Oxide Confined GaAs/AlGaAs Vertical Cavity Surface Emitting Lasers

By

KENG YEAM CHANG

A thesis submitted for the
degree of Doctor of Philosophy
at the University of Sheffield
Department of Electronic and Electrical Engineering

April 1999

Abstract

This thesis presents the design, fabrication, characterisation and theoretical modelling of oxide confined GaAs/AlGaAs VCSELs operating around 850nm wavelength. Three VCSEL structures utilising different oxide aperture thickness were designed. The oxide apertures contained in these VCSELs can be easily formed through the selective wet oxidation process. Detailed experimental investigations were performed on these devices with emphasis placed on the dependence of the resonant wavelength characteristics, the threshold and modal properties on the aperture size and oxide thickness. A feasibility study of polarisation control through using non-symmertical apertures was also carried out. These experimental activities were supplemented by theoretical modelling which included calculation of resonant wavelengths and eigenmode sizes using a scalar variational method that assumed Hermite-Gaussian transverse field variations. In addition, the light-current characteristics of the first two eigenmodes were also simulated by solving the photon and carrier rate equations, after their modal reflectance and transmittance had been calculated. The theoretical predictions were then compared with the experimental findings and ways of improving the model have also been suggested.

The oxide apertures in these VCSELs provides both current constriction and optical confinement. The resultant index guiding strength is dependent on the thickness as well as on the longitudinal position of the oxide. Devices with stronger guiding have smaller mode sizes which results in lower modal reflectance, larger blue shifts in resonant wavelengths from that of plane wave values, and larger wavelength separations between the fundamental mode and the higher order modes. Devices with smaller aperture sizes also have larger spectral separations and blue shift in resonant wavelengths. When the symmetry in aperture shape is broken, the wavelength degeneracy between the TEM_{10} and TEM_{01} mode is also broken. Among the three VCSEL structures, the one with the strongest guiding provides single mode operation at larger aperture size and is less affected by thermal lensing effects. However, lower threshold currents and higher efficiencies can be obtained from devices with weakest guiding. Despite being more susceptible to thermal lensing effects, single mode power up to 1.72mW and threshold current as low as 350μA can be obtained from devices with weakest guiding design.

Acknowledgements

I would like to thank my project supervisor, Dr. J.Woodhead, for offering me the opportunity to conduct a Ph.D. research study at Sheffield. The many stimulating and thought provoking discussions we have had, are certainly essential for developing my research skills.

I wish to express my utmost gratitude to Professor P.N.Robson for his valuable advice and guidance on the theoretical study carried out in this work. His kindness and warm encouragement throughout my study are greatly appreciated.

I would like to thank Dr. E.A.Khoo for sharing his skills and views on conducting useful experiments. My appreciation is also extended to Dr. C.K.Chia, Dr. P.J.Hor, Dr. K.F.Li, Dr. D.S.Ong, for their friendships and helpful advice. I am thankful to Dr. J.S.Roberts for supplying the VCSEL materials needed in this work, and Dr. J.P.R.David for his useful technical advice. The useful technical assistance from Dr. R.Airey and Dr.M.Steer are also appreciated. Acknowledgements are also extended to Dr. G.Hill and Dr. J.Clark for performing reactive ion etching on some of the devices used in this work. I must also acknowledge the professional technical support provided by Mr.P.Haines, Mr.A.Walker, Ms.S.Cross, Mr.J.E.Thompson and Mr. C.Harrisons. Last but not least, I would like to thank my tutor, Dr. G.J.Rees for his helpful advice.

Publications

Journal Papers :

1. K.Y.Chang, J.Woodhead and P.N.Robson, "Modal and Threshold Analysis of Dielectric Apertured Vertical Cavity Surface Emitting Lasers", Appl. Phys. Lett., vol.72, pp.335-337, 1998.

2. K.Y.Chang, J.Woodhead, J.Roberts and P.N.Robson, "Scalar Variational Method for eigenmode of Oxide-Confined Vertical Cavity Surface Emitting Lasers", (submitted to J. of Applied Physics, May 1999)

3. K.Y.Chang, J.Woodhead, J.Roberts and P.N.Robson, "Spectral Splitting of First Higher Order Modes in Rectangular Shape Oxide-Apertured Vertical Cavity Lasers", (submitted to Electron. Lett., June 1999)

4. K.Y.Chang, J.Woodhead, J.Roberts and P.N.Robson, "A Comparative Study on the Modal and Threshold Properties of Oxide-Confined Vertical Cavity Surface Emitting Lasers", (in preparation)

Conference/Workshop/Co-authored Papers :

1. K.Y.Chang, J.Woodhead and P.N.Robson, "Theoretical Analysis of Dielectric Apertured Vertical Cavity Surface Emitting Lasers", ESPRIT MEL-ARI Optoelectronics 1st Annual Workshop, OCT 1997, Swiss Federal Institute of Technology, Zurich.

2. MA.Al-Khafaji, H.Meidia, A.G.Cullis, K.Y.Chang, J.Woodhead, J.S.Roberts, " TEM Investigation of Wet oxidised AlAs in VCSEL Structures", Proceeding of 11th. Int. Conference on Microscopy of Semiconductor Materials, March 1999, Univ. of Oxford, U.K..

3. K.F.Li, D.S.Ong, J.P.R.David, R.C.Tozer, G.J.Rees, S.A.Plimmer, K.Y.Chang and J.S.Roberts, "Avanlanche Noise Characteristics of Thin GaAs Structures with Distributed Carrier Generation", (*submitted to IEEE Trans. Elec. Dev, Jan 99*)

4. C.Shearwood, C.Williams, R.Yates, P.Mellor, K.Y.Chang, J.Woodhead and C.Whitehouse, "Electro-magnetically levitated micro-discs", IEE Colloquium on Microengineering applications in optoelectronics, IEE Colloquium (Digest) n 96039, pp. 6/1-6/3, February 1996.

CONTENTS

Chapter 1 Introduction

Since its invention in 1979 [1], there have been intensive research efforts on Vertical Cavity Surface Emitting Laser (VCSEL) for applications in optical communication, optical recording, free space and fiber based optical interconnects, as well as short distance data links [2,3]. VCSELs are attractive for such wide ranging commercial interests because they offer surface normal, circularly symmetric and low divergence laser beams. This relaxes alignment tolerances in any optical system, and results in high direct fiber coupling efficiency without the need for expensive optics [2,4]. In addition, they can also be easily fabricated into densely packed two-dimensional arrays on a wafer scale, and the possibility of on-wafer testing and screening also makes them ideal for high volume, low cost mass production [5,6].

Over the past four years, the selective wet oxidation of AlAs and high Al composition $Al_xGa_{1-x}As$ layers ($x > 0.8$) has become a popular technique for producing the oxide apertures used for current constriction as well as providing optical confinement in both VCSELs [7-11] and edge emitting lasers [13,14]. The schematic of a typical top emitting VCSEL containing a single oxide aperture, which also applied for the VCSELs studied in this work, is shown in Figure 1.1. This technology has been utilized with such great success that a record breaking wall-plug efficiency of 57% [7] and single mode power of 4.8mW [8] has been achieved recently in 850nm GaAs based oxidized VCSELs. Significant reduction in threshold current down to a mere 9μA has also been achieved in the InGaAs based 980nm oxidized VCSELs [9]. In addition, ultra small working VCSELs with an aperture size down to about 0.5μm have also been successfully fabricated [10]. In fact, selectively oxidised VCSELs consistently exhibit lower threshold currents and voltages than the implanted VCSELs fabricated from the same wafer [11]. In addition, selective oxidation technology has also been used to fabricate low threshold current VCSELs incorporating high index contrast ratio $Al_xGa_{1-x}As/Al_xO_y$ Distributed Bragg Stacks (DBRs) which are more tolerant to variation in layer thickness [12]. This oxide technology has also been proposed for incorporation in $Al_xGa_{1-x}As$-based MESFET [15] and HBT [16] devices, fabrication of optical elements like micro-lenses[17] and optical waveguides [18], with varying degrees of success. Thus, just as the ease of formation of native silicon

oxide has made possible the existence of Si integrated circuit technology, the AlGaAs based oxide is making increasingly significant impact on optoelectronic devices even though various aspects of its formation are still under intensive research [19].

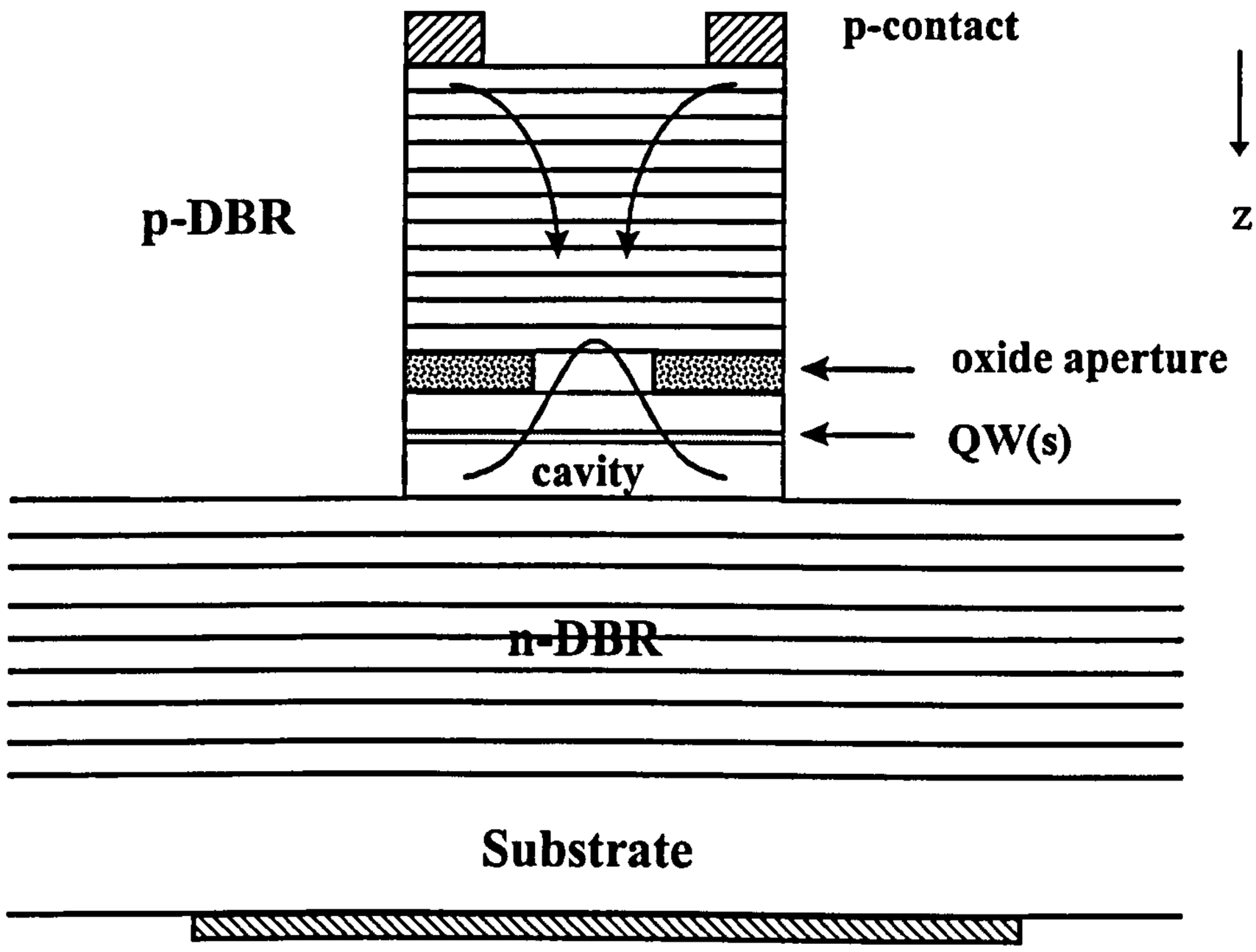

Figure 1.1 : Schematic of a typical oxide-confined top emitting VCSEL. The arrow shows the z-axis convention used in this thesis.

Presently, VCSELs with an emission wavelength of about 850nm are of great interest as transmitters for optical interconnections and short distance high speed data links [2,20]. The performance requirements for VCSELs in such applications are low threshold current, high power output single mode emission and a fixed predetermined polarisation orientation. While low threshold current is needed for low power consumption and ease of thermal management, a stable linearly polarised single mode light output is essential for achieving minimum relative intensity noise (RIN) and maximum bit error rates (BER) [21]. Because of the significant impact that the oxide aperture has on the VCSEL performance, there have also been intensive research efforts to provide qualitative models as well as quantitative numerical analysis [22-25], for explaining the mechanisms of mode confinement /selection and the aperture size dependent optical losses in this type of laser. Hence, in accordance with these

global aims, the main objective of this work is to evaluate the dependence of lasing performance of GaAs/AlGaAs VCSELs on the oxide aperture through theoretical simulations as well as experimental studies. By varying the thickness and position (with respect to an antinode of the optical standing wave) of the oxide aperture, three VCSEL layers with different index guiding strengths have been designed and studied in detail in this work. In addition, the effects of asymmetry in the aperture shape on the modal and polarisation characteristics are also examined.

The rest of this thesis is organised as follows, and is summarised in the flow chart in Fig. 1.2. Chapter 2 reviews the relevant background theory that is necessary for understanding the physics of VCSELs in particular and lasers in general. In Chapter 3, design assessments based on the theoretical predictions and experimental results obtained from the (plane wave) lasing performance of broad area VCSELs and broad area in-plane lasers made from VCSEL material are discussed. Next, the scalar variational method for analysing the frequency and mode size characteristics of the eigenmodes confined in the oxide apertured VCSELs is described in chapter 4. Comparisons between the theoretical and experimental results are also discussed in this chapter. This is followed by the purely theoretical chapter 5 which analyses the dependence of the modal reflectivities, photon lifetimes and threshold current densities, on the aperture sizes and shapes. Then, the experimental results on the lasing performance of the oxidised VCSELs studied in this work are presented in chapter 6. These experimental findings are also compared with the theoretical predictions calculated using the approaches described in chapter 5. Finally, the conclusions of this work are given in chapter 7, which also include recommendations for future work.

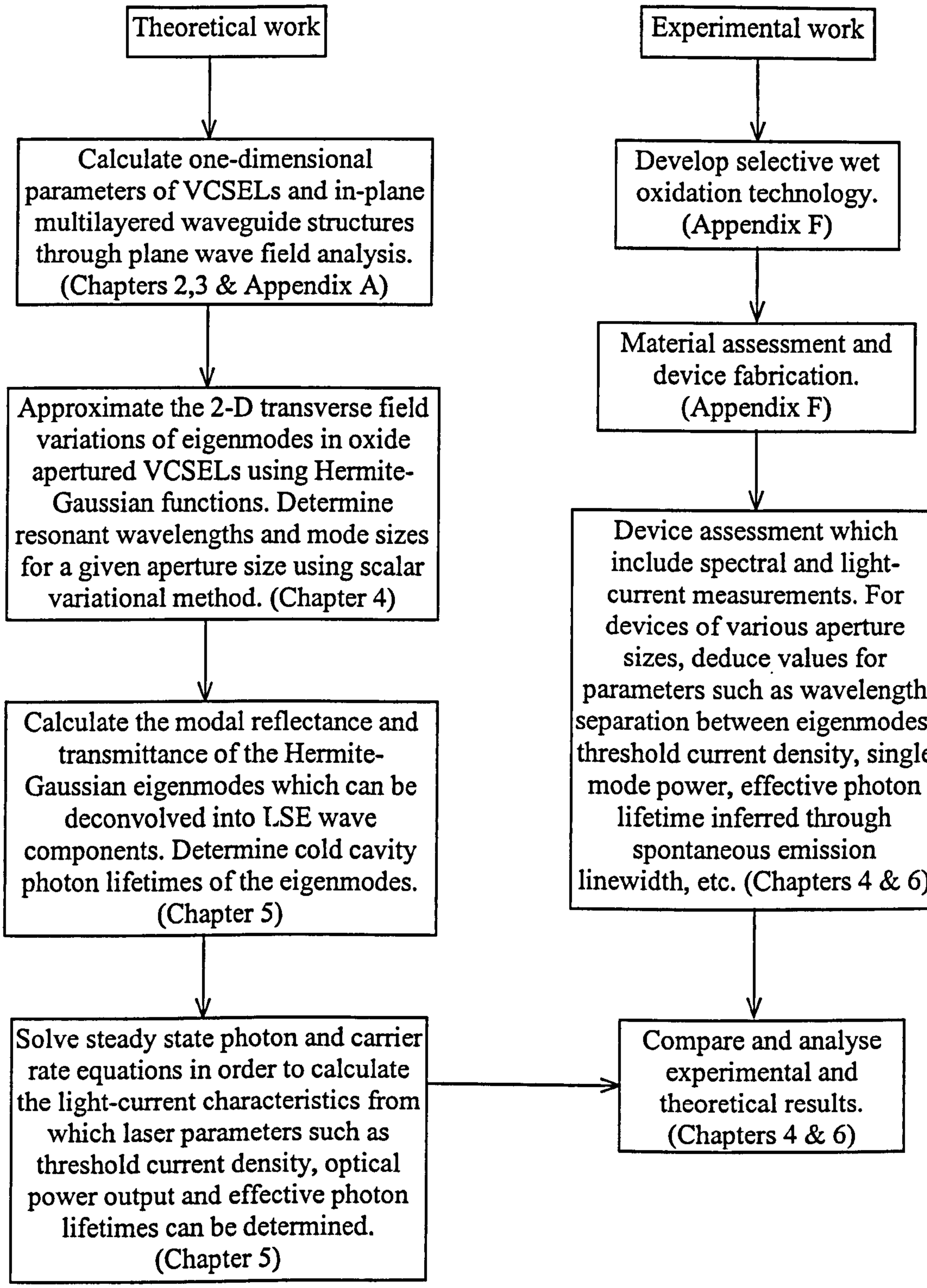

Figure 1.2 : Flow chart of the work carried out for this Ph.D. thesis.

References for Chapter 1

[1] H.Soda, K.Iga, C.Kitahara, and Y.Suematsu, "GaInAsP/InP surface emitting injection lasers", Jpn. J.Appl. Phys., vol.18, pp.2329-2330, 1979.

[2] K.J.Ebeling, U.Fiedler, R.Michalzik, G.Reiner and B.Weigl, "Recent advances in semiconductor vertical cavity lasers for optical communications and optical interconnects", Proc. of 22nd European Conference on Optical Communication, ECOC'96, TUC2.1, pp.81-83., 1996.

[3] T.E.Sale, "*Vertical cavity surface emitting lasers*",(Research Studies Press Ltd., England, 1995).

[4] K.Tai, G.Hasnain, J.D.Wynn, and A.Y.Cho, "90% coupling of top surface emitting GaAs/AlGaAs quantum well laser output into 8μm diameter core silica fibre", Electron. Lett., vol.26, pp.1628-1629, 1990.

[5] W.Yuen, G.S.Li and C.J.Chang-Hasnain, "Multiple wavelength vertical cavity surface emitting laser arrays with a record wavlength span", IEEE Photon. Technol. Lett., vol.8, pp.4-6, 1994.

[6] D.L.Hufaker, L.A.Graham, and D.G.Deppe, "Fabrication of high packing density vertical cavity surface emitting lasers using selective oxidation", IEEE Photon. Technol.Lett., vol.8, pp.596-598, 1996.

[7] R.Jager, M.Grabherr, C.Jung, R.Michalzik and K.J.Ebeling, "57% wallplug efficiency oxide-confined 850nm wavelength GaAs VCSELs", Electron. Lett., vol. 33, pp.330-331, 1997.

[8] C.Jung, R.Jager, M.Grabherr, R.Michalzik and K.J.Ebeling, "4.8mW single mode oxide confined top surface emitting vertical cavity laser diodes", Electron. Lett., vol.33, 1790-1791, 1997.

[9] G.M.Yang, M.H.MacDougal and P.D.Dapkus, "Ultralow threshold current vertical cavity surface emitting lasers obtained with selective oxidation", Electron. Lett., vol.31, pp.886-888, May 1995

[10] H.Deng, Q.Deng and D.G.Deppe, "Very small oxide-confined vertical cavity surface emitting lasers with a bulk active region", Appl. Phys. Lett., vol.70, pp. 741-743, 1997.

[11] K.D.Choquette, K.L.Lear, R.P.Schneider, and K.M.Geib, "Cavity characteristics of selectively oxidised vertical cavity lasers", Appl. Phys. Lett., vol.66, pp.3413-3415, 1995.

[12] M.H.MacDougal, G.M.Yang, A.E.Bond, C.K.Lin, D.Tishinin and P.Daniel Dapkus, "Electrically pumped vertical cavity lasers with Al_xO_y-GaAs reflectors", IEEE Photon. Technol. Lett., vol.8, pp.310-312, Mar 1996.

[13] J.M.Dallesasse and N.Holonyak Jr, "Native oxide stripe geometry $Al_xGa_{1-x}As$-GaAs quantum well heterostructure lasers", Appl. Phys. Lett., vol.58, pp. 394-396, Jan 1991.

[14] J.J.Wierer, P.W.Evans and N.Holonyak Jr., "Buried tunnel contact junction AlGaAs-GaAs-InGaAs quantum well heterostructure lasers with oxide-defined lateral currents", Appl. Phys. Lett., vol.71, pp. 2286-2288, Oct 1997.

[15] A.E.Bond, C.K.Lin, M.H.MacDougal, P.D.Dapkus and R.Nottenburg, "Backgating reduction in MESFETs using an AlAs native oxide buffer layer", Electron. Lett., vol.32, pp.2271-2273, Nov. 1996.

[16] A.Massengale, M.C.Larson., C.Dai and J.S.Harris Jr, "Collector-up AlGaAs/GaAS heterojunction bipolar transistors using oxidised AlAs for current confinement", Electron. Lett., vol.32, pp.399-401, Feb 1996

[17] O.Blum, K.L.Lear, H.Q.Hoi and M.E.Warren, "Buried refractive microlenses formed by selective oxidation of AlGaAs", Electron. Lett., vol. 32, pp.1407-1409, July 1996.

[18] A.Fiore, V.Berger, E.Rosencher, N.Laurent and J.Nagle, "Huge birefringence in selectively oxidized GaAs/AlAs optical waveguides", Appl. Phys. Lett., vol.68, pp.1320-1322, Mar 1996.

[19] K.D.Choquette, K.M.Geib, C.I.H.Ashby, "Advances in selective wet oxidation of AlGaAs Alloys", IEEE Journal of Selected Topics in Quantum Electronics, vol.3, pp.916-926, June 1997

[20] EU ESPRIT RODCI Project Work Plan for 1997-1998.

[21] D.V.Kuksenkov, H.Temkin and S.Swirhun, "Polarisation instability and relative intensity noise in vertical cavity surface emitting lasers", Appl. Phys. Lett., vol.67, pp.2141, 2143, vol.67, 1995.

[22] E.R.Hegblom, D.I.Babic, B.J.Thibeault, and L.A.Coldren, "Scattering losses from dielectric apertures in vertical cavity lasers", IEEE J. of Selected Topics in Quantum Electronics, vol.3, pp.379-389, April. 1997.

[23] H.K.Bissessur, F.Koyama and K.Iga, "Modelling of oxide-confined vertical cavity surface emitting lasers", IEEE J. of selected topics in Quantum Electronics, vol.3, pp.344-352, April 1997.

[24] G.R.Hadley, K.L.Lear, M.E.Warren , K.D.Choquette, J.W.Scott and S.W.Corzine, "Comprehensive numerical modeling of vertical cavity surface emitting lasers", IEEE J. of Quantum Electronics, vol. 32, pp.607-616, April 1996.

[25] K.Y.Chang, J.Woodhead and P.N.Robson, "Modal and threshold analysis of dielectric aperture vertical cavity surface emitting lasers", Appl. Phys. Lett., vol.72, pp.335-337, 1998.

Chapter 2 VCSEL Background Theory

2.1 Introduction

This chapter is intended to provide some of the basic background in laser physics needed for Vertical Cavity Surface Emitting Lasers (VCSELs). Firstly, Maxwell's equations which are indispensable for electromagnetic analysis of VCSEL properties are noted. The transfer matrix method is then introduced as a versatile mathematical tool needed for the simulation of electromagnetic wave propagation inside a VCSEL cavity. This is followed by a revision of some basic laser formulae. Finally, the numerical method for analyzing multilayered planar waveguide using the transverse wave admittance is also discussed. This is relevant since some useful parameters can be determined from in-plane lasers that are made from VCSEL material.

2.2 Maxwell's Equations and Wave Equations

Electric and Magnetic fields that vary with time are governed by physical laws described by a set of first order differential equations known collectively as Maxwell's equations. For linear, isotropic and homogeneous medium, these equations in the so-called time implicit form ($e^{j\omega t}$ dependece) are [1][2]

$$\nabla \times \mathbf{E} = -j\omega\mu\mathbf{H} \tag{2.1}$$

$$\nabla \times \mathbf{H} = \mathbf{J} + j\omega\varepsilon\mathbf{E} \tag{2.2}$$

$$\nabla \cdot \mathbf{E} = \frac{\rho}{\varepsilon} \tag{2.3}$$

$$\nabla \cdot \mathbf{H} = 0 \tag{2.4}$$

where **E** and **H** are the space vector complex phasors of the time harmonic fields, carrying information of magnitude and phase on the corresponding fields. ω ($=2\pi f$ where f is oscillation frequency of the fields) is the angular frequency; ε and μ are the permittivity and permeability respectively of the medium traversed by the wave, **J** is

the total current density vector and ρ is the charge density. These equations are complemented by the so-called constitutive relations that describe the relationship between the field and flux densities. They are given by

$$\mathbf{D} = \varepsilon\mathbf{E} \tag{2.5}$$

$$\mathbf{B} = \mu\mathbf{H} \tag{2.6}$$

$$\mathbf{J} = \mathbf{J}_s + \sigma\mathbf{E} \tag{2.7}$$

where σ is the conductivity of medium, $\mathbf{J}_s$ is the source current density vector, **D** and **B** are the vector electric and magnetic flux densities respectively.

In order to derive a single equation for **E** from Maxwell's equations for a source free region, one has to take the curl of equation (2.1). Then, using the well known vector identity $\nabla \times (\nabla \times \mathbf{F}) = \nabla(\nabla \cdot \mathbf{F}) - \nabla^2\mathbf{F}$, plus the relations in (2.2) and (2.7), the time independent *vector wave equation* (or *Helmholtz equation*) for the electric field is obtained as

$$\nabla^2\mathbf{E} + k^2\mathbf{E} = 0 \tag{2.8}$$

where k is known as the wave number. In a source free medium where ε and μ are spatially constant, it is given by

$$k^2 = \omega^2\mu\varepsilon \tag{2.9}$$

A similar equation exists for the magnetic field, and can be written in the form as (2.8) by replacing **E** with **H**. Most semiconductor material has a very weak magnetic response and thus $\mu \cong \mu_0$ (i.e. = permeability of free space). However, its permittivity ε is complex if it is absorptive [3,4]. Hence, in this case the wave number is also complex and is related to the complex refractive index N by

$$k = \omega\sqrt{\mu_0\varepsilon_0\varepsilon_r} = k_0\sqrt{\varepsilon_r} = k_0 N \tag{2.10}$$

$$\text{where } k_0 = \omega\sqrt{\mu_0\varepsilon_0} = \frac{\omega}{c} = \frac{2\pi}{\lambda_0} \tag{2.11}$$

is the wave number in free space; ε_r is the complex relative permittivity, λ_0 and c are the free space wavelength and velocity respectively. The complex refractive index N is related to the absorption loss by

$$N = \sqrt{\varepsilon_r} = n - jk_{ext} = n - j\left(\frac{\alpha}{2k_0}\right) \tag{2.12}$$

where n is the real refractive index, k_{ext} is the so-called field extinction coefficient, and α is the power absorption coefficient in per unit length.

For undoped intrinsic semiconductors, the main source of absorption loss is due to interband absorption when incident photons with energy above the bandgap energy are attenuated. If the material is doped through impurity doping, then free carrier absorptions and/or band-tail absorption can also attenuate waves with photon energies below the bandgap. In the gain medium of lasers such as quantum wells (QWs) in VCSELs, where the injected carriers recombine radiatively to produce stimulated emission, α becomes zero when the injected carrier density reaches the transparency value i.e. the onset of population inversion. Above transparency, optical gain becomes available and the complex refractive index of the gain medium can still be expressed in the form of (2.12) by allowing $\alpha = -g$ where g is the power gain coefficient in per unit length.

In equation (2.8), the vector fields **E** and **H** can be separated into three scalar field components in rectangular coordinates. Thus, this give rise to a set of *scalar wave equations* which for each component of electric field is given by

$$\nabla^2 E_i + k^2 E_i = 0 \qquad (2.13)$$

where E_i can be either E_x, E_y or E_z and is now a scalar phasor. Again, a similar form of this equation exists for the magnetic field and can be obtained by replacing E_i with H_i.

2.3 Electromagnetic Waves and Transfer Matrices

In an unbounded medium, the simplest solution to the vector wave equation (2.8) is the plane wave solution whose complex wave function can be written in rectangular co-ordinates as

$$\Psi(x,y,z) = \Psi(\mathbf{r}) = A\exp(\pm j\mathbf{k}\cdot\mathbf{r}) = A\exp\left[\pm j\left(k_x x + k_y y + k_z z\right)\right] \qquad (2.14)$$

where $\Psi(x,y,z)$ or $\Psi(\mathbf{r})$ is the vector wave function for **E** or **H**, A is a complex constant. The wave propagation vector, **k** is equivalent to $\mathbf{k} = k_x\hat{x} + k_y\hat{y} + k_z\hat{z}$ where k_x, k_y and k_z are the phase constants in their respective directions. The vector **r** gives the direction and traveled distance of the waves and can be written as $\mathbf{r} = x\hat{x} + y\hat{y} + z\hat{z}$. For equation (2.14) to satisfy the vector wave equation (2.8), the following must hold :

$$k^2 = k_x^2 + k_y^2 + k_z^2 \qquad (2.15)$$

These types of waves are called plane waves because the phase front where the field amplitude is constant (or **k.r** = constant) is a plane. Although they are the most fundamental type of waves allowed by the wave equation, the guided modes in many types of the waveguides can be viewed as being made up by superposition of a number of such plane waves.

A plane wave approaching a planar dielectric discontinuity plane between two homogenous media (with real or complex ε) can be considered as a TE, TM or TEM wave, depending on the incident angle as well as the polarisation direction of the fields. Referring to Figure 2.1, assume that the dielectric discontinuity boundaries are along the x-y plane, and the directions of the incident plane waves are such that there is no field variation in the x-direction i.e. $\partial / \partial x = 0$ and $k_x = 0$. The definitions of these waves (which can be deduced from the Maxwell curl equations) are :-

(i) Transverse Electromagnetic (TEM, to z) waves which are incident normally upon the discontinuity. Their scalar E or H fields components lie entirely parallel to the boundary and have zero normal field components i.e. $E_z = 0$, $H_z = 0$. Following Fig. 2.1(a), the tangential component pairs available are E_x and H_y

(ii) Transverse Electric (TE, to z) waves which are plane waves incident upon the normal of the interface at an oblique angle. In this case $E_z = 0$ but H_z is finite. Following Fig. 2.1(b), the other two tangential field components are E_x and H_y.

(iii) Transverse Magnetic (TM, to z) waves which are also oblique incident plane wave but with finite E_z and $H_z = 0$. According to Fig. 2.1(c), the other two scalar tangential field components are H_x and E_y.

From (2.14), the general wave functions for these two-dimensional waves are given by

$$\Psi(y,z) = A \exp(-jk_y y)\exp(-j\beta z) \qquad (2.16)$$

where the phase constant in the z-direction is given a new symbol β to indicate the direction normal to the discontinuity plane i.e. x-y plane. It is given by

$$\beta = k \qquad \text{for } (TEM)_z \text{ wave since } k_y = 0; \qquad (2.17\ a)$$

$$= \sqrt{k^2 - k_y^2} \qquad \text{for } (TE)_z \text{ and } (TM)_z \text{ waves} \qquad (2.17\ b)$$

as can be deduced from (2.15). For VCSEL which contains many such boundaries, the z-axis is often called the longitudinal axis since it is perpendicular to the reflecting

mirrors and β is called the propagation constants of the guided modes. The x-y directions are usually collectively known as transverse or lateral directions.

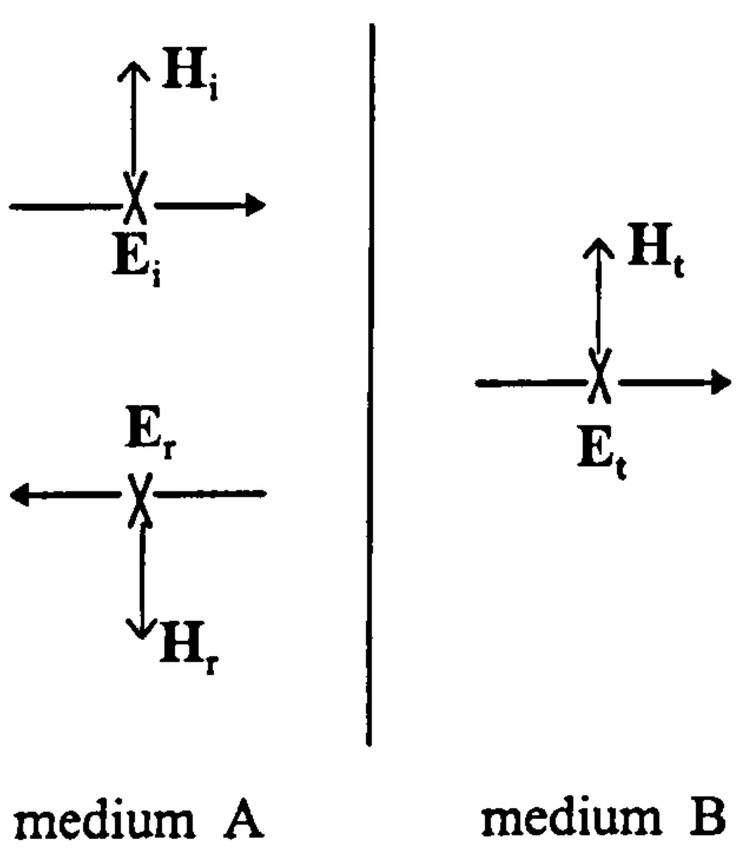

(a) TEM to z wave

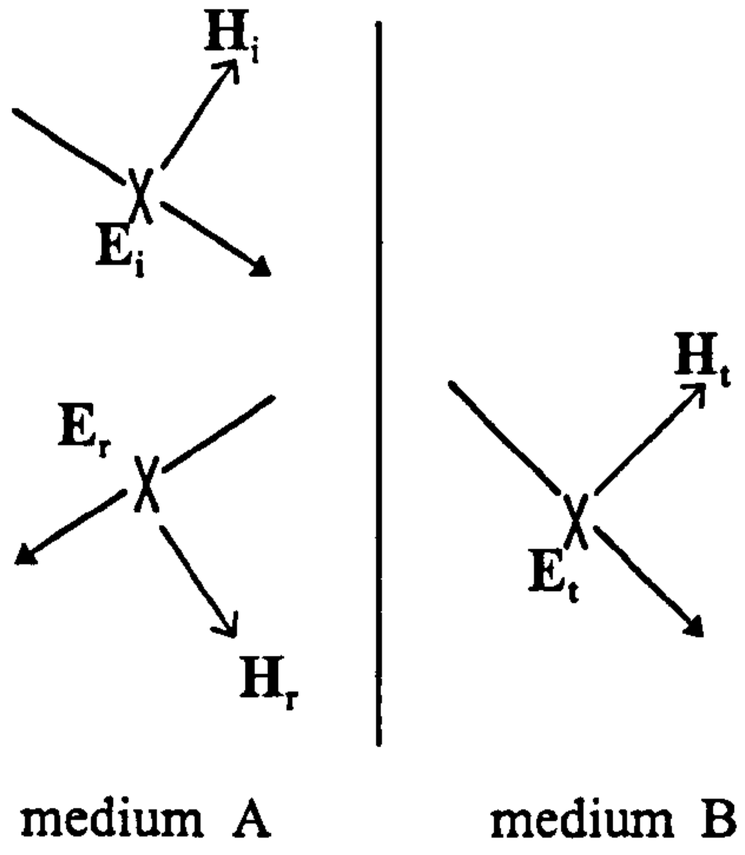

(b) TE to z wave

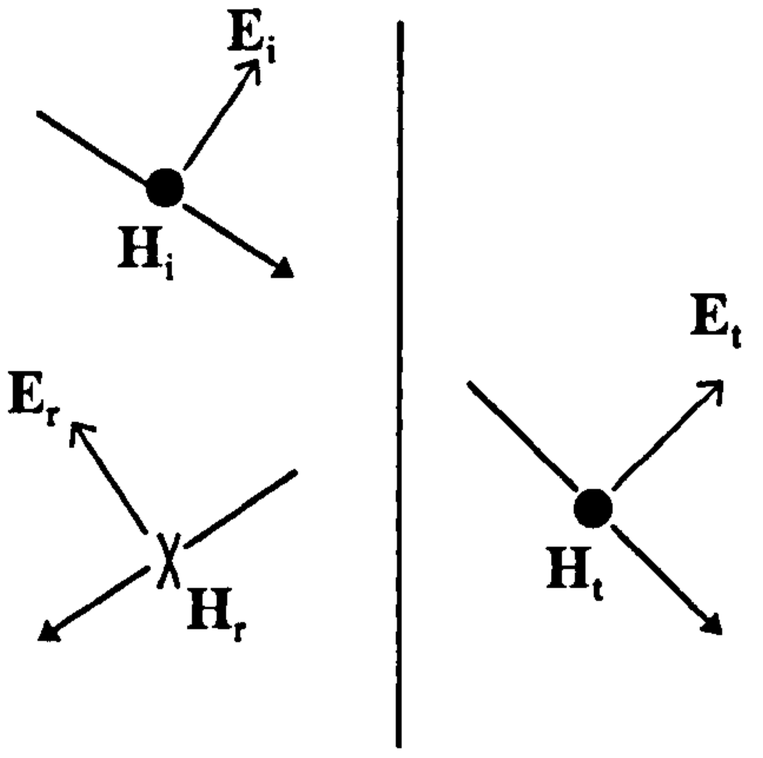

(c) TM to z wave

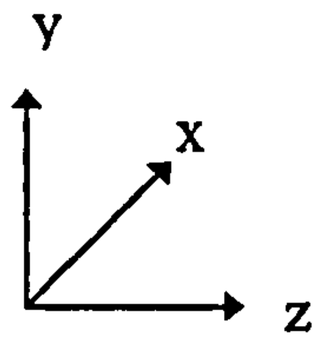

(d) coordinate systems

Figure 2.1 : Classifications of waves (2D) incident on a dielectric discontinuity, together with the definitions of the coordinate systems. The subscripts " i ", " t " and " r " denote the incident, transmitted and reflected waves respectively. The symbol (X) represents direction into the paper i.e. positive x-direction while the symbol (•) represents otherwise.

2.3.1 Formulations of Transfer Matrix Method

When plane waves are incident upon a plane of dielectric discontinuity between two homogenous media, their energy is partly reflected from or transmitted

through the interface. The Distributed Bragg Reflector (DBR) is a wavelength dependent reflector made up by a number of such discontinuities between homogeneous media. It usually consists of an assembly of dielectric thin layers with alternating refractive indices. It is the combined effects of all the discontinuities on the incident waves that give rise to the unique reflection and transmission properties of the DBR. Before the power reflectance from and transmittance through a dielectric thin layer or an assembly of thin layers like DBR can be calculated, the relations between the field amplitudes at each individual boundary are needed. These relations can be readily obtained from applying the boundary condition at the interfaces involved. The boundary condition at the interface between two dissimilar dielectric materials requires that the tangential components of **E** and **H** are continuous across it. In the following derivations which are generalized for TEM, TE and TM waves, the complex amplitude of the tangential field components are simply denoted as E and H with specific subscripts and/or superscripts to indicate their origins.

Firstly, consider layer 1 of the multilayered structure shown in Figure 2.2 existing from $z = 0$ to $z = d_1$ (where the z-axis is the vertical direction shown in the VCSEL schematic in Fig. 1.1). The summation of the fields within this layer at the boundary $z = 0$ is given by

$$E_0 = E_0^+ + E_0^- \tag{2.18}$$

$$H_0 = H_0^+ - H_0^- = Y_1\left(E_0^+ - E_0^-\right) \tag{2.19}$$

where E_0^+ and H_0^+ are the positive-going (in +z direction) resultant wave amplitudes, E_0^- and H_0^- are the negative-going (in -z direction) resultant wave amplitudes, and Y_1 is the characteristic wave admittance of layer 1. Dielectric media present different values of admittance to TEM, TE and TM waves and the derivations of these admittance values are detailed in ***Appendix A***. The fields at boundary 1 can be determined by altering the phase factor of the waves to allow for a shift in the z-coordinate from 0 to $+d_1$. The resultant tangential fields within the layer at boundary $z = d_1$ are thus given by

$$E_1 = E_1^+ + E_1^- = E_0^+ \exp(-j\beta_1 d_1) + E_0^- \exp(+j\beta_1 d_1) \tag{2.20}$$

$$H_1 = H_1^+ - H_1^- = Y_1\left[E_0^+ \exp(-j\beta_1 d_1) - E_0^- \exp(+j\beta_1 d_1)\right] \tag{2.21}$$

After some manipulations using equations (2.18) to (2.21), the following "transfer" equations are obtained :

$$E_0 = E_1\cos(\beta_1 d_1) + H_1 \frac{j\sin(\beta_1 d_1)}{Y_1} \tag{2.22}$$

$$H_0 = jY_1 E_1 \sin(\beta_1 d_1) + H_1\cos(\beta_1 d_1) \tag{2.23}$$

Together, equations (2.22) and (2.23) can be written in a matrix notation as

$$\begin{bmatrix} E_0 \\ H_0 \end{bmatrix} = \begin{bmatrix} \cos(\beta_1 d_1) & j\sin(\beta_1 d_1)/Y_1 \\ jY_1\sin(\beta_1 d_1) & \cos(\beta_1 d_1) \end{bmatrix} \begin{bmatrix} E_1 \\ H_1 \end{bmatrix} \tag{2.24}$$

The 2x2 matrix on the right hand side of (2.24) is usually called the "characteristic matrix" or "transfer matrix" of layer 1.

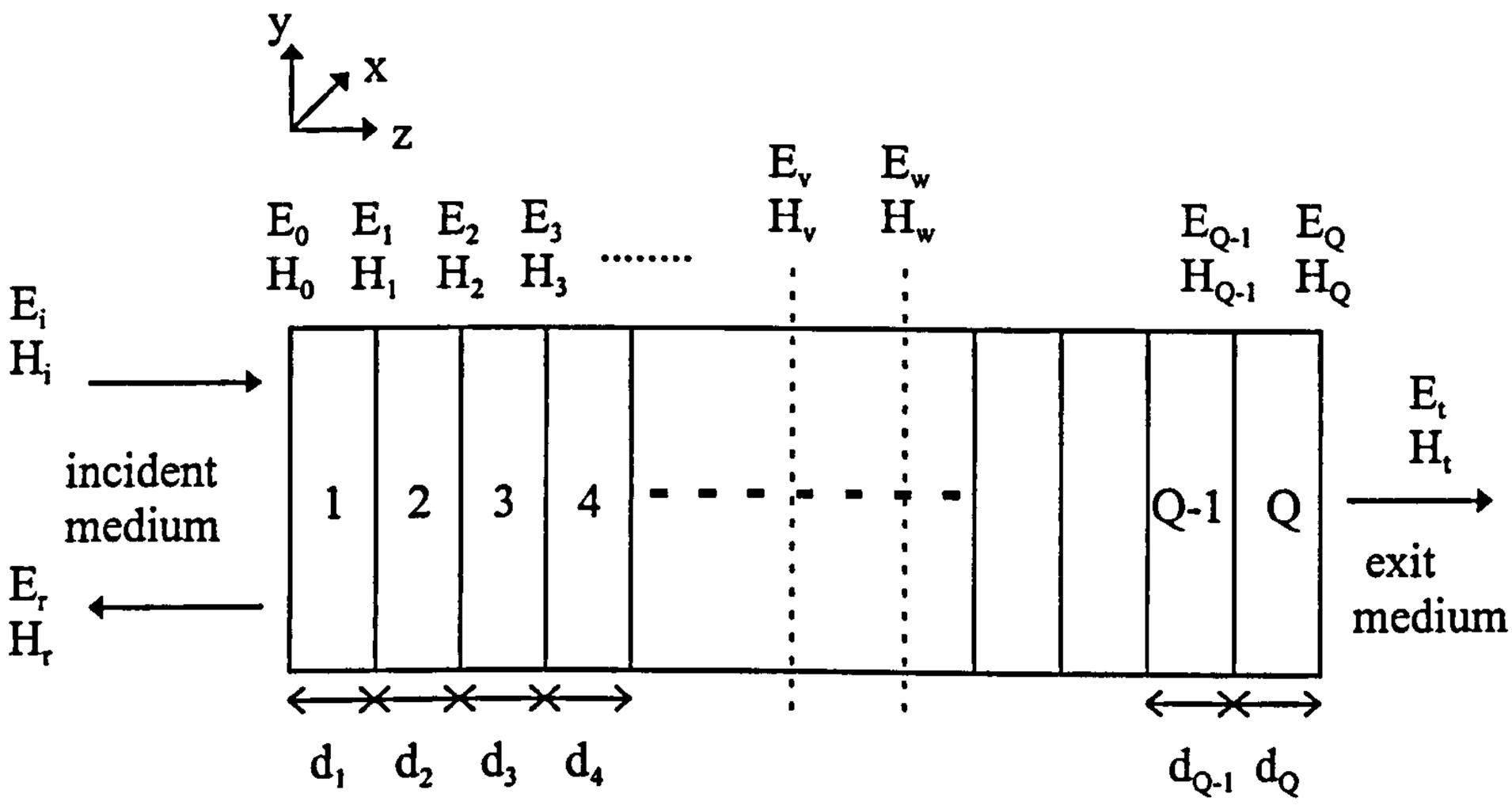

Figure 2.2 : Tangential electric and magnetic field components of a multilayer structure made up by Q number of dielectric layers.

In order to obtain the relation between the fields at the entrance boundary 0 and exit boundary Q, the boundary conditions are then applied repeatedly at the rest of the interfaces between the layers shown in Fig. 2.2. The resultant characteristic matrix for the assembly of the stacks is then given by

$$\begin{bmatrix} E_0 \\ H_0 \end{bmatrix} = \left(\prod_{q=1}^{Q} \begin{bmatrix} \cos(\beta_q d_q) & j\sin(\beta_q d_q)/Y_q \\ jY_q\sin(\beta_q d_q) & \cos(\beta_q d_q) \end{bmatrix} \right) \begin{bmatrix} E_Q \\ H_Q \end{bmatrix} \tag{2.25}$$

which is simply the product of the characteristic matrix of each constituent layer q with thickness d_q, admittance Y_q and propagation constant β_q, taken in the correct order i.e. layer 1 is the closest layer to the incident medium and layer Q is the next to the exit medium. In the exit medium, since there are only transmitted fields (E_t, H_t) but no reflected fields, the continuity condition thus ensures that $E_t = E_Q$ and $H_t = H_Q$.

The (2x2) matrix of equation (2.25) can then be reduced to just involving refractive indices as in

$$\begin{bmatrix} E_0 / E_t \\ H_0 / E_t Y_0 \end{bmatrix} = \left(\prod_{q=1}^{Q} \begin{bmatrix} \cos(\beta_q d_q) & j\sin(\beta_q d_q) / Y_q \\ jY_q \sin(\beta_q d_q) & \cos(\beta_q d_q) \end{bmatrix} \right) \begin{bmatrix} 1 \\ Y_s \end{bmatrix} = \begin{bmatrix} B \\ C \end{bmatrix} \qquad (2.26)$$

where as defined in Appendix A, Y (in *italic Arial* font) is the wave admittance normalised with respect to the TEM wave admittance in free space Y_0 i.e. $Y = Y / Y_0 = N$. Thus, Y_s and Y_q are the normalised admittance of the exit medium/substrate and layer-q respectively. Note that the symbols B and C are assigned to the elements of the resultant (2x1) matrix. Using the similar definition of characteristic admittance for the constituent layers, the input admittance of the whole assembly of stacks, Y_M , can then be determined by

$$Y_M = \frac{H_0}{E_0} = Y_M Y_0 = \frac{C}{B} Y_0 \qquad (2.27)$$

where Y_M is the normalized input admittance of the assembly given by the ratio C/B.

2.3.2 Reflectance, Transmittance, Absorptance and Resonant Wavelength

Referring to Fig. 2.2, the resultant field amplitudes at the entrance boundary 0 are also related to that of incident field (E_i , H_i) and reflected fields (E_r , H_r). These relations are governed by

$$E_0 = E_i + E_r = E_i(1+r) \qquad (2.28)$$

$$H_0 = H_i - H_r = Y_i E_i(1-r) \qquad (2.29)$$

where Y_i is the admittance of the incident medium. Using equations (2.27) through (2.29), the field reflection coefficient r which is defined as the ratio of the reflected field amplitude to the incident field amplitude can be obtained by

$$r = \frac{E_r}{E_i} = \frac{Y_i - Y_M}{Y_i + Y_M} = \frac{Y_i - Y_M}{Y_i + Y_M} \qquad (2.30)$$

On the other hand, the field transmission coefficient, t , is defined as the ratio of the transmitted field amplitude to the incident field amplitude. As can be deduced from (2.26) and (2.30), t is given by

$$t = \frac{1+r}{B} \qquad (2.31)$$

Electromagnetic waves carry energy along when they propagate through a medium. For time harmonic waves, the time averaged power per unit area, P (also called Intensity), carried by the fields is given by [1]

$$P = \frac{1}{2}\,\mathrm{Re}(\mathrm{EH}^*) = \frac{1}{2}\mathrm{Re}(\mathrm{Y})\,\mathrm{EE}^* \qquad (2.32)$$

where E and H are complex amplitudes of the orthogonal scalar fields. The direction of the vector **E** x **H** which is known as Poynting vector, gives the direction of the power flow. The reflectance, R, which is defined as the ratio of the total reflected power (P_r) to the total incident power (P_i) is simply given by

$$\mathrm{R} = \frac{\mathrm{P_r}}{\mathrm{P_i}} = r\,r^* \qquad (2.33)$$

for these plane waves. The transmittance, T, which is defined as the ratio of the total power transmitted (P_T) through the multilayer stacks into the exit medium (or substrate) to the total incident power, can be calculated using

$$\mathrm{T} = \frac{\mathrm{P_T}}{\mathrm{P_i}} = \frac{\mathrm{Re}(Y_s)}{\mathrm{Re}(Y_i)}\,t\,t^* \qquad (2.34)$$

Usually, part of the incident power will be attenuated by the doped constituent semiconductor layers making up the DBR. Thus, the absorptance A which gives the fraction of the incident power absorbed in the assembly of stacks is given by

$$\mathrm{A} = 1 - \mathrm{R} - \mathrm{T} \qquad (2.35)$$

as a direct result of conservation of power.

While designing a VCSEL structure, it is very important to ensure that its cavity resonant wavelength closely matches the gain peak wavelength of the gain medium (usually quantum wells) in order to achieve low threshold gain. In analogy with the classical Fabry Perot interferometer theory, the passive cavity resonant wavelength of a properly designed VCSEL can be readily identified from the sharp, narrow "resonant dip" which appears in the high reflectance region of the calculated or measured reflectivity spectrum (or equivalently as the transmission peak in the transmission spectrum). This calculated reflectivity spectrum is thus useful in material assessment since it allows comparison of features present in the experimental spectrum obtained through Photo-Reflectance (PR) measurement with the theoretical predictions.

2.3.3 Electromagnetic Standing Wave, Confinement Factor and Plane Wave (1-D) Threshold Gain

In a multilayer structure like a VCSEL (refer to Fig. 2.1), an electromagnetic standing wave is formed within the whole structure due to the superposition of the forward-going and backward-going traveling waves within each constituent layer. From the design viewpoint, it is useful to compute the spatial variation of the standing wave since it provides information on regions within the VCSEL where the field amplitudes are high and thus heavy doping must be avoided to prevent absorption. The gain medium should also be positioned to centre on the antinode of the standing wave in the cavity to enhance the available stimulated gain. As will also be shown in chapters 4 and 5, the relative position of the oxide aperture with respect to an antinode or node of the standing wave in a selectively oxidised VCSEL will determine the transverse waveguiding strength (index guiding) as well as the amount of the aperture size dependent optical loss suffered by the device.

Referring to Fig. 2.2 again, the amplitude of the electric field E_v at an arbitrary position v, can be easily computed by slightly modifying (2.26) into the form of

$$\begin{bmatrix} E_v / E_t \\ H_v / Y_0 E_t \end{bmatrix} = [M_v] \begin{bmatrix} 1 \\ Y_s \end{bmatrix} = \begin{bmatrix} B_v \\ C_v \end{bmatrix} \tag{2.36}$$

where M_v is the product of the characteristic matrices taken from the exit medium up to position v. Then, the normalized squared magnitude of the electric field can be easily computed from $|B_v|^2$ (with respect to the transmitted field), $|tB_v|^2$ (with respect to incident field) or $|tB_v / r|^2$ (with respect to reflected field). It is also possible to calculate the absorption loss (A_{vw}) suffered between any two positions of interest, say positions v and w, as a fraction of the incident power. This simply involves calculating the difference in the normalized field intensity (with respect to incident field) at these positions as given by

$$A_{vw} = \frac{P_v}{P_i} - \frac{P_w}{P_i} = (tB_v)\left(tB_v^*\right)\frac{\mathrm{Re}(Y_v)}{\mathrm{Re}(Y_i)} - (tB_w)\left(tB_w^*\right)\frac{\mathrm{Re}(Y_w)}{\mathrm{Re}(Y_i)} \tag{2.37}$$

where B_w is the matrix element (1,1) of the resultant (2x1) product matrix calculated up to position w.

Since the threshold gains of VCSELs are highly dependent on the thickness as well as the relative position of the gain medium within the spatial field distribution, it is useful to define a figure of merit which measures the "effectiveness" of the gain

medium. This usually appears as the so called *optical confinement factor*, Γ, which is the ratio of the integral of the electric field magnitude squared within the gain region of thickness d to that within the whole laser structure over the 3D space [5],

$$\Gamma = \frac{\iiint_{\text{gain rmedium}} |E|^2 (x,y,z)\, dxdydz}{\iiint_{\text{whole structure}} |E|^2 (x,y,z)\, dxdydz} = \Gamma_{xy}\Gamma_z = \Gamma_x\Gamma_y\Gamma_z \qquad (2.38)$$

where the ratio in the longitudinal z-direction (w.r.t the definitions in Fig. 2.1), Γ_z, is usually called the longitudinal confinement factor for a VCSEL, and the combined product ratio in the x-y direction (i.e. $\Gamma_{xy} = \Gamma_x\Gamma_y$) is often known as the transverse confinement factor. Using the transfer matrix method for plane waves described above, Γ_z can be calculated by simply dividing the sum of the area of the squared electric field magnitude standing wave distribution within the gain region by the sum of the area over the whole structure. As will be discussed in section (2.5), the transverse confinement factor for stripe lasers can be calculated in similar fashion.

Using the transfer matrix method discussed in preceding sections, it is possible to calculate the plane wave (1-D) threshold gain of a VCSEL numerically with great accuracy. A laser is said to have achieved self oscillation (i.e. lasing) when the "internal" gain provided by the gain medium is sufficient to balance the net loss. Referring to Fig. 2.2 again, this implies that the amplitude of the incident field E_i is zero and this occurs only when the QW(s) have finite gain rather than absorption. Consequently, it can be deduced from (2.30) that the oscillation threshold is : -

$$Y_M = -Y_i \quad \text{or} \quad Y_M = -Y_i \qquad (2.39)$$

i.e. the (complex) admittance are matched at the incident boundary. In actual fact, this impedance matching condition is also met at any other boundaries along the structure. The computation of the threshold gain then simply involves varying the wavelength and material gain of the QW(s) until the condition specified in (2.39) is fulfilled for the real and imaginary parts. This procedure will thus yield the plane wave (1-D) threshold gain g_{th} as well as the lasing wavelength. The latter is almost identical to the passive cavity resonant wavelength determined in sub-section 2.3.2. Compared to the analytical formulae that will be discussed in section 2.4, this numerical method has the advantage that it is exact and there is no need to estimate the longitudinal optical confinement factor through the approximation of the so called effective cavity length

[6]. It also correctly takes into account the possible absorption within the cavity and the DBRs.

2.4 Basic Laser Formulae

Although the numerical approach of using the transfer matrix method discussed in preceding sections is precise, it is useful to examine some analytical laser formulae that can reveal the significance of relevant parameters affecting the laser performance in a more explicit manner.

2.4.1 Threshold and Resonance Conditions

A laser is said to reach its threshold when the gain provided by the active medium compensates all the propagation and mirror transmission losses so that the magnitude and phase of the electric field of the cavity resonant mode(s) is/are conserved after one round trip in the cavity. The need to conserve magnitude (or stored energy inside the cavity) gives rise to the threshold gain condition and the requirement on phase constitutes the resonance condition. This can then be expressed as [4]

$$r_f r_b \exp(-j2\beta_c L_c) = 1 \tag{2.40}$$

where r_f and r_b are the field reflection coefficients of the front and back mirrors, L_c is the cavity length. β_c is the complex propagation constant inside the cavity region and is given by

$$\beta_c = k_c + j\left(\frac{\Gamma g_{th} - \alpha_C}{2}\right) \tag{2.41}$$

where k_c is the real part of the complex propagation constant , Γ is the confinement factor. The terms expressed in power coefficients per unit length, g_{th} and α_c, are the threshold gain provided by the gain medium and the average internal loss of the cavity respectively. Then by equating the real and imaginary parts of (2.40), the threshold and phase conservation conditions can be obtained. The threshold condition is given by

$$\Gamma g_{th} = \alpha_c + \alpha_m = \alpha_c + \frac{1}{2L_c}\ln\left(\frac{1}{R_f R_b}\right) \tag{2.42}$$

where R_f and R_b ($R = |r|^2$) are the reflectance of the front and back mirrors, and α_m represents the total mirror loss in per unit length. The product Γg_{th} is also usually referred to as modal threshold gain. This equation implies that in order to achieve low threshold gain, the total optical loss i.e.($\alpha_c + \alpha_m$), has to be minimised and the confinement factor must be maximised. Meanwhile, the phase conservation leads to

$$\exp[\, j(-2k_c L_c + \phi_f + \phi_b)] = 1 \qquad (2.43)$$

where ϕ_f and ϕ_b are the phase shift on reflection from the front and back mirrors as deduced from $r = |r|\, e^{j\phi}$. Rearranging, (2.43) leads to the resonance condition for modal resonant wavelength

$$\frac{2\pi n_c}{\lambda_0} L_c - \frac{(\phi_f + \phi_b)}{2} = m\pi \qquad (2.44)$$

where n_c is the real refractive index of the cavity medium and m is an integer number.

Although the threshold and resonance formulae given by (2.42) and (2.44) are generally applicable to both VCSELs and in-plane stripe lasers, the implications of certain parameters are actually different for the two types of laser. For most in-plane stripe lasers, except for multi-section lasers, the gain lengths are equivalent to the cavity lengths between the cleaved mirrors. Hence, the longitudinal (i.e. direction normal to the mirror planes) confinement factor is unity for all the guided modes, although the transverse and lateral confinement factors have to be calculated numerically or by using analytical solutions available for simpler structures [4]. In VCSELs, thin quantum wells that make up the gain media are usually placed at or close to the antinode of the optical standing wave formed in the longitudinal direction normal to the plane of the DBRs. Since the standing wave actually extends into the DBRs (as will be shown in Chapter 3), strictly speaking it can only be calculated accurately using the numerical approach discussed in section 2.3.3. However, this problem is usually circumvented by introducing a term called effective cavity length, L_{cav} [6], which is given by $L_{cav} = L_c + L_{pen(f)} + L_{pen(b)}$ where $L_{pen(f)}$ and $L_{pen(b)}$ are the so-called energy penetration depths (L_{pen}) of the front and back mirrors. This effective cavity length term is used to take account of the field penetration into the mirrors in the calculation of Γ_z. Assuming that the spatial field variation of the optical standing wave can be approximated by a $\cos(k_c z)$ profile, the longitudinal confinement factor Γ_z of VCSEL is simply given by

$$\Gamma_z = \frac{d_{qw}}{L_{cav}} \sum_{q}^{n_{qw}} \left(1 + \frac{\cos(2k_c l_q)\sin(k_c d_{qw})}{k_c d} \right) = \Gamma_{enh} \frac{n_{qw} d_{qw}}{L_{cav}} \qquad (2.45)$$

where n_{qw} is the total number of quantum wells, d_{qw} is the quantum well thickness, l_q is the distance between antinodes and the centres of each quantum well. Γ_{enh} is the so-called enhancement factor and indicates the dependence of Γ_z on the positions and thickness of the quantum wells. If all the quantum wells are centred on the antinodes and are sufficiently thin such that $\sin(k_c d_{qw}) \approx k_c d_{qw}$, Γ_{enh} then approaches the maximum value of 2. There have been a few suggestions on how to approximate the value of L_{pen} analytically, but the most commonly adopted are derived from the coupled mode theory [6], expressed by

$$L_{pen} = \frac{\tanh(2\kappa L)}{2\kappa} \qquad (2.46)$$

where κ and L are the coupling constant and total length of the mirrors respectively. For DBR consisting of pairs of quarter wave thickness layers, κ is given by $2\Delta n / \lambda_0$ where Δn is the index difference between the paired layers. (Note : in section 4.2, an alternative formula is derived based on a scalar variational expression)

2.4.2 Threshold Current, Power Output and Efficiencies

The relation between the material peak gain (g_{peak}) of a quantum well with injected current density can usually be fitted both theoretically and experimentally by a simple two-parameter semilogarithmic expression [5]

$$g_{peak} = g_{0J} \ln\left(\frac{J}{J_{tr}} \right) \qquad (\text{for } J > J_{tr}) \qquad (2.47)$$

where g_{0J} is an empirical gain coefficient and J_{tr} is the transparency current density. Combining (2.42) and (2.47), the threshold current density J_{th} for a multiple quantum well laser that lases at the gain peak wavelength is then given by

$$J_{th} = \frac{n_{qw} J_{tr}}{\eta_{int}} \exp\left(\frac{\alpha_c + \alpha_m}{\Gamma g_{0J}} \right) = \frac{n_{qw} J_{tr}}{\eta_{int}} \exp\left(\frac{2\alpha_c L_c - \ln(R_f R_b)}{2 L_c \Gamma g_{0J}} \right) \qquad (2.48)$$

where η_{int} is the internal quantum efficiency representing the fraction of the injected current that contributes to the radiative recombination in the gain media. The threshold current is then the product of current injection area and threshold current density.

Above threshold, the steady state optical power output from the laser is given by

$$P_{out} = \eta_{ext} \frac{hf}{q}(I - I_{th}) \qquad (\text{for } I > I_{th}) \qquad (2.49)$$

where hf is the photon energy of the laser light, q is the electronic charge, I is injected current, I_{th} is the threshold current; η_{ext} is the so-called external quantum efficiency expressed by

$$\begin{aligned} \eta_{ext} &= \frac{dP_{out} / dI}{hf / q} = \eta_{int} \frac{\alpha_m}{\alpha_c + \alpha_m} \\ &= \eta_{int} \frac{\ln(1/R_f R_b)}{2\alpha_c L_c + \ln(1/R_f R_b)} \end{aligned} \qquad (2.50)$$

and gives the ratio of the total number of photons emitted by the laser above threshold to the number of carriers injected into the active region of the laser. Rearranging, (2.50) can be rewritten as

$$\frac{1}{\eta_{ext}} = \frac{1}{\eta_{int}}\left(1 + \frac{2\alpha_c L_c}{\ln(1/R_f R_b)}\right) \qquad (2.51)$$

For stripe lasers, equation (2.51) is frequently used to extract the experimental values of the cavity loss α_c and internal quantum efficiency η_{int} from the measurements of η_{ext} on broad area lasers of different cavity length. To a good approximation, $R_f = R_b$ for this type of laser. From the plot of $1/\eta_{ext}$ against L_c , the intercept of the resulting straight line gives the value of $1/\eta_{int}$ which in turn can be used to infer α_c from the slope, if the reflectivities are known. This experimental value of α_c can then be substituted into (2.42) to determine the modal threshold gain Γg_{th} . Assuming unity lateral confinement factor for these broad area lasers and since the transverse confinement factor can be calculated, a plot of material gain g of the gain medium against radiative current density J_{rad} (where $J_{rad} = \eta_{int} J_{th}$) can then be obtained. As will be shown in chapter 3, the experimental plot of g_{QW} vs. J_{rad} obtained through this procedure can be compared with the theoretical one, using stripe lasers made from VCSEL material.

In contrast to the uncoated in-plane stripe lasers, the reflectivity of the bottom (back) mirror of a top (front) emitting VCSEL is always designed to be higher than that of the output top (front) mirror to maximise the extraction of light output. Taking into account of the fact that some portion of light may be absorbed in the output

mirror, the external differential quantum efficiency ($\eta_{ext(top)}$) for top emitting VCSEL can be estimated as

$$\eta_{ext\,(top)} = \eta_{int}\eta_{top} \cong \eta_{int}\frac{T_{top}}{2\alpha_c L_c + \ln(1/R_{top}R_{bot})} \cong \eta_{int}\frac{T_{top}}{2\alpha_c L_c + (1-R_{top}R_{bot})} \quad (2.52)$$

where $\ln(R^{-1}) \cong (1-R)$ if $R \approx 1$, η_{top} is the output coupling efficiency through the top DBR, T_{top} and R_{top} are the transmittance and reflectance of the top DBR, R_{bot} is the reflectance of the bottom DBR and α_c is the cavity loss (different value from that of an in-plane laser). Another figure of merit on the laser performance is the power conversion (or wall-plug) efficiency (η_{wp}) which is current injection dependent and is defined as the ratio of optical power output to the electrical input. For top emitting VCSELs, it is given by

$$\eta_{wp} \cong \eta_{ext(top)}\frac{(I-I_{th})}{I}\frac{V_g}{V_g+IR} \quad (2.53)$$

where I is injection current, I_{th} is the threshold current, V_g is the bandgap energy and R is the series resistance of DBRs.

2.5 Transverse Wave Admittance and Planar Waveguide

As discussed in section 2.4.2, it is possible to estimate the gain-current relation of the quantum wells by making broad area in-plane stripe lasers (60μm stripe width is used in this work) using the same material as used for the VCSEL. However, before this can be done the value of the transverse confinement factor must be known. To obtain this value theoretically, an approach similar to the "transverse resonance" method [2] was employed. Referring to Fig. 2.2, assume that the cleaved facets for such broad area stripe laser are parallel to the x-z plane such that the cavity length is determined by the distance between the mirrors along y-axis. Since the stripe width along the lateral x-axis is many times the lasing wavelength, this laser appears like a planar multilayered waveguide whose guided modes propagate in the "longitudinal" y-direction and are guided only in the "transverse" z-direction, i.e. $\partial / \partial x = 0$, $k_x = 0$ and thus $\Gamma_x = 1$. The guided modes in such a waveguide are classified as TE or TM

modes. They can be considered to be a superposition of a pair of TE or TM waves that are propagating along the y-axis with identical propagation constant k_y but with $\pm\beta$ phase constants in the z-direction (or a pair of TEM plane waves that are making an plus/minus oblique angle with the z-axis). Hence, the standing wave formed extends in the z-direction. As before, the relation between β and k_y can be readily obtained from (2.17b). Note that the definitions of longitudinal and transverse directions of these stripe lasers / planar waveguides are different from that of VCSEL.

Using the transfer matrix method described earlier, the propagation constant k_y and phase constant β of the guided modes can be determined as follows. Firstly, it is assumed that the modes are purely decaying in the media above the topmost layer and below the lowest layer of the waveguide structure, but either propagating or evanescently decaying waves are allowed in any other layers. Then for any guided modes, the impedance matching condition as given by (2.39) must be met. As in that instance, the matching condition are also met automatically at other interfaces. Depending on the layer dimensions and actual structure design, only a set of discrete values of k_y and β will be found to satisfy this condition. The guided mode with the largest value of propagation constant k_y and lowest value of phase constant β (related to k_y by (2.17b)) is considered to be the fundamental mode. Subsequently, the transverse standing wave pattern can be calculated easily using the procedure described in section 2.3.3. Then, the "transverse" confinement factor Γ_z for any guided modes can be evaluated according to their respective field profiles.

References for Chapter 2

[1] S.Ramo, J.R.Whinnery, T.V.Duzer, "Fields and Waves in Communication Electronics", (John Wiley & Sons , 1994)

[2] R.F.Harrington, "Time-Harmonic Electromagnetic Fields", (McGraw Hill, 1961)

[3] M.Born and E.Wolf, "Principles of Optics" (Pergamon 1984).

[4] G.P.Agrawal and N.K.Dutta, "Semiconductor Lasers", (Van Nostrand Reinhold, NY,1993)

[5] S.L.Chuang, "Physics of Optoelectronic Devices", (John Wiley & Sons, 1995)

[6] D.I.Babic and S.W.Corzine, "Analytic expressions for the reflection delay, penetration depth, and the absorptance of quarter-wave dielectric mirrors", IEEE J. of Quantum Electronics, vol. 28, pp 514-524, 1992.

Chapter 3 Design Issues

3.1 Introduction

This chapter deals with design aspects for oxide apertured VCSELs used in this work. It begins with an overview which includes details of the practical limitations that constrain the design flexibility. This is then followed by assessments of the plane wave values of reflectivity, threshold gain, threshold current density and output coupling efficiency of the designed VCSEL structures. Finally, some preliminary experimental results from broad area VCSELs and in-plane lasers are presented so that certain devices parameters can be estimated for use chapter 5.

3.2 Design Overview

The VCSEL materials used in this work were grown using the Metal-Organic Vapour Phase Epitaxy (MOVPE) technique. The details of these VCSEL structures are shown in Figure 3.1. Several growth constraints and practical device fabrication problems affected the design flexibility of these VCSELs. For 850nm GaAs VCSELs, $Al_xGa_{1-x}As$ is the natural material choice for the reflector stacks since it can be easily grown (the difference in lattice constant between GaAs and AlAs is less than 0.16% [2]) and provides sufficiently high refractive index contrast ratio for producing working VCSELs [3,4]. At the optical wavelength of 850nm, available data on the absorption coefficients [2,3] shows that while $Al_{0.1}Ga_{0.9}As$ is absorptive to light, $Al_{0.2}Ga_{0.8}As$ should be transparent. Therefore, $Al_{0.2}Ga_{0.8}As$ is chosen as one of the constituents of the DBR.

In the ideal absorption free case, the maximum normal incident reflectivity (R_{max}) at the designed central wavelength of a DBR formed by exact quarter-wave thick stacks, can be deduced from equations (2.26) and (2.30) as

$$R_{max} = \left(\frac{1 - \frac{n_e}{n_i}\left(\frac{n_1}{n_2}\right)^{2p}}{1 + \frac{n_e}{n_i}\left(\frac{n_1}{n_2}\right)^{2p}} \right)^2 \qquad (3.1)$$

where n_1 and n_2 are the refractive indices of the mirror layers (stacks start with the layer having n_1), n_i and n_e are the refractive indices of the incident and exit media, and p is the number of mirror pairs. For a fixed number of mirror pairs, the reflectance of the mirror is thus dependent on the index contrast ratio n_1/n_2. For a large number pair of stacks (i.e. $p \rightarrow \infty$), R_{max} approaches unity and the bandwidth ($\Delta\lambda$) of the first order reflectivity stopband can be estimated by [1]

$$\Delta\lambda = \frac{2\lambda_o}{\pi}\sin^{-1}\left[\frac{|n_2 - n_1|}{n_1 + n_2}\right] \qquad (3.2)$$

Again, this formula indicates that a DBR with a large index difference/contrast ratio offers a wider stopband width. Hence, in order to achieve the desired mirror reflectance using a minimum number of layers as well as with wide high reflectance bandwidth, the material with lowest refractive index i.e. AlAs would be the most logical option for making up the mirror pair. However, for single oxide apertured VCSELs, $Al_xGa_{1-x}As$ with $x<0.95$ [5] must be used in order to provide sufficient lateral oxidation selectivity so that oxide apertures do not form elsewhere within the mirrors other than the designated location. Unfortunately, due to the limitation of the growth reactor mass flow controllers for Trimethylaluminium (TMA) [6], the highest Al content $Al_xGa_{1-x}As$ with $x<1.0$ available for this work is $Al_{0.8}Ga_{0.2}As$. Hence, $Al_{0.2}Ga_{0.8}As/Al_{0.8}Ga_{0.2}As$ mirror pairs are used for the top DBR except for the first period where AlAs replaces $Al_{0.8}Ga_{0.2}As$ to form the oxide aperture.

During device fabrication, mesas were etched through the top DBR to expose the AlAs layer for oxidation (refer to Fig 1.1 in chapter 1), and usually stopped at the upper end of the bottom DBR in order to avoid unnecessary increase in mirror electrical series resistance. Thus, two different DBR material combinations can be used for the bottom DBRs : they are 15.5 pairs $Al_{0.2}Ga_{0.8}As/Al_{0.8}Ga_{0.2}As$ in the upper part of the bottom DBR to provide an extra etch depth tolerance of about 2μm, and the $Al_{0.2}Ga_{0.8}As$/AlAs combination making up the rest of the bottom DBRs to minimise the number of mirror pairs required to achieve the desired reflectivity.

p^+ - GaAs	50 Å
p - $Al_{0.2}Ga_{0.8}As$	424 Å
p - $Al_{0.5}Ga_{0.5}As$	200 Å
p - $Al_{0.8}Ga_{0.2}As$	471 Å
p - $Al_{0.5}Ga_{0.5}As$	200 Å
p - $Al_{0.2}Ga_{0.8}As$	424 Å
p - $Al_{0.5}Ga_{0.5}As$	200 Å
p - AlAs	*600 / 350 / 200 Å*
p - $Al_{0.8}Ga_{0.2}As$	*0 / 240 / 385 Å*

→ capping layer

x M (= 27) — Top DBR

→ Oxide aperture

i - $Al_{0.3}Ga_{0.7}As$	980 Å
i - GaAs QW1	100 Å
i - $Al_{0.3}Ga_{0.7}As$	100 Å
i - GaAs QW2	100 Å
i - $Al_{0.3}Ga_{0.7}As$	100 Å
i - GaAs QW3	100 Å
i - $Al_{0.3}Ga_{0.7}As$	990 Å

3 QWs in a 1λ cavity

n - $Al_{0.8}Ga_{0.2}As$	580 Å
n - $Al_{0.5}Ga_{0.5}As$	200 Å
n - $Al_{0.2}Ga_{0.8}As$	424 Å
n - $Al_{0.5}Ga_{0.5}As$	200 Å
n - $Al_{0.8}Ga_{0.2}As$	471 Å
n - $Al_{0.5}Ga_{0.5}As$	200 Å
n - $Al_{0.2}Ga_{0.8}As$	424 Å
n - $Al_{0.5}Ga_{0.5}As$	200 Å
n - AlAs	492 Å
n - $Al_{0.5}Ga_{0.5}As$	200 Å
n - buffer layers	
n - GaAs substrate	

x P (= 15) — Bottom DBR

x Q (= 27)

Figure 3.1 : Details of the full VCSEL structures used in this work. The structures containing 600Å, 350Å and 200Å AlAs layer in the first pair of top DBR are referred to as strong, medium and weak guiding designs in this thesis.

Besides providing the necessary optical feedback for lasing, the DBRs also act as the current carrying media for carrier injection into the gain region. While a large refractive index difference between the two constituents of the DBR structure is responsible for high optical reflectivity, the accompanying energy bandgap difference which increases with index difference, also results in potential barriers (spikes) at the "reverse biased" heterojunctions [4]. These barriers impede carrier flow in the DBR structures and constitute series resistance which is usually higher for the p-DBR than the n-DBR, due to the much higher effective mass of holes than electrons. Besides limiting the power conversion (i.e. wall-plug) efficiency through causing a higher biasing voltage, as can be deduced from equation (2.53), the series resistance also gives rise to device internal thermal heating. This promotes carrier leakage in the active region and thus further deteriorating the laser efficiency. The electrical conduction of the DBR can be improved by compositional grading and modulation doping of the heterojunctions to enhance thermionic and tunnelling currents through the potential barriers [7,8]. However, such schemes for reducing the series resistance of DBRs require sophisticated growth control that is not easily implemented at Sheffield. Therefore in this work, a single step grading scheme [4] is used, where a 200Å $Al_{0.5}Ga_{0.5}As$ intermediate layer is inserted at each heterojunction. The mirror stacks are also uniformly doped throughout to dopant concentrations of ~3.0 x 10^{18} cm^{-3}(C doped) for the p-type top DBR and ~2.0 x 10^{18} cm^{-3} (Si doped) for the n-type bottom DBR.

As can be deduced from (2.44), the resonant wavelength is very sensitive to the total optical thickness (nL) of the cavity. Thus, the VCSEL cavity design should be made as simple as possible to avoid misplacement of resonant wavelength. On the other hand, it is also desirable to grade the QW-cladding regions using a grading scheme such as the GRINSCH structure [9] or the staircase structure [10] to provide more efficient carrier capture in the quantum wells. Neither of these schemes were adopted since it is more difficult to ensure cavity optical thickness uniformity across the VCSEL wafer [6]. Thus, the VCSELs used in this work only contain three 100Å GaAs quantum wells that are clustered around the only antinode of the optical standing wave available in the 1-λ (optical thickness) cavity, and are separated by $Al_{0.3}Ga_{0.7}As$ barriers/cladding layers from each other and the mirrors.

As mentioned in Chapter 1, the main objective of this work is to study the effects of the oxide thickness on the VCSEL operating characteristics. For this purpose, the three VCSEL structures used are nominally identical except for the thickness of the oxide apertures embeded in the first mirror pair of the top DBR. The details of these structures are shown in Fig. 3.1. In order to vary the strength of the index guiding, the thickness of the to- be- oxidised AlAs layers are chosen to be 200Å, 350Å or 600Å respectively. As shown in Fig. 3.8(b) to 3.8(d) in section 3.3.2, these AlAs layers are designed to be situated between the antinode and the node of the optical standing wave. As will be shown later in chapter 4, the index guiding strength in an oxide apertured VCSEL is dependent on the thickness and the longitudinal position (i.e. distance from an antinode/node of the optical standing wave) of the oxide. Therefore, for ease of identification, these VCSEL structures are addressed as "strong guiding" (600Å oxidised AlAs), "medium guiding" (350Å oxidised AlAs) and "weak guiding" (200Å oxidised AlAs) respectively in the rest of this thesis.

3.3 Design Assessments

In this section, the dependence of the mirror reflectance, threshold gain and threshold current density, and output coupling efficiency on absorption loss and number of mirror pairs will be discussed. From these considerations, VCSEL designs which give a target threshold current density of around 1kA/cm^2 for broad area devices (diameter > 10μm) are determined. The VCSEL structures under consideration are those illustrated in Figure 3.1. The values of the layer thickness were calculated assuming a plane wave resonant wavelength of 850nm. The presence of the thin degenerately doped (1x10^{19} cm^{-3}) 50Å GaAs capping layer on top of the top DBR is necessary to reduce the formation of the surface oxide as well as for obtaining a low resistance ohmic contact. The $Al_{0.8}Ga_{0.2}As$ layer in the dotted box exists only for the cases of medium guiding (350Å AlAs) and weak guiding (200Å AlAs) layers, to ensure zero phase shift on reflection from the top mirror. The numerical calculations involved below are based on the transfer matrix method discussed in the previous chapter and the widely accepted refractive index values of $Al_xGa_{1-x}As$ from S.Adachi [3].

3.3.1 Plane Wave Reflectivity of Top and Bottom DBRs

In order to achieve high output efficiency and low threshold gain, the reflectance of the bottom mirror must be made as close to unity as possible. Figure 3.2 illustrates the effects of using two different DBR constituents (refer to Fig. 3.1), i.e. P pairs of ($Al_{0.2}Ga_{0.8}As/Al_{0.5}Ga_{0.5}As/Al_{0.2}Ga_{0.8}As/Al_{0.5}Ga_{0.5}As$) and Q pairs of ($Al_{0.2}Ga_{0.8}As$ /$Al_{0.5}Ga_{0.5}As$ /AlAs/$Al_{0.5}Ga_{0.5}As$), as well as that arises from inserting intermediate layers on the reflectance stopband bandwidth of the bottom DBR. For meaningful comparisons, all mirror stacks are assumed to be absorption-free and the total number of mirror pairs are kept at 30. As expected, the mirror with the largest index contrast ratio i.e. P=0, Q = 30 pairs (curve (iii)) has a wider stopband width than the other two mirrors designs with lower (curve (i)) and hybrid (curve (ii)) index contrast ratios. Therefore, by adopting the hybrid design (ii), some reduction in bandwidth of the stopband was traded for fabrication tolerance on the mesa etch depth. Curve (iv) also shows that ideal abrupt step-junction mirror without intermediate layers has the widest bandwidth among the four designs.

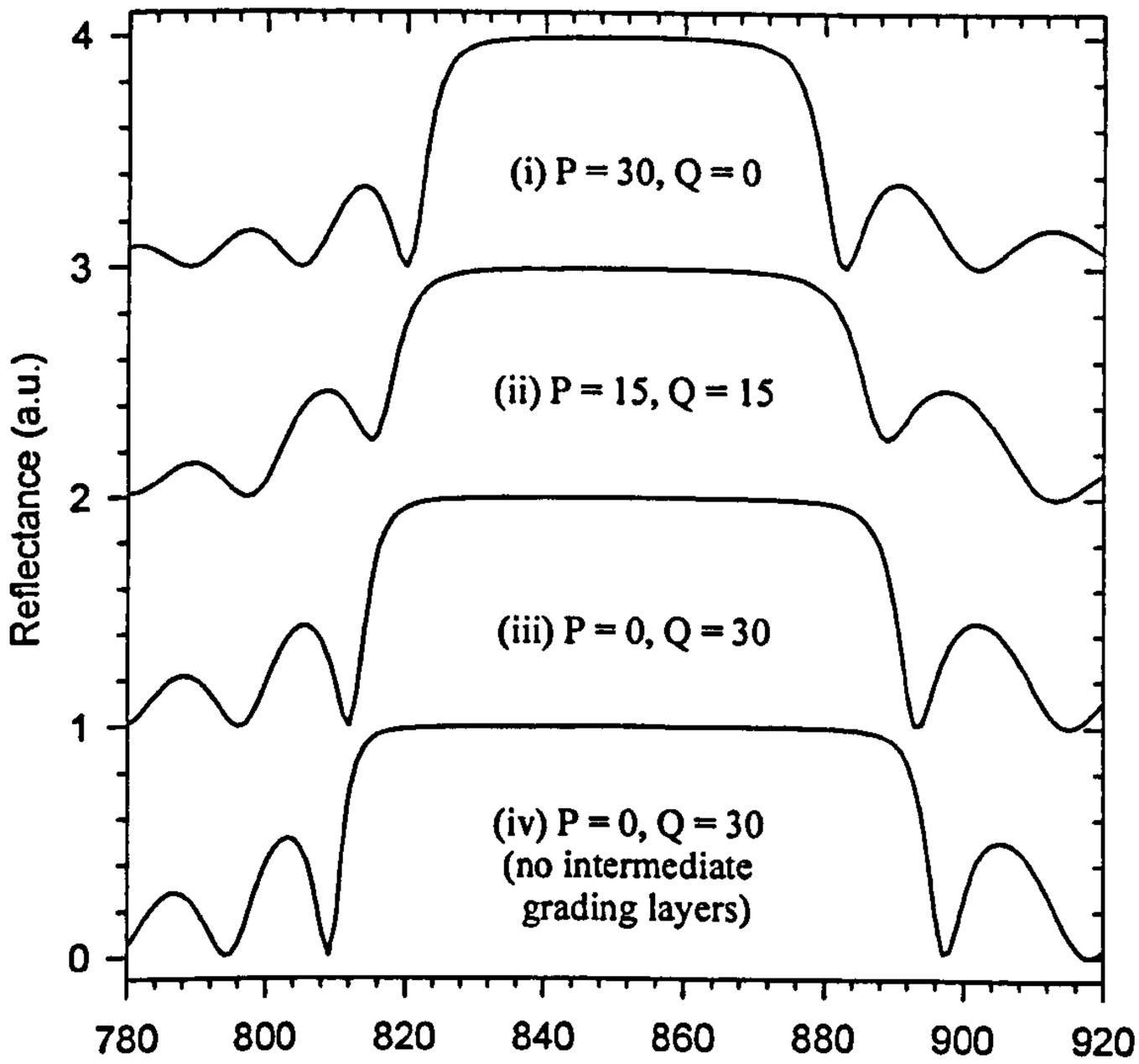

Fig 3.2 : Calculated reflectivity spectrum of bottom DBRs with different combinations of mirror periods P and Q. Curves (i), (ii) and (iii) have been offset for the sake of clarity.

By fixing P mirror pairs to 5,10 or 15, Fig 3.3 illustrates the variation of peak reflectance with (P+Q) mirror pairs for various values of uniform absorption coefficient. The peak reflectance curves flatten off for a large number of total mirror periods, and the maximum peak reflectance that can be obtained is dependent on the mirror combination as well as on the amount of absorption. As expected, a larger value of P mirror pairs results in larger total number of mirror pairs (P + Q) required for a particular value of reflectance in all cases. For P = 15, increasing the total number of mirror pairs beyond 42 (i.e. Q > 27 pairs) results in little improvement in reflectance and might also increase the mirror series resistance unnecessarily. Thus, a 42 pair DBR (P=15, Q=27) is chosen for forming the bottom mirror of the VCSELs used in this work. The advantages of using a DBR with larger index difference is obvious from Figures 3.2 and 3.3 (and also equations (3.1) and (3.2)). Although not adopted for the VCSELs studied in this work, the feasibility of making high index contrast ratio mirrors using $Al_xO_y/Al_{0.2}Ga_{0.8}As$ and $Al_xO_y/Al_{0.5}Ga_{0.5}As$ has also been investigated. These results are detailed in ***Appendix B***.

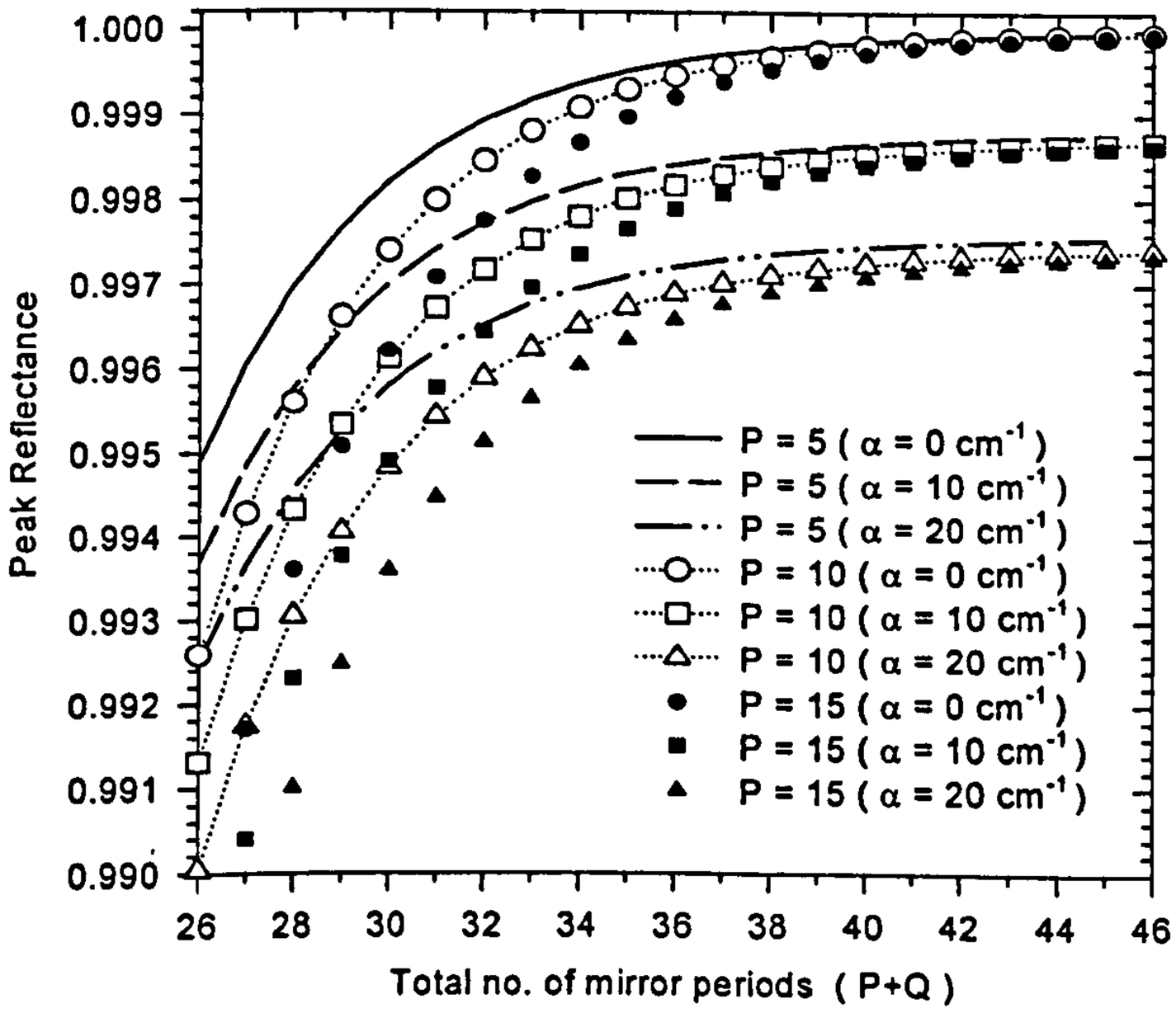

Fig 3.3 : Peak Reflectance of bottom DBR versus (P+Q) x no. of mirror periods for different values of uniform absorption coefficients in all layers.

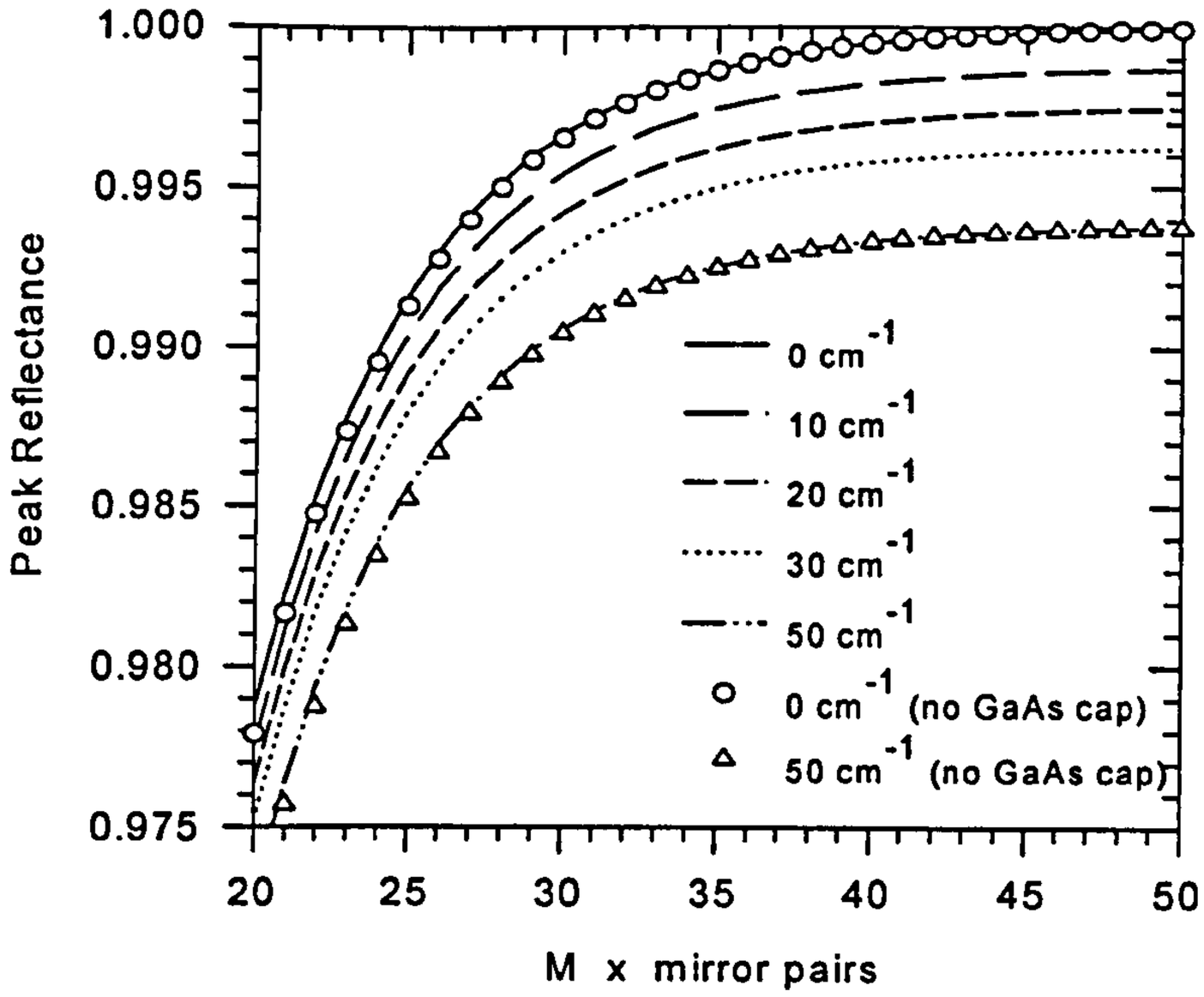

Fig 3.4 : Peak reflectance of top DBR of strong guiding design versus M number of mirror pairs for different values of uniform absorption coefficients.

Fig. 3.4 shows the variation of peak reflectance of the top DBR with increasing number (M) of mirror pairs in the top DBR for the strong guiding design. Its stopband bandwidth is similar to that shown in the curve(i) of Fig 3.2. As in the case of the bottom DBR, the peak reflectance reaches a different limit for a large number of mirror pairs for different values of absorption coefficient. The effect of the degenerately doped GaAs capping layer is negligible and in fact slightly increases the reflectance for M<35 pairs. This is because the extra index step provided is more than sufficient to offset the absorption loss in such a thin layer where the electric field is very weak. The peak reflectance of the top DBRs containing 200Å or 350Å AlAs in the first pair are very close to that with 600Å AlAs with a difference in reflectance no more than 0.03%.

3.3.2 VCSEL Plane Wave Properties : Threshold Gain, Output Coupling Efficiency and Optical Standing Wave

The threshold condition of a laser requires sufficient gain to overcome the optical losses before oscillation can be achieved. Besides the mirror transmission losses, the absorption losses also play very important parts in determining the lasing performance of VCSEL. The use of impurity doping in DBRs results in absorption losses which are mainly due to free carrier absorption and the so-called band-tail

absorption [12-13]. Free carrier loss involves the absorption of photons whose energy are below bandgap, by free carriers which are consequently raised to a higher energy state within the same conduction or valence band. The free carrier absorption coefficient can be estimated by [12]

$$\alpha_{fc} = \frac{n_c q^2 \lambda^2}{4\pi^2 m^* n c^3 \varepsilon_0 \tau_c} \qquad (3.3)$$

where n_c is the free carrier concentration, n is the refractive index, m^* is the effective mass of the carriers and τ_c is the effective scattering time, the inverse of which is the damping rate of the free carrier oscillation. The value τ_c is usually estimated from the carrier mobility μ_c where $\tau_c = m^* \mu_c / q$. On the other hand, band-tail absorption usually involves near bandgap transitions between ionised impurity states (i.e. band-tail states formed by donor/acceptor states) and the opposite band-edge. It has been suggested by Casey [13,14] that the total free carrier absorption loss due to doping impurities near the bandgap energy for GaAs at room temperature, can be estimated as

$$\alpha\,(\mathrm{cm}^{-1}) \approx 3\times10^{-18}\, n + 7\times10^{-18}\, p \qquad (3.4)$$

where n and p are the n-type and p-type dopant concentrations respectively. However, this estimation includes both free carrier absorption and band-tail absorption where the low energy bandtail states extended as far as 120meV from the bulk GaAs band edge (1.424eV) as deduced from figures in ref. [13]. Thus, this phenomenological formulae is not suitable for the case where the bandtail state energy levels of $Al_xGa_{1-x}As$ are far higher than the photon energy.

For the VCSELs discussed here (excluding the GaAs capping, buffer and substrate layers), $Al_{0.2}Ga_{0.8}As$ has a direct bandgap energy (1.66 eV) closest to the emission photon energy (≈1.46eV). Due to the lack of reported results, it is not certain whether the extent of the bandtail states of $Al_{0.2}Ga_{0.8}As$ is similar to that of GaAs. Hence, calculations were carried out assuming the absorption losses in $Al_{0.2}Ga_{0.8}As$ are given either by (3.4) which includes bandtail absorption, or purely due to free carrier losses estimated by (3.3). As for the other constituent reflector stacks with higher Al fractions, only free carrier absorption losses are considered. The relevant values for effective mass are taken from reference [2] where heavy hole masses are used for p-doped layers and an extrapolated conduction band effective mass is used for n-doped $Al_{0.2}Ga_{0.8}As$. For n-doped $Al_xGa_{1-x}As$ with x=0.5,0.8,1.0, the x-valley conductivity masses are adopted due to the indirect nature of their bandgaps. For

carrier mobility, the values for p and n-doped GaAs at $2x10^{18}$ cm^{-3} [4] are used for $Al_{0.2}Ga_{0.8}As$ while values for $Al_{0.5}Ga_{0.5}As$, taken from references [15] and [16], are also used for $Al_{0.8}Ga_{0.2}As$ and AlAs layers due to lack of published data. The estimated free carrier absorption losses for the p-type top DBR stacks (doping concentrations ≈ $3.0x10^{18}$ cm^{-3}) and n-type bottom DBR stacks (doping concentrations ≈ $2.0x10^{18}$ cm^{-3}) at 850nm are shown in Table 3.1. As for the nominally undoped cavity, the free carrier loss is assumed to be negligibly small. It is obvious that the estimated free carrier losses for $Al_{0.2}Ga_{0.8}As$ given in Table 3.1 are much lower than that given by equation (3.4) of Casey, i.e. $21cm^{-1}$ for p-type and 6 cm^{-1} for n-type $Al_{0.2}Ga_{0.8}As$ at similar doping concentrations. This seems logical since equation (3.4) includes the effects of both free carrier and band-tail absorption.

Having estimated the absorption coefficients of the DBR constituent layers, the threshold gain was then calculated using the numerical approach described in section (2.3.3). Figure 3.6 illustrates the dependence of the plane wave threshold gain for the strong guiding VCSEL layer on the number of top mirror pairs for three different sets of absorption values. Case A assumes all the constituents of VCSEL are absorption free, thus gives the lowest threshold gain among the three curves. Case B considers only free carrier losses in all layers and this assumption also applies to Case C except for the $Al_{0.2}Ga_{0.8}As$ layers where absorption losses obtained from Casey's equation (3.4) are adopted. As expected, the threshold gain reduces with increasing mirror pairs and reduction in mirror absorption. It is also found that the threshold gains for the "medium" and "weak" guiding designs are just slightly higher by no more than 40 cm^{-1} in both cases. Therefore, any difference in threshold gain (or threshold current density) among the oxidised devices with different oxide aperture thickness will be mainly due to the oxide thickness dependent excess optical losses.

Materials	$Al_{0.2}Ga_{0.8}As$		$Al_{0.5}Ga_{0.5}As$		$Al_{0.8}Ga_{0.2}As$		AlAs	
Dopant types	p	n	p	n	p	n	p	n
α_{fc} (cm^{-1})	0.56	1.95	1.37	2.74	1.28	3.29	1.24	3.75

Table 3.1 : Estimated free carrier absorption coefficients at 850nm using equation (3.3) for p and n-type DBRs with dopant concentrations of $3.0x10^{18}$ cm^{-3} and $2.0x10^{18}$ cm^{-3} respectively.

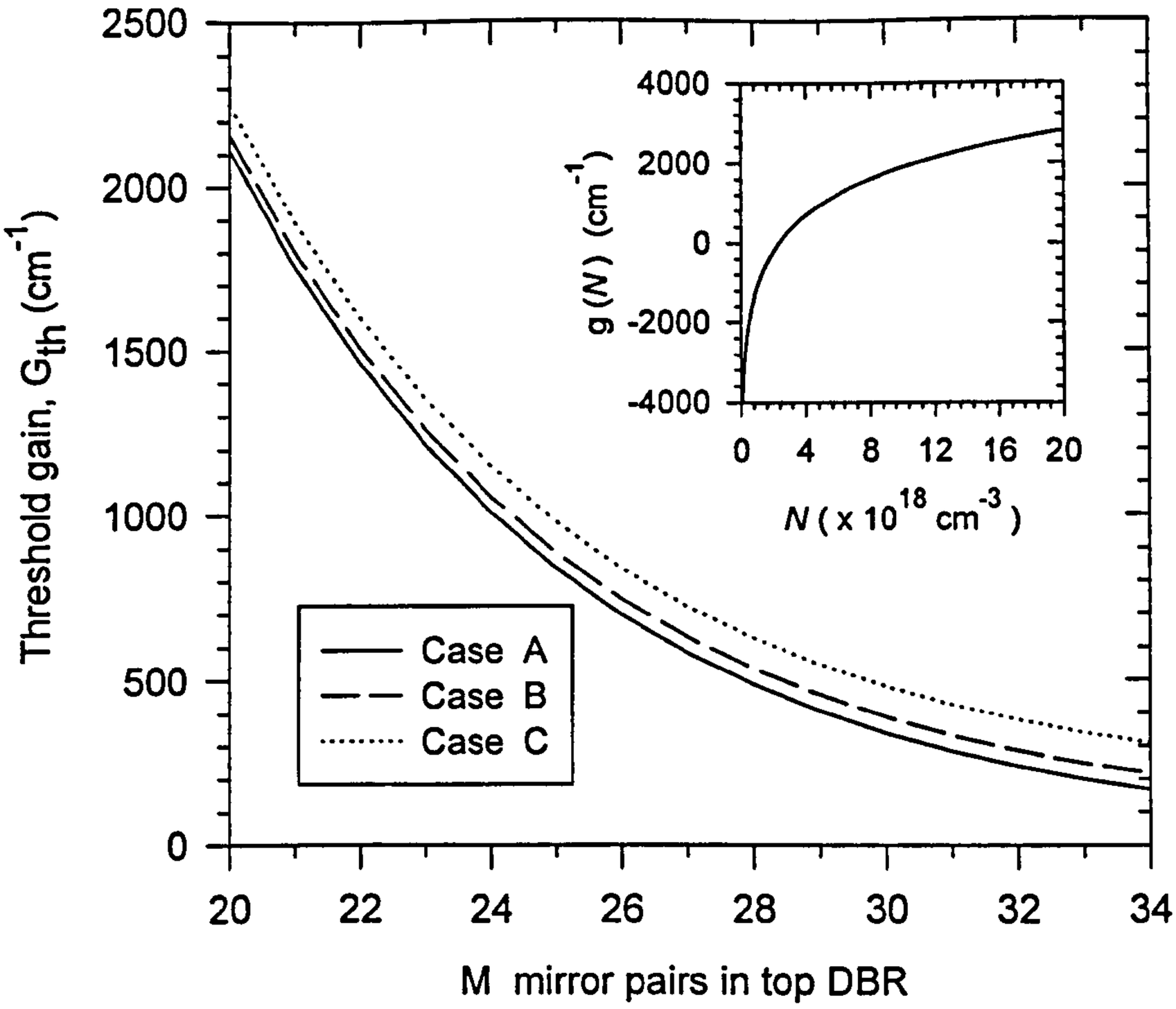

Figure 3.6 : Variation of plane wave threshold gain (G_{th}) with P x (mirror pairs) in the top DBR. Case A : no absorption loss in any layer; Case B : only free carrier loss in all layers; Case C : Free carrier loss in all layers except for $Al_{0.2}Ga_{0.8}As$ where absorption losses near band-edge from eqn.(3.4) are assumed.

For a given injected carrier density, the optical gain g(N) generated by a 100Å $GaAs/Al_{0.3}Ga_{0.7}As$ QW at 300K is given by [17]

$$g(N) = g_{0N} \ln\left(\frac{N + N_{min}}{N_{tr}}\right) \qquad (3.5)$$

where the gain coefficient, g_{0N} , is 1373.3 cm^{-1} , N_{tr} is the transparency carrier density given by 2.36 x 10^{18} cm^{-3} and N_{min} = 1.62 x 10^{15} cm^{-3} is the value inserted by the author to ensure that an unpumped (i.e. N = 0) QW has only a maximum absorption coefficient of 10^4 cm^{-2} [18]. The relation of gain - injected carrier concentration (g - N) calculated from equation (3.5) is shown in the inset of Fig. 3.6. In the absence of significant optical field (i.e. below threshold), and ignoring the carrier diffusion as well as carrier leakage effects, the carrier density concentration N is related to the injected current density (J) into the active region by

$$\frac{dN}{dt} = \frac{J}{qn_{qw}d_{qw}} - R_{spon}(N) - \frac{N}{\tau_{nr}} - CN^3 \qquad (3.6)$$

where $R_{spon}(N)$ is the spontaneous recombination rate and can be considered to vary as BN^2 at moderate carrier density. B is the bimolecular recombination coefficient and has a typical value of $1x10^{-10}$ cm^3s^{-1} for GaAs [19], corresponding to a radiative lifetime (i.e. $\tau_{rad}(N) = 1/BN$) of 10ns for $N = 1 \times 10^{18}$ cm^{-3}. The non-radiative recombination lifetime τ_{nr} is a function of interface quality as well as the number of impurity and defect states in the vicinity of the well. It is usually independent of injected carrier concentration and has value in the range of a few ns [19-21]. Thus, non-radiative recombination consumes quite a significant portion of injected carriers at low injection carrier density level. The last term in (3.6) represents the Auger recombination rate which is insignificant in GaAs since C is in the order of 10^{-30} cm^6/s [22], corresponding to a few hundreds of nanoseconds at the carrier density of interest. Thus at steady state, the injected current density can be estimated as

$$J = J_{rad} + J_{nr} = q\, n_{qw} d_{qw} \left(BN^2 + \frac{N}{\tau_{nr}} \right) \qquad (3.7)$$

where J_{rad} is the radiative current density due to the spontaneous recombination and J_{nr} is the non-radiative current density due to the non-radiative recombination.

Figure 3.7 shows the variation of the predicted threshold current density (J_{th}) for the strong guiding layer with M mirror pairs in the top DBR, where either only radiative current density or both radiative and non-radiative current density are considered assuming τ_{nr} = 5ns. These curves were calculated using the threshold gains obtained under the conditions set by cases A, B and C in Fig. 3.6 From this figure, it was decided to use M = 27 mirror pairs in the top DBR, corresponding to an ideal absorption free (i.e. case A) threshold current density ($J_{rad} + J_{nr}$) of 967 A/cm^2. Taking account of the absorption losses set by case C, the predicted threshold current density for the strong, medium and weak guiding designs are almost identical at 1.15 kA/cm^2, 1.17 kA/cm^2 and 1.20 kA/cm^2 respectively.

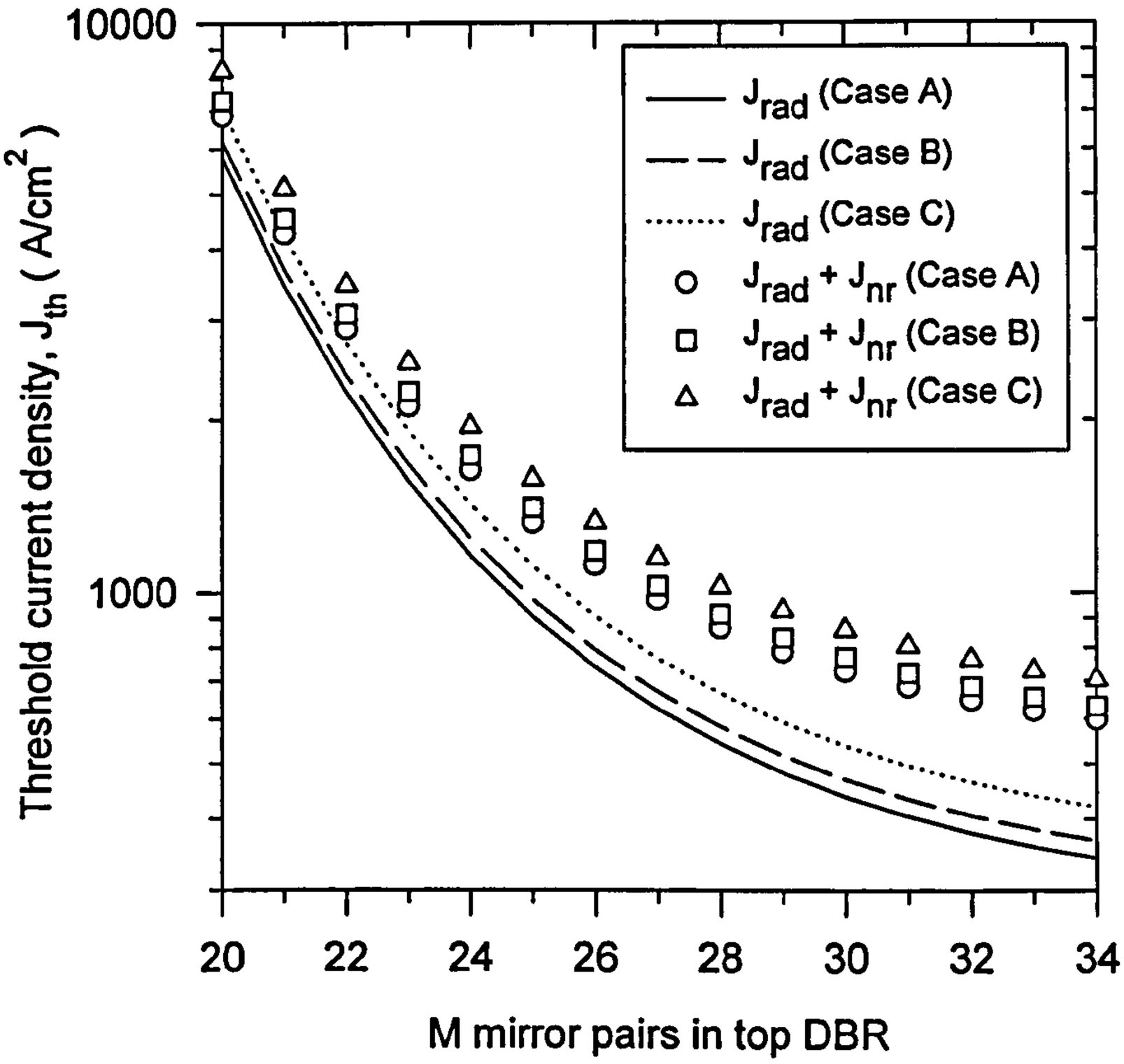

Figure 3.7 : Variation of predicted threshold current density (J_{th}) taking into account only radiative current density (J_{rad}) or, both radiative and non-radiative (J_{nr}) current density for strong guiding VCSEL layer.

Fig 3.8(a) shows the typical plane wave "squared electric field profile" formed within the whole VCSEL structure (such as that shown schematically in Fig. 1.1) at threshold and at the resonant wavelength of 850nm, normalised with respect to the field at the boundary between the last layer of bottom DBR and the substrate, i.e. buffer layers are neglected. Enlarged versions, emphasising the spatial field variation in the vicinity of the cavity region and the positions of the AlAs (oxide aperture) layers, are illustrated in Figure 3.8(b), (c) and (d) for the strong, medium and weak guiding VCSEL layers respectively. In the strong guiding design, the AlAs layer is thicker and closer to the antinode than in medium and weak guiding designs. The implications of the thickness and longitudinal positions of the oxide on the lasing performance will be discussed theoretically in Chapter 5, and based on experimental results in Chapter 6.

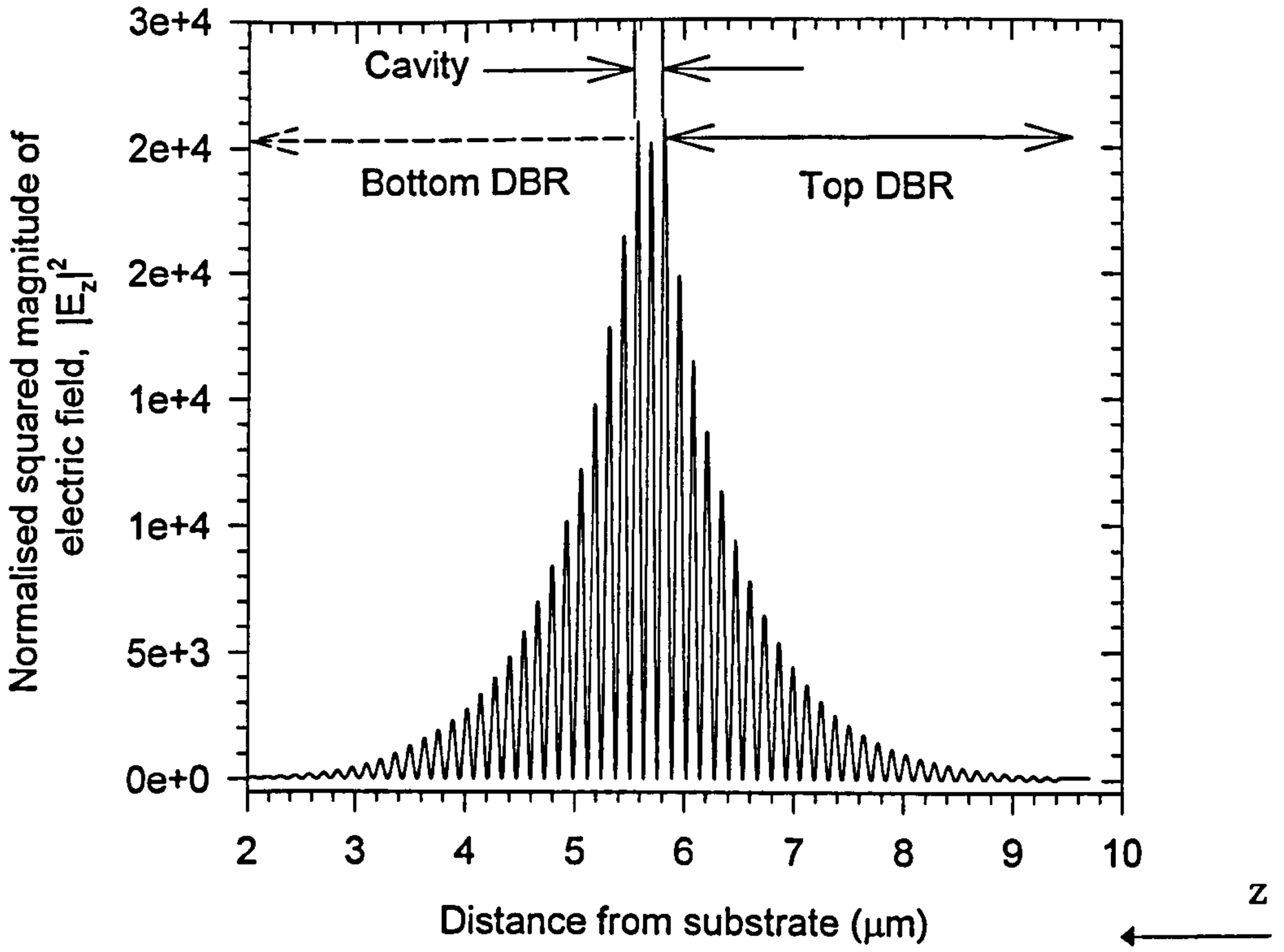

Figure 3.8(a) : Typical optical standing wave formed within the VCSEL structure at resonant wavelength (850nm).

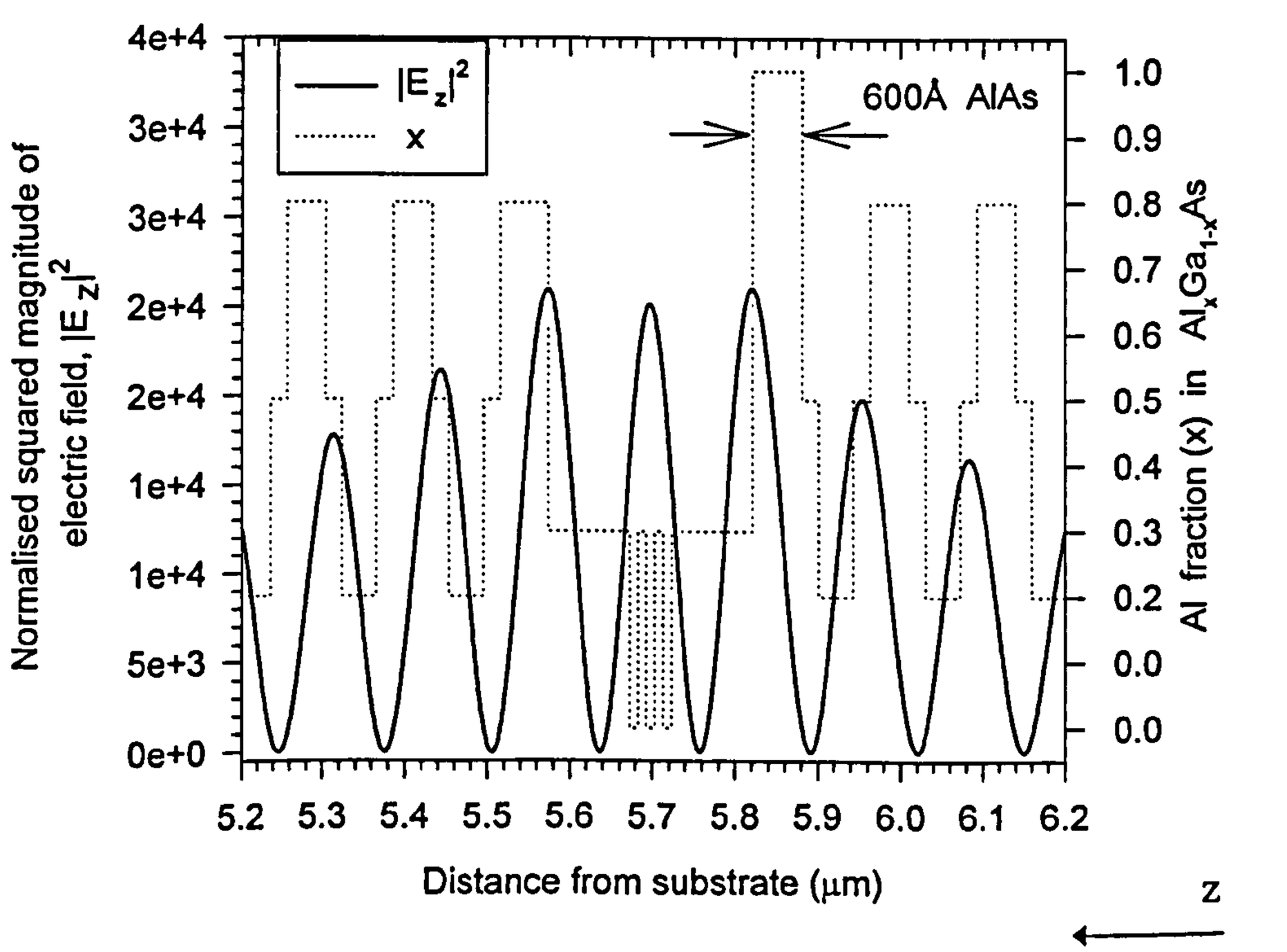

Figure 3.8 (b) : Variation of the optical standing wave in the vicinity of cavity region for the "strong guiding" (i.e. 600Å AlAs) VCSEL design.

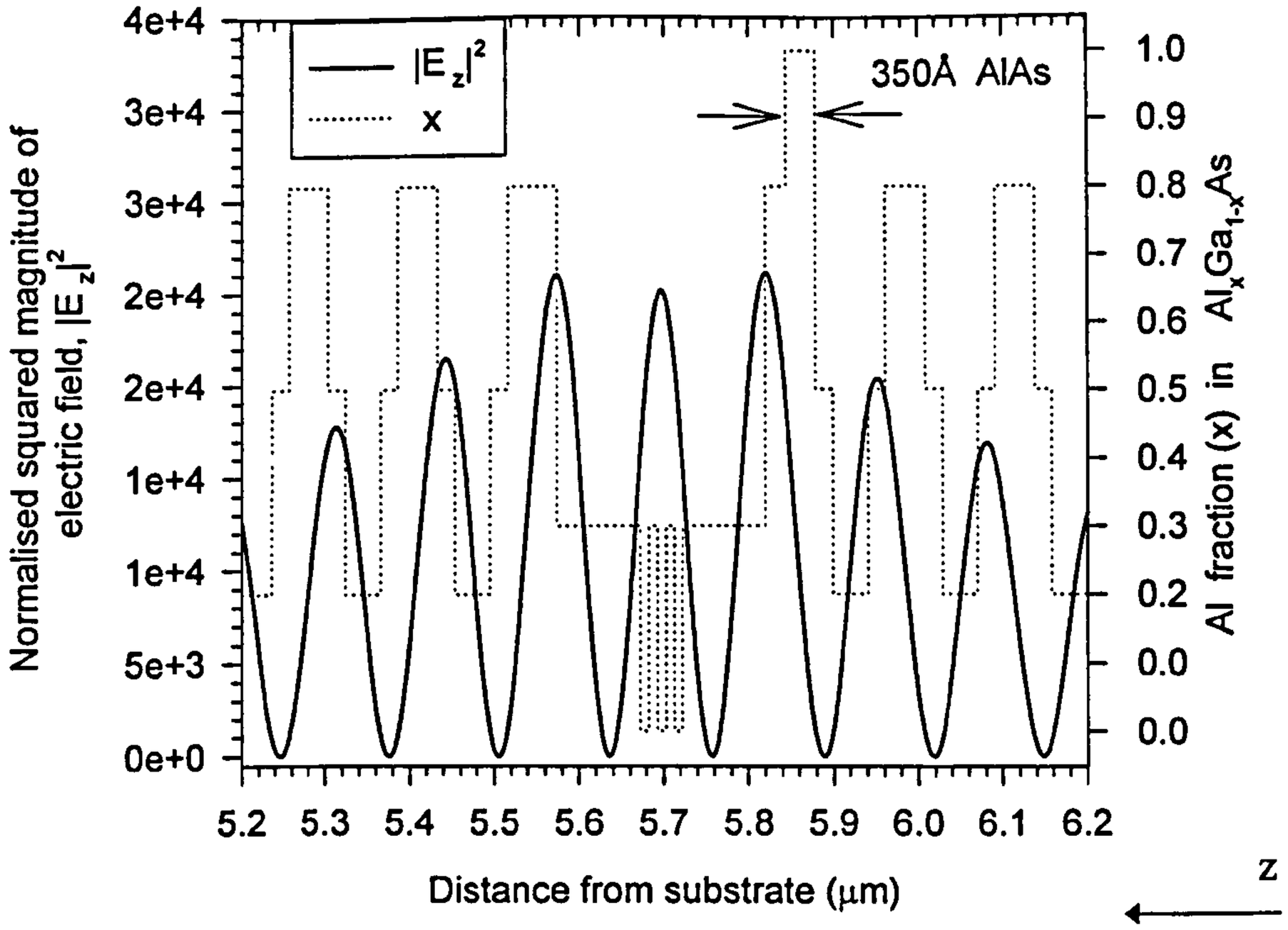

Figure 3.8 (c) : Variation of the optical standing wave in the vicinity of cavity region for the "medium guiding" (i.e. 350Å AlAs) VCSEL design.

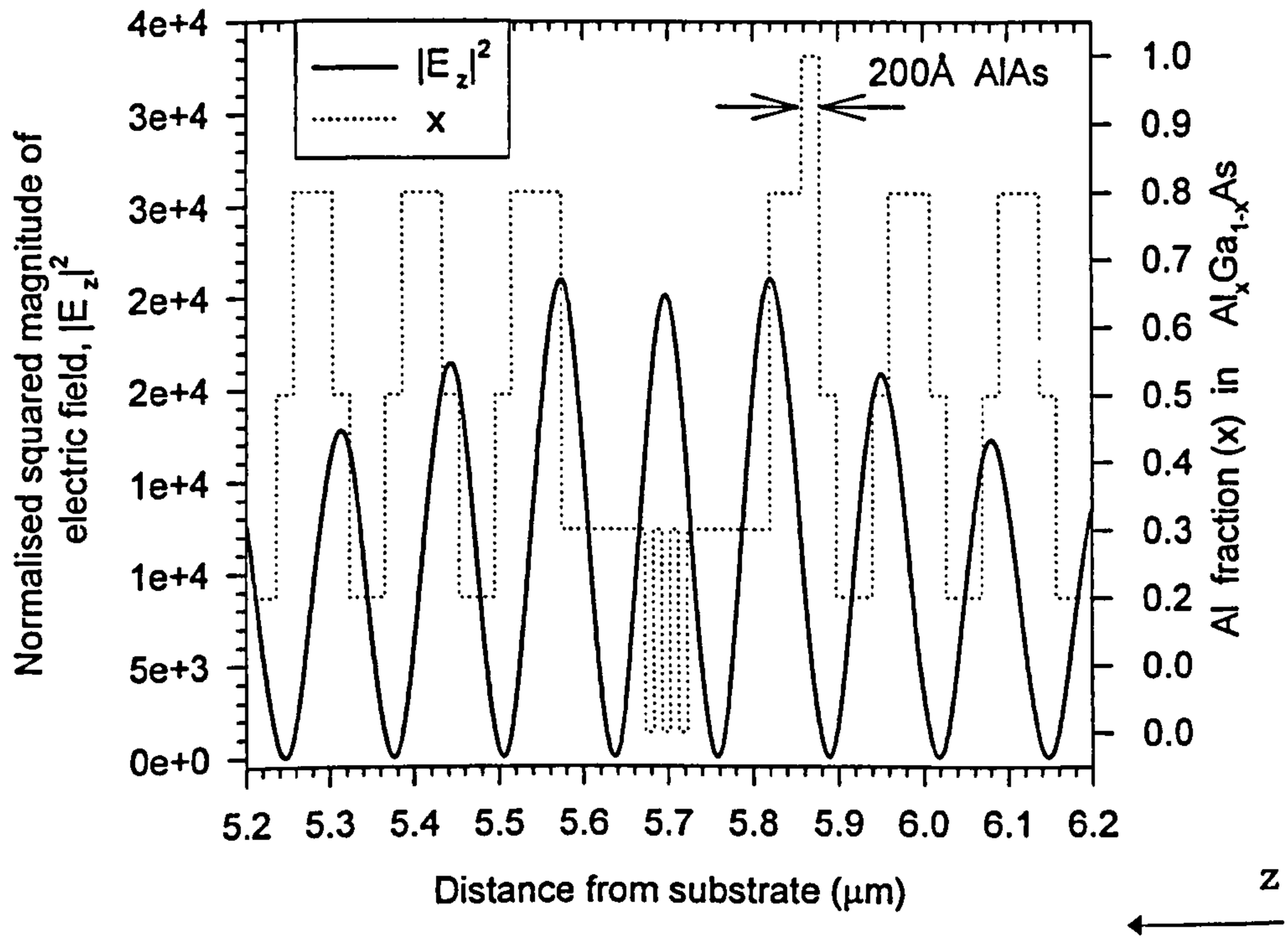

Figure 3.8 (d) : Variation of the optical standing wave in the vicinity of cavity region for the "weak guiding" (i.e. 200Å AlAs) VCSEL design.

It is also possible to evaluate the net power flow in the VCSEL structure by calculating the spatial variation of the time averaged power density (P_z) given by (2.32) i.e. ½ real(E_x x H_y) according to the co-ordinate systems in Fig. 2.1(d). Mathematically, using eqn.(2.18), (2.19) and (2.32), P_z can be shown to be equal to the summation of the forward-going (+) and backward-going (-) power density flows, i.e. $\left(\frac{1}{2}E^{+}H^{+}\right) + \left(-\frac{1}{2}E^{-}H^{-}\right)$. As in the case of a standing wave distribution, it is normalised with respect to the value obtained at the boundary between the last layer of bottom DBR and the substrate. Figures 3.9(a) and 3.9(b) show the spatial variation of (plane wave) P_z inside a strong guiding VCSEL at threshold where the latter figure offers an enlarged illustration for the region surrounding the cavity. The sign of the power density is negative in the top DBR because the direction into the substrate is defined as the positive z-axis. This means that values of $P_z > 0$ represent the transport of energy towards the substrate and those of $P_z < 0$ represent power flow towards the surface of top DBR. In Fig. 3.9(b), the amplification of the power flux by the QWs can be easily recognised. This suggests that the output coupling efficiency (η_{top}) from the top DBR can be obtained by

$$\eta_{top} = \frac{|P_{Z(top\_out)}|}{|P_{Z(top)}| + |P_{Z(bottom)}|} \tag{3.8}$$

where as shown in Fig 3.9(a), $|P_{Z(top)}|$ is the maximum magnitude of the power density in the upward direction (-z direction), $|P_{Z(bottom)}|$ is the corresponding value towards the substrate and $|P_{Z(top\_out)}|$ is the transmitted power output from the top DBR i.e. value at the interface between the air/VCSEL surface.

Using the definition given by eqn.(3.8), the output coupling efficiencies through the top DBR were calculated for cases A, B and C and the results are plotted in Figure 3.10. For M = 27 mirror pairs chosen for the three VCSEL designs used in this work, the predicted plane wave values of η_{top} are very similar for the strong, medium and weak guiding structures at 0.783, 0.785 and 0.787 respectively, using values of absorption coefficients set by case C. The corresponding values of η_{top} calculated using the phenomenological eqn.(2.52) are 0.774, 0.776 and 0.778 respectively, very close to those calculated using eqn. (3.8). Thus, in subsequent chapters eqn. (2.52) is used to calculate η_{top}.

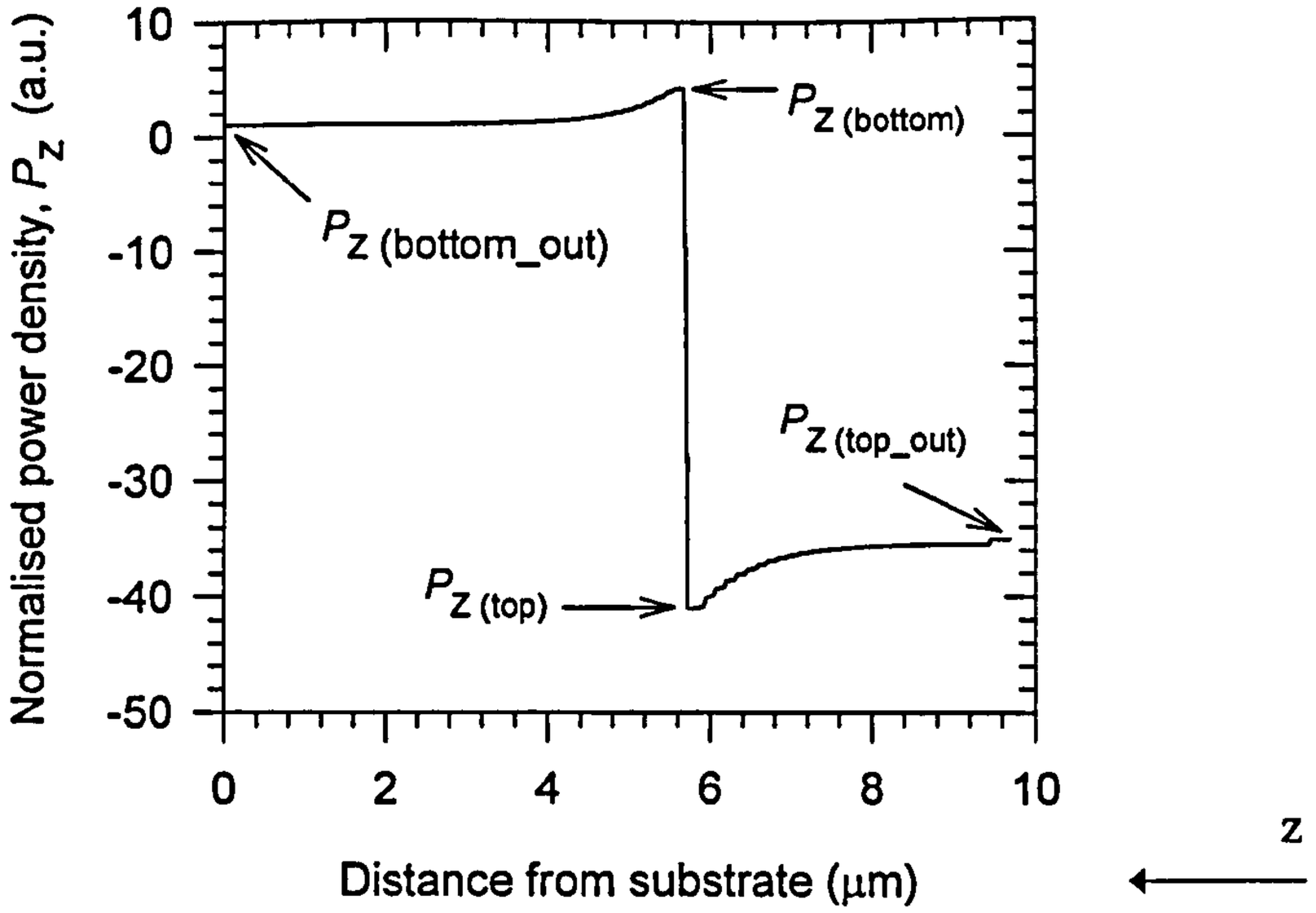

Figure 3.9(a) : Spatial variation of the time averaged power density, P_z across the whole strong guiding VCSEL structure, which is normalised to the value at the boundary between the last layer in bottom DBR and substrate i.e. buffer layers are neglected. The curve was calculated under the condition set by " Case C ".

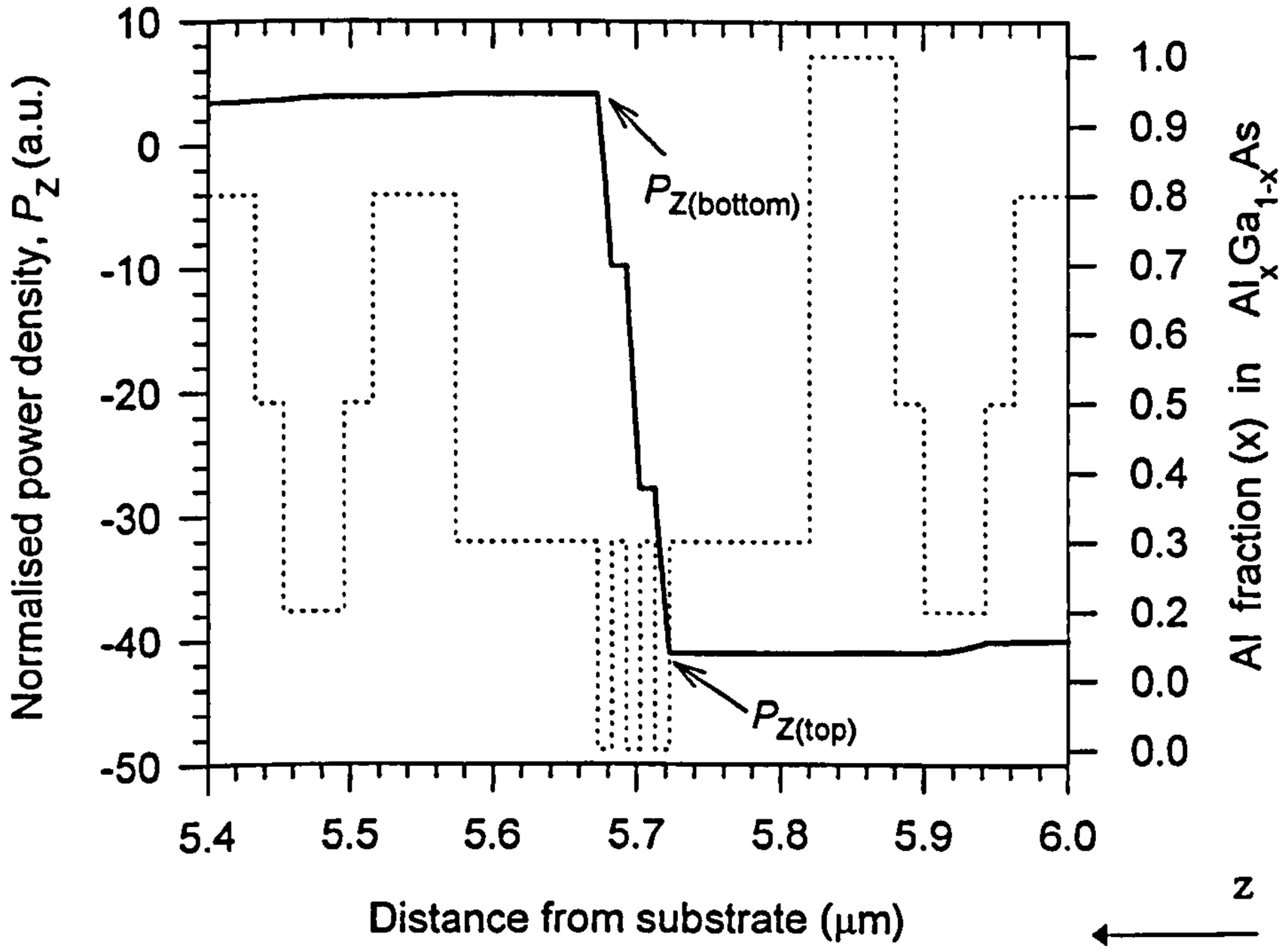

Figure 3.9(b) : Spatial variation of time average power density, P_z in the vicinity of cavity region for the strong guiding VCSEL structure.

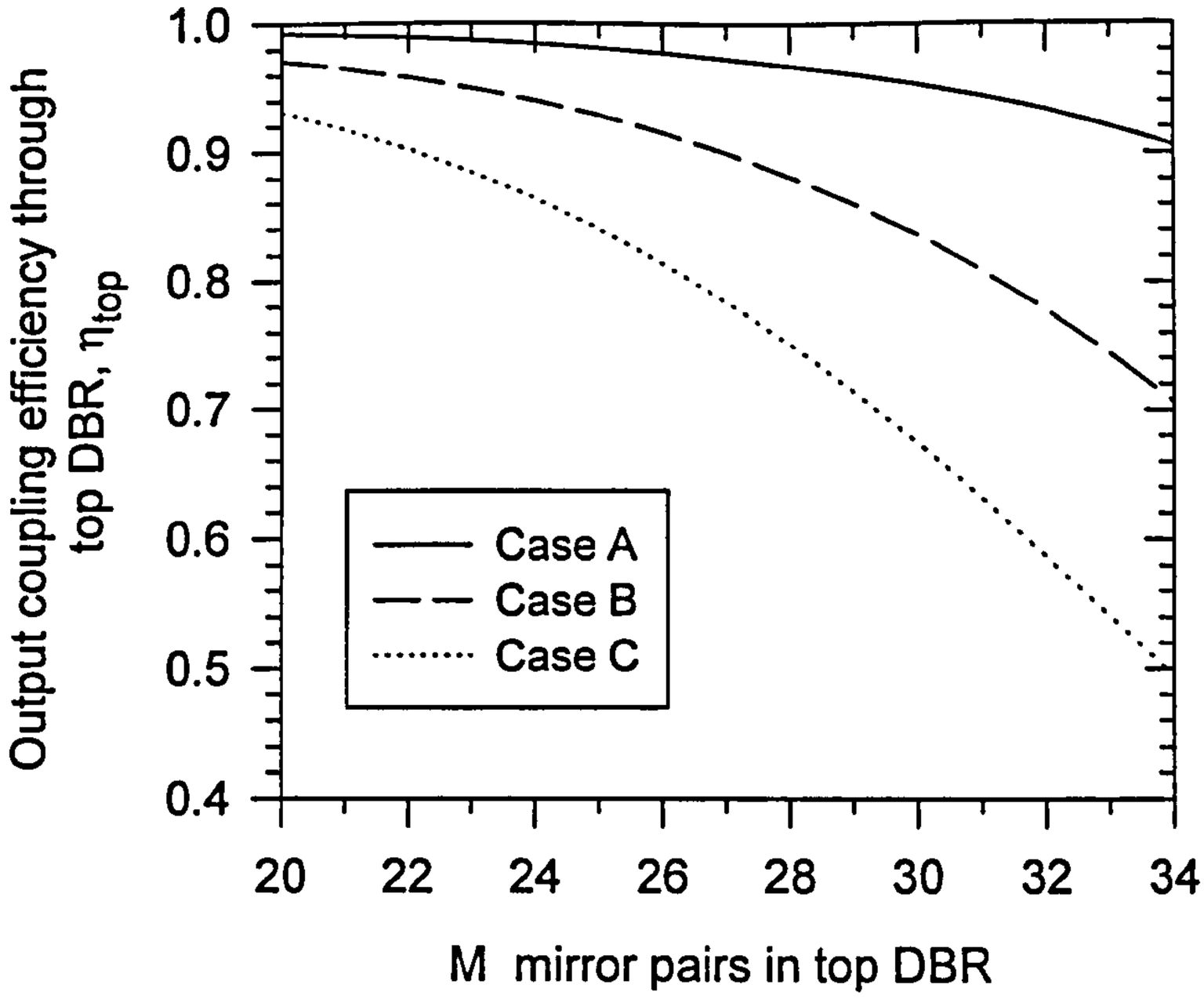

Figure 3.10 : Output coupling efficiencies through top DBR (η_{top}) calculated using eqn.(3.8) for absorption coefficients values set by cases A, B and C, for the strong guiding VCSEL structure.

3.3.3 Transverse Confinement Factor for Stripe Laser made from VCSEL layer

Using the method described in section 2.5, the transverse field variation in a planar multilayer longitudinal waveguide formed from the strong guiding VCSEL material was calculated. Figure 3.11 shows the spatial field variation for the lowest order TE_0 mode ($n_{eff} = 3.325$) guided in such a waveguide together with the refractive index profiles of the $Al_xGa_{1-x}As$ layers. The calculated value of the transverse confinement factor (Γ_t) deduced from this field variation is 9.6%. The highest value for a higher order mode is much smaller at 1.5% for the TE_2 mode, where most of the field energy is spread out into the DBRs rather than being contained within the cavity region. Note that a TE mode is assumed since the GaAs QWs offer higher TE gain than TM gain. In addition, the TE modal reflectivity is also higher at the semiconductor/air interface.

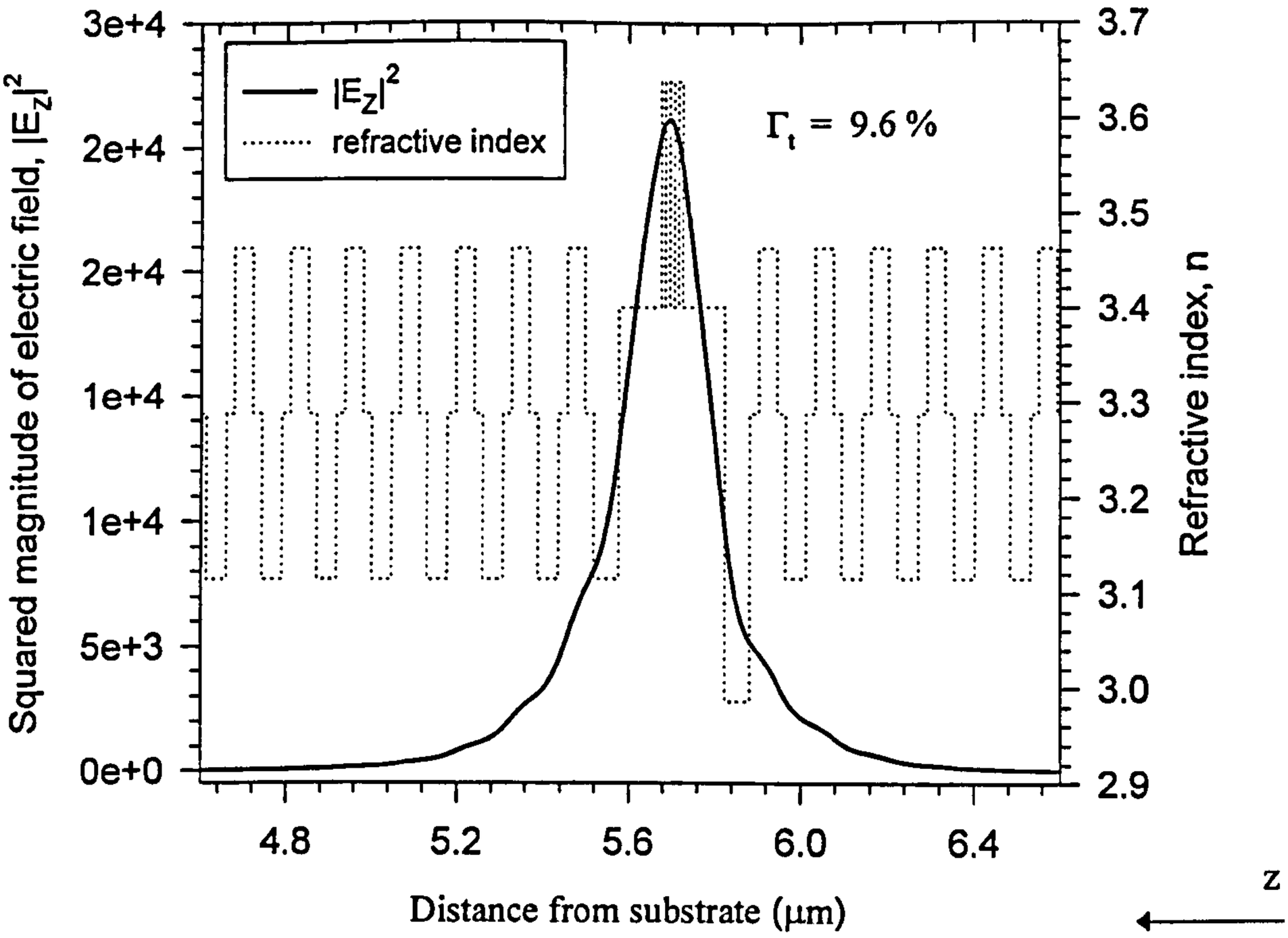

Figure 3.11 : Spatial variation of the transverse electric field of the fundamental TE_0 mode guided by the multilayer waveguide made from VCSEL structure of "strong guiding" design.

3.4 Assessments of Broad Area Devices

Broad area devices are useful for extracting some of the parameters used in VCSEL simulations. From in-plane stripe lasers, the gain-current relation, the internal quantum efficiency, and the gain peak wavelengths can all be estimated. For the broad area (>10μm diameter/size) oxide apertured VCSELs, where size dependent diffraction losses are negligible, the absorption loss in the DBRs can also be estimated.

3.4.1 Broad area in-plane stripe lasers

Using the VCSEL material from the "strong guiding" layer, broad area (60μm metal stripe width) in-plane stripe lasers with various cleaved cavity lengths had been made and assessed under pulsed conditions (1μs pulse length, 10kHz repetition rate).

Figure 3.12 illustrates the variations of the inverse differential quantum efficiency ($1/\eta_{ext}$) with cavity length (L_C) measured at just above threshold.

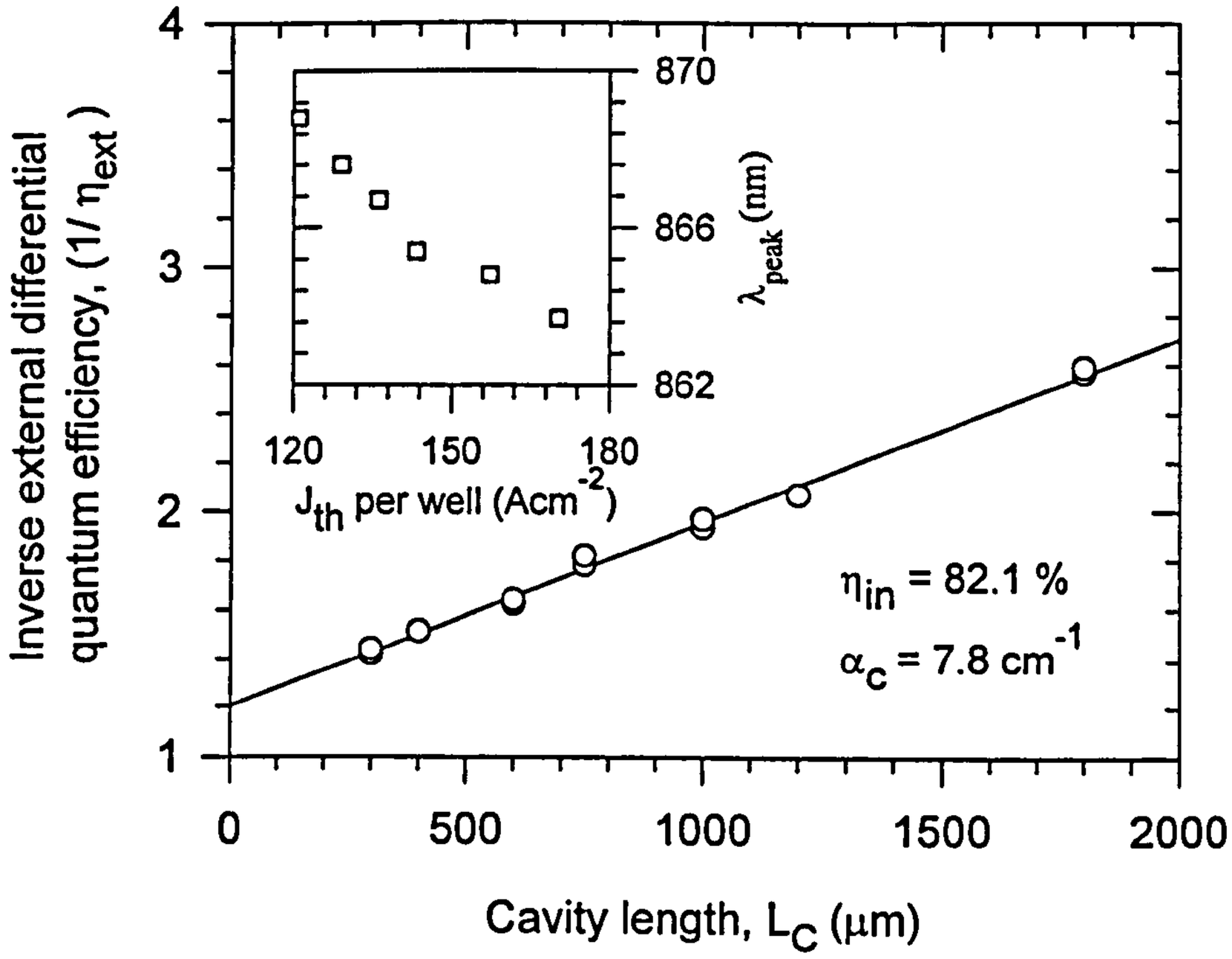

Figure 3.12 : Variation of inverse external differential quantum efficiency vs. cavity length of broad area in-plane stripe laser made from strong guiding VCSEL material. The inset shows the gain peak wavelength as a function of threshold current density per-well.

From equation (2.51) discussed in section 2.4.2, the inferred values of internal quantum efficiency (η_{int}) and cavity optical loss (α_C) from the slope and intercept of the fitted curve are 0.821 and 7.8 cm^{-1} respectively where R = 0.29 was assumed. The inset of the figure also shows the corresponding lasing wavelengths which can assumed to be the gain peak wavelength for various injection current density per-well. Obviously, the blue shift in the gain peak wavelength slows down with increasing injection current density as the band-tail states are filled up and bandgap re-normalisation comes into play. At an injection current density of about 500 A/cm^2 per-well (i.e. predicted value at threshold for the VCSELs designed), the gain peak wavelength should thus be below 863nm.

Using the experimental values of η_{int} and α_C, the relation of experimental peak gain (g_{peak}) vs. radiative current density ($J_{rad} = \eta_{int} J_{th}$) for a single QW can also be deduced from

$$g_{peak} = \frac{1}{\Gamma_t}\left[\alpha_C + \frac{1}{L_C}\ln\left(\frac{1}{R}\right)\right] \qquad (3.10)$$

where Γ_t is the calculated transverse confinement factor. Figure 3.13 shows both the experimental and the theoretical curves of g_{peak} vs. J_{rad}. The theoretical curve was calculated assuming $J_{rad} = BN^2$ where $B = 10^{-10}$ cm^3/s and the relation between g_{peak} and N was deduced from eqn.(3.5).

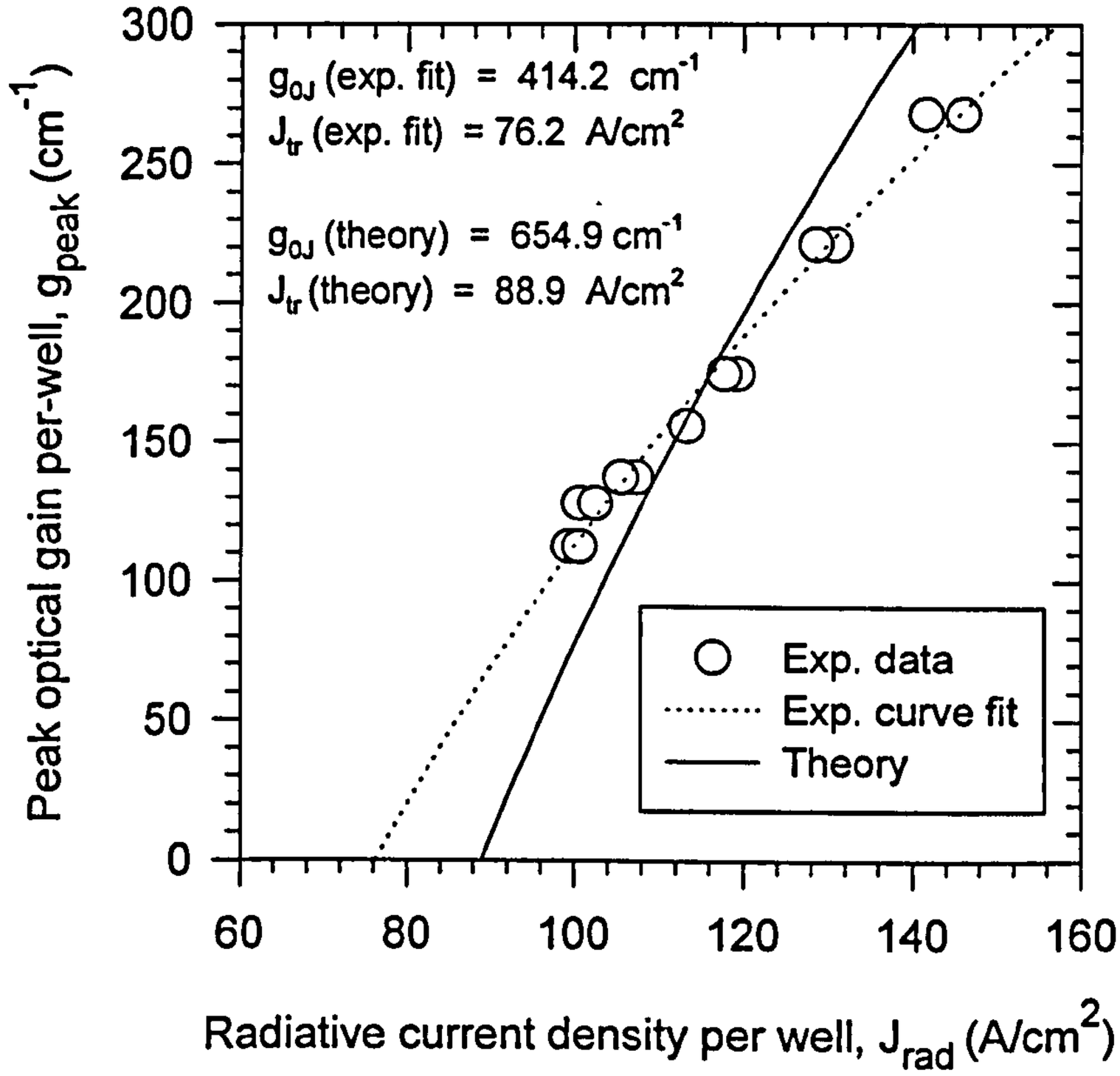

Figure 3.13 : Plots of peak gain vs. radiative current density (per well), inferred from experimental results and theoretical calculations.

The two curves were then fitted using the 2-parameter logarithmic relation expressed by eqn.(2.47). These yield a lower gain coefficient $g_{0J(rad)}$ for the experimental fit (414.2 cm^{-1}) than that from the theoretical prediction (654.9 cm^{-1}). The experimentally determined radiative transparency current density $J_{tr(rad)}$ of 76.2 A/cm^2 is also lower than the expected value or 88.9 A/cm^2. Although not a perfect match, this comparison does show that the theoretical values assumed are in the right range. The reason for the lower experimentally deduced $J_{tr(rad)}$ could be due to the reduction in the total spontaneous recombination rate, caused by the inhibition of spontaneous emissions in the vertical direction and/or the photon recycling effect [23].

This would cause an increase in effective carrier lifetime and a corresponding decrease in radiative current. As for the lower experimental value of gain coefficient, it could be because the modal facet reflectivity and/or the transverse confinement factor are lower than that assumed.

It should also be noted that the experimental g_{peak} vs. J_{rad} curves in Figure 3.13 were plotted under the assumption that the internal quantum efficiency at sub-threshold (also referred to as the radiative efficiency [24]) is similar to that above threshold (also called the "differential" internal quantum efficiency [24]). Strictly speaking, this is not true since both radiative and non-radiative currents are dependent on the injected carrier density and the regime of laser operation. In reference [24] where a more sophisticated method has been employed to determined η_{int} , the experimental results indicate that the value for below-threshold internal quantum efficiency could be about 5% lower than that above threshold. It also suggests that current spreading and recombination in the barriers are the major reasons for $\eta_{int} < 1$ above threshold, which otherwise would approach unity since the carrier density in the QWs is approximately pinned yielding a radiative efficiency of >98%. Bearing this uncertainty in mind, the simple method presented here does provide a way for checking the gain peak wavelength and the lasing quality of the quantum wells.

3.4.2 Broad area VCSELs

As will be shown in Chapter 5, oxidised VCSELs with large aperture sizes (>10μm) suffer from negligible size dependent optical diffraction loss and thus their modal reflectance are almost identical to the value of plane-wave (1-D) reflectivity. In order to estimate absorption losses in the DBRs, the threshold current densities and external differential quantum efficiencies of these broad area VCSELs (about 15um near-square device size) have been measured under pulsed condition using a shorter pulse length of 40ns and a 50kHz repetition rate. The devices chosen for assessments have lasing wavelengths of about 865-866nm, close enough to the projected gain peak wavelength. The average threshold current densities are found to be (1.62 ± 0.04) kA/cm^2, (1.48 ± 0.04) kA/cm^2 and (1.39 ± 0.04) kA/cm^2 respectively for the strong, medium and weak guiding devices respectively. The corresponding average external differential quantum efficiencies are 41.3%, 45.0% and 48.4%. Obviously, these values are quite different from those predicted in section 3.3.2. Results from polaron

profiling performed on these wafers [25] shows that the doping concentration in the p-DBR fluctuates between 2 x10^{18} to 6x10^{18} cm^{-3} as compared to the expected value of 3 x 10^{18} cm^{-3}. These fluctuations also seems to be more serious in the strong guiding wafer, which may explain why its efficiency and threshold are slightly inferior to other wafers. During the wafer growth, while the $Al_{0.2}Ga_{0.8}As$ and $Al_{0.5}Ga_{0.5}As$ layers in p-DBR were intentionally carbon doped, the aluminium rich p-$Al_{0.8}Ga_{0.2}As$ layers were unintentionally doped due to the presence of intrinsic carbon background doping of 2x10^{18} to 3x10^{18} cm^{-3} from the decomposition of the metal organic precursor [6]. Thus it is likely that the polaron profiling results indicate the p-$Al_{0.2}Ga_{0.8}As$ and p-$Al_{0.5}Ga_{0.5}As$ layers have about twice the doping concentration expected. For the n-type bottom DBR which was Si doped, the polaron profiling results (not so accurate now since the etched depth needed to penetrate well into the stacks) shows that the doping concentrations are about as expected at between 1.5x10^{18} to 2x10^{18} cm^{-3}.

By doubling the power absorption coefficients for the p-$AlGa_{0.2}Ga_{0.8}As$ and p-$Al_{0.5}Ga_{0.5}As$ layers in the simulation under condition set by case C, the recalculated value of output coupling efficiency η_{top} becomes about 70.2% for the strong guiding design. Assuming that the experimental value of η_{int} determined from the broad area in-plane stripe lasers is also applicable to the VCSELs made from same wafer, the predicted external differential quantum efficiency (i.e. $\eta_{int}\eta_{top}$) for the strong, medium and weak guiding devices becomes 57.7%, 57.8% and 58.0% respectively, which are still higher than the measured values for these three wafers. Recognising the possibility that the free carrier absorption losses might have been underestimated in section 3.3 due to the lack of information, it is found that the theoretical values of η_{ext} only match closely the experimental values when all the absorption losses are scaled up by a factor of 2.4, 2.0 and 1.7 correspondingly. Using these new absorption values in the analysis in section 3.3.2, the new predicted threshold current densities calculated assuming $J_{th} = J_{rad}/\eta_{int}$ are now 1.67 kA/cm^2, 1.50 kA/cm^2, 1.41 kA/cm^2 for the strong, medium and weak guiding layers respectively, reasonably close to their corresponding measured values. However, the other predicted values calculated simply by $J_{th} = J_{rad(th)} + J_{nr(th)}$ are slightly higher at 1.88 kA/cm^2, 1.72 kA/cm^2 and 1.63 kA/cm^2 respectively.

The new values of absorption coefficients in the DBRs inferred from the experimental results of broad area devices discussed above, will be used later in

chapter 5 for numerical calculations of the modal reflectance of the DBRs and the expected threshold current densities as a function of aperture size. Using eqn (5.14) or eqn. (2.52) (assuming the cavity is absorption free) as well as the inferred internal quantum efficiency, the predicted external differential quantum efficiency of the 15μm square devices are 41.1%, 44.7% and 48% for the strong, medium and weak guiding layers respectively. For circular apertured devices of equivalent area (i.e. 225 μm^2), the corresponding expected values of threshold current densities (calculated through solutions of rate equations) are 1.66 kA/cm^2 , 1.54 kA/cm^2 and 1.46 kA/cm^2. Since these values are quite close to the measured values, the assumed values of B = 10^{10} $cm^{-3}s^{-1}$ and τ_{nr} of 5ns in the simulations can thus be considered realistic in this typical injection current range for a VCSEL.

3.5 Summary

Based on the expected values of doping concentrations in the DBRs, the threshold current density and the output coupling efficiency of the three broad area VCSEL structures used in this work, namely the strong guiding (≈ 600Å thick aperture), medium guiding (≈ 350Å thick aperture) and weak guiding (≈ 200Å thick aperture) designs, are predicted using the numerical methods for plane wave lasing properties described in chapter 2. However, it is later found that the actual absorption coefficients in the DBRs are higher than expected, as deduced from the preliminary experimental results obtained from broad area stripe lasers and oxidised VCSELs. By recalculating the theoretical values such that they match the experimental inferred values, new values of absorption coefficients in the stacks are inferred. These values are adopted for the calculation of the modal reflectance of various eigenmodes in chapter 5.

Chapter 3 References

[1] M.Born and E.Wolf, "Principles of Optics" (Pergamon 1984).

[2] S.Adachi, "GaAs, AlAs and $Al_xGa_{1-x}As$: Material parameters for use in research and device applications", J.Appl. Phys., vol.58, pp.R1-R29.

[3] S.Adachi, "Optical properties of AlGaAs : Table (0.5-6.0 eV)", Emis Datareview series No.2, August 1989

[4] T.E.Sale, "Vertical cavity surface emitting lasers",(Research Studies Press Ltd., England, 1995).

[5] K.D.Choquette, K.M.Geib, C.I.H.Ashby, "Advances in selective set oxidation of AlGaAs alloys", IEEE Journal of Selected Topics in Quantum Electronics, vol.3, pp.916-926, June 1997

[6] J.S.Roberts, *private communication*.

[7] S.A.Chalmers, K.L.Lear and K.P.Killeen, "Low resistance wavelength reproducible p-type AlGaAs DBR grown by molecular beam epitaxy", Appl. Phys. Lett., vol.62, pp.1585-1587, April 1993.

[8] K.L.Lear and R.P.Schneider, Jr., "Uniparabolic mirror grading for vertical cavity surface emitting lasers", Appl. Phys. Lett.,vol.68, pp.605-607, Jan 1996.

[9] S.L.Chuang, "Physics of Optoelectronics Devices", (John Wiley & Sons, NY)

[10] B.Weigl, M.Grabherr, C.Jung, R.Michalzik and K.J.Ebeling, "High Performance Oxide Confined GaAs VCSELs", IEEE J. of Selected Topics in Quantum Electronics, Vol.3, pp. 409-414, 1997.

[11] G.R.Hadley, "Effective index model for vertical cavity surface emitting lasers", Optics Lett., vol.20, pp.1483-1486, 1995.

[12] P.Bhatacharya, "Semiconductor Optoelectronic Devices", (Prentice-Hall, New Jersey ,1994)

[13] H.C.Casey, D.D.Sell and K.W.Wecht, "Concentration dependence of the absorption coefficient for n and p type GaAs between 1.3 and 1.6 eV", J. of Applied Physics, Vol. 46, No.1, pp.250-257, Jan 1975.

[14] H.C.Casey and M.B.Panish, "Heterostructure Lasers Part A : Fundamental Principles", (Academic Press 1978)

[15] Y.H.Chen, "AlGaInP/AlGaAs Visible Vertical Cavity Surface Emitting Lasers", Ph.D thesis, Univ. of Sheffield, 1996.

[16] J.Saito and K.Kondo, "High temperature growth of Si-doped AlGaAs by molecular beam epitaxy", J.Vac. Sci. Technol. B, Vol. 6, pp.1264-1269, 1990.

[17] S.F.Yu, "Theoretical analysis of polarisation bistability in vertical cavity surface emitting semiconductor lasers", J. of Lightwave Technology, Vol.15, pp.1032-1041, 1997.

[18] M.Whitehead, "Optimisation of normal incidence GaAs-AlGaAs multiple quantum well optical modulators", Ph.D thesis, Univ. College London, 1990,

[19] G.P.Agrawal and N.K.Dutta, "Semiconductor Lasers", (Van Nostrand Reinhold, NY, 1993)

[20] R.Olshansky, C.C.Su and W.Powazinik, "Measurement of radiative and nonradiative recombination rates in InGaAsP and AlGaAs light sources", IEEE J. of Quantum Electronics, Vol.20, pp.838 - 854, 1984.

[21] P.Blood, E.Dennis, K.Woodbridge and A.R.Adams, "Influence of barriers on the temperature dependence of threshold current in GaAs/AlGaAs Quantum well lasers", IEEE J. of Quantum Electronics, vol.25, pp.1459-1467, 1989.

[22] M.Takeshima, "Effect of Auger recombination on laser operation in $Ga_{1-x}Al_xAs$", J.Appl.Phys., vol.58, pp.3846-3848, 1985.

[23] F.Yang and P.Blood, "Edge-emitting quantum well laser with Bragg reflectors", Appl. Phys. Lett., vol.66, pp. 2949-2952, 1995.

[24] P.M.Smowton and P.Blood, "The differential efficiency of quantum well lasers", IEEE J. of Selected Topics in Quantum Electronics, vol.3, pp. 491 - 498, 1997.

[25] J.Roberts, *Growth reports for wafers QT1084R, QT1089R and QT1092.*

Chapter 4 Scalar Variational Method for Oxide Apertured VCSELs

4.1 Introduction

In this chapter, the scalar variational method for calculating the resonant frequencies/wavelengths as well as the mode sizes of the eigenmodes guided by an oxide apertured VCSEL is discussed. It begins with the derivation of the general scalar variational formula for a resonator. Next, under the assumption of a Hermite-Gaussian transverse field variation , the scalar variational formulae for circular, square and rectangular oxide apertured resonators are derived. Then, the theoretical predictions on the eigenmode frequencies and mode sizes of the three VCSEL layers used in this work are presented. Finally, comparisons are made between the relevant theoretical and experimental results.

4.2 Variational Methods for Mode Sizes and Resonant Wavelengths

Variational methods [1-3] have been used for many years in various engineering disciplines, particularly in the microwave engineering field for determining characteristics quantities such as resonant frequency, impedance, etc. In contrast to other integration-formulae based approaches such as perturbation techniques, the variational procedure gives an approximation to the desired quantity itself rather than to changes in the quantity. When used to solve an electromagnetic field problem, the variatonal formula is relatively insensitive to variations in an assumed trial field about the correct field. Thus, the variational formula is said to be "stationary" about the correct solution [1-2]. If the desired quantity is real, the solution given by the variational formula will be either an upper or lower bound to the quantity, depending on the form of formula chosen.

4.2.1 Scalar Variational Formula for a Resonant Cavity

In order to derive a scalar variational formula for a resonant cavity enclosing an inhomogeneous region of dielectric in the rectangular co-ordinate system, the scalar wave equation for electric field E, given by (2.13) in section 2.1, is first scalar multiplied by the E field. The resulting equation is volume integrated throughout the entire resonator volume V. Rearranging, the following expression is obtained

$$-\frac{\omega^2}{c^2}\iiint_V n^2E^2\,dxdydz = \iiint_V E\left(\frac{\partial^2E}{\partial x^2}+\frac{\partial^2E}{\partial y^2}+\frac{\partial^2E}{\partial z^2}\right)dx\,dy\,dz \qquad (4.1)$$

where the trial E field and the refractive index n are functions of position within the integrated volume, i.e. E(x,y,z) and n(x,y,z). To proceed further, the following scalar identity [1] are needed :

$$E\frac{\partial^2E}{\partial i^2} = \frac{\partial}{\partial i}\left(E\frac{\partial E}{\partial i}\right)-\left(\frac{\partial E}{\partial i}\right)^2 \qquad (4.2)$$

where i can be x, y or z. Then, equation (4.1) becomes

$$-\frac{\omega}{c^2}^2\iiint_V n^2E^2\,dxdydz = -\iiint_V\left(\frac{\partial E}{\partial x}\right)^2+\left(\frac{\partial E}{\partial y}\right)^2+\left(\frac{\partial E}{\partial z}\right)^2 dxdydz \qquad (4.3)$$

provided the integral

$$\int\frac{\partial}{\partial i}\left(E\frac{\partial E}{\partial i}\right)di = 0 \qquad (4.4)$$

vanishes at the resonator boundary [1]. This is the case for all the geometries to be considered in the following sections. From (4.3), the scalar variational integral formula for the resonant frequency ω of the resonator is then given by

$$\frac{\omega^2}{c^2} = \frac{\iiint_V\left[\left(\frac{\partial E}{\partial x}\right)^2+\left(\frac{\partial E}{\partial y}\right)^2+\left(\frac{\partial E}{\partial z}\right)^2\right]dxdydz}{\iiint_V n^2E^2\,dxdydz} \qquad (4.5)$$

This expression will provide an upper bound for ω if the trial electric field satisfies the necessary boundary conditions [4]. Hence, the best trial field is the one that minimises ω^2/c^2. The proof of the stationary property of this scalar variational integral is detailed in ***Appendix C***.

4.2.2 Scalar Variational Formulae for Circular Oxide Apertured VCSELs

Figure 4.1 shows the cross-sectional schematic of the "passive-cavity" (i.e. no active medium in the cavity) oxide apertured resonator under consideration, together with the chosen co-ordinate system. In order to simplify the analysis, it is assumed that the resonator is terminated by infinitely long DBRs extending many wavelengths in the transverse (x,y) directions. This is a sufficiently good assumption for VCSELs utilising highly reflective DBRs that are considered here. The top and bottom DBRs are also assumed to be identical and made up by pairs of $Al_{0.2}Ga_{0.8}As/Al_{0.8}Ga_{0.2}As$ "plane" quarter-wave stacks (at free space wavelength λ_0), with their refractive indices and thickness denoted by n_1, n_2 and $L_1(= \lambda_0/4n_1)$, $L_2(= \lambda_0/4n_2)$ respectively. (Note: although the bottom DBR of the real VCSEL structure is made up of two different paired combinations, most of the electromagnetic energy is contained within the first 15 pairs which are of $Al_{0.2}Ga_{0.8}As/Al_{0.8}Ga_{0.2}As$, as can be seen from Fig.3.8(a)) The oxide aperture of diameter 2a, has thickness d_{ox} and refractive index n_{ox}. It is placed within the first layer of the top DBR, at a distance *l* from the antinode of the standing wave formed at the cavity - top DBR interface. The "passive" $Al_{0.3}Ga_{0.7}As$ cavity has a physical length of L_c and refractive index n_c, i.e. there is no gain medium inside the cavity. Hence, strictly speaking, the variational formulae to be derived in the following is for a "cold cavity" [6] resonator, a term used to emphasise the absence of optical gain within the cavity.

It can be deduced from (2.18) to (2.21) that in the plane wave approximation, the scalar tangential electric field variations in the absorption free quarter-wave DBR stacks are expressed by

$$ {}^{2}E_q(z) = E_0\left[\left(-\frac{n_2}{n_1}\right)^{q-1}\cos(\beta_2 z) - j\left(-\frac{n_1}{n_2}\right)^{q-1}\frac{Y_M}{n_2}\sin(\beta_2 z)\right] \qquad (4.6a) $$

in the q^{th}-pair stacks with refractive index n_2, and

$$ {}^{1}E_q(z) = E_0\left[\left(-\frac{n_2}{n_1}\right)^{q}\sin(\beta_1 z) - j\left(-\frac{n_1}{n_2}\right)^{q-1}\frac{Y_M}{n_2}\cos(\beta_1 z)\right] \qquad (4.6b) $$

in the q^{th}-pair stacks with refractive index n_1 where $n_1>n_2$, z is distance from the start of each layer and E_0 is the field at entry to DBR. For large number pairs of stacks, the value of the normalised characteristic admittance Y_M of the whole DBR given by $n_s(n_2/n_1)^{2q}$, is very small. Thus, under the assumption of an infinitely long DBR, the field variations in the stacks are solely given by the real terms in equations (4.6a) and

(4.6b). This means that for quarter-wave DBR stacks, the amplitudes of the field at the m^{th} antinode interface is given by $E_0(n_2/n_1)^m$ whereas the fields are zero at all the node positions, as defined schematically in Fig. 4.1(a). Fig 4.1(b) shows the schematic of the cross-sectional view of a circular oxide apertured device with some of the parameters defined in Fig. 4.1(a).

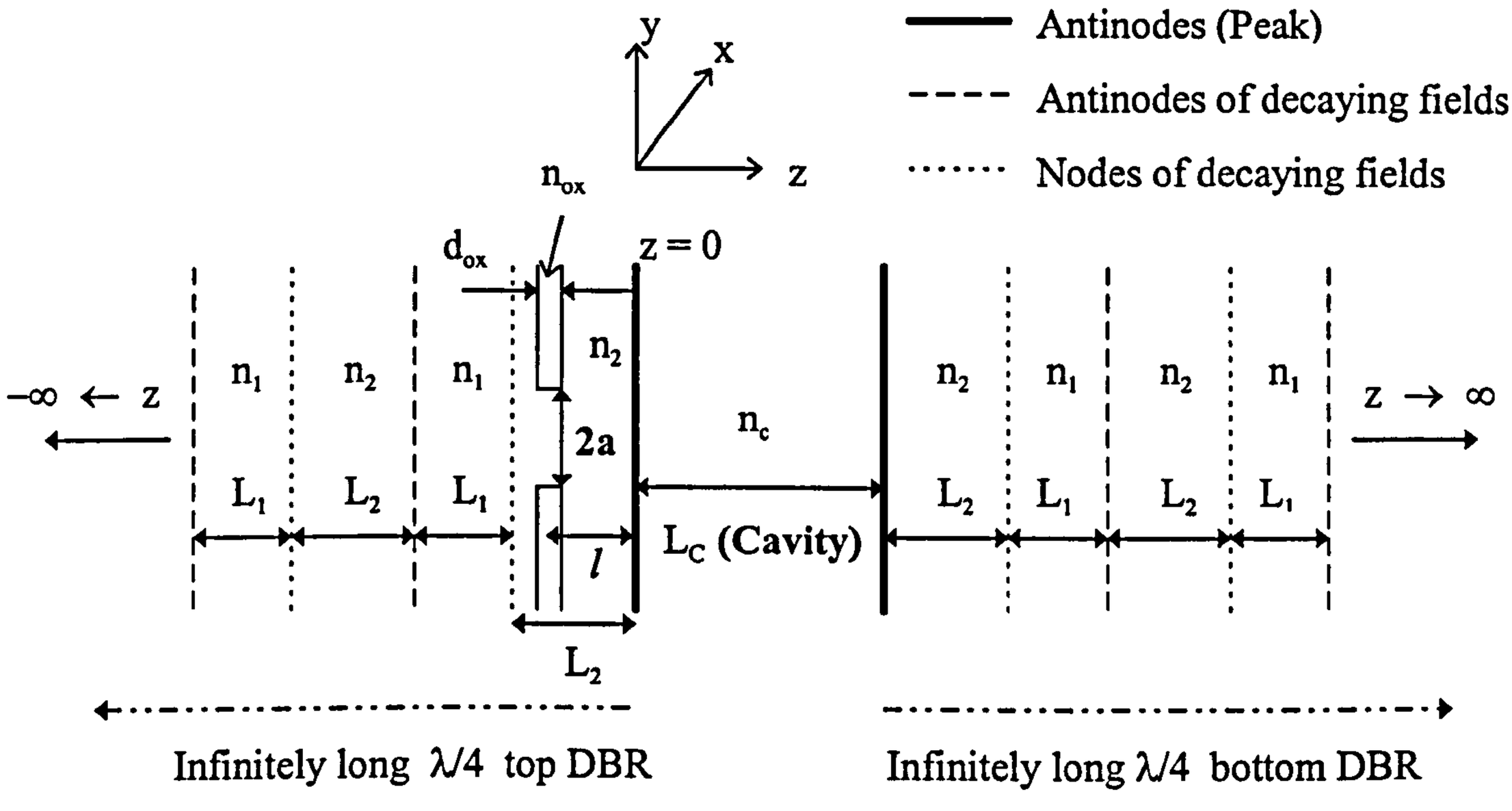

Figure 4.1(a) : Schematic illustration showing the important parameters for the dielectric apertured resonant cavity and the assumed co-ordinate system. Note that the legends on the top right corner of the figures indicate the positions of the antinodes and nodes that occur at the interfaces.

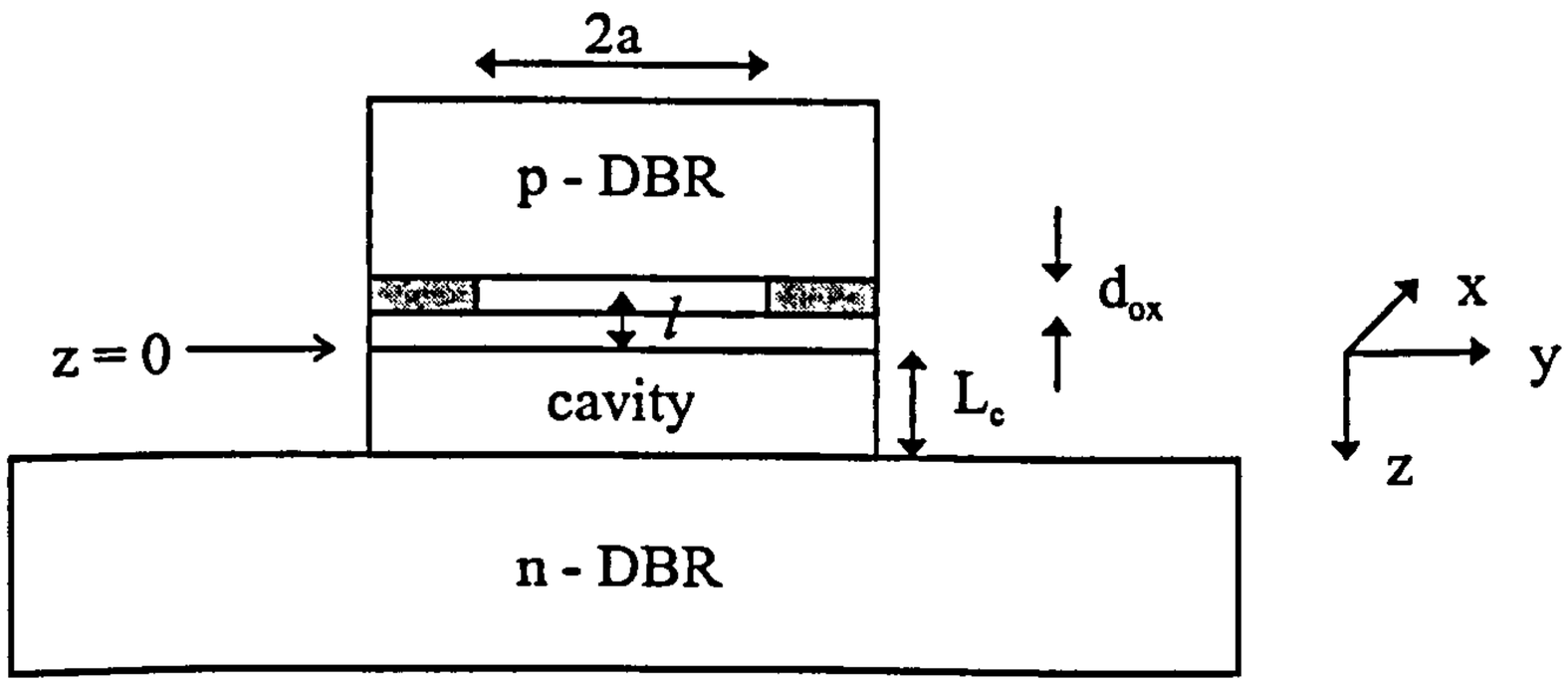

Figure 4.1(b) : Schematic illustration of the cross-sectional view of a circular oxide apertured device with some of the parameters defined in Fig. 4.1(a).

The transverse variations for the trial fields used in the variational formulae, in the presence of an oxide aperture, are chosen to be of the Hermite-Gaussian form [5]. For circular apertured resonators, the trial fields for the first four lowest order *circular* Hermite-Gaussian modes (TEM_{mp}) for $m, p \leq 1$, normalised to E_0, are given by

$$E_{mp} = x^m y^p \exp\left(-\frac{x^2+y^2}{w_{mp}^2}\right) \begin{cases} \cos(\beta_c z) & \text{in the cavity} \\ \left(-\frac{n_2}{n_1}\right)^{q-1} \cos(\beta_2 z) & \text{in the } q^{th} \text{ pair stacks with } n_2 \\ \left(-\frac{n_2}{n_1}\right)^{q} \sin(\beta_1 z) & \text{in the } q^{th} \text{ pair stacks with } n_1 \end{cases} \tag{4.7}$$

where z is distance from the start of each layer. The symbol w_{mp} is usually referred to as the 1/e beam spot size or 1/e half mode width, and the mode numbers (m,p) represent the number of zeros or intensity nulls in the (x,y) directions respectively. The Guoy phase shift term and z-dependent change of beam size [6] are not included in (4.7) as these are negligible for the short cavity length under consideration. The longitudinal propagation constants are given by $\beta_c = k_0 n_c$ within the cavity and $\beta_1 = k_0 n_1$ or $\beta_2 = k_0 n_2$ in the mirror stacks where k_0 ($= 2\pi / \lambda_0$) is plane wave number of the resonator, i.e. λ_0 may be considered as the plane wave resonant wavelength (in free space) of the structure in Fig. 4.1 with $n_{ox} = n_2$. It should be noted that this type of transverse field distributions has been found to match closely the modal patterns of VCSELs observed experimentally in this work as well as by other researchers [7]. Moreover, they are the near exact solutions to the paraxial wave equation and they form an orthogonal set which is particularly convenient to integrate in closed form. Furthermore, their modal patterns are also quite similar to those of the linearly polarised LP_{lm} modes used by other researchers in the modal simulation of gain (weakly) guided VCSELs [8] or the hybrid EH_{lm} / HE_{lm} and TE_{0n}, TM_{0m} modes (i.e. nomenclature for step index fiber modes) for the simulation of air-post index guided VCSELs [9]. In these cases, the field variations are described by the Bessel and Hankel functions [5] while *l* and *m* denote the azimuthal and radial orders respectively.

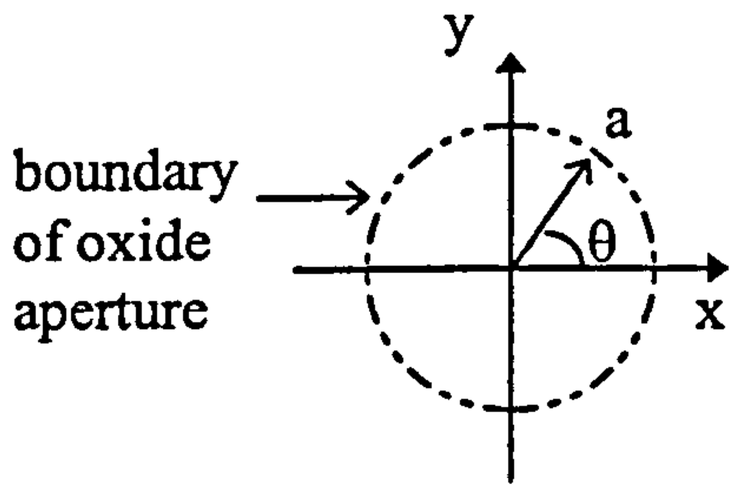

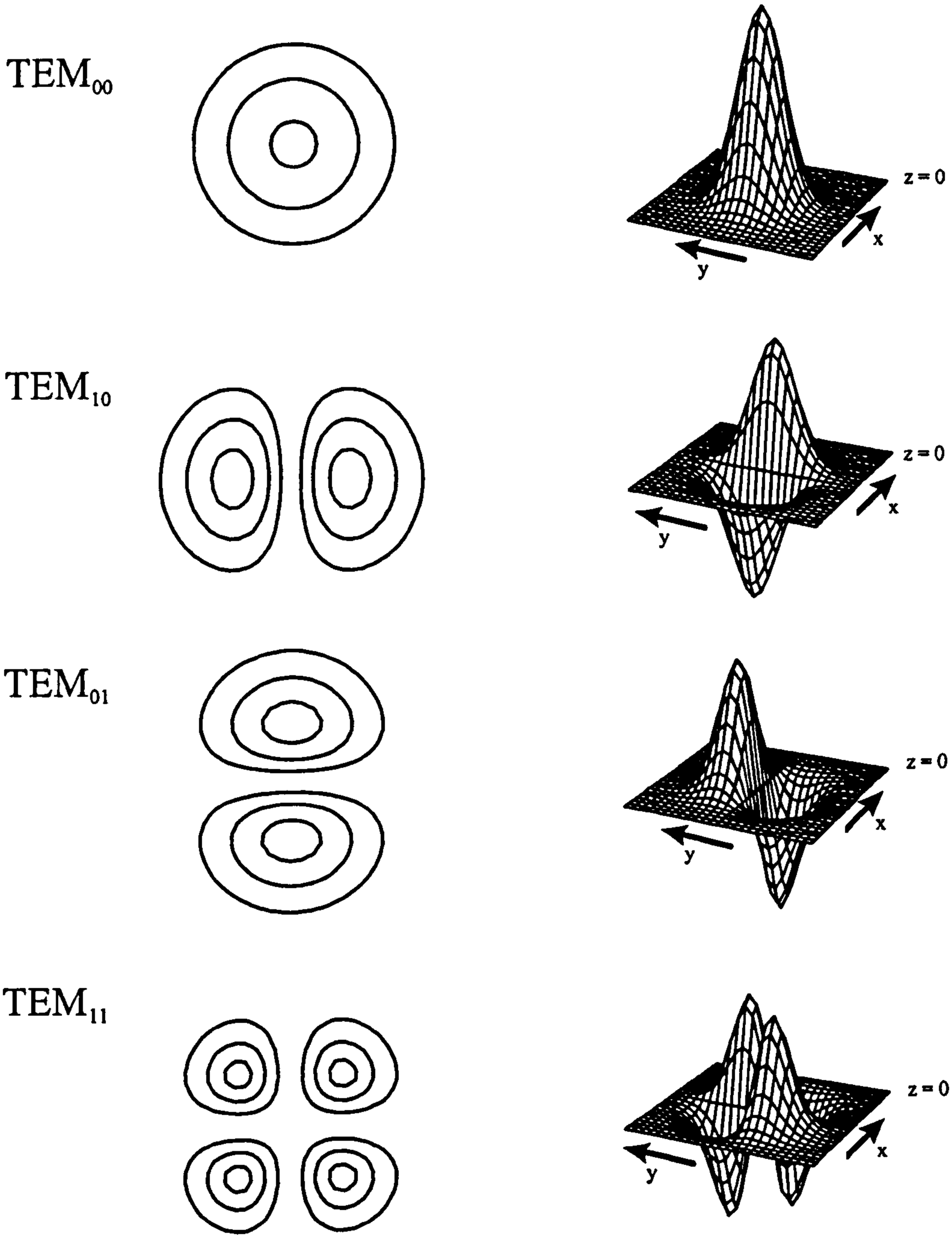

Figure 4.2 : Intensity contour patterns and 2-D transverse field variations of the first four lowest order ***circular*** Hermite - Gaussian modes, together with the information on the dielectric aperture.

Under the scalar approximation assumed here, the modal solutions from (4.7) for TEM_{mp} modes linearly polarised in either the x or y direction are similar. The 2D transverse field variations and intensity contour patterns of these *circular* Hermite-Gaussian modes are illustrated in Figure 4.2. The TEM_{00} mode can be viewed as similar to the LP_{01} or HE_{11} modes, while TEM_{01} and TEM_{10} modes are similar to the LP_{11} or HE_{21} mode, and TEM_{11} is similar to the LP_{21} or linear combination of HE_{31} and EH_{11} modes [5]. Subsequently, by substituting the trial field distribution for a particular eigenmode from (4.7) into (4.5), the resonant frequency (and thus resonant wavelength) can be obtained through minimisation of the values obtained from (4.5). This can be done by searching for the mode size w_{mp} that results in the lowest values of ω. This procedure will yield the resonant wavelength and mode size of that particular eigenmode for a given aperture size.

Due to the difference in the propagation constants β_1, β_2 and β_c, the scalar variational integral given by (4.5) has to be evaluated separately for the cavity and DBR regions. The numerator of (4.5) is thus given by

$$\text{numerator} = \iiint_{\text{cavity}} \left[\left(\frac{\partial E}{\partial x}\right)^2 + \left(\frac{\partial E}{\partial y}\right)^2 + \left(\frac{\partial E}{\partial z}\right)^2 \right] dV + 2 \iiint_{\text{DBR}} \left[\left(\frac{\partial E}{\partial x}\right)^2 + \left(\frac{\partial E}{\partial y}\right)^2 + \left(\frac{\partial E}{\partial z}\right)^2 \right] dV \tag{4.8}$$

where the volume element dV = dxdydz. Beginning with the fundamental circular TEM_{00} mode for circular apertured VCSELs, the differential components of the numerator *inside the cavity* are given by

$$\left(\frac{\partial E}{\partial x}\right)^2 = \frac{4x^2}{w_{00}^4} \exp\left(\frac{-2x^2 - 2y^2}{w_{00}^2}\right) \cos^2(\beta_c z) \tag{4.9}$$

$$\left(\frac{\partial E}{\partial y}\right)^2 = \frac{4y^2}{w_{00}^4} \exp\left(\frac{-2x^2 - 2y^2}{w_{00}^2}\right) \cos^2(\beta_c z) \tag{4.10}$$

$$\left(\frac{\partial E}{\partial z}\right)^2 = \beta_c^2 \exp\left(\frac{-2x^2 - 2y^2}{w_{00}^2}\right) \sin^2(\beta_c z) \tag{4.11}$$

By making use of the integral solutions (D.1) and (D.3) of the Gaussian functions listed in ***Appendix D***, the volume integral for the cavity region is found to be

$$\int_0^{L_c}\int_{-\infty}^{\infty}\int_{-\infty}^{\infty}\left[\left(\frac{\partial E}{\partial x}\right)^2+\left(\frac{\partial E}{\partial y}\right)^2+\left(\frac{\partial E}{\partial z}\right)^2\right]_{cavity} dxdydz$$

$$= \frac{L_c}{2}\left[2\left(\frac{4}{w_{00}^4}\right)\left(\sqrt{\frac{\pi}{2}}w_{00}\right)\left(\frac{1}{4}\sqrt{\frac{\pi}{2}}w_{00}^3\right) + \beta_c^2\left(\sqrt{\frac{\pi}{2}}w_{00}\right)^2\right] \qquad (4.12)$$

$$= \frac{\pi L_c}{4}\left(2+\beta_c^2 w_{00}^2\right)$$

The integration within the DBR region can be deduced using the relevant expressions in eqn.(4.7). The volume integral originating from the x and y-derivatives of E is given by

$$\int_0^{\infty}\int_{-\infty}^{\infty}\int_{-\infty}^{\infty}\left[\left(\frac{\partial E}{\partial x}\right)^2+\left(\frac{\partial E}{\partial y}\right)^2\right]_{DBR} dxdydz$$

$$= 2\int_{-\infty}^{\infty}\int_{-\infty}^{\infty}\frac{4x^2}{w_{00}^2}\exp\left(\frac{-2x^2-2y^2}{w_{00}^2}\right)dxdy\left\{\left[\int_0^{L_2}\cos^2(\beta_2 z)\,dz+\int_0^{L_1}\left(\frac{n_2}{n_1}\right)^2\sin^2(\beta_1 z)\,dz\right]\sum_{m=0}^{\infty}\left(\frac{n_2}{n_1}\right)^{2m}\right\}$$

$$= 2\left(\frac{4}{w_{00}^4}\right)\left(\sqrt{\frac{\pi}{2}}w_{00}\right)\left(\frac{1}{4}\sqrt{\frac{\pi}{2}}w_{00}^3\right)\left\{\left[\frac{1}{2}\left(\frac{\lambda_0}{4n_2}\right)+\frac{1}{2}\left(\frac{\lambda_0}{4n_1}\right)\left(\frac{n_2}{n_1}\right)^2\right]\left[1-\left(\frac{n_2}{n_1}\right)^2\right]^{-1}\right\}$$

$$= \left(\frac{\pi\lambda_0}{8n_2}\right)\left[1+\left(\frac{n_2}{n_1}\right)^3\right]\left[1-\left(\frac{n_2}{n_1}\right)^2\right]^{-1}$$

(4.13)

where the terms inside the curly bracket result from the integration along the z-axis. The integration of the z-derivative of E results in

$$\int_0^{\infty}\int_{-\infty}^{\infty}\int_{-\infty}^{\infty}\left[\left(\frac{\partial E}{\partial z}\right)^2\right]_{DBR} dxdydz$$

$$= \int_{-\infty}^{\infty}\int_{-\infty}^{\infty}\exp\left(\frac{-2x^2-2y^2}{w_{00}^2}\right)dxdy\left\{\left[\int_0^{L_2}\beta_2^2\sin^2(\beta_2 z)\,dz+\int_0^{L_1}\left(\frac{n_2}{n_1}\right)^2\beta_1^2\cos^2(\beta_1 z)\,dz\right]\sum_{m=0}^{\infty}\left(\frac{n_2}{n_1}\right)^{2m}\right\}$$

$$= \frac{\pi w_{00}^2}{2}\left\{\left[\frac{\pi^2 n_2}{2\lambda_0}+\frac{\pi^2 n_1}{2\lambda_0}\left(\frac{n_2}{n_1}\right)^2\right]\left[1-\left(\frac{n_2}{n_1}\right)^2\right]^{-1}\right\}$$

$$= \frac{\pi^3 w_{00}^2 n_2}{4\lambda_0}\left(1-\frac{n_2}{n_1}\right)^{-1} = \frac{\pi^3 w_{00}^2 n_1 n_2}{4\lambda_0(n_1-n_2)}$$

(4.14)

where again the terms originating from the integration along the z-axis are placed inside the curly bracket. Combining the final expressions in (4.12) to (4.14), the numerator is thus given by

$$\textit{numerator} = \frac{\pi L_c}{4}\left(2+\beta_c^2 w_{00}^2\right) + 2\left\{\left(\frac{\pi\lambda_0}{8n_2}\right)\left[1+\left(\frac{n_2}{n_1}\right)^3\right]\left[1-\left(\frac{n_2}{n_1}\right)^2\right]^{-1} + \frac{\pi^3 w_{00}^2 n_1 n_2}{4\lambda_0(n_1-n_2)}\right\}$$

$$= \frac{\pi L_c w_{00}^2}{4}\left\{\left(2w_{00}^{-2}+\beta_c^2\right) + \frac{\lambda_0}{n_2 L_c w_{00}^2}\left[\frac{1+(n_2/n_1)^3}{1-(n_2/n_1)^2}\right] + \frac{2\pi^2 n_1 n_2}{L_c\lambda_0(n_1-n_2)}\right\} \tag{4.15}$$

As in the case of the numerator, the denominator of (4.5) also has to be calculated independently for the cavity and DBR regions as expressed by

$$\textit{denominator} = \iiint_{\text{Cavity}} n^2E^2\,dV + \iiint_{\text{Top DBR}} n^2E^2\,dV + \iiint_{\text{Bottom DBR}} n^2E^2\,dV \tag{4.16}$$

where in this case the term due to the top DBR is different from that of bottom DBR because of the presence of the oxide aperture. Since the oxide aperture has a circular geometry, the area integral element dxdy is converted to $2\pi r dr$ and the radius r is equivalent to $\sqrt{x^2+y^2}$. With the help of the integral solution (D.2), the volume integration within the cavity thus yields

$$\iiint_{\text{Cavity}} n^2E^2\,dV = 2\pi\int_0^{L_c} n_c^2\cos^2(\beta_c z)\,dz\int_0^{\infty}\exp\left(\frac{-2r^2}{w_{00}^2}\right)rdr$$

$$= 2\pi\left(\frac{n_c^2 L_c}{2}\right)\left(\frac{w_{00}^2}{4}\right) = \frac{\pi n_c^2 w_{00}^2 L_c}{4} \tag{4.17}$$

where the z =0 position is as defined in Fig. 4.1(b). As for the integration within the top DBR where the oxide aperture is placed in the first layer, it can be obtained as

$$\iiint_{\text{Top DBR}} n^2E^2\,dV$$

$$= 2\pi\int_0^{\infty}\exp\left(\frac{-2r^2}{w_{00}^2}\right)rdr\left\{\left[\int_0^{L_2} n_2^2\cos^2(\beta_2 z)\,dz + \int_0^{L_1} n_1^2\sin^2(\beta_1 z)\left(\frac{n_2}{n_1}\right)^2 dz\right]\sum_{m=0}^{\infty}\left(\frac{n_2}{n_1}\right)^{2m}\right\}$$

$$- 2\pi\int_a^{\infty}\exp\left(\frac{-2r^2}{w_{00}^2}\right)rdr\int_{-l+d_{ox}/2}^{-l-d_{ox}/2}\left(n_2^2-n_{ox}^2\right)\cos^2(\beta_2 z)\,dz$$

$$= 2\pi\left(\frac{w_{00}^2}{4}\right)\left[\frac{n_2\lambda_0}{8}+\frac{n_1\lambda_0}{8}\left(\frac{n_2}{n_1}\right)^2\right]\left[1-\left(\frac{n_2}{n_1}\right)^2\right]^{-1} - 2\pi\left[\frac{w_{00}^2}{4}\exp\left(\frac{-2a^2}{w_{00}^2}\right)\right]\left(n_2^2-n_{ox}^2\right)\left(\frac{F_{ox}d_{ox}}{2}\right)$$

$$= \frac{\pi w_{00}^2 L_c}{4}\left[\frac{n_1 n_2\lambda_0}{4L_c(n_1-n_2)} - \frac{F_{ox}d_{ox}}{L_c}\left(n_2^2-n_{ox}^2\right)\exp\left(\frac{-2a^2}{w_{00}^2}\right)\right] \tag{4.18}$$

where the integral expression (D.9) and solution (D.2) have been employed. Also, in calculating the integral

$$\int_{-l+d_{ox}/2}^{-l-d_{ox}/2} \cos^2(\beta_2 z)\, dz = \frac{d_{ox}}{2}\left(1 + \frac{\cos(2\beta_2 l)\sin(\beta_2 d_{ox})}{\beta_2 d_{ox}}\right) = F_{ox}\frac{d_{ox}}{2} \qquad (4.19),$$

the longitudinal propagation constant within the oxide of thickness d_{ox} is assumed to be β_2. Note that F_{ox} is an important "weighing" factor dependent on the thickness and position of the oxide aperture and is actually identical to the enhancement factor Γ_{enh} used in (2.45) for the QWs. On the other hand, the volume integration of the bottom DBR where there is no dielectric aperture is simply given by

$$\iiint_{\text{Bottom DBR}} n^2 E^2\, dV = \frac{\pi w_{00}^2 L_c}{4}\left[\frac{n_1 n_2 \lambda_0}{4L_c(n_1 - n_2)}\right] \qquad (4.20)$$

Summing up the final expressions given by (4.17),(4.18) and (4.20), the denominator is then obtained as

$$denominator = \frac{\pi w_{00}^2 L_c}{4}\left[n_c^2 - \left(n_2^2 - n_{ox}^2\right)\frac{F_{ox} d_{ox}}{L_c}\exp\left(\frac{-2a^2}{w_{00}^2}\right) + \frac{n_1 n_2 \lambda_0}{2L_c(n_1 - n_2)}\right] \qquad (4.21)$$

Combining the expressions for numerator and denominator from (4.15) and (4.21) respectively, the variational formula for the fundamental TEM_{00} mode guided in a circular apertured VCSEL is given by

$$\frac{\omega_{00}^2}{c^2} = \frac{\beta_c^2 + 2w_{00}^{-2} + \dfrac{2\pi^2 n_1 n_2}{\lambda_0 L_c(n_1 - n_2)} + \dfrac{\lambda_0}{n_2 L_c w_{00}^2}\left[\dfrac{1+(n_2/n_1)^3}{1-(n_2/n_1)^2}\right]}{n_c^2 + \dfrac{n_1 n_2 \lambda_0}{2L_c(n_1 - n_2)} - \left(n_2^2 - n_{ox}^2\right)\dfrac{F_{ox} d_{ox}}{L_c}\exp\left(\dfrac{-2a^2}{w_{00}^2}\right)} \qquad (4.22)$$

Note that by inspection eqn.(4.21), the so-called plane wave "effective cavity length" can be obtained as $L_c + \dfrac{n_1 n_2 \lambda_0}{2(n_1 - n_2)n_c^2}$, whilst the "effective length of the DBR" is simply given by $\dfrac{n_1 n_2 \lambda_0}{4(n_1 - n_2)n_c^2}$. Assuming $n_1 = 3.46$, $n_2 = 3.11$, $n_c = 3.4$ and $\lambda_0 = 0.85\mu m$, the effective length of the DBR considered here is thus $0.57\mu m$. This value is slightly lower than that given by eqn. (2.46) of $0.61\mu m$, for an infinitely long DBR.

For the next three higher order circular Hermite - Gaussian modes i.e. TEM_{01}, TEM_{10} and TEM_{11} modes, the azimuthal angular dependence of their transverse field

variations requires the conversion of integral element dxdy to rdrdθ and (x,y) = (r sinθ, r cosθ) while deriving the denominator. Then using a similar procedure to that for TEM_{00} mode described above as well as the relevant integral solutions/expressions listed in *Appendix D*, it can be shown that the variational formulae for both TEM_{01} and TEM_{10} modes are identical in form and can be expressed by

$$\frac{\omega_{01}^2}{c^2} = \frac{\omega_{10}^2}{c^2} = \frac{\beta_c^2 + 4w_{mp}^{-2} + \dfrac{2\pi^2 n_1 n_2}{\lambda_0 L_c (n_1 - n_2)} + \dfrac{2\lambda_0}{n_2 L_c w_{mp}^2}\left[\dfrac{1+(n_2/n_1)^3}{1-(n_2/n_1)^2}\right]}{n_c^2 + \dfrac{n_1 n_2 \lambda_0}{2L_c(n_1 - n_2)} - (n_2^2 - n_{ox}^2)\dfrac{F_{ox} d_{ox}}{L_c}\left(1+\dfrac{2a^2}{w_{mp}^2}\right)\exp\left(\dfrac{-2a^2}{w_{mp}^2}\right)} \tag{4.23}$$

where w_{mp} is either w_{01} or w_{10} accordingly. As for the TEM_{11} mode, a similar derivation leads to the variational formula given by

$$\frac{\omega_{11}^2}{c^2} = \frac{\beta_c^2 + 6w_{11}^{-2} + \dfrac{2\pi^2 n_1 n_2}{\lambda_0 L_c (n_1 - n_2)} + \dfrac{3\lambda_0}{n_2 L_c w_{11}^2}\left[\dfrac{1+(n_2/n_1)^3}{1-(n_2/n_1)^2}\right]}{n_c^2 + \dfrac{n_1 n_2 \lambda_0}{2L_c(n_1 - n_2)} - (n_2^2 - n_{ox}^2)\dfrac{F_{ox} d_{ox}}{L_c}\left(1+\dfrac{2a^2}{w_{11}^2}+\dfrac{2a^4}{w_{11}^4}\right)\exp\left(\dfrac{-2a^2}{w_{11}^2}\right)} \tag{4.24}$$

As a final check for the plane wave limit when $d_{ox} \to 0$ and $w_{mp} \to \infty$, the resonant wavelength given by expressions (4.22) to (4.24) are seen to be λ_0 in all cases.

4.2.3 Scalar Variational Formulae for Square and Rectangular Oxide Apertured VCSELs

For square and rectangular apertured resonators, the transverse variation of the trial fields are chosen to be of *elliptical* Hermite-Gaussian (TEM_{mp}) form [5]. The complete expressions for the trial fields of the first four order modes ($m,p \leq 1$) in different regions of the resonator are thus given by

$$E_{mp} = x^m y^p \exp\left(-\frac{x^2}{w_{x,mp}^2} - \frac{y^2}{w_{y,mp}^2}\right) \begin{cases} \cos(\beta_c z) & \text{in the cavity} \\ \left(-\dfrac{n_2}{n_1}\right)^{m-i} \cos(\beta_2 z) & \text{in the } m^{th} \text{ pair stack with } n_2 \\ \left(-\dfrac{n_2}{n_1}\right)^{m} \sin(\beta_1 z) & \text{in the } m^{th} \text{ pair stack with } n_1 \end{cases} \tag{4.25}$$

where $w_{x,mp}$ and $w_{y,mp}$ are the mode sizes in x and y direction respectively. Together with the dimensions of the oxide aperture, the schematic modal patterns of these elliptical Hermite-Gaussian modes are illustrated in Figure 4.3. Note that the cross sectional schematic shown in Fig. 4.1 is still applicable in this case except that the aperture dimensions are 2a in the x-direction and 2b in the y-direction.

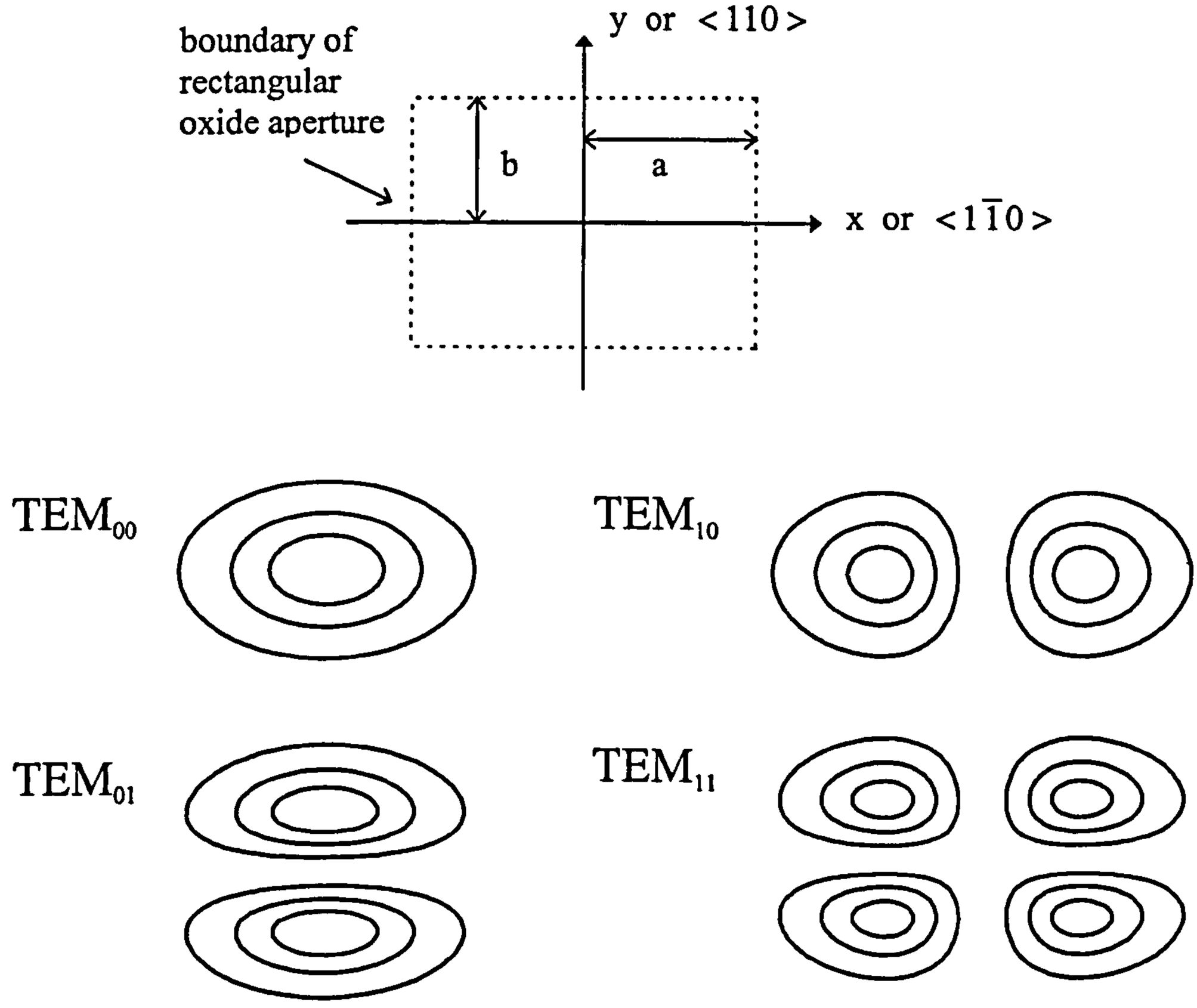

Figure 4.3 : Intensity contour patterns of the first four lowest order ***elliptical*** Hermite - Gaussian modes (assumes $w_x > w_y$), together with the information on the dielectric aperture. The assignments of crystal axes are meant for discussion of experimental result to be presented later in section 4.3.2.

Since the square apertured resonator is actually a special case of the rectangular apertured resonators simply by setting a = b, it is sufficient to work out the general variational formulae for resonators with rectangular apertures. As in the case of a circular apertured resonator, the numerator and denominator of the variational integral formula (4.5) have to be evaluated separately for the cavity and DBR regions.

Beginning with the fundamental elliptical TEM_{00} mode with mode sizes w_{x00} and w_{y00}, the differential components of the numerator within the cavity are given by

$$\left(\frac{dE}{dx}\right)^2 = \frac{4x^2}{w_{x00}^4}\exp\left(\frac{-2x^2}{w_{x00}^2}\right)\exp\left(\frac{-2y^2}{w_{y00}^2}\right)\cos^2(\beta_c z) \tag{4.26}$$

$$\left(\frac{dE}{dy}\right)^2 = \frac{4y^2}{w_{y00}^4}\exp\left(\frac{-2x^2}{w_{x00}^2}\right)\exp\left(\frac{-2y^2}{w_{y00}^2}\right)\cos^2(\beta_c z) \tag{4.27}$$

$$\left(\frac{dE}{dz}\right)^2 = \beta_c^2\exp\left(\frac{-2x^2}{w_{x00}^2}\right)\exp\left(\frac{-2y^2}{w_{y00}^2}\right)\sin^2(\beta_c z) \tag{4.28}$$

Again, by making use of the integral solutions (D.1) and (D.3), the volume integral of the cavity region is reduced to

$$\begin{aligned}&\int_0^{L_c}\int_{-\infty}^{\infty}\int_{-\infty}^{\infty}\left[\left(\frac{dE}{dx}\right)^2+\left(\frac{dE}{dx}\right)^2+\left(\frac{dE}{dx}\right)^2\right]_{cavity}dxdydz\\ &=\frac{\pi w_{x00}w_{y00}L_c}{4}\left(\frac{1}{w_{x00}^2}+\frac{1}{w_{y00}^2}+\beta_c^2\right)\end{aligned} \tag{4.29}$$

For the DBR region, the volume integral product due to the x and y-derivatives of E is given by

$$\begin{aligned}&\int_0^{\infty}\int_{-\infty}^{\infty}\int_{-\infty}^{\infty}\left[\left(\frac{dE}{dx}\right)^2+\left(\frac{dE}{dy}\right)^2\right]_{DBR}dxdydz\\ &=2\int_{-\infty}^{\infty}\int_{-\infty}^{\infty}\frac{4x^2}{w_{x00}^2}\exp\left(\frac{-2x^2}{w_{x00}^2}\right)\exp\left(\frac{-2y^2}{w_{y00}^2}\right)dxdy\left\{\left[\int_0^{L_2}\cos^2(\beta_2 z)\,dz+\int_0^{L_1}\left(\frac{n_2}{n_1}\right)^2\sin^2(\beta_1 z)\,dz\right]\sum_{m=0}^{\infty}\left(\frac{n_2}{n_1}\right)^{2m}\right\}\\ &=\left(\frac{w_{x00}}{2w_{y00}}+\frac{w_{y00}}{2w_{x00}}\right)\left(\frac{\pi\lambda_0}{8n_2}\right)\left[1+\left(\frac{n_2}{n_1}\right)^3\right]\left[1-\left(\frac{n_2}{n_1}\right)^2\right]^{-1}\end{aligned} \tag{4.30},$$

whereas the volume integration of the z-derivative results in

$$\begin{aligned}&\int_0^{\infty}\int_{-\infty}^{\infty}\int_{-\infty}^{\infty}\left[\left(\frac{dE}{dz}\right)^2\right]_{DBR}dxdydz\\ &=\int_{-\infty}^{\infty}\int_{-\infty}^{\infty}\exp\left(-\frac{2x^2}{w_{x00}^2}-\frac{2y^2}{w_{yx00}^2}\right)dxdy\left\{\left[\int_0^{L_2}\beta_2^2\sin^2(\beta_2 z)\,dz+\int_0^{L_1}\left(\frac{n_2}{n_1}\right)^2\beta_1^2\cos^2(\beta_1 z)\,dz\right]\sum_{m=0}^{\infty}\left(\frac{n_2}{n_1}\right)^{2m}\right\}\\ &=\frac{\pi w_{x00}w_{y00}}{2}\left[\frac{\pi^2 n_1 n_2}{2\lambda_0(n_1-n_2)}\right]=\frac{\pi^3 w_{x00}w_{y00}\,n_1 n_2}{4\lambda_0(n_1-n_2)}\end{aligned} \tag{4.31}$$

Then evaluating the numerator according to eqn.(4.8), using the final expressions from (4.29) to (4.31) gives

$$numerator = \frac{\pi L_c w_{x00} w_{y00}}{4}\left\{\begin{array}{l}\left(w_{x00}^{-2}+w_{y00}^{-2}+\beta_c^2\right)+\dfrac{2\pi^2 n_1 n_2}{L_c\lambda_0\left(n_1-n_2\right)}\\ +\dfrac{\lambda_0}{2n_2 L_c}\left(w_{x00}^{-2}+w_{y00}^{-2}\right)\left[\dfrac{1+\left(n_2/n_1\right)^3}{1-\left(n_2/n_1\right)^2}\right]\end{array}\right\} \tag{4.32}$$

For the evaluation of the denominator which requires separate area integration inside and outside the aperture, the quarter symmetry of the rectangular or square shape is exploited. Then, volume integration of the cavity region yields

$$\begin{aligned}\iiint_{\text{Cavity}} n^2E^2\,dV &= 4\left\{\int_0^{L_c} n_c^2\cos^2\left(\beta_c z\right)dz\int_0^{\infty}\int_0^{\infty}\exp\left(-\frac{2x^2}{w_{x00}^2}-\frac{2y^2}{w_{y00}^2}\right)dxdy\right\}\\ &= 4\left(\frac{n_c^2L_c}{2}\right)\left(\frac{1}{2}\sqrt{\frac{\pi}{2}}w_{x00}\right)\left(\frac{1}{2}\sqrt{\frac{\pi}{2}}w_{y00}\right) = \frac{\pi n_c^2 w_{x00}w_{y00}L_c}{4}\end{aligned} \tag{4.33}$$

Within the top DBR, the volume integration is given by

$$\begin{aligned}&\iiint_{\text{Top DBR}} n^2E^2\,dV\\ &=4\int_0^{\infty}\int_0^{\infty}\exp\left(-\frac{2x^2}{w_{x00}^2}-\frac{2y^2}{w_{y00}^2}\right)dxdy\left\{\left[\int_0^{L_2} n_2^2\cos^2\left(\beta_2 z\right)dz+\int_0^{L_1} n_1^2\sin^2\left(\beta_1 z\right)\left(\frac{n_2}{n_1}\right)^2dz\right]\sum_{m=0}^{\infty}\left(\frac{n_2}{n_1}\right)^{2m}\right\}\\ &-4\left[\int_0^{b}\int_a^{\infty}\exp\left(-\frac{2x^2}{w_{x00}^2}-\frac{2y^2}{w_{y00}^2}\right)dxdy+\int_b^{\infty}\int_0^{\infty}\exp\left(-\frac{2x^2}{w_{x00}^2}-\frac{2y^2}{w_{y00}^2}\right)dxdy\right]\int_{-l+d_{ox}/2}^{-l-d_{ox}/2}\left(n_2^2-n_{ox}^2\right)\cos^2\left(\beta_2 z\right)dz\\ &=\frac{\pi w_{x00}w_{y00}L_c}{4}\left[\frac{n_1n_2\lambda_0}{4L_c\left(n_1-n_2\right)}-\frac{F_{ox}d_{ox}}{L_c}\left(n_2^2-n_{ox}^2\right)\left[1-erf\left(\frac{\sqrt{2}a}{w_{x00}}\right)erf\left(\frac{\sqrt{2}b}{w_{y00}}\right)\right]\right]\end{aligned} \tag{4.34}$$

where F_{ox} is defined in (4.19) and the integral expression (D.8) that involves the error function *erf* has been used. Since there is no aperture in the bottom DBR, the volume integration in this region gives

$$\iiint_{\text{Bottom DBR}} n^2E^2\,dV = \frac{\pi w_{x00}w_{y00}L_c}{4}\left[\frac{n_1n_2\lambda_0}{4L_c\left(n_1-n_2\right)}\right] \tag{4.35}$$

Using the final expressions given by (4.33) to (4.35), the evaluation of denominator according to (4.16) thus gives

denominator

$$= \frac{\pi w_{x00} w_{y00} L_c}{4}\left\{n_c^2 - \left(n_2^2 - n_{ox}^2\right)\frac{F_{ox} d_{ox}}{L_c}\left[1 - erf\left(\frac{\sqrt{2}a}{w_{x00}}\right) erf\left(\frac{\sqrt{2}b}{w_{y00}}\right)\right] + \frac{n_1 n_2 \lambda_0}{2L_c(n_1 - n_2)}\right\}$$

(4.36)

Combining the expressions for numerator and denominator from (4.21) and (4.23), the variational formula for the elliptical TEM_{00} mode in rectangular apertured resonator is thus given by

$$\frac{\omega_{00}^2}{c^2} = \frac{\left(\beta_c^2 + w_{x00}^{-2} + w_{y00}^{-2}\right) + \frac{2\pi^2 n_1 n_2}{\lambda_0 L_c(n_1 - n_2)} + \frac{\lambda_0}{2n_2 L_c}\left(w_{x00}^{-2} + w_{y00}^{-2}\right)\left[\frac{1 + (n_2/n_1)^3}{1 - (n_2/n_1)^2}\right]}{n_c^2 + \frac{n_1 n_2 \lambda_0}{2L_c(n_1 - n_2)} - \left(n_2^2 - n_{ox}^2\right)\frac{F_{ox} d_{ox}}{L_c}\left[1 - erf\left(\frac{\sqrt{2}a}{w_{x00}}\right) erf\left(\frac{\sqrt{2}b}{w_{y00}}\right)\right]}$$

(4.37)

Note that the variational expression for a square apertured resonator can be obtained by simply putting $a = b$.

By working through the similar steps and exploiting fully the list of integral solutions/expressions of *Appendix D*, the variational formulae for the elliptical TEM_{01}, TEM_{10} and TEM_{11} modes guided by a *rectangular apertured resonator* are found to be expressed by : -

for the *elliptical* TEM_{01} mode,

$$\frac{\omega_{01}^2}{c^2} = \frac{\left(\beta_c^2 + w_{x10}^{-2} + 3w_{y10}^{-2}\right) + \frac{2\pi^2 n_1 n_2}{\lambda_0 L_c(n_1 - n_2)} + \frac{\lambda_0}{2n_2 L_c}\left(w_{x10}^{-2} + 3w_{y10}^{-2}\right)\left[\frac{1 + (n_2/n_1)^3}{1 - (n_2/n_1)^2}\right]}{n_c^2 + \frac{n_1 n_2 \lambda_0}{2L_c(n_1 - n_2)} - \left(n_2^2 - n_{ox}^2\right)\frac{F_{ox} d_{ox}}{L_c}\left[1 + \frac{2\sqrt{2}\,b}{\sqrt{\pi} w_{y10}}\exp\left(\frac{-2b^2}{w_{y10}^2}\right)\operatorname{erf}\left(\frac{\sqrt{2}a}{w_{x10}}\right) - \operatorname{erf}\left(\frac{\sqrt{2}a}{w_{x10}}\right)\operatorname{erf}\left(\frac{\sqrt{2}b}{w_{y10}}\right)\right]}$$

(4.38)

for the *elliptical* TEM_{10} mode,

$$\frac{\omega_{10}^2}{c^2} = \frac{\left(\beta_c^2 + 3w_{x01}^{-2} + w_{y01}^{-2}\right) + \frac{2\pi^2 n_1 n_2}{\lambda_0 L_c (n_1 - n_2)} + \frac{\lambda_0}{2n_2 L_c}\left(3w_{x01}^{-2} + w_{y01}^{-2}\right)\left[\frac{1+(n_2/n_1)^3}{1-(n_2/n_1)^2}\right]}{n_c^2 + \frac{n_1 n_2 \lambda_0}{2L_c(n_1 - n_2)} - (n_2^2 - n_{ox}^2)\frac{F_{ox} d_{ox}}{L_c}\left[1 + \frac{2\sqrt{2}\,a}{\sqrt{\pi} w_{x01}} \exp\left(\frac{-2a^2}{w_{x01}^2}\right) \operatorname{erf}\left(\frac{\sqrt{2}b}{w_{y01}}\right) - \operatorname{erf}\left(\frac{\sqrt{2}b}{w_{y01}}\right) \operatorname{erf}\left(\frac{\sqrt{2}a}{w_{x01}}\right)\right]} \quad (4.39)$$

and finally for the *elliptical* TEM_{11} mode,

$$\frac{\omega_{11}^2}{c^2} = \frac{\left(\beta_c^2 + 3w_{x11}^{-2} + 3w_{y11}^{-2}\right) + \frac{2\pi^2 n_1 n_2}{L_c \lambda_0 (n_1 - n_2)} + \frac{\lambda_0}{2n_2 L_c}\left(3w_{x11}^{-2} + 3w_{y11}^{-2}\right)\left[\frac{1+(n_2/n_1)^3}{1-(n_2/n_1)^2}\right]}{n_c^2 + \frac{n_1 n_2 \lambda_0}{2L_c(n_1 - n_2)} - (n_2^2 - n_{ox}^2)\frac{F_{ox} d_{ox}}{L_c}\left[\begin{array}{l} 1 - \operatorname{erf}\left(\frac{\sqrt{2}a}{w_{x11}}\right) \operatorname{erf}\left(\frac{\sqrt{2}b}{w_{y11}}\right) \\ + \frac{2\sqrt{2}\,b}{\sqrt{\pi} w_{y11}} \operatorname{erf}\left(\frac{\sqrt{2}a}{w_{x11}}\right) \exp\left(\frac{-2b^2}{w_{y11}^2}\right) \\ + \frac{2\sqrt{2}\,a}{\sqrt{\pi} w_{x11}} \operatorname{erf}\left(\frac{\sqrt{2}b}{w_{y11}}\right) \exp\left(\frac{-2a^2}{w_{x11}^2}\right) \\ - \frac{8ab}{\pi\, w_{x11} w_{y11}} \exp\left(-\frac{2a^2}{w_{x11}^2} - \frac{2b^2}{w_{y11}^2}\right) \end{array}\right]} \quad (4.40)$$

4.3 Results and Comparisons

In this section, simulation results calculated using the scalar variational model described above are presented first. Then, comparisons are made between the relevant experimental and theoretical results. Note that the theoretical values are calculated assuming refractive index value of 1.52 for the oxide, and no shrinkage in the oxide thickness from that of original AlAs after oxidation. The latter assumption is reasonable since a negligible 3% thickness shrinkage has been measured recently, for AlAs that was oxidised under the similar conditions adopted in this work [17].

4.3.1 Simulation Results

Using the scalar variational formulae discussed in preceding sections, the resonant wavelengths and the corresponding mode sizes for circular, square or rectangular oxide apertured VCSELs can be calculated numerically in a couple of seconds. While the calculations for square and rectangular apertured resonators involve searching for a minimum in ω by varying the mode size in the x and y domains, those for circular devices are simpler and require only a one dimensional search.

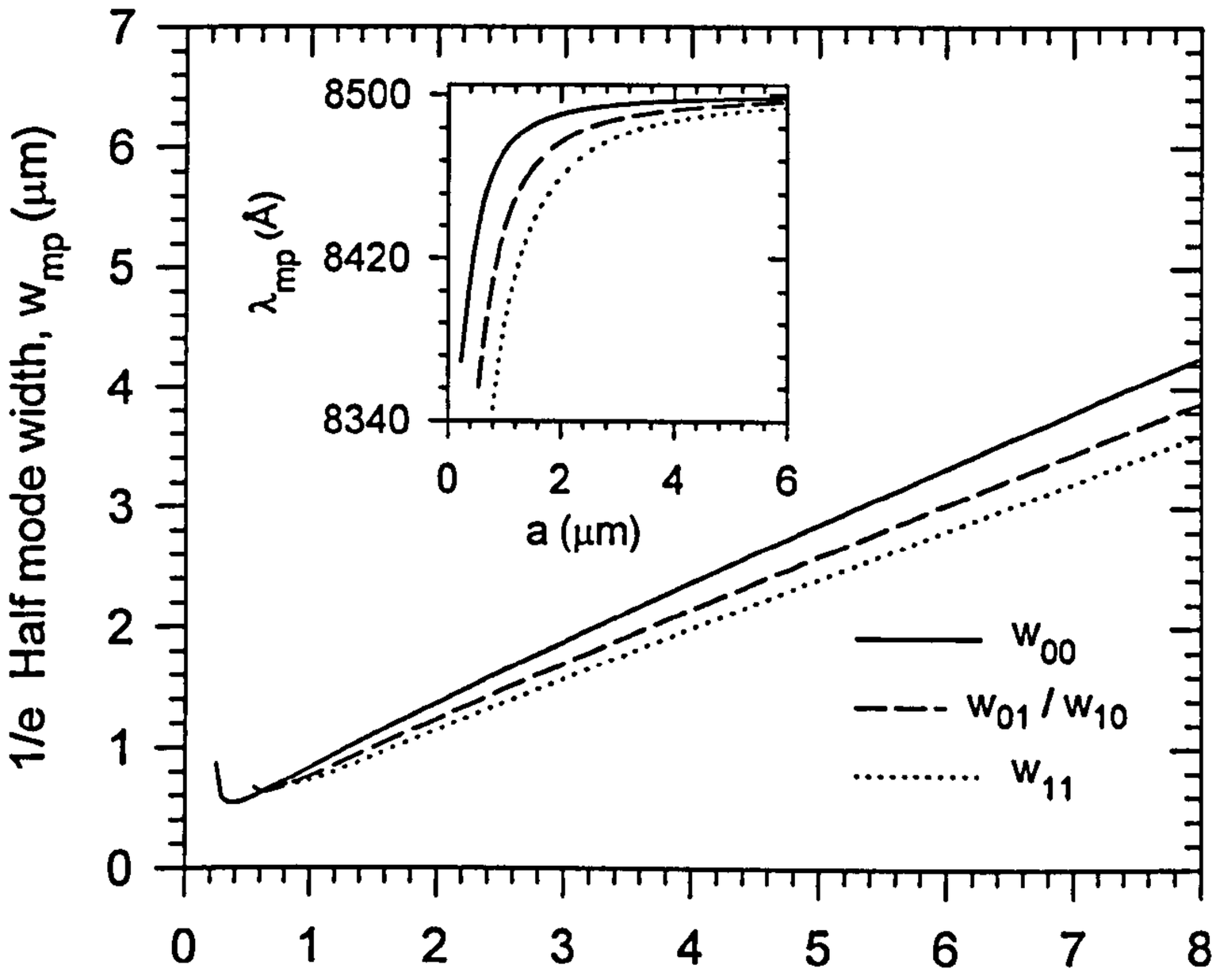

Figure 4.4 : Variation of 1/e half mode width (main) and resonant wavelengths (inset) with aperture radius for the first four lowest order eigenmodes guided by circular apertured passive resonators with 600Å thick oxide aperture.

For the **circular** apertured resonators with 600Å thick oxide (strong guiding case, assuming no shrinkage from the original AlAs thickness), the main illustration in Figure 4.4 shows that the mode radii of the four lowest order eigenmodes including the degenerate TEM_{01} and TEM_{10} modes, shrink as the aperture size becomes smaller. After the minimum mode radii are achieved, the mode sizes then expand rapidly with further reduction in oxide aperture size due to the increasing loss of optical confinement. Eventually, the oxide aperture ceases to provide any optical guiding and

no longer supports an eigenmode. The inset of Fig. 4.4 also shows that the resonant wavelengths of the eigenmodes blueshift while the modal wavelength separations between the eigenmodes increase with reduction in aperture size. These variations provide a convenient means of checking the accuracy of the theoretical models.

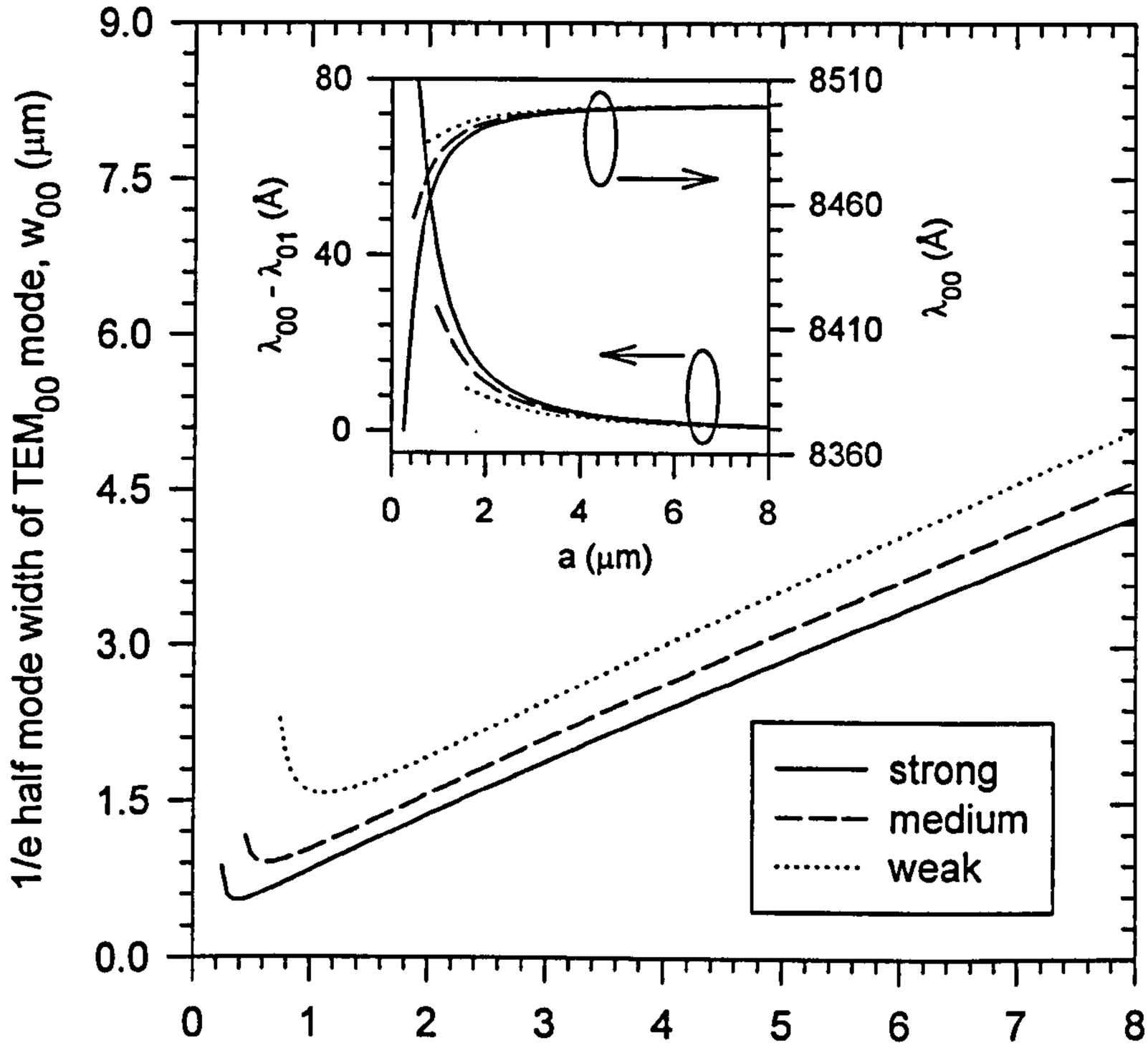

Figure 4.5 : Variation of mode radius of the fundamental TEM_{00} mode with aperture radius for circular apertured passive resonator with strong (600Å oxide), medium (350Å oxide) or weak guiding (200Å oxide) designs. The inset shows the corresponding modal wavelength separations between the TEM_{00} mode and the degenerate TEM_{01} / TEM_{10} modes.

Similar trends as depicted in Fig.4.4 also occur for resonators of medium and weak guiding designs although the corresponding mode radii are bigger and the blueshift in resonant wavelength is smaller for a given aperture size. These are shown in Figure 4.5 where the main illustration compares the variation of the TEM_{00} mode 1/e half mode width as a function of aperture radius, for oxide apertured resonators with strong, medium and weak guiding designs. Note that the minimum mode radius of the weakly guiding resonator is always larger, and the cut-off of the TEM_{00} modes

also occur at a bigger aperture radius (≈ 0.7μm) when compared to those of medium (≈ 0.4μm) and strong guiding (≈ 0.2μm) designs. The inset of Fig. 4.5 also shows the variation of the resonant wavelength of the TEM_{00} mode with aperture radius, as well as the corresponding wavelength separations between the TEM_{00} mode and the degenerate TEM_{01} / TEM_{10} modes. Obviously, the resonators with thinner oxide aperture give smaller wavelength separations (λ_{00} - λ_{01}) and become inherently single moded at a bigger aperture radius (a ≈ 1.55 μm) as compared to medium (a ≈ 0.90 μm) and strong (a ≈ 0.50 μm) guiding designs. This is due to the modal cut-off of the degenerate TEM_{01} / TEM_{10} modes. Also, the blue shift of the resonant wavelength from the plane wave value is larger for the resonators with strong guiding design.

Qualitatively, the observations made and conclusions drawn above for circular apertured resonators also apply to the *square*-shaped resonators. The only exception, as shown in Figure 4.6, is that although the TEM_{01} and TEM_{10} modes are still degenerate in resonant frequency/wavelength, anisotropy exist in their mode sizes i.e. $w_{x01} \neq w_{y01}$ and $w_{x10} \neq w_{y10}$, but $w_{x01} = w_{y10}$ and $w_{x10} = w_{y01}$. Thus, their transverse field variations are of *elliptical* Hermite-Gaussian form. However, for the TEM_{00} and TEM_{11} modes, their field variations remain *circular* Hermite-Gaussians.

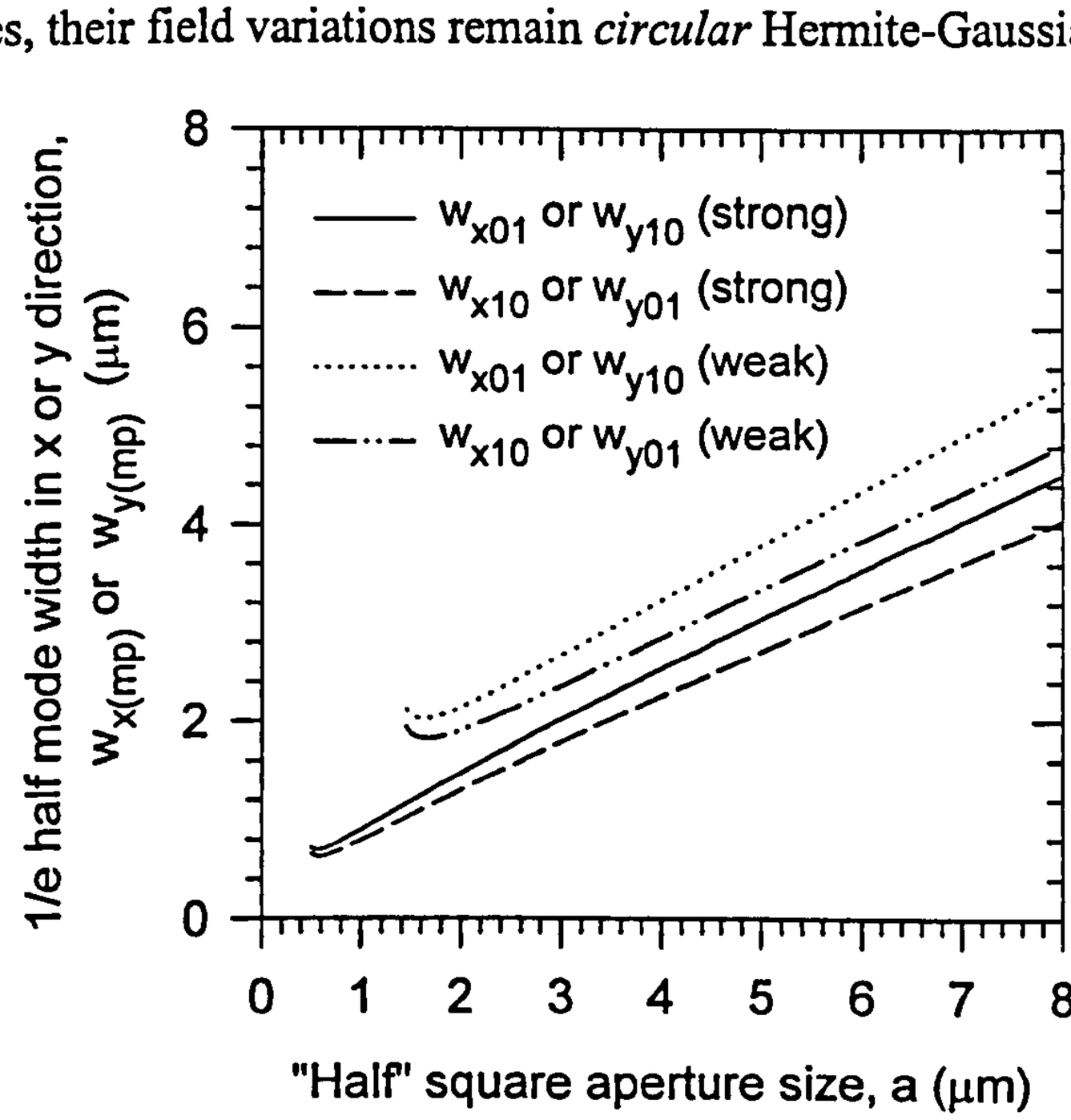

Figure 4.6 : Variation of mode sizes of TEM_{01} and TEM_{10} modes as a function of half aperture size(square) for strong and weak guiding cases.

For a given aperture area, Figure 4.7 shows that the mode size of the fundamental TEM_{00} mode is similar for both the square and circular apertured resonators, especially for areas below $30\mu m^2$ (i.e. 5.5μm square device or circular device with 3.1μm radius). In all cases, the TEM_{00} mode sizes of the square apertured resonators are slightly lower than their circular counterparts, implying that the eigenmodes are slightly more confined in the former case. Note that this close matching also happens in the modal wavelength separation between the eigenmodes as indicated in the inset (as well as the variation of resonant wavelength with aperture area which is not shown here).

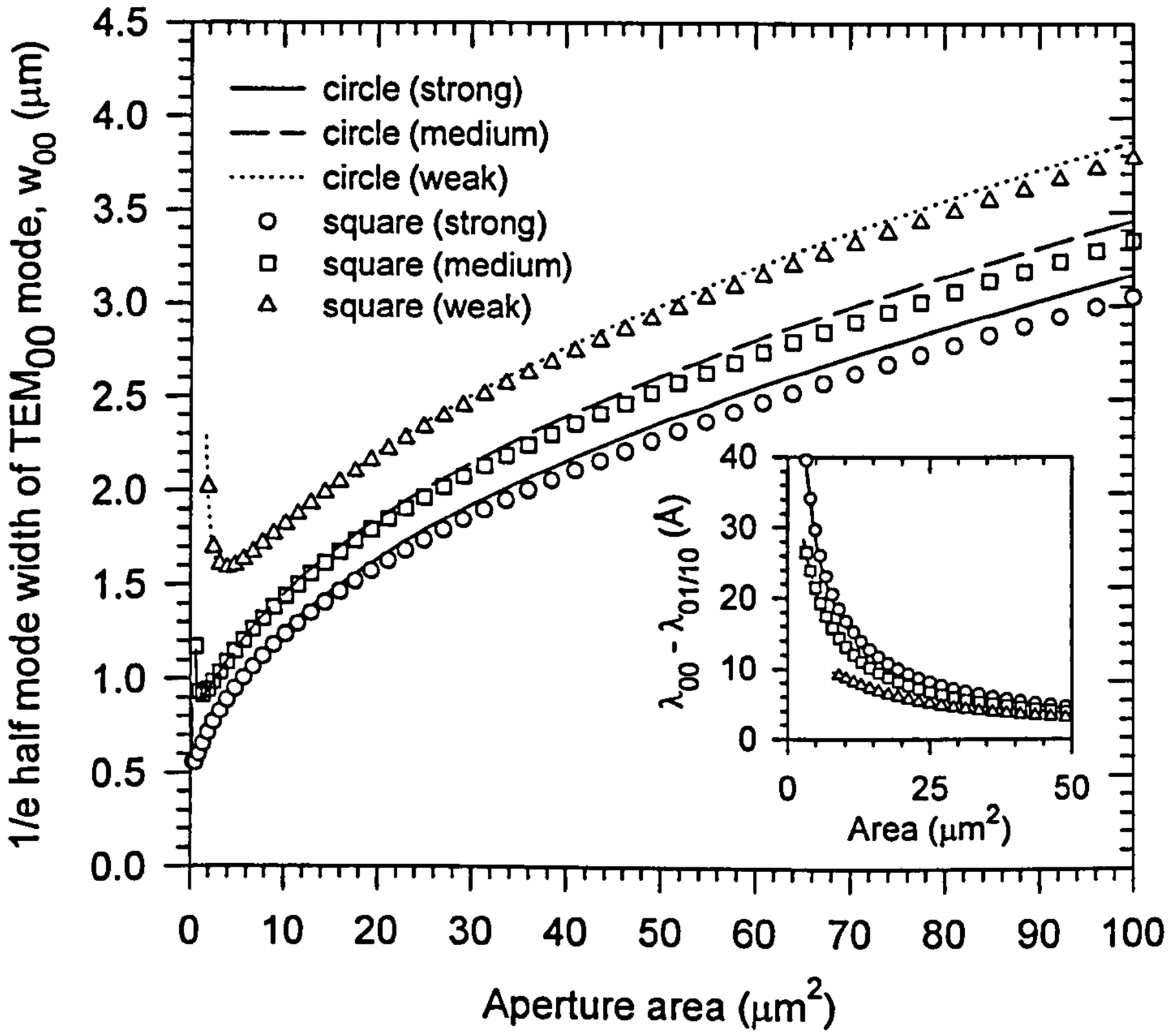

Figure 4.7 : Variation of 1/e half mode width of TEM_{00} mode as a function of aperture area for circular and square apertured resonators. The inset shows the corresponding modal wavelength separations between the TEM_{00} and degenerate TEM_{01} and TEM_{10} modes.

Two major effects occur when the aspect ratio of the oxide aperture is higher/lower than unity, i.e. frequency splitting occurs between the TEM_{01} and TEM_{10} modes, and the transverse field variations of the eigenmodes become elliptical. For instance, Figure 4.8 illustrates the variation of eigenmode resonant wavelengths with

aspect ratio (2b/2a), for rectangular apertured resonators of strong guiding design and with the length 2a of the oxide aperture fixed at 4μm. Note that the resonant wavelengths of the TEM_{00} and TEM_{10} modes which have no field/intensity null in the y-direction only vary slightly with change in aspect ratio, as compared to the other two modes. When the aspect ratio (2b/2a) is larger than unity, the resonant wavelength of TEM_{01} mode approaches that of TEM_{00} mode. Conversely, when the aspect ratio is less than unity, it is then that the TEM_{10} mode is closer to the fundamental mode with little change in their wavelength separation as the aperture aspect ratio reduces. This results in a rapid increase in the "net" wavelength separation between TEM_{01} and TEM_{10} modes as the aspect ratio deviates from unity. The inset of Fig 4.8 shows that this spectral splitting varies in a near parabolic manner with aspect ratio. From the experimental point of view, the degree of spectral splitting between TEM_{01} and TEM_{10} provides a useful means of checking the asymmetry in the aperture geometry and it is also found to be relatively insensitive to reasonable changes in the plane wave resonant wavelength.

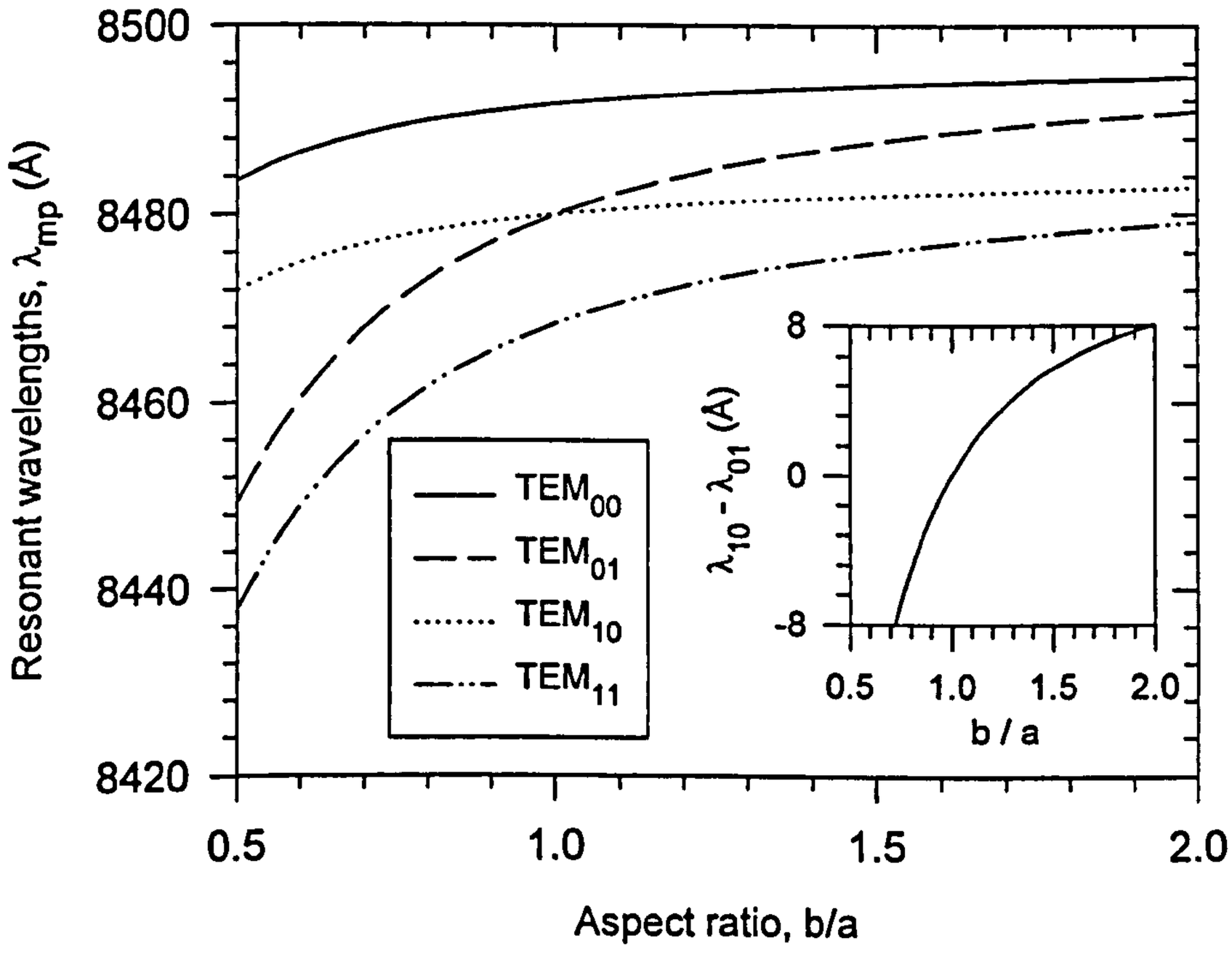

Figure 4.8 : Variations of resonant wavelengths with aspect ratio for rectangular apertured resonators with the length 2a (refer to Fig. 4.3) of oxide aperture fixed at 4μm. The inset shows the change in spectral splitting between TEM_{01} and TEM_{10} modes with the aspect ratio.

Figure 4.9 shows that the eigenmodes become increasingly elliptical, with the 1/e half mode width in the y-direction i.e. $w_{y(mp)}$, varying almost linearly with aspect ratio whilst those in the x-direction hardly change. Notice that the mode sizes of the TEM_{00} mode in the x-direction is similar to that of the TEM_{01} mode in the x-direction, whilst in the y-direction its mode size is similar to that of TEM_{10} mode. As will be shown in chapter 5, the anisotropy in the transverse modal field variation shown here causes a difference in the modal reflectance of the eigenmodes with similar mode number but polarised in the orthogonal directions.

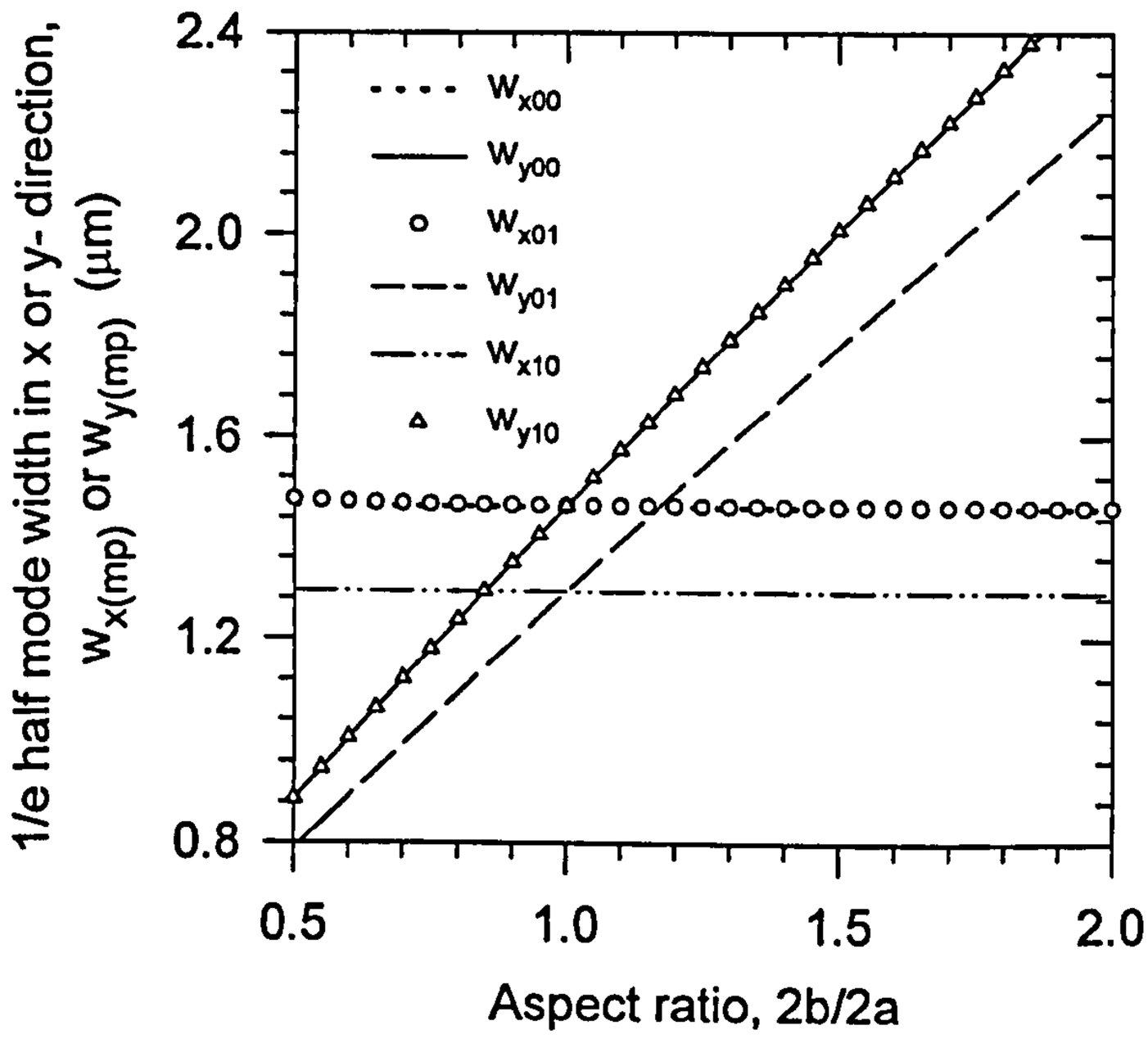

Figure 4.9 : Variation of mode sizes of the elliptical Hermite-Gaussian eigenmodes guided with aspect ratio of rectangular apertured resonators where the length 2a (refer to Fig. 4.3) of the oxide aperture fixed at 4μm.

4.3.2 Experimental Results and Comparisons

In order to investigate the accuracy of the scalar variational model presented above, devices were made from the three VCSEL layers whose designs were discussed in Chapter 3, using the fabrication procedures detailed in ***Appendix F***. Two major problems were encountered. Firstly, considerable variations in plane resonant wavelength (measured by photo-reflectance measurement) exist across the three wafers due to the growth non-uniformity. It was found that the wafer regions where the plane resonant wavelength is between 861 - 866nm, the variation in wavelength is

less rapid for all the three VCSEL layers and thus most suitable for performance comparison. Also, the gain peak wavelength of the QWs is projected to be in the range of 855-860nm at a current density of about 1.5kA/cm^2, as deduced from the lasing wavelengths of in-plane stripe lasers in section 3.4. This small few nannometers gain offset would thus ensure that the resonant wavelengths of the eigenmodes are not too far away from the gain peak. (This will be proven later in chapter 6 through the temperature dependence of the pulsed threshold current density).

Secondly, as mentioned in the section on selective oxidation in ***Appendix F***, it was found that the oxide apertures resulting from circular and square mesas were elliptical and rectangular in shape respectively with the longer side parallel to $<110>$. This geometric anisotropy in the oxide apertures is generally attributed to a difference in the lateral oxidation rate along the $<110>$ and $<1\bar{1}0>$ (faster) crystal axes [10]. On the other hand, it was found in this work that by orientating the rectangular shaped VCSEL mesas parallel to the direction where oxidation rate was higher, near square shape devices with the aspect ratio in the range of $0.93 \leq (2b/2a) \leq 1.07$ can be obtained. Consequently, comparisons between the theoretical predictions and experimental results are only available for square and rectangular devices and not the circular one, in this chapter as well as in chapter 6 where the threshold and modal behaviours are discussed. For convenience and in order to avoid confusion, the assignment of mode numbers particularly regarding TEM_{01} and TEM_{10} modes for the experimental results presented hereafter, assumes that *the* $<1\bar{1}0>$ *direction is parallel to x-axis while the* $<110>$ *direction is parallel to the y-axis* of the co-ordinate system as indicated in Figure 4.3.

The oxide aperture sizes were measured using modified infra-red microscope fitted with a 100x microscope objective with numerical aperture value of 0.95 (described in more detail in ***Appendix F***). During this measurement, the contrast of the interface between the oxidised and unoxidised regions of an aperture is broadened by the resolving power of the microscope to a distance of $\approx 0.61\ \lambda_0 / NA$ [18] where λ_0 is the wavelength in free space and NA is the numerical aperture of the optical system. Based on the simulated reflectivity spectra for oxidised and unoxidised VCSEL structures (not shown), the image contrast between the oxidised and unoxidised regions of the oxide aperture is mainly due to light of wavelength around 800nm (in free space). Hence, assuming NA = 0.95 and $\lambda_0 = 0.8\mu m$, this maximum

broadened distance is estimated to be ≈ 0.5μm. However, the random uncertainty in measured values should be better than this value since it is possible for an observer to estimate the "mean" transition interface between oxidised and unoxidised regions quite comfortably through the enlarged image. In this work, the random error in estimating this mean distance is estimated to be about 0.1μm, corresponding to uncertainty of ±0.2μm in full aperture size. This uncertainty is sufficiently small that it does not affect the qualitative observations and conclusions made in subsequent sections.

All the spectral measurement carried out in this work were made using a 0.75m SPEX spectrometer and nitrogen cooled Ge-detector. The optical set-up allows spectral measurement with resolution as high as 0.16Å as deduced from the full-width-half-maximum (FWHM) of the emission lines when a slit width of 10μm is used. It was found that using such a narrow slit width poses no detection sensitivity problem at (not far) below, and above threshold, for devices of all sizes. In fact, far above threshold, a neutral density filter as high as ND3 had to be used to avoid saturating the detector. However, the below threshold spontaneous emissions peaks became too weak to be measurable when a Dichroic sheet polariser (Melles Griot) was used to separate out the peaks polarised in orthogonal directions. This is due to the fact that the polariser attenuates the signal output by about 5 to 6 times. For this reason, it was finally decided that all the spectral assessment carried out in this work should be obtained using a 30μm slit width which offers spectral resolution of about 0.35Å. This ensures that low intensity spontaneous emission at currents well below threshold (as low as 50μA) can be measured even with the available polariser. Spectral measurements under pulsed conditions (40ns, 50kHz) were also attempted, but unfortunately the emissions were too weak to be observed at well below threshold. The need to use a polariser in the spectral measurements is because of the spectral splitting between orthogonally polarised sets of eigenmodes. This is exemplified by Figure 4.10 which shows the below threshold CW emission spectra of a 3.8μm near-square strong guiding device measured at a current density of (0.5 x J_{th}), where J_{th} ≈ 4.9 kA/cm^2. The actual dimension of this device is (3.9 x 3.7)μm with longer side parallel to $<1\bar{1}0>$ i.e. the x - direction, and the resulting aspect ratio, 2b/2a, is thus 0.95.

The spectra shown in Figure 4.10 demonstrates the importance of using polariser while performing spectral measurements on VCSELs if accurate spectral information is to be obtained. Otherwise, the double peaks of the near-degenerate TEM_{10} and TEM_{01} modes would not be discernible under normal measurement condition. In addition, as will be discussed in chapter 6, crucial information like the effective photon lifetime that can be deduced from the spectral linewidth of the eigenmodes would also be affected as a result of the over-estimation of the linewidth. The assignment of the order of eigenmodes for each resonant peak, shown in Fig. 4.10, is decided by comparing the sequence of resonant wavelengths with that shown in Fig.4.8. However, it is also possible to confirm these assignments through the spectral resolved near field patterns; which can be observed by placing a viewing camera at the output slit of the spectrometer, at the respective resonant wavelength of interest.

For this particular device, the spectral splittings between the orthogonally polarised modes of TEM_{00} and of TEM_{10} are both 1.0Å, while those of TEM_{01} and TEM_{11} modes are 0.7Å and 0.4Å respectively. The breaking of the frequency degeneracy between the orthogonally polarised eigenmodes of similar mode number is generally attributed to the birefringence effect [11] that causes slight differences in the refractive indices as seen by the fields that polarise in orthogonal directions. This birefringence can be induced by unintentional stress that incurs either during the fabrication process [11] or possibly due to conversion of AlAs to oxide [10]. On the other hand, the slight residual geometry asymmetry of this nearly square device also breaks the frequency degeneracy between the TEM_{01} and TEM_{10} modes, in accordance to the simulation results discussed earlier in section 4.3.1. At half the threshold current density, this spectral splitting was measured to be about 1.2Å, very close to the predicted value of 1.1Å for a device with aspect ratio 0.95. The measured wavelength separations between TEM_{00} and TEM_{10} modes, and between TEM_{10} and TEM_{11} modes are 9.9Å and 10.9Å respectively. These values are also quite close to the respective predicted values of 11.4Å and 12.2Å. Note that the corresponding predicted values for a "perfectly" square 3.8μm devices are at 12.39Å and 12.6Å respectively. This particular device eventually lased under single mode condition, with the dominant TEM_{00} mode linearly polarised in the direction parallel to the <110> crystal axis.

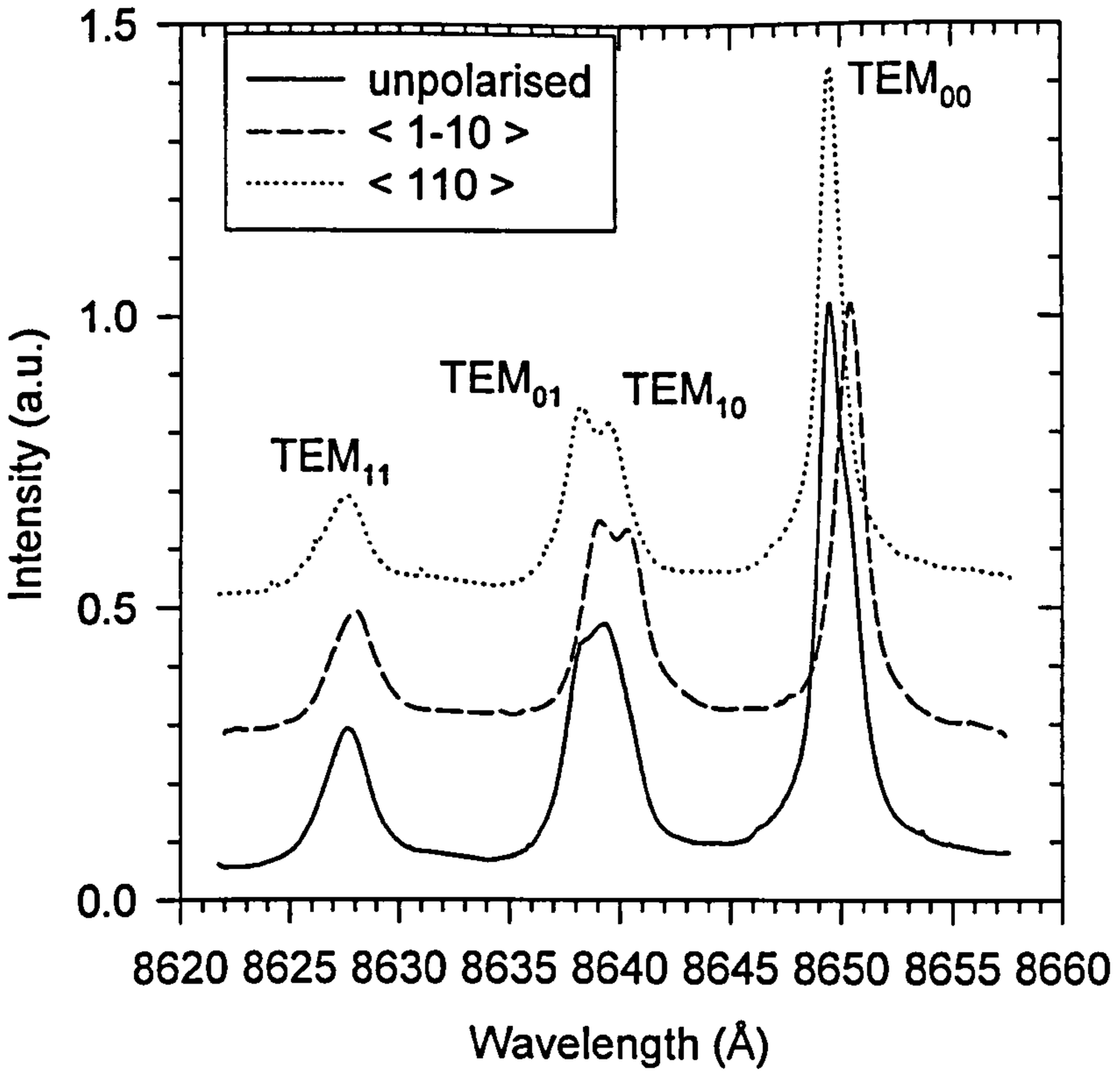

Figure 4.10 : Below threshold cw emission spectra from a 3.8μm near square device (strong guiding) measured under polarisation and non-polarisation resolved conditions. The injected current density was at (0.5 x J_{th}).

As mentioned in section 4.2, the "cold cavity" resonant wavelengths and wavelength separation between the eigenmodes provide a useful and convenient way of comparing the theoretical and experimental results. Unfortunately, in reality the measured resonant wavelengths of oxide apertured VCSELs vary with injection current and thus complicate the comparison efforts. Figure 4.11 shows the variations of resonant/lasing wavelength of various eigenmodes polarised in the <110> direction with injected current. These variations are attributed to the combined effects of carrier injection into the gain region and device internal heating on the profile of the refractive index within the cavity. It is well known that injected free carriers result in a decrease of real refractive index ($\Delta n_{carrier}$) [12], and thus results in the blue shift of resonant wavelengths illustrated in Fig. 4.11. For GaAs, it was estimated that the rate reduction of real refractive index n with injected free carrier density N is $\partial n/\partial N \approx -10^{-20}$ cm^3 [12].

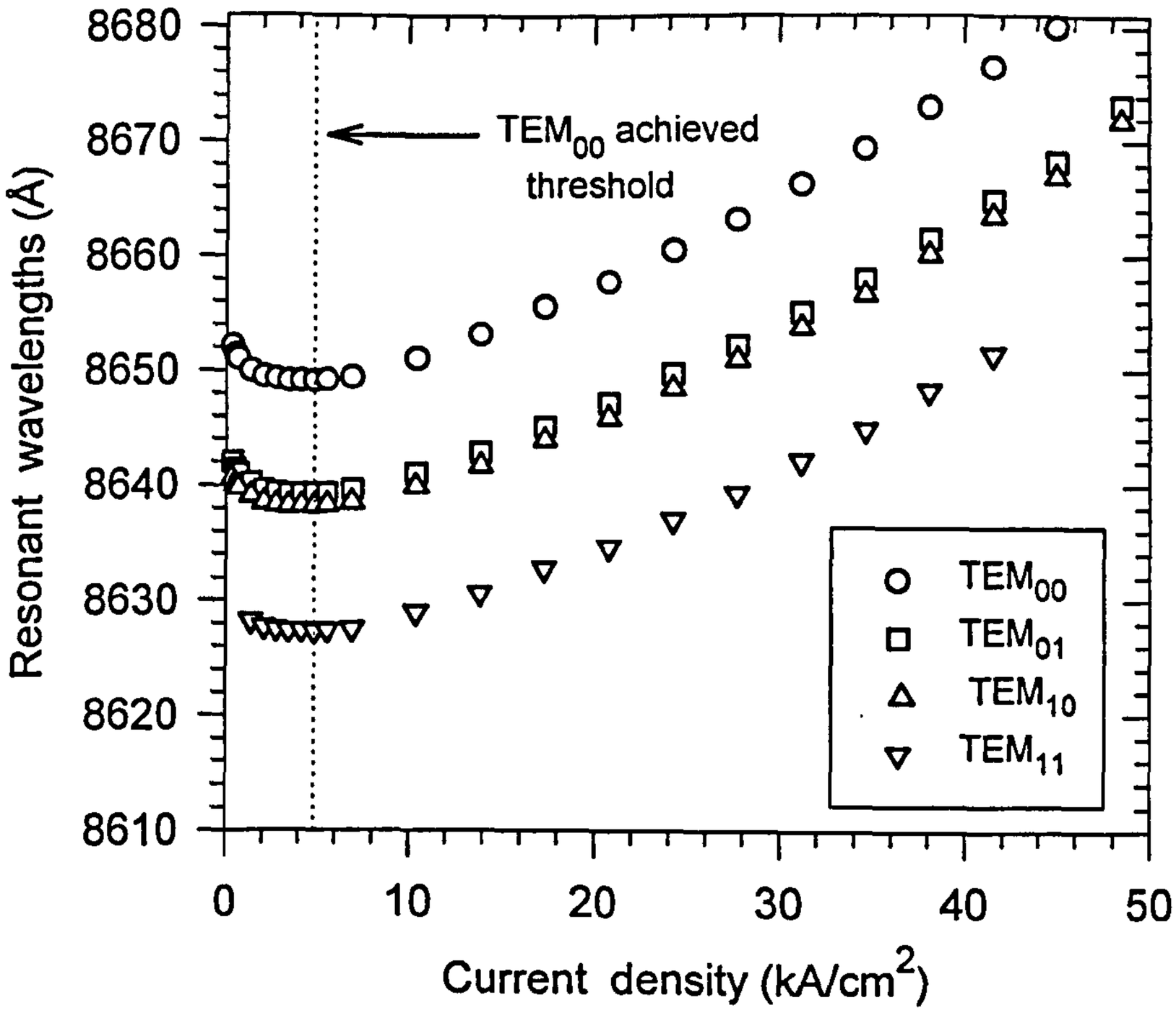

Figure 4.11 : Variation of resonant wavelengths with injected current density (CW) for the 3.8μm near square device of strong guiding design, polarised in the <110> direction.

On the other hand, a temperature rise increases both the refractive index (Δn_{ther}) and the dimension (Δl_{ther}) of the semiconductor material due to thermal expansion. At 850nm, the refractive index of GaAs changes almost linearly with temperature as $\partial n/\partial T = 4 \times 10^{-4}$ K^{-1} [13], while the thermal expansion coefficient for $Al_xGa_{1-x}As$ is given by $\alpha_{ther} = (\partial l/\partial T) / l = (6.4\text{-}1.2x) \times 10^{-6}$ K^{-1} [14]. Therefore, any change in the device temperature will result in the change of optical path length nl of the cavity and thus the resonant wavelengths. Taking into account both the carrier and thermal induced effects, the observed initial net blue-shift at below threshold in Fig 4.11 thus indicates that the carrier induced effect is stronger in this regime. The near parabolic manner in which the frequency blue shift reduces, reflects the non-linear $J \alpha N^2$ and thus $J \alpha (\Delta n_{carrier})$ relation. Once the threshold is reached, the carrier density in the QWs remains almost pinned in the centre region of aperture with increasing injected current and this eventually leads to a halt in the increase in blue shift of the resonant frequencies. Hence, above threshold, the thermal effect becomes dominant and results in the net red shift of resonant wavelengths seen in Fig. 4.11. In

this regime, the resonant wavelengths red shifts almost linearly with injected current density. Hence, assuming the thermally induced $(d\lambda_{mp}/dJ)_{ther}$ can be described by a linear relation close to the threshold region, it is estimated through extrapolation that the maximum blue shift due to carrier induced effect alone is about 10Å at threshold. Using the simple plane wave hard mirror formula $nL = \lambda$, the value of $\Delta n_{carrier}$ needed to give a 10Å blue shift is roughly estimated to be about -0.03, and the corresponding injected carrier density is 3×10^{18} cm^{-3} which is close to the typical value of threshold carrier density in a VCSEL (see Fig. 5.19).

Due to the inherent heat-sinking capability of a VCSEL, thermal gradients exist within a VCSEL when it is operated under cw condition [13]. In the transverse direction, the local temperature tends to peak at the centre of device and decays radially. In the longitudinal direction, the cavity region is expected to be hotter than the DBRs [15]. The transverse temperature variation particularly affects the modal behaviours of VCSELs because it creates a thermally induced transverse variation in the refractive index profile. Besides the built-in index guiding afforded by the oxide, this leads to an extra thermally induced waveguiding effect that is usually referred to as thermal lensing [16]. This effect is exemplified by Figure 4.12 which shows the variation of the wavelength separations between the eigenmodes with the current density. The spectral splittings between the TEM_{00} and TEM_{01} modes, and that between TEM_{01} and TEM_{11} modes increases by up to 17% and 11% respectively beyond threshold. This phenomenon is believed to be due to the continuing contraction in mode sizes as the thermal lensing effect becomes more severe with increasing difference between peak temperature at the aperture centre and the ambient. The lower rate of increase in spectral splitting in the latter case is likely to be because of the field of the TEM_{11} mode extending further out from the centre of the oxide aperture, thus experiencing smaller interaction with the thermal lens. It is also interesting to note that the spectral splitting between TEM_{01} and TEM_{10} changes little ($\approx$ 0.3Å), suggesting that the thermal lens and indeed the oxide aperture are quite symmetrical. Otherwise, the asymmetrical thermal lens would have caused asymmetry in the transverse refractive index profile, resulting in larger increased spectral splitting between TEM_{01} and TEM_{10} modes as well.

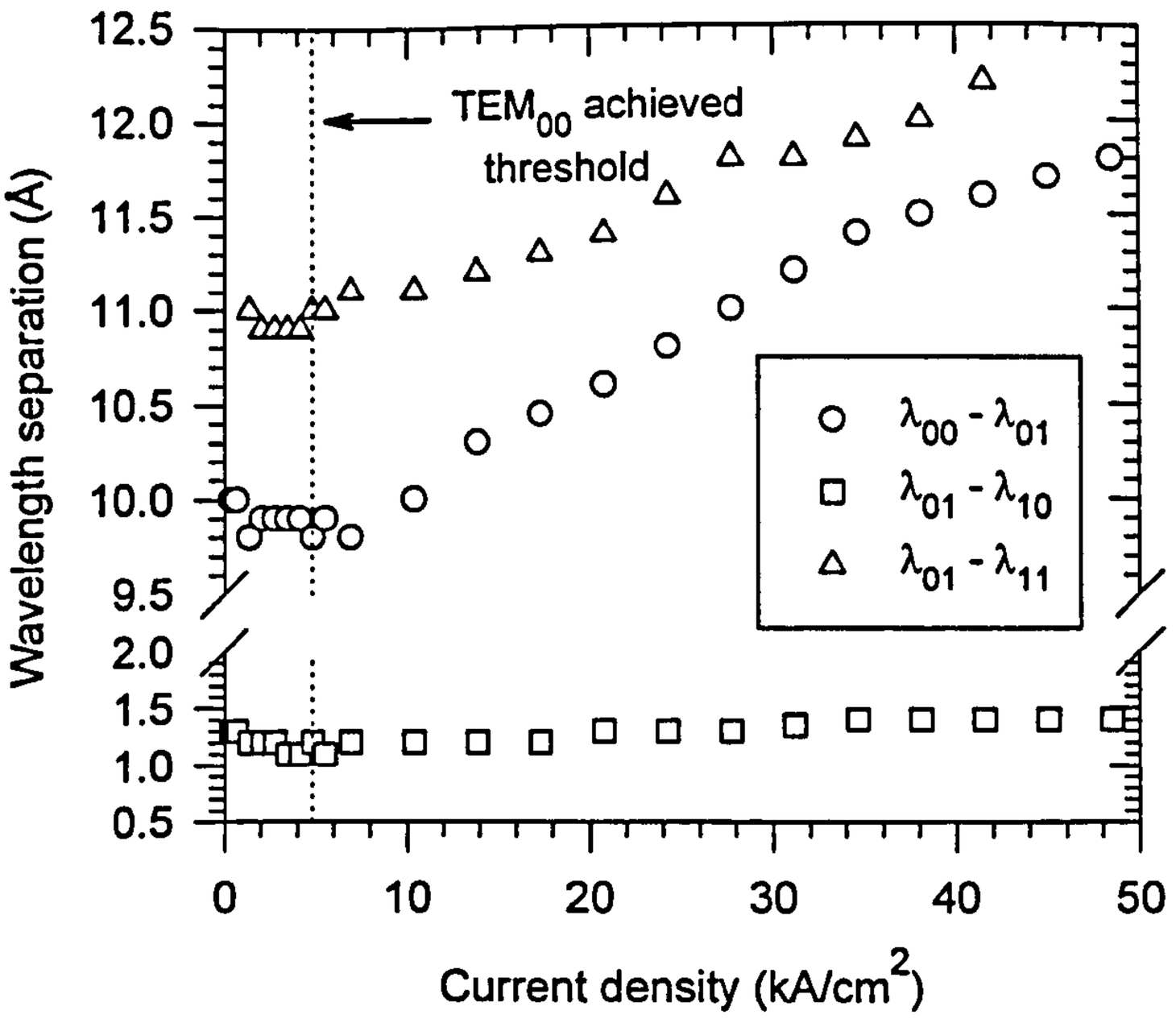

Figure 4.12 : Variation of wavelength separations between the eigenmodes with injected current density (cw) for the near-square 3.8μm device of strong guiding design

Ideally, the experimental values that are used to compare with the theoretical predictions for "passive-cavity" resonator discussed in this chapter, should be those measured from the actual devices under the "cold cavity" condition i.e. when the modal gain of the eigenmode concerned is zero (more about this issue in chapter 5). However, as shown in Figures 4.11 and 4.12, it is almost impossible to pinpoint the current densities at which the cavity appears "cold" to each eigenmode. In the absence of a better alternative, it was finally decided that the comparison should be made between the wavelength separations measured at **half** the threshold current density with those predicted by theory. This decision is reasonable since both the resonance wavelengths and modal spectral splittings changed little (i.e. 0.4Å and 0.2Å respectively) at below threshold as indicated in Figure 4.12. At such low current injection level, the thermal lensing effect is also minimum and can be neglected. For devices with three different oxide thickness namely the strong, medium and weak guiding designs, Figure 4.13 illustrates the variation of spectral splittings between the fundamental TEM_{00} mode and the nearest higher order mode i.e. TEM_{10} or TEM_{01} modes, with average square oxide aperture sizes (S) where $S = 2\sqrt{ab}$. The

asymmetry in the aperture shape of these devices are in the range of $0.93 \leq (2b/2a) \leq 1.07$. Due to the small spectra splittings involved, the values for devices bigger than 11μm are estimated from non-polarisation resolved spectrum measured by using a 10μm spectrometer slit width.

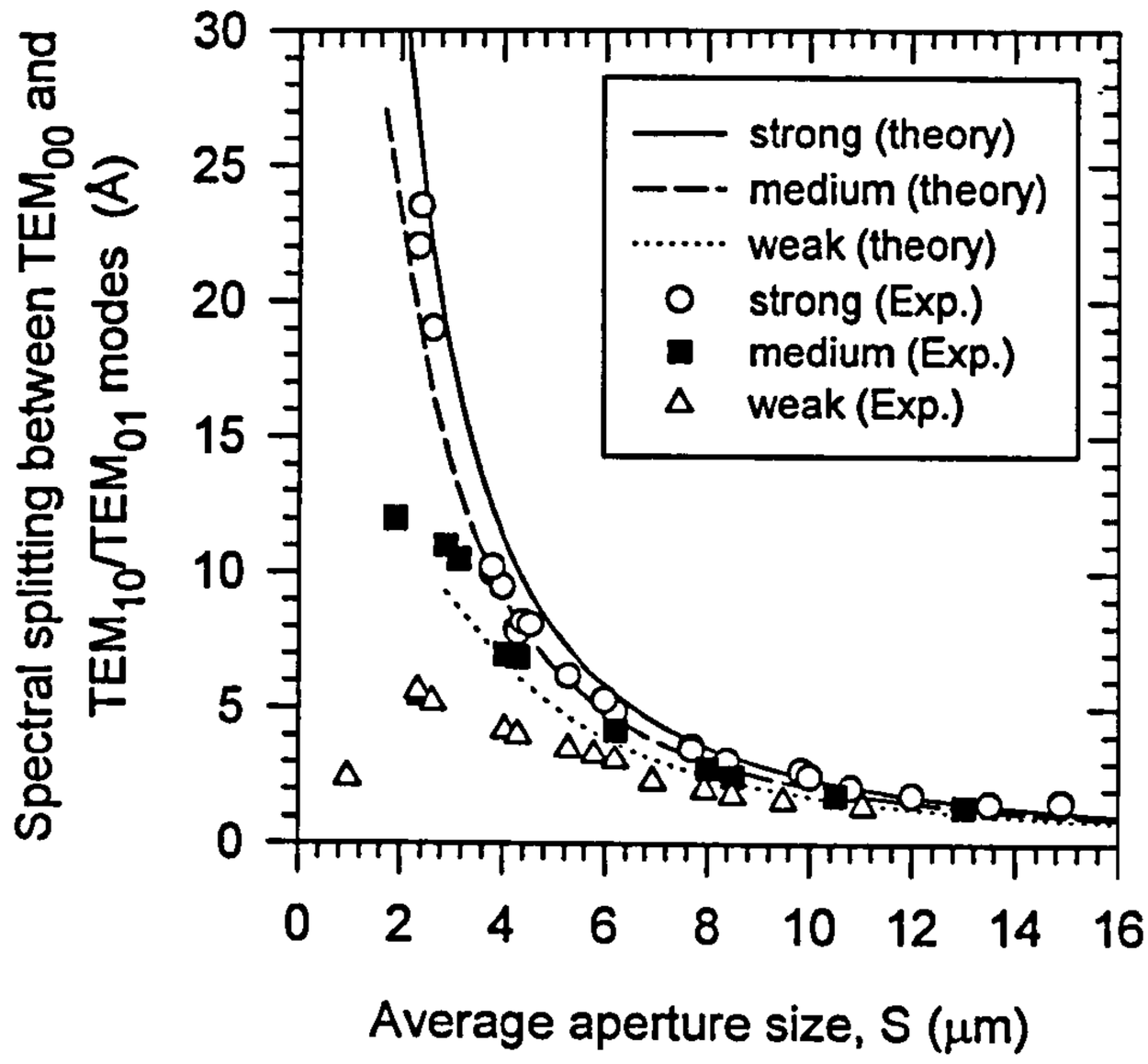

Figure 4.13 : Variation of spectral splitting between the TEM_{00} mode and the closest TEM_{10} or TEM_{01} modes with average aperture size. Values are evaluated at 0.5 x $J_{th(00)}$ except that for the 1.0μm weak guiding devices which is taken at the onset of the higher order mode

The experimental results shown in Fig 4.13 were obtained from the devices fabricated from the wafer region where the plane resonant wavelengths are between 861 and 866nm. The theoretical curves were computed assuming perfect square apertured devices with plane resonant wavelength of 865nm. Theoretical calculations show that the small variation (≈ 5nm) in the plane resonant wavelengths of actual devices, causes negligible difference in the modal spectral splitting (<0.05Å). The calculated values on spectral splitting seems to fit the experimental results quite well. Generally speaking the experimental values are always lower than predicted values. These differences are especially significant for the weak guiding devices smaller than 4.5μm as well as the 1.9μm medium guiding device. The dimensions of these devices are very close to the regime where the higher modes expand rapidly. As shown in Fig. 4.13, the predicted minimum square aperture sizes before the cut-off of higher

order modes occurs are 1.0μm, 1.7μm and 2.9μm for the strong, medium and weak guiding devices respectively. In this regime, besides the perturbation in transverse refractive index variation caused by the oxide aperture, the effect of carrier induced refractive index change which is not taken into account in the present model, becomes increasingly significant to the overall waveguiding strength as the aperture size reduces. In fact, for the 1.0μm weak guiding device in which even the TEM_{00} mode should have been cut off (its theoretical limit is 1.2μm for weak guiding), its spectral splitting value does not follow the trend of previous values. For this particular device, the spectral splitting value is that taken at the onset of the higher order mode as it was not detectable in the below-threshold spontaneous emission.

In order to investigate the blue shift of the eigenmode resonant wavelengths from the plane wave values, results obtained from devices taken from the same cell were plotted in the main illustrations of Figure 4.14(a), (b) and (c) respectively for strong, medium and weak guiding designs. In such a small chip area of about 1.8 x 0.5 mm^2, the variation of plane resonant wavelength due to growth non-uniformity is minimum and thus any significant change in resonant wavelength should be due to the effect of the oxide apertures. Based on the resonant wavelengths of the biggest devices measured (using 10μm slit width and no polariser), the plane resonant wavelengths are estimated to be about 8660Å, 8648Å and 8650Å for strong, medium and weak guiding devices respectively. As in Fig.4.13, the results shown in Figures 4.14 were measured at half the threshold current density (cw). In all cases, although some scatter of data does exist, the matching of experimental and theoretical results can be considered to be very good. Also shown in the insets of these figures are the resonant wavelengths measured under pulsed condition, but now at threshold. This is because the emission peaks were too weak to be observable at half the threshold under pulsed condition. In these cases, the experimental values appear to be slightly lower than the theoretical predictions. Considering the carrier and thermal induced effects discussed earlier, these results are expected since once the thermal effects were removed by pulsing, the enhanced carrier induced negative index change due to doubling the current would cause a larger blue shift in resonant wavelength.

As mentioned earlier, the spectral splitting between the TEM_{01} and TEM_{10} modes provides a good indication of the asymmetry in the aperture shape. For the near-square devices whose asymmetry in aspect ratios are determined to be in the

range of $0.93 \leq (2b/2a) \leq 1.07$ through infra-red microscopy, the measured values of these spectral splittings are plotted in Figure 4.15 as a function of the dimension of the shorter side of the oxide aperture. Together with these experimental results are the predicted splitting values represented by the line traces, for rectangular devices with an aspect ratio of 1.07. Clearly, the experimental values are either close to or below the theoretical limits predicted for all the strong, medium and weak guiding devices. This suggests that the asymmetry in aperture dimension of these devices are indeed well within the specified range. It is also obvious that besides the aspect ratios, the spectral splitting between the TEM_{01} and TEM_{10} modes is also dependent on the aperture sizes (shorter dimension) as well as the guiding strength i.e. thickness and position of oxide.

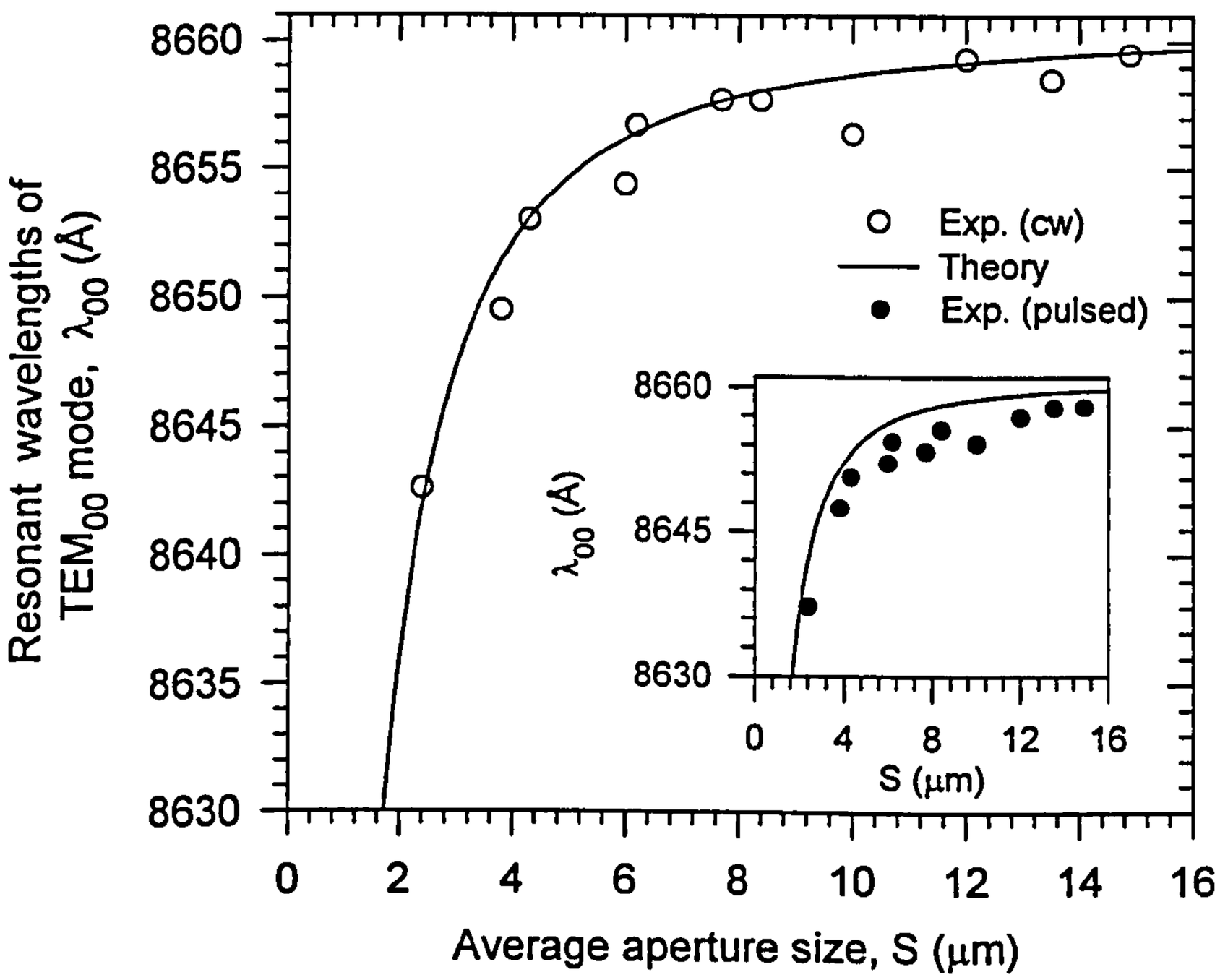

Figure 4.14(a) : Variation of TEM_{00} mode resonant wavelength with average aperture size for near-square "*strong guiding*" devices.

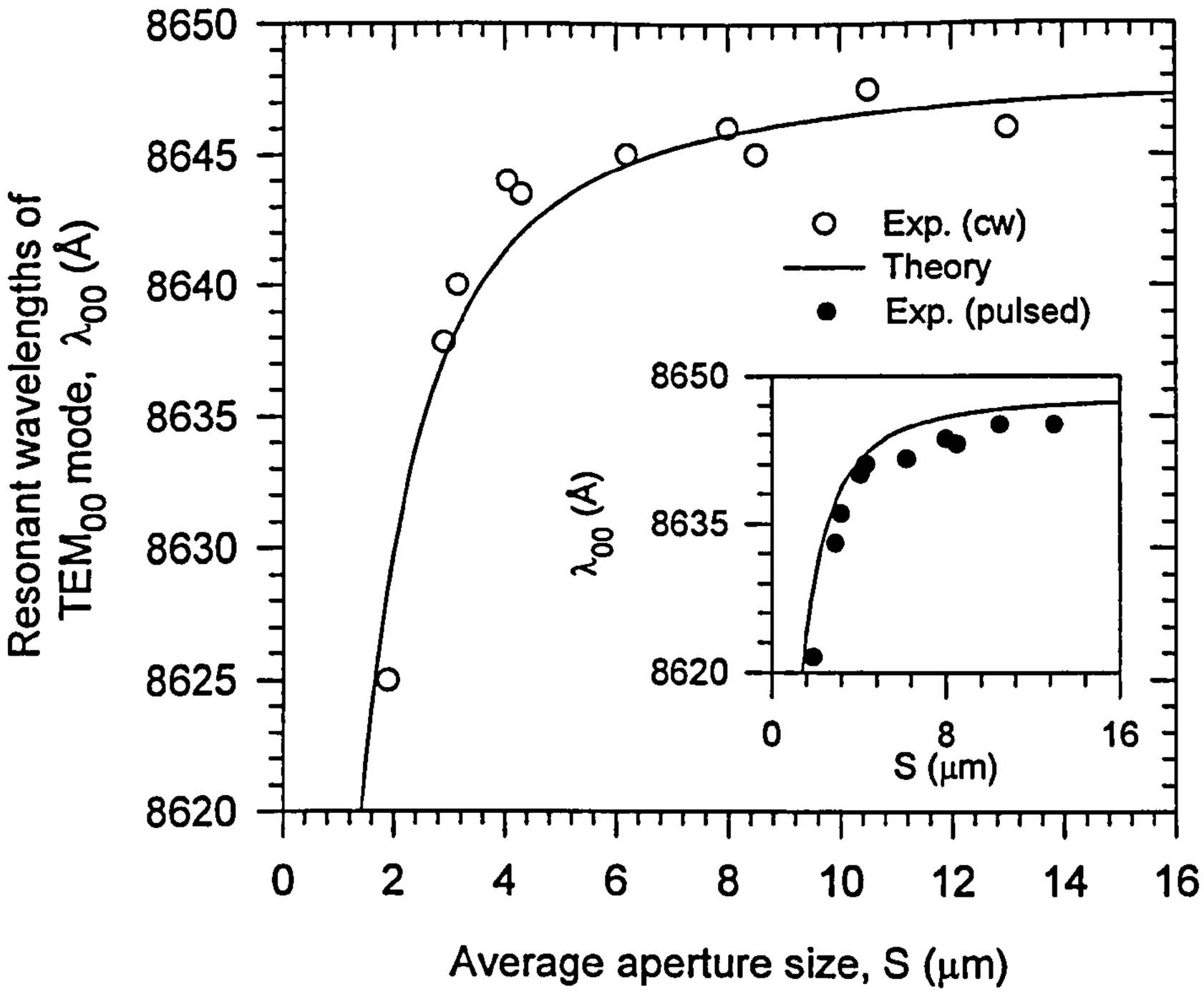

Figure 4.14(b) : Variation of TEM_{00} mode resonant wavelength with average aperture size for near-square "*medium guiding*" devices.

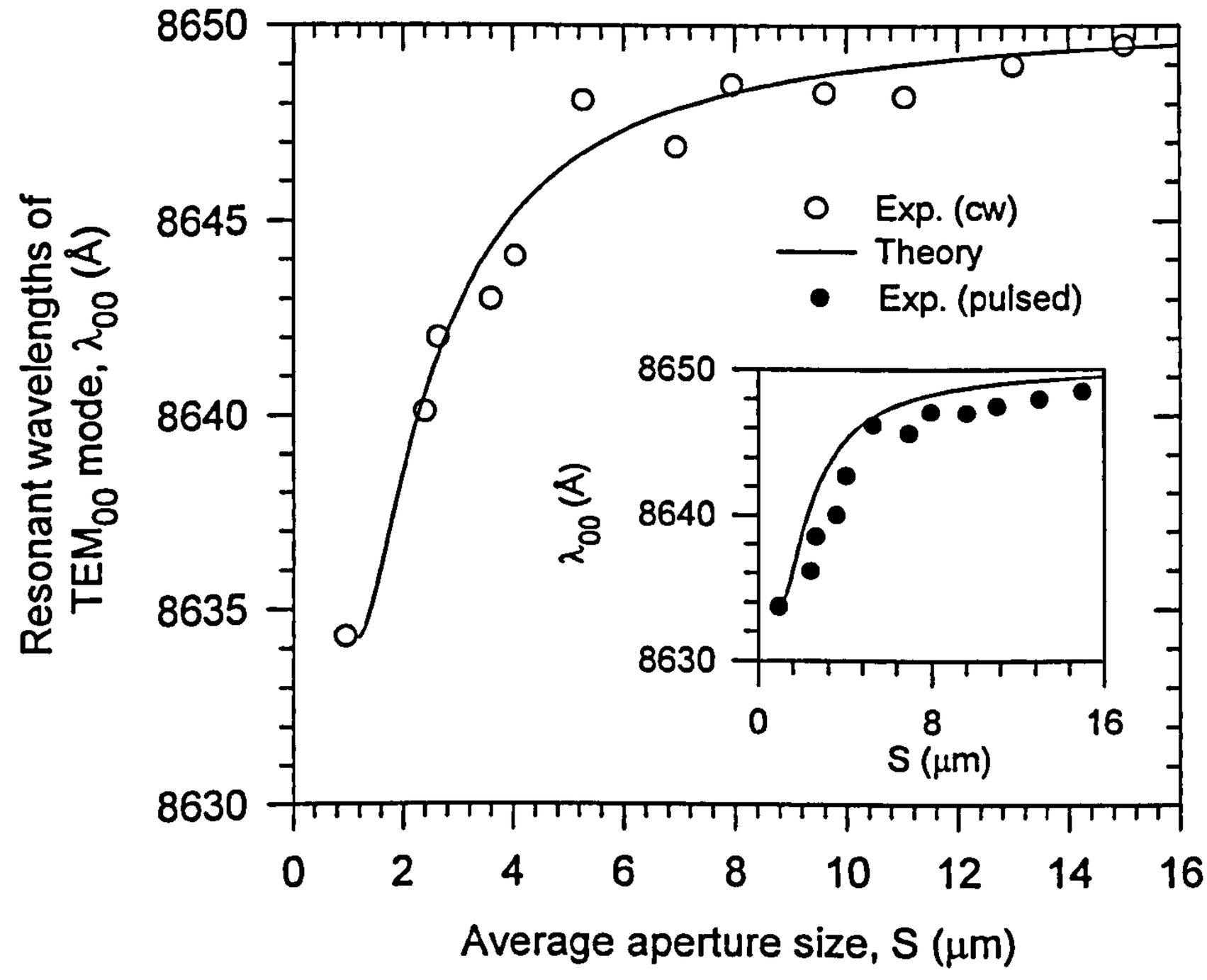

Figure 4.14(c) : Variation of TEM_{00} mode resonant wavelength with average aperture size for near-square "*weak guiding*" devices.

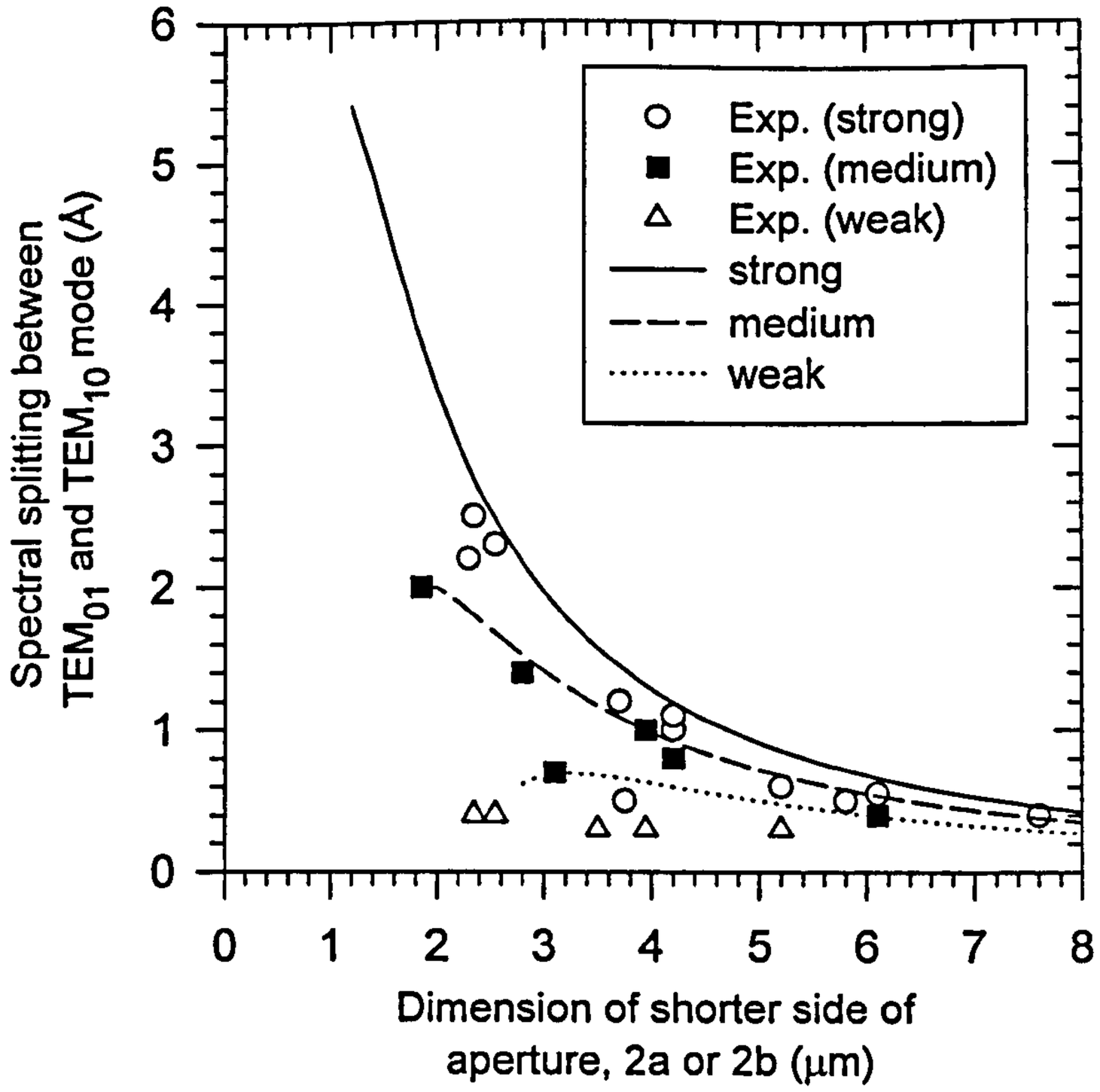

Figure 4.15 : Spectral splitting between the TEM_{01} and TEM_{10} modes as a function of the dimension of the shorter side of aperture. The line traces are the predicted splitting for devices with aperture aspect ratio of 1.07.

As shown in Fig. 4.15, while the spectral splitting between the TEM_{01} and TEM_{10} mode for the near-square devices are usually less than 2.0Å except for the relatively small strong/medium guiding devices (< 2.5μm); rectangular devices with aspect ratio of (2b/2a) > 1.1 or (2b/2a) < 0.9 can easily exceed 2.0 Å especially in the cases of strong guiding devices. Two good examples of these devices are shown in Figures 4.16(a) and 4.16(b). In these figures, the polarisation and non-polarisation resolved spectra were measured at half the threshold for the (5.0 x 4.3)μm (aspect ratio = 0.86) and (2.6 x 3.4)μm (aspect ratio = 0.76) strong guiding devices respectively. The measured spectral splitting between the TEM_{10} and TEM_{01} modes are 2.5Å and 7.0Å respectively, as compared to the predicted values of 2.4Å and 8.4Å. Meanwhile, the spectral splitting between the TEM_{02} and TEM_{20} modes, that are now closer to the TEM_{00} mode than the TEM_{11} mode (not shown), are 1.1Å and 2.0Å respectively. On the other hand, the birefringence splitting between orthogonally polarised TEM_{00} modes are relatively small at 0.5Å and 0.3Å respectively.

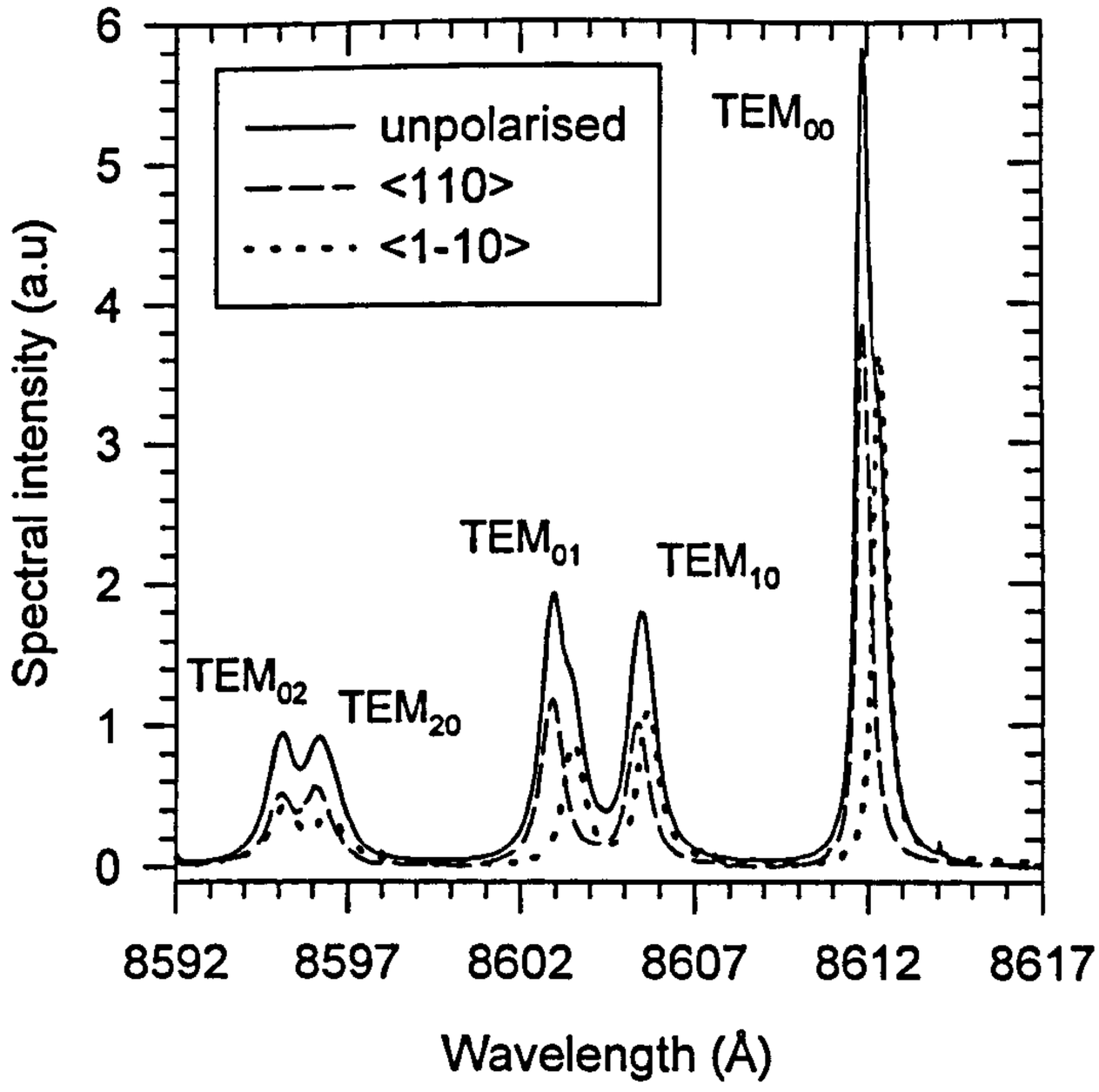

Figure 4.16(a) : Spontaneous emission spectra of (5.0 x 4.3) μm strong guiding device at half the threshold current density

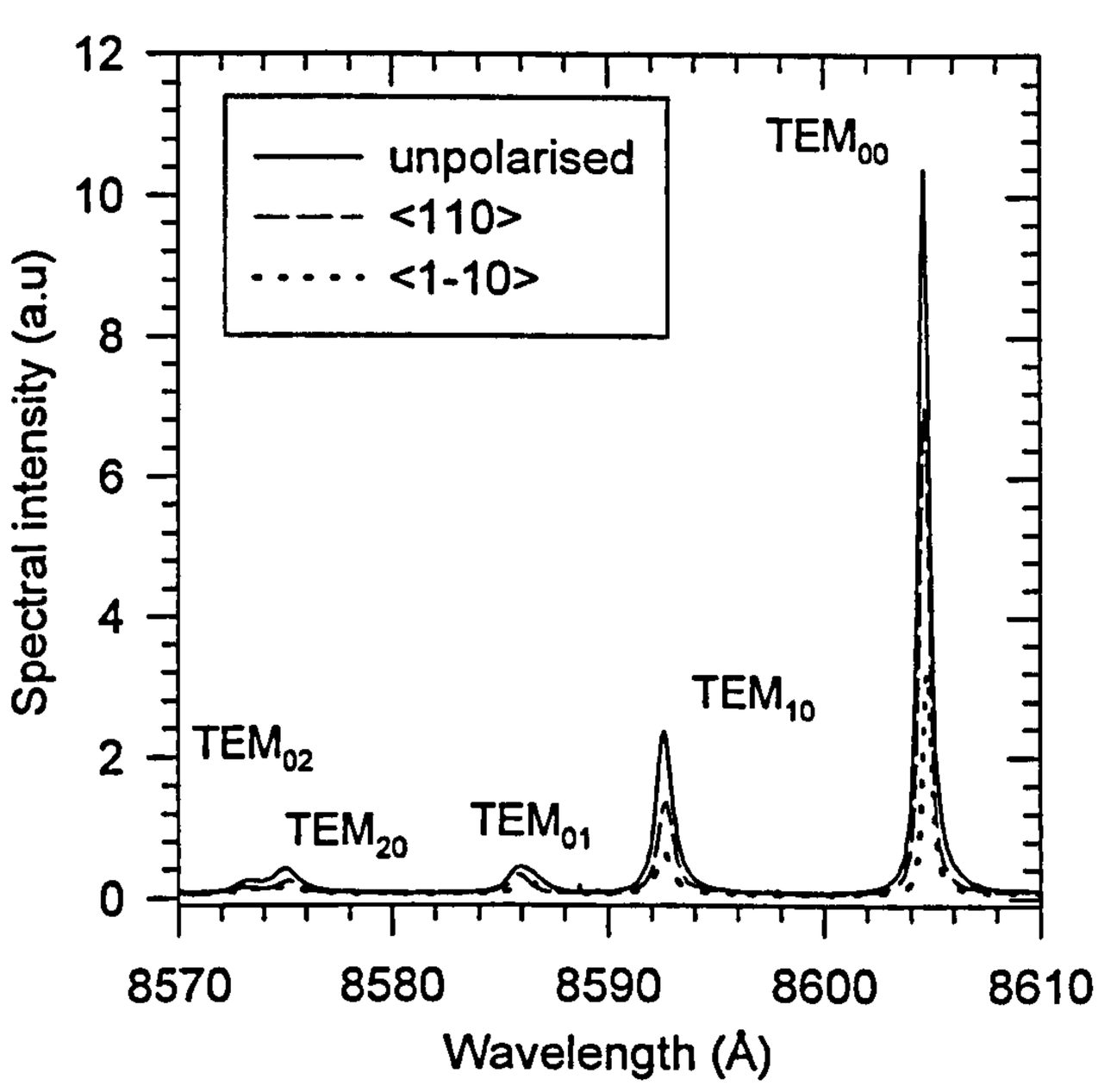

Figure 4.16(b) : Spontaneous emission spectra of (3.4 x 2.6) μm strong guiding device at half the threshold current density

For aspect ratio in the range of $1.12 < (2b/2a) < 1.20$, Figure 4.17 compares the predicted and experimental values of the spectral splitting between the TEM_{01} and TEM_{10} modes for several strong guiding devices whose dimensions of the shorter side of the aperture are in the range of $2.5\ \mu m < a < 4.5\ \mu m$. Clearly, the experimental and theoretical values agree quite well. However, for larger values of aspect ratio the predicted splitting tend to be always larger than the measured values. For instance, the measured spectral splitting for (2.4 x 2.9)μm, (2.2 x 3.1)μm and (2.9 x 4.3)μm devices (aspect ratios are 1.21, 1.31,1.48 respectively) were found to be 5.6Å, 8.3Å, and 7.1Å in each case, but the predicted values are 7.0Å, 12.8Å and 9.6Å respectively. This may be because the simulation does not take account of the dispersive nature of the refractive indices of the DBR constituents, which might limit the spectral splitting through its effect on the resonant wavelengths. Besides that, as the dimension of the shorter length reduces, the rate of change in spectral splitting also becomes very sensitive to the aspect ratio. Thus, any possible measurement error in the dimensions of the aperture could also contribute to the discrepancies.

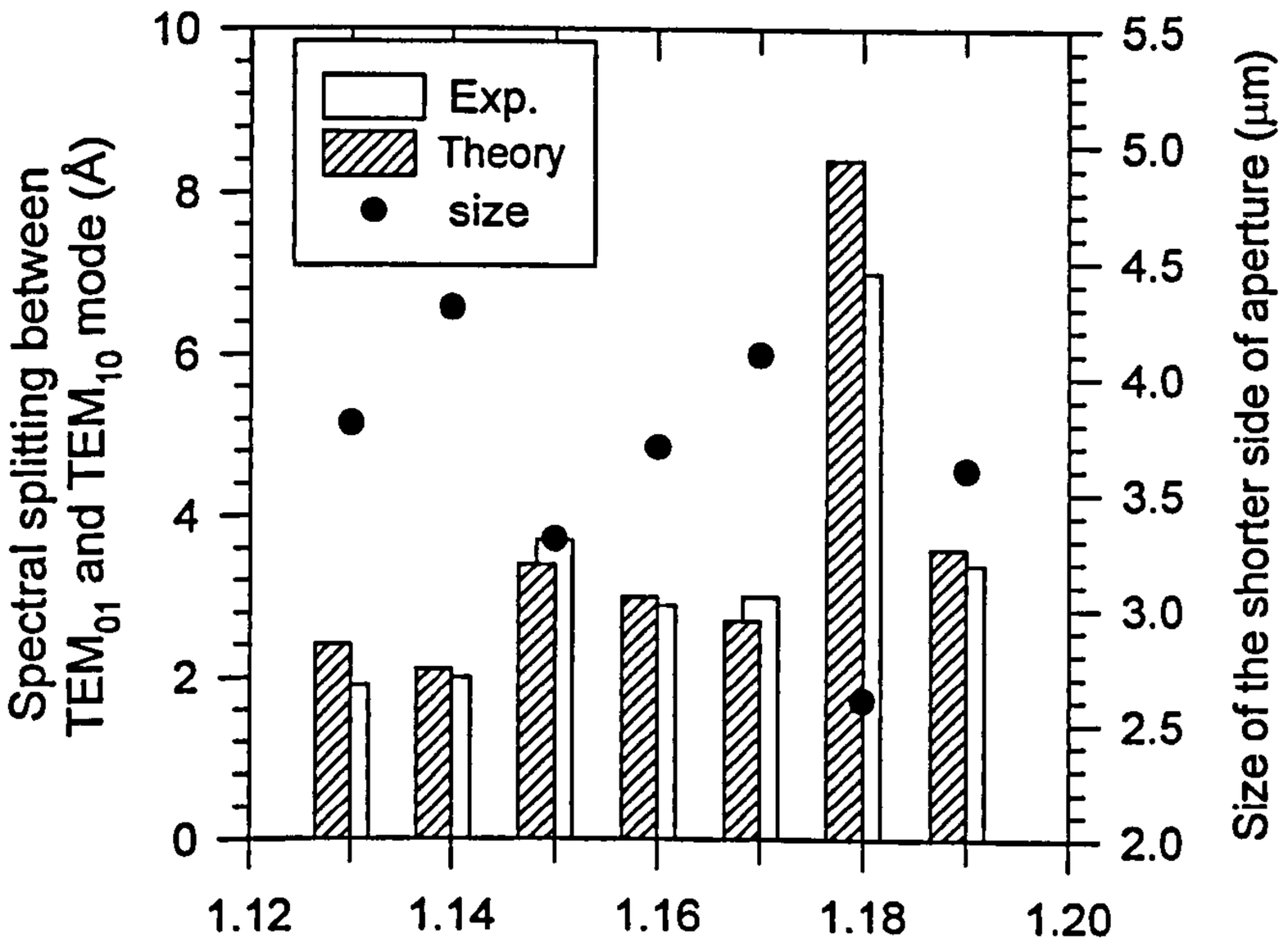

Figure 4.17 : Spectral splitting between the TEM_{01} and TEM_{10} modes as a function aperture aspect ratio (2b/2a).

4.4 Summary

This chapter describes how the scalar variational method can be used to determine the resonant wavelength and mode sizes of the eigenmodes that exist in oxide apertured "passive cavity" resonators, or equivalently in active devices under the "cold cavity" condition. Under the assumption of a Hermite-Gaussian transverse field variation, the scalar variational formulae for circular, square and rectangular oxide apertured resonators have been derived for the TEM_{00}, TEM_{01}, TEM_{10} and TEM_{11} modes. It is found that :-

- The blue shift in the resonant wavelength of a given eigenmode from that of the plane wave value, as well as the wavelength splittings between the eigenmodes, increases with reduction in aperture size or area.
- Conversely, the mode size decreases as the aperture size becomes smaller until it reaches a minimum value, beyond which the mode expands rapidly and eventually becomes no longer guided in the apertured resonator. The loss of confinement of the higher order modes occurs at a larger aperture sizes than the lower order modes.
- For a given aperture size or area, it is the strong guiding device that has the largest eigenmode wavelength splitting and blue shift in resonant wavelength. This is followed by the medium and weak guiding devices. However, the eigenmode sizes are smallest in the strong guiding device, and biggest in the weak guiding device.
- Wavelength splitting between the TEM_{01} and TEM_{10} modes occurs when the symmetry in the aperture shape is broken. It is always the mode with the field null along the longer side of a rectangular aperture, that has the longer resonant wavelength, i.e. TEM_{01} mode for $b/a > 1$ and TEM_{10} mode for $b/a < 1$.
- For a given aspect ratio, the wavelength splitting between the TEM_{01} and TEM_{10} modes increases with the reduction the aperture area or effective aperture size. Also, for the same aspect ratio and aperture area, it is the strong guiding device that exhibits the largest splitting. This is followed by the medium and weak guiding devices.

Due to the stationary nature of this method, as discussed in *Appendix C*, it is expected to be relatively insensitive to errors arising from the assumptions made to simplify form of trial fields. This is confirmed by the fact that the theoretical predictions on the eigenmode resonant wavelengths and wavelength separations match

closely the experimental results measured from the VCSEL devices with different aperture sizes and oxide thickness.

References for Chapter 4

[1] R.F.Harrington, "*Time-Harmonic Electromagnetic Fields*", (McGraw-Hill, New York, 1961), Chapters 4 & 7.

[2] P.N.Robson, private communication.

[3] A.W.Snyder, "*Optical Waveguide Theory*",(Chapman and Hall, 1983),chapter 15

[4] A.W.H.Beck, "*Space Charge Waves*", (Pergamon Press, 1958), p.332

[5] A.Yariv, "*Optical Electronics*", (Sauders College Publishing, 1991), chapters 2 & 4.

[6] A.E.Siegman, "*Lasers*", (University Science Books, 1986), chapters 14, & 17.

[7] C.J.Chang-Hasnain, M.Orenstein, A.V.Lehmen, L.T.Florez, J.P.Harbison and N.G.Stoffel, " Transverse mode characteristics of vertical cavity surface emitting lasers", Appl. Phys. Lett., vol.57, pp.218-220, 1990.

[8] R.Michalzik and K.J.Ebeling, "Generalised BV diagrams for higher order transverse modes in planar vertical cavity laser diodes", IEEE Journal of Quantum Electronics, vol.31, pp.1371-1379, 1995.

[9] D.Burak and R.Binder, "Electromagnetic characterisation of vertical cavity surface emitting lasers based on a vectorial eigenmode calculation", Appl. Phy. Lett., vol.72, pp. 891-893, 1998.

[10] K.D.Choquette, K.M.Geib, C.I.H.Ashby, "Advances in selective wet oxidation of AlGaAs Alloys", IEEE J. of Selected Topics in Quantum Electronics, vol.3, pp.916-926, 1997.

[11] A.K.Jansen van Doorn, M.P. van Exter and J.P.Woerdman, "Elasto-optical anisotropy and polarisation orientation of vertical cavity surface emitting semiconductor lasers", Appl. Phys. Lett., vol. 69, pp.1041-1043, aug 1996.

[12] J.G.Mendoza, F.D.Nunes and N.B.Patel, "Refractive index dependence on free carriers for GaAs", J.Appl. Phys., Vol. 51, pp.4365-4367, 1980.

[13] T.E.Sale, " *Vertical Cavity Surface Emitting Lasers*", (John Willey & Sons Inc., 1995), Chapter 8.

[14] S.Adachi, "GaAs, AlAs, and $Al_xGa_{1-x}As$: Material parameters for use in research and applications", J.Appl. Phys., vol. 58, pp. R1-R29, 1985.

[15] J.Woodhead, *private communication on the thermal modelling of oxidised VCSELs using finite element technique.*

[16] N.K.Dutta, L.W.Tu, G.Hasnain and A.Y.Cho, "Anomalous temporal response of gain guided surface emitting lasers", Electron. Lett., vol.27, pp.208-210, 1991.

[17] P.Heremans, M.Kuiik, R.Windisch, J.Vanderhaegen, H.De Neve and G.Borghs, "Angular Spectroscopic analysis : An optical characterisation technique for laterally oxidised AlGaAs layers", J.Appl. Phys., vol.81, pp. 5265-5267, Nov. 1996.

[18] M.Born & E.Wolf, "*Principles of Optics*", (Pergamon Press, 1970), Chapter 8.

Chapter 5 Theoretical Analysis of Oxide Apertured VCSELs

5.1 Introduction

This chapter describes the numerical approaches adopted in this work for analysing the lasing characteristics of oxide apertured VCSELs. Firstly, the method for calculating the modal reflectance and transmittance of arbitrary Hermite-Gaussian eigenmodes is detailed. Then, using the values of mode sizes and resonant wavelengths obtained from the closed form variational expression discussed in Chapter 4, the oxide aperture size dependence of modal reflectance for the three VCSEL structures under consideration are predicted. This is followed by the derivation of the relationship between the eigenmode photon lifetime, cavity Q-factor and spontaneous emission linewidth. Finally, the light-current characteristics of the first two lowest order eigenmodes are also calculated through the self consistent solution of photon and carrier rate equations.

The simulation results presented below were calculated assuming that the DBRs of the strong and medium VCSEL layers have the same absorption coefficients deduced experimentally and presented in chapter 3 for the weak guiding layer. This is necessary so that meaningful comparisons and deductions regarding the effect of using different oxide thickness can be made. The theoretical curves that take account of the different absorption levels in the DBRs among the three VCSEL structures will be presented later in chapter 6, when comparisons between experimental and theoretical results are made.

5.2 Modal Reflectivity of Distributed Bragg Reflectors (DBRs)

For an optical beams, the modal reflectance of a DBR is limited by the diffraction loss as a result of beam spreading during propagation. This diffraction loss

is dependent on the size, shape, mode number of the particular transverse mode concerned as well as its polarisation direction. In this section, the modal reflection properties of Hermite - Gaussian beams incident upon a DBR are studied, in accordance with the trial fields chosen for the scalar variational formulae discussed in chapter 4. From these simulation results, the possible implications on the threshold and polarisation properties of oxide apertured VCSELs are also discussed.

5.2.1 Modal Reflections of Hermite - Gaussian Beams

In order to calculate the modal reflection properties of Hermite - Gaussian beams, the spatial Fourier decomposition method which involves transforming the beam profile into the "spatial frequency" or the "k-vector space" domain has to be employed. The Fourier transform pair in two dimensional space is given by [1]

$$F(k_x,k_y) = \int_{-\infty}^{\infty}\int_{-\infty}^{\infty} f(x,y)\exp(-jk_x x)\exp(-jk_y y)\,dxdy \qquad (5.1)$$

$$f(x,y) = \frac{1}{4\pi^2}\int_{-\infty}^{\infty}\int_{-\infty}^{\infty} F(k_x,k_y)\exp(jk_x x)\exp(jk_y y)\,dk_x dk_y \qquad (5.2)$$

where f(x,y) is the transverse spatial function of the field, and $F(k_x, k_y)$ is the corresponding Fourier transform function in terms of the transverse phase constants (or spatial frequencies), $f(x,y)$ is the spatial Fourier integral functions obtained through "inverse" Fourier transform of $F(k_x,k_y)$.

For the first two order 1-D Hermite - Gaussian functions in the form of

$$f_0(x) = \exp\left(\frac{-x^2}{r_0^2}\right) \qquad (5.3a)$$

$$f_1(x) = x\exp\left(\frac{-x^2}{r_1^2}\right) \qquad (5.3b),$$

it can be shown (see ***Appendix E***) that the corresponding Fourier transforms in k-space are given by

$$F_0(k_x) = \sqrt{\pi}r_0\exp\left(\frac{-k_x^2 r_0^2}{4}\right) \qquad (5.4a)$$

$$F_1(k_x) = \frac{-j\sqrt{\pi}r_1^3 k_x}{2}\exp\left(\frac{-k_x^2 r_1^2}{4}\right) \qquad (5.4b)$$

respectively. Note that the Fourier transform of a Hermite-Gaussian spatial function is

also expressed by a Hermite-Gaussian function in the k-space. Consequently, the expressions in equation (5.4) can be further "inverse" Fourier transformed to yield the Fourier spatial integral functions *f* involving both space distance and phase constants. They are expressed by

$$f_0(x) = \frac{r_0}{\sqrt{\pi}} \int_0^{\infty} \exp\left(\frac{-k_x^2 r_0^2}{4}\right) \cos(k_x x)\, dk_x \qquad (5.5a)$$

$$f_1(x) = \frac{r_0^3}{2\sqrt{\pi}} \int_0^{\infty} k_x \exp\left(\frac{-k_x^2 r_0^2}{4}\right) \sin(k_x x)\, dk_x \qquad (5.5b)$$

Note that the derivations leading to expressions (5.4) and (5.5) are detailed in ***Appendix E.***

By making use of the Fourier identities (5.4) to (5.5) as well as equations (5.1) and (5.2), the spatial Fourier transform pairs of the first four lowest order Hermite-Gaussian modes can be easily derived. For the sake of generalisation, the expressions for spatial Fourier transforms and spatial Fourier integral functions (i.e. inverse spatial Fourier transforms) of the *elliptical* Hermite-Gaussian modes are shown in Table 5.1 and Table 5.2 respectively. The corresponding expressions for *circular* TEM_{mp} modes can be obtained by simply allowing for $w_x = w_y$. As expected, the expressions for the Fourier transforms listed in Table 5.1 implies that the 1/e "spread" of the transform functions changes in opposite trend to the mode sizes of the spatial functions, i.e. beams with narrower spot size are "larger" in the k-space but with lower scaled "amplitude". However, it is the Fourier integral functions tabulated in Table 5.2 that reveal the composition of a Hermite-Gaussian beam.

These functions indicate that the Hermite Gaussian modes actually consist of an infinite sum of component waves with scaled amplitudes dependent on the modes sizes and transverse phase constant. These component waves have different transverse field variations of the form $\cos(k_x x)\cos(k_y y)$, $\cos(k_x x)\sin(k_y y)$, $\sin(k_x x)\cos(k_y y)$ and $\sin(k_x x)\sin(k_y y)$ for the TEM_{00}, TEM_{01}, TEM_{10} and TEM_{11} modes respectively and are polarised in either x or y directions depending on the original polarisation of the TEM_{mp} mode assumed. These waves are called Longitudinal Section Electric (LSE) waves [2 - 4] since the electric field is wholly in either the longitudinal x-z plane or longitudinal y-z plane, and they are characterised by having transverse variations of the form $\begin{matrix}\cos \\ \sin\end{matrix}(k_x x)\begin{matrix}\cos \\ \sin\end{matrix}(k_y y)$. The field reflection and transmission coefficients for

these LSE waves propagating in the z-direction can be calculated in the similar manner for the plane waves as discussed in section 2.3. The derivations of the wave admittance for these LSE waves are detailed in *Appendix A.2* where the wave admittance is shown to be different for the x or y-polarised waves.

Modes	Spatial functions, $f_{mp}(x,y)$	Fourier transforms in k-space, $F_{mp}(k_x,k_y)$
TEM_{00}	$\exp\left(\frac{-x^2}{w_{x00}^2}\right)\exp\left(\frac{-y^2}{w_{y00}^2}\right)$	$\pi w_{x00} w_{y00} \exp\left(\frac{-k_x^2 w_{x00}^2}{4}\right)\exp\left(\frac{-k_y^2 w_{y00}^2}{4}\right)$
TEM_{01}	$y \exp\left(\frac{-x^2}{w_{x01}^2}\right)\exp\left(\frac{-y^2}{w_{y01}^2}\right)$	$\frac{-j\sqrt{\pi}\, w_{x01}\, w_{y01}^3\, k_x}{2} \exp\left(\frac{-k_x^2 w_{x01}^2}{4}\right)\exp\left(\frac{-k_y^2 w_{y01}^2}{4}\right)$
TEM_{10}	$x \exp\left(\frac{-x^2}{w_{x10}^2}\right)\exp\left(\frac{-y^2}{w_{y10}^2}\right)$	$\frac{-j\sqrt{\pi}\, w_{y10} w_{x10}^3\, k_y}{2} \exp\left(\frac{-k_x^2 w_{x10}^2}{4}\right)\exp\left(\frac{-k_y^2 w_{y10}^2}{4}\right)$
TEM_{11}	$xy \exp\left(\frac{-x^2}{w_{x11}^2}\right)\exp\left(\frac{-y^2}{w_{y11}^2}\right)$	$\frac{-\sqrt{\pi}\, w_{y11}^3 w_{x11}^3 k_x k_y}{4} \exp\left(\frac{-k_x^2 w_{x11}^2}{4}\right)\exp\left(\frac{-k_y^2 w_{y11}^2}{4}\right)$

Table 5.1 : Fourier transforms (in k-space) of the first four lowest order *elliptical* Hermite - Gaussian TEM_{mp} modes.

Modes	Spatial Fourier Integral Functions, $f_{mp}(x,y)$
TEM_{00}	$\frac{w_{x00}\, w_{y00}}{\pi} \int_0^\infty\int_0^\infty \exp\left(\frac{-k_x^2 w_{x00}^2}{4}\right) \exp\left(\frac{-k_y^2 w_{y00}^2}{4}\right) \cos(k_x x) \cos(k_y y)\, dk_x dk_y$
TEM_{01}	$\frac{w_{x01}\, w_{y01}^3}{2\pi} \int_0^\infty\int_0^\infty k_y \exp\left(\frac{-k_x^2 w_{x01}^2}{4}\right) \exp\left(\frac{-k_y^2 w_{y01}^2}{4}\right) \cos(k_x x) \sin(k_y y)\, dk_x dk_y$
TEM_{10}	$\frac{w_{x10}^3 w_{y10}}{2\pi} \int_0^\infty\int_0^\infty k_x \exp\left(\frac{-k_x^2 w_{x10}^2}{4}\right) \exp\left(\frac{-k_y^2 w_{y10}^2}{4}\right) \sin(k_x x) \cos(k_y y)\, dk_x dk_y$
TEM_{11}	$\frac{w_{x11}^3 w_{y11}^3}{4\pi} \int_0^\infty\int_0^\infty k_x k_y \exp\left(\frac{-k_x^2 w_{x11}^2}{4}\right) \exp\left(\frac{-k_y^2 w_{y11}^2}{4}\right) \sin(k_x x) \sin(k_y y)\, dk_x dk_y$

Table 5.2 : Spatial Fourier integral functions of the first four lowest order *elliptical* Hermite- Gaussian TEM_{mp} modes.

The spatial Fourier integral function at the reference interface for the *reflected* beam, $f^{r}_{mp}(x,y)$, originating from a given order incident Hermite-Gaussian mode is similar to those given in Table 5.2 except for the inclusion of an additional $r_{x(LSE)}(k_x,k_y)$ or $r_{y(LSE)}(k_x,k_y)$ term in the integrand depending on whether the incident wave is x or y polarised. The reflected integral function $f^{r}_{mp}(x,y)$, is thus different from the incident one $f_{mp}(x,y)$, and may be considered to be made up of the reflected original mode with reduced amplitude, as well as modes of other orders. It can be written as

$$f^{r}_{mp}(x,y) = r_{mp}\, f_{mp}(x,y) + \text{functions of other modes} \qquad (5.6)$$

where r_{mp} is the modal reflection coefficient. To extract $r_{mp,}$ it is necessary to calculate the overlap integral for the eigenmode concerned. For this purpose, each term in eqn.(5.6) is multiplied by $f^{*}_{mp}(x,y)$ and then integrated over the transverse x-y plane. This results in

$$\int_{-\infty}^{\infty}\int_{-\infty}^{\infty} f^{r}_{mp}(x,y)\, f^{*}_{mp}(x,y)\, dxdy = \int_{-\infty}^{\infty}\int_{-\infty}^{\infty} r_{mp}\, f_{mp}(x,y)\, f^{*}_{mp}(x,y)\, dxdy + \int_{-\infty}^{\infty}\int_{-\infty}^{\infty}(\text{functions of other modes})\, f^{*}_{mp}(x,y)\, dxdy \qquad (5.7)$$

Then by making use of the orthogonality property of the Hermite-Gaussian function [1] which states that

$$\int_{-\infty}^{\infty} f_a(x)\, f^{*}_b(x)\, dx = \begin{cases} 0, & \text{if } a \neq b \\ \text{real constant}, & \text{if } a = b \end{cases} \qquad (5.8),$$

the modal reflection coefficient can be determined from eqn.(5.7) and eqn.(5.8) as

$$r_{mp} = \frac{\int_{-\infty}^{\infty}\int_{-\infty}^{\infty} f^{r}_{mp}(x,y)\, f^{*}_{mp}(x,y)\, dxdy}{\int_{-\infty}^{\infty}\int_{-\infty}^{\infty} f_{mp}(x,y)\, f^{*}_{mp}(x,y)\, dxdy} \qquad (5.9)$$

where $f^{*}_{mp}(x,y) = f_{mp}(x,y)$ for the real incident Hermite-Gaussian functions discussed here.

By making use of the integral identities in *Appendix D*, the denominator of (5.9) which involves integration of Hermite-Gaussian function can always be reduced to a simple expression. For instance, for the elliptical TEM_{00} mode polarised in a

given transverse direction, the denominator of (5.9) is given by $\pi w_{x00} w_{y00} / 2$ as deduced from solution (D.1). As for the numerator, it can be simplified to :-

numerator

$$= \frac{w_{x00} w_{y00}}{\pi} \int_0^\infty \int_0^\infty \left\{ \left[\int_{-\infty}^{\infty} \int_{-\infty}^{\infty} \exp\left(\frac{-x^2}{w_{x00}^2}\right) \exp\left(\frac{-y^2}{w_{y00}^2}\right) \cos(k_x x) \cos(k_y y)\, dx dy \right] \right.$$
$$\left. r_{LSE}(k_x, k_y) \exp\left(\frac{-k_x^2 w_{x00}^2}{4}\right) \exp\left(\frac{-k_y^2 w_{y00}^2}{4}\right) \right\} dk_x dk_y$$

$$= \frac{w_{x00} w_{y00}}{\pi} \int_0^\infty \int_0^\infty F_{00}(k_x, k_y)\, r_{LSE}(k_x, k_y) \exp\left(\frac{-k_x^2 w_{x00}^2}{4}\right) \exp\left(\frac{-k_y^2 w_{y00}^2}{4}\right) dk_x dk_y$$

$$= w_{x00}^2 w_{y00}^2 \int_0^\infty \int_0^\infty r_{LSE}(k_x, k_y) \exp\left(\frac{-k_x^2 w_{x00}^2}{2}\right) \exp\left(\frac{-k_y^2 w_{y00}^2}{2}\right) dk_x dk_y \quad (5.10)$$

where $r_{LSE}(k_x,k_y)$ is the reflection coefficient of the LSE wave polarised in the direction specified. Thus, the modal reflection coefficient for the TEM_{00} mode, r_{00} , is given by

$$r_{00} = \frac{2 w_{x00} w_{y00}}{\pi} \int_0^\infty \int_0^\infty r_{LSE}(k_x, k_y) \exp\left(\frac{-k_x^2 w_{x00}^2}{2}\right) \exp\left(\frac{-k_y^2 w_{y00}^2}{2}\right) dk_x dk_y \quad (5.11)$$

The modal reflection coefficients for other higher order modes can be obtained through a similar procedure by making use of eqn.(5.4b) as well as other relevant solutions listed in *Appendix D*. The final expressions are shown in Table 5.3. Having computed the modal reflection coefficients, the modal power reflectance, R_{mp} can then be calculated through $R_{mp} = r_{mp} r_{mp}^*$. Note that the expressions for the corresponding modal transmission coefficients t_{mp} are similar to those listed in Table 5.3 except for replacing the field reflection coefficient $r_{LSE}(k_x,k_y)$ with field transmission coefficient $t_{LSE}(k_x,k_y)$. The modal power transmittance is then simply given by the $t_{mp} t_{mp}^* [\mathrm{Re}(Y_s)/\mathrm{Re}(Y_i)]$, in similar form to eqn.(2.34).

Modes	Modal Reflection Coefficients, r_{mp}
TEM_{00}	$\frac{2w_{x00}w_{y00}}{\pi}\int_0^\infty\int_0^\infty r_{LSE}(k_x,k_y)\exp\left(\frac{-k_x^2w_{x00}^2}{2}\right)\exp\left(\frac{-k_y^2w_{y00}^2}{2}\right)dk_xdk_y$
TEM_{01}	$\frac{2w_{x01}w_{y01}^3}{\pi}\int_0^\infty\int_0^\infty r_{LSE}(k_x,k_y)\,k_y^2\exp\left(\frac{-k_x^2w_{x01}^2}{2}\right)\exp\left(\frac{-k_y^2w_{y01}^2}{2}\right)dk_xdk_y$
TEM_{10}	$\frac{2w_{x10}^3w_{y10}}{\pi}\int_0^\infty\int_0^\infty r_{LSE}(k_x,k_y)\,k_x^2\exp\left(\frac{-k_x^2w_{x10}^2}{2}\right)\exp\left(\frac{-k_y^2w_{y10}^2}{2}\right)dk_xdk_y$
TEM_{11}	$\frac{2w_{x11}^3w_{y11}^3}{\pi}\int_0^\infty\int_0^\infty r_{LSE}(k_x,k_y)\;k_x^2k_y^2\exp\left(\frac{-k_x^2w_{x11}^2}{2}\right)\exp\left(\frac{-k_y^2w_{y11}^2}{2}\right)dk_xdk_y$

Table 5.3 : Modal reflection coefficients of the first four lowest order elliptical Hermite - Gaussian TEM_{mp} modes.

5.2.2 Simulation Results I : Dependence of Diffraction Loss on Mode Size and Mode Number

Using the approach described above, the modal reflectance of the Hermite-Gaussian modes from any DBR structure can be calculated numerically. For a LSE component wave having k-vectors (k_x,k_y), its reflection coefficient and transmission coefficient are readily obtained using the transfer matrix method discussed in chapter 2, using the wave admittance and propagation constants of LSE waves. As an example, Figure 5.1 illustrates the 2-D variation of the y-polarised LSE wave reflectance at the designed 850nm central wavelength from the 28 pair top DBR (with 600Å AlAs) in k-vector space, while Fig 5.2 selectively shows only those with $k_x = 0$ (TM wave), $k_y = 0$ (TE wave), $k_x = k_y$, $k_x = 0.5k_y$ and $k_x = 2k_y$ (Note: the variable of the x-axis is k_x except for the TM waves).

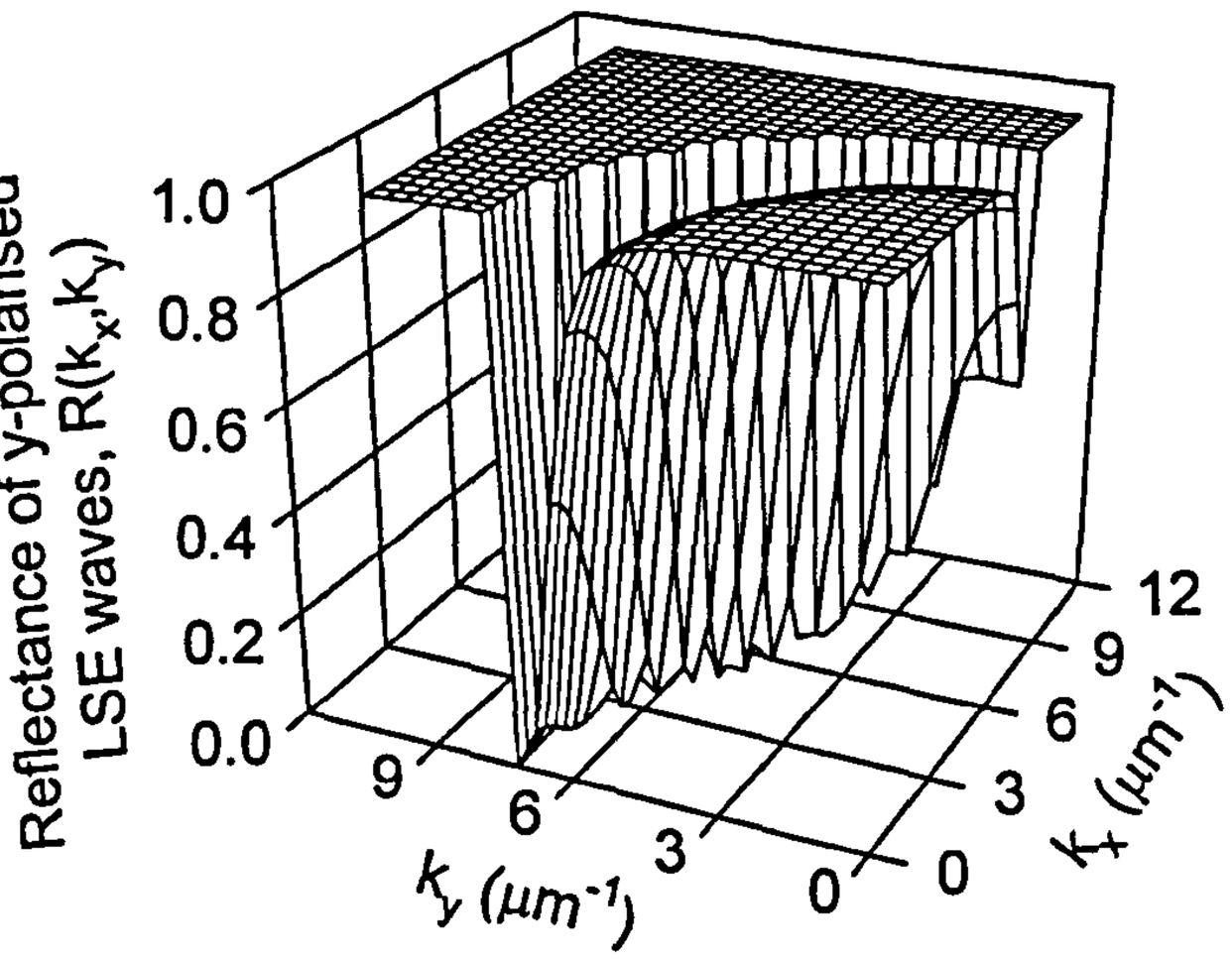

Figure 5.1 : Variation of the y-polarised LSE wave reflectance in the k-vector space at the designed 850nm central wavelength from the 28 pair top DBR.

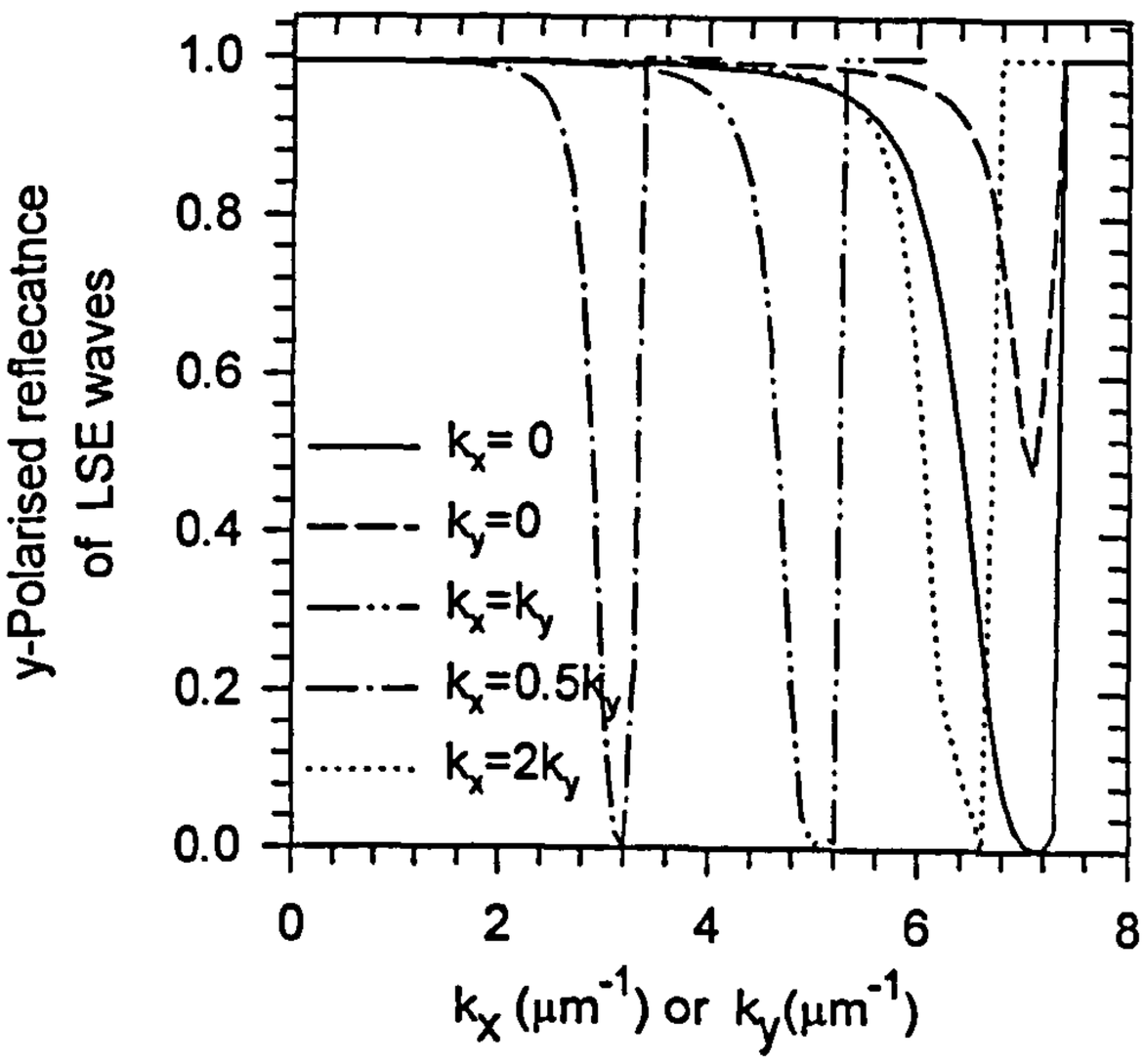

Figure 5.2 : y-polarised reflectance of the selected LSE waves.

In all cases, the wave reflectance drops with increasing k_x or/and k_y until it reach a minimum, after which it increases rapidly to give unity reflectance as a result of total internal reflection. Note that the incident angle (given by $\sin^{-1}(k_y/k_{inc})$ where k_{inc} is the wave number of the incident medium) at which the reflectance of the TM waves drop to zero is commonly known as the Brewster angle. The curves for the cases of $k_x = 2k_y$ and $k_x = 0.5k_y$ indicates that the reflectance and thus the reflection coefficients of the LSE waves are not symmetrical along the $k_x = k_y$ plane. This is

perhaps better illustrated in Figure 5.3 which shows the difference in reflectance between the y-polarised LSE waves with k-vector co-ordinates of (k_x,k_y) and (k_y,k_x), i.e. $R(k_x,k_y) - R(k_y,k_x)$ (e.g. R(5,2) - R(2,5) = 0.028187). As can be seen, this difference in reflectance is quite small when both k_x and k_y are less than $3\mu m^{-1}$. But beyond this range, the difference increases rapidly until reaching the maximum values, before decreasing to zero when the total internal reflections happen to both waves.

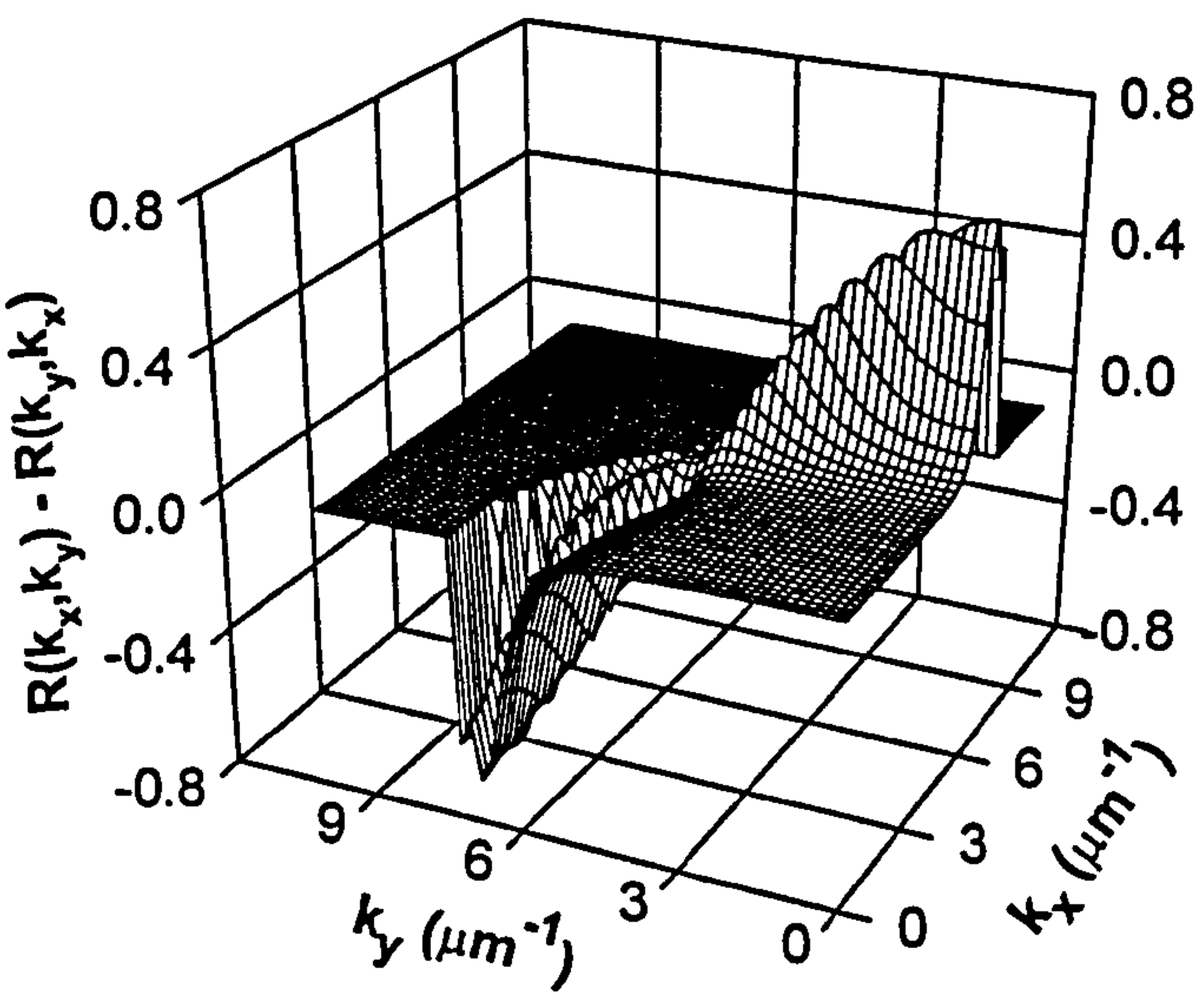

Figure 5.3 : Difference in reflectance between the y-polarised LSE waves with k-vector co-ordinates of (k_x,k_y) and (k_y,k_x), i.e. $R(k_x,k_y) - R(k_y,k_x)$.

Having calculated the reflection coefficients of LSE waves, the remaining numerical task for computing the modal reflectance then simply involves 2-D integration in the k-space of the expressions for modal reflection coefficients listed in Table 5.3. In this work, the uniform element sizes chosen ($\Delta k_x = \Delta k_x = 0.02\mu m^{-1}$) are sufficiently small and the required resolution imposed in terms of modal reflectance is better than 0.0005%. As an example, Figures 5.4(a) and 5.4(b) show the modal reflectivity spectra of the 28 pair top DBR for the first four order y-polarised Hermite-Gaussian modes with 1/e half mode widths of 1.0μm and 0.5μm respectively. The spectra for the plane wave are also included for comparison.

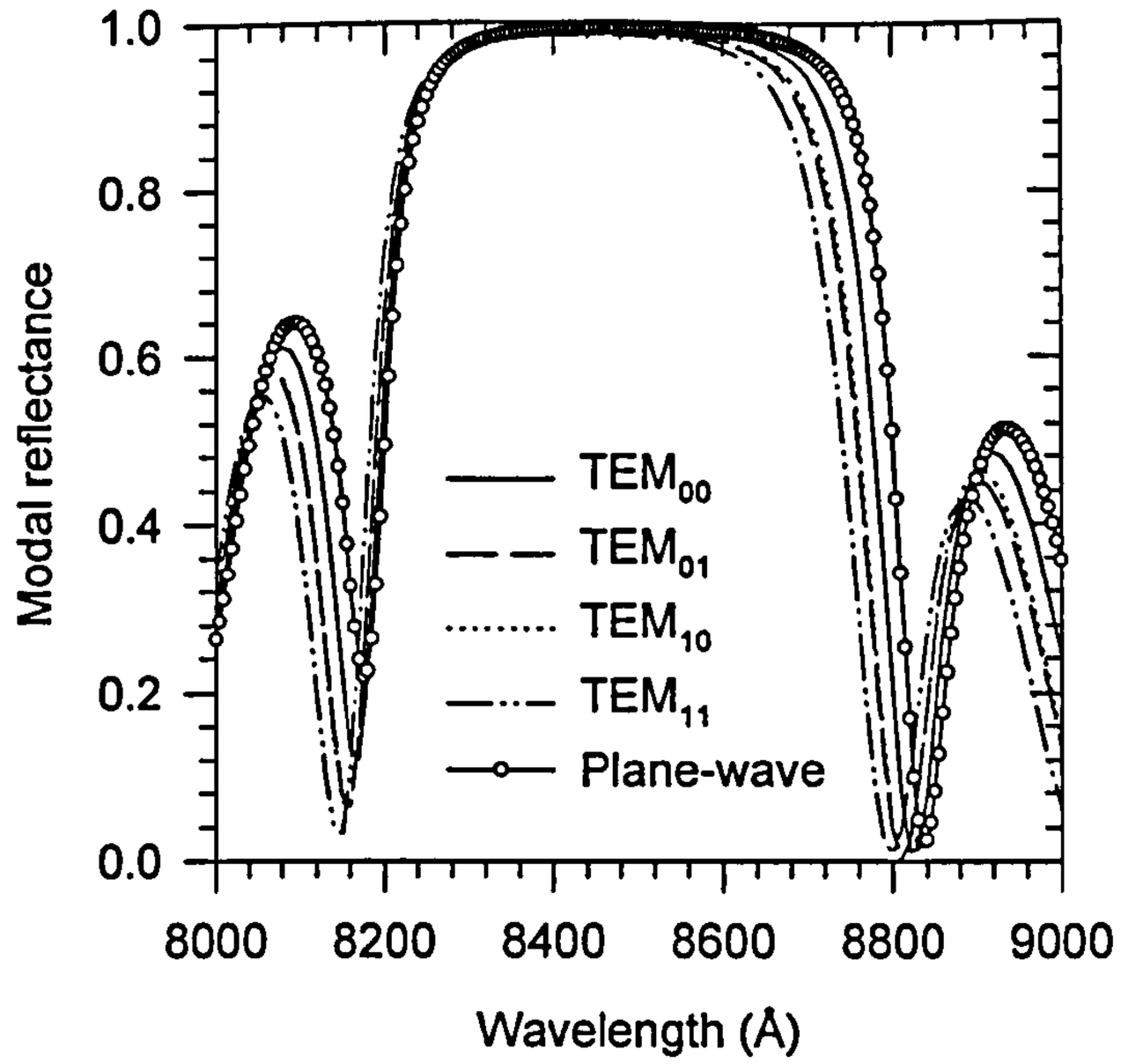

Figure 5.4(a) : Modal reflectivity spectra of the four lowest order eigenmodes with 1/e half mode width of **1.0μm**, for the 28 pair top DBR.

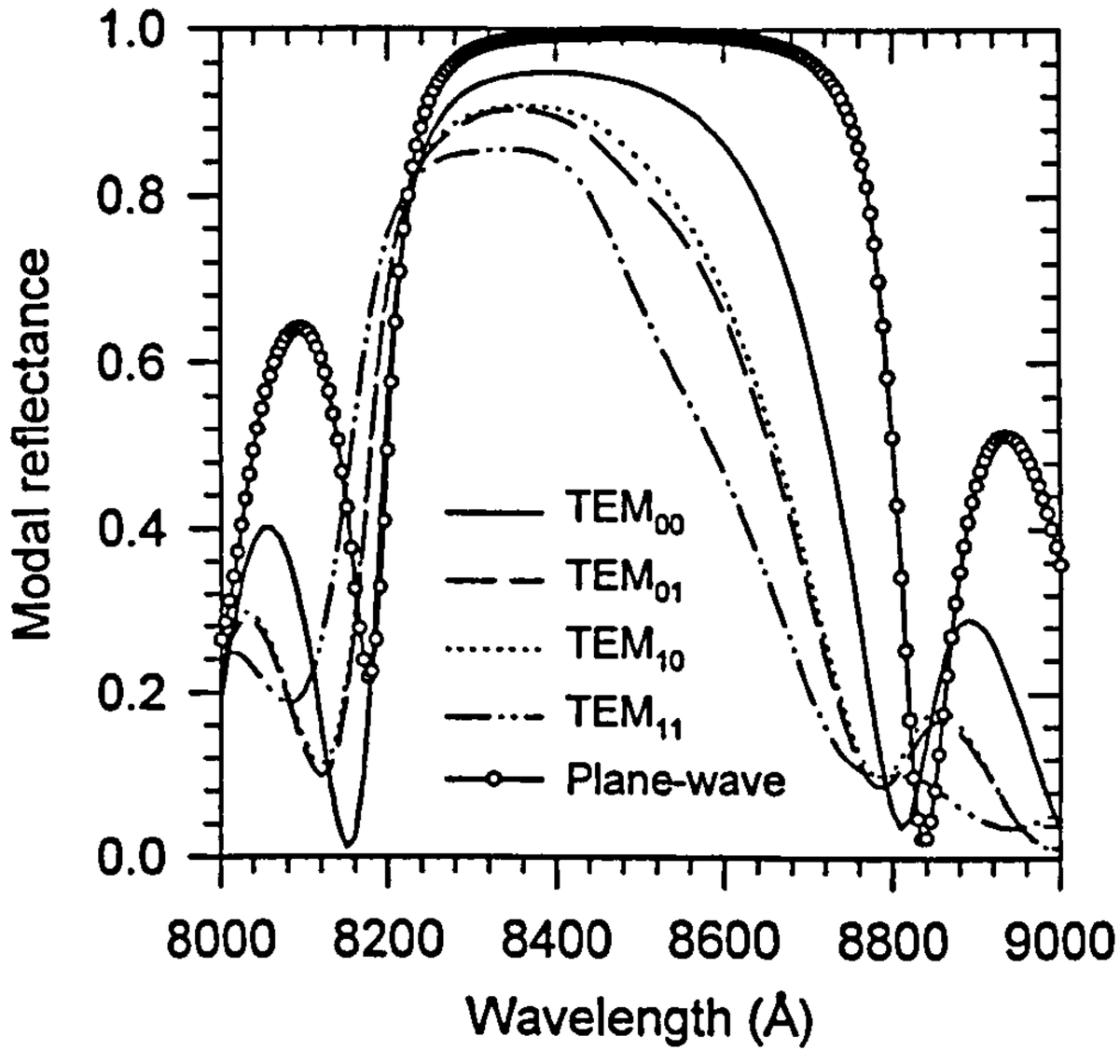

Figure 5.4(b) : Modal reflectivity spectra of the four lowest order eigenmodes with 1/e half mode width of **0.5μm**, for the 28 pair top DBR.

Clearly, the modal reflectance of the higher order modes are lower than those of lower order modes. In additional, its "bandwidth" of high reflectance region is also narrower. Comparing the values for a particular 1/e half mode width, those obtained

from the 0.5μm are always lower than that of 1.0μm especially in the higher order cases. This is attributed to the larger diffraction loss experienced by the eigenmodes with smaller mode sizes whereby the larger spreading in the k-space results in a lower modal reflection coefficient derived from the overlap integral given by (5.9). The modal reflectance of the y-polarised TEM_{10} mode is higher than the y-polarised TEM_{01} mode because of the different scaling factors in the respective modal reflection Fourier integrals given in Table 5.3 (i.e. k_x^2 for the former and k_y^2 for the latter), in addition to the non-symmetrical nature of LSE reflection coefficients along the $k_x = k_y$ plane as exemplified by Fig. 5.3. This difference also increases for smaller mode size as the beam spreads wider in k-space.

For the first four lowest order *circular* Hermite Gaussian modes, Figure 5.5(a) illustrates the dependence of y-polarised modal reflectance from the top DBR ($R_{T(mp)}$, main) and bottom DBR ($R_{B(mp)}$, inset) used in this work, as a function of the 1/e half mode width. The corresponding modal transmittance ($T_{T(mp)}$) and total optical loss from the top DBR ($1-R_{T(mp)}$) are also shown in Fig. 5.5(b). In all cases, the modal reflectance decreases and transmittance increases rapidly when the mode sizes become smaller than 1.0μm. However, the reduction in the modal reflectance of the bottom DBR is less severe than the top DBR since it is designed to have near-unity plane wave reflectance. For the same reason, the transmittance through the bottom DBR is also much smaller than that of the top DBR. Therefore, for the VCSELs used in this work the diffraction losses suffered by the eigenmodes with small mode sizes are mainly due to that from the top DBR. It should also be noted that the difference in modal reflectance of the fundamental mode and other higher order modes increases rapidly with reduction in mode size. From the "single mode" operation point of view, this implies that the suppression of the higher order modes in a multi-moded oxide apertured VCSEL should be better when the oxide apertures are small. Conversely, as the mode sizes get larger these modal reflectances approach the plane wave value and reduce the difference in modal reflectance between different eigenmodes. Therefore, larger devices are more susceptible to the onset of higher order modes. It should also be noted that the absorption losses in the DBR do not affect the qualitative observations made above. Indeed, the same conclusions have also been drawn, based on the results obtained from absorption-free DBR [19].

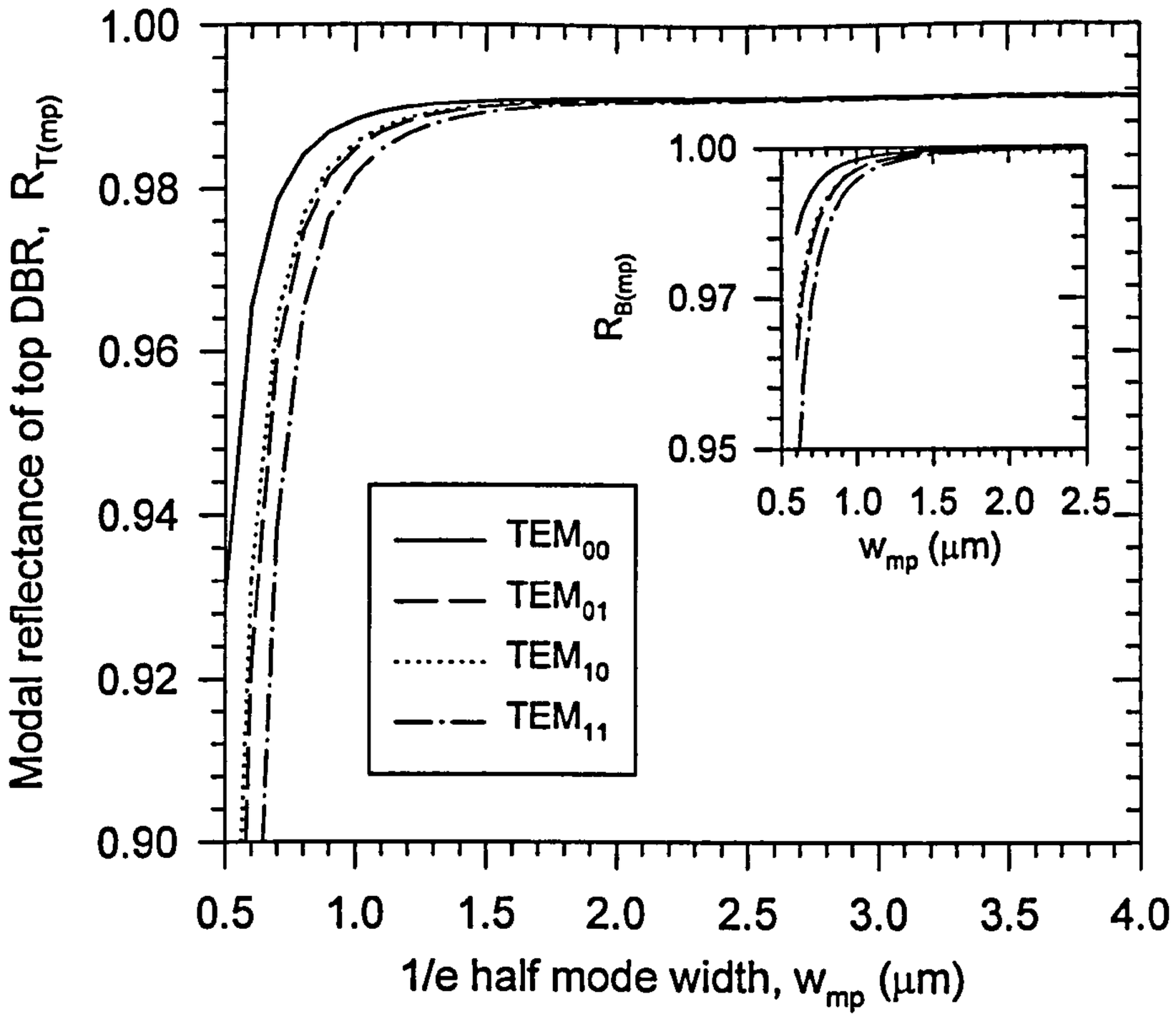

Figure 5.5(a) : y-polarised modal reflectance from the top DBR, $R_{T(mp)}$ (main), and bottom DBRs, $R_{B(mp)}$ (inset) for the first four lowest order circular TEM_{mp} modes.

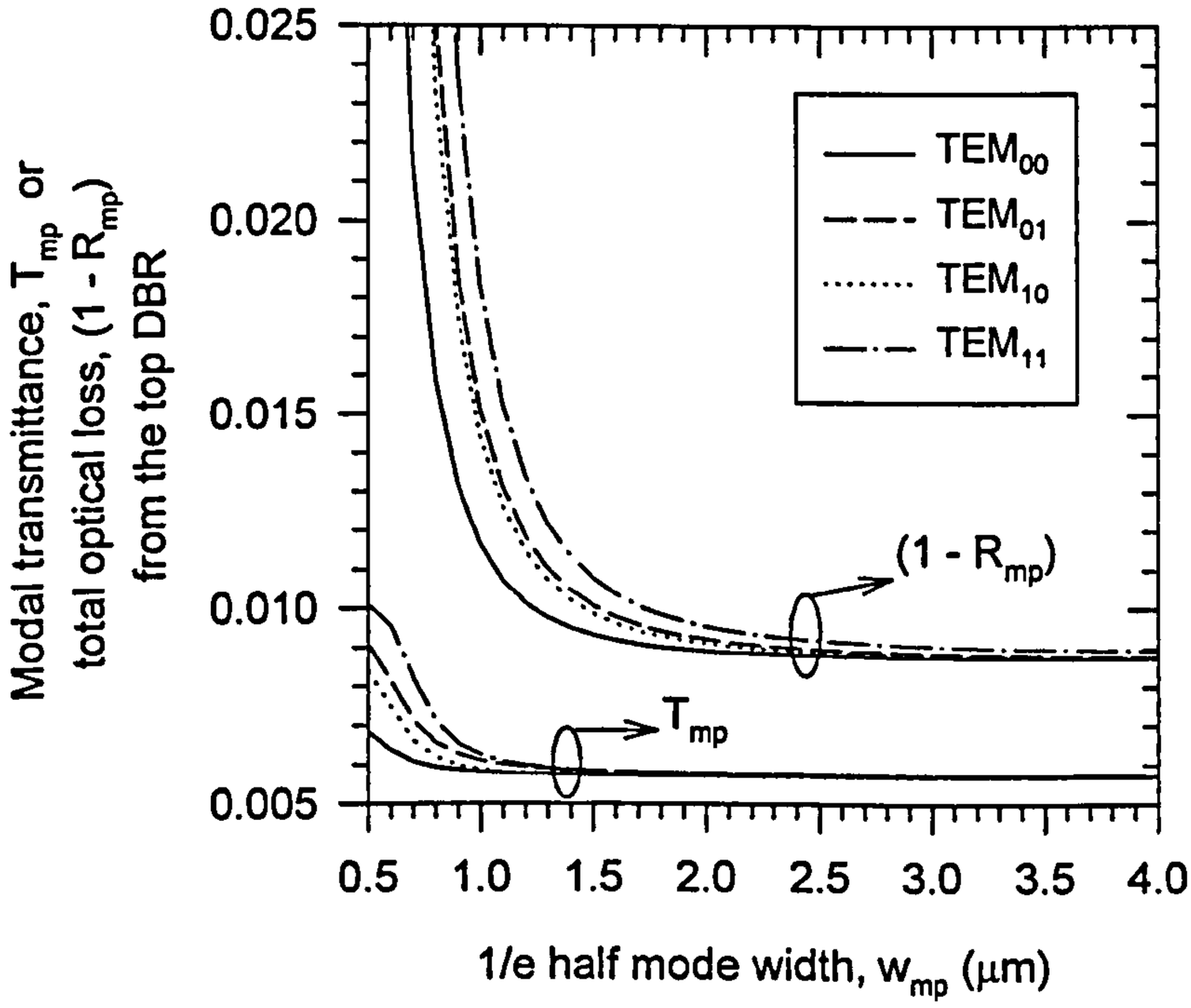

Figure 5.5(b) : y-polarised modal transmitance, $T_{T(mp)}$ and total optical loss from the top DBR, $(1-R_{T(mp)})$.

As an aside and also in order to illustrate the dependence of the modal diffraction loss on the refractive index contrast ratio of the DBR constituent stacks, Figure 5.6 also shows the change in modal reflectance with 1/e half mode width of an alternative high index contrast ratio Al_xO_y based top DBR which can be readily obtained through selective oxidation. This DBR has similar plane-wave reflectivity to the all-semiconductor counterpart described above, and the TEM_{00} mode curve for the latter is also included in the figure for comparison. The layer structure of this particular oxide-DBR under consideration is composed of Air / ($\lambda/14$ $Al_{0.2}Ga_{0.8}As$ / Al_xO_y) / 3 x (Al_xO_y / $Al_{0.2}Ga_{0.8}As$) / ($3\lambda/4$ $Al_{0.2}Ga_{0.8}As$ / AlAs) / cavity, where all the layers are of quarter wave thick unless stated otherwise. The $3\lambda/4$ $Al_{0.2}Ga_{0.8}As$ layer is meant for ohmic contacting while the AlAs layer is for the formation of an oxide aperture.

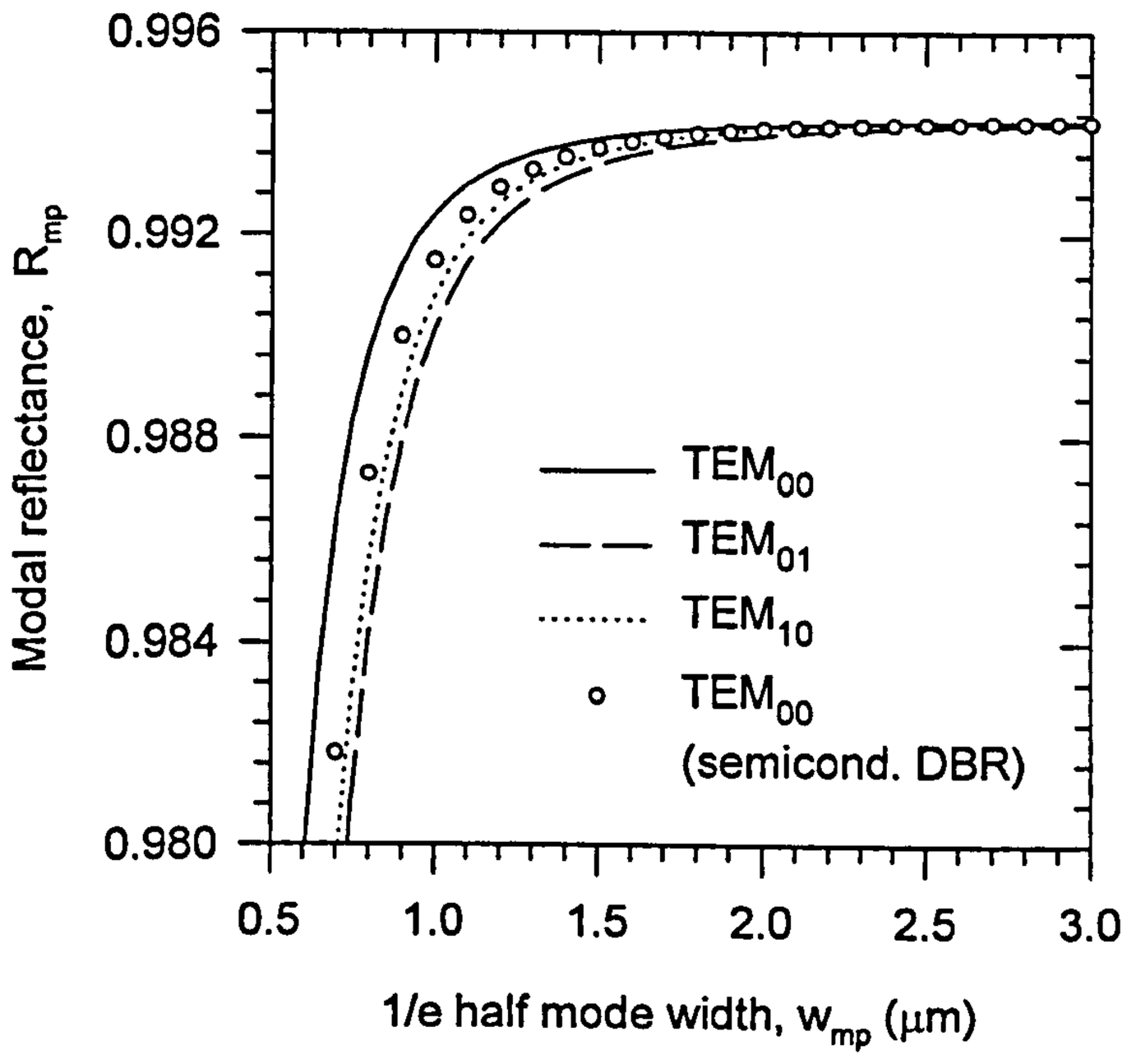

Figure 5.6 : Modal reflectance for the Al_xO_y based DBR which has similar plane wave reflectance as the all-semiconductor DBR.

Obviously, the modal reflectance dependence on the 1/e mode size is less serious for this type of high index contrast DBR than those made up by lower index contrast semiconductor pairs. In spite of the extra fabrication complexity involved, threshold current as low as 53μA [5] has been achieved in a 2μm (2a) square oxide apertured VCSELs using a high index contrast Al_xO_y-contained bottom DBR and

ZeSe/MgF dielectric top DBR. Although suffering from lower diffraction loss, devices with a high index contrast DBR also have smaller difference in modal reflectance between the fundamental and higher order modes for a given mode size, when compared to those utilise DBRs with higher index contrast ratio. Therefore, single mode operation may be more difficult to achieve in these devices.

Using the values of mode sizes and resonant wavelengths calculated earlier through the scalar variational formulae in chapter 4, the modal reflectivities of the oxide apertured VCSELs with strong, medium and weak guiding designs can be calculated. For the **circular** oxide apertured VCSELs of these three different designs, the predicted variation of the product of y-polarised modal reflectance from top and bottom DBRs (i.e. $R_{T(mp)}R_{B(mp)}$) with aperture size, considering only mirror absorption and diffraction losses, are shown in Figures 5.7(a) to 5.7(c) respectively. As expected, the modal reflectance product of all the eigenmodes decreases with reduction in aperture size until the region where loss of optical confinement occurs is reached. In this region, the mode size expands rapidly and thus so does the modal reflectance product. In all cases, the fundamental TEM_{00} mode always has the highest modal reflectance product for a given aperture size, followed by the TEM_{10}, TEM_{01} and TEM_{11} modes in descending order. As the aperture sizes (and thus the mode sizes) get larger, the modal reflectance products especially that of the TEM_{00} mode approach the plane wave values.

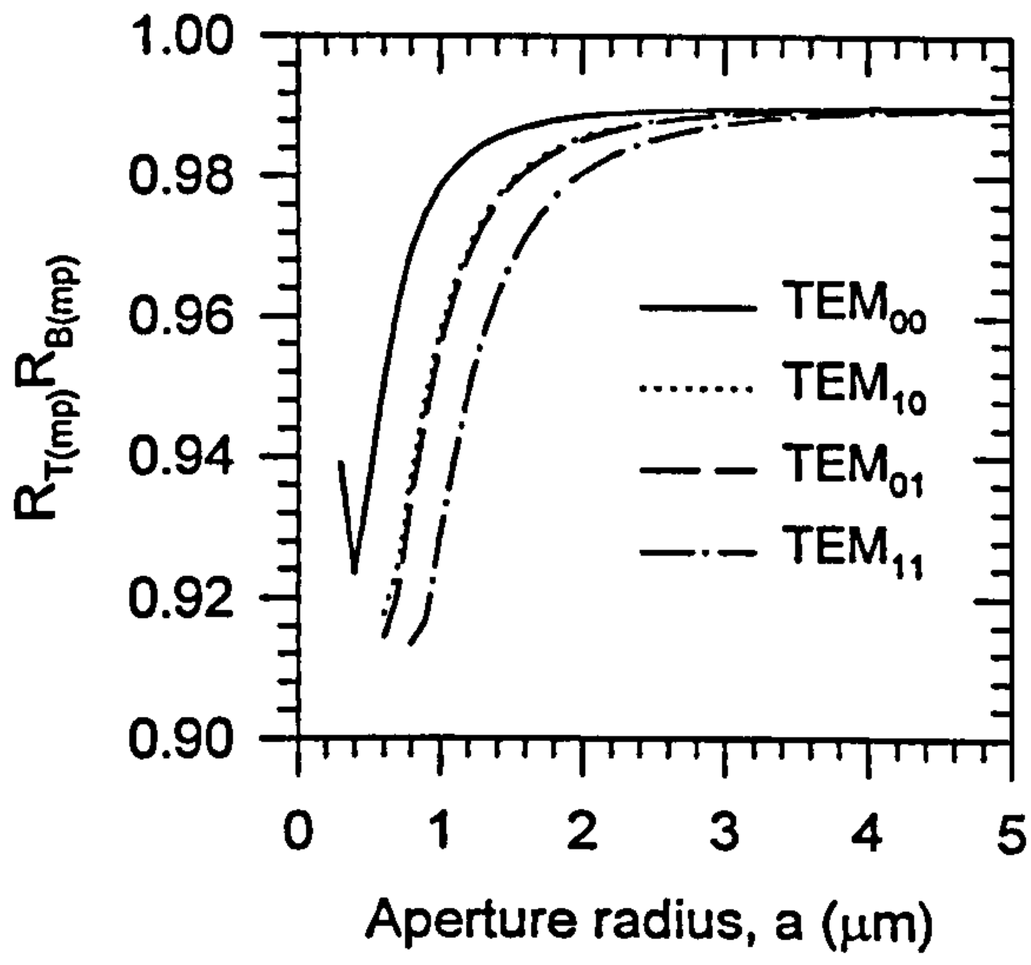

Figure 5.7(a) : Modal reflectance product of the four lowest order eigenmodes as a function aperture radius for the "strong" guiding devices.

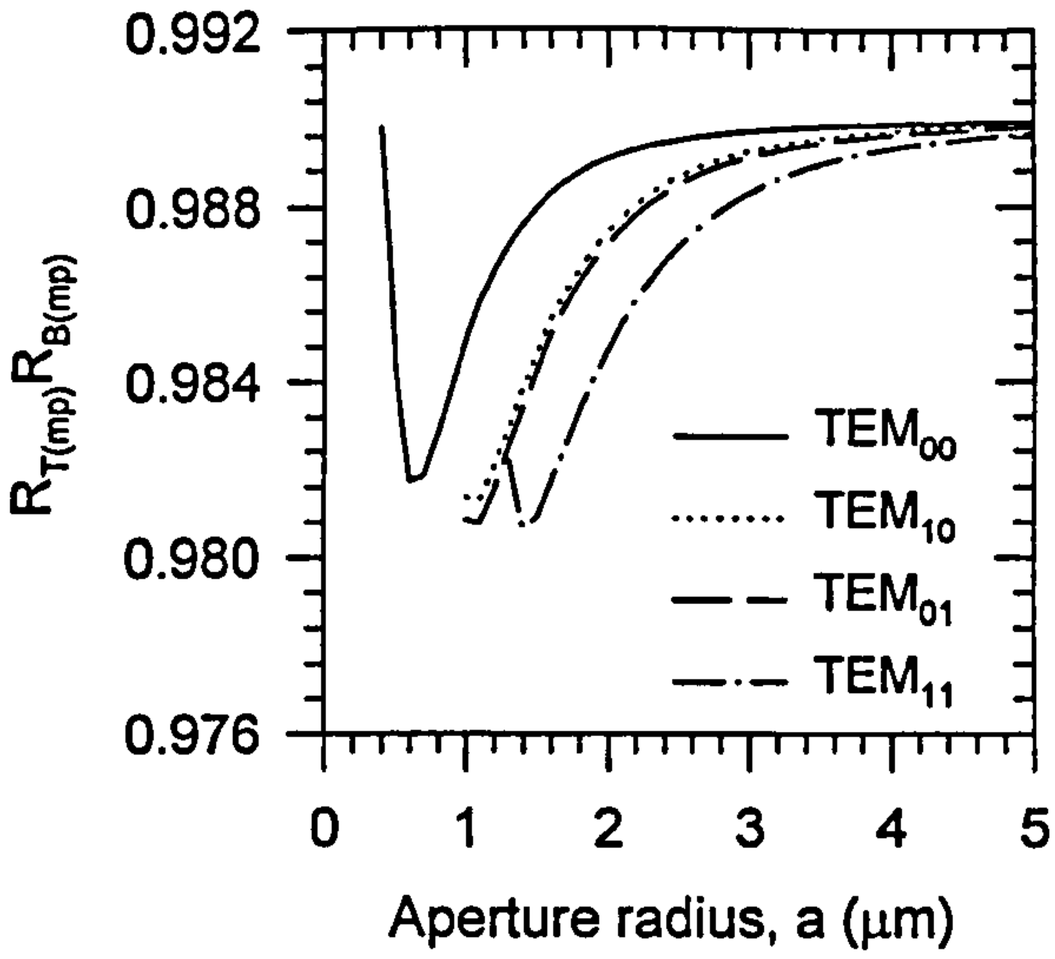

Figure 5.7(b) : Modal reflectance product of the four lowest order eigenmodes as a function aperture radius for the "medium" guiding devices.

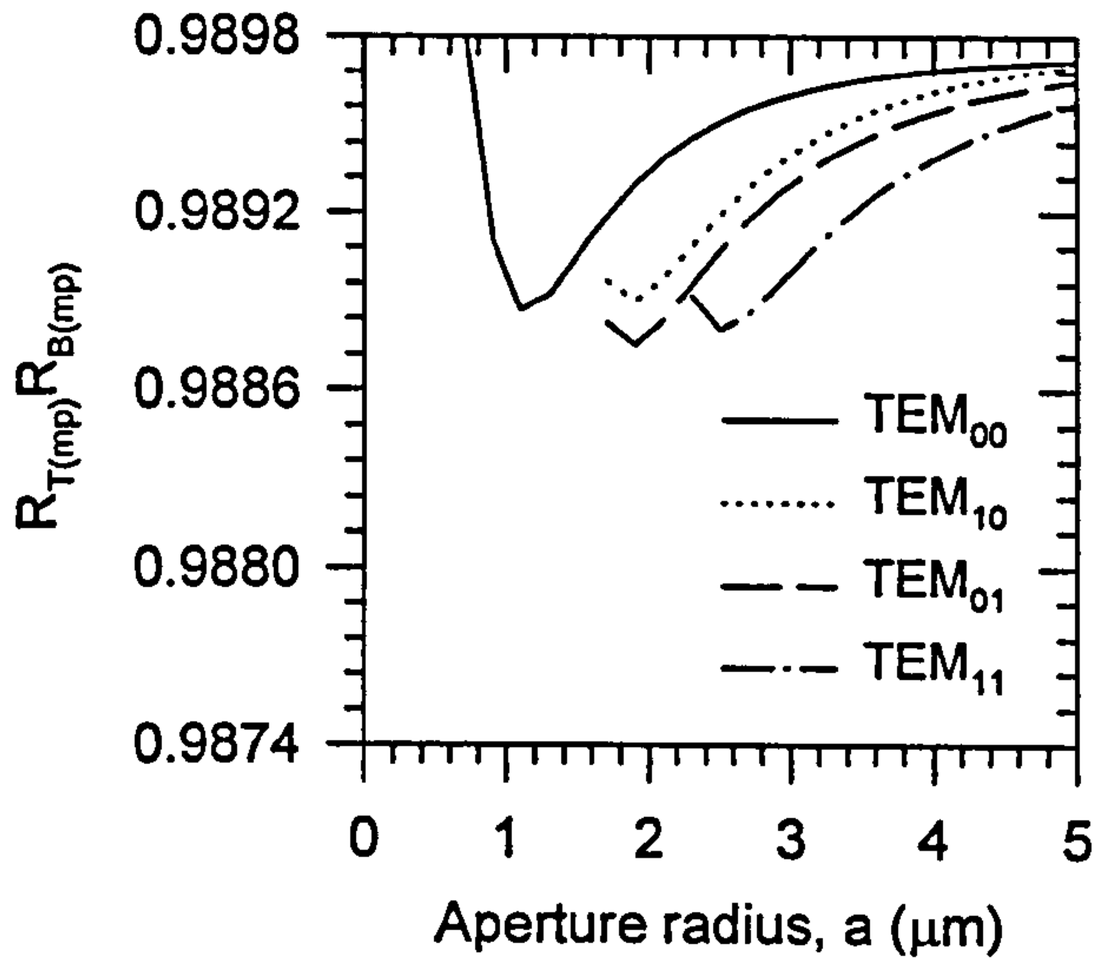

Figure 5.7(c) : Modal reflectance product of the four lowest order eigenmodes as a function aperture radius for the "weak" guiding devices.

For comparison purposes, the modal reflectance product of the fundamental TEM_{00} (main) and the TEM_{10} modes (inset) for the three VCSEL designs are also re-plotted on the same graphs shown in Figure 5.8. Clearly, the weak guiding devices are the least affected by the size dependent diffraction loss among the three type of devices. Comparing the modal reflectance between the TEM_{00} and TEM_{10} modes, however, it is the strong guiding devices that provide the larger reflectance difference especially for $a \leq 1.0\mu m$ where the modal reflectance product of the TEM_{10} mode are very low (< 0.98). Therefore, from the diffraction loss point of view, strong guiding

devices should provide better suppression of higher order modes. On the other hand, for the weak and medium guiding devices the higher modes are completely cut off for aperture radius smaller 1.6 and 0.9μm respectively. It should be noted that the results obtained by assuming no absorption in the DBRs (not shown here), also offer similar qualitative conclusions.

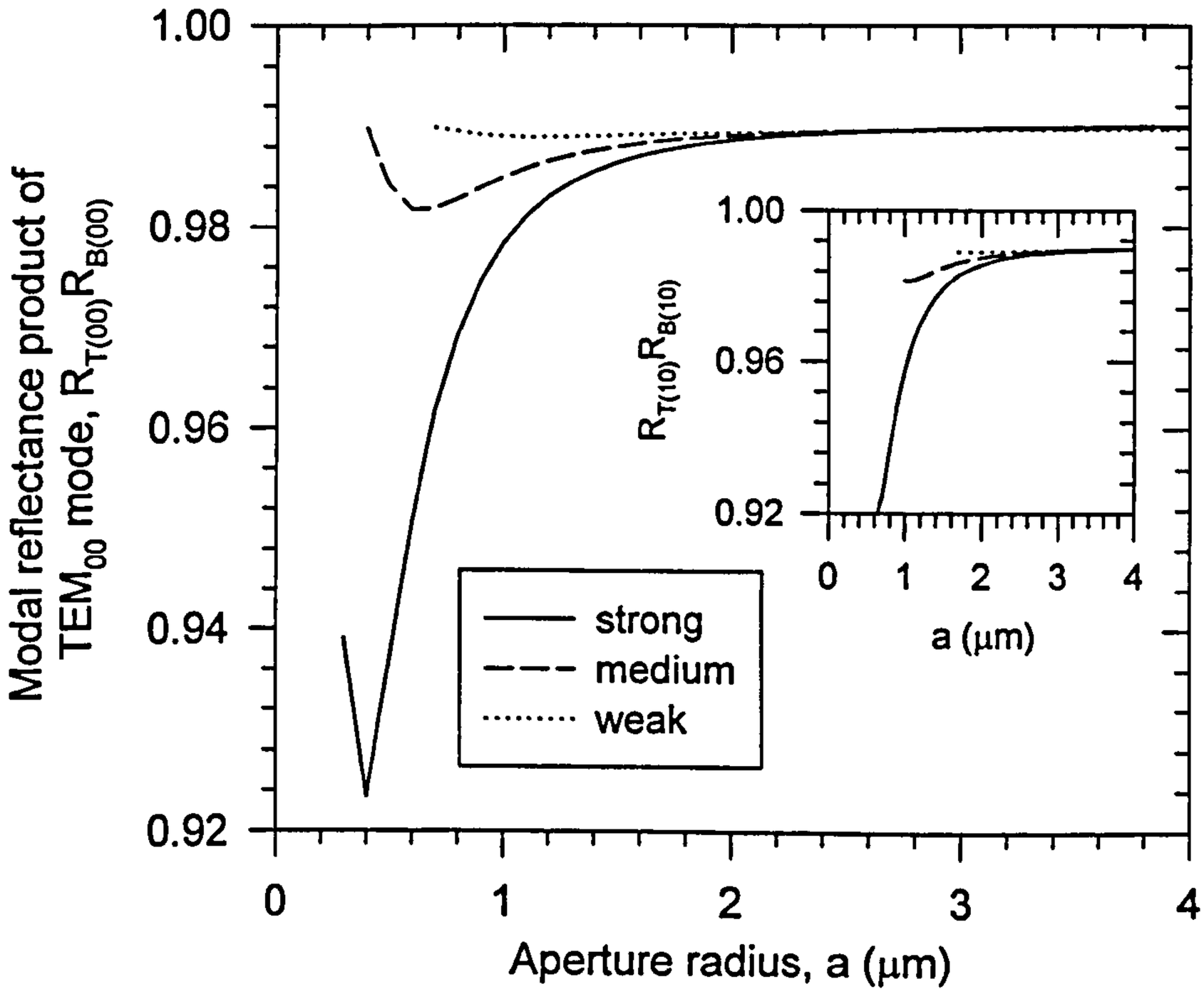

Figure 5.8 : Comparison of modal reflectance product of y-polarised TEM_{00} mode (main) and TEM_{10} mode (inset) as a function of aperture radius among the strong, medium and weak guiding devices.

An alternative way of comparing the diffraction loss is to extract the so-called round-trip "excess optical loss" (L_s) when the active region in the cavity is transparent i.e. at zero gain [6,7]. This excess optical loss is aperture size dependent and is given by the difference between the 2-D total round trip losses experienced by an eigenmode (L_{mp}) and the 1-D "broad area" round trip loss encountered by the plane wave in the oxide apertured optical resonator (L_{plane}). Assuming negligible absorption loss in the cavity medium for the devices considered here, the round trip loss can be estimated as (1 - $R_{T(mp)}R_{B(mp)}$) in a high-Q cavity. Thus, the excess optical loss of a particular eigenmode, $L_{S(mp)}$, is given by

$$\begin{aligned} L_{S(mp)} &= L_{(mp)} - L_{plane} \\ &\cong R_{T(mp)}R_{B(mp)} - R_{T(plane)}R_{B(plane)} \end{aligned} \tag{5.12}$$

where $R_{T(mp)}$, $R_{B(mp)}$ are the (modal) reflectance of a given eigenmode from the top and bottom DBRs respectively, and $R_{T(plane)}$, $R_{B(plane)}$ are the corresponding plane wave values. For the VCSELs used in this work, the predicted excess optical losses for the TEM_{00} mode (main) and TEM_{10} mode (inset) are plotted in Figure 5.9.

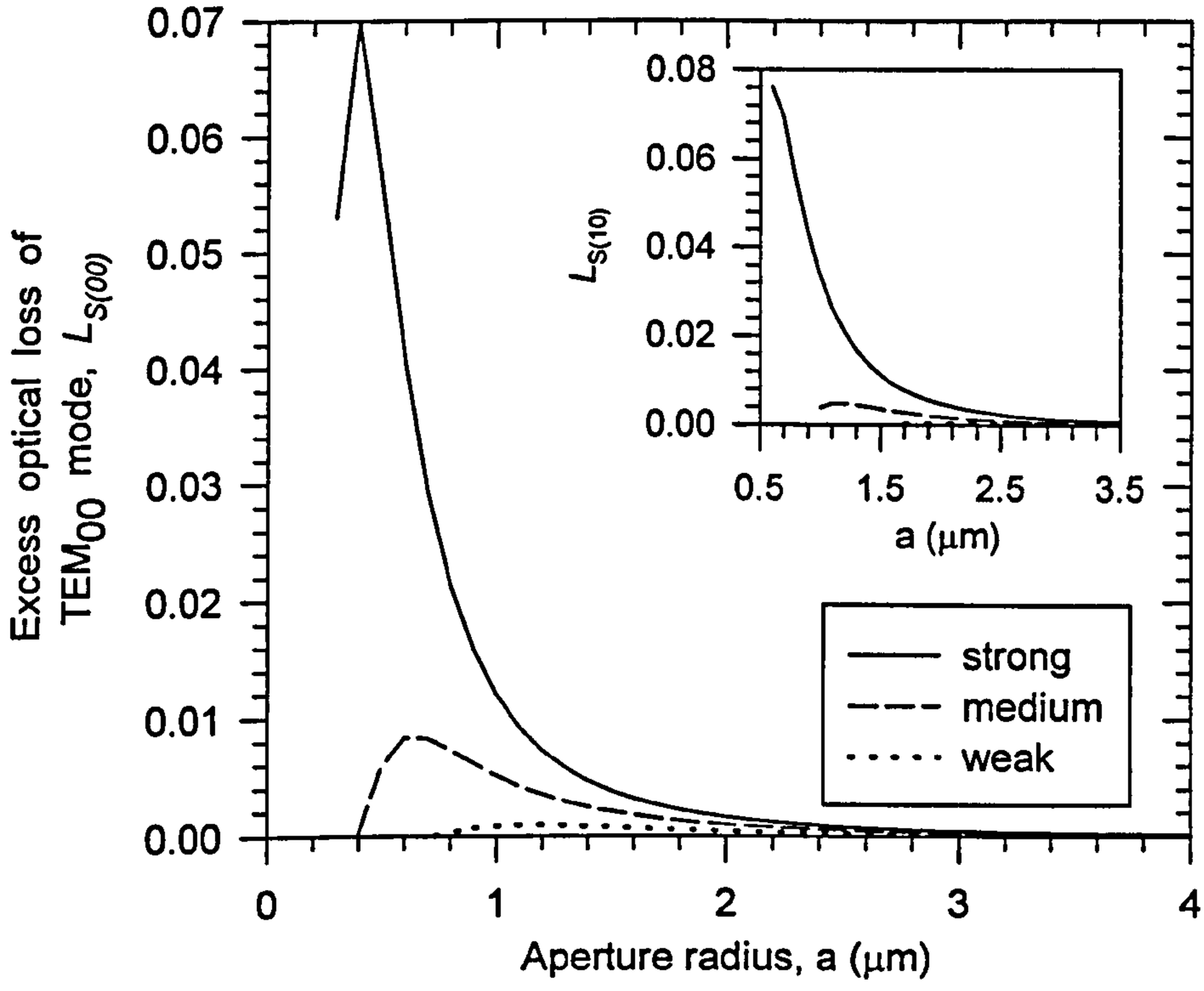

Figure 5.9 : Excess optical loss of TEM_{00} (main illustration) and TEM_{10} (inset) modes for the strong, medium and weak guiding devices.

As expected, the excess optical losses are much lower for a given aperture radius in the weak guiding devices than other type of devices, for both the fundamental TEM_{00} and higher order TEM_{10} mode. Qualitatively, the conclusion made here that devices with thicker oxide aperture suffered from higher excess optical loss, agrees well with the theoretical work by other researchers [6,7]. In spite of such a distinct difference in the excess optical loss, however, one still can not make any early conclusion regarding the difference in threshold between devices of different guiding strengths or between different eigenmodes guided by a particular device. This is because the threshold gains and thus the threshold current densities are also dependent on the transverse confinement factor, as evident in eqn.(2.42). Therefore, this

difference in threshold must be calculated numerically by solving self consistently the photon-carrier rate equations including the carrier diffusion effect. These issues shall be addressed later in section 5.4.

Besides the threshold gain, the excess optical losses caused by the use of oxide apertures also have significant impacts on the output coupling efficiency through the top DBR ($\eta_{T(mp)}$), which is defined as the ratio of the transmitted power through the top DBR to the total optical losses experienced by optical field in the resonator. In a high finesse cavity with negligible cavity absorption loss, η_T is given by

$$\eta_{T(mp)} \approx \frac{T_{T(mp)}}{1 - R_{T(mp)} R_{B(mp)}} \tag{5.13}$$

Using eqn. (5.13), the variation of the output coupling efficiencies of the TEM_{00} (main illustration) and TEM_{10} (inset) modes with aperture radius are calculated and shown in Figure 5.10.

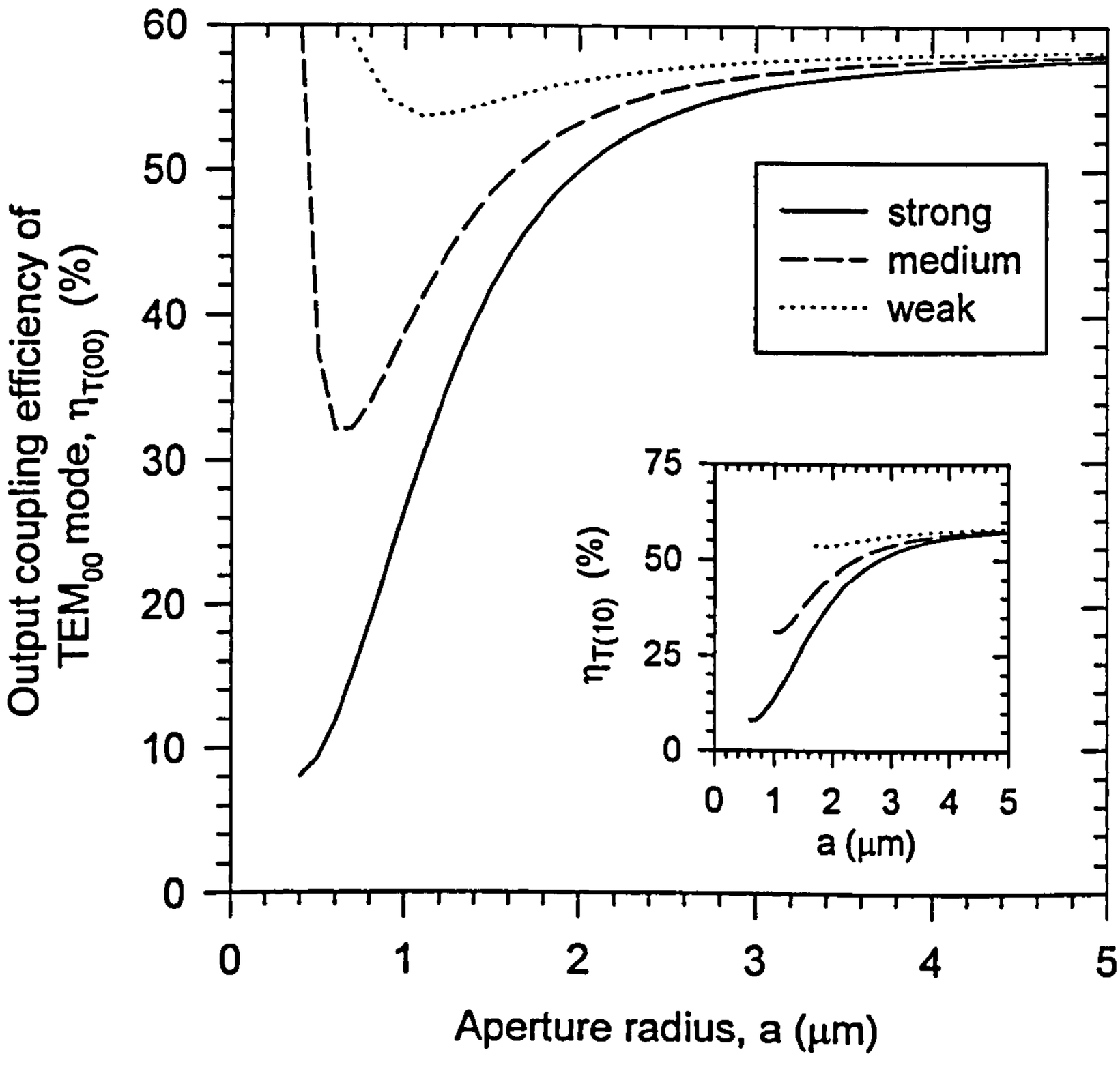

Figure 5.10 : Output coupling efficiencies through the top DBR of the TEM_{00} mode (main illustration) and the TEM_{10} mode (inset).

Clearly, due to the much lower excess optical losses experienced by the eigenmodes, the weak guiding devices are much more efficient in coupling out the light from the cavity. In fact, for aperture radius as small as 1.0μm, the drop in the coupling efficiency with respect to that of the plane wave value (or devices with large aperture radius) is merely 4.8% for the weak guiding device while those of medium and strong guiding devices are as high as 19.5% and 31.7% respectively. It should be noted that this output coupling efficiency directly affects the external quantum efficiencies as well as the wall-plug efficiencies of VCSELs (see eqn. (2.50) and eqn. (2.52)). Thus, it is expected that the weak guiding devices will yield higher power outputs and efficiencies than their medium and strong guiding counterparts. This statement is also true even when absorption-loss DBRs are assumed in the calculations (results not shown here).

The external quantum efficiency of a top emitting oxide apertured VCSEL at just above threshold can be roughly estimated from

$$\eta_{ext(top)} \cong \eta_{int}\eta_{T(00)} \cong \eta_{int}\frac{T_{T(00)}}{(1-R_{T(00)}R_{B(00)})} \tag{5.14}$$

by assuming a constant internal quantum efficiency for devices of all sizes, and similar modal reflectance and transmittance to that of TEM_{00} mode for all the eigenmodes. In actual fact, the internal quantum efficiency is weakly dependent on the carrier diffusion and spatial hole burning effects [6]. The second assumption is reasonable for the devices operated single mode with large side mode suppression ratio, SMSR (ratio of peak intensity of dominant mode with respect to the "side" modes) and even in the case of multimode devices, the modal reflectance and transmittance of the higher order mode approach that of the fundamental mode. It should also be noted that the so-called "scattering loss" [6,7] due to perturbation of fields caused by the oxide aperture has been neglected in the optical loss analysis discussed so far. This issue is treated in more detail in chapter 6. Consequenly, the excess size dependent optical losses calculated above only take account of the diffraction loss, and are the expected minimum values. By the same reason, the values of external quantum efficiency given by eqn.(5.14) are the expected upper limits.

In Fig 4.7 of section 4.3, it is shown that for a given total oxide aperture area (i.e. current injection area), the 1/e mode sizes and resonant wavelengths of the circular and square devices are very similar. Since the modal reflectance are

dependent on these two parameters, it is thus expected that circular and square devices of similar aperture area have similar excess optical losses. To illustrate this point, Figures 5.11 shows the change in output coupling efficiency of the TEM_{00} mode with aperture for the circular and square devices. Clearly, the efficiencies and thus excess optical losses are very similar for these devices of equivalent aperture area.

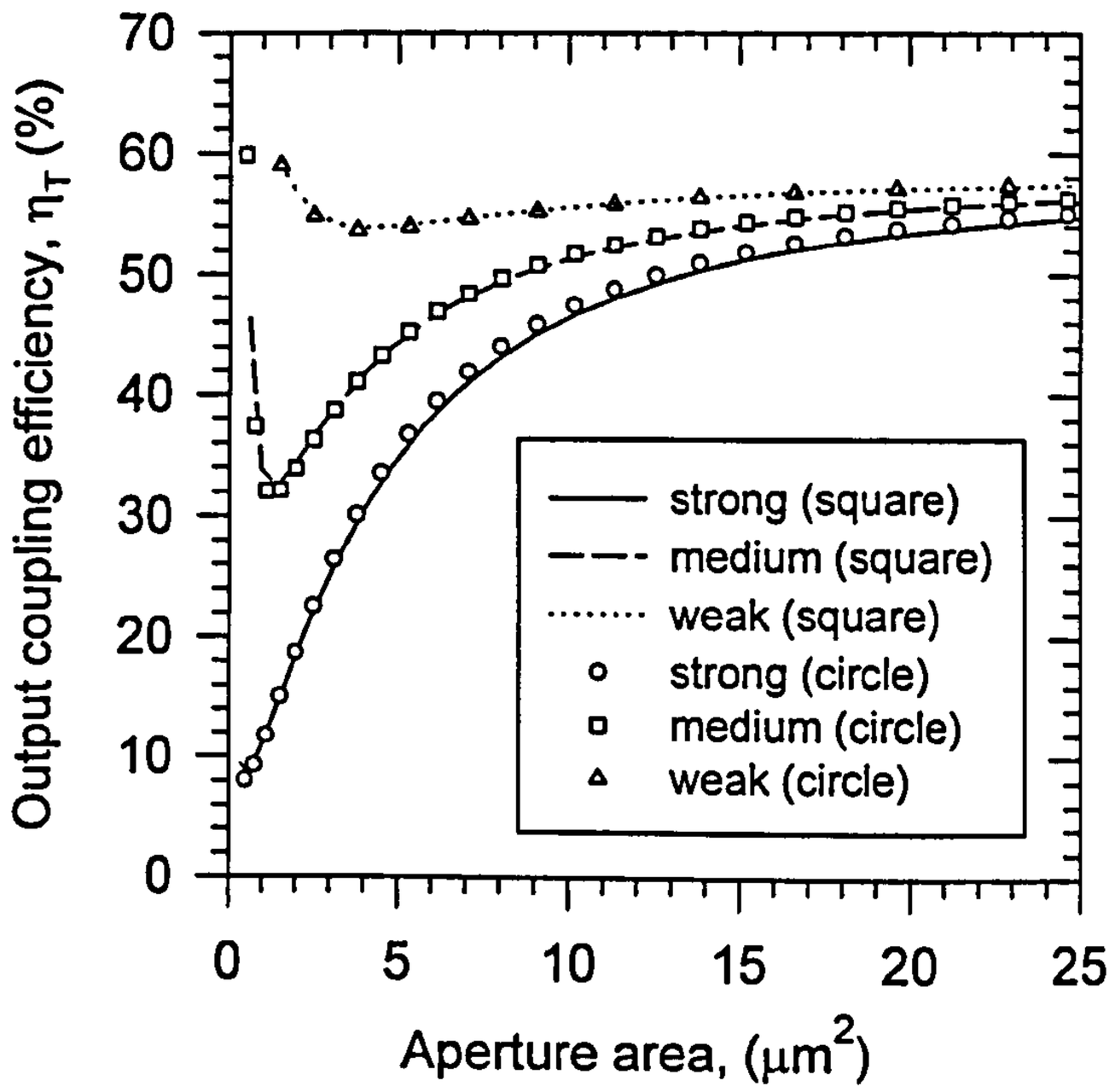

Figure 5.11 : Output coupling efficiencies of the TEM_{00} mode as a function of aperture area for square and circular devices.

5.2.3 Simulation Results II : Effects of Asymmetry in Mode Shape on the Modal Reflectance in Orthogonal Polarisation Directions

As discussed in section 4.3, the eigenmodes confined by a rectangular oxide apertured VCSELs have elliptical Hermite-Gaussian transverse field variations and spectral splittings also exists between the TEM_{01} and TEM_{10} modes. Due to the asymmetry in the 1/e mode sizes ((i.e. $w_{x(mp)} \neq w_{y(mp)}$), different diffraction loss is experienced depending on whether the mode is polarised along the x or y direction. Therefore, the modal reflectance $R_{x(mp)}$ and $R_{y(mp)}$ where the first subscript gives the direction of polarisation, are different for a given elliptical Hermite-Gaussian mode. As an example, Figure 5.12 shows the 2-D variations of the difference in the modal reflectance of the fundamental TEM_{00} mode in the orthogonal polarisation directions, (R_{x00} - R_{y00}), from the 28 pair top DBR. These results are calculated in a similar manner to that outlined in section 5.2.2.

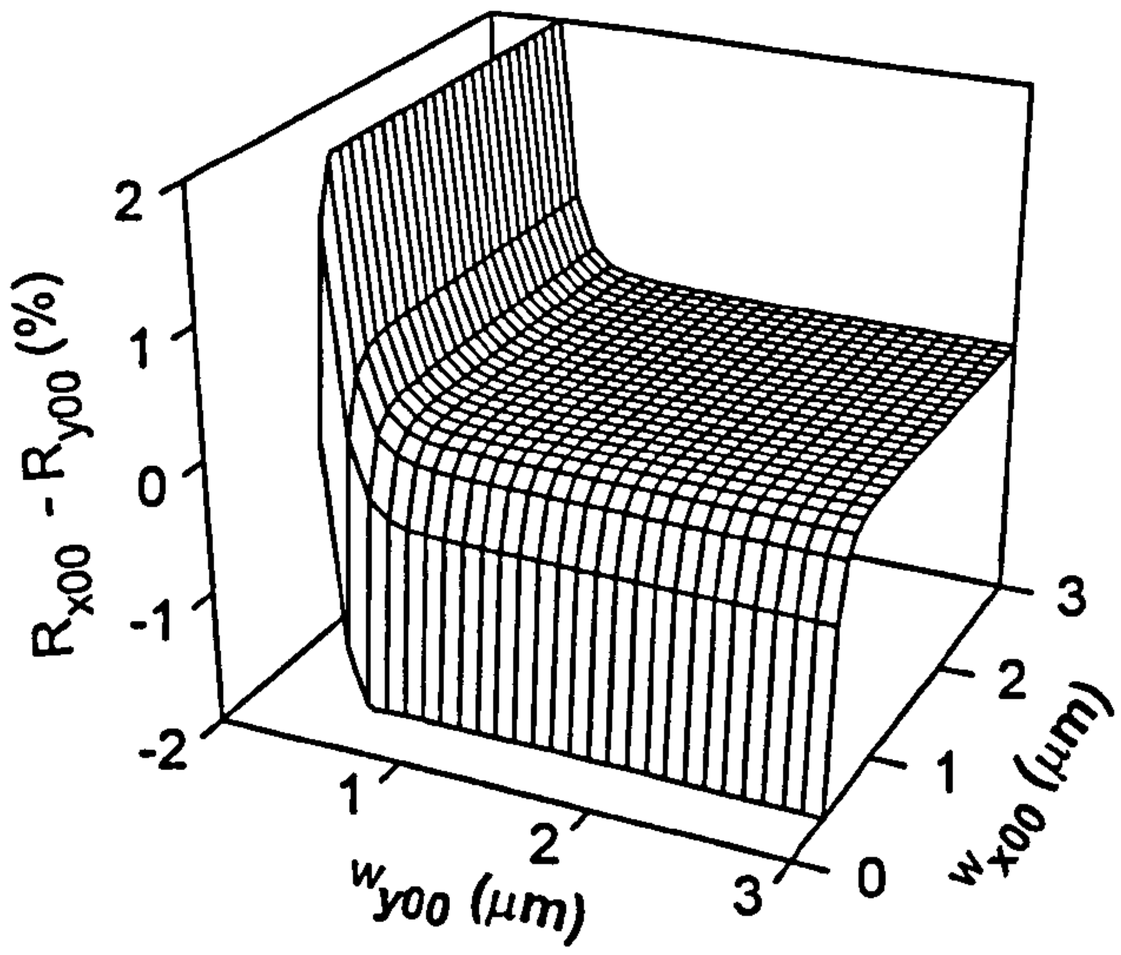

Figure 5.12 : Variation of difference in modal reflectance of the TEM_{00} mode along the x and y polarisation directions with modes sizes, for the 28 pair top DBR.

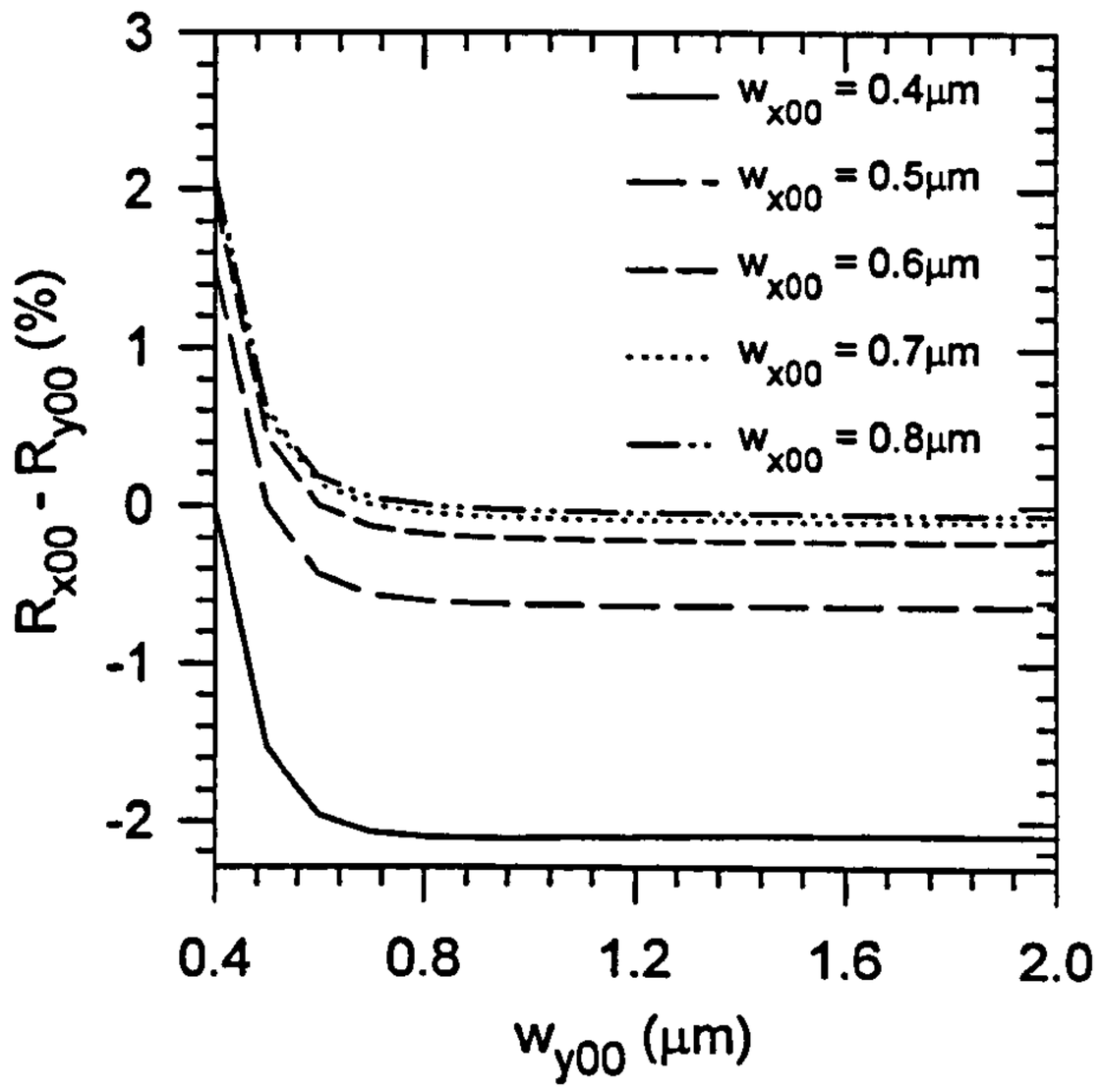

Figure 5.13 : Variation of difference in modal reflectance of the TEM_{00} mode along the x and y polarisation directions for fixed w_{x00} but variable w_{y00}. (for the 28 pair top DBR)

Clearly, this difference changes sign from when the mode size in one of the direction varies from being smaller to become bigger than the those in the other direction, or vice versa. It is therefore always the mode with its electric field polarised along the direction of the longer side of aperture that has the higher modal reflectance. This is perhaps more obvious in Figure 5.13 where the modal reflectance difference is

plotted as a function of w_{y00} for a range of fixed w_{x00}. As can be seen, the difference in modal reflectance increases with the ratio of the mode sizes. However, in order to obtain the maximum difference, it seems that the mode size in one of the direction, say w_{y00}, has to be kept bigger than 0.8μm while minimising the mode size in the other direction, w_{x00}.

Although the analysis above indicates that it is possible to produce a modal reflectance difference as high as 2% between the orthogonal polarised eigenmodes, the mode width in one of the direction has to be made very small, i.e. <0.5μm. As discussed in chapter 4, the mode widths of the eigenmodes confined by the oxide apertured resonator are dependent on the thickness and position of the oxide aperture, i.e. the "guiding strength" provided. Therefore, from the viewpoint of the diffraction loss difference between the orthogonal polarisation directions, the strong guiding devices should provide better polarisation control among the three designs adopted in this work. As an example, for the strong guiding rectangular devices with the aperture size in the x-direction fixed at 2μm, Figure 5.14 shows the x-(smooth lines) and y-(dotted lines) polarised modal reflectance product (i.e. $R_{T(mp)}R_{B(mp)}$) of various eigenmodes as a function of aperture aspect ratio, 2b/2a.

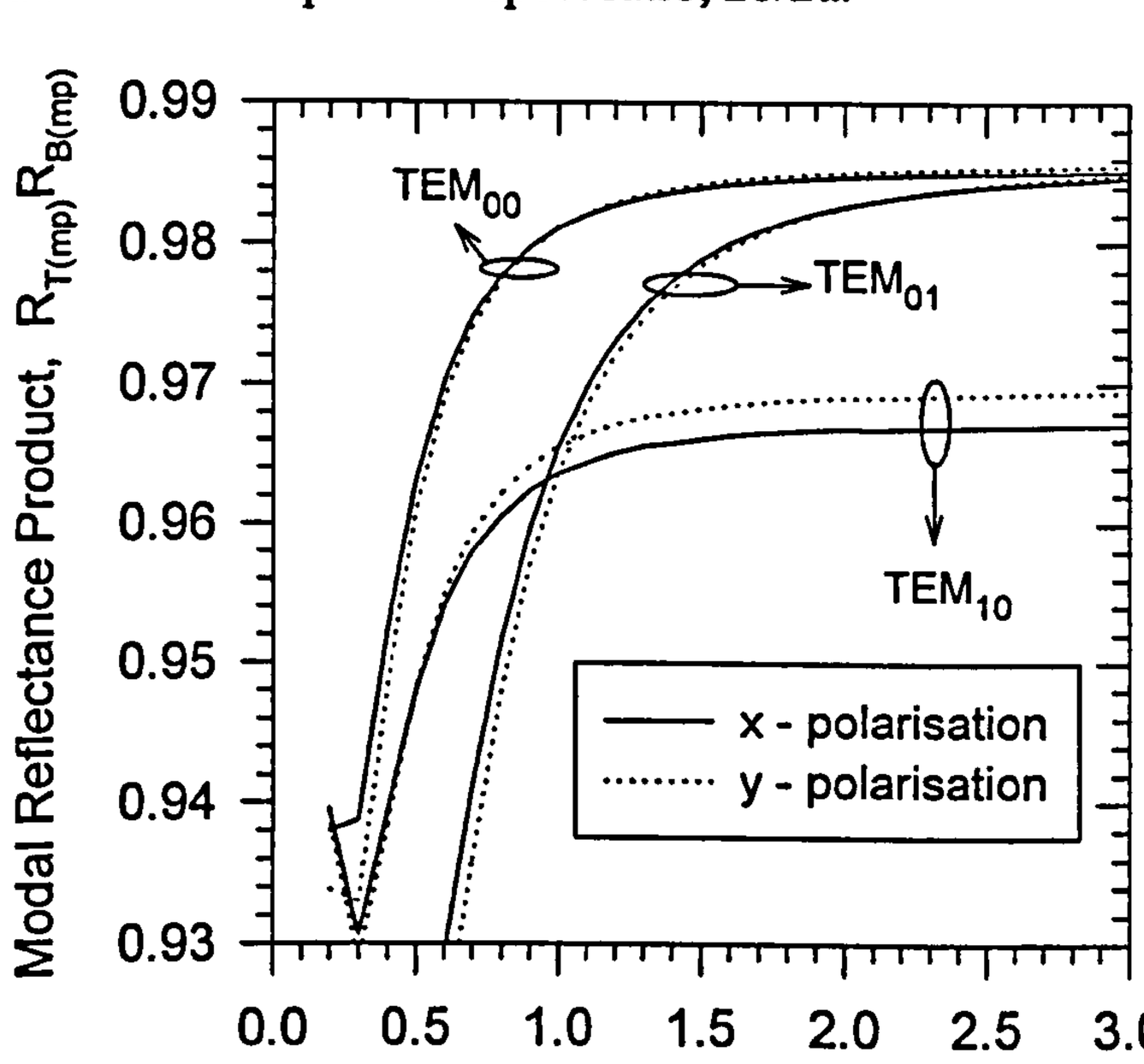

Figure 5.14 : Variation of y-polarised and x-polarised modal reflectance product with oxide aperture size in the y-direction, 2b, for the case of 2a = 2μm.

As expected, when the aspect ratio is *larger* than unity i.e. 2b>2a and thus the aperture is elongated in y-direction, the fundamental TEM_{00} mode (Note: as well as TEM_{11} mode whose traces are not shown) suffers from *lower* diffraction losses in the y polarisation direction. Conversely, when the aspect ratio is less than unity, the TEM_{00} (ditto TEM_{11} mode) is more reflective in the x-direction. Between the TEM_{01} and TEM_{10} modes, it is always the one with field/intensity null along the longer side of the aperture, that has higher modal reflectance, i.e. TEM_{01} mode for b/a > 1 and TEM_{10} mode for b/a <1. Referring to Fig. 4.8 in chapter 4, it is also the mode that has longer resonant wavelength. However, for the TEM_{01} mode the y-polarised modal reflectance is always *higher* than that in the x-direction unless the aspect ratio is more than 2.1. On the other hand, for the TEM_{10} mode the y-polarised modal reflectance is always *lower* than that in the x-direction except for aspect ratios lower than 0.5. Consequently, when the aspect ratio is in the range of $1.0 \leq (2b/2a) \leq 2.1$, the eigenmodes with modal reflectance in the decreasing order are : $y\text{-}TEM_{00} > x\text{-}TEM_{00} > x\text{-}TEM_{01} > y\text{-}TEM_{01} > y\text{-}TEM_{10} > x\text{-}TEM_{10} > y\text{-}TEM_{11} > x\text{-}TEM_{11}$ modes for this particular example. Meanwhile, when the aspect ratio is in the range of $0.5 \leq (2b/2a) \leq 1.0$, the eigenmodes with modal reflectance in the decreasing order are : $x\text{-}TEM_{00} > y\text{-}TEM_{00} > y\text{-}TEM_{10} > x\text{-}TEM_{10} > x\text{-}TEM_{01} > y\text{-}TEM_{01} > x\text{-}TEM_{11} > y\text{-}TEM_{11}$ modes. In another words, the higher order mode with highest modal reflectivity (i.e. could be TEM_{01} or TEM_{10} mode) is always orthogonally polarised with respect to the the fundamental TEM_{00} if the aspect ratio falls in the range of $0.5 \leq (2b/2a) \leq 2.1$.

It is also obvious that the difference in modal reflectance product between the orthogonally polarised TEM_{00} modes is not that significant. For instance, the net value of this reflectance difference increases only from 0.015% to 0.034% when the aspect ratio increases from 1.2 to 2.0, and increases from 0.013% to 0.23% when the aspect ratio decreases from 0.9 to 0.5. This is mainly because the mode width in the x-direction (w_{x00}) when the corresponding dimension of the oxide aperture is fixed at 2.0μm, stays almost constant at 0.88μm. Nevertheless, by comparison the weak guiding device of similar dimension hardly changes from 0.006% to 0.017% and 0.0015% to 0.0058% for the similar aspect ratio range. Thus, strong guiding devices seems to provide a larger difference in the modal reflectance of the orthogonally polarised TEM_{00} modes.

5.3 Q-Factor, Photon Lifetime and Linewidth

In this section, the expressions for Q-factor, photon lifetime and linewidth are derived. These relations are very useful in both theoretical modelling and experimental investigation of the performance of an optical resonator.

5.3.1 Definitions

The performance of a resonator is characterised by a quantity called the quality factor, Q. The theoretical definition of Q-factor at resonance is expressed by [8]

$$\begin{aligned} Q &= 2\pi \frac{\text{time averaged energy stored in the system at resonance}}{\text{energy lost in one cycle of oscillation}} \\ &= \omega_r \frac{\text{time averaged energy stored in the system at resonance}}{\text{average power loss}} \\ &= \omega_r \frac{U}{P_{ave}} \end{aligned} \tag{5.15}$$

where ω_r is the resonant angular frequency and the average power loss P_{ave} is equal to the (decreasing) time rate of change in the stored energy U if the resonator is allowed to dissipate naturally, i.e. $P_{ave} = -dU/dt$. Rearranging, this leads to the energy rate equation, written as

$$\frac{dU}{dt} = -\frac{\omega_r}{Q} U \tag{5.16}$$

The solution to (5.16) in the time domain is

$$U(t) = U_{(0)} \exp\left(-\frac{\omega_r}{Q} t\right) \tag{5.17}$$

where $U_{(0)}$ is the initial value of stored energy at $t = 0$ and, for an optical resonator is equal to the initial number of photons $N_{p(0)}V$ (where V = cavity volume, N_p = photon density) times photon energy *hf*. Thus, equation (5.17) can be recast into a more specific form to describe the change of photon density inside the optical resonator with time as

$$N_p(t) = N_{p(0)} \exp\left(-\frac{\omega_r t}{Q}\right) = N_{p(0)} \exp\left(-\frac{t}{\tau_p}\right) \tag{5.18}$$

where the constant τ_p expressed by

$$\tau_p = \frac{Q}{\omega_r} \tag{5.19}$$

is the photon lifetime. This gives the decay time duration for the photon density (or stored photon energy) to decrease to 1/e (≈ 36.8%) of its initial value, $N_{p(0)}$.

The Q-factor or photon lifetime given by eqns. (5.15) and (5.19) respectively, can be used for predicting the performance of a laser cavity. Thus, it is useful to acquire an experimental method to measure them. The simplest and most direct approach would be through the spectrum of the emission from the optical resonator. From (5.17), and noting that the energy is proportional to E^2, the corresponding time dependence of the electric field, $E(t)$ is (for $t>0$)

$$E(t) = E_{(0)} \exp(-j\omega_r t) \exp\left(-\frac{t}{2\tau_p}\right) \tag{5.20}$$

where $E_{(0)}$ is the initial field amplitude. Taking the Fourier transform of (5.20), the transfer function of the resonator in the frequency domain is thus of the Lorentzian form given by

$$H(\omega) = \frac{1}{1 + (\omega - \omega_r)^2 (2\tau_p)^2} \tag{5.21},$$

which is similar to that of a damped LCR resonant circuit. From (5.21), it can be easily deduced that the full-width half-maximum (FWHM) linewidth, $\Delta\omega_{1/2}$, of the Lorentzian spectral frequency response is given by

$$\Delta\omega_{FWHM} = \frac{1}{\tau_p} = \frac{\omega_r}{Q} \tag{5.22}$$

Hence, the FWHM spectral linewidth of the light emission peak detected in the wavelength domain ($\Delta\lambda_{FWHM}$) is related to the photon lifetime through

$$\Delta\lambda_{FWHM} = \frac{\lambda_r^2}{2\pi c \tau_p} \tag{5.23}$$

As implied in the derivations above, the photon lifetime τ_p is related to the decay rate of the photon energy inside the optical resonator, and the relations given by (5.16) and (5.20) hold for every kind of resonator. For a resonator which has an active gain region, the photon lifetime depends on the optical gain. From the relation between photon lifetime and Q-factor expressed by (5.19), a generalised definition of photon lifetime inside a laser cavity can be deduced from (5.15) as

$$\tau_p = \frac{\text{time averaged stored energy in the system at resonance}}{\text{"net" average power loss}} = \frac{U}{P_{ave}} \tag{5.24}$$

where the word "net" emphasises the existence of optical gain inside the cavity, i.e. the net power loss is the difference between the passive power loss and the active power gain. The energy density in the resonator, W_e, is given in terms of the electric field E by [2]

$$W_e = \frac{1}{2}\varepsilon E^2 \tag{5.25},$$

Thus, the total stored energy for a particular eigenmode U_{mp} (i.e. numerator of (5.15)) is given by

$$U_{mp} = \iiint_V W_{e(mp)}\, dV = \frac{1}{2} \iiint_V \varepsilon E_{pk(mp)}^2 E_{mp}^2\, dV = \frac{1}{2}\varepsilon_0 E_{pk(mp)}^2 \iiint_V n^2 E_{mp}^2\, dV \tag{5.26}$$

where $E_{pk(mp)}$ is the peak field amplitude of the optical standing wave and E_{mp} is the 3-D field variation defined earlier in chapter 4. In accordance with the Hermite - Gaussian field variations assumed in this work, the general expression of E_{mp} for either circular or elliptical eigenmode (normalised with respect to the antinode peak amplitude in the cavity) is that given by (4.25).

For each eigenmode, it is the overlapping of the counter propagating waves each associated with a time average power density (i.e. intensity) flow of $P_{0(mp)}$ that results in the formation of standing wave within the resonator. From (2.32), the power density flow is thus given by

$$P_{0\,(mp)} = \frac{1}{2} n_c Y_0 \left(\frac{E_{pk(mp)}\, E_{tr(mp)}}{2} \right)^2 = \frac{1}{8} n_c Y_0\, E_{pk(mp)}^2 E_{tr(mp)}^2 \tag{5.27}$$

where n_c is the real refractive index of the cavity medium, Y_0 is the admittance of free space ($\approx 1/120\pi$) and $E_{tr(mp)}$ is the transverse field variations for the Hermite-Gaussian eigenmode ($m,p \leq 1$) expressed by

$$E_{tr(mp)} = x^m y^p \exp\left(-\frac{x^2}{w_{x(mp)}^2} - \frac{y^2}{w_{y(mp)}^2} \right) \tag{5.28}$$

Note that as in section 4.2, the field perturbation due to the dielectric discontinuity between thin gain medium and cavity medium is neglected, thus allowing the use of n_c for the position within the quantum wells where the standing wave peaks. In the presence of optical gain, the net average power loss of a given eigenmode from both highly reflecting reflectors can be deduced from the surface S integral given by

$$P_{ave(mp)} = \oiint_S P_{0(mp)} \left[1 - R_{T(mp)} R_{B(mp)} \exp\left(-2\alpha_{(mp)}\right) \exp\left(+2G_{(mp)}\right)\right] \, dS$$

$$\cong \frac{1}{8} n_c Y_0 E_{pk(mp)}^2 \left[1 - R_{T(mp)} R_{B(mp)} \exp\left(-2\alpha_{(mp)}\right) \exp\left(+2G_{(mp)}\right)\right] \oiint_S E_{tr(mp)}^2 \, dS \tag{5.29}$$

where $\alpha_{(mp)}$ and $G_{(mp)}$ represent the total (one-pass) modal loss and modal gain experienced in the cavity respectively, $R_{T(mp)}$ and $R_{B(mp)}$ are the modal reflectance of the top and bottom reflectors. Combining eqns. (5.24), (5.27) and (5.29), the general expression for photon lifetime of particular eigenmode inside an optical resonator with gain medium is thus given by

$$\tau_{p(mp)} \cong \frac{4}{c\, n_c \left[1 - R_{T(mp)} R_{B(mp)} \exp\left(-2\alpha_{mp}\right) \exp\left(+2G_{mp}\right)\right]} \frac{\oiiint_V n^2 E_{mp}^2 \, dV}{\oiint_S E_{tr(mp)}^2 \, dS} \tag{5.30}$$

5.3.2 "Cold Cavity" Photon Lifetime of Oxide Apertured Resonators

In the absence of optical gain i.e. the gain medium is transparent, the "cold cavity" photon lifetime [1], $\tau'_{p(mp)}$, can be deduced from (5.30) to be

$$\tau'_{p(mp)} \cong \frac{4}{c\, n_c \left[1 - R_{T(mp)} R_{B(mp)} \exp\left(-2\alpha_{mp}\right)\right]} \frac{\oiiint_V n^2 E_{mp}^2 \, dV}{\oiint_S E_{tr(mp)}^2 \, dS} \tag{5.31}$$

Note that the cold cavity photon lifetime is given a new symbol $\tau'_{p(mp)}$ in order to differentiate it from the photon lifetime in the presence of gain i.e. $\tau_{p(mp)}$, which is more usually quoted as "effective" photon/cavity lifetime [1]. Under the plane wave picture, the cold cavity photon lifetime for a resonator formed by "hard" mirrors (i.e. no decaying field penetration into the mirrors) and with negligible cavity absorption loss is thus simply given by

$$\tau_p' \text{ (plane wave, hard mirrors)} = \frac{2\, n_c\, L_c}{c\,(1 - R_T R_B)} \tag{5.32}$$

where $\iiint_V n^2 E^2 dV \;/\; \iint_S E^2_{tr(mp)}\, dS = n_c^2 L_c / 2$. However, in the case of oxide apertured VCSELs where the assumed transverse field variation of the eigenmodes are in Hermite-Gaussian form as well as with significant field penetration into the DBRs, the surface and volume integral of (5.31) have to be evaluated accordingly. By making use of the integral solutions given by *Appendix D*, it can be shown that the surface integration term of (5.31) is given by

$$\iint_S E^2_{tr(mp} \, dS = \left(\frac{\pi}{2}\right)\left(\frac{1}{2}\right)^{2m+2p} r_{x(mp)}^{1+2m}\; r_{y(mp)}^{1+2p} \tag{5.33}$$

where for the sake of generalisation, the normalised field variations of an elliptical Hermite-Gaussian expressed by (4.25), is assumed. It is also easy to recognise that the numerator of the integral term $\iiint_V n^2 E^2\, dV$ in (5.31) is actually identical to the denominator of the scalar variational integral formula given by (4.5). Thus by recycling the expressions for denominators of scalar variational formulae derived previously in section 4.2.2 and 4.2.3 for circular, square and rectangular apertured resonators, together with the general expression given by (5.33), the expressions for cold cavity photon lifetimes of the circular and elliptical Hermite - Gaussian eigenmodes can be obtained. Assuming negligible cavity absorption loss, these expressions are given in Table 5.4 and Table 5.5 respectively. Note that the photon lifetimes for these Hermite-Gaussian modes can also be written in a similar form to (5.32) by replacing L_c with $L_{eff(mp)}$ which is the "effective cavity length" taking into account the field penetration into the DBRs. By inspection, $L_{eff(mp)}$ is simply the product of L_c and the cumulative terms inside the curly brackets of the expressions in Tables 5.4 and 5.5.

Mode	Cold Cavity Photon Lifetime, $\tau'_{p(mp)}$
TEM_{00}	$\frac{2\,n_c L_c}{c\,(1-R_{T(00)}R_{B(00)})}\left\{1-\frac{\left(n_2^2-n_{ox}^2\right)}{n_c^2}\frac{F_{ox}d_{ox}}{L_c}\exp\left(\frac{-2a^2}{w_{00}^2}\right)+\frac{n_1 n_2 \lambda_0}{2n_c^2 L_c (n_1-n_2)}\right\}$
TEM_{01}	$\frac{2\,n_c L_c}{c\,(1-R_{T(01)}R_{B(01)})}\left\{1-\frac{\left(n_2^2-n_{ox}^2\right)}{n_c^2}\frac{F_{ox}d_{ox}}{L_c}\left(1+\frac{2a^2}{w_{01}^2}\right)\exp\left(\frac{-2a^2}{w_{01}^2}\right)+\frac{n_1 n_2 \lambda_0}{2n_c^2 L_c (n_1-n_2)}\right\}$
TEM_{10}	$\frac{2\,n_c L_c}{c\,(1-R_{T(10)}R_{B(10)})}\left\{1-\frac{\left(n_2^2-n_{ox}^2\right)}{n_c^2}\frac{F_{ox}d_{ox}}{L_c}\left(1+\frac{2a^2}{w_{10}^2}\right)\exp\left(\frac{-2a^2}{w_{10}^2}\right)+\frac{n_1 n_2 \lambda_0}{2n_c^2 L_c (n_1-n_2)}\right\}$
TEM_{11}	$\frac{2\,n_c L_c}{c\,(1-R_{T(11)}R_{B(11)})}\left\{1-\frac{\left(n_2^2-n_{ox}^2\right)}{n_c^2}\frac{F_{ox}d_{ox}}{L_c}\left(1+\frac{2a^2}{w_{11}^2}+\frac{2a^4}{w_{11}^4}\right)\exp\left(\frac{-2a^2}{w_{11}^2}\right)+\frac{n_1 n_2 \lambda_0}{2n_c^2 L_c (n_1-n_2)}\right\}$

Table 5.4 : "Cold cavity" photon lifetime of the circular Hermite-Gaussian eigenmodes guided by the *circular* oxide apertured resonator.

Mode	Cold Cavity Photon Lifetime, $\tau'_{p(mp)}$
TEM_{00}	$\frac{2\,n_c\,L_c}{c\,(1-R_{T(00)}R_{B(00)})}\left\{1-\frac{\left(n_2^2-n_{ox}^2\right)}{n_c^2}\frac{F_{ox}d_{ox}}{L_c}\left[1-erf\left(\frac{\sqrt{2}a}{w_{x00}}\right)erf\left(\frac{\sqrt{2}b}{w_{y00}}\right)\right]+\frac{n_1n_2\lambda_0}{2n_c^2L_c(n_1-n_2)}\right\}$
TEM_{01}	$\frac{2\,n_c\,L_c}{c\,(1-R_{T(01)}R_{B(01)})}\left\{1-\frac{\left(n_2^2-n_{ox}^2\right)}{n_c^2}\frac{F_{ox}d_{ox}}{L_c}\left[1-erf\left(\frac{\sqrt{2}a}{w_{x01}}\right)erf\left(\frac{\sqrt{2}b}{w_{y01}}\right)+\frac{2\sqrt{2}\,b}{\sqrt{\pi}\,w_{y01}}\exp\left(\frac{-2b^2}{w_{y01}^2}\right)erf\left(\frac{\sqrt{2}a}{w_{x01}}\right)\right]+\frac{n_1n_2\lambda_0}{2n_c^2L_c(n_1-n_2)}\right\}$
TEM_{10}	$\frac{2\,n_c\,L_c}{c\,(1-R_{T(10)}R_{B(10)})}\left\{1-\frac{\left(n_2^2-n_{ox}^2\right)}{n_c^2}\frac{F_{ox}d_{ox}}{L_c}\left[1-erf\left(\frac{\sqrt{2}\,b}{w_{y10}}\right)erf\left(\frac{\sqrt{2}\,a}{w_{x10}}\right)+\frac{2\sqrt{2}\,a}{\sqrt{\pi}\,w_{x10}}\exp\left(\frac{-2a^2}{w_{x10}^2}\right)erf\left(\frac{\sqrt{2}b}{w_{y10}}\right)\right]+\frac{n_1n_2\lambda_0}{2n_c^2L_c(n_1-n_2)}\right\}$
TEM_{11}	$\frac{2\,n_c\,L_c}{c\,(1-R_{T(11)}R_{B(11)})}\left\{1-\frac{\left(n_2^2-n_{ox}^2\right)}{n_c^2}\frac{F_{ox}d_{ox}}{L_c}\left[1-erf\left(\frac{\sqrt{2}\,b}{w_{11}}\right)erf\left(\frac{\sqrt{2}\,a}{w_{x11}}\right)+\frac{2\sqrt{2}\,a}{\sqrt{\pi}\,w_{x11}}\exp\left(\frac{-2a^2}{w_{x11}^2}\right)erf\left(\frac{\sqrt{2}b}{w_{y11}}\right)+\frac{2\sqrt{2}\,b}{\sqrt{\pi}\,w_{y11}}\exp\left(\frac{-2b^2}{w_{y11}^2}\right)erf\left(\frac{\sqrt{2}a}{w_{x11}}\right)-\frac{8ab}{\pi w_{x11}w_{y11}}\exp\left(-\frac{2a^2}{w_{x11}^2}-\frac{2b^2}{w_{y11}^2}\right)\right]+\frac{n_1n_2\lambda_0}{2n_c^2L_c(n_1-n_2)}\right\}$

Table 5.5 : "Cold cavity" photon lifetime of the elliptical Hermite-Gaussian eigenmodes guided by the *rectangular/square* oxide apertured resonator.

5.3.3 Simulation Results

Figures 5.15(a) to 5.15(c) shows the variation of the eigenmode "cold cavity" photon lifetime, $\tau'_{p(mp)}$ (main illustrations) and spectral FWHM linewidth, $\Delta\lambda'_{(FWHM)}$ (insets) with oxide aperture radius for the strong, medium and weak guiding resonators respectively. Clearly, the decrease in cold cavity photon lifetime with

reduction in aperture radius is much more gradual in the case of weak guiding as compared to the strong guiding device, and these trends are reflected in the corresponding variations of the cold cavity linewidth as well. As expected, in all cases the fundamental TEM_{00} mode always has the highest photon lifetime (or narrowest linewidth), followed by the TEM_{10}, TEM_{01} and TEM_{11} modes for these y-polarised eigenmodes. For comparison, the cold cavity photon lifetimes and linewidths for the TEM_{00} mode (main) and TEM_{10} mode (inset) for the strong, medium and weak guiding devices are also re-plotted on the same graph in Figures 5.16 and 5.17 respectively. Note that for big aperture size, strong guiding devices have the highest cold cavity photon lifetime, as a result of the slightly higher plane wave reflectance of top DBR over the medium and weak guiding devices (see section 3.3.1). However, since the strong and medium guiding devices suffer from larger size dependent diffraction losses, the weak guiding devices will have the highest photon lifetime and thus narrowest linewidth when aperture radius becomes smaller than 2.5μm. For the square devices of equivalent area, their values are also very close to those shown in Fig. 5.16 and Fig. 5.17 since, as demonstrated in Fig. 5.11, their modal reflectance are almost identical to those of the circular devices.

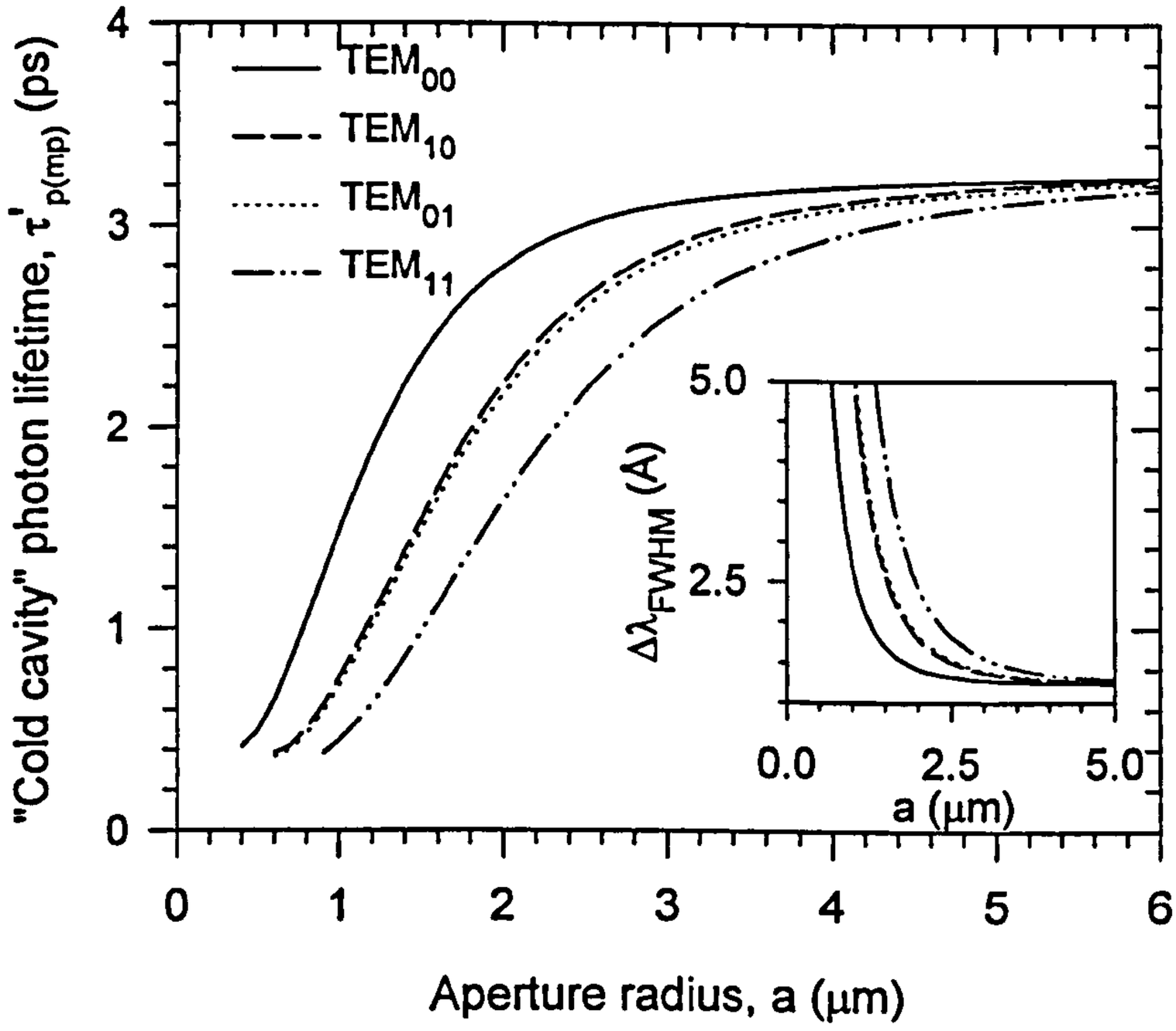

Figure 5.15(a) : Cold cavity photon lifetime (main) and FWHM linewidth (inset) as a function of aperture radius for *strong* guiding devices.

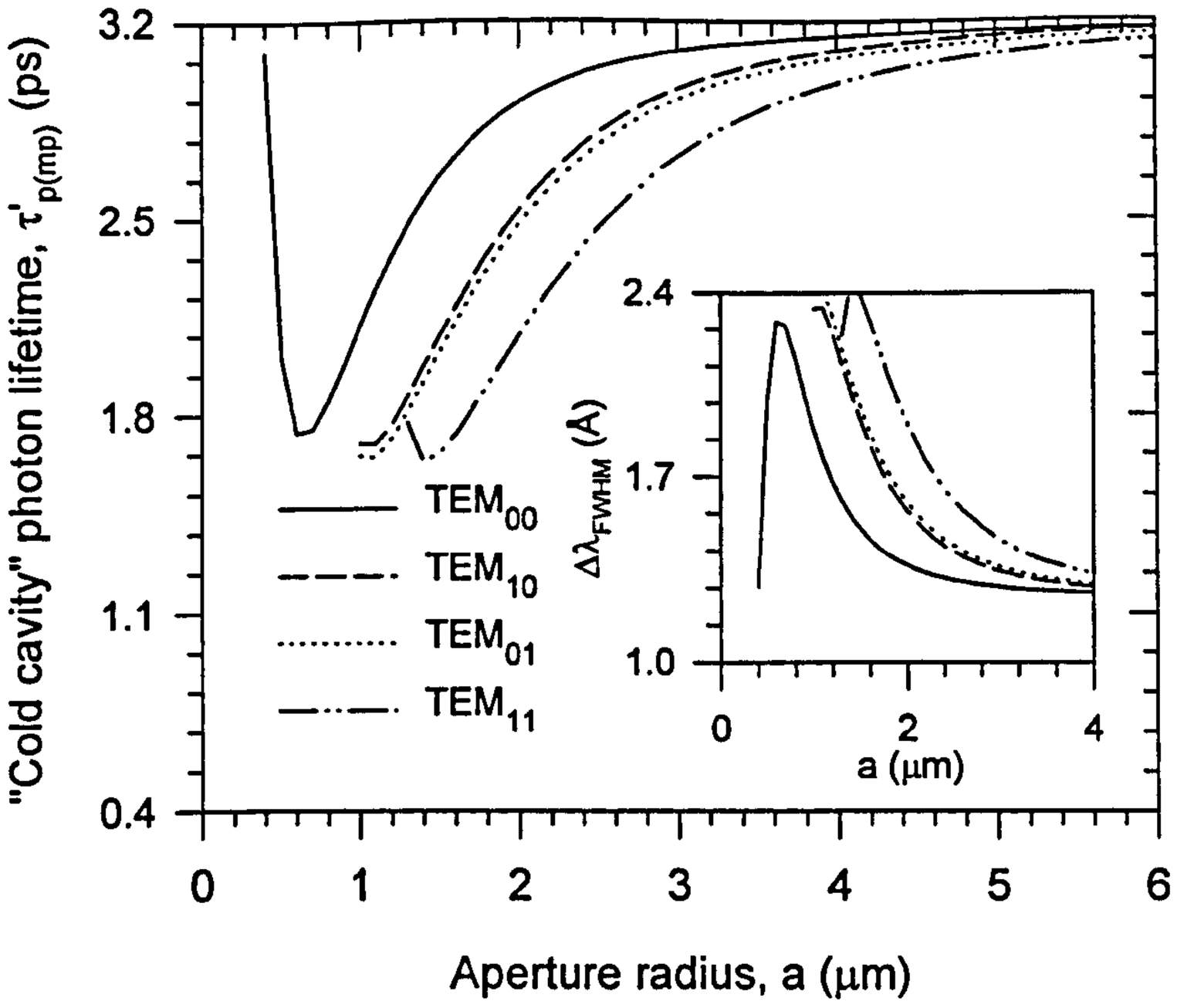

Figure 5.15(b) : Cold cavity photon lifetime (main) and FWHM linewidth (inset) as a function of aperture radius for *medium* guiding devices.

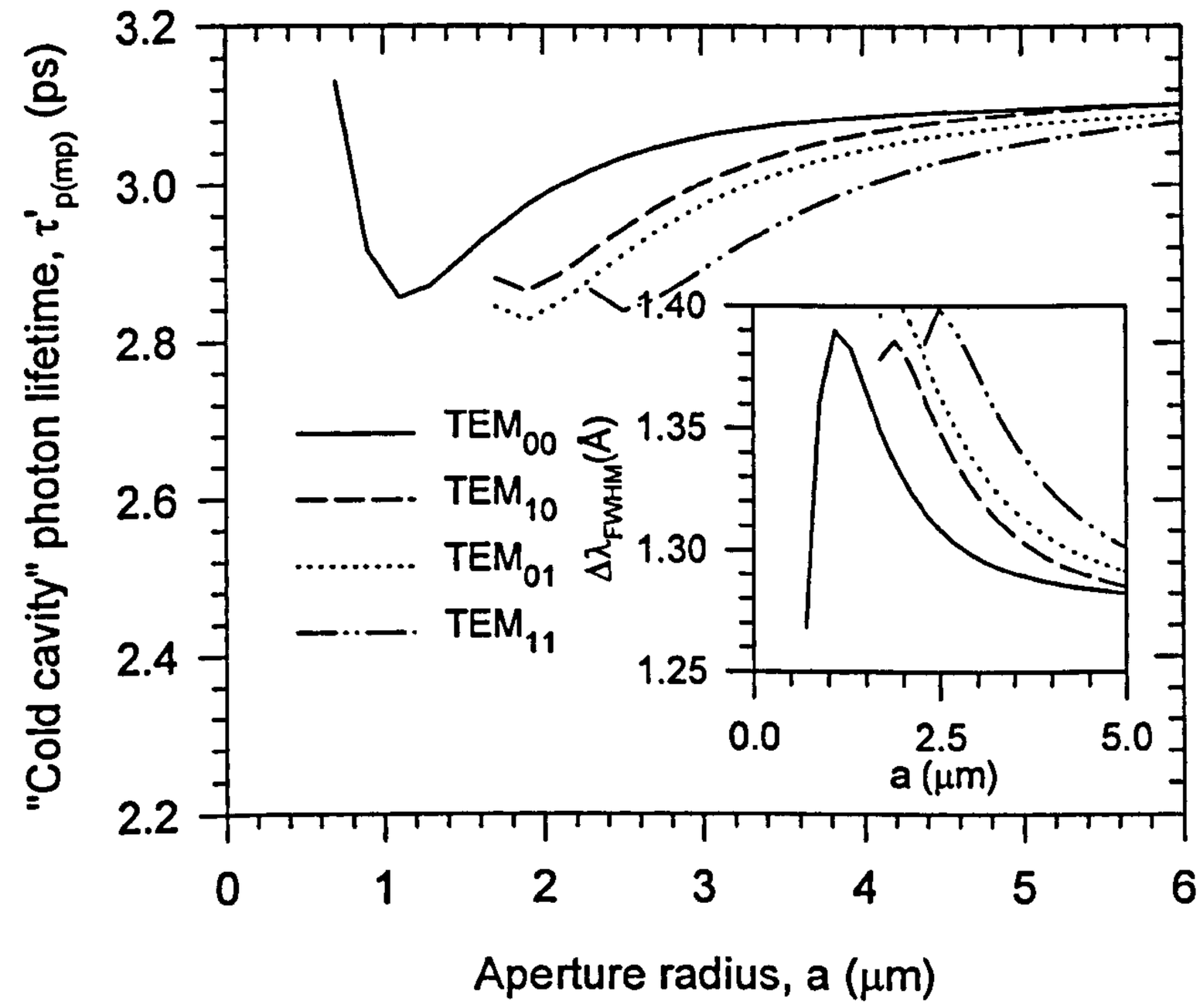

Figure 5.15(c) : Cold cavity photon lifetime (main) and FWHM linewidth (inset) as a function of aperture radius for *weak* guiding devices.

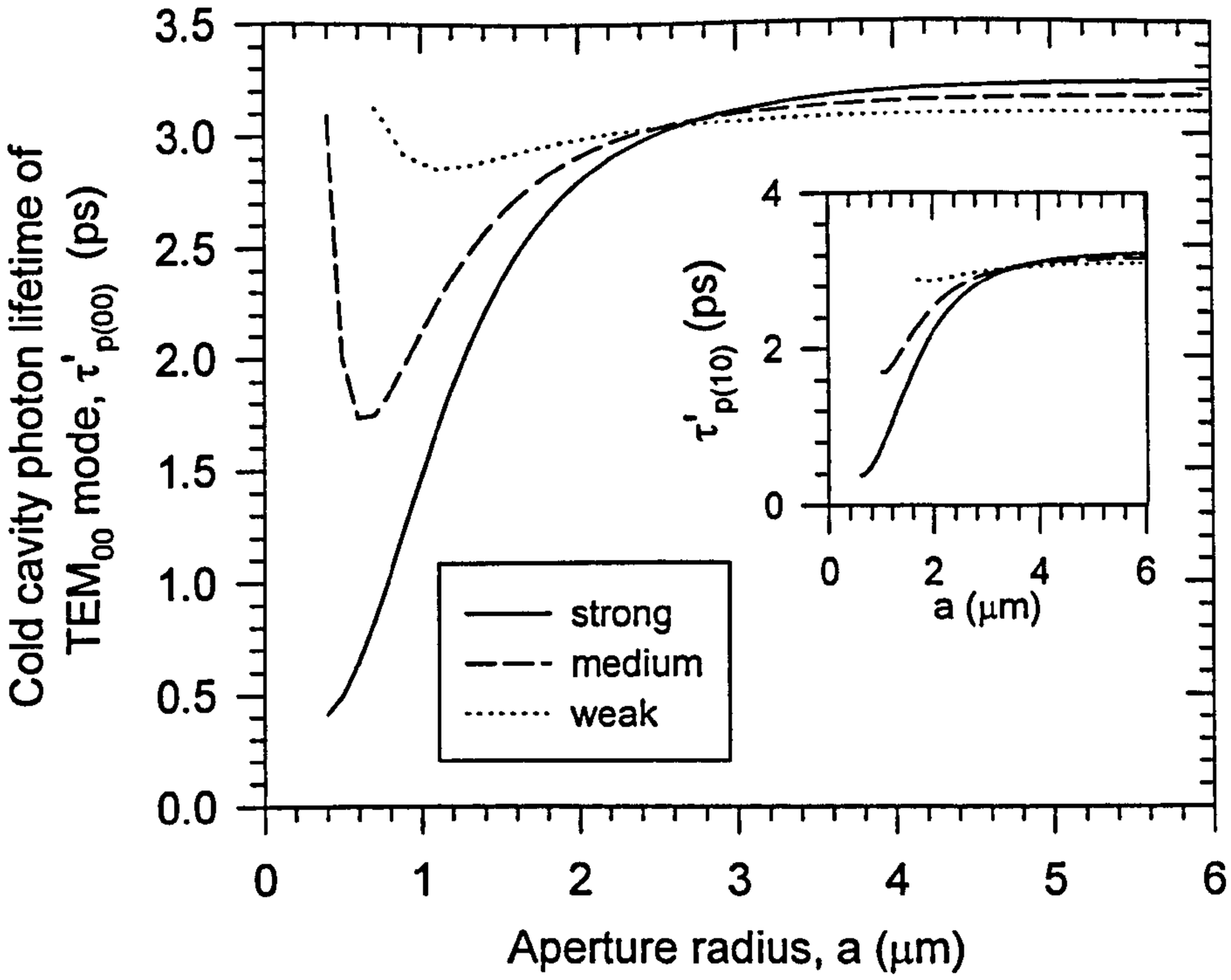

Figure 5.16 : "Cold cavity" photon lifetime of TEM_{00} mode (main) and TEM_{10} mode (inset) as a function of aperture radius.

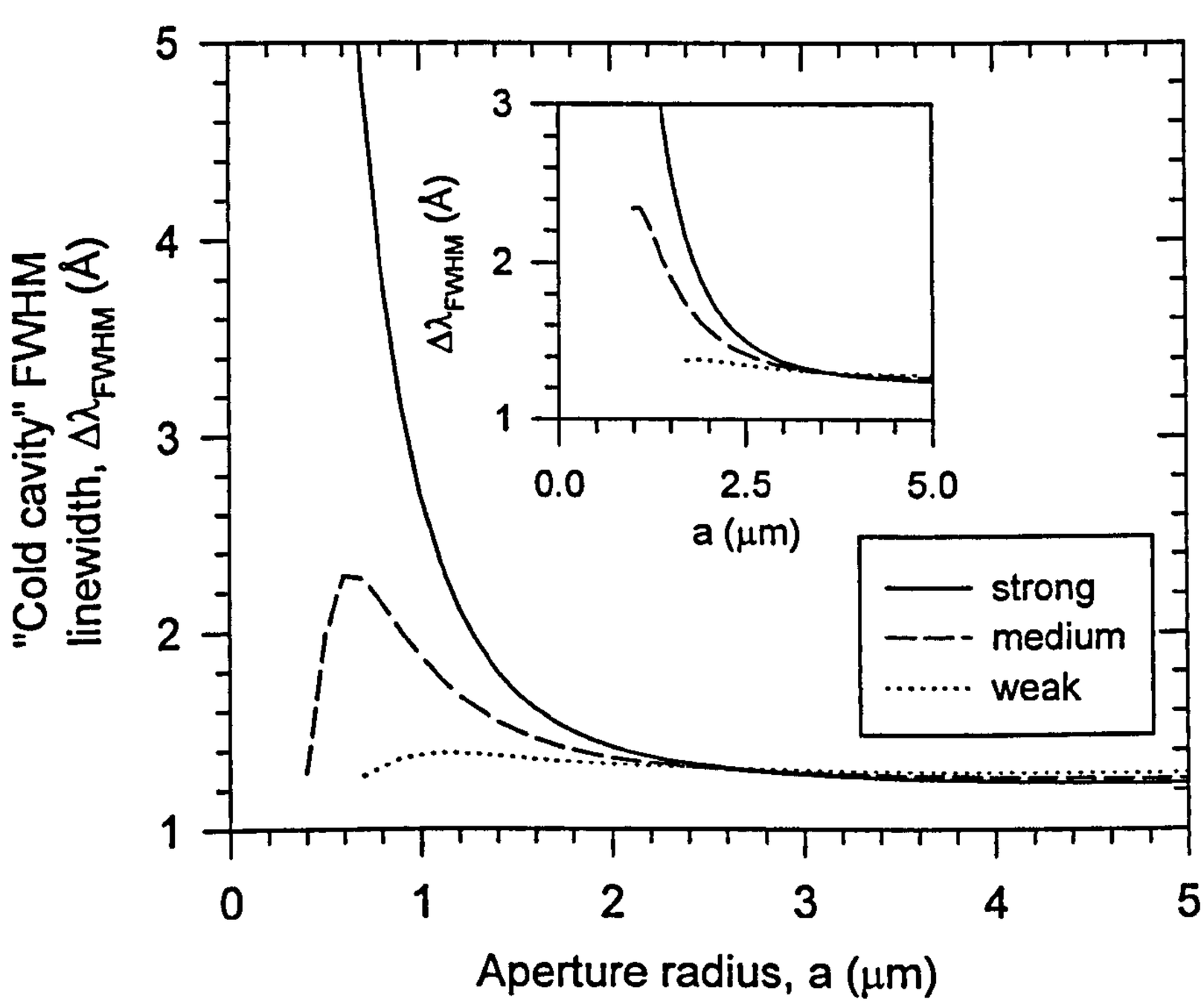

Figure 5.17 : "Cold cavity" FWHM linewidth of TEM_{00} mode (main) and TEM_{10} mode (inset) as a function of aperture radius.

5.4 Modelling of Steady State Light-Current Characteristic of Oxide Apertured VCSELs

In this section, a simplified approach to the modelling of the steady state light - current characteristic of an oxide apertured VCSEL is presented. This involves solving the photon and carrier rate equations self consistently to fully describe the photon-carrier interaction.

5.4.1 Photon and Carrier Rate Equations for VCSEL Resonator

Considering the conservation of photon generation and loss, the rate equation for the total number of photons carried by a particular mode inside a laser resonator is expressed by [11]

$$\frac{\partial}{\partial t}\iiint_{V} N_p \, dV = \iiint_{V_{qw}} vgN_p \, dV + \iiint_{V_{qw}} \beta_{sp} B N^2 \, dV - \frac{1}{\tau_p'}\iiint_{V} N_p \, dV \qquad (5.34)$$

where N_p is the photon density, N is the carrier density, V and V_{qw} are the volume of the resonator and the gain media (i.e. quantum wells) respectively. The first term on the right hand side of (5.31) represents the photon generation through stimulated emissions where v is the group velocity of the light in the medium and g is the gain provided by the gain media. The second term is due to the spontaneous emission where β_{sp} is the spontaneous emission factor which accounts for the fraction of the spontaneous emission generated that is coupled into the resonant mode of interest, B is the bimolecular recombination coefficient and N is the carrier density. (Note : β_{sp} can take a wide range of values and the effects of using different values of β_{sp} are discussed in section 5.4.4.) The spontaneous emission can be viewed as the optical "noise" that is needed to initiate the lasing oscillation. The last term represents the combined losses of photons either through various absorption mechanisms within the resonator or light transmission through the reflectors, and as defined earlier τ_p' is the cold cavity photon lifetime. Note that in (5.34), N_p and N are all position dependent parameters i.e. 3-dimensional functions of (x,y,z) or (r,ϕ,z) co-ordinates whereas the local optical gain g is directly related to N through the logarithmetric g-N relation expressed by eqn. (3.5).

In order to solve (5.34), firstly the photon density of a particular eigenmode ($N_{p(mp)}$) can be deduced from (5.25) as

$$N_{p(mp)} = \frac{\varepsilon E_{mp}^2 E_{pk(mp)}^2}{2hf} \tag{5.35}$$

where E_{mp} is the normalised 3-D field variations given by (4.25), $E_{pk(mp)}$ is the peak amplitude of the electric field at an antinode inside the cavity and hf is the photon energy. Consequently, the total number of photon for a particular eigenmode inside the resonator is given by

$$\iiint_V N_{p(mp)}\, dV = \frac{\varepsilon_0 E_{pk(mp)}^2}{2hf} \iiint_V n^2 E_{mp}^2\, dV \tag{5.36}$$

Again, it is easy to recognise that the familiar integral on the right hand side of (5.36) is identical to the denominator of the scalar variational integral formula expressed by eqn.(4.5).

Next, the stimulated photon emissions due to n_{qw} number quantum wells each of thickness d_{qw} placed a distance l from the peak of standing wave can be evaluated as

$$\begin{aligned}\iiint_{V_{qw}} v\, g\, N_{p(mp)}\, dV &= \frac{n_c^2 \varepsilon_0 v\, E_{pk(mp)}^2}{2hf} \sum_{i=1}^{n_{qw}} \left(\int_{l_i - d_{qw}/2}^{l_i + d_{qw}/2} \cos^2(\beta_c z)\, dz \right) \iint g\, E_{tr(mp)}^2\, dS \\ &= \frac{n_c^2 \varepsilon_0 v E_{pk(mp)}^2 \Gamma_{enh}\, n_{qw}\, d_{qw}}{4hf} \iint g\, E_{tr(mp)}^2\, dS\end{aligned} \tag{5.37}$$

where $E_{tr(mp)}$ is the generalised transverse field variation given by (5.28) and, Γ_{enh} is the "average" gain enhancement factor due to the placement of all the QWs with respect to the peak of the standing wave, which can be obtained by

$$\Gamma_{enh} = \frac{1}{n_{qw}} \sum_{i=1}^{n_{qw}} \left(1 + \frac{\cos(2\beta_c l_i) \sin(\beta_c d_{qw})}{\beta_c d_{qw}} \right) \tag{5.38}$$

Note that in (5.37), the refractive index of the cavity medium is assumed for the quantum wells since the field perturbations due to the dielectric discontinuity between thin QWs and the cavity medium are neglected. Photon generation due to spontaneous emission which is not field dependent, is simply given by

$$\iiint_{V_{qw}} \beta_{sp} B N^2\, dV = \beta_{sp} B n_{qw} d_{qw} \iint N^2\, dS \tag{5.39}$$

where the bimolecular recombination coefficient B is assumed to be independent of carrier density and the spontaneous emission factor β_{sp} is considered to be the same

for all the eigenmodes. It should be noted that in both expressions (5.37) and (5.39), uniform carrier density is assumed in the longitudinal z-direction within the closely placed thin QWs i.e. $\partial N / \partial z = 0$. Combining eqns. (5.36), (5.37) and (5.39), the photon number rate equation given by (5.34) can thus be rewritten as

$$\frac{\varepsilon_0 E_{pk(mp)}^2}{2hf}\frac{\partial}{\partial t}\iiint_V n^2 E_{mp}^2\, dV = \frac{n_c^2 \varepsilon_0 v \Gamma_{enh} n_{qw} d_{qw} E_{pk(mp)}^2}{4hf}\iint g\, E_{tr(mp)}^2\, dS + \beta_{sp} B n_{qw} d_{qw}\iint N^2 dS - \frac{\varepsilon_0 E_{pk(mp)}^2}{2hf\tau'_{p(mp)}}\iiint_V n^2 E_{mp}^2\, dV \quad (5.40)$$

In order to solve the photon rate equation expressed by (5.40), obviously the carrier distribution in the gain region must be known. Thus, a carrier number rate equation that considers the conservation of carrier in the gain medium is needed to complete the description of the photon-carrier interactions inside the laser resonator. Including the carrier diffusion effect, it is in the form of [11]

$$\iiint_{V_{qw}}\frac{\partial N}{\partial t}\, dV = \frac{I}{q} + \iiint_{V_{qw}} D\left(\nabla^2 N\right) - \frac{N}{\tau_{nr}} - BN^2 - \sum_{\text{All modes}} v g N_{p(mp)}\, dV \quad (5.41)$$

where I is the current injection, q is the charge constant, D is the ambipolar diffusion coefficients, τ_{nr} is the non-radiative carrier lifetime. For gain medium whose thickness is much less than the diffusion length (in the order of μm), as is the case of the QWs used for a VCSEL, uniform longitudinal carrier distribution can be assumed. Hence, substituting for N_p and g using equations (5.35) and (3.5) into (5.41), as well as taking into account of the positions of the QWs with respect to the antinode of the standing wave, the carrier *density* rate equation can be written as

$$\frac{\partial N}{\partial t} = \frac{J}{q\, n_{qw} d_{qw}} + D\left(\nabla_{tr}^2 N\right) - \frac{N}{\tau_{nr}} - BN^2 - \sum_{\text{All modes}} \frac{\Gamma_{enh} n_c Y_0 E_{pk(mp)}^2 g_{0N}}{4hf}\ln\left(\frac{N + N_{min}}{N_{tr}}\right) E_{tr(mp)}^2 \quad (5.42)$$

where J is the injection current density, ∇_{tr}^2 is the "transverse" Laplacian operator, and it is assumed that the group velocity $v \cong c/n_c$, and the expression for the gain has been taken from eqn. (3.5).

5.4.2 Steady State Solution of Photon and Carrier Rate Equations

The steady state solutions of the rate equations (5.40) and (5.42) can be found by setting the time derivatives to zero i.e. when $\partial / \partial t = 0$. Solving (5.40) for steady state peak field amplitude (and thus photon density), $E_{pk(mp)}$ is given by

$$E_{pk(mp)}^2 = \frac{4hf\beta_{sp}B\, n_{qw}d_{qw}\oiint N^2 dS}{\frac{2\varepsilon_0}{\tau'_{p(mp)}}\oiiint_V n^2 E_{mp}^2\, dV - n_c^2\varepsilon_0 v\Gamma_{enh} n_{qw}d_{qw}g_{0N}\oiint_S \ln\left(\frac{N+N_{min}}{N_{tr}}\right) E_{tr(mp)}^2\, dS} \tag{5.43}$$

Meanwhile, solving eqn (5.42) for dc current results in the carrier continuity equation expressed by

$$\frac{J}{q\, n_{qw}d_{qw}} + D\left(\nabla_{tr}^2 N\right) = \frac{N}{\tau_{nr}} + BN^2 + \sum_{\text{All modes}} \frac{\Gamma_{enh} n_c Y_0 E_{pk(mp)}^2 g_{0N}}{4hf} \ln\left(\frac{N+N_{min}}{N_{tr}}\right) E_{tr(mp)}^2 \tag{5.44}$$

In order to obtain any solution that fully describes the effects of photon-carrier interactions, equation (5.43) and (5.44) have to be solved self-consistently taking into account the two dimensional variations of the fields and carrier density profile. However for this work, in the quest to ease the computational workload, only the lasing characteristics of circular apertured devices are modelled. Besides that, the influence of the higher order mode on the transverse carrier density profile through stimulated emission at below threshold is neglected since its photon density is negligibly small in this operating region. In this way, the numerical task of solving (5.43) and (5.44) is reduced to a one dimensional problem along the radial direction i.e. r-axis. Furthermore, only the first two "least lossy" circular Hermite-Gaussian modes guided in the circularly apertured VCSELs are considered. Assuming y-polarised modes, they are thus the TEM_{00} and the TEM_{10} modes (since the TEM_{10} mode has a higher cold cavity photon lifetime than the TEM_{01} mode).

With the above mentioned assumptions in place, the cross sectional integral of the carrier density in the numerator of (5.43) is reduced to

$$\oiint_S N^2\, dS = \int_0^{2\pi}\int_0^{\infty} N^2(r,\phi)\, r dr\, d\phi = 2\pi\int_0^{\infty} N^2(r)\, r dr \tag{5.45}$$

where any azimuthal variation in the carrier density profile due to the presence of higher order modes is neglected. Also, the spontaneous emission rate of the higher order mode is assumed to be similar to that of the fundamental mode. For the volume

integral in the denominator of (5.43), which is identical to the denominator of the scalar variational formula in (4.5), the resulting final expressions for the TEM_{00} mode can be written as

$$\iiint_V n^2 E_{00}^2 \, dV = \frac{\pi w_{00}^2 n_c^2 L_c}{4}\left[1 - \frac{\left(n_2^2 - n_{ox}^2\right)}{n_c^2}\frac{F_{ox} d_{ox}}{L_c}\exp\left(\frac{-2a^2}{w_{00}^2}\right) + \frac{n_1 n_2 \lambda_0}{2n_c^2 L_c (n_1 - n_2)}\right]$$

$$= \frac{\pi w_{00}^2 n_c^2 L_{eff(00)}}{4} \qquad (5.46)$$

and for the TEM_{10} mode as

$$\iiint_V n^2 E_{10}^2 \, dV = \frac{\pi w_{10}^4 n_c^2 L_c}{16}\left\{1 - \frac{\left(n_2^2 - n_{ox}^2\right)}{n_c^2}\frac{F_{ox} d_{ox}}{L_c}\left(1 + \frac{2a^2}{w_{10}^2}\right)\exp\left(\frac{-2a^2}{w_{10}^2}\right) + \frac{n_1 n_2 \lambda_0}{2n_c^2 L_c (n_1 - n_2)}\right\}$$

$$= \frac{\pi w_{10}^4 n_c^2 L_{eff(10)}}{16} \qquad (5.47)$$

where as defined earlier in section (4.4), $L_{eff(00)}$ and $L_{eff(10)}$ are the "effective" cavity lengths for the TEM_{00} and TEM_{10} mode respectively. Similarly, as can be deduced from the general solution expressed by (5.33) for surface integration of the Hermite-Gaussian modes, the carrier density dependent surface integral in the denominator of (5.43) can be reduced to

$$\iint_S \ln\left(\frac{N(r) + N_{min}}{N_{tr}}\right) E_{tr(00)}^2 \, dS = \int_0^{2\pi} d\phi \int_0^{\infty} \ln\left(\frac{N(r) + N_{min}}{N_{tr}}\right) \exp\left(\frac{-2r^2}{w_{00}^2}\right) rdr$$

$$= 2\pi \int_0^{\infty} \ln\left(\frac{N(r) + N_{min}}{N_{tr}}\right) \exp\left(\frac{-2r^2}{w_{00}^2}\right) rdr \qquad (5.48)$$

for the TEM_{00} mode, and

$$\iint_S \ln\left(\frac{N(r) + N_{min}}{N_{tr}}\right) E_{tr(10)}^2 \, dS = \int_0^{2\pi} \cos^2\phi \, d\phi \int_0^{\infty} \ln\left(\frac{N(r) + N_{min}}{N_{tr}}\right) r^2 \exp\left(\frac{-2r^2}{w_{10}^2}\right) rdr$$

$$= \pi \int_0^{\infty} \ln\left(\frac{N(r) + N_{min}}{N_{tr}}\right) r^3 \exp\left(\frac{-2r^2}{w_{10}^2}\right) dr \qquad (5.49)$$

for the TEM_{10} mode. Using equations (5.45) to (5.49), the expression for the peak field amplitude of the TEM_{00} mode is reduced to

$$E^2_{pk(00)} = \frac{8\pi hf\,\beta_{sp} B\, n_{qw} d_{qw} \int_0^\infty N^2(r)\, rdr}{\frac{\pi\varepsilon_0 w_{00}^2 n_c^2 L_{eff(00)}}{2\,\tau'_{p(00)}} - 2\pi\, n_c^2 \varepsilon_0 v\Gamma_{enh} n_{qw} d_{qw}\, g_{0N} \int_0^\infty r \exp\left(\frac{-2r^2}{w_{00}^2}\right) \ln\left(\frac{N(r)+N_{min}}{N_{tr}}\right) dr}$$

$$= \frac{16\, hf\,\tau_{p(00)}\,\beta_{sp} B\, n_{qw} d_{qw}}{w_{00}^2 L_{eff(00)} n_c^2 \varepsilon_0} \int_0^\infty N^2(r)\, rdr \qquad (5.50)$$

where the "effective" photon lifetime of the TEM_{00} mode $\tau_{p(00)}$ i.e. photon lifetime in the presence of gain, is given by

$$\tau_{p(00)} = \left[\frac{1}{\tau'_{p(00)}} - \frac{4\, g_{0N} v\Gamma_{enh} n_{qw} d_{qw}}{w_{00}^2 L_{eff(00)}} \int_0^\infty r \exp\left(\frac{-2r^2}{w_{00}^2}\right) \ln\left(\frac{N(r)+N_{min}}{N_{tr}}\right) dr\right]^{-1} \qquad (5.51)$$

As for TEM_{10} mode, its peak field amplitude is given by

$$E^2_{pk(10)} = \frac{8\pi hf\,\beta_{sp} B\, n_{qw} d_{qw} \int_0^\infty N^2(r)\, rdr}{\frac{\pi\varepsilon_0 w_{10}^4 n_c^2 L_{eff(10)}}{8\,\tau'_{p(10)}} - \pi\, n_c^2 \varepsilon_0 v\Gamma_{enh} n_{qw} d_{qw}\, g_{0N} \int_0^\infty r^3 \exp\left(\frac{-2r^2}{w_{10}^2}\right) \ln\left(\frac{N(r)+N_{min}}{N_{tr}}\right) dr}$$

$$= \frac{64\, hf\,\tau_{p(10)}\,\beta_{sp} B\, n_{qw} d_{qw}}{w_{10}^4 L_{eff(10)} n_c^2 \varepsilon_0} \int_0^\infty N^2(r)\, rdr \qquad (5.52)$$

where the effective photon lifetime of TEM_{10} mode ($\tau_{p(10)}$) is given by

$$\tau_{p(10)} = \left[\frac{1}{\tau'_{p(10)}} - \frac{8\, g_{0N} v\Gamma_{enh} n_{qw} d_{qw}}{w_{10}^4 L_{eff(10)}} \int_0^\infty r^3 \exp\left(\frac{-2r^2}{w_{10}^2}\right) \ln\left(\frac{N(r)+N_{min}}{N_{tr}}\right) dr\right]^{-1} \qquad (5.53)$$

On the other hand, taking into account only the effect of the fundamental mode and allowing only the radial variation in the carrier density profile, the steady state solution of carrier rate equation of (5.44) can be reduced to

$$\frac{J}{q\, n_{qw} d_{qw}} + D\left(\nabla_r^2 N\right) = \frac{N}{\tau_{nr}} + BN^2 + \frac{\Gamma_{enh} n_c Y_0 E_{pk(00)}^2 g_{0N}}{4hf} \ln\left(\frac{N(r) + N_{min}}{N_{tr}}\right) \exp\left(\frac{-2r^2}{w_{00}^2}\right) \tag{5.54}$$

where now ∇_r^2 is the "radial" Laplacian operator.

It is also possible to write a compact general expressions for the steady state solutions of the photon rate equation in terms of the photon density of a particular eigenmode, $N_{p(mp)}$. By inspecting eqn.(5.50),(5.52) and (5.34), it is given by

$$N_{p(mp)} = R_{sp(mp)}\, \tau_{p(mp)} \tag{5.55}$$

where $R_{sp(mp)}$ is the average spontaneous emission rate per unit volume that is coupled into the eigenmode, and is expressed by

$$R_{sp(mp)} = \frac{\beta_{sp(mp)} n_{qw} d_{qw} B \oiint N^2\, dS}{\oiiint_V E_{mp}^2\, dV} \tag{5.56}$$

The expression for effective photon lifetime can also be simplified into

$$\tau_{p\,(mp)} = \left[\frac{1}{\tau'_{p\,(mp)}} - vG_{mp}\right]^{-1} \tag{5.57}$$

where the modal gain $G_{(mp)}$ obtained by

$$G_{mp} = \frac{\oiiint_{\text{gain region}} E_{mp} E_{mp}^* g\, dV}{\oiiint_V E_{mp} E_{mp}^*\, dV} \tag{5.58},$$

is a function of modal field distribution in the resonator as well as the local carrier distribution that affects the local optical gain in the active region. Obviously, besides the total cavity loss represented by cold cavity photon lifetime, the effective photon lifetime is also affected by the modal gain.

As discussed in section 5.3, the light emission linewidth from an optical resonator is inversely proportional to the effective photon lifetime. Using eqn.(5.23) and eqns.(5.55) to (5.58), the relation among the emission linewidth (FWHM), effective photon lifetime, cold cavity photon lifetime and modal gain can be expressed by

$$\Delta\lambda_{FWHM\,(mp)} = \frac{\lambda_r^2}{2\pi c\,\tau_p} = \frac{\lambda_r^2}{2\pi c}\left(\frac{1}{\tau'_{p(mp)}} - vG_{mp}\right) = \Delta\lambda'_{FWHM\,(mp)} - \frac{\lambda_r^2 G_{mp}}{2\pi n_c} \tag{5.59}$$

or simply by

$$\Delta\lambda_{FWHM\,(mp)} = \frac{R_{sp(mp)}\,\lambda_r^2}{2\pi c\,N_{p(mp)}} \tag{5.60}$$

where $\Delta\lambda'_{FWHM(mp)}$ is the "cold cavity" linewidth and eqn.(5.60) is equivalent to the famous Schawlow-Townes linewidth formula [1,9]. Therefore, as the modal gain increases with current injection, the emission linewidth reduces while the "effective" photon lifetime (τ_p) and the photon density/number grows. Eventually when the photon density grow very large at the lasing onset of the eigenmode, the emission linewidth collapses into a very narrow spectral line, which is one of the defining characteristics of lasers. However, eqn (5.60) which considers only the effect of spontaneous emission noise is only valid for the below-threshold amplified spontaneous emission linewidth. Above threshold, the coupling between the amplitude and phase fluctuations of the optical fields caused by carrier induced noise, broaden the laser linewidth such that it is larger that that predicted by eqn.(5.60) [1,10,11]. Phenomenologically, the broadened laser linewidth is usually estimated by multiplying the "modified" Schawlow-Townes linewidth limit (i.e. ½ of that predicted by eqn.(5.60) due to the stabilisation of field amplitude fluctuations at above threshold [1]) by a factor of $(1+\alpha_e^2)$ where α_e is commonly referred to as linewidth enhancement factor [10,11]. Therefore, from eqn.(5.60), the expected laser linewidth in the frequency domain, Δf, is given by

$$\Delta f = \frac{\Gamma_{sp(mp)} R_{sp(mp)}}{4\pi N_{p(mp)}}\left(1+\alpha_e^2\right) \tag{5.61}$$

Finally, it should also be noted that under the steady state conditions, the threshold modal gain (G_{mp}) is actually lower than the total cavity loss $(\tau'_{p(mp)}v)^{-1}$, i.e. the threshold condition ($G_{mp} = (\tau'_{p(mp)}v)^{-1}$) is only approached asymptotically. Otherwise, as can be deduced from eqn.(5.59) and eqn.(5.60), a zero laser linewidth and infinite photon density would be implied. Therefore, as the threshold current is approached and exceeded, the modal gain must saturate slightly below the threshold value. Hence,

the laser can be considered to be a very high gain, very narrow bandwidth regenerative amplifier of spontaneous emission noise.

5.4.3 Computational Procedures

In order to solve (5.54) numerically, the standard Finite Difference Method (FDM) [12] whereby uniform grids of equal annular width constructed along the radial direction is adopted. Hence, the carrier diffusion term in (5.54) can be solved as

$$\begin{aligned} \mathrm{D}\left(\nabla_r^2 N\right) &= \frac{\partial^2 N}{\partial \mathrm{r}^2} + \frac{1}{\mathrm{r}}\frac{\partial N}{\partial \mathrm{r}} \\ &= \mathrm{D}\left\{ \frac{1}{\Delta \mathrm{r}}\left[\left(\frac{N_{s+1}-N_s}{\Delta \mathrm{r}}\right)-\left(\frac{N_s-N_{s-1}}{\Delta \mathrm{r}}\right)\right] + \frac{1}{\mathrm{s}\,\Delta \mathrm{r}}\left(\frac{N_{s+1}-N_{s-1}}{2\Delta \mathrm{r}}\right)\right\} \\ &= \frac{\mathrm{D}}{\Delta \mathrm{r}^2}\left[N_{s+1}\left(1+\frac{1}{2s}\right) + N_{s-1}\left(1-\frac{1}{2s}\right) - 2N_s\right] \end{aligned} \tag{5.62}$$

where s = 1, 2, 3.....M (s=0 at centre of device), (M+1) is the total number of grid points and Δr is the dimension of the radial grid element. The boundary condition needed to be imposed are :

(i) $\frac{\partial N}{\partial \mathrm{r}} = 0$ at r = 0, thus requires that $N_1 = N_2$ where N_1 is the carrier density in first grid element extending from the centre of resonator to a distance Δr.

(ii) $N = 0$ at r = ma where a is the radius of the oxide aperture, and m is any integer number which is sufficiently large such that any change in this number causes negligible difference to the final solutions.(i.e. $N_M = 0$ where M = (ma/Δr))

Substituting eqn. (5.62) into eqn.(5.54), the steady state solution of carrier rate equation for the s-th grid point can thus be written as

$$\begin{aligned} &\frac{\mathrm{J_s}}{\mathrm{q}\,n_{qw}\mathrm{d_{qw}}} + \frac{\mathrm{D}}{\Delta \mathrm{r}^2}\left[N_{s+1}\left(1+\frac{1}{2s}\right) + N_{s-1}\left(1-\frac{1}{2s}\right) - 2N_s\right] \\ &= \frac{N_s}{\tau_{nr}} + \mathrm{B}N_s^2 + \frac{\Gamma_{enh}\mathrm{n_c}\mathrm{Y_0}\mathrm{E}^2_{pk(00)}\mathrm{g}_{0N}}{4hf}\ln\left(\frac{N_s+N_{min}}{N_{tr}}\right)\exp\left[\frac{-2\left(\mathrm{s}\,\Delta \mathrm{r}\right)^2}{\mathrm{w}_{00}^2}\right] \end{aligned} \tag{5.63}$$

where J_s is the injected current density that assumed to be uniform across the oxide aperture but zero elsewhere i.e. $J_s = J$ for $s \le (a/\Delta r)$, $J_s = 0$ for $s > (a/\Delta r)$. Equation

(5.63) has to be applied at successive grid points repetitively until the carrier density at each element in present iteration does not differ significantly from that of the previous iteration i.e. stabilisation of carrier density profile achieved. In order to speed up the convergence of the carrier density profile, a method called "Successive Over-Relaxation" (SOR) [12] was employed. From eqn. (5.63), the carrier density for s-th grid point at the *i*-th iteration is thus given by

$$|N_s|^i = |N_s|^{i-1} + SOR\left\{\frac{\frac{J_s}{q\, n_{qw} d_{qw}} + \frac{D}{\Delta r^2}\left[|N_{s+1}|^{i-1}\left(1+\frac{1}{2s}\right) + |N_{s-1}|^{i-1}\left(1-\frac{1}{2s}\right)\right] - |Stim|^{i-1}}{\left(\frac{2D}{\Delta r^2} + B|N_s|^{i-1} + \frac{1}{\tau_{nr}}\right)} - |N_s|^{i-1}\right\} \tag{5.64}$$

where the term due to stimulated emissions, $|Stim|$ is given by

$$|Stim|^{i-1} = E_{pk(00)}^2 \frac{\Gamma_{enh} n_c Y_0 g_{0N}}{4hf} \ln\left(\frac{|N_s|^i + N_{min}}{N_{tr}}\right) \exp\left[\frac{-2(s\,\Delta r)^2}{w_{00}^2}\right] \tag{5.65}$$

The successive over- relaxation factor, *SOR*, can be chosen to be any value between 1 and 2 whereby the higher value of *SOR* allows faster convergence. It should be noted that superscripts *i* associated with the carrier density *N* in (5.64) and (5.65) represents the corresponding values for the (*i*-1)-th or the *i*-th iteration rather their exponential power.

Similarly, the solutions for peak field amplitudes can also be obtained using the finite difference method described above. For a particular carrier density level and profile, the peak field amplitude for TEM_{00} mode can be deduced from (5.50) as

$$E_{pk(00)}^2 = \frac{16\, hf\, \beta_{sp} B\, n_{qw} d_{qw} \tau_{p(00)}}{w_{00}^2 L_{eff(00)} n_c^2 \varepsilon_0} \sum_{s=2}^{M}\left[\left(\frac{N_s^2 + N_{s-1}^2}{2}\right) s\,\Delta r^2\right] \tag{5.66}$$

where the "effective" photon lifetime of the TEM_{00} mode ($\tau_{p(00)}$) is given by

$$\tau_{p(00)} = \left\{\frac{1}{\tau'_{p(00)}} - \frac{4\, g_{0N} v \Gamma_{enh} n_{qw} d_{qw}}{w_{00}^2 L_{eff(00)}} \sum_{s=2}^{M}\left[\exp\left(\frac{-2s^2\Delta r^2}{w_{00}^2}\right) \ln\left(\frac{(N_s + N_{s-1})/2 - N_{min}}{N_{tr}}\right) s\,\Delta r^2\right]\right\}^{-1} \tag{5.67}$$

As for the TEM_{10} mode, from (5.52) its peak field amplitude can be obtained by

$$E^2_{pk(10)} = \frac{64\, hf\, \beta_{sp} B\, n_{qw} d_{qw} \tau_{p(10)}}{w_{10}^4 L_{eff(10)} n_c^2 \varepsilon_0} \sum_{s=2}^{M} \left[\left(\frac{N_s^2 + N_{s-1}^2}{2} \right) s\, \Delta r^2 \right] \qquad (5.68)$$

where the effective photon lifetime of TEM_{10} mode ($\tau_{p(10)}$) is given by

$$\tau_{p(10)} = \left\{ \frac{1}{\tau'_{p(10)}} - \frac{8\, g_{0N} v \Gamma_{enh} n_{qw} d_{qw}}{w_{10}^4 L_{eff(10)}} \sum_{s=2}^{M} \left[\exp\left(\frac{-2s^2 \Delta r^2}{w_{10}^2} \right) \ln\left(\frac{(N_s + N_{s-1})/2 - N_{min}}{N_{tr}} \right) s^3\, \Delta r^4 \right] \right\}^{-1} \qquad (5.69)$$

As mentioned earlier in this section, the objective of this simulation is to calculate the optical power outputs through the peak electric field amplitudes associated with the TEM_{00} and TEM_{10} modes, as a function of the current density injection level into the gain media. From these light-current characteristics, the thresholds of both the fundamental and higher order modes can thus be determined. The variation of the effective photon lifetimes and thus the narrowing of the emission linewidths with current can also be predicted automatically in the course of calculation. At the beginning of the calculation for each injected current density value, an initial "guessed" input value of $E^2_{pk(00)}$ is used to calculate the carrier density profile using eqn. (5.64) and (5.65) iterated to a steady state. Then, the output value of $E^2_{pk(00)}$ is obtained using the above calculated carrier density profile through eqns (5.66) and (5.67). This process is repeated until the output value agrees with the input value within the resolution specified. When this happens, the final value of $E^2_{pk(00)}$ and the resulting carrier density profile are said to be the stable solutions of both the photon and carrier rate equation. Then, the peak field amplitude of the higher order mode $E^2_{pk(10)}$ can be calculated easily using eqns. (5.68) and (5.69). Subsequently, the optical power output of the TEM_{00} and TEM_{10} modes transmitted through the top reflector (i.e. part of the passive cavity loss) can be deduced from (5.29) by setting the modal gain to zero, and then multiplied the whole expression by the output coupling ratio $T_{T(mp)}/(1-R_{T(mp)}R_{B(mp)})$ where the cavity absorption loss is neglected. They are thus given by

$$P_{T(00)} \cong \frac{1}{16} \pi w_{00}^2 n_c Y_0 E^2_{pk(00)} T_{T(00)} \qquad (5.70)$$

and

$$P_{T(10)} \cong \frac{1}{64}\pi w_{10}^4 n_c Y_0 E_{pk(10)}^2 T_{T(10)} \tag{5.71}$$

respectively where $T_{T(mp)}$ is the modal transmittance of the top DBR.

It should be noted that the final results obtained are independent of the initial guess of $E_{pk(00)}^2$. However, a good "educated" initial field assumption e.g. making use of the near linear light-current relationship at above threshold, can save much computing time. On average, the calculation for a given current density takes about 4 to 12 minutes depending on aperture size, on a Pentium 166MHz personal computer for grid element size of 0.05μm. The values (MKS unit) of the material and fundamental constants adopted in the calculations are listed in Table 5.6. The values of ambipolar diffusion coefficients are general taken to be between about $5cm^2/s$ [13,14] and $10cm^2/s$ [15,16] for a GaAs based active region. In this work, the latter value of $10cm^2/s$ is adopted. The measured experimental values (e.g. 0.0021, obtained by analysing L-I characteristics and emission spectra [17]) of spontaneous emission factors for oxide apertured VCSELs are generally found to be an order higher than their implanted counterparts, and a value of 0.001 is used in the simulation here.

Material / Fundamental Constants	Symbols	Values	Units (MKS)
Bimolecular recombination coefficient	B	1×10^{-16}	m^3/s
Ambipolar diffusion coefficient	D	10^{-3}	m^2/s
Spontaneous emission factor	β_{sp}	10^{-3}	-
Non-radiative carrier lifetime	τ_{nr}	5×10^{-9}	s
Transparency carrier density	N_{tr}	2.36×10^{24}	m^{-3}
Gain coefficient (carrier density)	g_{0N}	1.37×10^{5}	m^{-1}
Electron charge constant	q	1.6×10^{-19}	C
Velocity of light in free space	c	3×10^{8}	m/s
Permittivity constant	ε_0	8.854×10^{-12}	F/m
Admittance of free space	Y_0	$(120\pi)^{-1}$	Ω
Planck constant	h	6.626×10^{-34}	Js

Table 5.6 : List of material and fundamental constants used in the simulation.

5.4.4 Simulation Results I : General Discussions

Before proceeding on to comparing the predicted lasing performance of the VCSEL designs used in this work, it is useful to first analyse how the threshold and modal behaviour of a VCSEL are influenced by certain device parameters that affect the modal gains. For this purpose, the light-current characteristic of a generic VCSEL with an uniform current injection region of 2μm radius (i.e. assumed to be the size of aperture) was simulated with variation of only one parameter at each occasion, so that the effect of that particular parameter can be ascertained independently. Except for the cases where the effects of mode size are considered, identical 1/e half mode size (w_{mp}) of 1.5μm were assumed for both TEM_{00} and TEM_{10} modes. Their cold cavity photon lifetimes (τ'_{mp}) were assumed to be identical at 3.0ps. Unless stated otherwise, the values of other constants needed for simulation are those given in Table 4.6.

(A) Effects of Carrier Diffusion and Spatial Hole Burning

As mentioned in section 4.5.2, the modal gain is affected by the distribution of the spatial distribution carriers in the laser active regions. Under the assumption of uniform transverse current density injection profile (valid since the QWs are very close to the oxide aperture i.e. ≈ 0.1μm) and uniform longitudinal carrier distribution in the quantum wells (i.e. $\partial N / \partial z = 0$), at below threshold the transverse carrier concentration profile is mainly dependent on the value of the ambipolar diffusion coefficient D. Above lasing threshold, the enhanced interaction between the carriers and photons through stimulated emission modify the carrier density profile according to the intensity profile of the first lasing mode, and thus affect the subsequent lasing threshold of other higher order eigenmodes. In order to illustrate these points, Figures 5.18(a) and 5.18(b) show the transverse carrier density profiles of the device with 2μm aperture radius at various current injection levels assuming diffusion coefficients of $10cm^2/s$ and $50cm^2/s$ respectively. The former is a typical value for the ambipolar diffusion coefficient [15,16] and is adopted in this thesis, whilst the latter is within the possible range of values for *electron* diffusion coefficient [18].

As expected, the larger value of diffusion coefficient causes the carriers to spread out further from the current injection region at below threshold, and there is thus a smaller number of carriers within the aperture. This in turn results in a lower modal gain available or possibly higher modal absorption experienced, depending on

the current injection level. Consequently, the threshold current density of the TEM_{00} mode $J_{th(00)}$ is lower at *2.55 kA/cm²* for the case of D=10cm²/s than at *5.15 kA/cm²* for the case of D=50cm²/s .

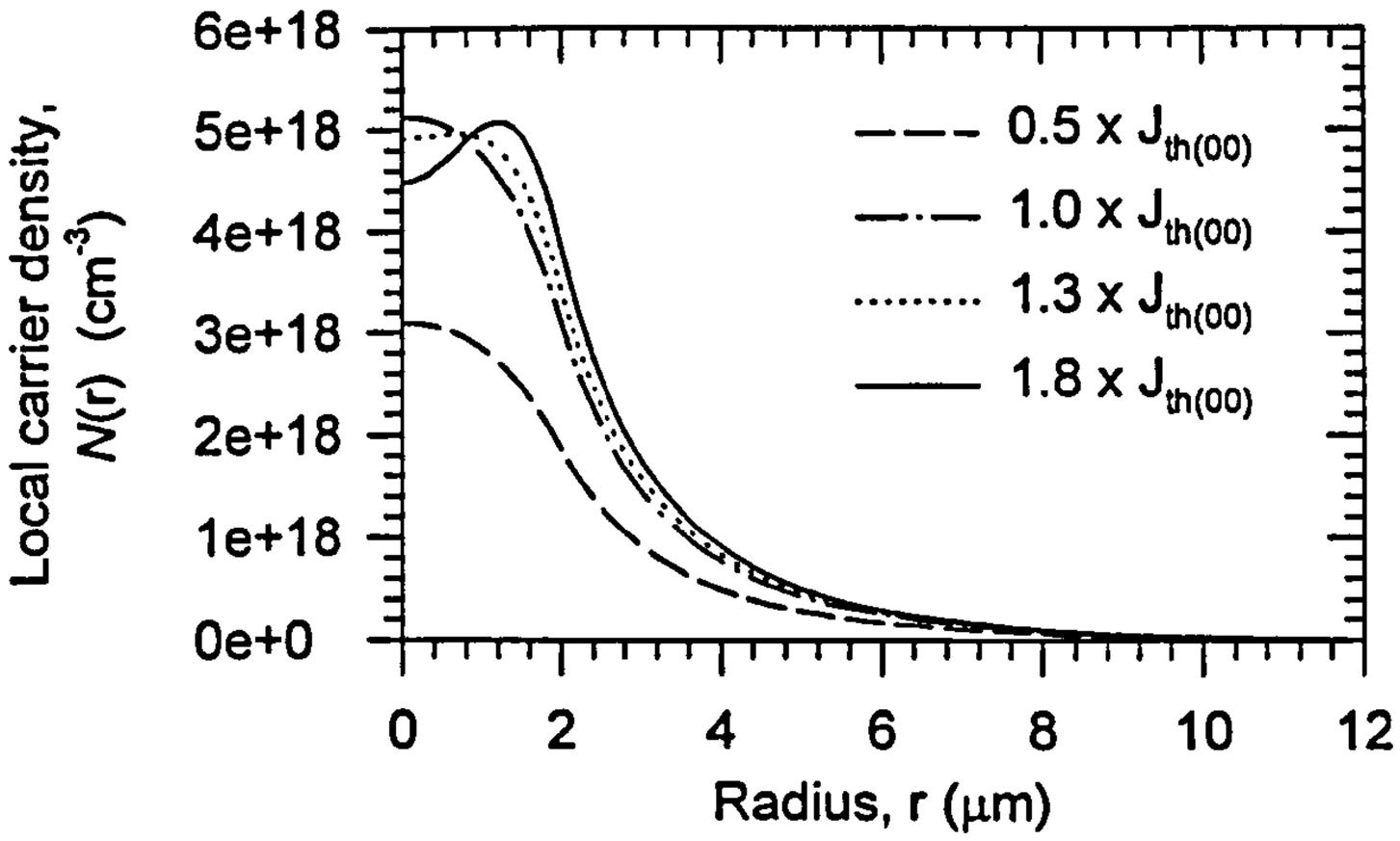

Figure 5.18(a) : Radial carrier density profile in the 2μm radius device, assuming diffusion coefficient (D) of *10 cm²/s*, and mode size (w_{mp}) of 1.5μm.

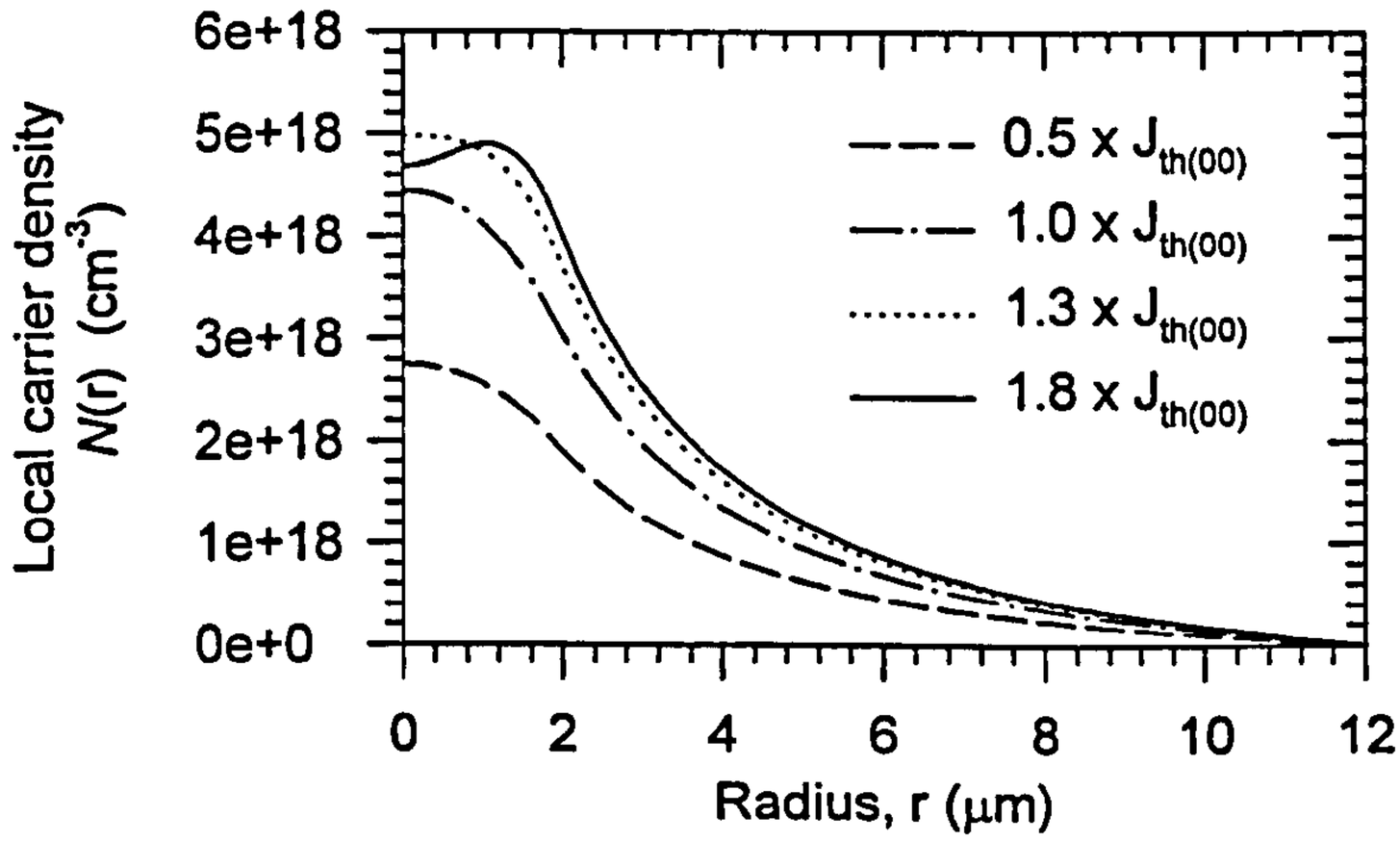

Figure 5.18(b) : Radial carrier density profile in the 2μm radius device, assuming diffusion coefficient (D) of *50 cm²/s*, and mode size (w_{mp}) of 1.5μm.

After the onset of the fundamental TEM_{00} mode, the enhanced carrier-photon interaction causes the local carrier density at the centre of the gain region/QWs where the optical intensity is high to decrease. On the other hand, the carrier density at the edges of the gain region where the optical intensity of the TEM_{00} mode is weak, is not clamped but continues rising with the current injection. This phenomenon is the well-known spatial hole burning (SHB) effect [11,13]. As a result of this spatial hole

burning effect, the modal gain of the higher order TEM_{10} mode which has a high intensity near the edge of aperture, increases with current injection even after the turn on of the fundamental mode. It will eventually reach its own threshold and results in multimode lasing operation. Comparing the carrier density profile above $J_{th(00)}$, it is obvious that larger value of diffusion coefficient is good for alleviating the SHB effect by "washing out"/reducing the carrier peak that appears near the edge of the aperture. This thus results in better suppression of the onset of the higher order mode. The threshold current density of the TEM_{10} mode ($J_{th(10)}$) for the case of $D = 50cm^2/s$ is *11.90 kA/cm²* as compared to *5.25kA/cm²* in the case of $D = 10cm^2/s$.

Despite the fact that identical cold/passive cavity photon lifetimes are assumed for both eigenmodes, the threshold of the higher order TEM_{10} mode is higher than that of the fundamental TEM_{00} mode as shown by the results discussed above. This is simply because the fields of the higher order mode extends further out of the aperture into the region where the local carrier density available is much lower than that within the aperture region. As illustrated in Figure 5.19 where the dependence of local carrier density and local optical gain on injected current density is shown, these regions either offer little optical gain (e.g. at r = 1.5a) or could even be absorptive (e.g. at r = 2a) as transparency is not reached yet. Consequently, the modal gain of the higher order mode for a given injected current is always lower than that of fundamental mode for the situations considered here, and thus leads to it having a higher threshold current density. Also note that at below threshold, while the local carrier densities increase almost linearly with injected current density, the corresponding local optical gains vary in a near parabolic manner as a direct consequence of the logarithmic gain-carrier relation.

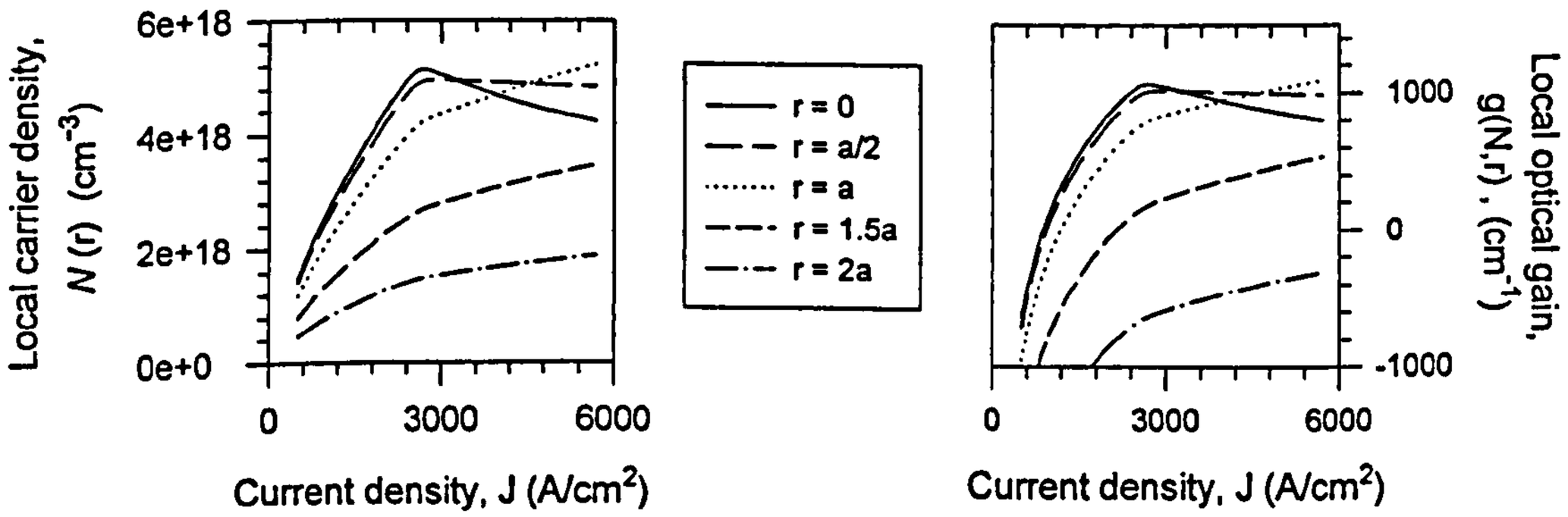

Figure 5.19 : Local carrier density $N(r)$ and local optical gain $g(r, N)$, as a function of injected current density at various radial positions.

The simulated light-current (L-I) characteristic (excluding the thermal effects) where a diffusion coefficient of $10cm^2/s$ is assumed for the 2μm radius device considered here, is also illustrated in Figure 5.20. The inset of this figure shows the corresponding variation of Side Mode Suppression Ratio (SMSR), which is define as the ratio of spectral peak intensity of the dominant mode to that of the side mode with highest peak value [11]. Here, that side mode is assumed to be the TEM_{10} mode, and the broadening of the TEM_{00} actual lasing linewidth above threshold is neglected. Note that since the photon-carrier interactions due to the higher order mode are neglected in the simulation (a reasonable assumption at below threshold since the photon density of the TEM_{10} mode is negligible when compared to that of the fundamental mode), solutions obtained after the onset of the TEM_{10} mode are not physically meaningful. Nevertheless, the threshold current densities of both eigenmodes can be determined easily by linearly extrapolating their respective L-I curves. It is also obvious that whilst the SMSR increases dramatically upon the lasing of the fundamental TEM_{00} mode, it also deteriorates rapidly just before the onset of the TEM_{10} mode.

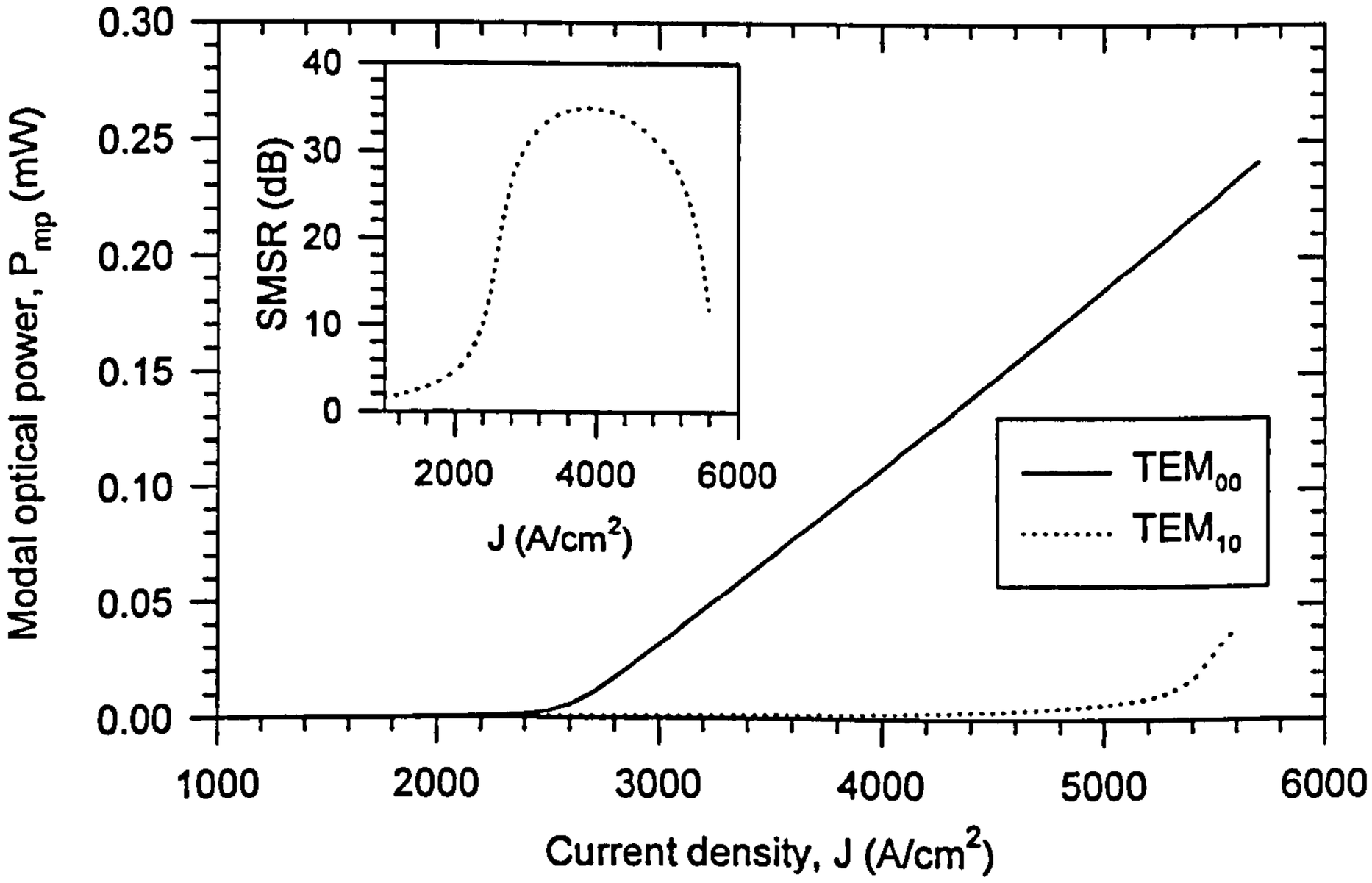

Figure 5.20 : Simulated light-current characteristics of the 2μm radius device assuming diffusion coefficient (D) of 10 cm^2/s and mode size (w_{mp}) of 1.5μm. The inset shows the corresponding variation of SMSR.

In section 5.4.2, it was shown that the effective photon lifetime and thus the linewidth of amplified spontaneous emission can be calculated directly through the solution of the rate equations. For the 2μm radius device with D = 10 cm^2/s considered above, Figure 5.21 and Figure 5.22 show the variations of the effective photon lifetimes and emission linewidths respectively for both the TEM_{00} and TEM_{10} modes. Whilst the inset of Fig 5.21 details variations of photon lifetime in the vicinity of the threshold of the TEM_{00} mode, the inset of Fig. 5.22 shows the variation of linewidth at well above threshold where the values for TEM_{10} mode are out of range. The black dots that appear in Fig. 5.21 (inset) and Fig. 5.22 (main illustration) mark the positions at where the respective eigemodes reach "transparency". As can be deduced from eqn.(5.58), this happens when the modal gain $G_{mp} = 0$ and this produces, by definition the cold cavity values of the photon lifetime and linewidth.

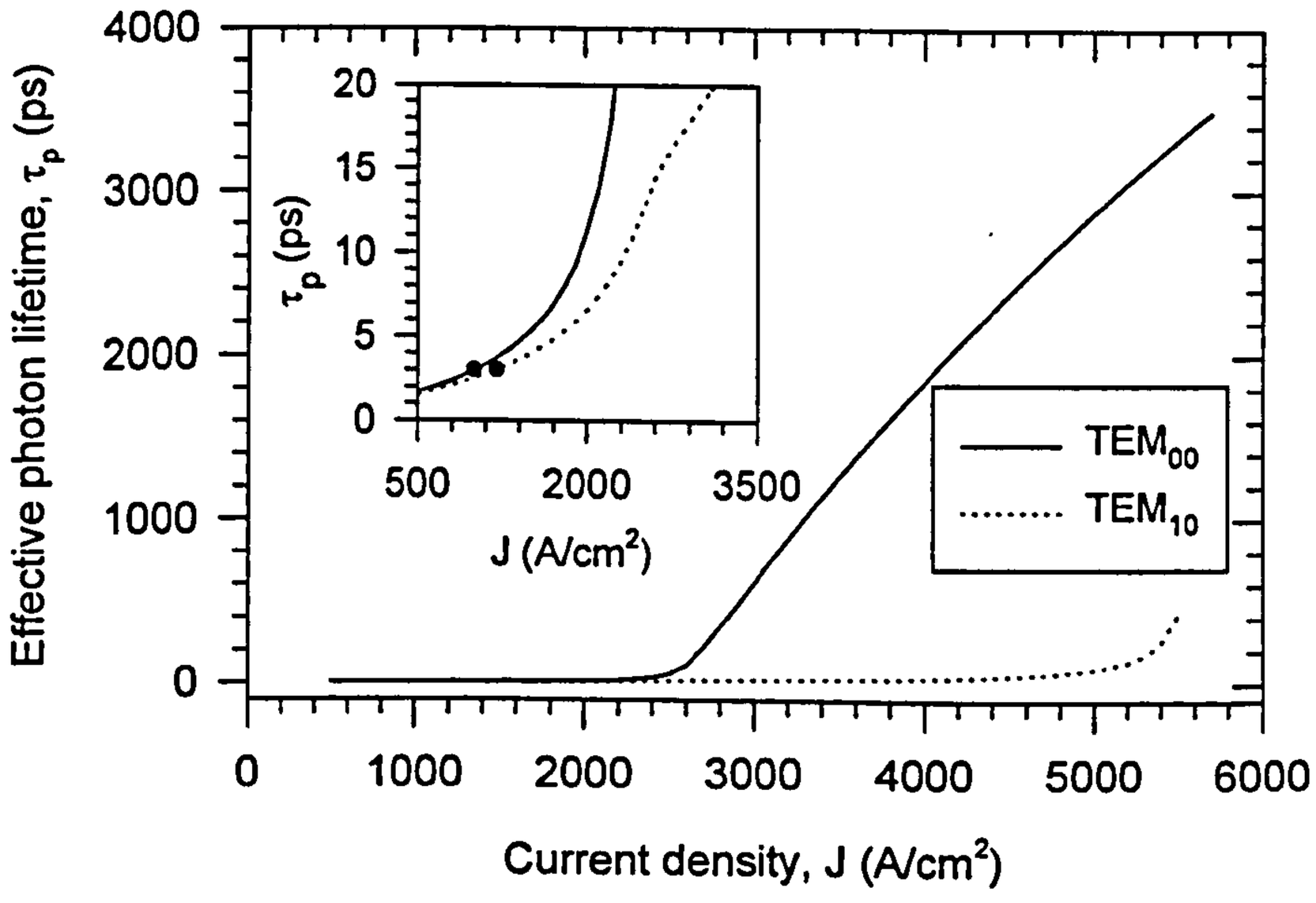

Figure 5.21 : Variation of effective photon lifetime with injected current density for the simulated 2μm radius device, assuming D = 10cm^2/s and w_{mp} = 1.5μm. The black solid dots represent the cold cavity values.

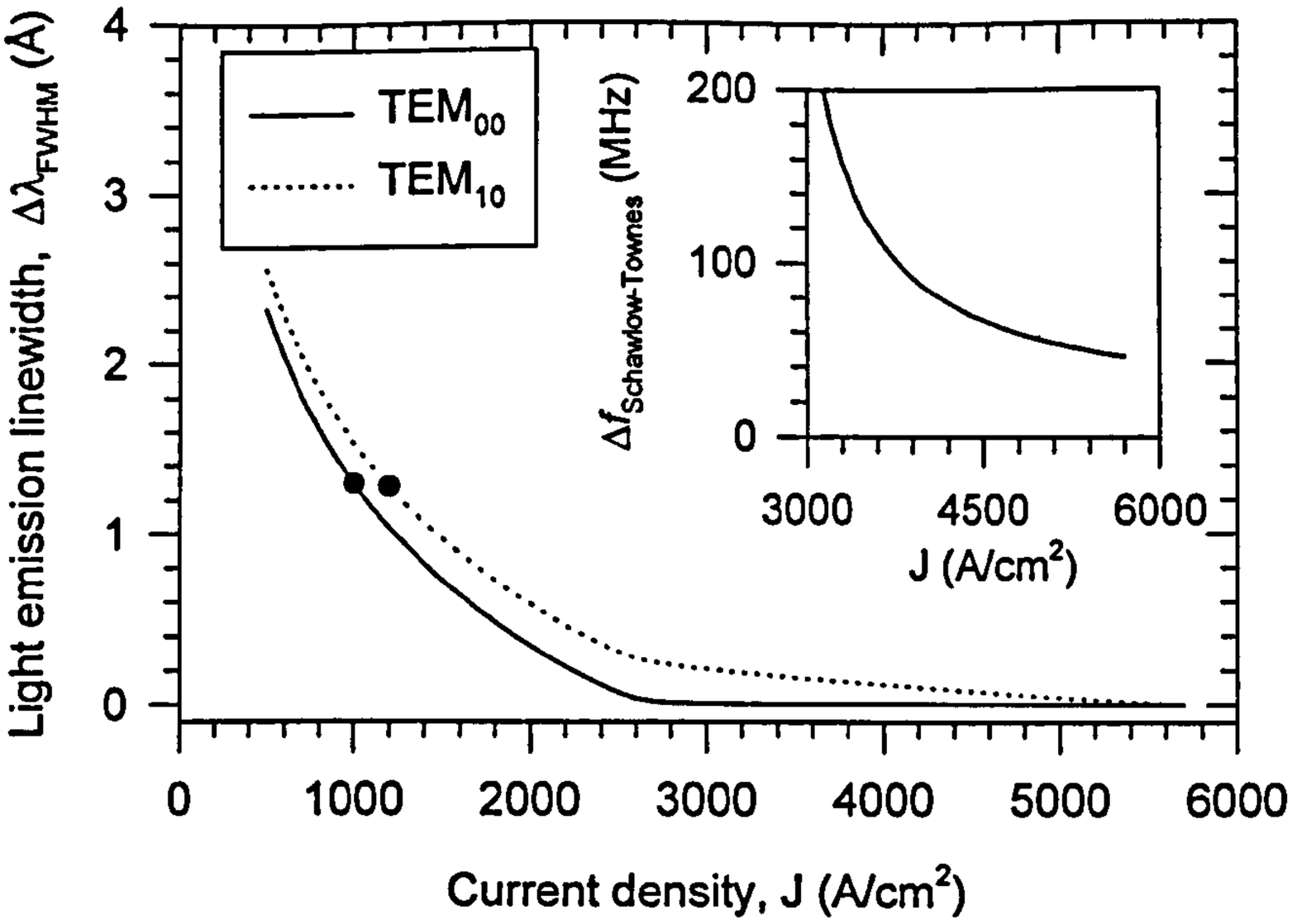

Figure 5.22 : Variation of light emission linewidth with injected current density for the simulated 2μm radius device, assuming D = 10cm²/s and w_{mp} = 1.5μm. The black solid dots represent the cold cavity values.

Beyond the transparency current densities, the effective photon lifetimes increase much more rapidly up to the threshold of the TEM_{00} mode. This is in accordance with discussions in section 5.4.3, that the lasing onset of each eigenmode is accompanied by the rapid increasing of its effective photon lifetime and therefore the rapid narrowing of the light emission linewidth. As reflected in the variation of the effective photon lifetime of the TEM_{00} mode at above threshold, the threshold condition ($G_{mp}=(\tau'_{p(mp)}v)^{-1}$) is only approached asymptotically due to the finite optical gain provided by the QWs. In addition, the Schawlow-Townes linewidth limit reduces with increasing current density and thus power output. Note that the non-linear manner the linewdith limit increases, clearly reflect the logarithmic gain-current relationship. As for the TEM_{10} mode, after the lasing of the TEM_{00} mode, its effective photon lifetime increases slower than before, and in this case does eventually reach its own threshold at higher current density. This is also reflected in the change of the reduction rate of its spontaneous emission linewidth.

Unfortunately, since there is no distinctive feature in the variation of the photon lifetime or linewidth that is associated with the position of the cold cavity value, it is very difficult experimentally to identify these values with great confidence.

Hence, as will be discussed in chapter 6, no comparison of the eigenmode cold cavity photon lifetime among the strong, medium and weak guiding devices is made from the effective photon lifetime variations that are deduced from the measured FWHM spontaneous emission linewidths. Instead, comparisons are made at current densities of 1.0 kA/cm^2 in the case of the TEM_{00} mode and at 1.0 x $J_{th(00)}$ for the TEM_{10} mode, in order to obtain some insights on the modal gains as well as the effects of excess optical losses on various devices of different sizes and different guiding designs.

(B) Effects of Mode Size

In order to clarify the effects of the mode size on the threshold and modal properties of VCSELs, the lasing characteristics for eigenmodes with 1/e half mode sizes of 1.0μm and 2.0μm were also calculated assuming D = 10cm^2/s. As can be deduced from Fig. 4.5, for aperture radius of 2.0μm, the values of 1/e mode size of 1.0, 1.5 and 2.0μm under consideration here are very close to those of strong, medium and weak guiding devices respectively. Interestingly, the threshold current densities of the TEM_{00} and TEM_{10} modes with 1.0μm mode sizes are lower at *2.35 kA/cm^2* and *2.70 kA/cm^2* respectively as compared to those with 1.5μm mode sizes calculated earlier (i.e. 2.60 kA/cm^2 and 5.25 kA/cm^2). However, the thresholds for the eigenmodes with 2.0μm mode sizes are the highest among the three cases at *3.05kA/cm^2* and > 100 kA/cm^2 respectively. At an injected current density of 1.0 kA/cm^2, the effective photon lifetime for the TEM_{00} and TEM_{10} modes are for *3.29ps and 3.07ps* for mode sizes of 1.0μm, *2.98ps and 2.51ps* for mode sizes of 1.5μm, and *2.58ps and 1.95ps* for modes of 2.0μm respectively. Since identical cold cavity photon lifetimes are assumed, these results thus indicate the eigenmodes with smaller mode sizes experiences larger modal gains or lower modal absorptions than those with bigger mode sizes. Between the TEM_{00} and TEM_{10} modes, the former also has larger modal gain (or lower modal absorption) in the cases considered here. After the lasing of the fundamental mode, another indication of how fast the higher order mode can achieve threshold, can be obtained through its effective photon lifetimes evaluated at $J_{th(00)}$. For mode sizes of 1.0μm, 1.5μm and 2.0μm, they are *28.1ps*, *14.4ps* and *7.1ps* respectively. Obviously, the order of these values are in accordance with the order of current density at which the TEM_{10} achieve lasing for different mode sizes.

It is now obvious that as the field of an eigenmode penetrates radially further into the region of the active layer which is below transparency, it will experience lower modal gain for a given injected current and thus a larger threshold current density is needed for lasing. Since the field of a higher order mode always extends further away from the radial centre, the resultant increase in its threshold current is thus also higher as indicated by the results discussed above. As will be shown in chapter 6, these findings are helpful when comparing the threshold and modal behaviours of a VCSEL under cw and pulsed condition, especially in the case of weak guiding device. This is because as noted in chapter 4, under cw operation the thermal lensing effect caused by the temperature gradient within the device, which is not considered in the simulation discussed above, results in the contraction of mode size with increasing current injection. If the associated increase in diffraction loss is less significant, the increase in modal gain will thus lead to threshold reduction. This is expected to be more significant for the higher order mode. The same argument also applies when comparing the threshold and modal performance of devices with identical aperture size but different oxide aperture thickness. Both modal gain and excess optical losses which are dependent on the mode sizes, are equally important in deciding the relative merits or demerits of these devices.

(C) Effects of Spontaneous Emission Factor

The reported experimental values of spontaneous emission factor, β_{sp}, for VCSELs is generally in the order of 10^{-4} to 10^{-3}, with a value of 0.002 having been measured recently for a 2μm square oxide apertured device [17]. In order to evaluate its effect on the eigenmode thresholds, the simulations were repeated for the device with mode sizes of 1.5μm using β_{sp} value of 0.01 or 0.0001 as well as assuming D = 10 cm^2/s. Within the range considered here, it is found that the thresholds of the eigenmodes are relatively insensitive to the value of β_{sp}. The threshold current densities of TEM_{00} and TEM_{10} modes are *2.45 kA/cm²* and *5.10 kA/cm²* respectively for β_{sp} = 0.01, and *2.60 kA/cm²* and *5.30 kA/cm²* respectively for β_{sp} = 0.0001, as compared to the values of *2.55 kA/cm²* and *5.25 kA/cm²* calculated earlier for β_{sp} = 0.01. Therefore, any possible error in the calculated threshold current densities due to the uncertainties in the value of β_{sp} should be negligible.

5.4.5 Simulation Results II : Strong, Medium and Weak Guiding Oxide-Confined VCSELs

Using the simulated values of cold cavity photon lifetime, mode sizes, resonant wavelengths, and modal transmittance obtained in the preceding sections for strong, medium and weak guiding devices, the threshold current densities were calculated by solving the rate equations. Besides the exclusion of thermal effects, the so-called optical scattering loss from the oxide aperture as well as carrier leakage are not taken into consideration in the model. In addition, the devices are also assumed to operate at the gain peak wavelength. Thus, the calculated values presented below are the predicted *minimum* threshold values.

Figure 5.23 shows the variation of the threshold current densities of TEM_{00} and TEM_{10} modes with aperture radius, for the strong, medium and weak guiding device. As expected, the thresholds of both eigenmodes increase with reduction in aperture size, mainly due to the decrease in cold cavity photon lifetime caused by the size dependent optical diffraction loss discussed earlier. Comparing the threshold values for the TEM_{00} mode among the three types of devices, it is the strong guiding devices that always have the lowest threshold current densities when the aperture radius is bigger than about 1.5μm, followed by the medium and weak guiding devices. Referring to Fig. 5.16, this is partly due to the values of TEM_{00} cold cavity photon lifetime that are in the opposite order, as well as the mode size effects that were discussed earlier in section 5.4.4(B) due to the smaller mode size of strong guiding devices (see Fig. 4.7). However, when aperture radius becomes smaller than 1.5μm, the thresholds of the strong guiding devices increases much more rapidly than other devices as a result of the much steeper drop in the cold cavity photon lifetime (see Fig. 5.16) or modal reflectance (see Fig. 5.8). Consequently, in this region it is now the weak guiding devices that produce the lowest threshold current densities, followed by the medium and strong guiding devices. For the TEM_{10} mode, the weak guiding devices always give the highest threshold current densities even at large aperture sizes. As discussed earlier in section 5.4.4(B), this is mainly due to the effect of the larger mode size for a given aperture size. Between the strong and medium guiding devices, the former have slightly lower threshold current density until the aperture size is smaller than about 2.5μm, i.e. when the cold cavity lifetime begins to drop at much faster rate (see Fig. 5.16(a)).

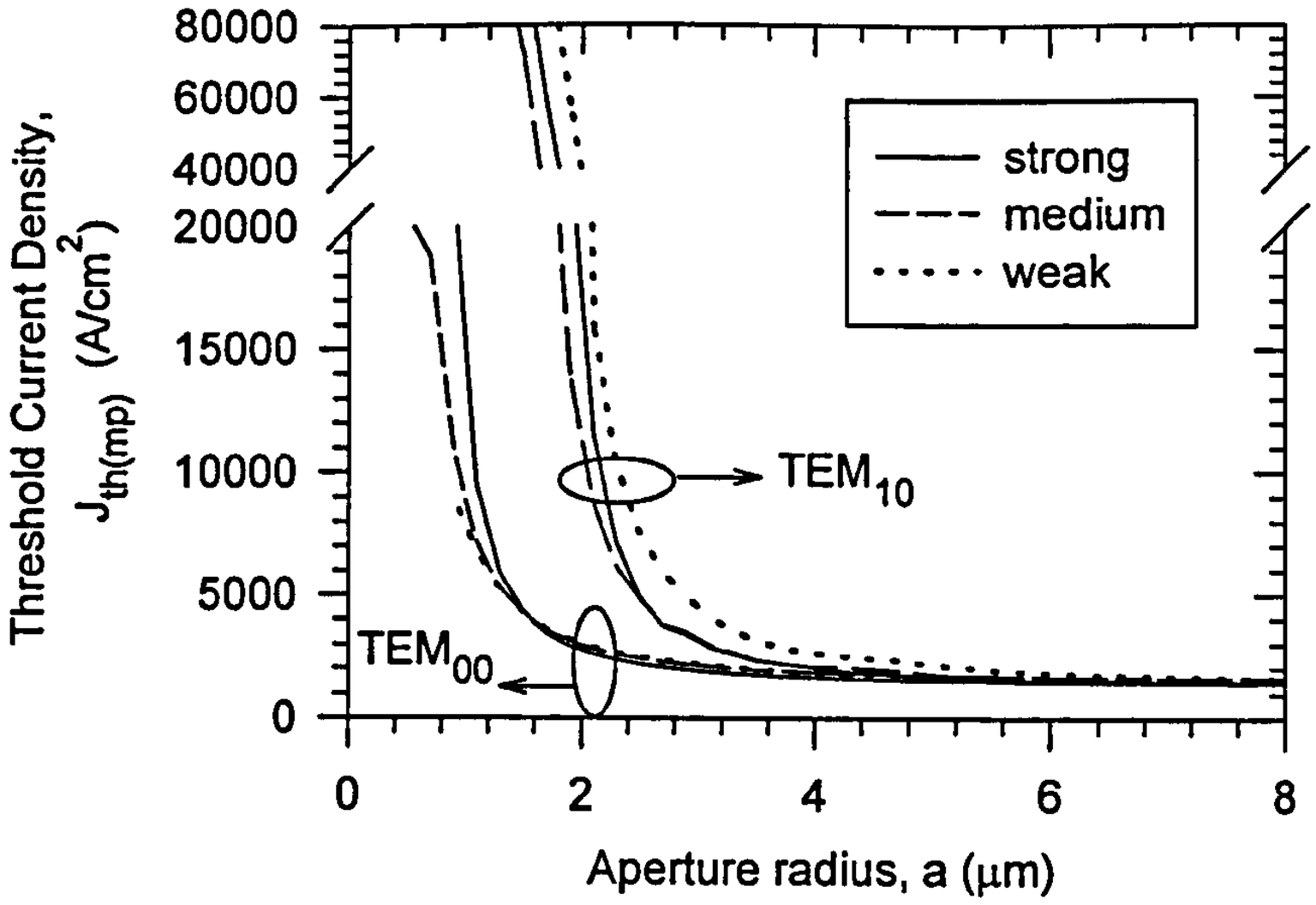

Figure 5.23 : Variation of the threshold current densities of TEM_{00} and TEM_{10} modes with aperture radius, for the strong, medium and weak guiding device.

Besides the threshold current densities, it is also interesting to compare the maximum power output obtainable from the strong, medium and weak guiding devices before the lasing of the higher order TEM_{10} mode. The aperture size dependence of this maximum "single mode" power output, defined here as the power carried by the fundamental TEM_{00} mode at 95% of the threshold current density of the TEM_{10} mode, is shown in Figure 5.24. These results are obtained assuming the three type of devices having identical absorption coefficients in their DBRs. Clearly, due to the higher output coupling efficiencies as well as the higher turn on currents of the TEM_{10} mode, the weak guiding devices always offer higher maximum single mode power output for aperture sizes bigger than 4.0μm. Between the strong and medium guiding devices, larger maximum single mode power output can be obtained from the former when the aperture radius becomes smaller than 2.5 μm. As can be seen from Fig. 5.23, this is mainly because the threshold current density of the TEM_{10} mode of the strong guiding device becomes larger than that of the medium guiding device for aperture radius smaller than this value.

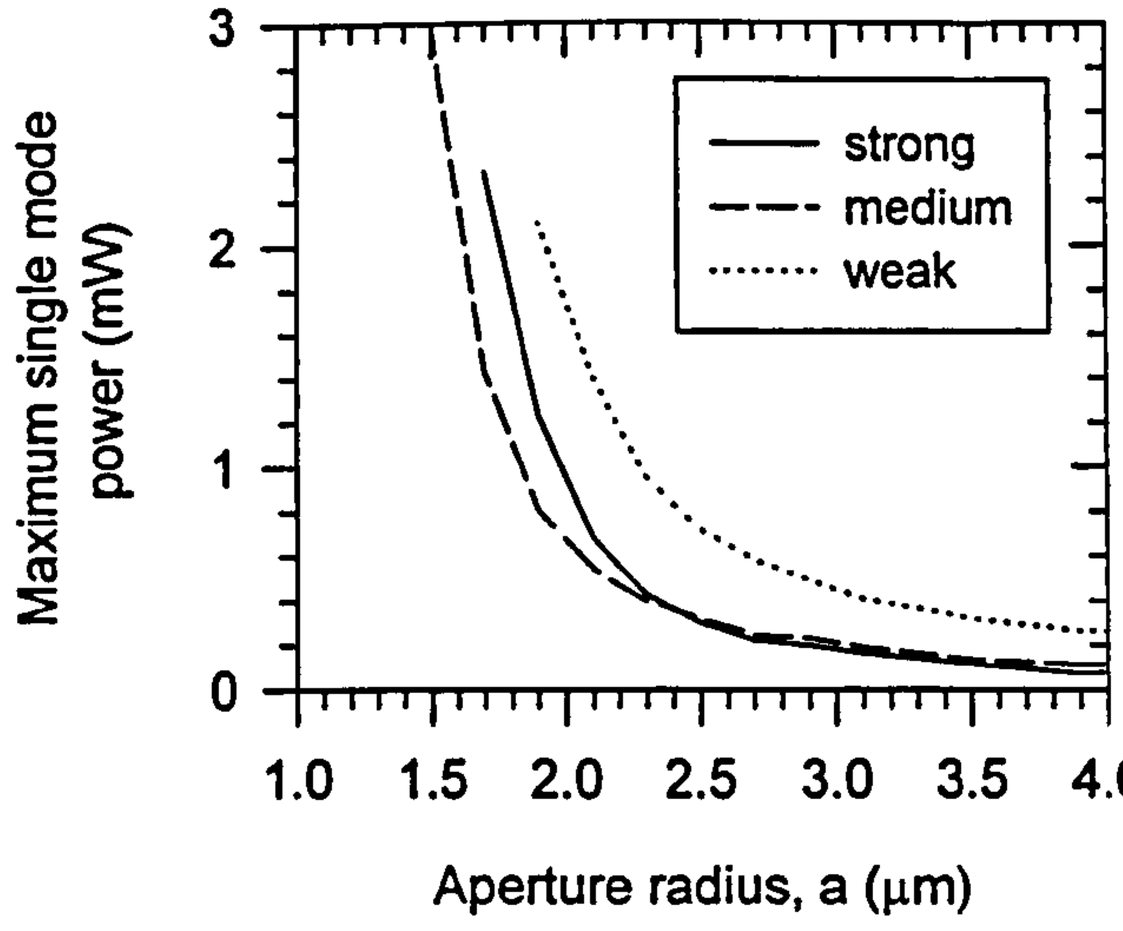

Figure 5.24 : Variation of maximum single mode power output as a function of aperture size for the strong, medium and weak guiding devices.

The corresponding Schawlow-Townes linewidth limits ($\Delta f_{\text{Schawlow-Townes}}$) evaluated at the current densities where the maximum single mode powers are assessed, are also shown in Figure 5.25. As a result of the higher turn on current densities of the TEM_{10} mode, as well as the larger cold cavity lifetime or lower total optical loss, these linewidth limits are the lowest for the weak guiding devices. For aperture size smaller than about 3.0μm radius, it is also found that the weak guiding devices always have the narrowest linewidth limits for a given injected current density, followed by the medium and strong guiding devices. Assuming the same linewidth enhancement factor for these three types of devices, the results above thus implies that weak guiding single mode devices may be more suited for any communication systems utilising coherent transmission/detection scheme such as the Wavelength Division Multiplexing (WDM) system, where narrow spectral lasing linewidth is an important requirement.

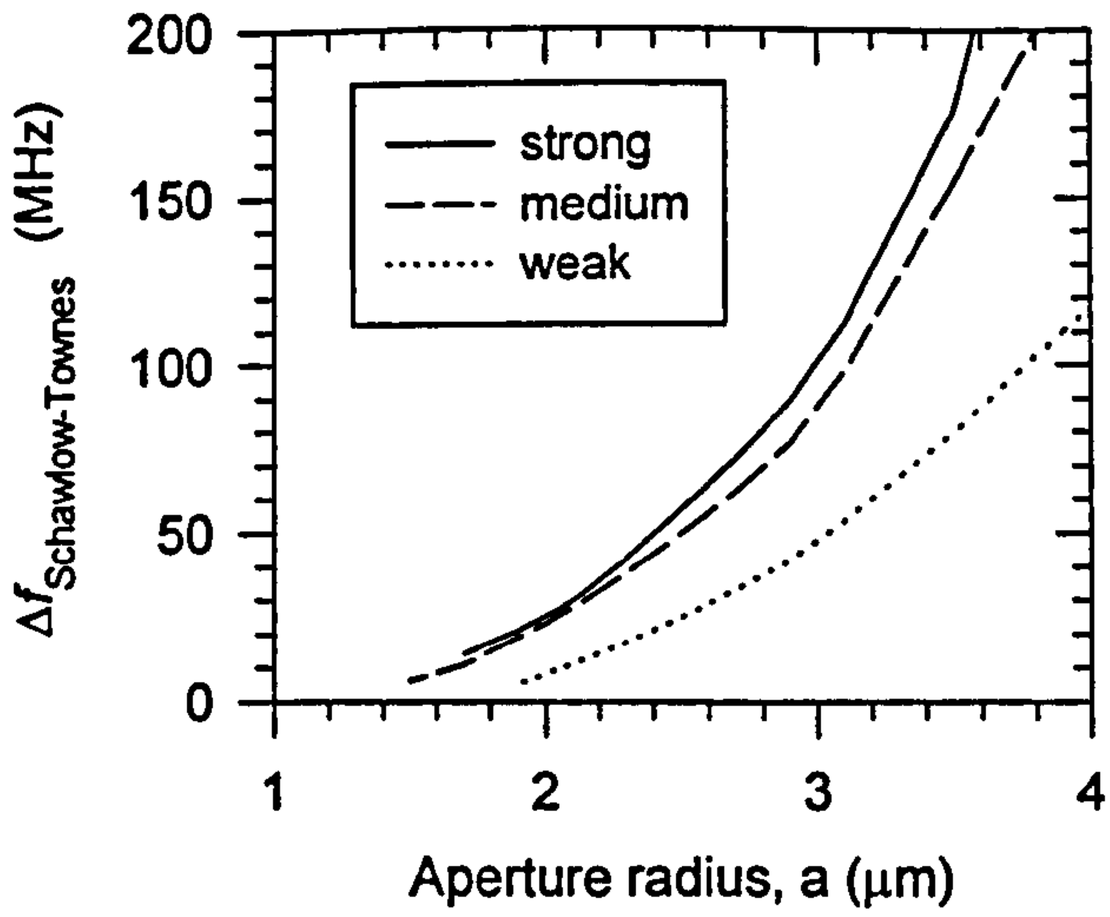

Figure 5.25 : Aperture size dependence of the Schawlow-Townes linewidth limit evaluated at the 95% of the TEM_{10} threshold current density.

5.5 Summary

This chapter begins by describing the numerical methods used for calculating the modal reflectance and transmittance of the Hermite-Gaussian eigenmodes by the DBRs. Firstly, this method involves decomposing the eigenmode concerned into an infinite number of Fourier components in k-space, by taking its two-dimensional spatial Fourier transform. Then for these Fourier components, which propagate through the Bragg stacks as longitudinal section electric (LSE) waves, their individual reflection and transmission coefficients are computed using the standard transfer matrix method, taking account of the differences in their wave admittances and propagation constants from that of a plane wave. Subsequently, the inverse Fourier transform is performed to obtain the total reflected field, and the modal overlap integral is carried out in order to calculate the modal reflection coefficients and modal reflectance. Using this numerical technique, it is found that :-

- The modal reflectance of various eigenmodes decreases with reduction in mode size as a result of diffraction loss.
- For a given mode size, the fundamental mode has higher modal reflectance than the higher order modes.

- DBRs with higher refractive index contrast ratio experience lower diffraction loss, and also have smaller difference in modal reflectance between the fundamental TEM_{00} mode and the higher order modes.
- As a result of their smaller mode size for a given aperture size, the strong guiding devices have largest diffraction loss. It therefore follows that diffraction loss experienced by medium guiding devices are intermediate whilst that of weak guiding devices are the smallest.
- For the rectangular devices whose eigenmodes have elliptical Hermite-Gaussian transverse field variations, the modal reflectance of the fundamental TEM_{00} mode polarised along the direction of the longer side of the aperture is found to be always higher than that polarised along the shorter side.
- Between the TEM_{01} and TEM_{10} modes, it is always the one with field null along the longer side of the aperture and thus with longer resonant wavelength, that has higher modal reflectance, i.e. TEM_{01} mode for $b/a > 1$ and TEM_{10} mode for $b/a < 1$.
- Within a certain range of aspect ratio, the higher order mode with the highest modal reflectance is found to be always orthogonally polarised with respect to the fundamental TEM_{00} mode.

The relationships between the Q-factor, emission linewidth and photon lifetime are derived. The distinction between the values obtained under cold cavity condition (i.e. when the gain media is transparent), and those under the active cavity environment (i.e. cavity with gain), is also clarified. The cold cavity photon lifetimes of the eigenmode are then calculated, taking account of the field penetration into the DBRs. As a consequence of diffraction loss, it is found that :-

- The cold cavity photon lifetime decreases whilst the linewidth increases with reduction in aperture size
- As in the case of modal reflectance, the values of photon lifetime and linewidth of the fundamental mode are always higher than those of the higher order modes.
- Strong guiding devices suffer from steeper decline in the photon lifetime with reduction in aperture size. This is followed by the medium and weak guiding devices.

The steady state light-current characteristics of oxide-confined VCSELs of various circular aperture radii are also computed by solving numerically the photon and carrier rate equations that incorporate the effects of carrier diffusion. Besides light power output, threshold current densities, effective photon lifetimes, spontaneous emission linewidths as well as above threshold Schalow-Townes linewidth limit, can also be calculated. It is found that :-

- Spatial hole burning effect promotes the lasing of higher order mode.
- Assuming identical cold cavity photon lifetimes, devices with smaller mode sizes have lower threshold current densities than those with bigger mode sizes. The former also experiences higher modal gain or lower modal absorption for a given current density.
- Considering only the effects of diffraction loss, weak guiding devices have the lowest TEM_{00} mode threshold current densities for aperture radii smaller than 1.5μm. This is followed by the medium guiding and strong guiding devices in ascending order. For bigger aperture sizes, the strong guiding devices have lower thresholds than medium and weak guiding devices.
- The threshold current densities of TEM_{10} mode for the weak guiding devices are always higher than that of the strong and medium guiding devices. The values for strong guiding devices only becomes larger than those of medium guiding device when the aperture size becomes smaller than 2.5μm

References for Chapter 5

[1] A.E.Siegman, "*Lasers*", (University Science Books, 1986), chapters 14, & 17.

[2] R.F.Harrington, "*Time-Harmonic Electromagnetic Fields*", (McGraw-Hill, New York, 1961), Chapters 4 & 7.

[3] P.N.Robson, *private communication.*

[4] R.E.Collin, "*Field Theory of Guided Waves*", (IEEE Press, 1991), chapter 4

[5] D.L.Huffaker and D.G.Deppe, "Low threshold vertical cavity surface emitting lasers based on high contrast distributed Bragg reflectors", Appl. Phys. Lett., 70, pp.1781-1783, 1997.

[6] H.K.Bissessur, F.Koyama and K.Iga, "Modelling of oxide-confined vertical cavity surface emitting lasers", IEEE J. of Selected Topics in Quantum Electronics, vol.3, pp.344-352, April 1997.

[7] E.R.Hegblom, D.I.Babic, B.J.Thibeault, and L.A.Coldren, "Estimation of scattering losses in dielectrically apertrued vertical cavity lasers", Appl. Phys. Lett., vol. 68, pp.1757-1759, March 1996.

[8] A.Yariv, "*Optical Electronics*", (Sauder College Publishing, 1991), chapter 4.
[9] A.L.Schawlow an C.H.Townes, Phys. Rev., vol.112, pp.1940, 1958.
[10] S.L.Chuang, "*Physics of Optoelectronic Devices*", (John Wiley & Sons, 1995), chapter 11.
[11] G.P.Agrawal and N.K.Dutta, "Semiconductor Lasers", (Van Nostrand Reinhold, New York, 1993), chapter 6.
[12] G.D.Smith, "*Numerical Solution of Partial Differential Equations*", (Oxford University Press, 1975).
[13] A.Valle, J.Sarma, and K.A.Shore, "Spatial hole-burning effects on the dynamics of vertical cavity surface emitting laser diodes", IEEE J. of Quantum Electronics, vol.31, pp. 1423 - 1431, Aug 1995.
[14] J.H.Shin, H.E.Shin and Y.H.Lee, "Effect of carrier diffusion in oxidised vertical cavity surface emitting lasers determined from lateral spontaneous emission", Appl. Phys. Lett., vol. 70, pp.2652-2654, May 1997.
[15] G.R.Hadley, K.L.Lear, M.E.Warren, K.D.Choquette, J.W.Scott and S.W.Corzine, "Comprehensive numerical modelling of vertical cavity surface emitting lasers", IEEE J. of Quantum Electronics, vol.32, pp.607-616, April 1996.
[16] R.P.Sarzala and W.Nakwaski, " Carrier diffusion inside active regions of gain-guided vertical cavity surface emitting lasers", IEE Proc. of Optoelectronics, vol.44, pp.421-425, Dec 1997.
[17] J.H.Shin, Y.G.Ju, H.E.Shin and Y.H.Lee, "Spontaneous emission factor of oxidised vertical cavity surface emitting lasers from the measured below threshold cavity loss", Appl. Phys. Lett., vol.70, pp.2344-2347, 1997.
[18] S.M.Sze, "*Physics of Semiconductor Devices*", (John Wiley & Sons, 1981)
[19] K.Y.Chang, J.Woodhead and P.N.Robson, "Modal and threshold analysis of dielectric-apertured vertical cavity surface emitting lasers", Appl. Phys. Lett., vol.72, pp.335-337, 1998.

Chapter 6 Experimental Results and Comparisons

6.1 Introduction

This chapter details the experimental results obtained from the strong, medium and weak guiding devices. Comparisons between the theoretical predictions and experimental results are also made whenever it is possible. It begins by discussing the lasing characteristics of the oxidised VCSELs with near-square shape oxide apertures. Detailed comparisons of the threshold and modal properties are made between the devices with different oxide thickness. The results on the polarisation and thermal characteristics of these devices are also presented. Effective photon lifetimes are also inferred from the spectral linewidths, and offer some insights into the modal gains and excess optical losses of these devices. Then, results obtained from devices with rectangular oxide apertures are presented. These include the modal and polarisation characteristics that are different from their near-square shaped counterparts.

6.2 Lasing Characteristics of Near-Square Shaped Oxide Apertured VCSELs

In this section, the threshold and modal properties of oxide apertured VCSELs are discussed based on the experimental results obtained from devices with near-square shaped apertures (i.e.$0.93 \leq (b/a) \leq 1.07$). Devices with variable oxide aperture sizes were fabricated from the VCSEL layers of strong, medium and weak guiding designs, using the device fabrication procedures described in ***Appendix F***. In order to minimise the effect of the relative spectral offset between the gain peak and resonant wavelength, the plane resonant wavelengths of these devices are estimated to be between 865-866 nm. (see section 4.3.2).

6.2.1 Dependence of Threshold Currents, Efficiencies and Power Output on Aperture Size and Oxide Thickness

As discussed earlier in chapters 4 and 5, the diffraction loss in an oxidised VCSELs is sensitive to eigenmode size which in turn is determined by the longitudinal position and the thickness of the oxide (i.e. waveguiding strength), as well as the aperture size. This size dependent optical loss result also affects the threshold gain and thus the threshold current density. To confirm these predictions experimentally, the threshold properties of the strong, medium and weak guiding devices were assessed at room temperature. For this and other useful characterisation purposes to be discussed later, the light-current-voltage (L-I-V) characteristics of these devices were measured when operated cw and under pulsed condition (40ns pulse length at 50kHz repetition rate) to remove the heating effects. Figure 6.1 shows L-I-V curves that are typical of all devices under investigation. This particular device of strong guiding design, has an average square aperture size of 4.3μm (actual dimension is 4.4 x 4.2μm) and its cw and pulsed threshold current are 830μA and 820μA respectively.

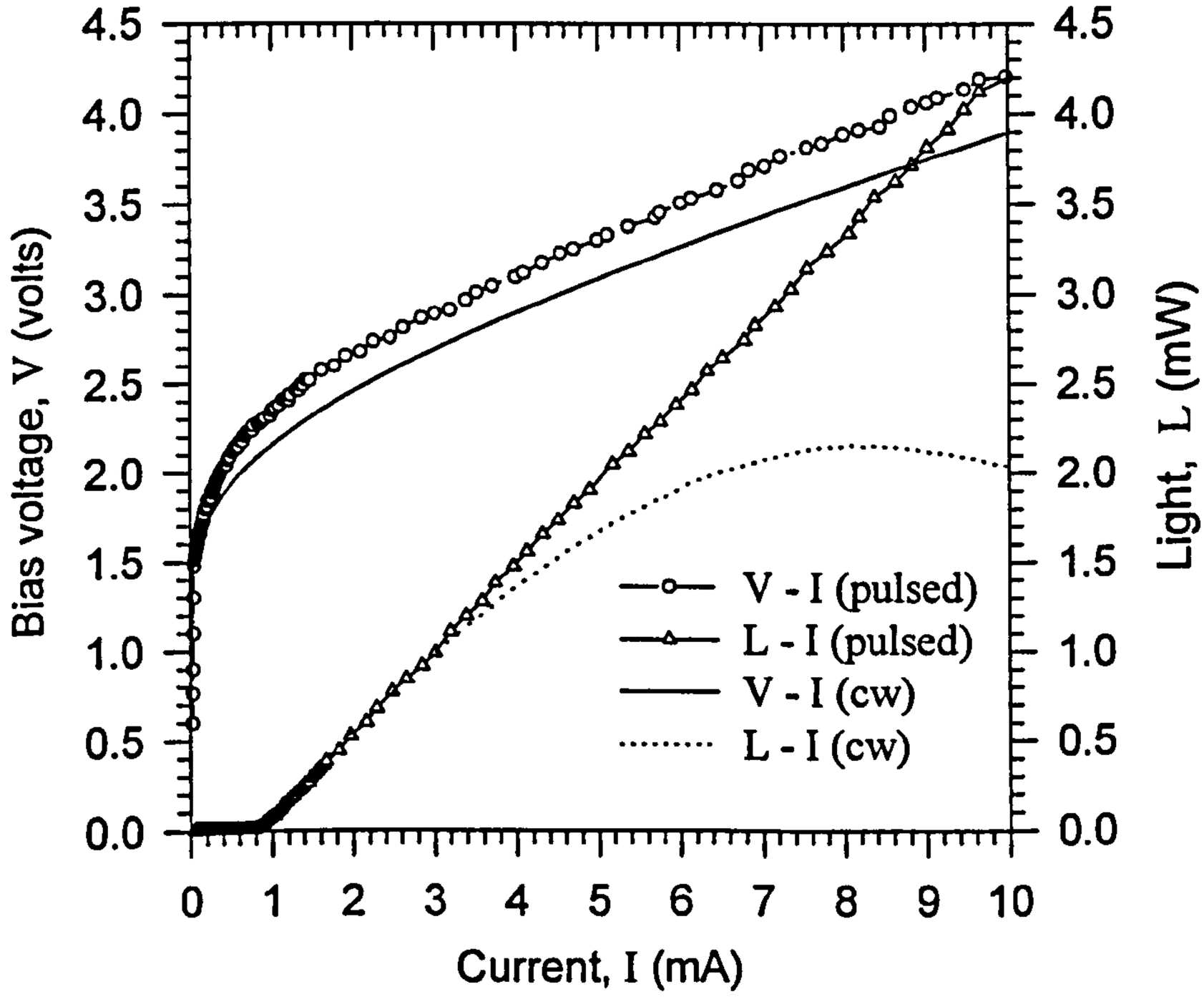

Figure 6.1 : Typical cw and pulsed L-I-V characteristics. This particular device of strong guiding design has an average aperture size of 4.3μm.

Evidently, while the pulsed L-I curve remains quite linear throughout the whole driving range, the cw L-I curve becomes increasingly non-linear after the thermal effects become significant at current injection larger than 3mA. This reduction in external quantum efficiency under cw operation is due to the thermal enhanced carrier leakage as well as the increasing spectral offset between the resonant wavelength and the QW gain peak. The device internal heating is mainly due to the electrical series resistance presented by the heterojunctions of non-optimised DBRs. Eventually, the thermal roll-over occurs at 8.1mA limiting the maximum optical power to 2.2 mW. The ohmic heating also results in lower biasing voltage, for a particular current injection level under cw operation, as a result of increased thermionic conduction through the hetero-barriers of the DBRs.

Figures 6.2(a), (b) and (c) illustrate the variation of the cw and pulsed threshold current with average oxide aperture size , S (where $S = 2\sqrt{ab}$), for devices of strong, medium and weak guiding designs respectively. For devices with aperture sizes smaller than 6μm, the threshold current measured is associated with the onset of the fundamental TEM_{00} mode. For devices with bigger aperture sizes, the TEM_{00}, TEM_{01} and/or TEM_{10} modes, and possibly other higher order modes, lase almost simultaneously. Comparing the cw and pulsed thresholds, there are negligible differences in all cases except for devices smaller than 3μm. In the strong guiding case, the cw threshold current for the 2.4μm device is higher than the corresponding value measured under pulsed conditions. On the other hand, the cw thresholds of the 2.4μm and 1.0μm devices of weak guiding design are in fact lower than the corresponding pulsed values. This behaviour is believed to be caused by thermally induced mode size shrinkage when the devices are driven under cw condition (see section 4.3.2). In the weak guiding case, it is most likely that the contraction in mode size results in a negligible increase in diffraction loss since the size dependent diffraction loss is quite insensitive to changes in the relatively large mode size of weak guiding devices (refer to Fig. 5.6 for modal reflectivity as a function of mode size). Instead, it markedly improves the overlap of the carrier - optical field distributions by pulling the optical field towards the device centre where carrier concentration is higher. This increases the net modal gain and thus reduces the threshold current. In the case of the strong guiding device which has a much smaller mode size, the increase in diffraction loss as a result of mode size contraction

probably outweighs any extra gain from the enhanced carrier-field overlap, and thus leads to an increased cw threshold.

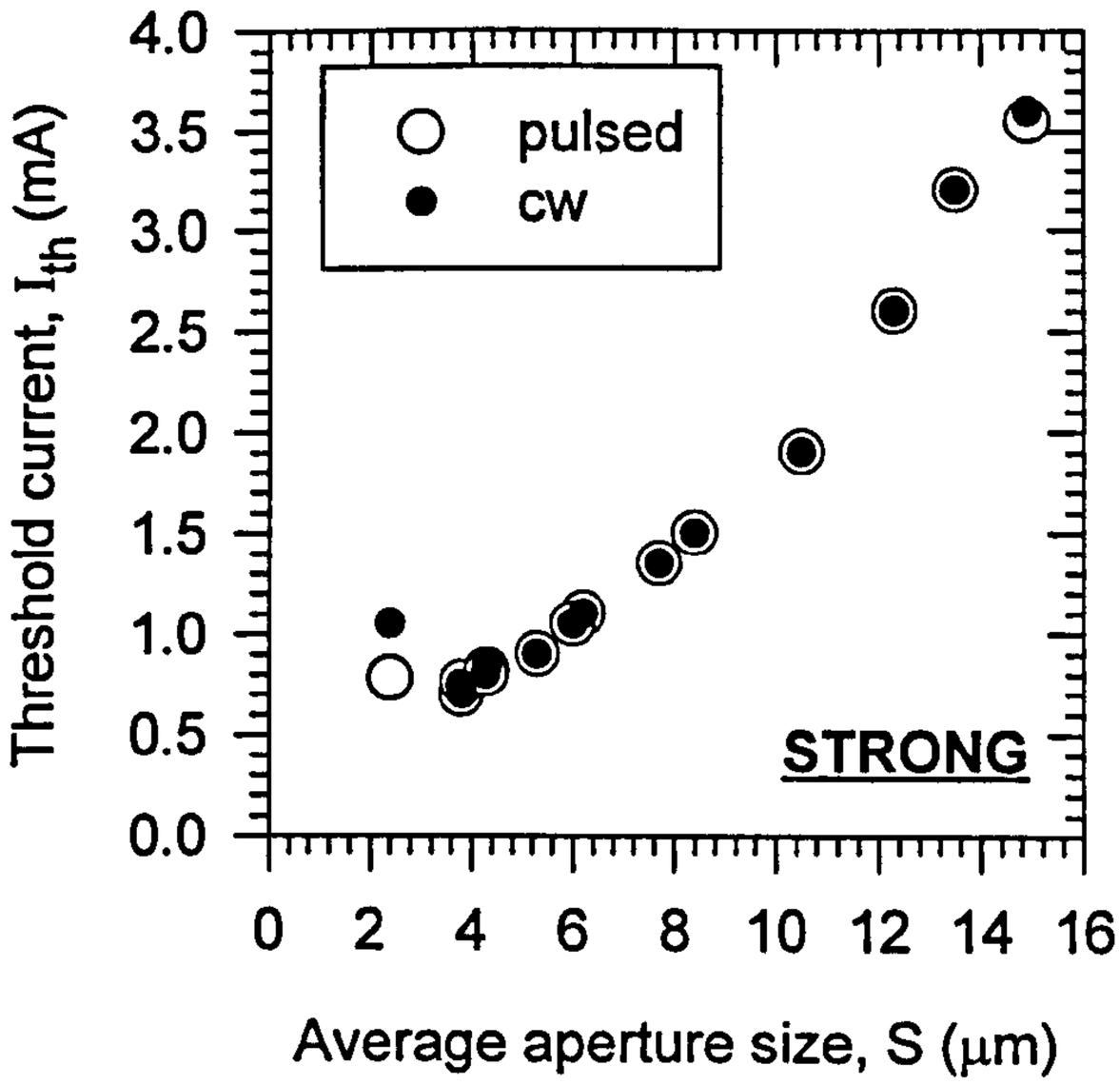

Figure 6.2(a) : Variation of threshold current with aperture size for devices of "strong guiding" design.

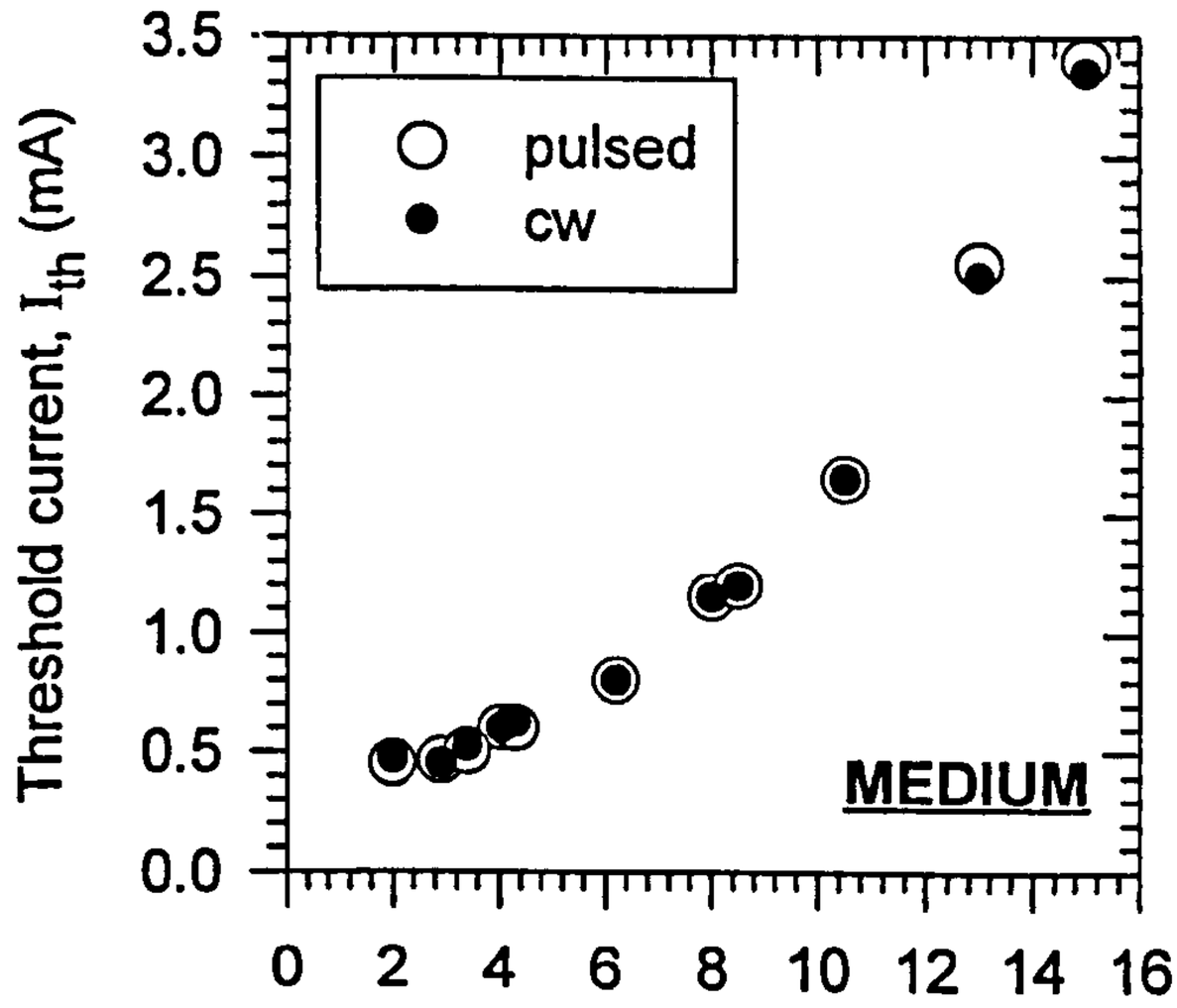

Figure 6.2(b) : Variation of threshold current with aperture size for devices of "medium guiding" design.

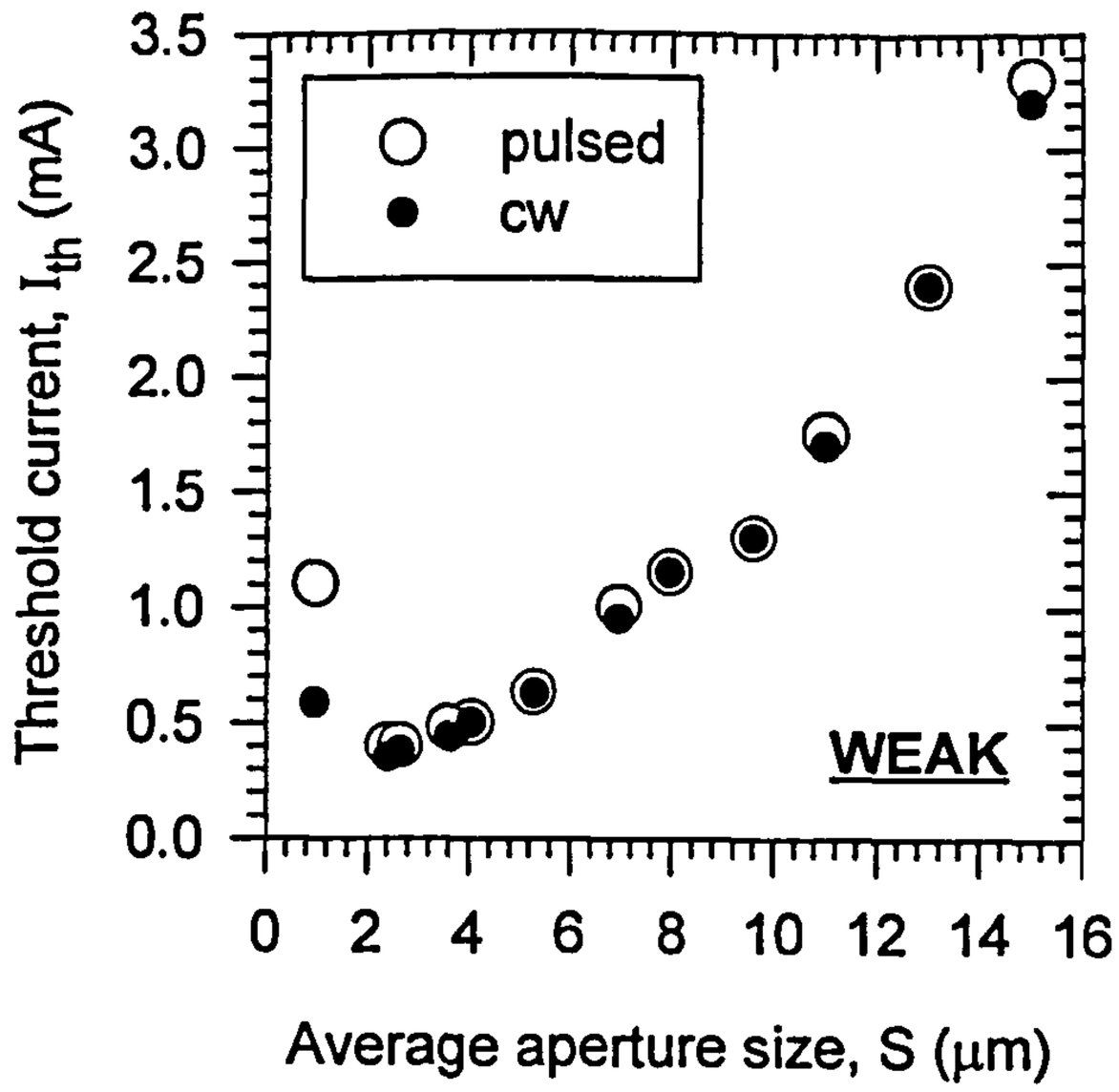

Figure 6.2(c) : Variation of threshold current with aperture size for devices of "weak guiding" design.

It is obvious from Fig. 6.2(a) to (c) that the decrease in threshold current does not scale with the reduction in current injection area determined by aperture size, and this eventually leads to an optimum aperture size where lowest threshold current is achieved. The lowest threshold currents achieved under pulsed and cw conditions are 400μA and 350μA respectively by the weak guiding device of 2.4μm aperture size. The very small 1μm device has much larger pulsed threshold current of 1.1mA but is reduced to 580μA when operated cw. For the strong guiding devices, the lowest pulsed threshold current achieved is 700μA (750μA cw) at aperture size of 3.8μm while devices smaller than 2.4μm do not lase under both pulsed and cw conditions. Meanwhile, in the medium guiding case the lowest pulsed threshold current of 450μA (470μA cw) is obtained from the 2.0μm device and devices with smaller size do not achieve lasing. The values for the 2.0μm device of medium guiding design are almost similar under both conditions, suggesting that in this case the increase in diffraction loss on heating is almost compensated by a corresponding increase in modal gain, as a result of an improvement in carrier-field overlap. For comparison purposes, the dependence of the pulsed threshold current density on the oxide aperture size for the strong, medium and weak guiding devices, are plotted on the main illustration of Figure 6.3, together with the theoretical values that take into account the different

absorption levels in the DBR of these VCSELs deduced in section 3.4.2. Since the calculated values are actually for circular devices while the experimental results are obtained from near-square devices, the theoretical values are plotted as a function of equivalent aperture size where $S = a\sqrt{\pi}$ and a is the aperture radius. As mentioned in section 5.4, the theoretical values are the predicted *minimum* threshold values, and since thermal effects are excluded in the model, they should be compared with the experimental results obtained under pulsed conditions. Nevertheless, the corresponding cw experimental values are also shown in the inset of Fig. 6.3.

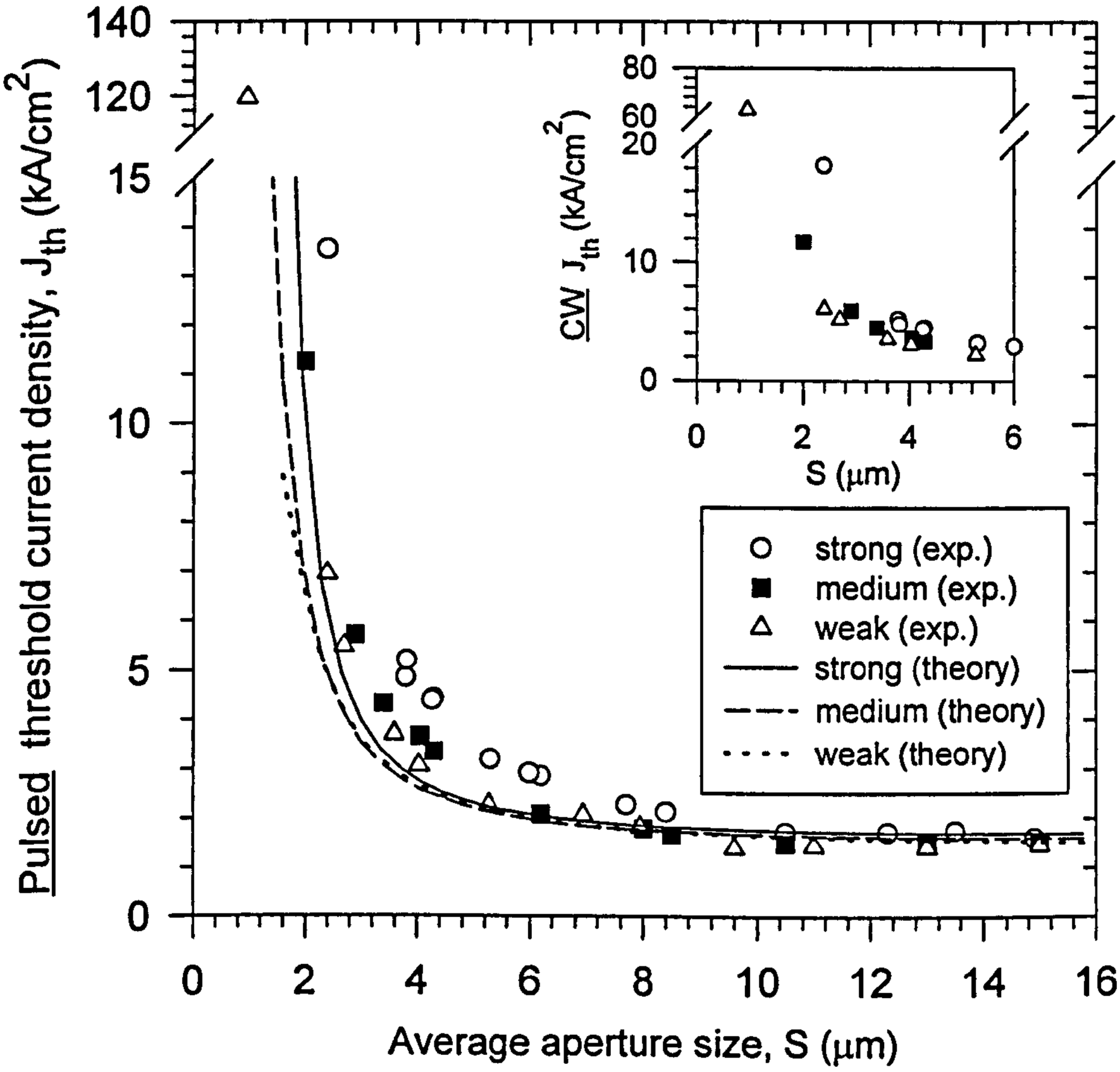

Figure 6.3 : Variation of threshold current density, J_{th} (pulsed : main illustration, cw: inset) with average square aperture size, S. The theoretical curves are also included for comparison

In all cases, the values of theoretical curves fall below the experimental values. However, the theoretical predictions do agree with the experimental results in predicting that the threshold current densities of the strong guiding devices are always the highest for a given aperture size. Between the medium and weak guiding devices,

the former has the higher measured threshold current densities when the aperture size becomes smaller than about 4μm. For bigger aperture size, their threshold values are almost identical. This is also predicted by the simulations, but is expected to be maintained until the aperture size becomes smaller than about 2μm. Based on the results discussed above, it is thus fair to conclude that the oxidised VCSEL design with thinner oxide aperture is best suited for achieving ultra low threshold current. This is due to the smaller size dependent excess optical loss experienced in the DBRs, which results in lower rate of increase in threshold current density with reduction in aperture. This conclusion and the experimental observations presented here are indeed in good qualitative agreement with those obtained by other researchers [1,2].

In addition to the threshold current, the differential quantum efficiency (η_{ext}) which can determined easily from the L-I curve is also a sensitive function of the optical losses existing in each device through the dependence on the output (top) coupling efficiency, η_{top}, as discussed earlier in section 5.2.2. Figure 6.4 illustrates how the differential quantum efficiency measured under the pulsed conditions varies with aperture size. The relevant theoretical results obtained through eqn.(5.14) using a value of $\eta_{int} = 0.821$ deduced in section 3.4.1, are also included for comparison. These theoretical curves predict the *maximum* attainable efficiency, and take account of the different absorption levels in the DBRs of the strong, medium and weak guiding devices. For the weak guiding devices which experience negligible diffraction loss, the theoretical predictions fit the experimental results quite well. However, the experimental values for the strong and medium guiding device are always below the predicted values. Nevertheless, both the theoretical and experimental results show that the rate of decrease in the efficiency with reduction in aperture size from that of the plane wave value estimated from the ≈15μm device, is the fastest in the strong guiding devices. For instance, while the efficiencies of weak guiding devices decrease gradually by just about 4.9% even down to an aperture size of 2.4μm, the reduction suffered by the strong guiding device of identical size is about 24.2%. As for the medium guiding devices whose reduction rate is in between those of the other two designs, the efficiency drops by about 13.2% at aperture size of 2.0μm. Comparatively, the corresponding theoretical values for these devices are 3.5% (weak, 2.4μm), 13.7% (strong, 2.4μm) and 12.1% (medium, 2.0μm) respectively. Therefore, this is consistent with the predictions that strong guiding devices suffer from higher

size dependent excess optical losses than the medium and weak guiding devices. Although the devices measured here have slightly different absorption levels in their DBRs, the above statement is still valid, as it has already been vindicated by the simulation results in section 5.2.2 which assume similar DBR absorption levels as for these devices.

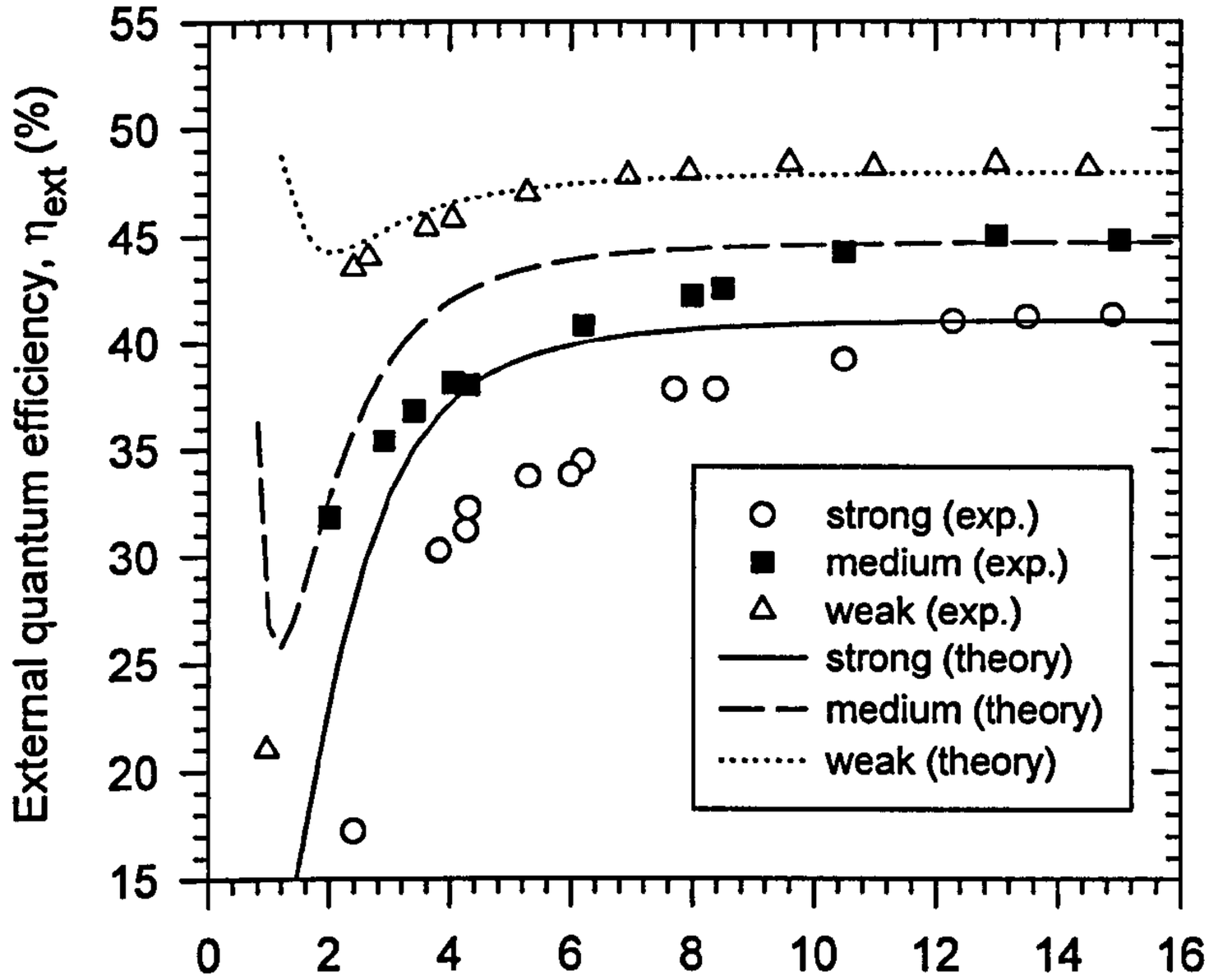

Figure 6.4 : Variation of pulsed external quantum efficiency with aperture size for the strong, medium and weak guiding devices.

It is also interesting to note that the efficiency of 1μm weak guiding device drops dramatically to 21% which does not follow the trend set by the bigger devices. This behaviour is most likely due to its large mode size/oxide aperture size ratio as a result of loss of optical confinement. The small carrier-field overlap results in the under-utilisation of the injected carriers, and thus leads to the poor efficiency performance. However, while the cw external quantum efficiencies measured at close to the threshold (results not shown here) of most devices are quite similar to those measured under pulsed condition, those of the 1μm weak guiding device is about *twice* as high (i.e. from 21% to 43.6%) when operated cw. Such a marked improvement reflects the threshold current results obtained from the same device when operated cw, and is believed to be due to same reason, namely the improvement in carrier-field overlap which leads to increased modal gain. This leads to an increase

in the internal quantum efficiency both at and above threshold. This thermal induced effect also results in an increase of 2.1% and reduction of 1.7% in the efficiencies of the 2.4μm weak and strong guiding devices respectively.

As mentioned in section 5.2, the theoretical efficiency values shown in Fig. 6.4 were calculated by taking account of the size dependent diffraction loss only, but not the "scattering loss" [1] due to the oxide. Therefore, the discrepancies between the theoretical and experimental results shown in Fig. 6.4 may be due to this scattering loss. As an attempt to fit the experimental values using the existing model, the following empirical equation for output coupling efficiency through the top DBR, which includes the "scattering loss" is used (Note : the total optical loss can be inferred from eqn. (5.29)) :

$$\eta_{top(mp)} = \frac{\text{transmitted optical power through top DBR}}{\text{total optical power loss}} = \frac{T_{T(mp)}}{1 - R_{T(mp)} R_{B(mp)} \exp\left(-2\alpha'_{ox(mp)}\right)} \tag{6.1}$$

where $\alpha'_{ox(mp)}$ is the "modal scattering loss" due to the oxide given by

$$\alpha'_{ox(mp)} = \alpha_{ox} F_{ox} d_{ox} \frac{\text{oxide edge} \to \infty}{\oiint E^2_{tr(mp)} dS} \tag{6.2}$$

In eqn.(6.2), α_{ox} is the "effective oxide loss" expressed in per unit length, whilst F_{ox} and d_{ox} are the oxide weighing factor and thickness respectively (as defined in eq.(4.19) earlier), and $E_{tr(mp)}$ is the transverse field variation.

Using equations (6.1) and (6.2) for the TEM_{00} mode, it is found that the experimental results are best fitted when $\alpha_{ox} = 6 \times 10^5$ cm^{-1} for strong guiding devices, $\alpha_{ox} = 1 \times 10^5$ cm^{-1} for medium guiding devices and $\alpha_{ox} = 4000$ cm^{-1} for weak guiding devices. These fitted values are shown in Fig.6.5, together with the relevant experimental results obtained by assuming $\eta_{int} = 0.821$. The size dependent exponential factors $\exp\left(-2\alpha'_{ox(00)}\right)$ that represent the additional "attenuation" of light due to the scattering loss, are also shown in the inset of this figure. As in the case of diffraction loss, this "scattering loss" also increases with reduction in aperture size and is the largest for the strong guiding devices. Assuming that the higher order modes also experience the same amount of "effective oxide loss" α_{ox} as the TEM_{00} mode, from (5.31) the cold cavity photon lifetimes that take account of the scattering losses

can be calculated using

$$\tau'_{p\,(mp)} \cong \frac{4}{c\, n_c \left[1 - R_{T(mp)} R_{B(mp)} \exp\left(-2\alpha'_{ox(mp)}\right)\right]} \frac{\iiint_V n^2 E^2_{mp}\, dV}{\oiint_S E^2_{tr(mp)}\, dS} \qquad (6.3)$$

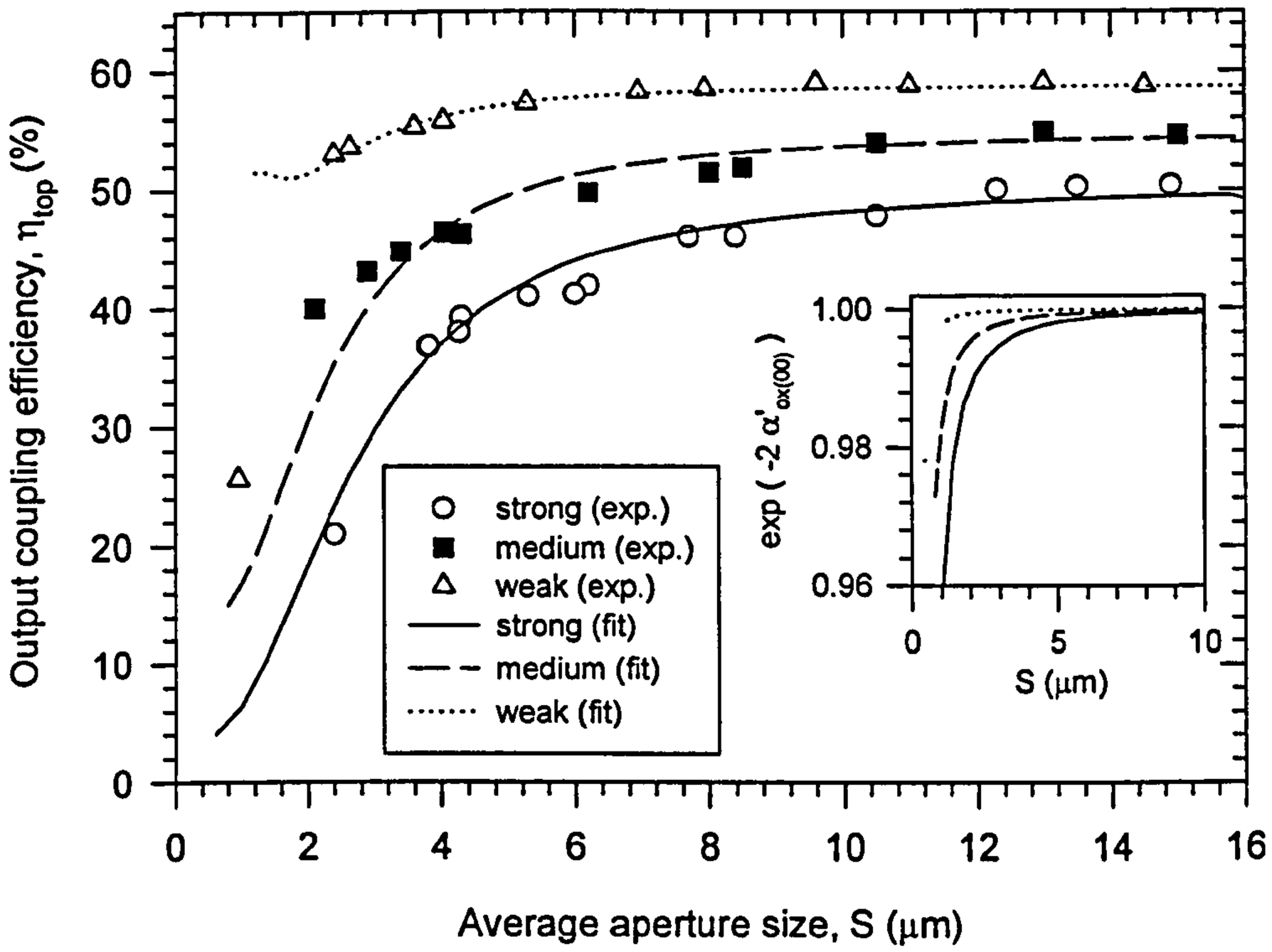

Figure 6.5 : Fitted and experimental values of output coupling efficiency for the strong, medium and weak guiding devices. The inset shows the size dependent exponential factors that represent the additional "attenuation" of light due to the modal "scattering loss".

Using the new values of cold cavity photon lifetime, the theoretical threshold current densities of TEM_{00} mode and TEM_{10} mode in circular apertured devices were recalculated. These values are shown in Figure 6.6, together with the experimental values. Compared to Fig 6.3, the theoretical results in Fig.6.6 clearly give a better "qualitative" match to the experimental results. For instance, it correctly predicts the larger difference in threshold current density between the strong guiding and the other two types of devices. In addition, the difference between the medium and weak guiding devices also becomes significant at aperture size of about 4.0μm, as in the case of the experimental results. The remaining discrepancies between the experimental and theoretical results shown in Fig. 6.6 are believed to be mainly due to the carrier leakage effect that has not been considered in the model.

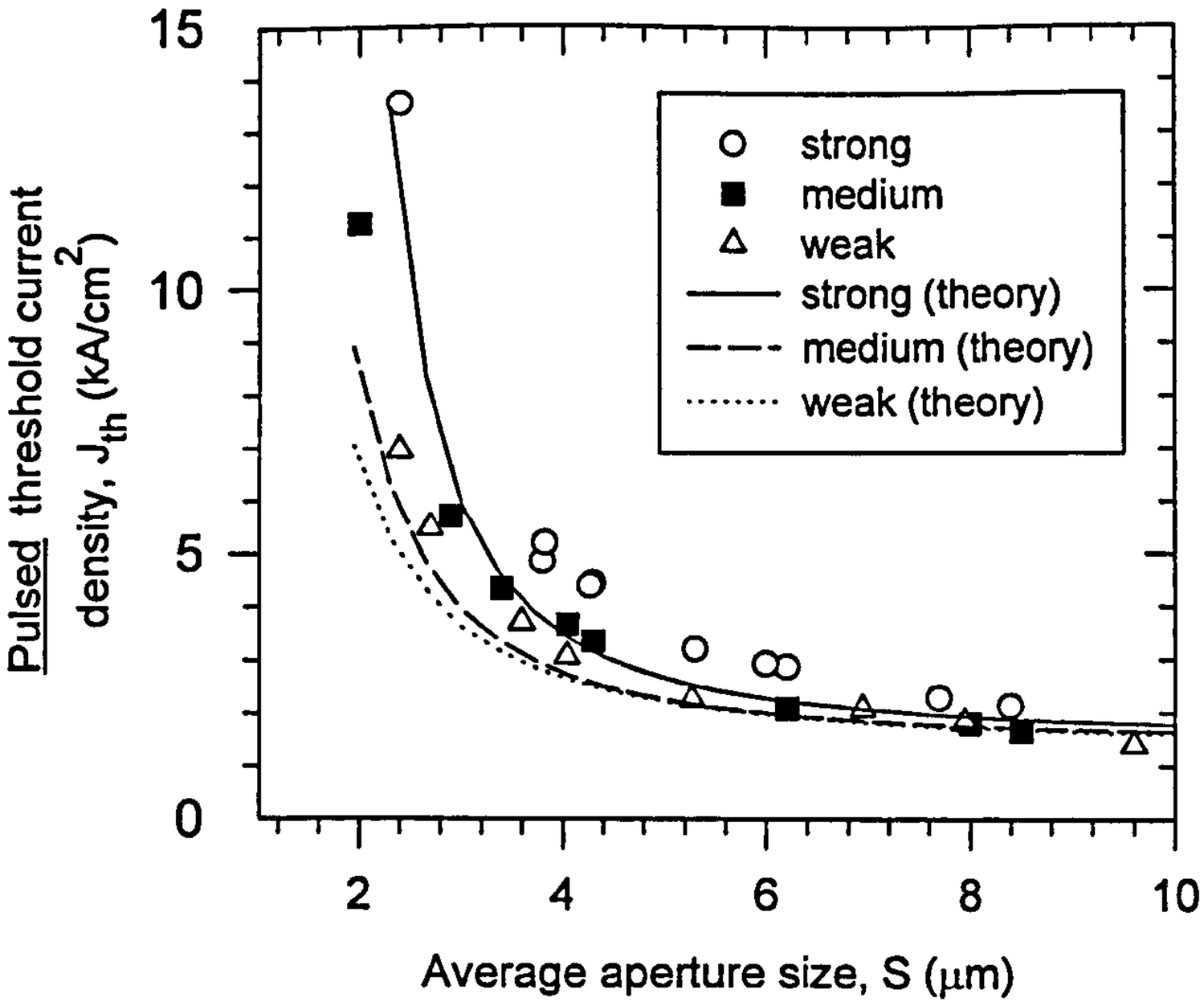

Figure 6.6 : Comparison between the calculated threshold current densities that take into account of "scattering loss" and the experimental results obtained under pulsed conditions.

The measured external quantum efficiencies are best compared to the theoretical results obtained directly from the solutions of the "multi-mode" rate equations. However, this is more numerically intensive and can not be done here since only the first two order modes are considered in this work. Nevertheless, in Figure 6.7, the measured "multimode" external quantum efficiencies are plotted alongside the predicted "single mode" external quantum efficiencies of the TEM_{00} mode, which takes into account the scattering losses. The arrows in this figure mark the experimental points from devices which manage to suppress the lasing of higher order modes within the "pulsed" driving range. The modal behaviours of these devices will discussed in more details in section 6.2.3 later. Clearly, the predicted "single mode" values are quite close to the measured external quantum efficiencies of the 2.4μm strong guiding and 2.0 medium guiding devices, which contain negligible contributions from the higher order modes. For devices that undergo multi-mode operation within the driving range, the "multi-mode" experimental values are higher than the "single-mode" theoretical values as expected.

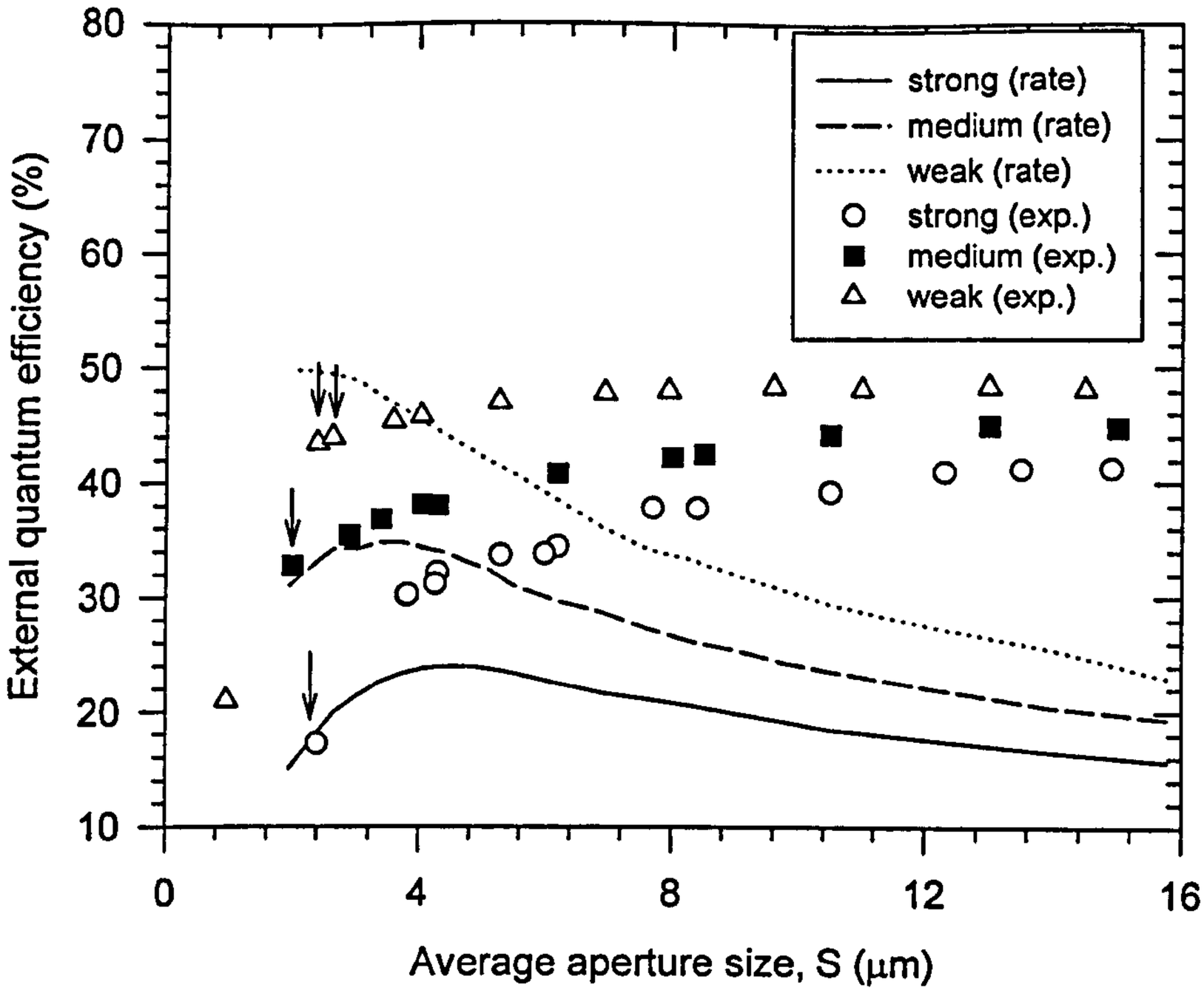

Figure 6.7 : Measured (i.e. multi-mode) external quantum efficiencies, and the predicted (single mode) external quantum efficiencies of TEM_{00} mode obtained through solutions of rate equations. The arrows mark the experimental points from devices in which the lasing of higher order modes are suppressed within the driving range.

The dependence of the external quantum efficiency on oxide aperture size and oxide thickness directly affects the maximum light power output and the wall-plug efficiency (i.e. the power conversion efficiency) of a particular device when driven under cw conditions. These are illustrated in Figures 6.8 and 6.9. The former shows the variation of the measured maximum power output taken at the brink of thermal roll-off and the latter the maximum wall-plug efficiency as a function of aperture size for the three different type of devices. The inset of Fig 6.9 also shows the wall-plug efficiency-current (η_{wp}-I) characteristic of the 4.3μm strong guiding device (whose L-I-V characteristic is illustrated in Fig. 6.1), which also typifies those of other devices. It is obvious from these figures that the weak guiding devices have the highest maximum powers and wall-plug efficiencies at all aperture sizes, with those of medium guiding devices falling between the other two type of devices. In short, if high multi-modal power and wall-plug efficiency devices are sought after, then a weak guiding design utilising thin oxide seems to be the best choice.

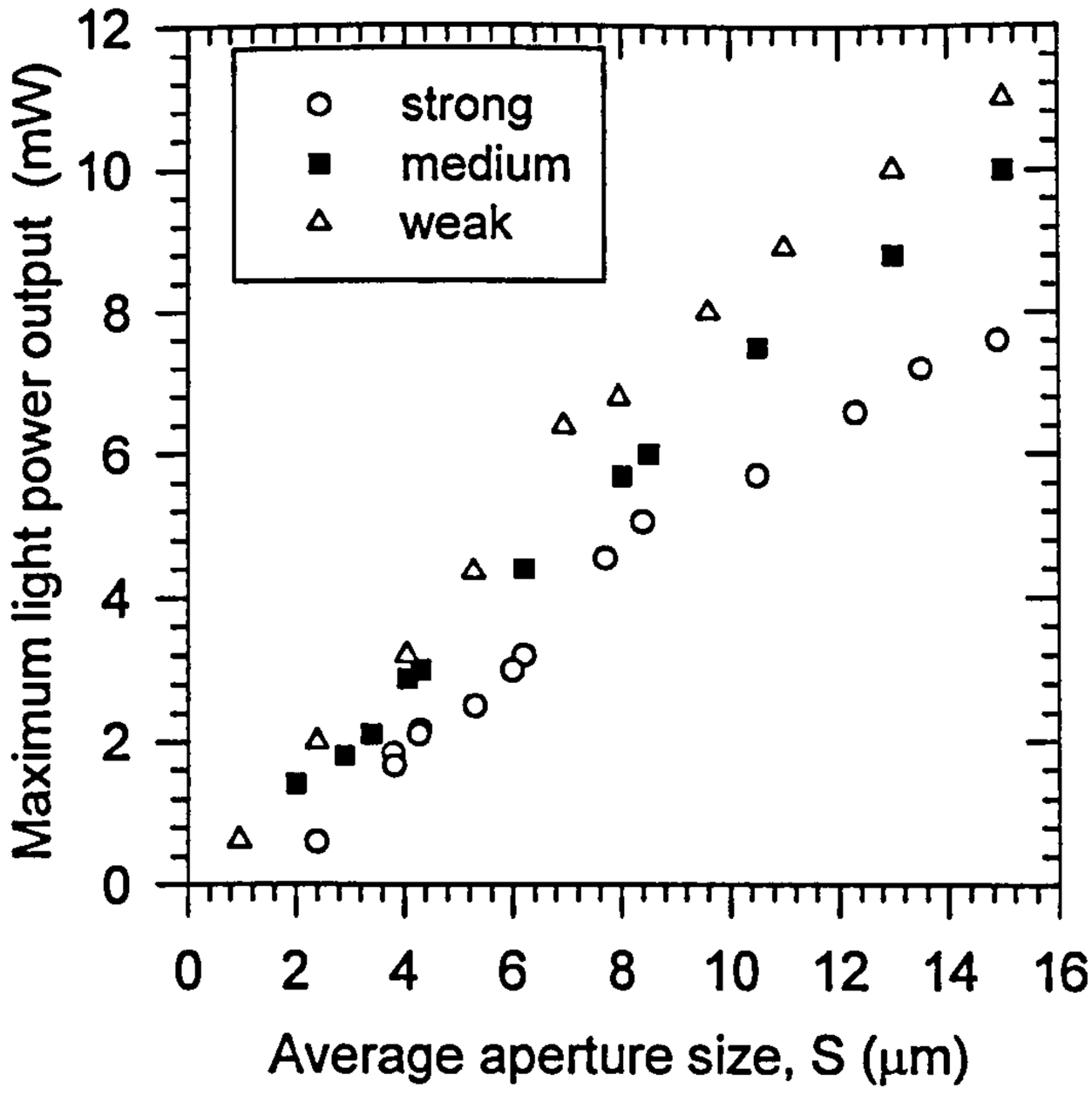

Figure 6.8 : Variation of maximum light power output with aperture size for the strong, medium and weak guiding devices.

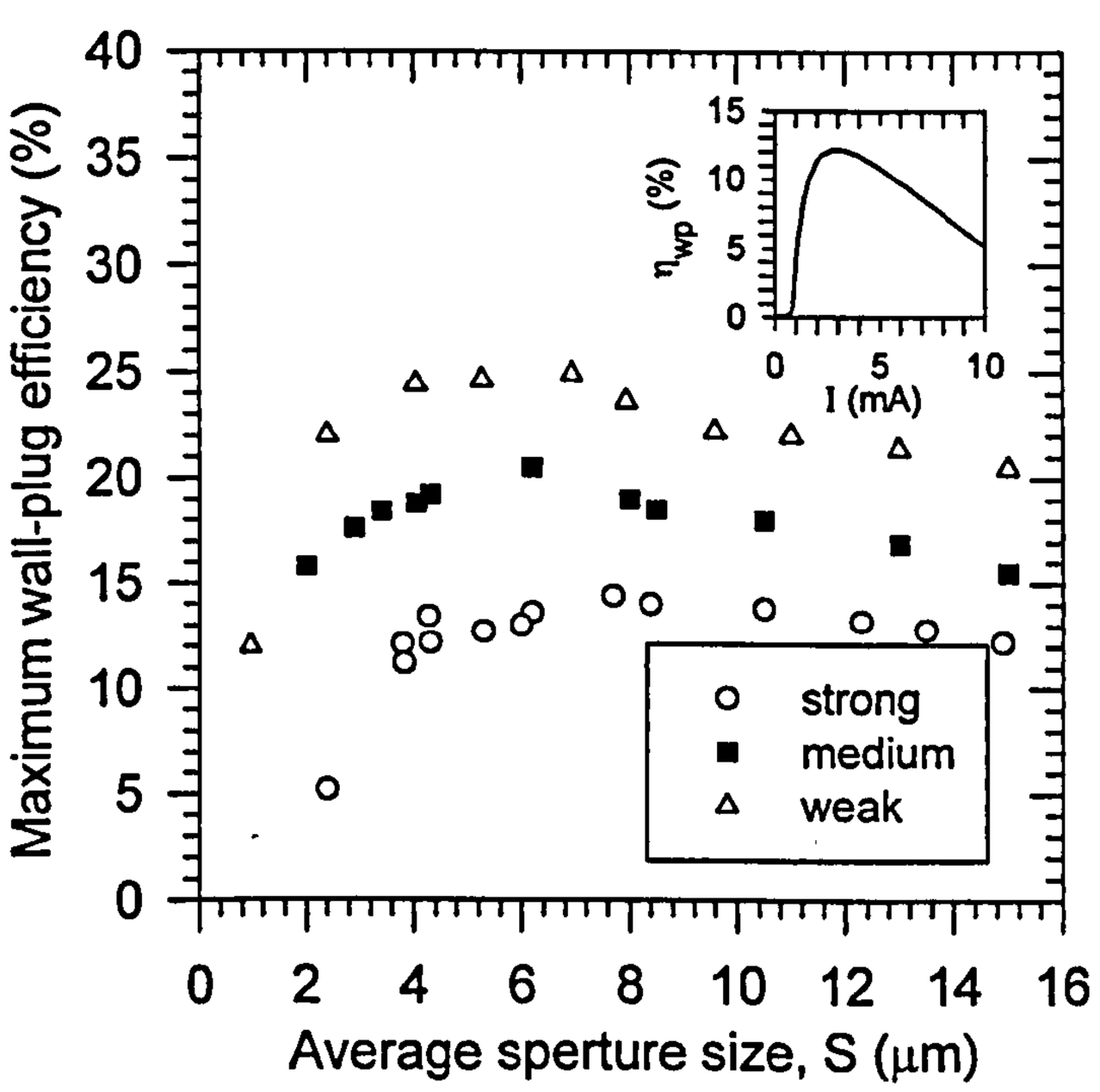

Figure 6.9 : Variation of maximum wall-plug efficiency with aperture size. The inset shows the η_{wp}-I characteristic of the 4.3μm strong guiding device.

In order to confirm that the trends shown in Fig. 6.8 and 6.9, are mainly due to the size dependence of the optical excess losses, the current densities at which the

thermal roll-off begins are also plotted as a function of aperture size in Figure 6.10. Clearly, these values are very similar for strong, medium and weak guiding devices of equal aperture size. This thus implies that for a given aperture size and injected current density, the internal temperature rise in the three different types of devices are also similar, i.e. they have similar thermal impedance. Therefore, the differences in power and efficiency among these devices of identical size, are mainly due to the differences in external quantum efficiency and thus excess optical losses. In addition, the results illustrated in Fig. 6.10 also implies that smaller devices have better intrinsic heat-sinking capabilities i.e. lower thermal impedance, than the bigger devices, in good agreement with theoretical predictions [3].

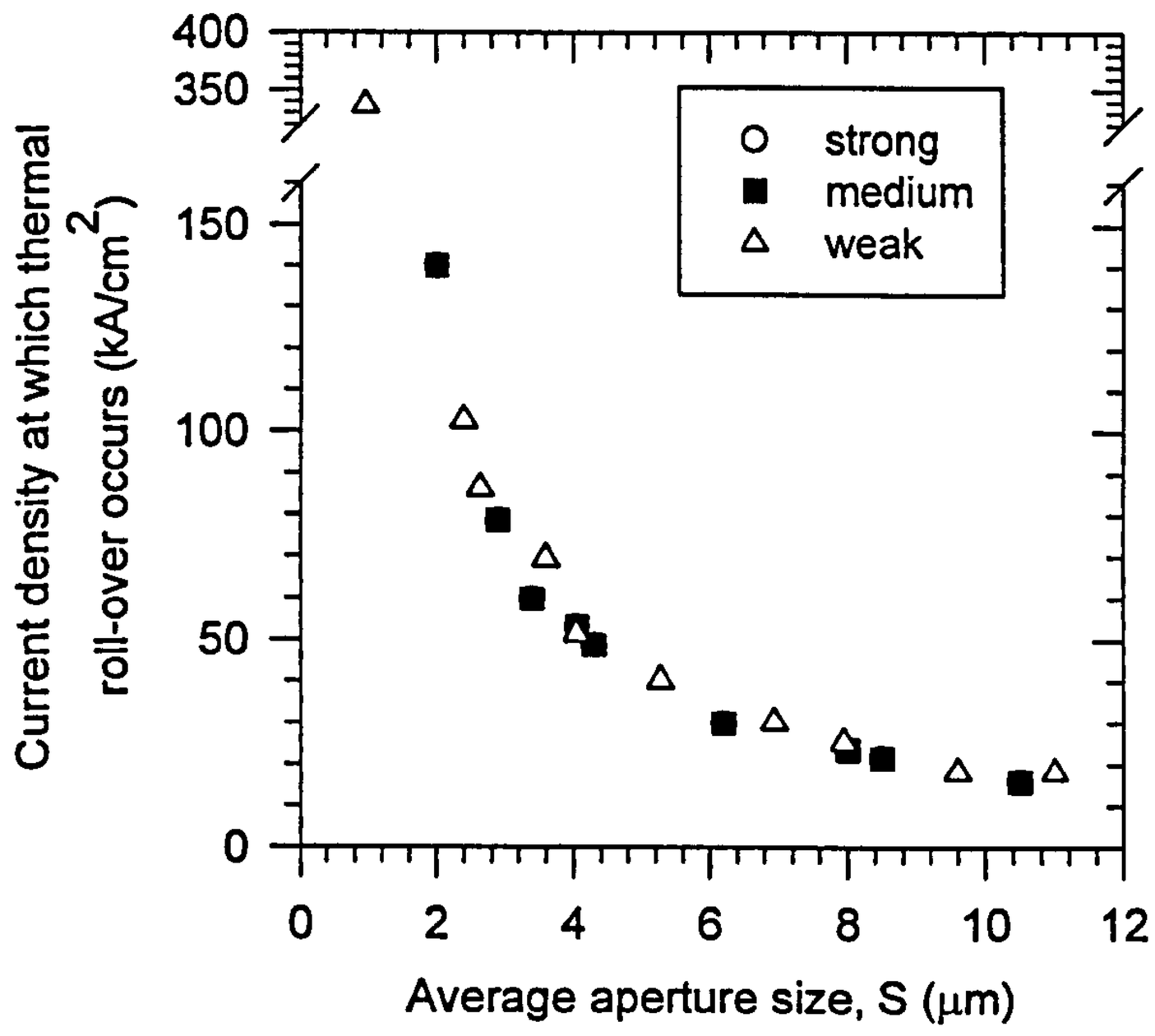

Figure 6.10 : Current densities at which thermal roll-off occurs as a function of average aperture size, S.

Finally, it should be noted that the small differences in the DBR absorption levels between the three different types of devices, only causes relatively small changes to their threshold values, since the effects of excess optical losses are more significant. Therefore, they do not affect the conclusion drawn above regarding the merits of using thinner oxide thickness for achieving lower threshold current. Likewise, in all cases they do not markedly affect the rate of reduction in the external quantum efficiency as the aperture size becomes smaller. Therefore, it is valid to conclude that weak guiding devices are preferable for achieving higher external

quantum efficiencies and thus higher light power output, especially for aperture sizes smaller than 10μm.

6.2.2 Polarisation Characteristics

Figures 6.11 to 6.13 illustrate the polarisation resolved light-current characteristics measured under both pulsed and cw conditions, for the strong guiding devices with average aperture sizes of 2.4μm (2.4 x 2.5μm), 3.8μm (3.7 x 3.9μm) and 4.3μm (4.4 x 4.2μm) respectively. While the 2.4μm device sustains "single mode" operation under both pulsed and cw conditions throughout the driving range shown, multimode operation occurs in the 4.3μm device under both pulsed and cw conditions, but only under cw condition in the 3.8μm device. The onset of the first higher order mode, a TEM_{01} mode in the 4.3μm device and a TEM_{10} mode in the 3.8μm device, are highlighted by the arrow markings in the figures for these devices. As will be discussed later in section 6.2.3, the lasing of the higher order mode can be confirmed through the spectral measurements. For the 4.3μm device, the cw "turn on" current of the first higher order mode at 4.5mA is slightly higher than the corresponding pulsed value of 4.1mA, most likely due to the higher thermal enhanced carrier leakage. At 6mA, it is found that the TEM_{00}, TEM_{01} and TEM_{10} modes lase in both polarisation directions. As for the 3.8μm device, no second higher order "lasing" mode or TEM_{00} mode were found lasing in the $<1\bar{1}0>$ direction for the pulsed current range shown.

These three devices of different aperture size also show different polarisation characteristics. While the 2.4μm device demonstrates stable polarisation along the <110> crystal axis, polarisation switching between the two polarisation states occurs when the 3.8μm and 4.3μm devices are operated under cw conditions. In addition, there is only one switching event between the two orthogonally polarised fundamental modes in the 3.8μm device, but two such polarisation flippings occur in the 4.3μm device, with the higher current one believed to be that corresponding to the higher order modes. However, before polarisation switching occurs in these devices, the lasing fundamental mode is polarised along the <110> crystal axis, as in the case of the 2.4μm device. Interestingly, under pulsed conditions, all the three devices show stable polarisation characteristics predominantly along the <110> direction. This thus suggests that the polarisation switching phenomenon has its origin in some thermally induced effects.

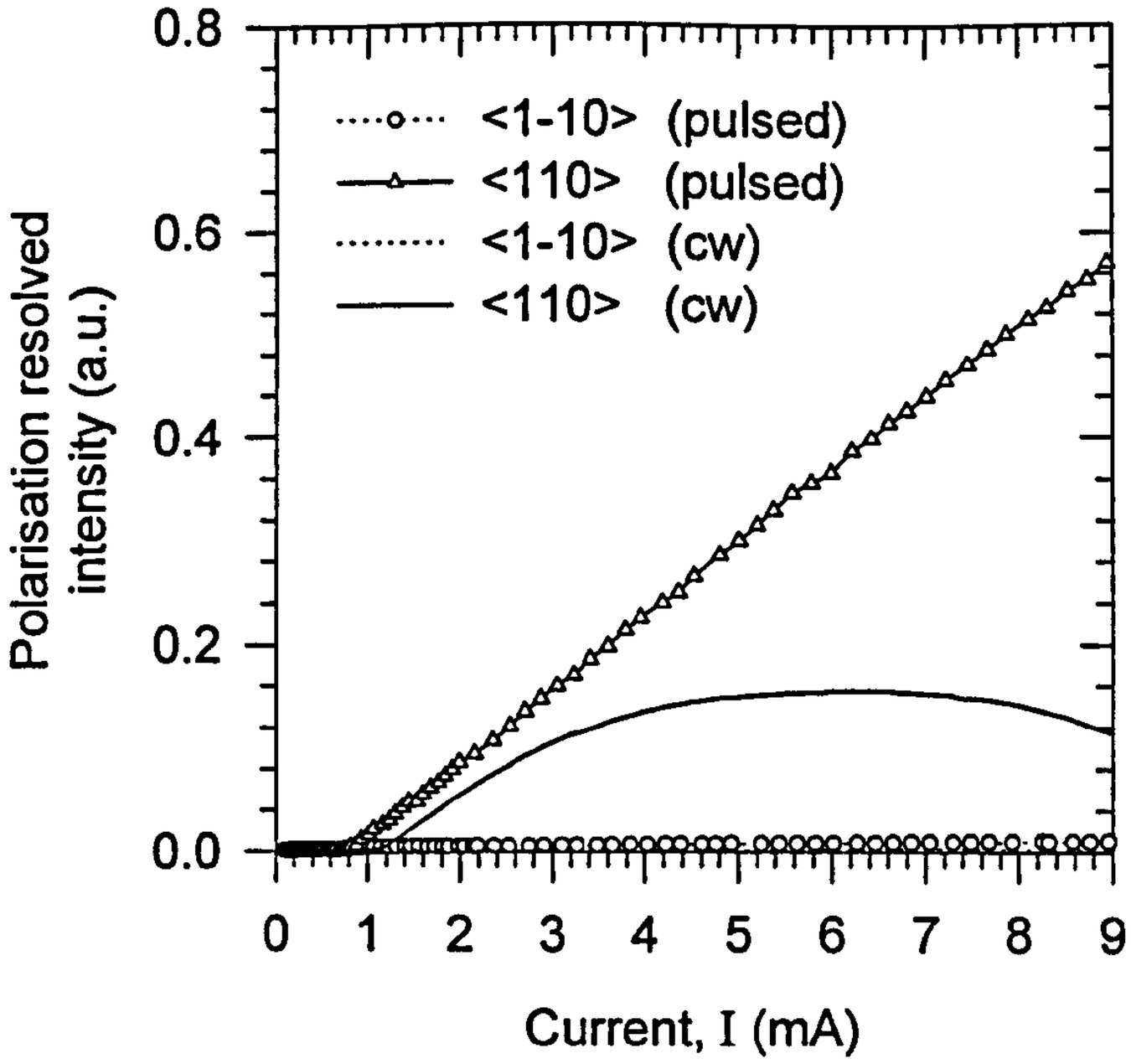

Figure 6.11 : Polarisation resolved light - current characteristic of the 2.4μm square devices of strong guiding design.

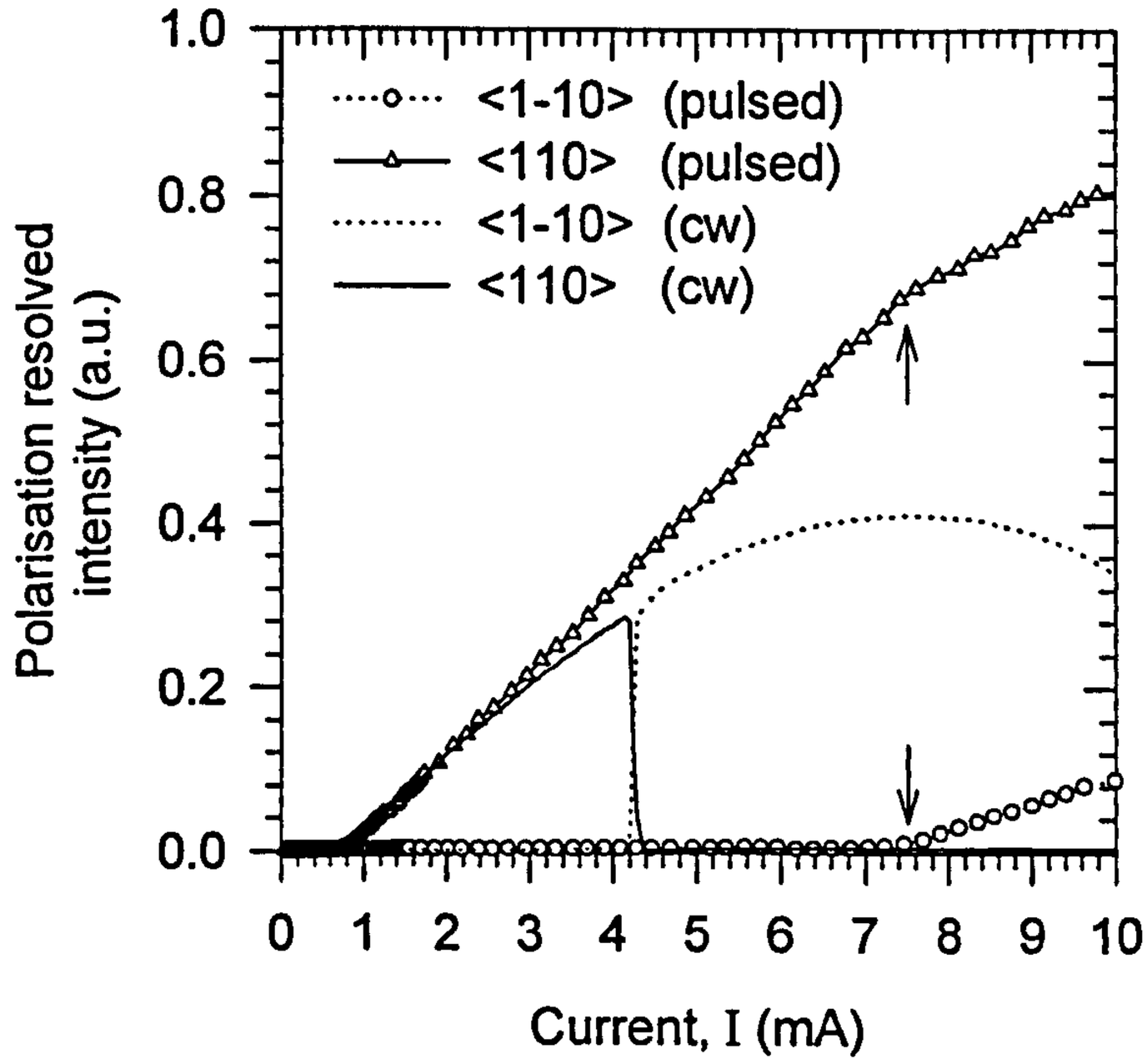

Figure 6.12 : Polarisation resolved light - current characteristic of the 3.8μm square devices of strong guiding design. The arrow marks the onset of the first higher order mode.

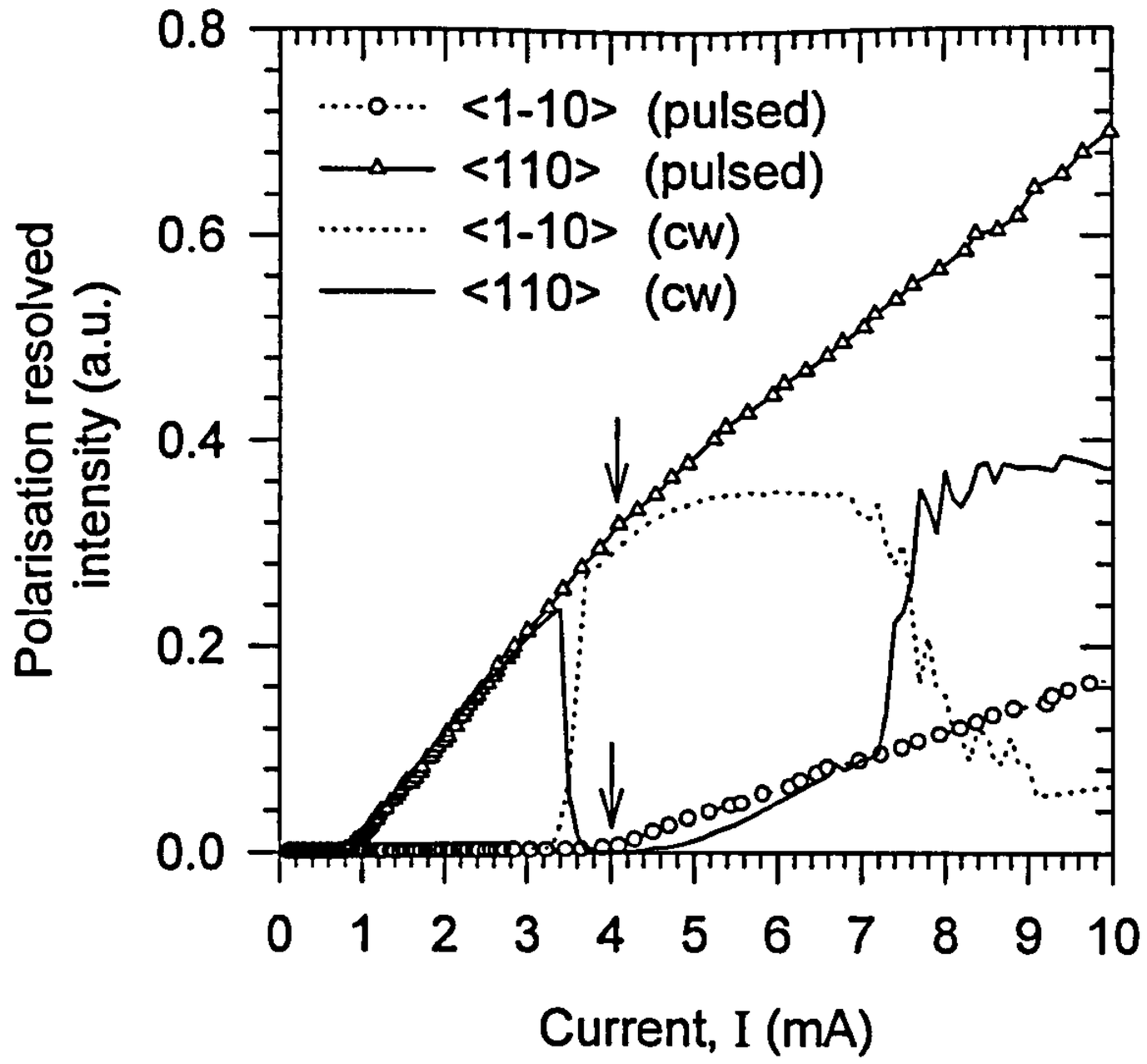

Figure 6.13 : Polarisation resolved light - current characteristic of the 4.3μm square devices of strong guiding design. The arrows mark the onset of the first higher order mode : left (pulsed), right (cw).

Several theories [4-7] had been put forward to explain the possible cause(s) of the polarisation switching phenomenon demonstrated here. Among the reasons proposed that cite thermal effects induced by device internal heating are those invoking the spectral shift of the gain peak relative to the resonant wavelengths of non-degenerate eigenmodes in orthogonal polarisation directions [4] and thermal lensing effects [5]. Both of these proposals are based on the assumption that the polarisation switching happens when the modal gain difference between the two orthogonal polarised eigenmodes changes sign. In both cases, spectral spliting between these two eigenmodes is certainly a pre-requisite. In the former case, it is assumed that the eigenmode closer to the gain peak always has higher modal gain and is thus more equipped to achieve lasing first. Hence, it is expected that in VCSELs where the gain peak is initially blue-shifted with respect to the eigenmodé resonant wavelengths (such are the cases for the devices considered here), the lasing TEM_{00} mode will be "switched" from the one which has shorter wavelength to the one with longer wavelength once the gain peak starts thermal red-shifting and sweeps across the resonant wavelengths. The thermal induced red shift of the gain peak wavelength is 5-6 times faster than that of the eigenmode resonant wavelengths with increasing

device temperature. The validity of this hypothesis has been confirmed by the occurrence of polarisation switching when the device is heated up intentionally [4]. This explanation is certainly plausible in the cases considered here since it is found that it is the fundamental mode with shorter wavelength that starts lasing first. On the other hand, the thermal lensing effect has also been proposed as the possible reason for causing the polarisation switching due to the change in modal gain difference, in VCSELs where the resonant wavelengths are blue shifted with respect to the gain peak [5]. In this work, polarisation switching under cw condition has also been observed in near-square devices with initial lasing wavelength of about 830nm, which is well blue-shifted with respect to the gain peak wavelength (results not shown).

However, the fact that the small 2.4μm device shown here has stable polarisation suggests that the real situation may no be as simple as suggested. For this particular device, it is possible that the slight asymmetry in aperture shape creates sufficient difference in the modal reflectance of the orthogonally polarised eigenmodes to overcome the two thermal effects mentioned above, and thus results in sustained stable polarisation operation. However, this modal reflectance difference is not adequate in the bigger devices because, as discussed in section 5.2.3, this difference is also a function of mode size. Other alternative non-thermal mechanisms suggested include those invoking the difference in the population of the magnetic sub-levels of the conduction and heavy hole valence bands in the QW [6], and spatial hole burning effects [7]. While the implications of the former proposal are quite subtle, the spatial hole burning effect alone certainly is not sufficient to cause switching as evident in the pulsed traces shown in figures 6.6. However, when operated cw, thermal lensing and spatial hole burning effects tend to reinforce each other and may thus lead to polarisation switching.

The polarisation behaviour of the medium and weak guiding devices are very similar to those shown above, although for unknown reasons, in certain cases polarisation switching only happens to the higher order mode but not the fundamental mode for devices with aperture size 3 - 4μm. In addition, the strong, medium and weak guiding devices also share other similarities in their polarisation characteristics. For the devices ($S < 6$ μm) that have single mode operation either throughout the whole driving range or for a limited current range only, almost all of them begin lasing in the polarisation direction parallel to the $<110>$ crystal axis. Since it is well

known that VCSEL layers grown on mis-orientated substrate have intrinsic anisotropy in the QW gain [8], the preferential direction of polarisation demonstrated by most of these devices may be due to the fact that VCSEL layers used here were grown on (100) substrates that are slightly off axis at 3° towards (110) plane. It is of course, also possible that the unintentional mechanical stress/strain induced by the conversion of AlAs to Al_xO_y or by fabrication processes such as etching or annealing, may introduce some extra anisotropy to the optical gain. In fact, anisotropic mechanical stress introduced intentionally by an elliptical etched substrate hole has been reported to result in reasonable polarisation control [9]. The only exception to the polarisation characteristic discussed above can only be found in some strong guiding rectangular devices of certain dimensions and aspect ratios, where the longer side of the apertures as well as the polarisation direction are perpendicular to the $<110>$ direction i.e. along the $<1\bar{1}0>$ direction. The polarisation characteristics of these rectangular devices will be discussed later in section 6.3.2.

6.2.3 Modal Properties

The modal behaviour of oxide apertured VCSELs are of great research interest since some of their potential applications specifically require either single mode operation (smaller far field divergence angle and larger coupling efficiency to optical components), such as in free space optical inter-connect systems; or multi-mode operation for use in short-distance communication systems utilising multi-mode optical fibres. Since most oxide apertured VCSELs are inherently multi-moded, multi-mode operation can be obtained readily from medium (>5μm) to large size devices. On the other hand, as pointed out in chapter 4, "pure" single mode devices can only be obtained from devices with very small aperture size where the cut-off of the first higher order mode has occurred. However, it was found in this work as well as by other researchers [1,10,11] that it is possible for certain inherently multi-moded devices to have the fundamental mode dominating over other modes throughout a certain driving range. In this work, a "complete" driving range is defined as the current range starting from threshold up to 30% above the thermal rollover under cw operation, since it is unusual for lasers to operate far beyond the thermal roll-off in most applications. From the system point of view, the suitability of a laser for single mode operation is usually decided by a figure called "Side Mode Suppression Ratio

(SMSR), which is given by the ratio of spectral peak intensity of the dominant mode to that of the side mode with highest peak value [12]. This figure is usually large so long as only the dominant mode achieves lasing while the other side modes remain below "threshold"; for instance, as shown in Fig. 5.20. Therefore, the current injection level at which the first higher order mode turns on is chosen as a figure of merit in this work for comparing the single mode performance of the three different type of devices. For comparison, the same batch of near-square shaped devices used in the investigation of the threshold properties discussed in section 6.2.1 were studied.

In the process of identifying the onset of the higher order mode, the presence of an abrupt increase in intensity or a kink, in the polarisation resolved light-current characteristic as shown in preceding sections, proved a useful tool for a "first guess". It is found that for the near-square devices with aperture sizes of 4.3μm or smaller, the "first" higher order TEM_{01} or TEM_{10} mode always turns on in the orthogonal polarisation to the fundamental TEM mode. (However, it is still possible that the higher order modes lased in the same polarisation direction as the fundamental modes at higher current injection levels) This behaviour was confirmed through spectral measurements where it was found that the distinct features in the polarisation resolved L-I curves mentioned above coincide with the degradation in SMSR as well as narrowing in the emission linewidths as will be described in the following paragraphs. However, for bigger devices (>4.3μm), it is possible for the side modes to start lasing in the same polarisation direction as the fundamental mode, before settling in the orthogonal direction. Therefore, in such cases, the identification of the onset of the higher order modes have to rely on the deduction from the linewidth measurement as well as the corresponding trend in the SMSR.

As an example, Figure 6.14 shows the measured cw lasing spectra of a 4.3μm (4.4 x 4.2μm) near-square device of strong guiding design measured at various current injection levels. The polarisation resolved L-I characteristics of this device are those shown in Fig. 6.13 while its normal L-I-V curves are illustrated in Fig. 6.1 earlier. Due to signal saturation from the N_2 cooled Ge-detector at injection currents well above threshold of the TEM_{00} mode, calibrated neutral density filters of various attenuation ratios had to be used in order to attenuate those emission peaks of very high intensity. The legends inside these graphs indicate the factor by which the intensity was attenuated during the measurement of the spectrum concerned.

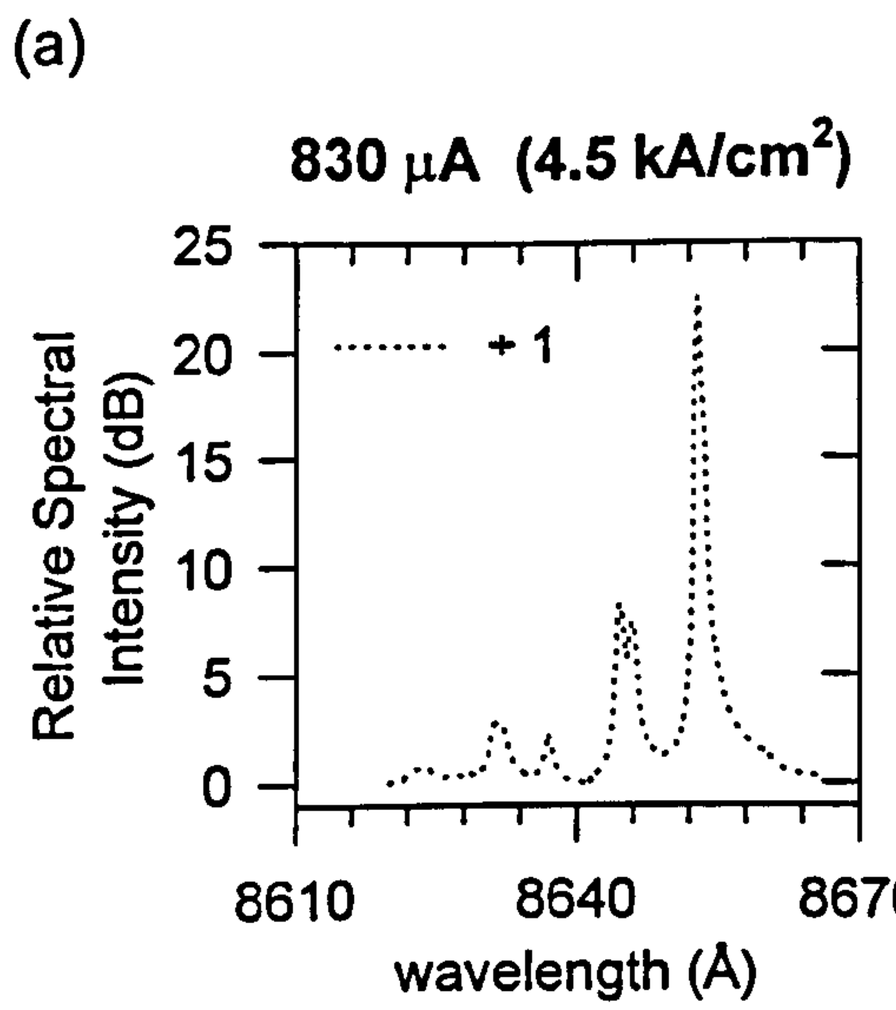

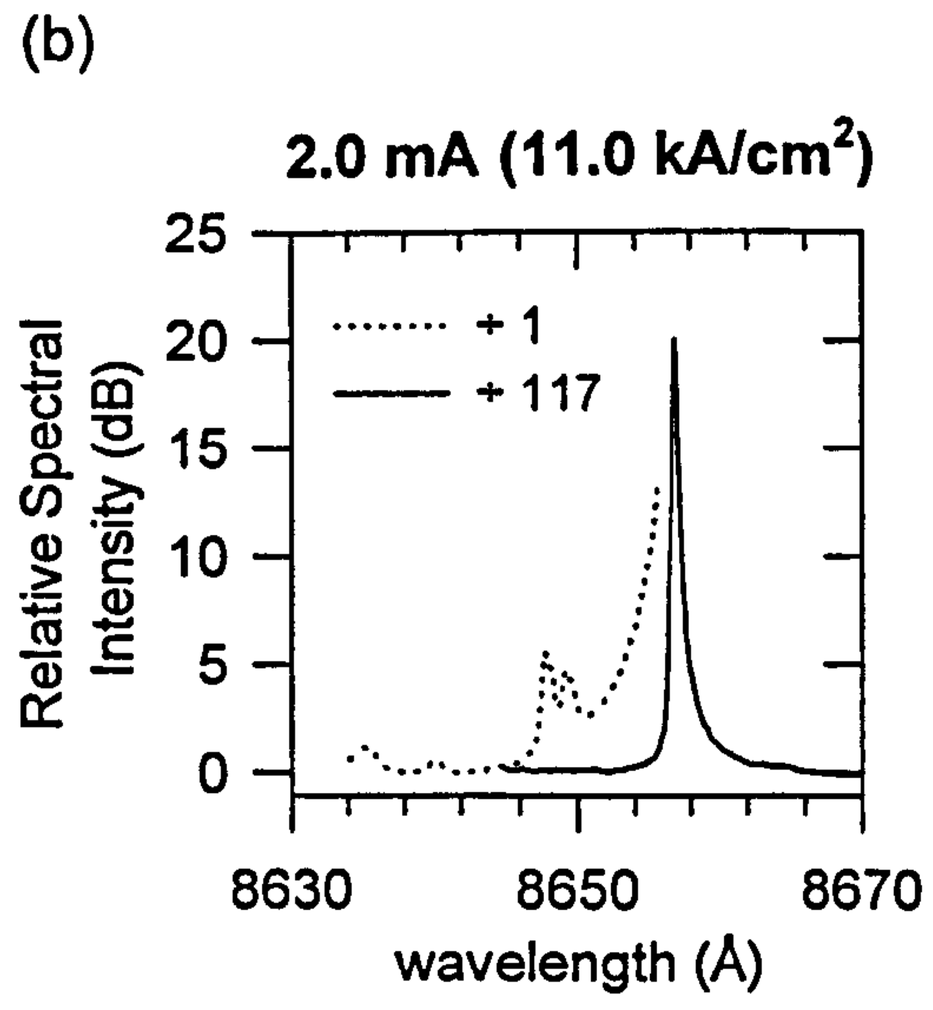

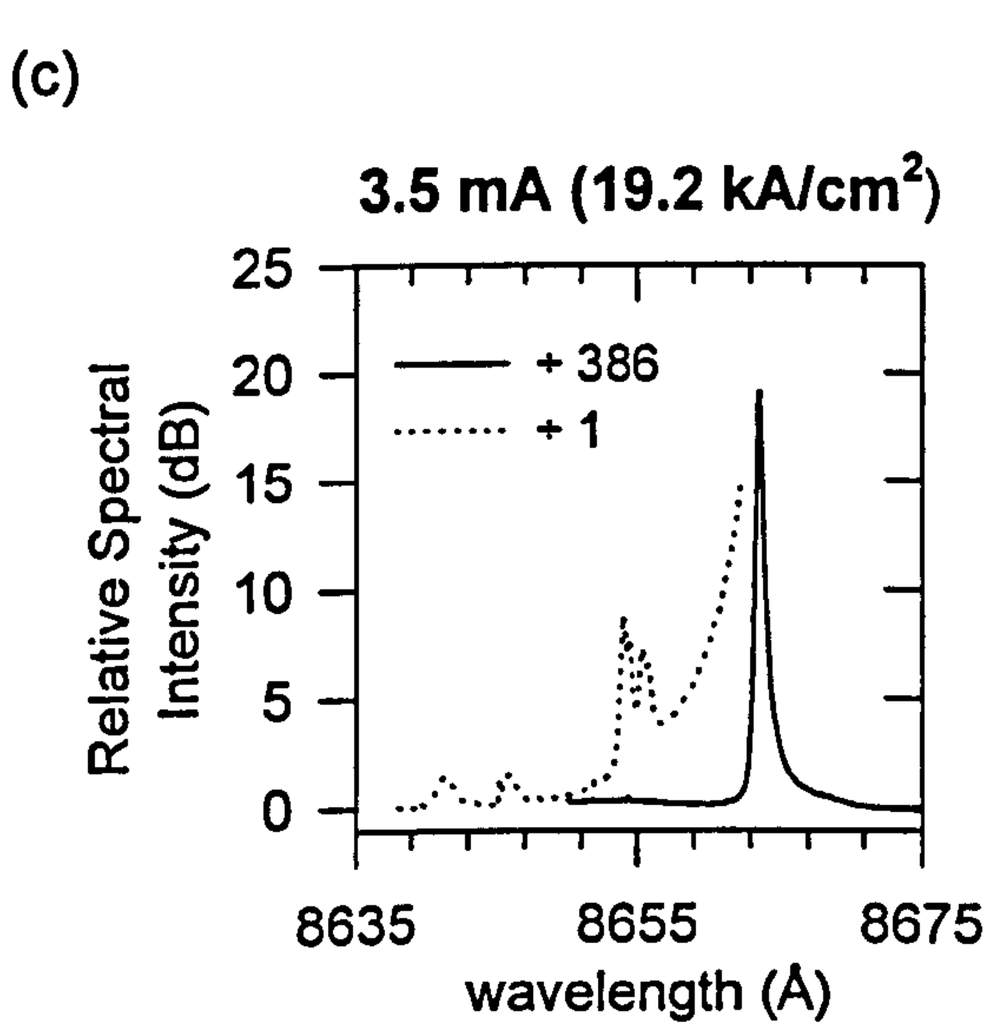

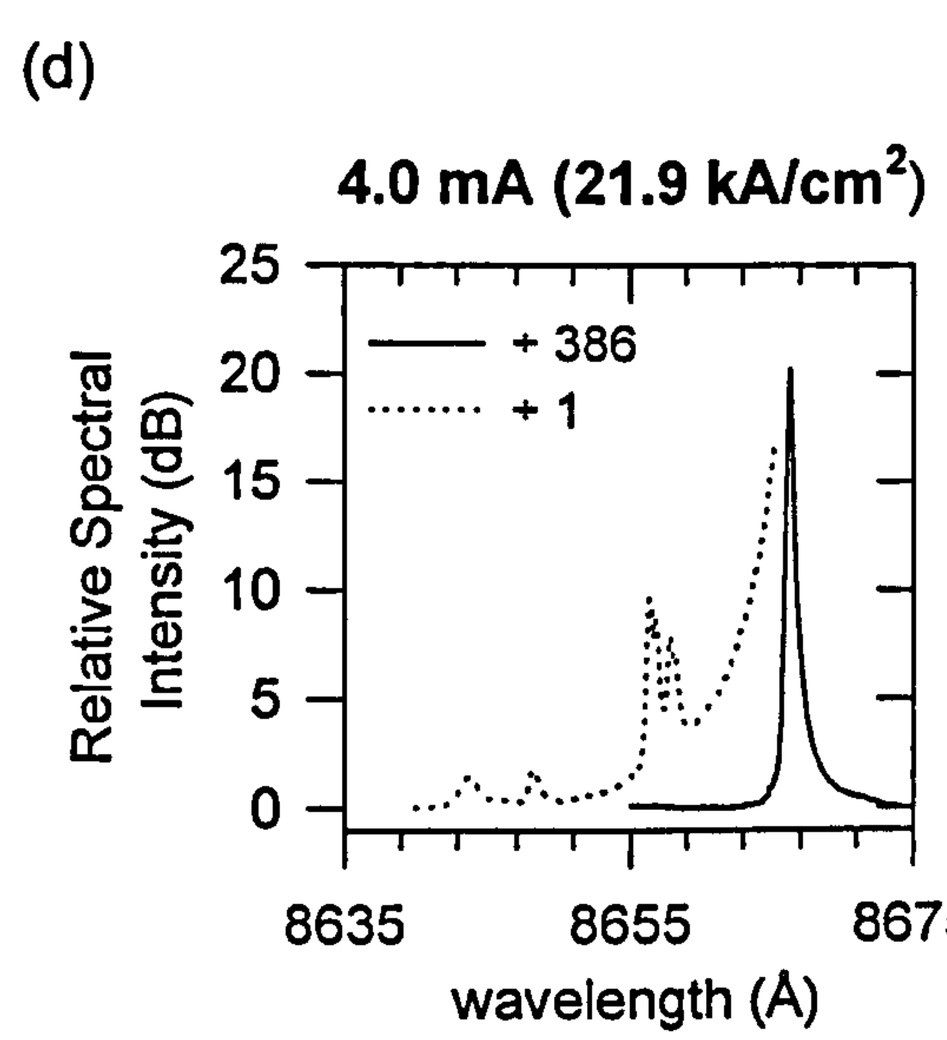

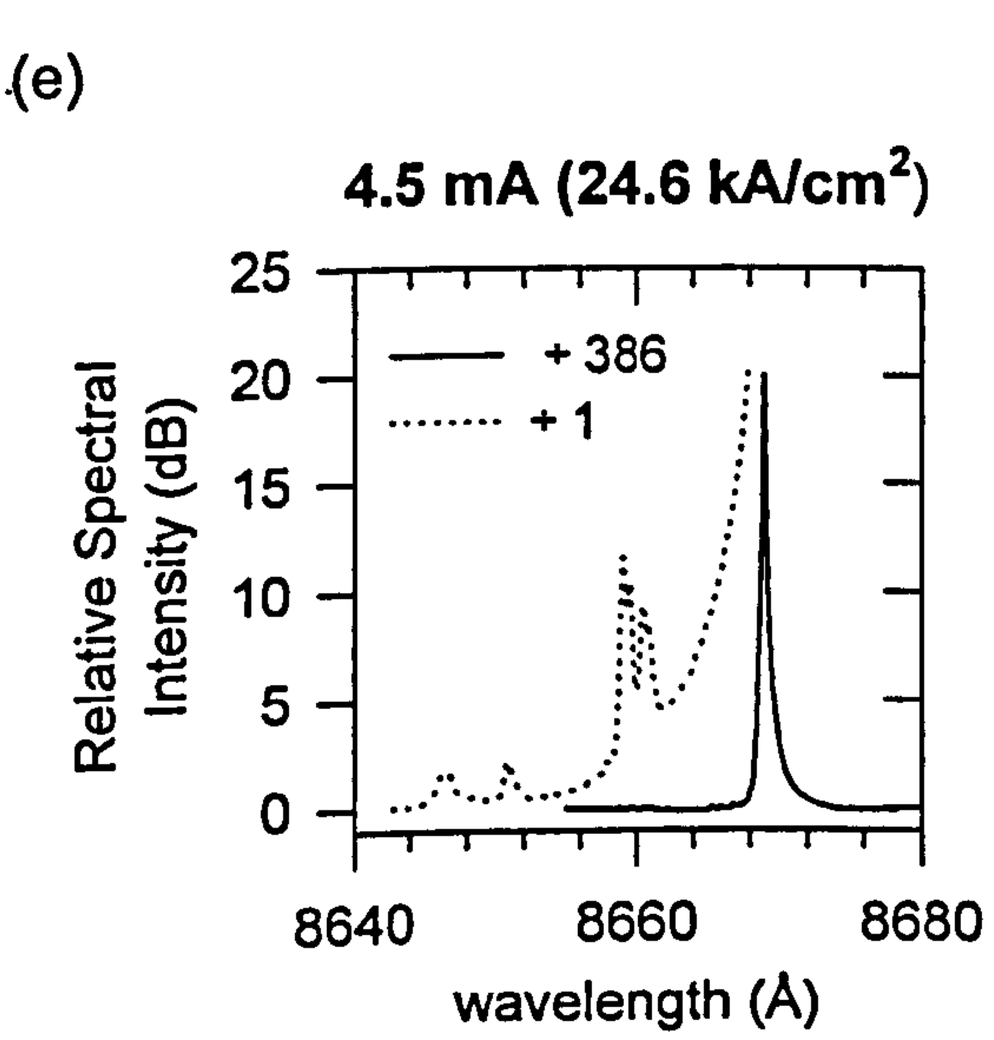

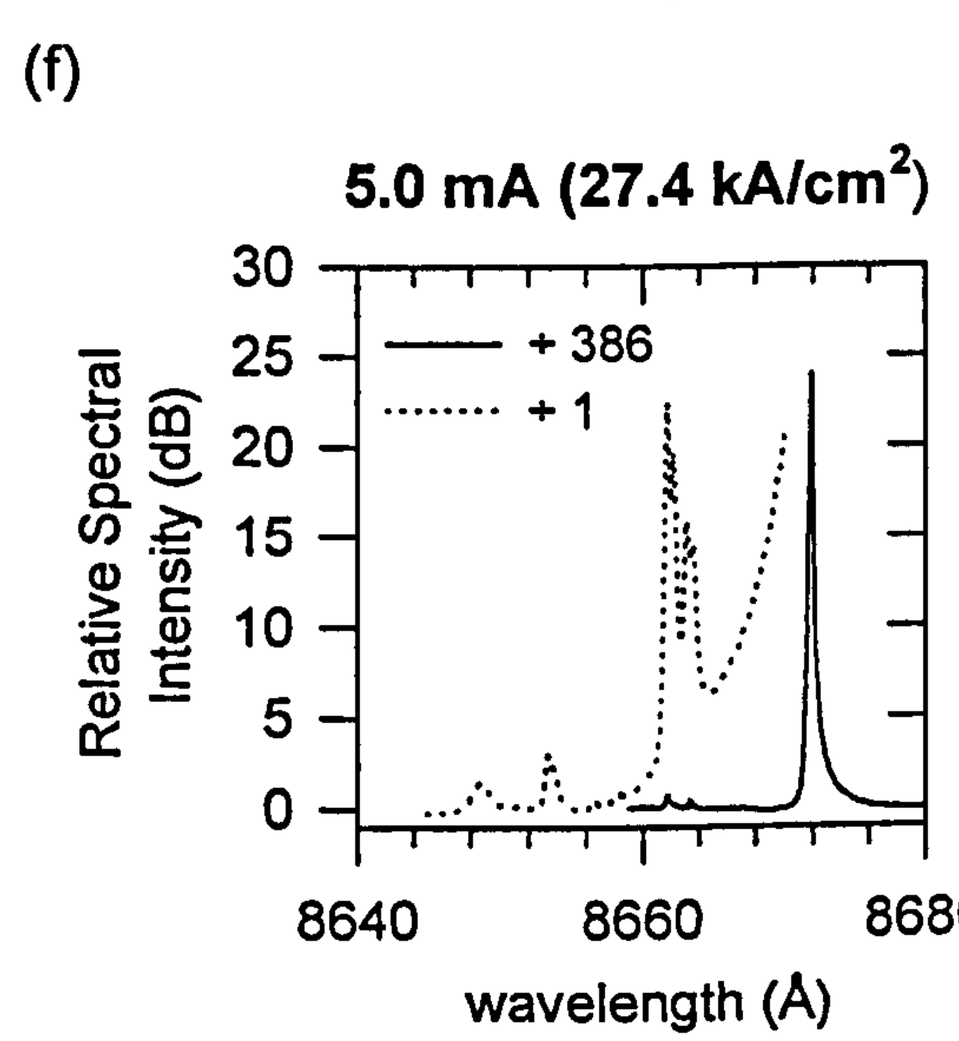

Figure 6.14 : (Continues overleaf)

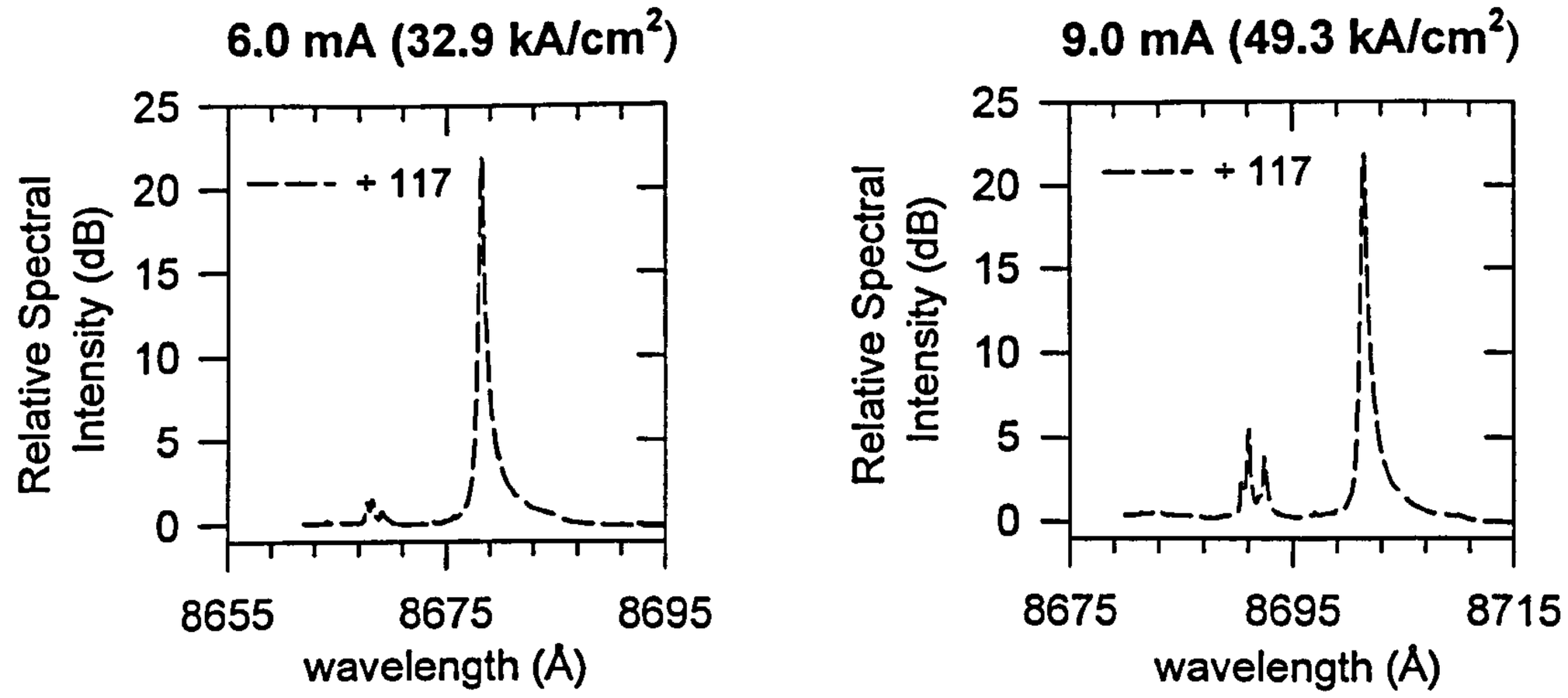

Figure 6.14 : Lasing spectra (cw) of the 4.3μm near-square device at various current injection levels. The threshold current of the TEM_{00} mode is 830μA, while that of TEM_{01}/TEM_{10} modes are 4.5mA/5.0mA respectively.

For the same device, the main illustration of Figure 6.15 also shows how the spontaneous emission linewidths (FWHM) of the eigenmodes polarised in the <110> direction varies with injected current. As discussed in section 5.3, these values can be extracted easily by curve-fitting the polarisation resolved spectra with Lorentzian lineshapes. As reasoned in section 4.3.2, the spectra were measured using a 30μm spectrometer slit width and sampling step size of 0.02Å. Although the theoretical resolution of the spectrometer is 0.30Å, the resolution of the whole measuring system is about 0.35Å as deduced from the measured FWHM linewidth of the lasing peak. The current densities at which the emission linewidths of the eigenmode reach the system resolution are marked by the arrows shown in this figure. The results shown in Fig 6.15 are as expected, i.e. the linewidth of the emission peaks reduces rapidly with increasing current density. Eventually, when the TEM_{00} mode achieves its threshold, its linewidth is limited by the system resolution of 0.35Å. This happens at the threshold current density of the TEM_{00} mode determined from the L-I characteristic, which is 830μA (4.4 kA/cm^2). After the lasing of the TEM_{00} mode, the linewdiths of the TEM_{01} and TEM_{10} modes reduce more gradually than previously, until reaching their threshold. It is found that the TEM_{01} mode which has a shorter resonant wavelength turns on slightly before the TEM_{10} mode despite the fact that the shape of

the oxide aperture (4.4 x 4.2μm) which is slightly elongated along the $\langle 1\bar{1}0 \rangle$, i.e. x-direction, should favour TEM_{10} modes in terms of diffraction loss. However, it is most likely that this difference in optical loss is negligible compared to the effect of relative gain offset which favours the TEM_{01} mode whose wavelength is closer to the gain peak. The current (density) at which the linewidth of the TEM_{01} mode approached that of system resolution is 4.5mA (24.3 kA/cm^2), coincided with its threshold value determined from the polarisation resolved L-I characteristic in Fig. 6.13. This is followed by the onset of the TEM_{10} mode, which lases at 5.0mA (27.0 kA/cm^2).

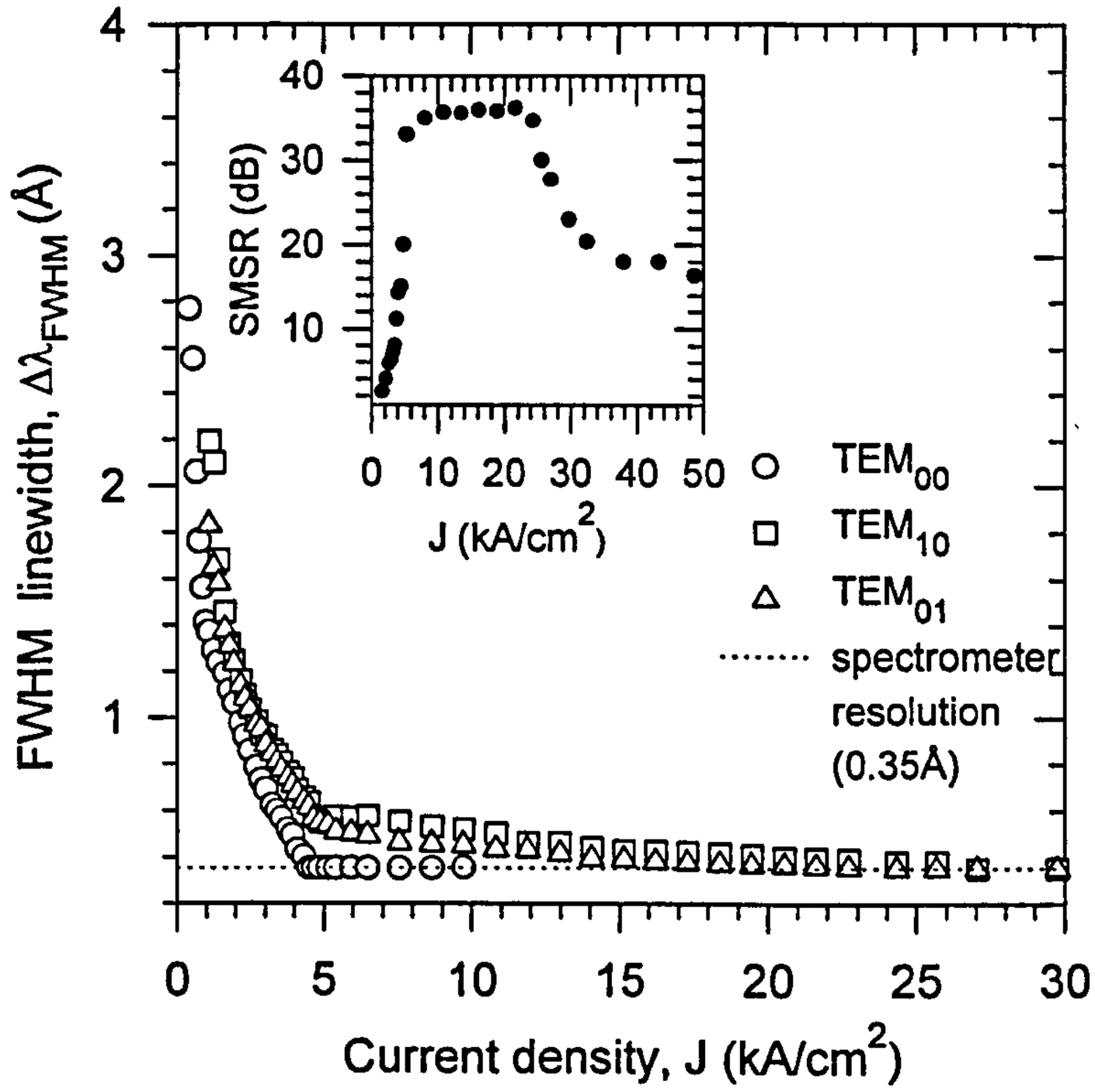

Figure 6.15 : Variation of FWHM spectral linewidth of the first three order eigenmodes polarised in the <110> direction with injected current density for the 4.3μm strong guiding device. The arrows mark the current densities at which the emission linewidths of the eigenmode reach the system resolution. The inset shows the corresponding change in the SMSR between the TEM_{00} and TEM_{01} modes.

As can be seen in the figure for 830μA in Fig 6.14(a), there are quite a number of eigenmodes resonant in this device, namely TEM_{00}, TEM_{10}, TEM_{01}, TEM_{11}, TEM_{20}, TEM_{02}, etc, with their resonant wavelengths in this descending order. However, since among the higher order modes it is the TEM_{01} mode that achieved lasing first, the

monitoring of the deterioration in the SMSR was mainly focused on the intensity ratio between this particular higher order mode and the fundamental TEM_{00} mode. Assuming the actual peak spectral intensity of the fundamental mode can be obtained by multiplying the filter attenuation factor by its measured peak value, the change in the intensity ratios between the TEM_{00} mode and TEM_{01} mode, i.e. SMSR, with current injection is shown in the inset of Figure 6.8. Note the qualitative resemblance of the SMSR variation shown in this inset with that in the inset of Fig. 5.20, up to the onset of the higher order mode. The SMSR increases dramatically from the value at threshold, and then saturates at around 36dB for a current density range of about 14kA/cm^2 before deteriorating rapidly due to the lasing of the TEM_{01} mode at about 24.3 kA/cm^2 as determined previously.

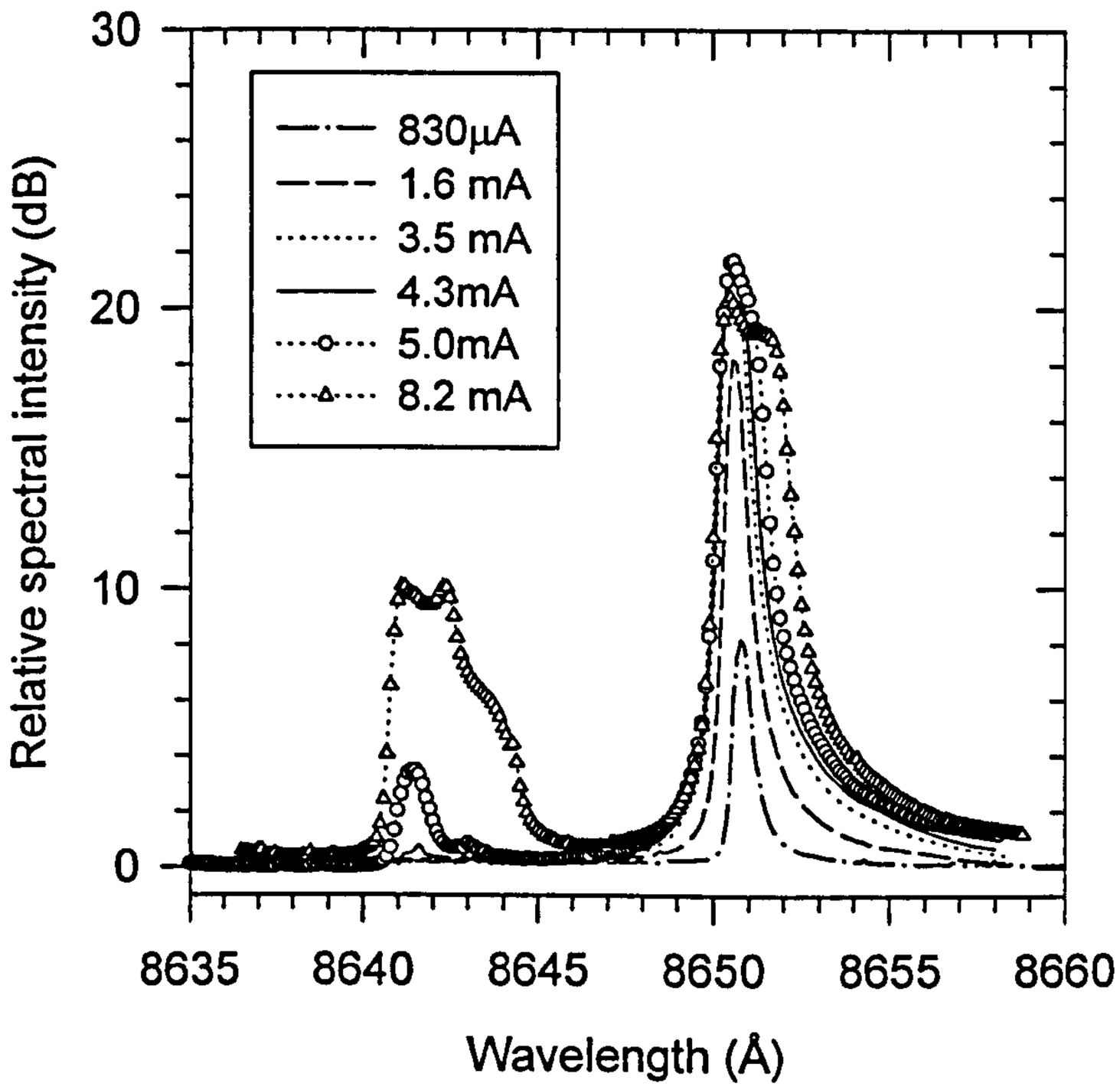

Figure 6.16 : Lasing spectra (pulsed) of the 4.3μm near-square device at various current injection levels. The threshold current of the TEM_{00} mode is 830μA while that of TEM_{01}/TEM_{10} mode is 4.1mA.

Figure 6.16 illustrates how the lasing spectra of the same 4.3μm device evolves when measured under pulsed conditions. The polarisation resolved pulsed L-I characteristics suggests that the higher order mode should turn on at 4.0mA, and indeed an obvious peak of the TEM_{01} mode appears at 4.3mA. Despite of the use of

short electrical pulse (40ns, 50kHz) and large mark-space ratio (500), the residual heating at high current injection results in frequency chirping in the lasing spectrum, i.e. thermal induced broadening of the spectral linewidth. It should also be noted that increasing the mark-space ratio to 2500 does not seems to affect the turn on of the higher order mode, but helps to slightly reduce the residual chirping effect.

Using the same approach as described above, the threshold current of the "first" higher order mode is determined for devices of various aperture sizes. These results for the strong, medium and weak guiding devices are illustrated in Figures 6.17 to 6.19 respectively, together with data points indicating the current density at which thermal rollover happens during cw operation. It was found that in all cases the fundamental TEM_{00} mode and the higher order TEM_{01} and TEM_{10} modes turn on almost simultaneously for devices with aperture size larger than 6.2μm. For smaller devices, the difference in the threshold currents of the fundamental and higher order modes widens rapidly with reduction in aperture size. Due to the near-square shape of the oxide apertures, the onset currents for the TEM_{01} and TEM_{10} modes are very close, and it is usually the one with the shorter resonant wavelength and thus closer to gain peak that turns on first.

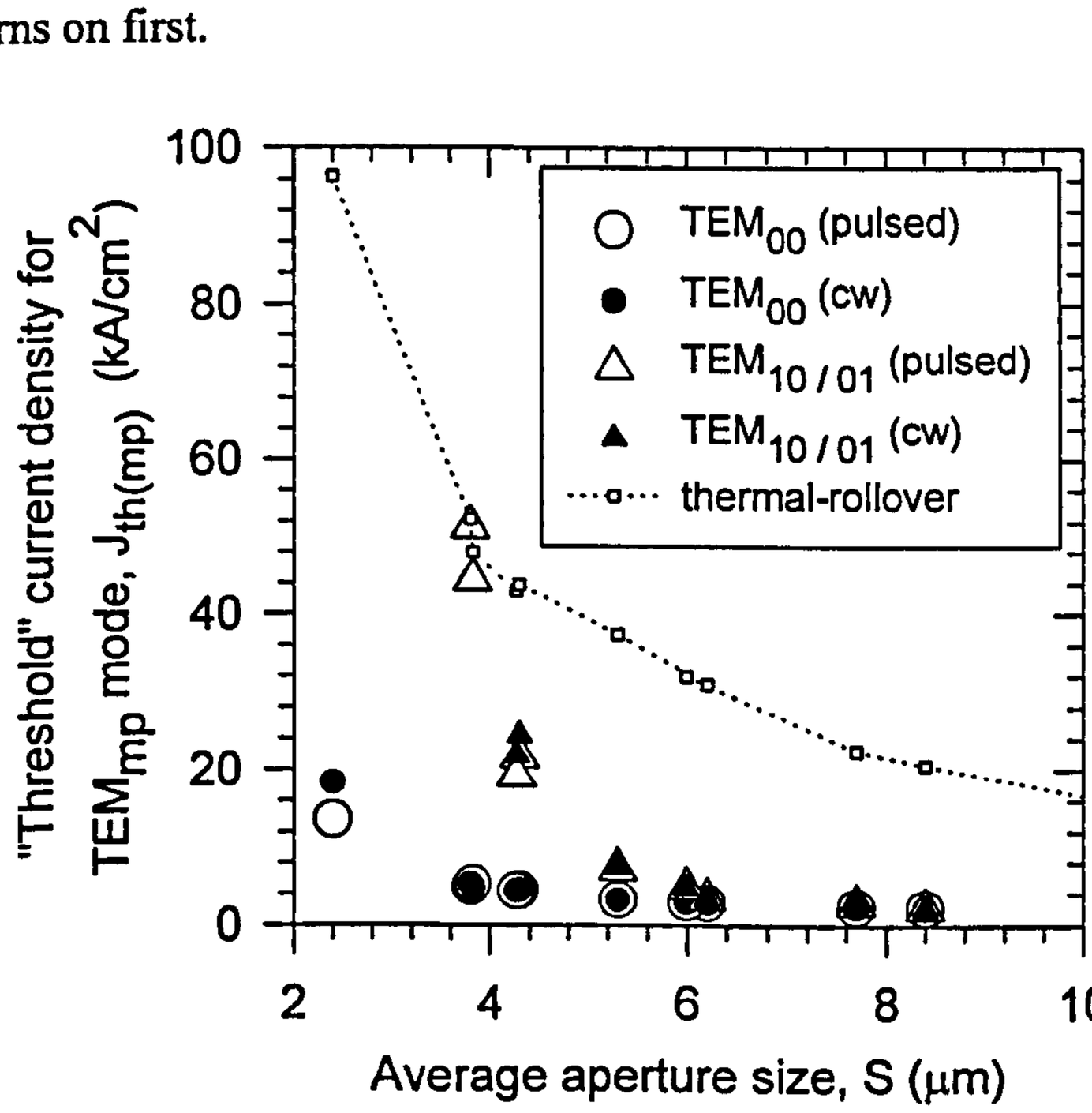

Figure 6.17 : Variations of threshold current densities of the TEM_{00} and TEM_{10}/ TEM_{01} modes with oxide aperture size for "strong guiding" devices.

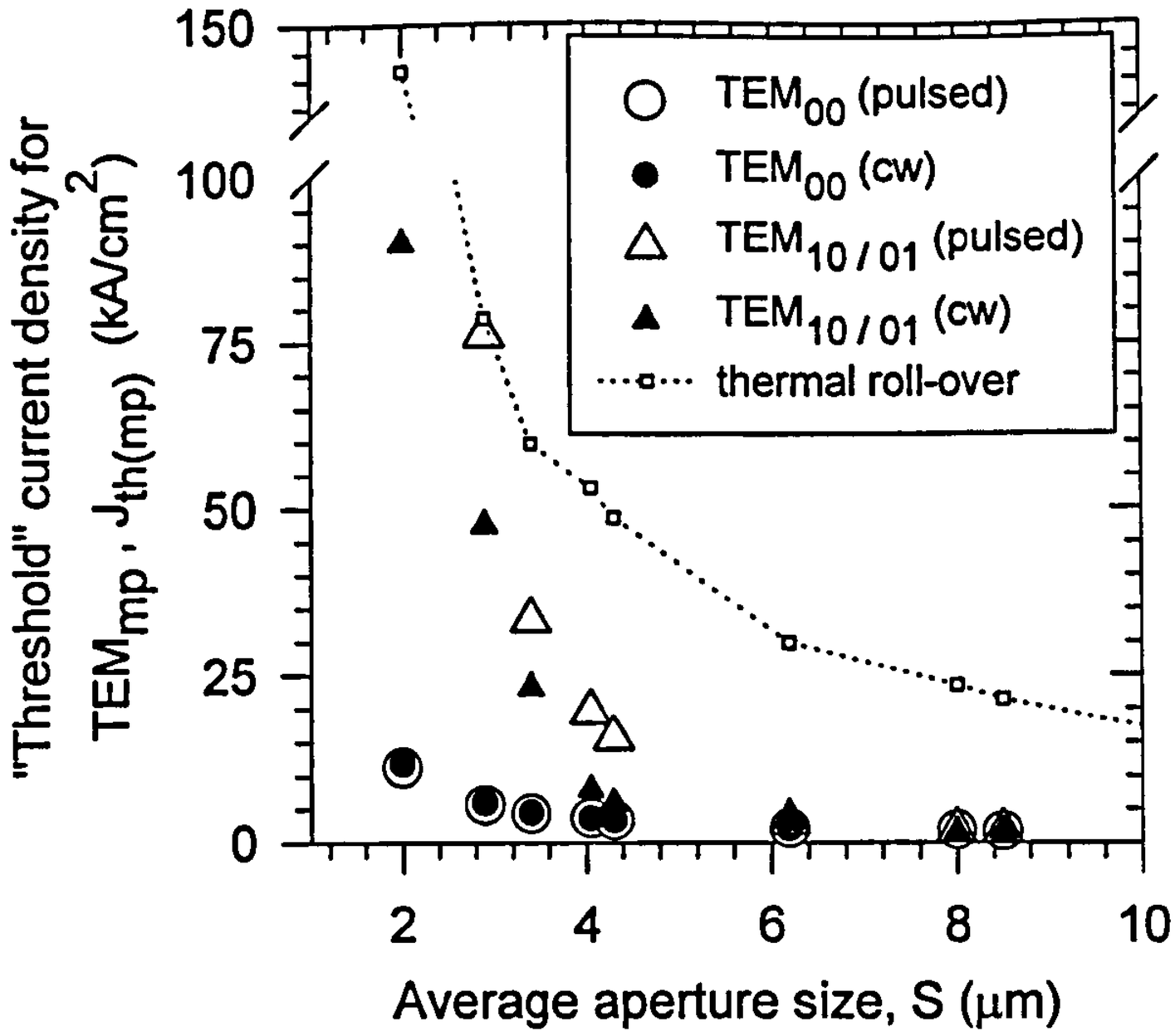

Figure 6.18 : Variations of threshold current densities of the TEM_{00} and TEM_{10}/ TEM_{01} modes with oxide aperture size for "medium guiding" devices

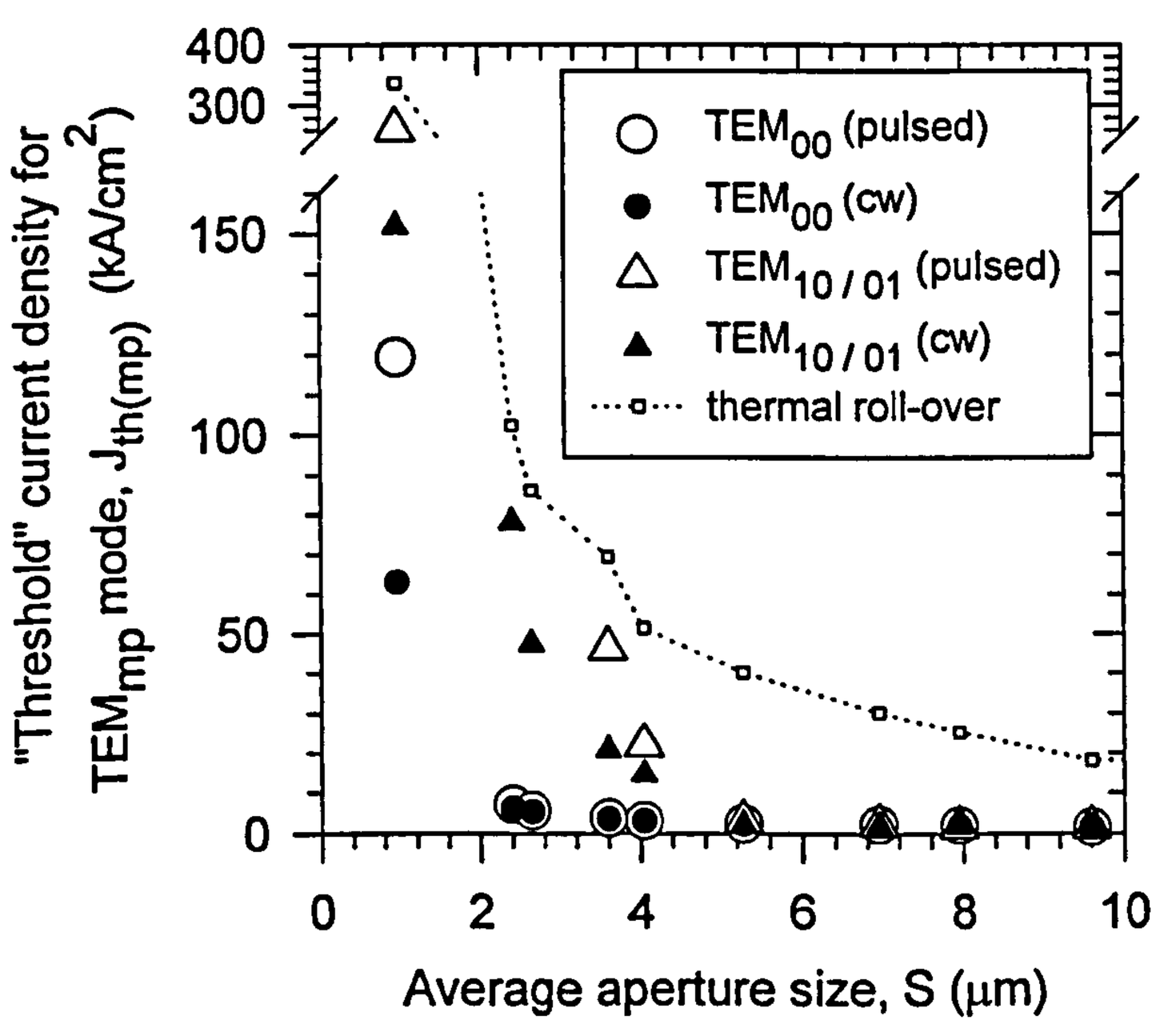

Figure 6.19 : Variations of threshold current densities of the TEM_{00} and TEM_{10}/ TEM_{01} modes with oxide aperture size for "weak guiding" devices.

For the strong guiding devices, no higher order mode achieves lasing throughout the whole driving range (i.e. defined as up to 30% above the thermal roll-

over) under the cw condition when the aperture size is 3.8μm or smaller. Under pulsed conditions, however, only the 2.4μm device allows no onset of higher order modes in a similar driving range. Thus, it is likely that thermal induced effects such as carrier leakage, thermal lensing or change in spectral gain offset, which become quite significant at the high current density injection level are helping to suppress the higher modes under cw operations in the 3.8μm strong guiding device. However, the opposite trend was observed for the medium and weak guiding devices with aperture size smaller than 6μm, where the cw thresholds of the higher order modes are always lower than that measured under pulsed conditions. It is believed that in these cases, the modal gains of the TEM_{01} and/or TEM_{10} modes improve under the cw condition as a result of mode size contraction caused by thermal lensing effect. As pointed out in section 5.4.4(B), if the associated increase in diffraction loss is less significant, as is most likely to occur in the cases considered here, the increase in modal gain thus leads to reduction in the threshold of the first higher order mode. However, under pulsed conditions, no higher order mode achieves lasing within the whole driving range for weak guiding device of 2.4μm and medium guiding device of 2.0μm.

The effects of thermal lensing on single mode operation are especially obvious in the 2.4μm and 2.6μm weak guiding devices as well as the 2.0μm medium guiding device, where the excitation of higher order modes occurs within the driving range under cw conditions but not under pulsed conditions. Referring to Fig.4.13 in chapter 4, ideally at these sizes all the higher order modes should have been cut off due to the loss of optical confinement by the oxide aperture. Hence, the higher order modes that appear under cw conditions are due to the combined index guiding from the oxide aperture and the thermal lens. This is of course, consistent with the distinctive change of trend in the measured resonant wavelength separations shown in Fig. 4.13 at these sizes. As for the 1μm weak guiding device, the near field pattern of the "higher" order mode (not shown here) that lases even under pulsed conditions, does not centre on that of the fundamental mode and the oxide aperture. Thus, it is most likely that the excitation of this higher order mode is mainly due to the carrier induced index change and possibly some residual heating effect during the short-pulsed excitation in such a highly resistive ultra-small device.

In order to compare the single mode performance of the devices with three different oxide thicknesses, the threshold current densities of the higher order modes

of these devices are plotted as a function of average aperture size (S) in Figure 6.20 for those measured under cw conditions, and both Figures 6.21 and 6.22 for pulsed conditions. In Fig.6.21, the theoretical predictions that take into account the difference in absorption levels of the DBRs between the three types of devices but excludes the "scattering losses" effects, are also included for comparison. In Fig. 6.22, however, the theoretical curves do take into account the scattering losses by using the same α_{ox} values determined earlier in section 6.2.1 to correct for the cold cavity photon lifetime of TEM_{10} mode.

Comparing the experimental results, the single mode performances of the strong and weak guiding devices are comparable under the pulsed conditions. Both types of device are superior to the medium guiding devices in suppressing the higher order modes, especially in those devices with aperture sizes in the range of 2.0 to 4.0μm. On the other hand, under cw conditions it is now the weak and medium guiding devices that are comparable in their single mode performance. Both types of device are much more affected by the thermal lensing effect than the strong guiding devices, where in these latter devices the higher order modes are suppressed within the driving range once the aperture size becomes 3.8μm or smaller. As shown in Fig. 6.10, thermal heating effects in these three types of devices are very similar since the aperture size dependence of the current density at which thermal rollover happens is almost identical. Therefore, it is fair to conclude that strong guiding devices (2.0 to 4.5μm) manage to suppress the lasing of higher order modes better than others under cw conditions.

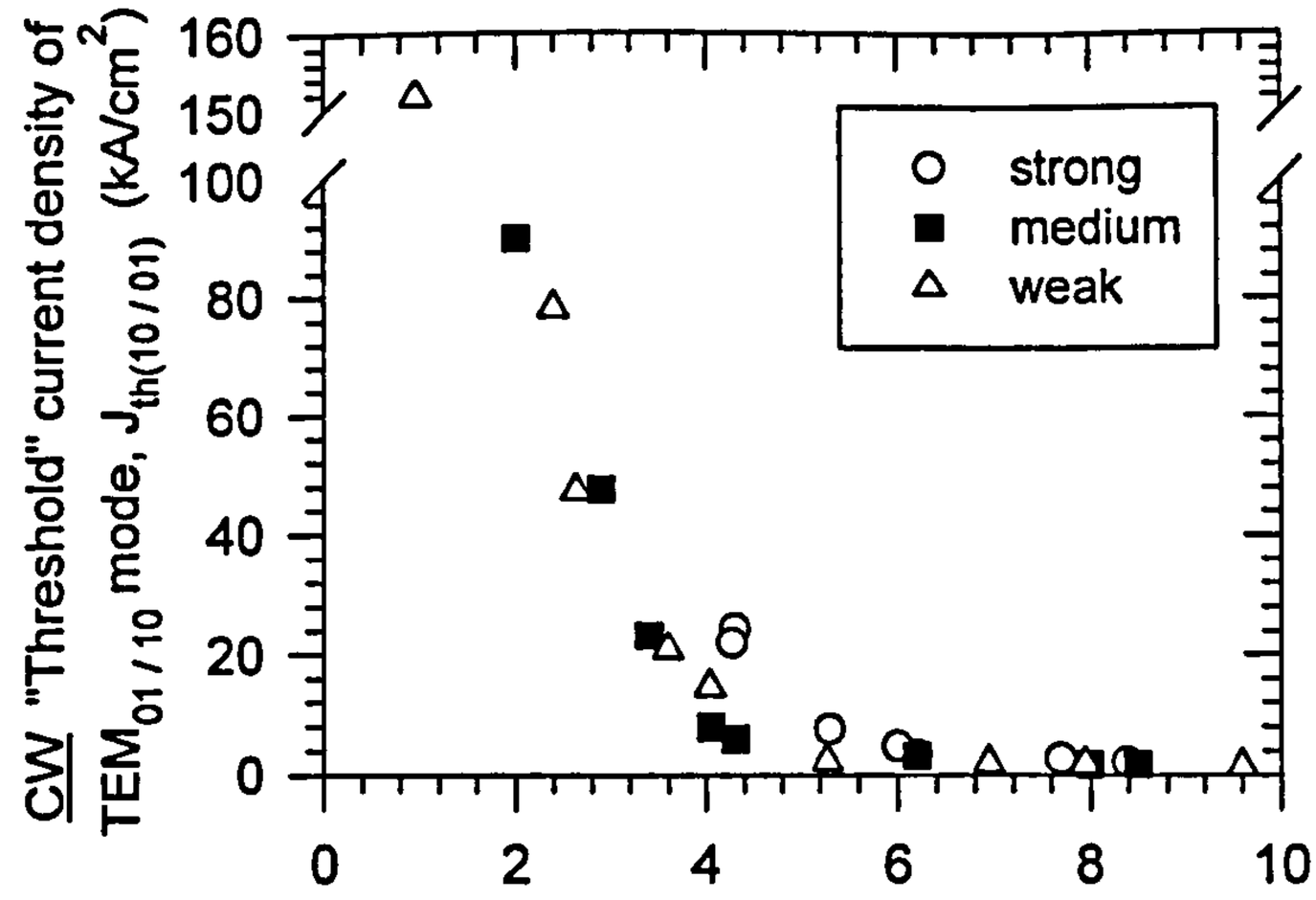

Figure 6.20 : Variation of *cw* threshold current densities of the TEM_{10} or TEM_{01} modes with oxide aperture size for the strong, medium and weak guiding devices. (Experimental values only)

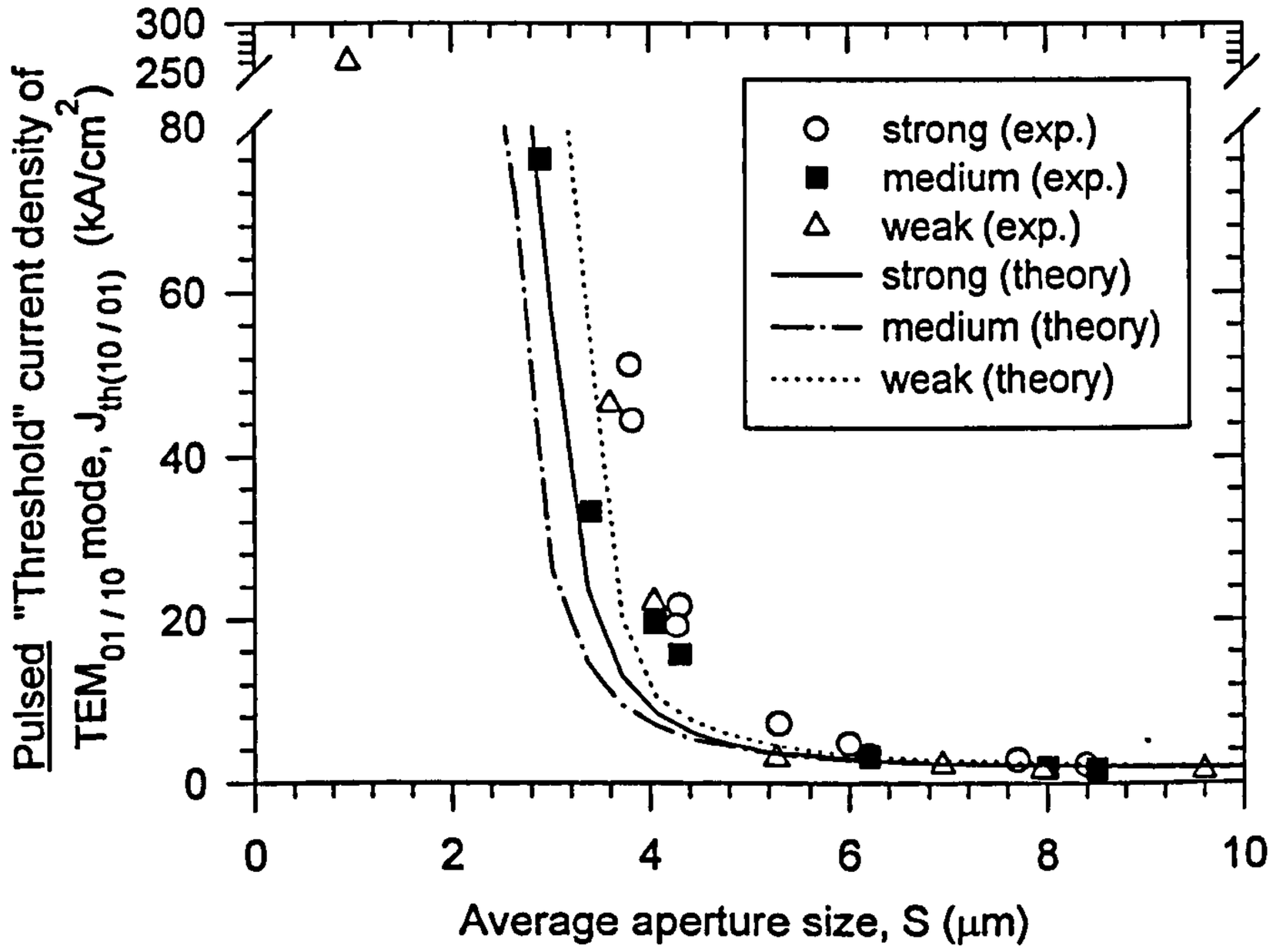

Figure 6.21 : Variations of ***pulsed*** threshold current densities of the TEM_{10} or TEM_{01} modes with oxide aperture size for the strong, medium and weak guiding devices. Theoretical predictions that **exclude** "scattering loss" effects are also included for comparison.

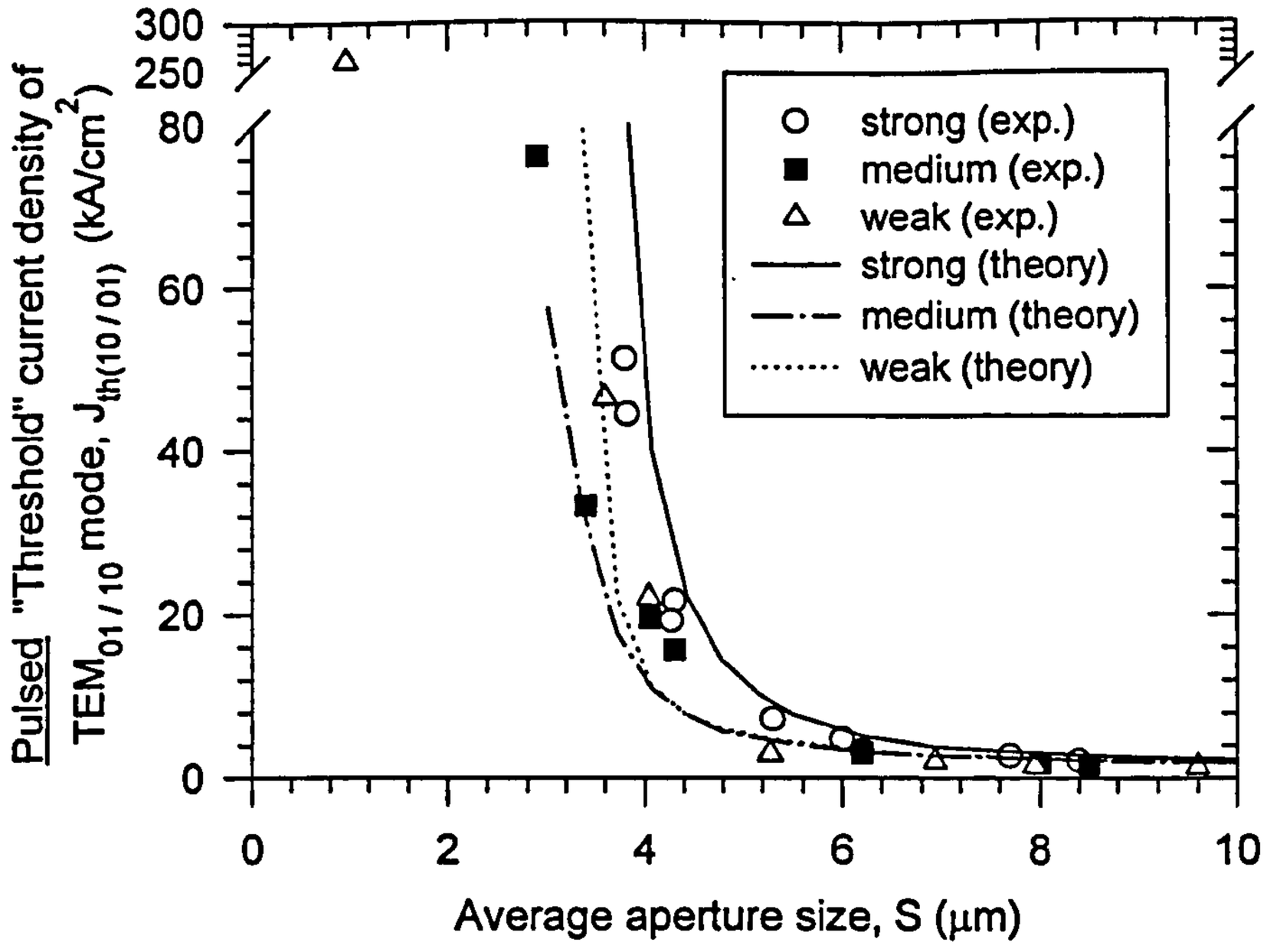

Figure 6.20 : Variations of ***pulsed*** threshold current densities of the TEM_{10} or TEM_{01} modes with oxide aperture size for the strong, medium and weak guiding devices. Theoretical predictions that **include** "scattering loss" effects are also included for comparison.

As for theoretical results, the weak guiding devices are predicted to be the best in suppressing the onset of the first higher order mode, followed by the strong and medium guiding devices, if the effects of scattering loss are *excluded* (Fig. 6.21). As expected, all these predicted "minimum" threshold values are lower than the experimental values. When the scattering losses are taken into account as in Fig.6.22, strong guiding devices are predicted to have the highest threshold of the first higher order mode for aperture size smaller than about 10.0μm. Between the medium and weak guiding device, the thresholds are almost identical until the aperture size becomes smaller than about 4.0μm, when that of the latter increase much rapidly than that of the former. Quantitatively, the predicted values are always higher than the experimental values for the strong guiding devices. However, the predicted values for the medium and weak guiding devices are lower than the experimental values, until the aperture size becomes smaller than about 4.0μm. When this occurs, the experimental values are very close to the predicted values.

Recall from section 6.2.1, where it is believed that the main reason for the predicted thresholds of the TEM_{00} mode in Fig.6.6 being lower than experimental

values when the effects of scattering losses are considered, is the exclusion of carrier leakage. Since carrier leakage should be even more severe at the higher current density at which the first higher order mode lases, the results in Fig. 6.22 thus imply that the scattering losses for the higher order mode must have been over-estimated by the simple model introduced in section 6.2.1, especially in the case of strong guiding devices. Nevertheless, the results in Fig.6.21 and Fig.6.22 do confirm that scattering losses must be considered in the theoretical model in order to correctly predict the modal behaviour. Also, when the scattering losses are included, the total excess optical losses are sufficiently large such that the small differences in the DBR absorptance between these three different types of devices have no effect on the conclusions drawn above.

For most optical applications, the amount of "single mode" light power available from the laser when operated cw is also a major concern. In this work, the maximum single mode light power is taken to be the light output at current injection 95% the cw turn on threshold of the first higher order mode. For those strong guiding devices that manage to suppress the lasing of the higher order modes, the maximum total light power recorded at the verge of thermal rollover is assumed. Using these definitions, the maximum *cw* "single mode" light powers measured from devices of various aperture sizes are shown Figure 6.23. It should be noted that in reality, the values quoted in this figure also contain a small fraction of spontaneous light powers from the higher order modes. However, as can be deduced from Figure 6.24 which shows the corresponding SMSRs at which these values are measured, the contributions from the higher order modes should be negligible since all the SMSRs are larger than 20dB. Among these devices, the largest single mode power is offered by the 3.8μm strong guiding device at 1.88mW with SMSR of 36.5dB. This is closely followed by the smaller 2.4μm weak guiding device at 1.72mW with SMSR of 40.7dB, despite the onset of higher order mode within the driving range. By comparison, the 2.4μm strong guiding device only manages much lower power of 0.61mW while the SMSR stands at 41.5dB.

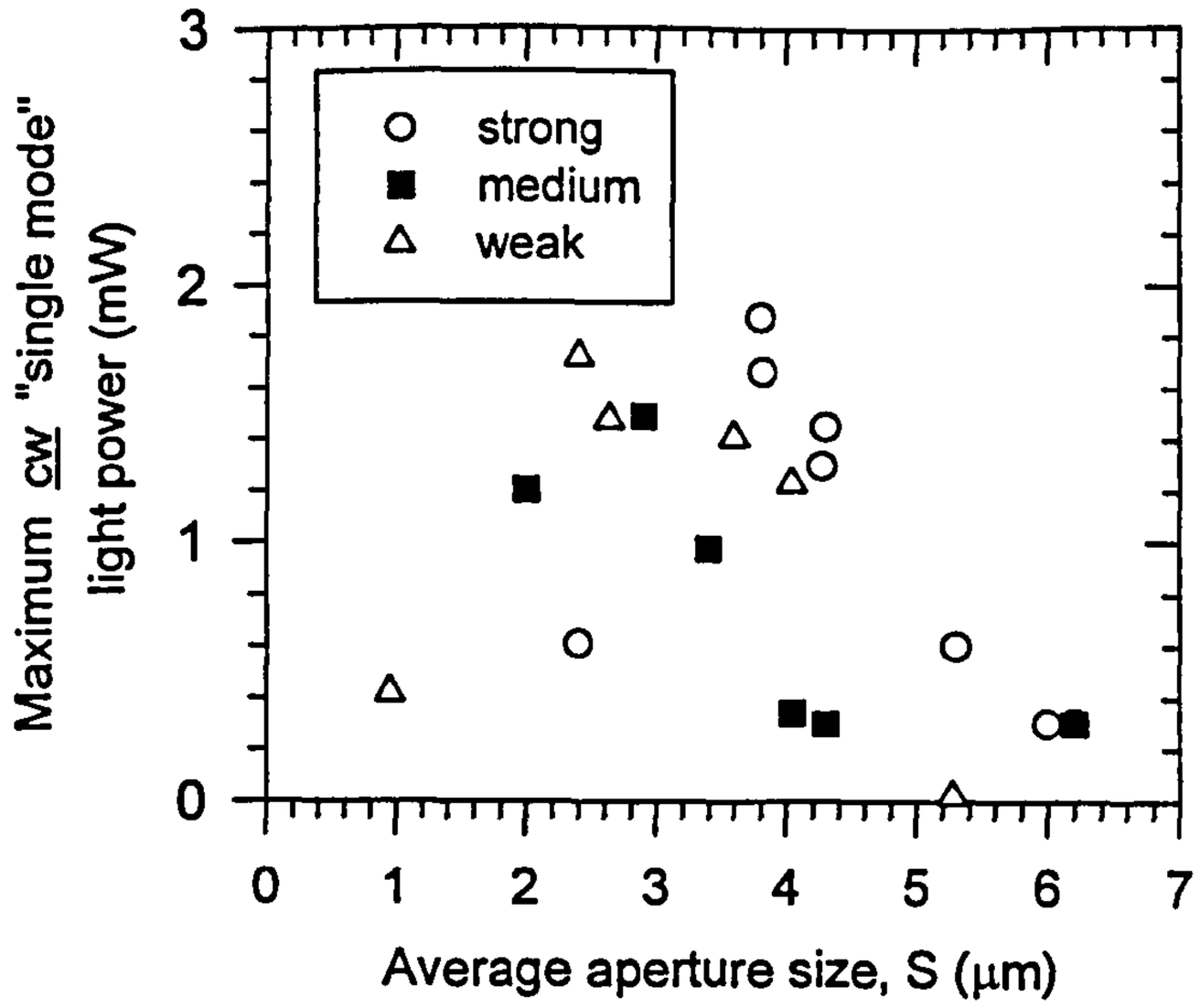

Figure 6.23 : Variation of maximum *cw* "single mode" light power with average aperture size.

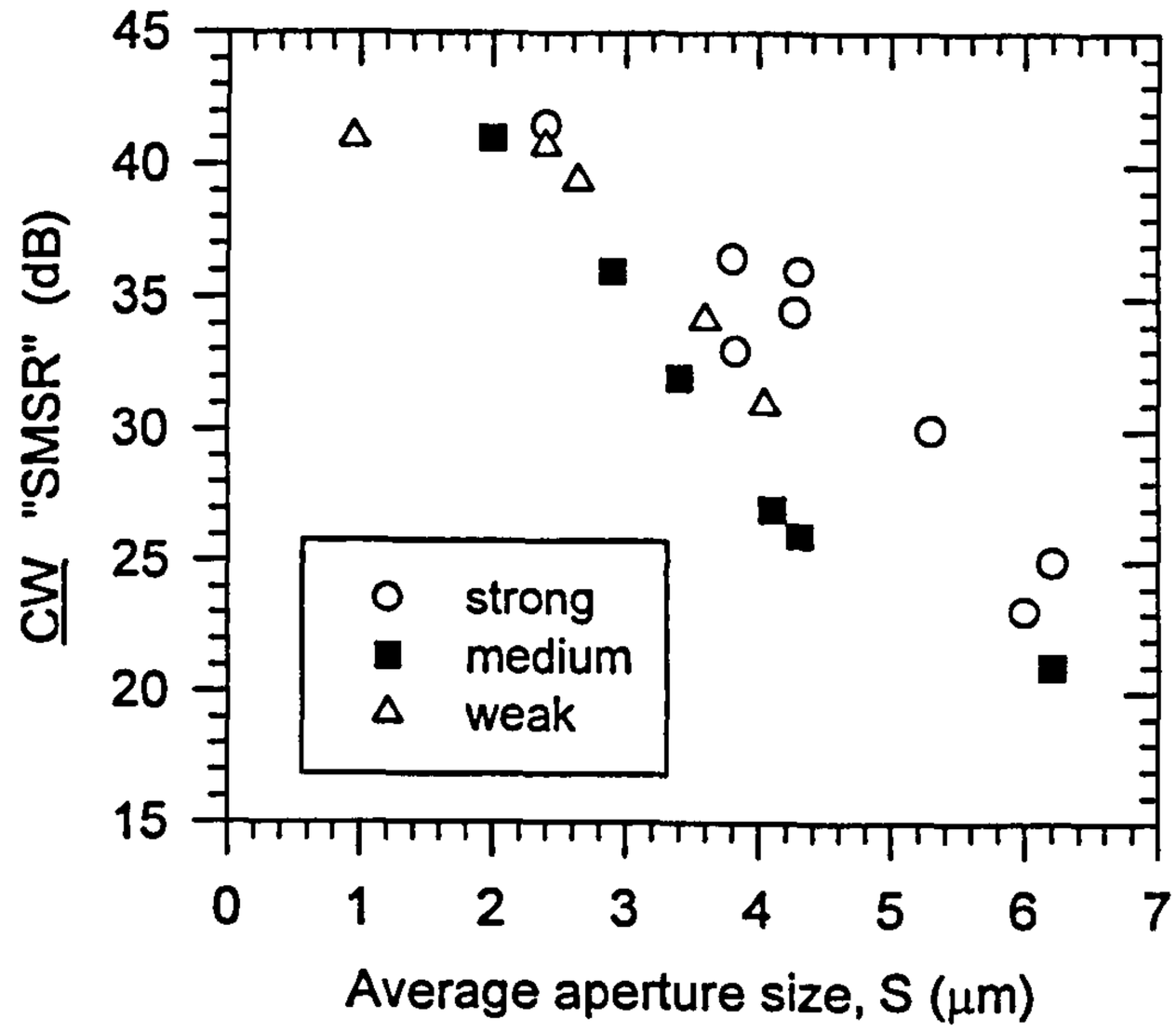

Figure 6.24 : Variation of **cw** "SMSR" with average aperture size. These values are recorded at which maximum single mode light powers are taken.

Overall, it can be said that the strong guiding devices achieve higher single mode powers when the aperture sizes are in the region around 4.0 μm. In these regions, it seems the weak guiding devices also perform better than their medium guiding counterpart. When the aperture size drops to about 2 to 2.6μm, however, the weak and medium guiding devices offer higher single mode power in spite of the fact

the higher order mode does turn on at some stage within the driving range. As for the SMSRs, these values hover around 31dB to 36dB for the strong and weak guiding devices when the aperture size are between 3.0 to 4.3μm. In this aperture size region, the values from medium guiding devices are always slightly lower. However, when the aperture sizes are smaller than about 2.6μm, these intensity ratios increase to about 40dB or higher in all cases.

When compared with the strong guiding devices, it is obvious that the weak guiding devices manage to offer comparable single mode light power for aperture sizes of between 3.5μm to 4.3μm but much higher power at smaller aperture sizes. This is mainly due to their higher differential quantum efficiencies as shown in Fig. 6.5. As illustrated in Figure 6.25, which shows the variation of the wall-plug efficiencies at which maximum single powers are recorded, this thus results in the better utilisation of electrical input power. Clearly, for aperture sizes <4μm, the weak guiding devices always yield highest "single mode wall-plug efficiency".

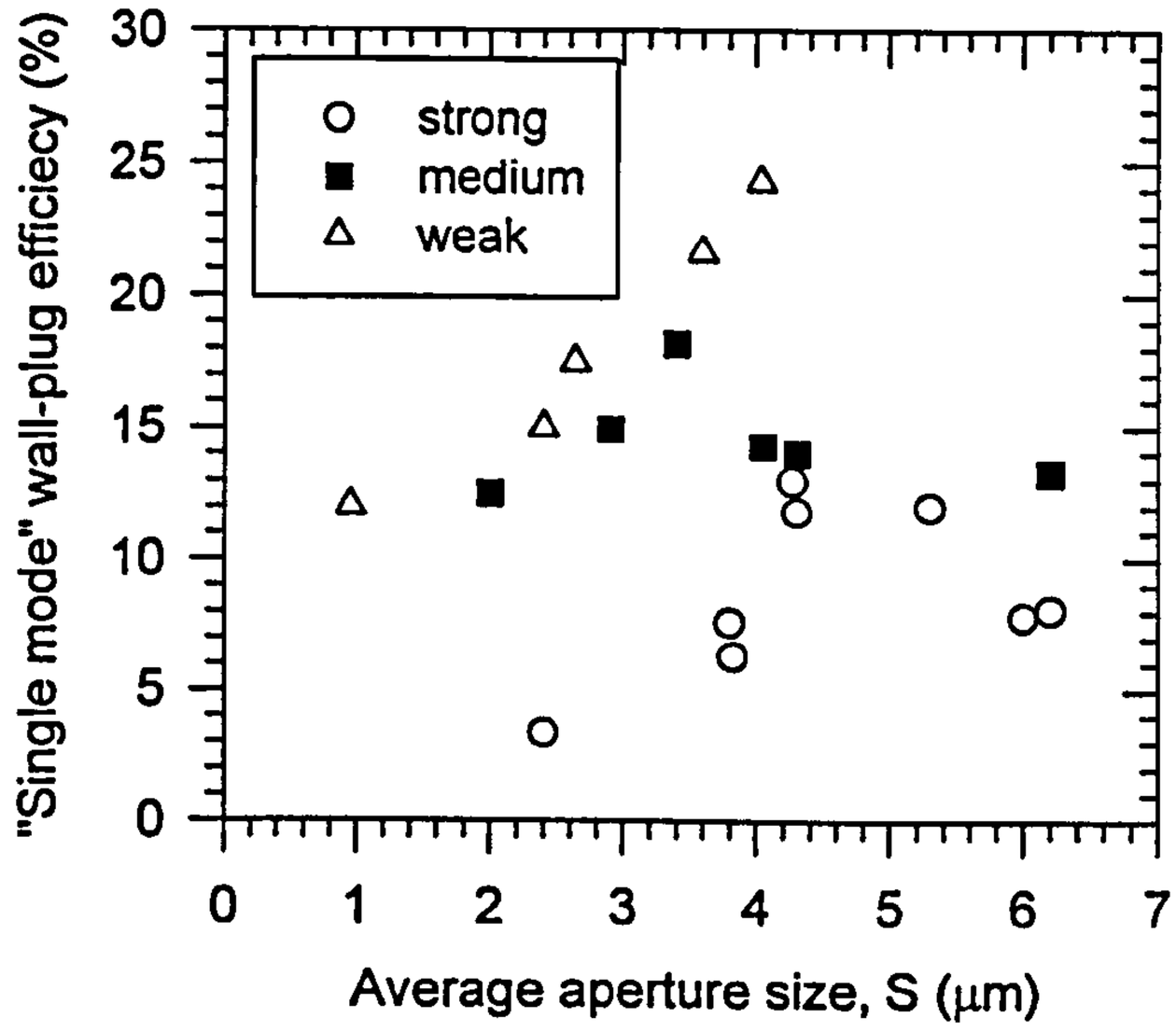

Figure 6.25 : Variation of "single mode" wall-plug efficiency with aperture size. These values are recorded at which maximum single mode light powers are taken.

In order to estimate the maximum single mode powers that can be obtained if the thermal induced effects such as thermal lensing are to be removed, Figure 6.26 plots the variations of the maximum ***pulsed*** single mode light power with aperture size. These values are obtained at current injection 95% the "pulsed" turn on threshold

of the first higher order mode except for those arrow-marked experimental points. For these devices that manage to suppress the onset of the higher order modes throughout the whole pulsed driving range, the deduced "pulsed powers" at the current density when thermal roll-over occurs are quoted. For comparisons, the predicted light powers of the fundamental TEM_{00} mode obtained at 0.95 x predicted threshold of the higher order TEM_{10} mode, are also included in this figure. The effects of scattering losses were considered during the calculations of these theoretical values.

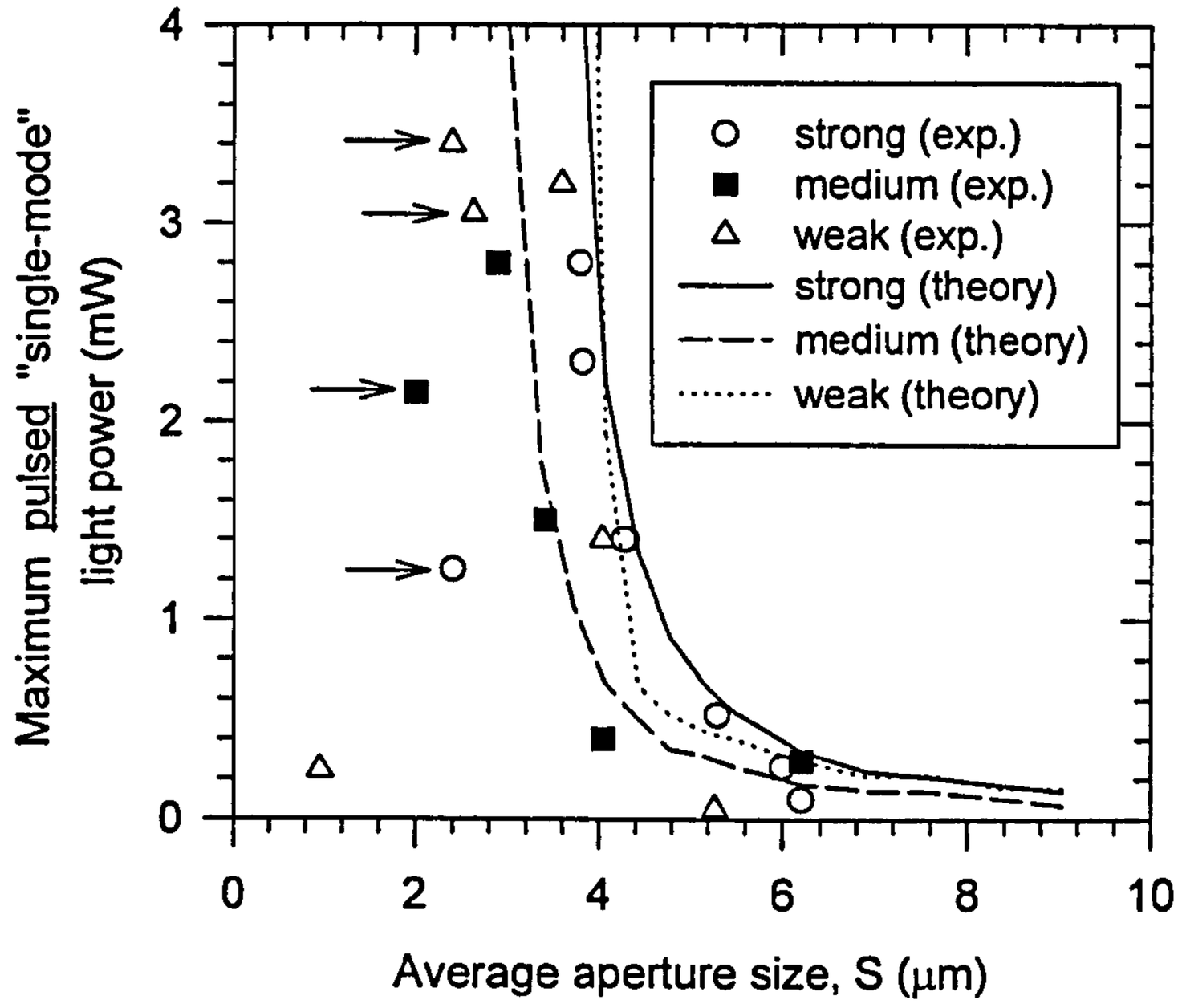

Figure 6.26 : Variation of the maximum ***pulsed*** "single mode" light power with average aperture size. The arrow-marked experimental points are the deduced pulsed light power at the current density thermal roll-off occurs. The theoretical results that take into account of the effects of scattering losses, give the predicted maximum single mode light power produced by the TEM_{00} mode.

Clearly, the predicted values are quite close to the experimental values for those non arrow-marked devices, especially for the strong and medium guiding devices. Comparing the experimental results in Fig.6.23 and Fig.6.26, in all cases when the aperture sizes are smaller than 4.0μm, the maximum single powers obtainable will be greatly improved if thermal induced effects can be minimised. These effects include thermal enhanced carrier leakage, increasing spectral offset between the resonant wavelength and the QW gain peak, reduction in peak gain, and

thermal lensing which the weak guiding devices are particularly susceptible to. At these aperture sizes (i.e. < 4.0μm), as indicated by both the experimental and theoretical results in Fig. 6.26, the maximum (pulsed) single power that can be obtained are the highest in the weak guiding devices

6.2.4 Effective Photon Lifetimes

Besides being useful in identifying the turn on current of the eigenmodes, the linewidth measurement also offer some insights into the modal gains and excess optical losses of a VCSEL. This is because the effective photon lifetime is directly related to the spontaneous emission linewidth as indicated by eqn.(5.23), as well as modal gain and optical losses as expressed in eqn. (5.58). Therefore, through the effective photon lifetime, the effectiveness of a particular eigenmode in acquiring optical gain for lasing can be monitored. Before this can be done, the actual linewidth of the emission peaks have to be deconvolved from the measured value obtained from the polarisation resolved spontaneous emission spectra. To simplify this deconvolution task, it is assumed that the frequency response of all the optical components involved in the measurement as well as the actual and resultant measured linewidths, have a Gaussian transfer function. Then, the actual linewidth can be approximated from

$$\Delta\lambda^2_{measured} = \Delta\lambda^2_{actual} + \Delta\lambda^2_1 + \Delta\lambda^2_2 + \ldots\ldots\ldots\ldots \quad (6.3)$$

where $\Delta\lambda_{measured}$ is the measured linewidth, $\Delta\lambda_{actual}$ is the actual linewidth, and $\Delta\lambda_1$, $\Delta\lambda_2$, etc. are the linewidth broadening factors of the optical components that make up the measuring system. In this work, the combined total linewidth broadening factor ($\Delta\lambda_{total}$) due to the optics such as microscope objective and polariser, and the spectrometer resolution limit is assumed to be the lasing linewidth measured at above threshold, which is about 0.35Å. (The "theoretical" resolution limit of the spectrometer is 0.30Å). Thus, the actual linewidth is extracted using

$$\Delta\lambda^2_{actual} = \Delta\lambda^2_{measured} - \Delta\lambda^2_{total} \quad (6.4)$$

This assumption is reasonable since the actual lasing linewidth of VCSELs have been determined by other researchers using various techniques, such as a scanning Fabry-Perot etalon [13] to be extremely narrow, in the order of ~ 30MHz or ~ 0.001Å.

For the 4.3μm strong guiding device whose measured spontaneous emission linewidth characteristics are shown in Fig.6.8, Figure 6.15(a) illustrates how the

effective photon lifetimes of the TEM_{00}, TEM_{01} and TEM_{10} modes polarised in <110> direction vary with cw current injection. The dotted lines demarcate the current densities at which the TEM_{00}, TEM_{01} and TEM_{10} mode turn on. The inset of Fig 6.27 also enlarges the variation of photon lifetimes at sub-threshold region. Clearly, the effective photon lifetimes of the eigenmodes increase rapidly with increased current injection. However, it is the TEM_{00} mode which has the lower optical loss and higher modal gain that achieves lasing first. After the lasing of this mode, the effective photon lifetimes and thus the modal gains of the higher order modes do not pin, but continue to increase at a slower rate than before. As discussed in section 5.4.4, this is due to the spatial hole burning by the TEM_{00} mode, which is accentuated by the thermal lensing effect under the cw conditions. Eventually, this leads to the onset of the TEM_{01} mode which is followed closely by that of TEM_{10} mode.

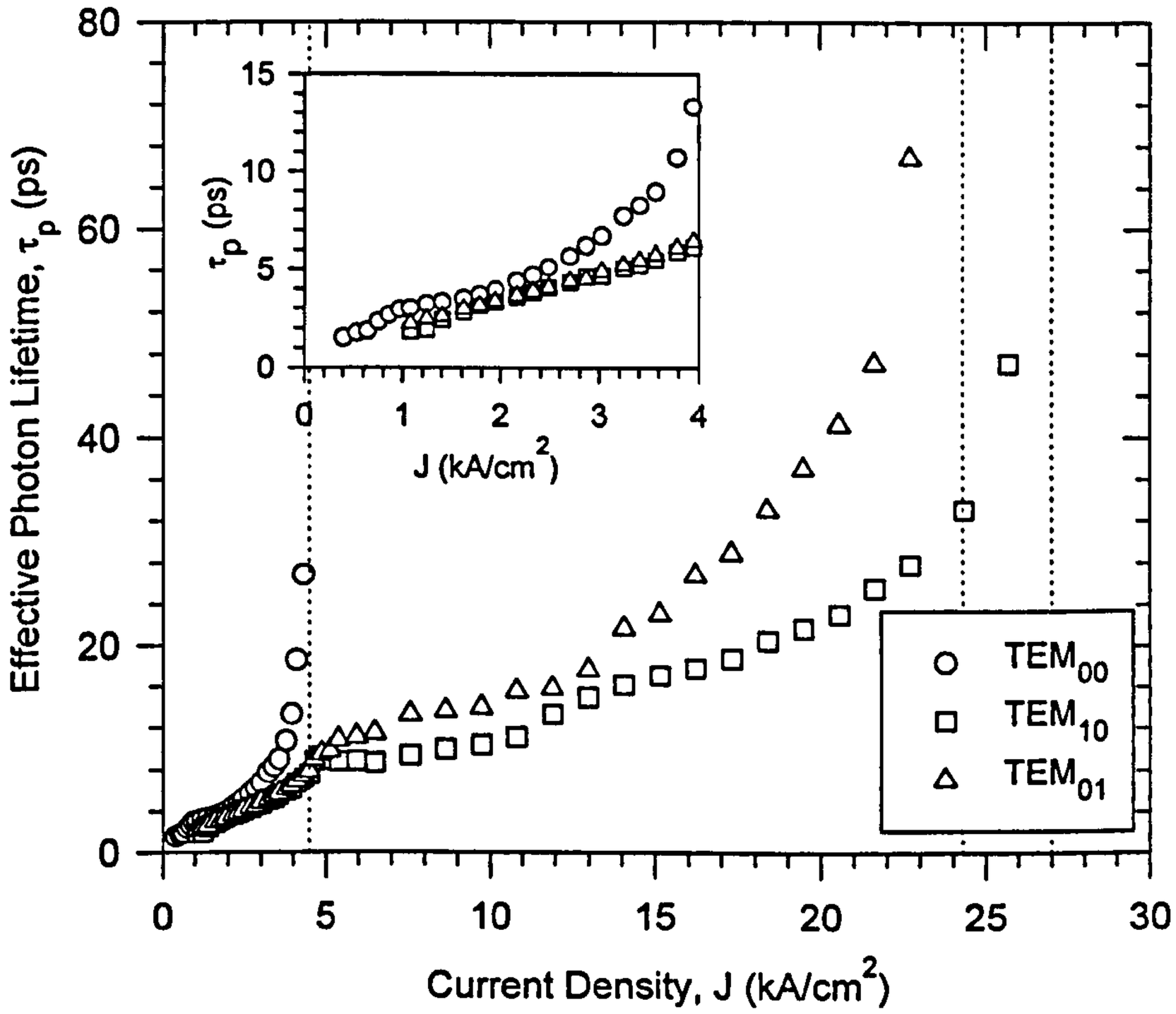

Figure 6.27 : Variation of effective photon lifetimes with current density for the 4.3μm strong guiding device. The dotted lines demarcate the threshold current densities for the TEM_{00}, TEM_{01} and TEM_{10} modes respectively.

The effective photon lifetime characteristic for the 3.8μm (3.9 x 3.7μm) strong guiding device is shown in Fig 6.28. In this case, the onset of the higher order modes

is well suppressed even beyond the thermal rollover (≈ 52.3 kA/cm^2) although the effective photon lifetimes of TEM_{01} and TEM_{10} modes do increase gradually after the lasing of the TEM_{00} mode. Nonetheless, these increases eventually taper off as the injected current density approaches the thermal rollover. According to the results from section 6.2.3, the turn on current density for the higher order mode under pulsed injection for the same device is about 51.2kA/cm^2. However, as also suggested in that section, the increased diffraction loss as a result of mode size contraction due to thermal lensing and/or thermal induced carrier leakage that becomes increasingly severe at high current injection level, may have helped to suppress the onset of higher order modes under cw operation. Other possible reasons could be the reduced optical gain from the QWs due to thermal broadening of the gain spectrum, and/or the increased spectral offset from the gain peak due to thermal induced red shift in resonant wavelengths .

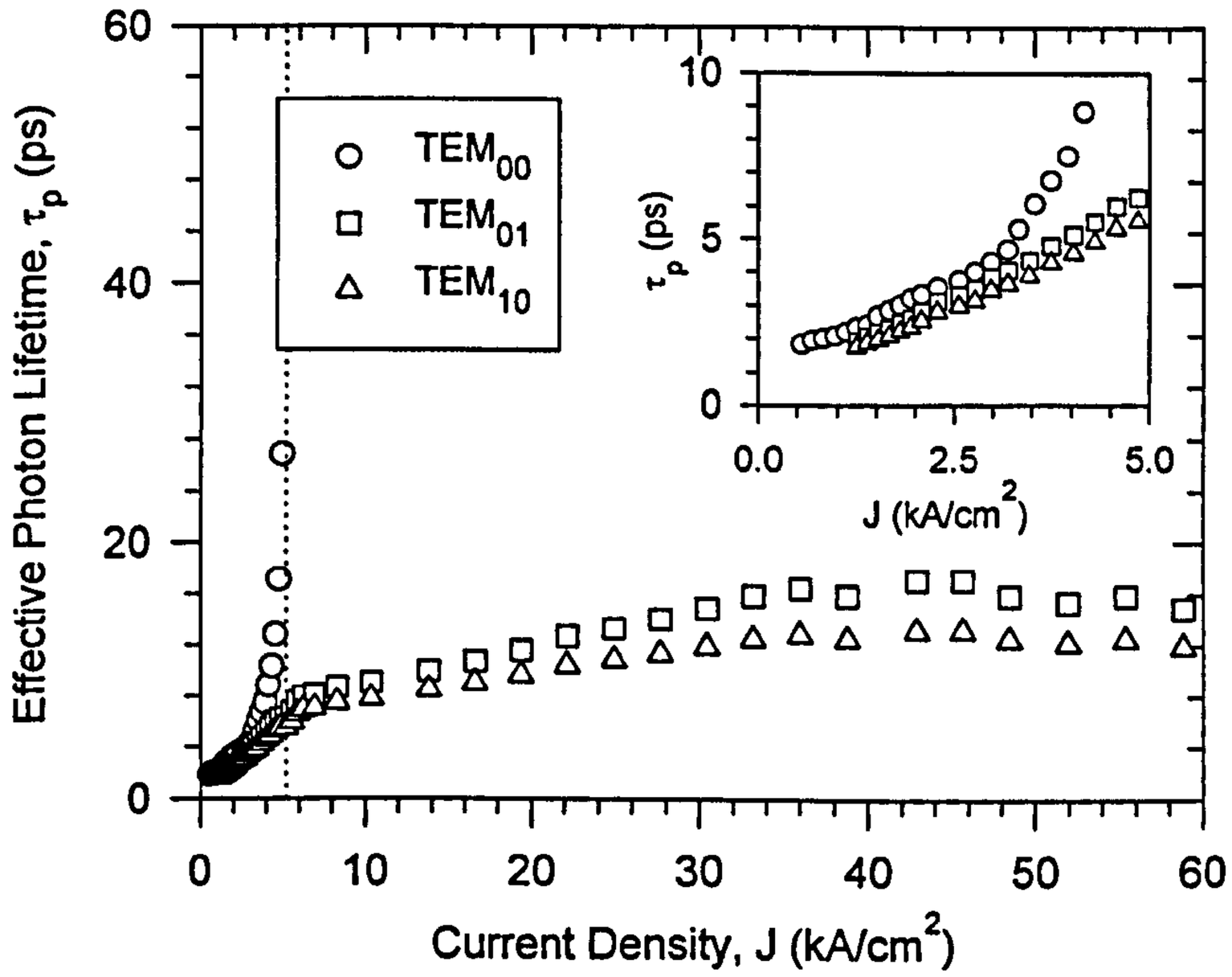

Figure 6.28 : Variation of effective photon lifetimes with current density for the 3.8μm strong guiding device. The dotted lines demarcate the threshold current densities for the TEM_{00} mode.

As mentioned in section 5.4.4, it is difficult to identify the cold cavity photon lifetime from the τ_p - J characteristics such as those shown in Fig. 6.27 and Fig. 6.28. Therefore, comparisons for the TEM_{00} mode are made through the effective photon lifetimes deduced at a particular injected current density below threshold for all

devices, which is chosen to be 1.0 kA/cm^2 in this work. The measured values obtained at this current densities for the strong, medium and weak guiding devices are shown in Figure 6.29, where the theoretical results that take account of the effects of scattering losses are also included for comparison. In all cases, as predicted, the effective photon lifetime decreases with reduction in aperture size. However, due to the lower size dependent excess optical losses experienced, the effective photon lifetimes of the weak guiding devices are always the highest at all aperture sizes, mainly because they have the highest cold cavity photon lifetime. This is followed by the medium and strong guiding devices in descending order. As for the theoretical results, the predicted values are very close to the measured values for the strong guiding devices, but underestimate those of medium and weak guiding devices, especially for devices bigger than 4.0μm. Nevertheless, qualitatively the theoretical model does correctly predict the order of the values for the three different type of devices i.e. weak guiding the highest and strong guiding the lowest.

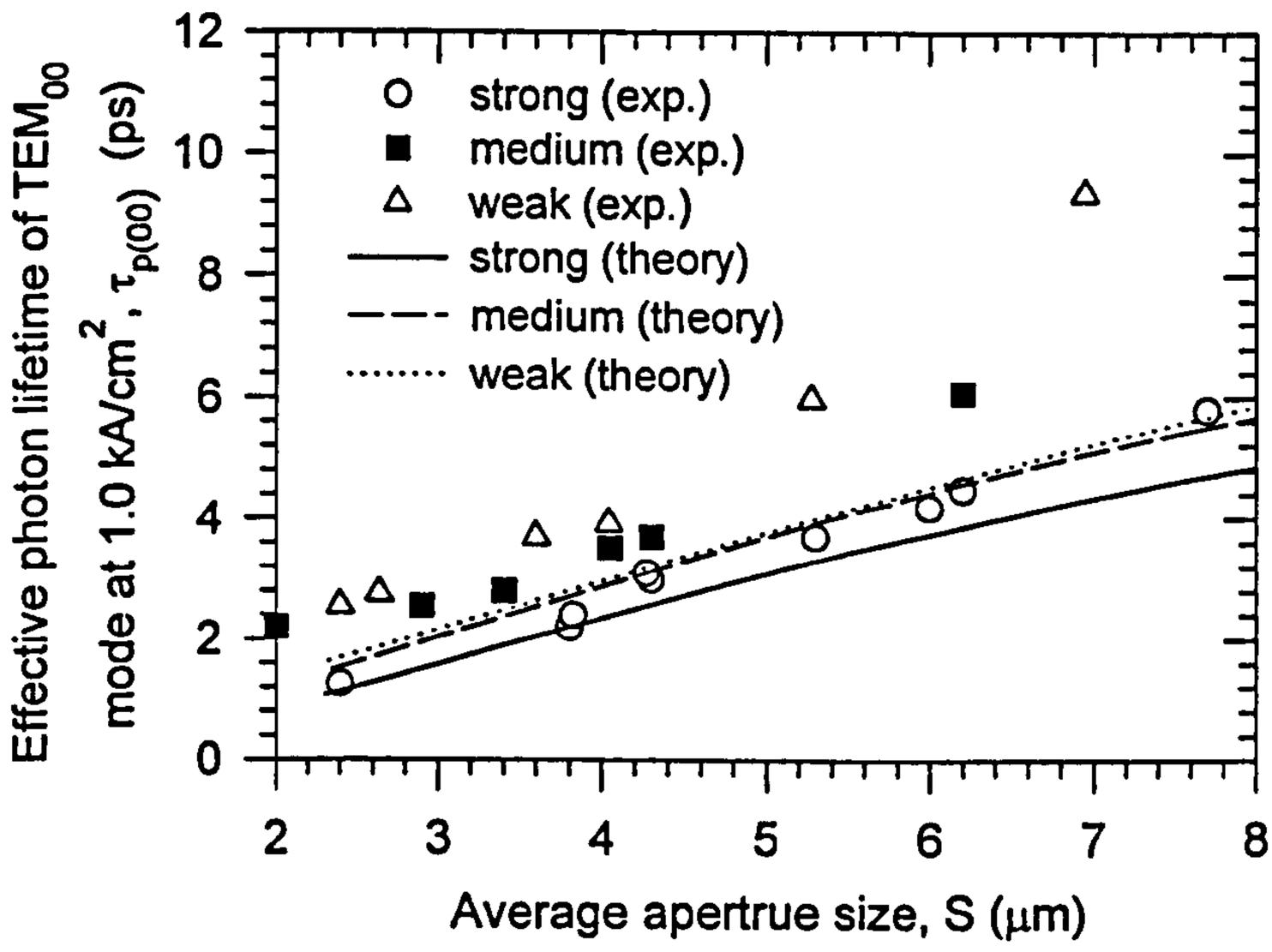

Figure 6.29 : Effective photon lifetimes of the TEM_{00} mode at injected current densities of 1.0 kA/cm^2. The effects of "scattering loss" have been taken into account of, in the theoretical results.

In section 5.4.4(B), it has been shown that eigenmode with smaller mode size experiences higher modal gain or lower modal absorption for a given current density. However, the experimental results in Fig. 6.29 indicate that the strong guiding devices which have smaller mode sizes than the medium and weak guiding devices, always

have lower effective photon lifetime. Therefore, this implies that strong guiding devices suffer from higher size dependent excess optical loss (i.e. lower cold cavity lifetimes) than the other two type of devices. Similarly, these results also imply that the excess optical losses are the least in the weak guiding devices.

Next, the effective photon lifetimes of the first higher order mode (i.e. TEM_{01}/ TEM_{10} mode) determined at threshold current density of the TEM_{00} mode ($J_{th(00)}$), are also illustrated in Figure 6.30 for the strong and medium guiding devices. The theoretical results that take account of the scattering loss using eq. (6.1) are also included for comparison. The results of weak guiding devices are not available because their much smaller spectral splitting between the TEM_{01} and TEM_{10} modes prevent any reasonable deduction of their linewidths. As in the case of the fundamental mode, the photon lifetimes decreases as the excess optical losses increases with reduction in aperture size. For both type of devices, the theoretical results also underestimate the effective photon lifetimes.

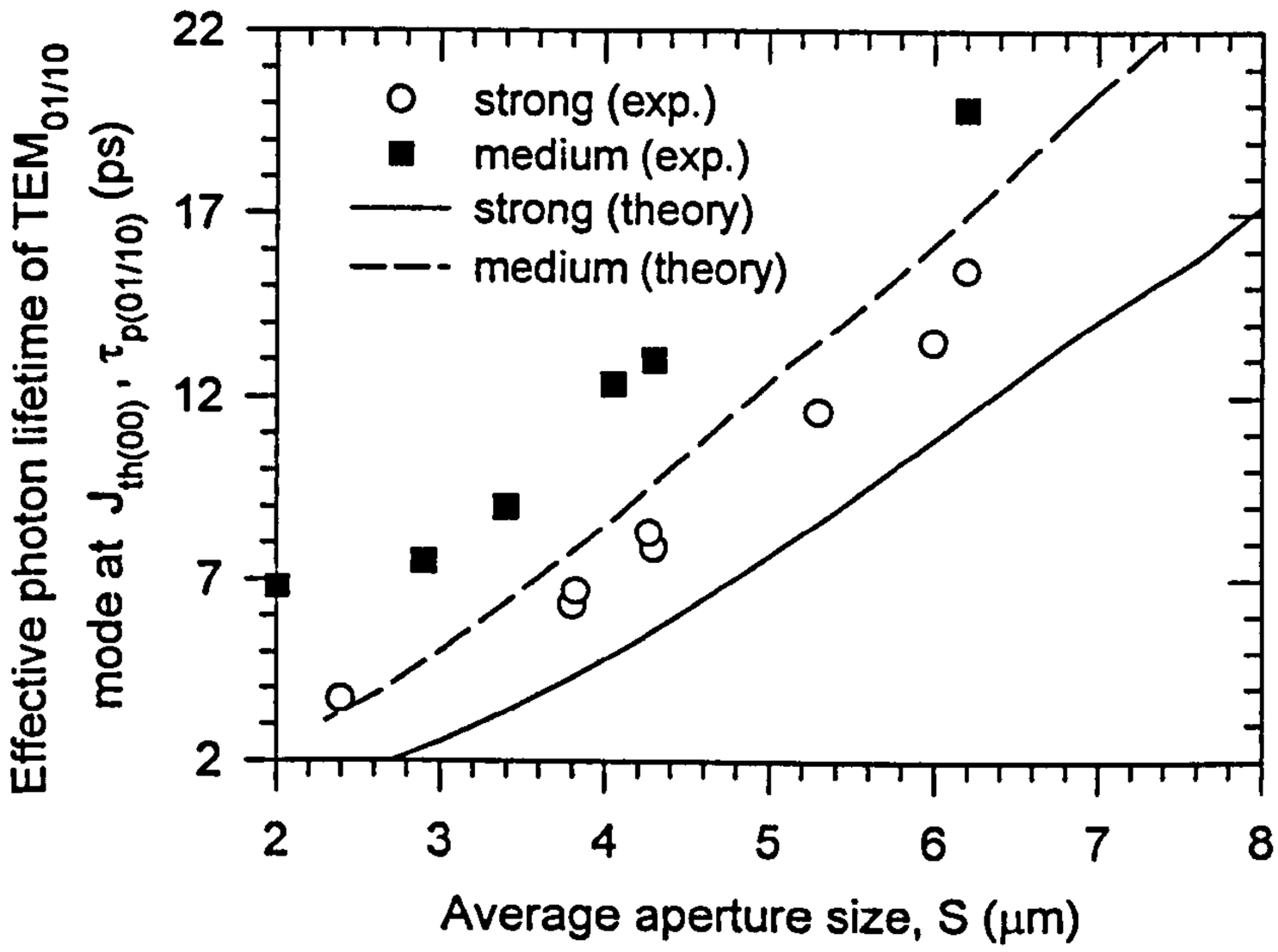

Figure 6.30 : Effective photon lifetimes of the TEM_{01}/TEM_{10} modes measured at threshold current density of TEM_{00} mode, $J_{th(00)}$.

Recall from section 6.2.3 (or Fig. 6.22) that the first higher order mode turns on at higher current density in the strong guiding devices. Since these devices have smaller mode sizes, they should thus have higher modal gain at $J_{th(00)}$ than the medium guiding devices. However, the results in Fig.6.30 indicate that strong guiding devices have lower effective photon lifetimes at all aperture sizes. Hence, these results imply

that the higher order modes suffer from larger excess optical losses in strong guiding devices than in medium guiding devices. This thus make the strong guiding devices better in suppressing the onset of higher order mode after the lasing of fundamental mode.

6.2.5 Thermal Characteristics

In section 3.4.1, based on the experimental results obtained from broad area stripe lasers made from the VCSEL materials, the gain peak wavelength is estimated to be below 863nm, which is blue shifted with respect to the resonant wavelengths of the devices assessed in previous sections. In order to confirm this, the temperature dependence of the threshold current densities were investigated by warming up devices intentionally on a Peltier heater stage. Although both the resonant and gain peak wavelengths increase with temperature, the latter usually increases at a rate of 4 - 6 times faster than the former [14]. Hence, for a device with blue shifted gain peak at ambient and operated under pulsed conditions, a minimum in the threshold current density is thus expected when the variation in stage temperature causes the offset between the resonant and gain peak wavelengths to change sign.

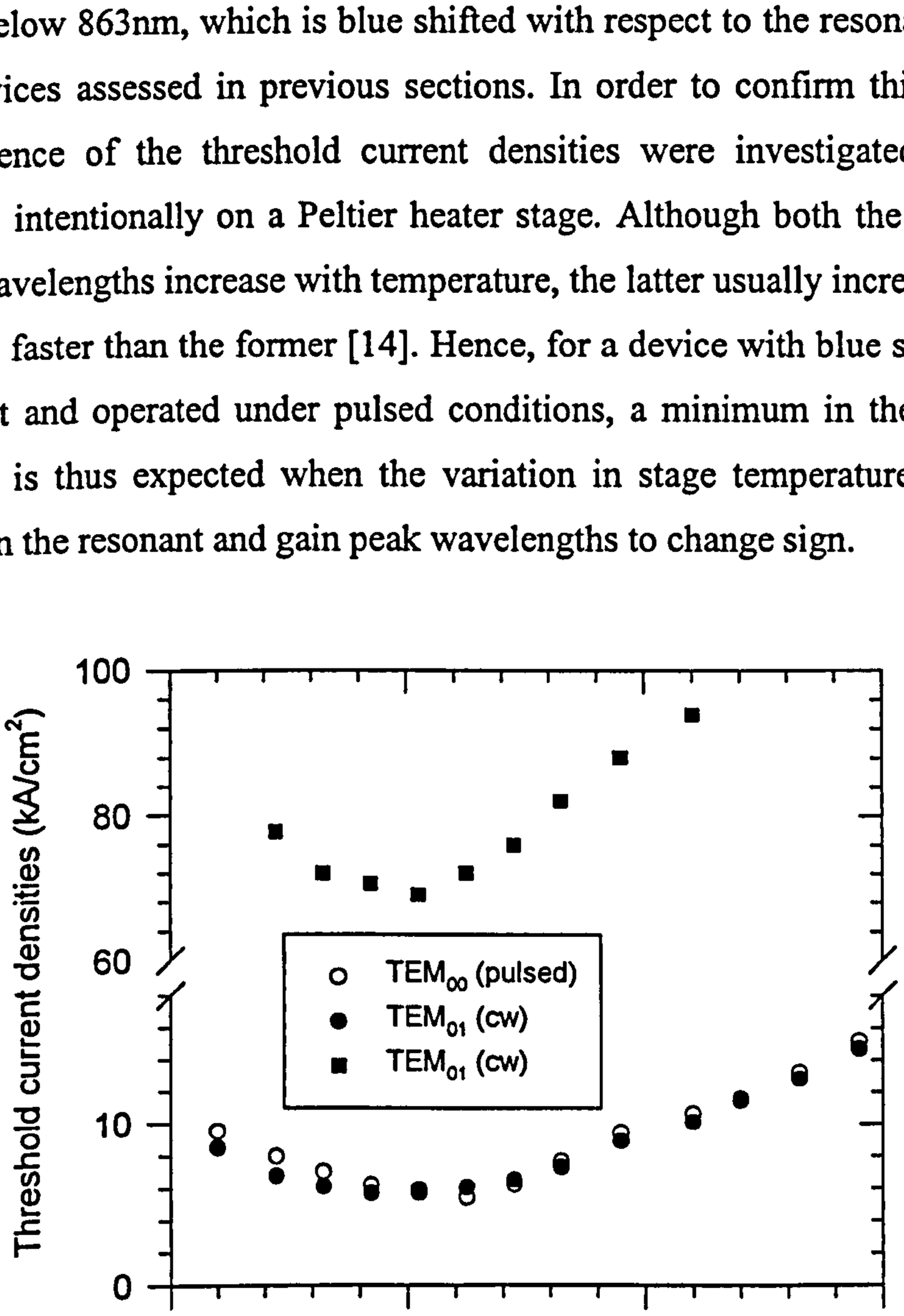

Figure 6.31 : Temperature dependence of threshold current densities for the 2.4μm weak guiding device.

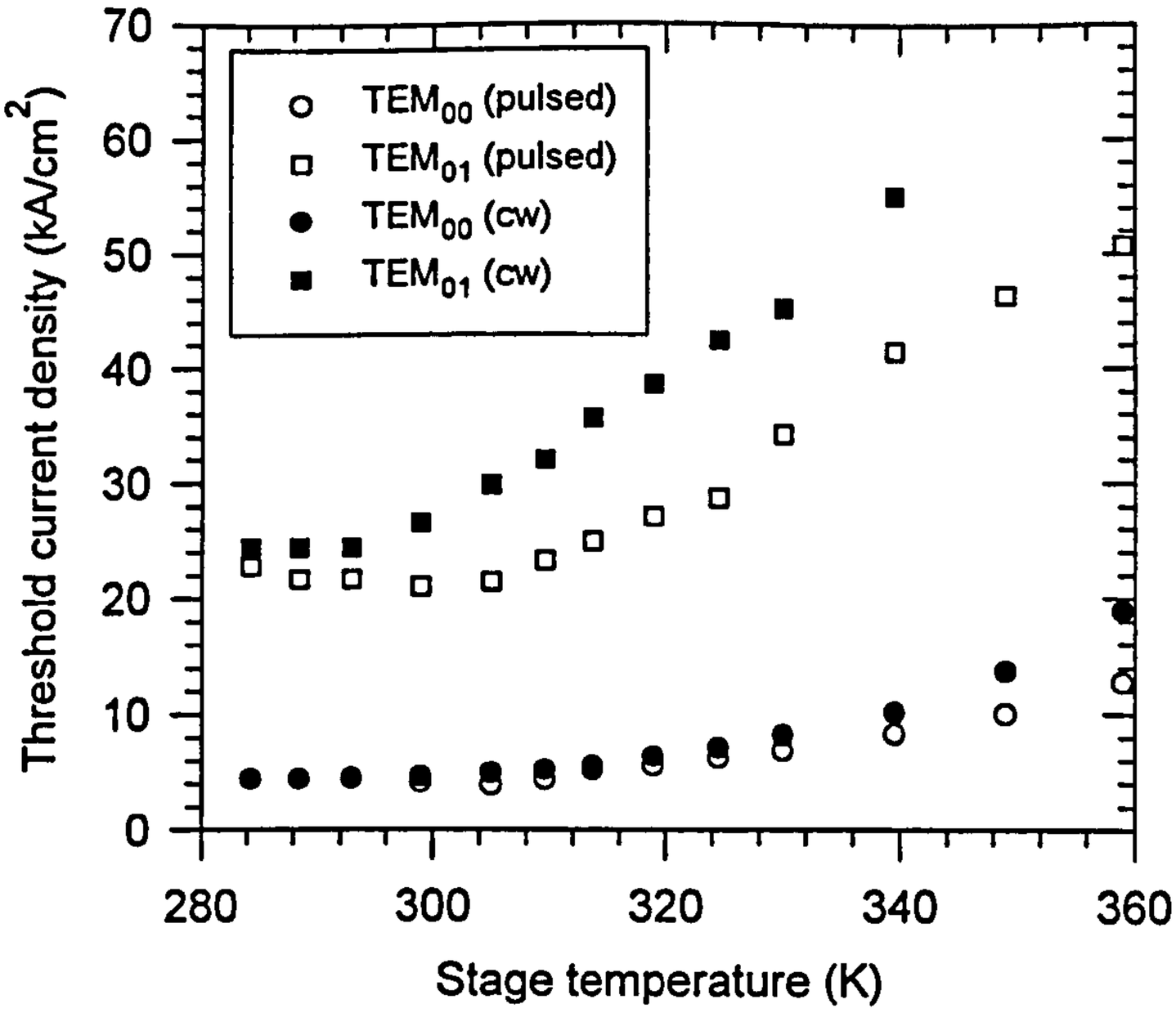

Figure 6.32 : Temperature dependence of threshold current densities for the 4.3μm strong guiding device.

The devices investigated are the 2.4μm weak guiding and 4.3μm strong guiding devices, and the temperature dependence of threshold current densities under both cw and pulsed conditions of these devices are illustrated in Figure 6.31 and Figure 6.32 respectively. As expected, minimum values of the threshold current densities could be obtained from both devices when the stage temperature was varied. For both devices, the minimum pulsed threshold current density of the TEM_{00} mode was achieved when the stage temperatures was raised to between 10K and 15K above the ambient temperature of 293K, assuming the device internal temperature is equivalent to the ambient during pulsed operation. Within the temperature range shown, it is found that the TEM_{00} lasing wavelength at pulsed threshold increases almost linearly with stage temperature at the rates of 0.77 Å/K and 0.73 Å/K for the 2.4μm and 4.3μm devices respectively (figures not shown). On the other hand, as a result of bandgap shrinkage the gain peak wavelength increases at a much faster rate of about 3.0 Å/K [14]. Based on the these values and the estimated minimum point of threshold, the gain peak wavelength is estimated to be around 861 to 862 nm at ambient, in good agreement with the deduction obtained earlier in section 3.4.1. These results thus confirm that the gain peak wavelength is indeed slightly blue shifted with respect to the resonant wavelengths of these devices at threshold, i.e. 8640Å and

8653Å respectively. This is consistent with the fact that the minima in thresholds are obtained at temperature slightly above ambient.

On the other hand, the threshold behaviour of the TEM_{01} mode is different between the two devices. For the 4.3μm strong guiding device, the cw threshold current density of the TEM_{01} mode is always higher than that obtained under pulsed pulsed conditions at the temperature range shown. However, the opposite was true for the 2.4μm weak guiding device, i.e. the TEM_{01} mode only lases under cw conditions within the driving range for the same temperatures. In section 6.2.3, the fact that the higher order mode achieves lasing at lower current density under cw conditions than under pulsed conditions for the weak guiding devices, is attributed to thermal lensing effects caused by the radial variations of the device internal temperature profile. The results for the 2.4μm weak guiding device discussed above support this interpretation. They show that "uniform" (external) heating does not reduce the pulsed threshold current denisty of the TEM_{01} mode, but the thermal lensing caused by the device radial temperature gradient under cw conditions, do result in a decrease in threshold. Hence, this is consistent with the proposition that thermal lensing reduces the cw threshold of TEM_{01} mode in the weak guiding devices.

Thermal lensing also causes an increase in wavelength separation between the eigenmodes, as exemplified by Fig. 4.12. However, separate measurements (results not shown here) shows that the wavelength separations between that of the TEM_{00} and the TEM_{01} modes measured at $0.5xJ_{th(00,\ ambient)}$ actually reduces slightly with increasing stage temperature, e.g. by about 0.4Å (2.4μm device) and 0.3Å (4.3μm device) with respect to the ambient value when stage temperature is raised by about 30K. Thus, the increase in wavelength separation between eigenmodes observed during cw operation, must be due to the thermal lensing effect and not a simple uniform rise in temperature.

6.3 Lasing Characteristics of Rectangular Shaped Oxide Apertured VCSELs

In this section, the influence of the oxide aperture anisotropy on the modal and polarisation properties of oxidised VCSELs will be discussed. The devices used in following discussions were fabricated from the wafer region close to those near-square shaped devices, and their planar resonant wavelengths are between 864 - 865nm.

6.3.1 Threshold and Modal Properties

Using the experimental approaches discussed in the preceding sections, the threshold and modal properties of devices with rectangular apertures were also examined. These results are summarised in Tables 6.1 and 6.2 for several *strong* and *weak* guiding devices of different aspect ratios, where devices with similar average aperture size (S) are grouped together. The results obtained from the near-square shaped devices, which appear at the top of each sub-group, are also included for comparisons. For both type of devices, the thresholds (of the fundamental mode) of these rectangular devices can be higher or lower than those of near-square devices, depending on the resulting average aperture size S. It is found that devices with smaller S usually exhibit higher current density, as in the case of the (1.9 x 2.9)μm strong and weak guiding rectangular devices. However, it seems that if the length of longer side is bigger than 4.0μm and the length shorter side is bigger than 2.5μm, for instance the (2.9 x 4.8) μm strong guiding and (2.9 x 5.3) weak guiding devices, then the threshold of the rectangular devices could be lower than the near-square devices even if they have a smaller S.

Regarding the single mode behaviour, as long as the lengths of both longer and shorter sides are kept smaller than about 3.5μm, the onsets of higher order modes can be suppressed throughout the whole driving range under both pulsed and cw operations, in the case of the strong guiding rectangular devices. However, when the length of longer side of these devices becomes bigger than 4.0μm, the higher order modes tend to lase at lower current densities than their near-square counterparts of similar S, even if the length of the shorter side is as small as 2.9μm. Subsequently, the maximum single mode power that can be obtained from these rectangular devices is also lower than that offered by the near square devices. For the weak guiding

rectangular devices, single mode operation can only be maintained under pulsed conditions, if both lengths are shorter than 3.0μm. When the length of the longer side of these devices becomes bigger than 4.0μm, the threshold current density of the higher order modes become lower than their near-square counterpart of similar S. Despite being more susceptible to the thermal lensing effect that gives rise to the onset of the higher order modes under cw conditions, the maximum single mode powers that can be obtained from the weak guiding rectangular devices are still always higher than their strong guiding counterparts of similar aperture area.

Average aperture size, S(μm)	Aperture dimension 2ax2b (μm)	Aspect ratio (2b/2a)	Pulsed $J_{th(00)}$ (kA/cm^2)	CW $J_{th(00)}$ (kA/cm^2)	Pulsed $J_{th(01/10)}$ (kA/cm^2)	CW $J_{th(01/10)}$ (kA/cm^2)	Max. "Single mode" Power (mW)
2.4	2.4 x 2.5	1.04	13.5	18.2	--	--	0.61
2.6	2.4 x 2.9	1.21	11.5	12.3	--	--	0.80
2.6	2.2 x 3.1	1.41	10.3	11.0	--	--	0.94
2.3	1.9 x 2.9	1.53	18.1	19.1	--	--	0.45
3.0	3.4 x 2.6	0.76	8.7	9.0	--	--	1.12
3.8	3.7 x 3.9	1.05	4.9	5.2	51.2	--	1.88
3.7	3.4 x 4.0	1.18	6.4	6.2	29.4	36.8	1.22
3.7	2.9 x 4.8	1.48	4.8	4.8	25.1	21.6	0.89
4.0	3.8 x 4.3	1.13	3.7	3.7	12.9	12.9	0.64
4.0	4.3 x 3.7	0.86	4.7	4.8	11.9	14.3	1.05
4.3	4.4 x 4.2	0.95	4.4	4.5	21.6	24.3	1.49
4.3	3.8 x 4.8	1.26	4.4	4.4	15.1	15.3	0.86
4.4	4.8 x 4.1	0.85	4.1	3.8	9.2	10.7	0.89
4.6	5.0 x 4.3	0.86	3.8	3.9	8.4	8.4	0.62

Table 6.1 : Threshold current densities of the fundamental and higher order modes as well as the maximum cw "single mode" power for rectangular and near squared *strong guiding* devices.

Average aperture size, S(μm)	Aperture dimension 2ax2b (μm)	Aspect ratio (2b/2a)	Pulsed $J_{th(00)}$ (kA/cm^2)	CW $J_{th(00)}$ (kA/cm^2)	Pulsed $J_{th(01/10)}$ (kA/cm^2)	CW $J_{th(01/10)}$ (kA/cm^2)	Max. "Single mode" Power (mW)
2.4	2.4 x 2.5	1.04	6.9	6.1	--	78.1	1.72
2.6	2.9 x 2.4	0.83	6.1	5.8	--	44.5	1.48
2.6	2.4 x 2.9	1.21	5.9	5.5	--	47.4	1.60
2.3	1.9 x 2.9	1.53	7.7	7.3	--	44.9	1.41
2.5	1.9 x 3.4	1.79	7.5	7.1	94.4	41.7	1.12
4.0	3.9 x 4.1	1.05	3.1	3.1	22.0	14.7	1.23
4.3	3.8 x 5.0	1.32	2.6	2.7	7.4	4.2	0.16
3.9	2.9 x 5.3	1.83	3.0	3.6	13.0	6.5	0.24
3.6	3.9 x 3.4	0.87	4.2	4.0	46.4	20.9	1.40

Table 6.2 : Threshold current densities of the fundamental and higher order modes as well as the maximum cw "single mode" power for rectangular and near squared *weak guiding* devices.

It was mentioned earlier in section 6.2.3 that for the near-square devices, between the TEM_{01} and TEM_{10} modes it is always the one closer to the gain peak (i.e. shorter resonant wavelength) that achieves lasing first, if ever. However, when the aspect ratio of the rectangular devices becomes larger than 1.15, it is the higher order TEM_{01} or TEM_{10} mode with the longer resonant wavelength i.e. the one with a field null along the longer side of the aperture, that turns on first when the device operation is multi-moded. This experimental observation is consistent with the theoretical results presented in section 5.2.3 on rectangular devices, which predicts that this particular higher order mode experiences lower diffraction loss than the one with shorter resonant wavelength (i.e. with a field null along the shorter side of the aperture). According to the values computed by using eqn (6.2), it also suffers from lower scattering loss. For these reasons, it has a larger effective photon lifetime for a given injected current density than the mode with shorter resonant wavelength. For an extreme case, the large modal reflectance difference between these two modes could

result in one of them eventually achieving lasing but not the other one. One of such devices is the (3.4 x 4.0)μm strong guiding device, where the onset of the TEM_{10} mode of shorter resonant wavelength is suppressed whilst the TEM_{01} mode does achieve lasing within the driving range. The effective photon lifetime characteristics of the TEM_{00} mode polarised in the $\langle 110 \rangle$ direction, and that of the TEM_{01} and TEM_{10} modes polarised in the $\langle 1\bar{1}0 \rangle$ direction, for this device are shown in Figure 6.33. In this figure, the dotted lines demarcate the threshold current densities of the TEM_{00} mode (6.2 kA/cm^2) and the TEM_{01} mode (36.8 kA/cm^2) respectively, and the inset details the variation of the lifetimes below the TEM_{00} threshold. As can be seen, even well below the TEM_{00} threshold, there is already a considerable difference in effective photon lifetime between the TEM_{01} and TEM_{10} modes. This difference continues to increase at a slower rate at above threshold, and eventually leads the lasing of the TEM_{01} mode whilst the TEM_{10} mode stays below threshold.

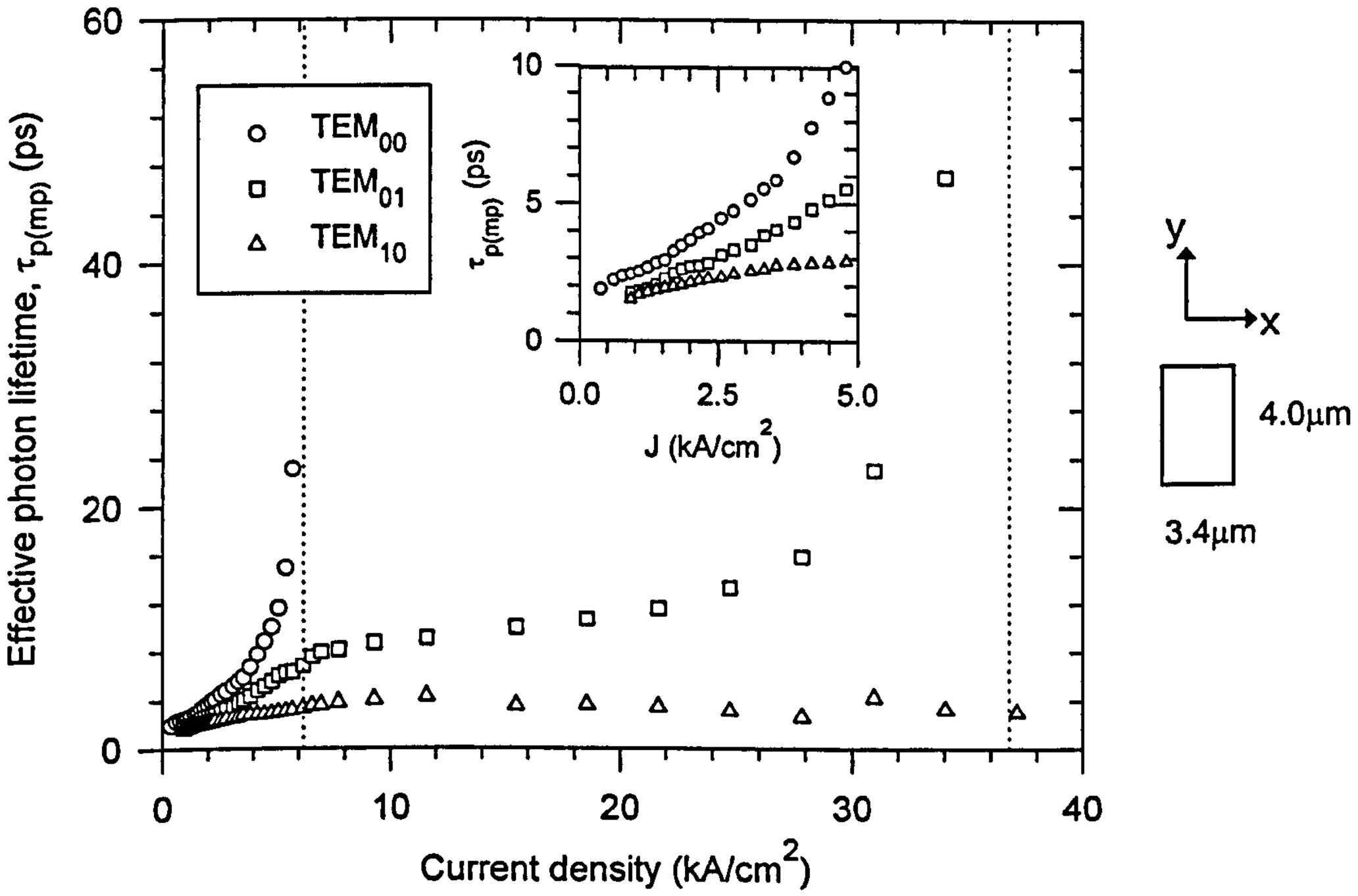

Figure 6.33 : Variation of effective photon lifetimes for the TEM_{00} mode polarised in the $\langle 110 \rangle$ or y direction, and that of the TEM_{01} and TEM_{10} modes polarised in the $\langle 1\bar{1}0 \rangle$ or x direction, for the 3.4 x 4.0μm strong guiding rectangular devices.

6.3.2 Polarisation Properties

The simulation results for rectangular device in section 5.2.3 also show that asymmetry in the mode shapes results in the difference in modal reflectance of the eigenmodes (of the same mode number) polarised in orthogonal directions. This thus gives rise to the possibility of controlling the polarisation of light output by using rectangular oxide apertures along the $\langle 110 \rangle$ and $\langle 1\bar{1}0 \rangle$ directions. Experimental results show that these efforts do seem to help in reducing the possibility of polarisation switching in strong guiding devices with apertures elongated along the $\langle 110 \rangle$ direction, i.e. the preferential polarisation direction of the near squared devices. For instance, Figure 6.34, Figure 6.36 and Figure 6.36 illustrate the polarisation resolved L-I characteristics of the (2.9 x 4.8)μm, the (3.4 x 4.0)μm (whose effective photon lifetime characteristic is shown in Fig. 6.33) and the (2.2 x 3.1)μm strong guiding rectangular devices whose apertures are all elongated along the $\langle 110 \rangle$ direction. Clearly, the polarisation switching events that happen in the 3.8μm and 4.3μm near squared devices as shown in Fig. 6.6(a) and (b) earlier, do not appear in these devices and the fundamental TEM_{00} mode lases in the same $\langle 110 \rangle$ direction. In particular, the (2.2 x 3.1)μm device has single mode and single polarisation operation throughout the whole driving range with maximum polarisation extinction ratio of 19dB at about 3 x $J_{th(00)}$. However, in the (3.4 x 4.0)μm and the (2.9 x 4.8)μm devices, the first higher order TEM_{01} mode still lases in the orthogonal polarisation direction from that of the dominant TEM_{00} mode, i.e. along the $\langle 1\bar{1}0 \rangle$ axis. In these devices, the TEM_{00} mode does eventually lase in the $\langle 1\bar{1}0 \rangle$ direction as well, but at higher current density after the onset of the first higher order mode.

These three devices are located not far away from those near-squared devices on the same chip, and thus the gain peak wavelength (≈ 861nm to 862nm) are blue shifted with respect to their TEM_{00} lasing wavelengths of 8653Å, 8651Å and 8642Å respectively. The difference in the spontaneous linewidths are quite small (≤ 0.03Å) between the orthogonally polarised TEM_{00} modes as measured at half the threshold current density. However, the corresponding values for the TEM_{01} mode (from 0.04Å to 0.07Å) and the TEM_{10} mode (from 0.16Å to as high as 0.3Å), especially the latter are more significant. In fact, the deduced effective photon lifetimes of these eigenmodes do seem to agree with the implications of the modal reflectance predicted

in section 5.2.3, i.e. the eigenmode effective photon lifetimes in descending order are that of y-TEM_{00} > x-TEM_{00} > x-TEM_{01} > y-TEM_{01} > y-TEM_{10} > x-TEM_{10} modes, assuming that the y and x directions are along the $\langle 110 \rangle$ and $\langle 1\bar{1}0 \rangle$ directions respectively. The elimination of polarisation switching shown in Figures 6.34 to 6.36 also happens to medium and weak guiding devices but only if the length of the longer side is smaller than 3.5μm and the aspect ratio is bigger than 1.20.

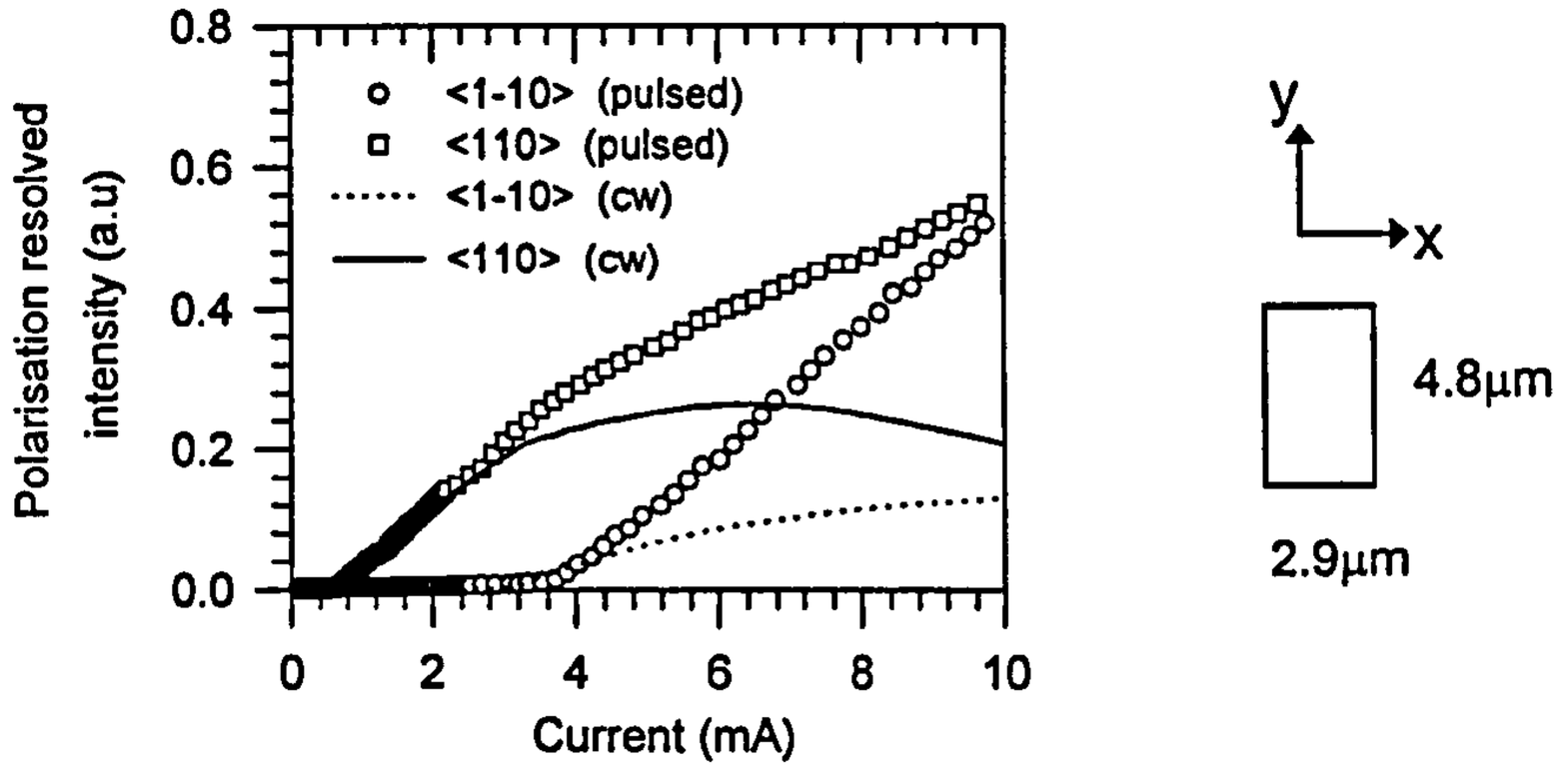

Figure 6.34 : Polarisation characteristics of strong guiding rectangular devices with aperture size of (2.9 x 4.8)μm.

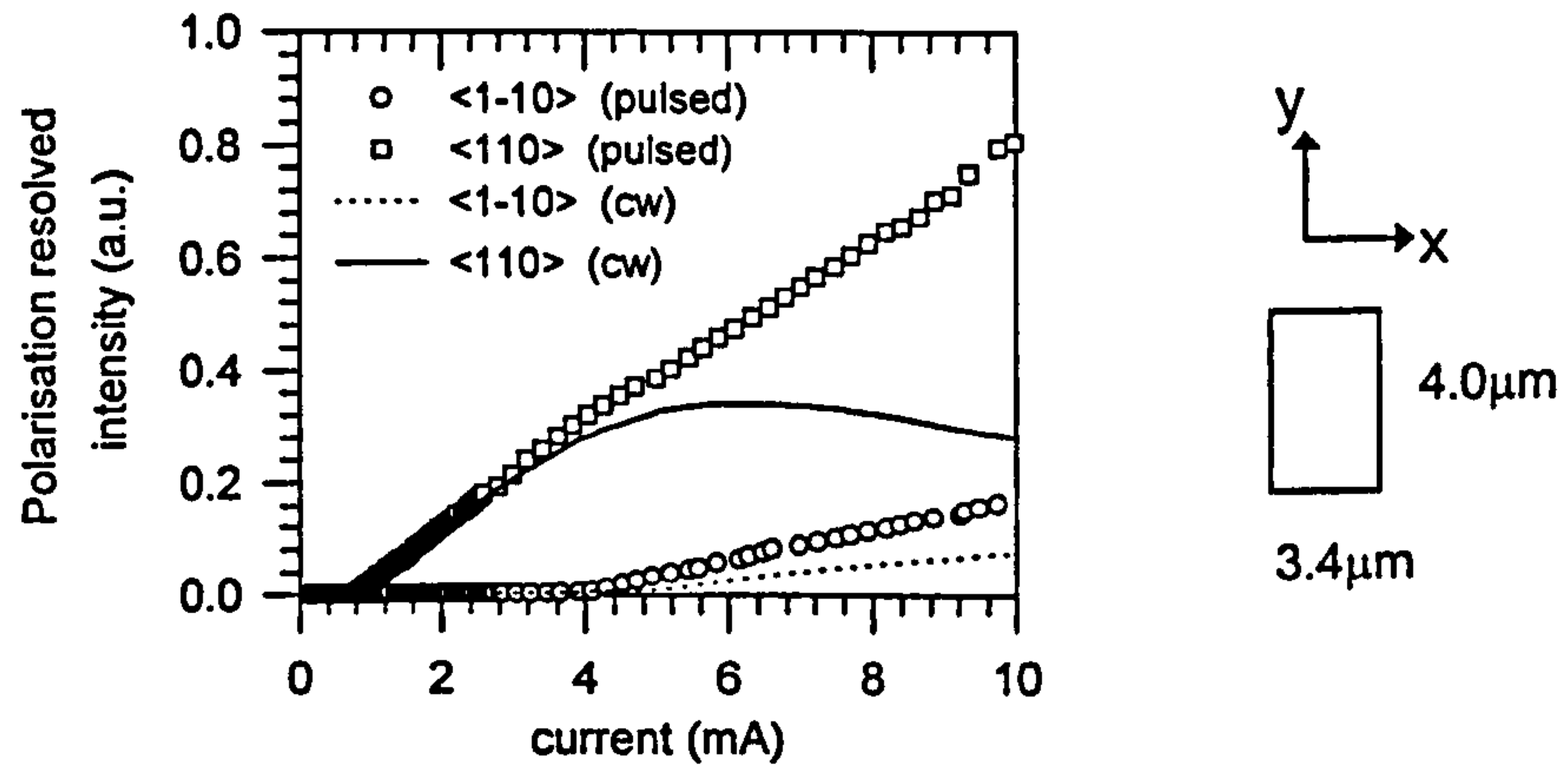

Figure 6.35 : Polarisation characteristics of strong guiding rectangular devices with aperture size of (3.4 x 4.0)μm

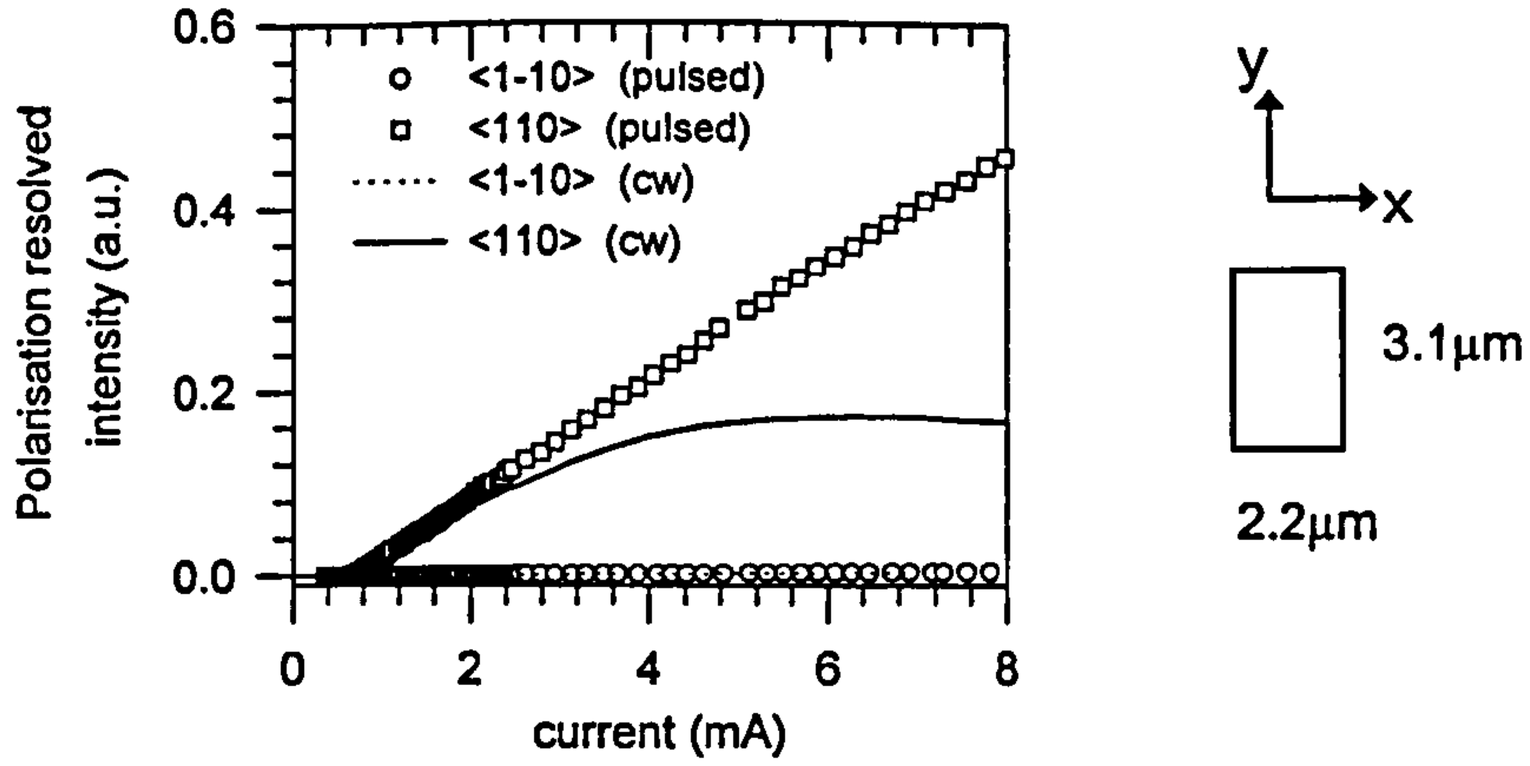

Figure 6.36 : Polarisation characteristics of strong guiding rectangular devices with aperture size of (2.2 x 3.1)μm.

Unfortunately, the controlling of the light polarised in the $\langle 1\bar{1}0 \rangle$ direction is less successful in most of the rectangular devices elongated along the $\langle 1\bar{1}0 \rangle$ direction even for the strong guiding devices. The fundamental mode still lases in the $\langle 110 \rangle$ direction with polarisation switching events occurring in certain cases and the onset of the first higher order mode is in the $\langle 1\bar{1}0 \rangle$ direction. The exceptions to this statement seems to be only for those strong guiding devices having both aperture dimensions below 3.5μm. One of these devices is the (3.4 x 2.6)μm strong guiding device whose spectra at half the threshold is that shown in Figure 4.16(b) in chapter 4. This device operates single mode throughout the driving range and its polarisation resolved L-I characteristics are shown in Figure 6.37. The spontaneous emission linewidth measurements indicate that the $\langle 1\bar{1}0 \rangle$-polarised TEM_{00} mode indeed has slightly higher effective photon lifetimes than that in the $\langle 110 \rangle$ direction at below threshold. However, for reasons that are not obvious, though believed to be strain related, repeated cw measurements or intentional application of pressure on the contact pad of this device and other devices that show similar characteristic initially, are able to change the polarisation direction of the lasing TEM_{00} mode between the $\langle 110 \rangle$ and $\langle 1\bar{1}0 \rangle$ directions, and eventually to along the $\langle 110 \rangle$ direction.

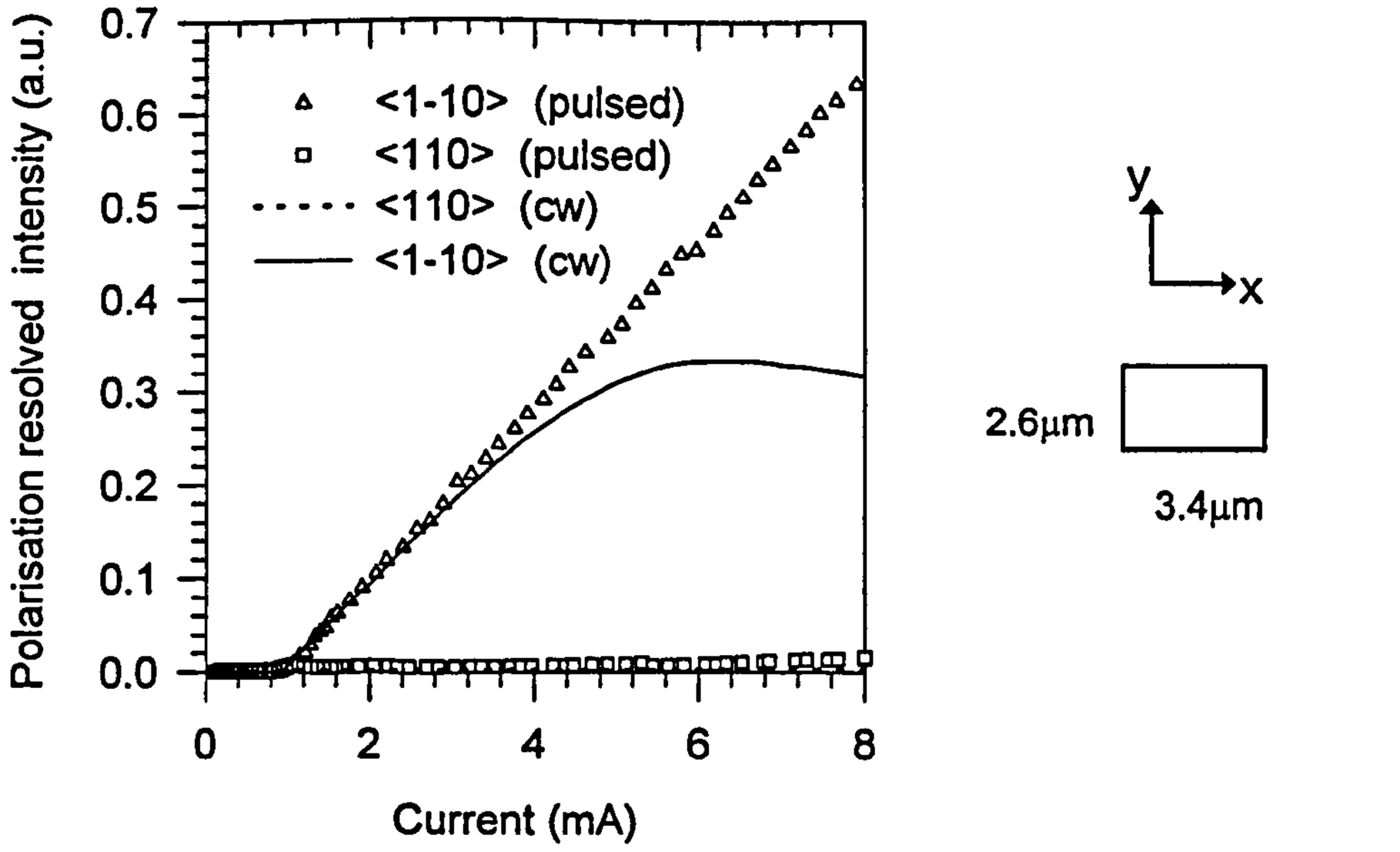

Figure 6.37 : Polarisation characteristics of strong guiding rectangular devices with aperture size of (2.6 x 3.4)μm.

6.4 Summary

Based on the experimental results obtained from the strong, medium and weak guiding devices, it is found that :-

- Weak guiding devices are the best for achieving low threshold currents, high efficiencies and high multi-mode power performances. In these aspects, the lasing performances of medium guiding devices are found to be always in between those of the weak and strong guiding devices.
- The lowest cw and pulsed threshold currents achieved are 350μA and 400μA respectively, obtained from a 2.4μm weak guiding device. Weak guiding devices as small as about 1.0μm also manage to achieve lasing with threshold currents of 580μA and 1.1mA under cw and pulsed conditions respectively.
- Thermal lensing effect is thought to help reduce the cw threshold values from that of pulsed values for small weak guiding devices (< 4.0μm). However, it seems to have the opposite effect for the strong guiding devices of 2.4μm or smaller.
- Polarisation switching events occur in all the three types of devices except for those with aperture size of about 2.4μm or smaller, when they are operated under

cw conditions. Since the polarisation switching do not occur under pulsed conditions, thermal induced effects such as thermal lensing and a change in the sign of the offset between gain peak and resonant wavelengths that affect the modal gains, are thought to be the most likely causes.

- Under pulsed conditions, the threshold current densities of the "first" higher order mode for the strong and weak guiding devices are comparable and higher than that of medium guiding devices, if the aperture sizes are smaller than 4.0μm. For these aperture sizes, no higher order mode can achieve lasing under cw conditions for the strong guiding devices. However, due to thermal lensing effects, the cw thresholds of the higher order modes tend to be lower than that measured under pulsed conditions in the cases of medium and weak guiding devices.
- In terms of maximum cw single mode power, strong guiding devices offer the highest values, followed by weak and medium guiding devices, if the aperture sizes are between 3.0 and 4.0μm. However, when the aperture size becomes smaller than 3.0μm, it is the weak guiding devices that have the highest maximum single mode power. Due to the much higher excess optical loss experienced, strong guiding device now offer the lowest light power. The maximum single mode power obtained are as high as 1.88 mW from a 3.8μm strong guiding device and 1.72 mW from a smaller 2.4μm weak guiding device.
- If thermal effects can be minimised, pulsed measurement as well as theoretical results imply that weak guiding devices will offer the highest maximum single mode power when the aperture sizes becomes smaller than 4.0μm.
- For aperture sizes between 4.0 and 7.0μm, single mode operation can be sustained in the strong and medium devices but not the weak guiding devices, but only for a short current range from the threshold. Both the single mode power and SMSR performance obtained for these devices are also relatively poor.
- The effective photon lifetimes of the TEM_{00} and TEM_{01}/TEM_{10} modes for a given current density decrease with reduction in aperture sizes, mainly due to the associated increases in the size dependent optical excess losses. The fundamental mode also has a longer effective photon lifetime than the higher order mode, partly because the former experiences lower excess optical losses. However, for identical aperture sizes, strong guiding devices have the shortest photon lifetimes since they

suffered from the largest excess optical losses when compared to medium and weak guiding devices.

- For devices with rectangular apertures, as long as the length of longer side is kept shorter than 3.5μm in the strong guiding case and 3.0μm in the weak guiding case, single mode operation can be maintained under pulsed conditions.
- In these rectangular devices, between the TEM_{01} and TEM_{10} modes, it is always the one with longer resonant wavelength (i.e. field null along the longer side of aperture), that has longer effective photon lifetime for a given current density. It eventually reaches threshold first, if ever. This is in accordance with the theoretical predictions that this particular mode has lower diffraction loss as well as scattering loss than the other one.
- For rectangular devices with the longer side of apertures orientated along the $\langle 110 \rangle$ direction, the dominant polarisation direction is also along the same direction. Polarisation switching also do not occur throughout the cw driving range for strong guiding devices, if the longer side is smaller than 5.0μm and the aspect ratio is more than 1.15. However, this is only the case for the weak guiding devices, if the longer side is smaller than 3.5μm and the aspect ratio is larger than 1.20.
- For multi-mode rectangular devices, however, the first higher order mode still lases in the orthogonal $\langle 1\bar{1}0 \rangle$ direction. In fact, at half the threshold of the TEM_{00} mode, the measured effective photon lifetimes of various eigenmodes in descending order are y-TEM_{00} > x-TEM_{00} > x-TEM_{01} > y-TEM_{01} > y-TEM_{10} > x-TEM_{10} modes, assuming that the y and x directions are along the $\langle 110 \rangle$ and $\langle 1\bar{1}0 \rangle$ directions respectively. This is in good qualitative agreement with the order of the predicted modal reflectance.
- Unfortunately, polarisation control in the $\langle 1\bar{1}0 \rangle$ direction proved unsuccessful in most of the rectangular devices with the longer side of the aperture orientated along the same direction. Even in the few strong guiding devices that achieved the desired polarisation pinning under pulsed conditions, repeated cw measurements or intentional application of pressure on the contact pad seemed to be able to destroy the control eventually.

Comparing the experimental results and theoretical predictions, it is found that the effects of "scattering loss" due to the oxide have to be considered,

- In order to fit the measured pulsed external quantum efficiency a constant value of internal quantum efficiency is assumed for all aperture sizes. Values of the "single mode" external quantum efficiency obtained directly from the solutions of the rate equations, also match fairly well with the experimental values of the strong and medium guiding devices with aperture sizes of 2.4μm or smaller.
- In order to achieve good qualitative agreement with the experimental results on the threshold current density of the TEM_{00} mode, for the strong, medium and weak guiding devices. The remaining discrepancies are believed to be mainly due to carrier leakage effects.

However, the simple model used to estimate the scattering losses seems to have over-estimated that for the higher order mode in the strong guiding devices, and for aperture sizes smaller than 4.0μm in the cases of medium and weak guiding devices. Nevertheless, the effects of "scattering loss" must be considered so that the theoretical predictions are in qualitative agreement with the experimental results, i.e. values for the three types of devices are in the correct order, especially for aperture sizes smaller than 4.0μm. Alternative models to calculate the scattering loss are thus needed.

References for Chapter 6

[1] B.J.Thibeault, E.R.Hegblom, P.D.Floyd, R.Naone, and L.A.Coldren, "Reduced optical scattering loss in vertical cavity lasers using a thin oxide apertrue", IEEE Photon. Tech. Lett., vol. 8 , pp. 593 - 595, 1996.

[2] K.D.Choquette, W.W.Chow, G.R.Hadley, H.Q.Hou and K.M.Geib, "Scalability of small aperture selectively oxidized vertical cavity lasers", Appl. Phys. Lett., pp.823 - 825, Feb 1997.

[3] J.Woodhead, *private communication on the thermal modelling of oxidised VCSELs using finite element technique.*

[4] K.D.Choquette, R.P.Schneider, K.L.Lear, and R.L.Leibenguth, "Gain-dependent polarisation properties of vertical cavity lasers", IEEE J. of Selected Topics in Quantum Electronics, Vol.1, pp. 661-666, 1995.

[5] K.Panajotov, B.Ryvkin, J.Danckaert, M.Peters and I.Veretenicoff, "Polarasation switching in VCSELs due to thermal lensing", IEEE Photon. Tech. Lett., vol. 10, pp.6-8,1998.

[6] A.Valle, L.Pesquera and K.A.Shore, "Polarization behaviour of birefringent multitransverse mode vertical cavity surface emitting lasers", IEEE Photon. Tech. Lett., vol.9, pp.557-559, 1997.

[7] J.M.Regalado, M.SanMiguel, N.N.Abraham and F.Prati, "Polarisation switching in quantum well vertical cavity surface emitting lasers", Opt. Lett., vol. 21, pp.351-353, 1996.

[8] Y.G.Ju and Y.H.Lee, "Strong polarisation selectivity in 780nm vertical cavity surface emitting lasers grown on misorientated substrate", Appl. Phys. Lett., vol. 71, pp. 741-743, 1997.

[9] T.Mukaihara, F.Koyama and K.Iga, "Engineered polarisation control of GaAs/AlGaAs surface emitting lasers by anisotropic stress from elliptical etched substrate hole", IEEE Photon. Tech. Lett., vol.5, pp.133-135, 1993.

[10] M.Grabherr, R.Jager, R.Michalzik, B.Weigl, G.Reiner and K.J.Ebeling, "Efficient single mode oxide-confined GaAs VCSEL emitting in the 850nm wavelength regime", IEEE Photon. Tech. Lett., vol.9, pp. 1304-1306, 1997.

[11] C.Jung, R.Jager, M.Grabherr, R.Michalzik, B.Weigl and K.J.Ebeling, "4.8mW singlemode oxide confined top surface emitting vertical cavity laser diodes", Electron. Lett, vol.33, pp.1790-1791, 1997.

[12] G.P. Agrawal and N.K.Dutta, "Semiconductor Lasers", (Van Nostrand Reinhold, New York, 1993), chapter 6.

[13] G.Reiner, E.Zeeb, B.Moller, M.Ries and K.J.Ebeling, "Optimisation of planar Be-doped InGaAs VCSEL with two-sided output", IEEE Photon. Technol. Lett., vol.7, pp.730-732, 1995.

[14] B.Tell, K.F.Brown-Goebeler, R.E.Leibenguth, F.M.Baez and Y.H.Lee, "Temperature dependence of GaAs/AlGaAs vertical cavity surface emitting lasers", Appl. Phys. Lett., vol.60, pp.683-685, 1992.

Chapter 7 Conclusions

7.1 Conclusions

A detailed description of the design, fabrication, characterisation and theoretical modelling of oxide apertured (confined) GaAs/AlGaAs VCSELs has been presented. The performance comparisons of the three different VCSEL designs used in this work, namely strong, medium and weak guiding, have produced much valuable insight. To begin with, experimental and theoretical results from broad area devices (≈15μm) are used to estimate the absorption coefficients in the DBRs. Although the absorption levels of the DBRs of the three VCSEL layers turn out to be different due to unintentional variations in doping concentrations, these differences are sufficiently small that valid conclusions can still be drawn from the comparison of results obtained from these three layers.

A scalar variational method is used to calculate the mode sizes and resonant wavelengths of the various eigenmodes guided by an oxide apertured VCSEL. This is done under the assumption of Hermite-Gaussian transverse field variations. As a result of the perturbation in transverse refractive index variation caused by the oxide aperture, the mode size of a given eigenmode is seen to reduce as the aperture size becomes smaller, until it reaches a minimum value beyond which the mode expands rapidly and eventually becomes no longer guided by the apertured resonator. The resonant wavelengths of the various eigenmodes are blue shifted from the plane wave value, and the blue shifts increase with reduction in the aperture size. Due to the larger index guiding strength provided by the thicker oxide, such strong guiding devices demonstrate the smallest mode sizes and biggest blue shifts in resonant wavelengths for a given aperture size. In addition, they also give the largest wavelength separations between the fundamental mode and the higher order modes. When the symmetry in the shape of oxide apertrue is broken, the degeneracy between the TEM_{01} and TEM_{10} modes is also lifted. The spectral splitting between these two modes increases with aspect ratio, and is also always the largest in the strong guiding devices. Comparisons between the experimental observations and the theoretical predictions of resonant

wavelengths and wavelength separations have produced close fits. Hence, these validate the use of the scalar variational method for oxide apertured VCSELs.

The presence of an oxide aperture in a VCSEL also gives rise to excess optical losses, namely diffraction loss and oxide "scattering loss". Both losses increase with reduction in aperture size and are larger in devices with thicker oxide. In additions, the higher order modes experience larger excess optical losses than the fundamental mode. On the other hand, modal gains tend to increase with reduction in the eigenmode sizes, as a result of better overlap between the optical fields and the local optical gains. Therefore, both modal gains and excess optical losses must be considered when comparing the performance of devices with identical aperture sizes but different mode sizes or oxide thickness.

Experimental observations show that the threshold current density (of the fundamental mode) increases at the fastest rate with reduction in aperture size in the strong guiding devices compared to the medium and the weak guiding devices. This is because the considerably higher excess optical losses caused by the use of the thickest oxide aperture in these strong guiding devices, more than offsets any advantage in terms of modal gain from their smaller mode sizes. It is also found that the oxide scattering loss has to be considered in order to obtain good qualitative agreement between the theoretical predictions and the experimental observations from pulsed measurements. The lowest threshold current obtained under cw conditions is 350μA, from a 2.4μm weak guiding devices. With more optimised doping schemes that will reduce the absorption in the DBRs, in principle threshold currents of about 100μA should be attainable, even if the present numbers of DBR pairs are maintained.

When operated under pulsed conditions, single mode operation can be maintained throughout the whole driving range, in devices with aperture sizes of about 2.4μm or smaller. The threshold current densities of the first higher order mode for the strong and weak guiding devices are comparable and higher than that of the medium guiding devices, if the aperture sizes are smaller than 4.0μm. As in the case of TEM_{00} threshold, if the scattering loss was considered, the theoretical predictions are in good qualitative agreement with the experimental observations from pulsed measurements. However, whilst the onset of higher order mode is suppressed under cw conditions in the strong guiding devices of these aperture sizes, thermal lensing effects help to reduce the cw thresholds of the higher order modes in the weak guiding and medium

guiding devices. This is mainly due to the fact that the built-in index guiding strengths of the latter two devices are smaller than their strong guiding counterpart, and become comparable to the thermally induced refractive index variation at high injected current density. Nevertheless, due to their higher external quantum efficiencies, the "single mode" powers that can be obtained from weak guiding devices are comparable or bigger than that of strong guiding devices. The two highest maximum single powers obtained in this work are 1.88 mW in a 3.8μm strong guiding device and 1.72 mW in a smaller 2.4μm weak guiding device.

Polarisation switching which is common in the near-square shaped devices, is suppressed throughout the cw driving range in strong guiding rectangular devices aligned along the $\langle 110 \rangle$ direction, if the longer side of the aperture is smaller than 5.0μm and the aspect ratio is more than 1.15. This is attributed to the difference in modal reflectance between the orthogonally polarised eigenmodes. In fact, at half the threshold of the TEM_{00} mode, the measured effective photon lifetimes of eigenmodes of one of these devices in descending order are, y-TEM_{00} > x-TEM_{00} > x-TEM_{01} > y-TEM_{01} > y-TEM_{10} > x-TEM_{10} modes, assuming that the y and x directions are along the $\langle 110 \rangle$ and $\langle 1\bar{1}0 \rangle$ direction respectively. This is in good qualitative agreement with the order of the modal reflectance predicted. Unfortunately, the attempt to obtain similar polarisation control in the $\langle 1\bar{1}0 \rangle$ direction is unsuccessful in the rectangular devices with the longer side of the aperture orientated along the same direction.

7.2 Suggestions for Future Work

The analysis carried in this work reveals that there is still room for improvement over the performance of present VCSEL structures. Below are several suggestions regarding the VCSEL designs :

- The VCSEL structures used in this work are not optimised in terms of optical power output and power efficiencies. However, provided the doping concentrations and absorption coefficients in the DBRs can be known accurately, the number of mirror periods in the top and bottom DBRs for optimisation of the plane wave threshold gain/current and power efficiency (for big multi-moded devices), can be ascertained easily using the procedures described in section 3.3.2.

- The electrical conduction of DBRs can be improved to reduce the series resistance and thus thermal dissipation, which will eventually result in increased cw light power output. Established schemes such as compositional grading and modulation doping of the hetero-junctions [1,2] will be very helpful in this aspect. In the latter approach, the reduction of absorption in DBRs by only doping the hetero-interfaces where the field amplitudes are low, will reduce the number of periods in the top DBR needed for achieving the desired threshold gain/current as well as light output. The reduced thermal dissipation will also help to minimise the thermal lensing effect, which has been shown in this work to be detrimental to single mode operation in VCSELs with small built-in index guiding strength.
- It is also desirable to grade the QW-cladding regions using a grading scheme such as the GRINSCH structure [3] or the staircase structure [4] to provide more efficient carrier capture in the quantum wells.
- The use of thicker oxide or DBRs with lower refractive index contrast ratios can also be employed for increasing the difference in modal reflectance between the fundamental mode and the higher order modes for a given aperture size. This will improve the single mode performance by suppression of the onset of the higher order modes, either throughout the whole driving range or only over a certain current range, and can be made to occur for even larger aperture size than is possible in present devices. In addition, the ensuing increased difference in modal reflectance between the orthogonally polarised TEM_{00} modes may also lead to better polarisation control.
- For complete stable polarisation control, VCSELs grown on non (100) substrates such as those on a (311)B substrate [5] can be used. In these types of VCSELs, the intrinsic anisotropic optical gain is believed to help stabilising the polarisation [6]. Alternatively, VCSELs grown on (100) mis-orientated substrate towards (111)A can also provide large polarisation selectivity [7].

On the theoretical modelling front, the following will be attempted by the author in the near future :

- A more exact approach for taking account of the oxide scattering losses needs to be devised, within the framework of the current model. This would require a more rigorous solution of the electromagnetic field perturbation due to the presence of

the oxide aperture. Although established numerically intensive schemes such as thebeam propagation method (BPM) [8,9] have been attempted for the calculation of the excess optical losses, verification of this model through full comparisons between the theoretical and experimental results on laser parameters such as threshold current density and single mode power, are still lacking.

- In addition, any realistic VCSEL modelling ought to consider the thermal induced effects when the devices are operated under cw conditions. In particular, the thermal lensing effect caused by thermally induced transverse refractive index variations within the device and the thermally enhanced carrier leakage that affects the optical gain provided by the QWs, must be taken into account if the correct modal and threshold properties are to be predicted. Hence, detailed optical gain calculations and modelling of the device thermal profile will be important for improving the present theoretical model.

References for Chapter 7

[1] S.A.Chalmers, K.L.Lear and K.P.Killeen, "Low resistance wavelength reproducible p-type AlGaAs DBR grown by molecular beam epitaxy", Apl. Phys. Lett., vol.62, pp.1585-1587, April 1993.

[2] K.L.Lear and R.P.Schneider, Jr., "Uniparabolic mirror grading for vertical cavity surface emitting lasers", Appl. Phys. Lett.,vol.68, pp.605-607, Jan 1996.

[3] S.L.Chuang, "Physics of Optoelectronics Devices", (John Wiley & Sons, NY)

[4] B.Weigl, M.Grabherr, C.Jung, R.Michalzik and K.J.Ebeling, "High performance oxide confined GaAs VCSELs", IEEE J. of Selected Topics in Quantum Electronics, Vol.3, pp. 409-414, 1997.

[5] N.Nishiyama, A.Mizutani, N.Hatori, F.Koyama and K.Iga, "A completely single mode and single polarisation vertical cavity surface emitting lasers Grown on GaAs (311)B Substrate", Jpn. J. Appl. Phys., vol. 37, pp L640-642, 1998.

[6] T.Ohtoshi, T.Kuroda, A.Niwa and S.Tsuji, "Dependence of optical gain on crystal orientation in surface-emitting lasers with strained quantum wells", Appl. Phys. Lett., vol. 65, pp.1886-1887, 1994.

[7] Y.G.Ju and Y.H.Lee, "Strong polarisation selectivity in 780nm vertical cavity surface emitting lasers grown on misorientated substrate", Appl. Phys. Lett., vol. 71, pp. 741-743, 1997.

[8] H.K.Bissessur, F.Koyama and K.Iga, "Modelling of oxide-confined vertical cavity surface emitting lasers", IEEE J. of Selected Topics in Quantum Electronics, vol.3, pp.344-352, April 1997.

[9] E.R.Hegblom, D.I.Babic, B.J.Thibeault, and L.A.Coldren, "Estimation of scattering losses in dielectrically apertured vertical cavity lasers", Appl. Phys. Lett., vol. 68, pp.1757-1759, March 1996.

Appendix A : Electromagnetic Wave Admittance

The Maxwell vector curl equations given by (2.1) and (2.2) can be separated into six scalar differential equation in the rectangular co-ordinate system . They are

$$\frac{\partial E_z}{\partial y} - \frac{\partial E_y}{\partial z} = -j\omega\mu H_x \qquad (A.1)$$

$$\frac{\partial E_x}{\partial z} - \frac{\partial E_z}{\partial x} = -j\omega\mu H_y \qquad (A.2)$$

$$\frac{\partial E_y}{\partial x} - \frac{\partial E_x}{\partial y} = -j\omega\mu H_z \qquad (A.3)$$

which originate from (2.1) and,

$$\frac{\partial H_z}{\partial y} - \frac{\partial H_y}{\partial z} = j\omega\varepsilon E_x \qquad (A.4)$$

$$\frac{\partial H_x}{\partial z} - \frac{\partial H_z}{\partial x} = j\omega\varepsilon E_y \qquad (A.5)$$

$$\frac{\partial H_y}{\partial x} - \frac{\partial H_x}{\partial y} = j\omega\varepsilon E_z \qquad (A.6)$$

which are obtained from (2.2). From these equations, a wave admittance Y, which is defined as the ratio of one of the components of magnetic field to an orthogonal component of electric field can be determined. Some examples used in this thesis are described below.

A.1 TEM plane waves, TE waves and TM waves

Following the orientations of waves and co-ordinate system shown in Fig. 2.1 and Fig. 2.2 of section 2.3, the wave admittance of TEM, TE or TM waves that are associated with power flow in the z-direction can be determined through the tangential field components polarised in the x and y directions. For the VCSEL, this admittance is sometimes called the longitudinal admittance since the power flow is normal to the reflectors. However, it is commonly known as the transverse wave admittance for in-plane stripe lasers or planar waveguides when it is used to calculate the transverse confinement in the y direction.

(a) TEM plane wave

The tangential field components are E_x and H_y and from (2.17a), $\beta = k$ where $k = \omega\sqrt{\varepsilon\mu}$. Using equation (A.2) or (A.4), the wave admittance is thus given by

$$Y_{TEM} = \frac{H_y}{E_x} = \frac{\beta}{\omega\mu} = N\sqrt{\frac{\varepsilon_0}{\mu_0}} = Y_{TEM}\, Y_0 \qquad (A.7)$$

where Y_0 ($= \sqrt{\varepsilon_0 / \mu_0}$.) is the TEM wave admittance in free space and has a approximate value of $1/120\pi$ and

$$Y_{TEM} = N \qquad (A.8)$$

is the normalised TEM wave admittance with respect to this free space TEM wave admittance Y_0.

(b) TE wave

The tangential field components are also E_x and H_y but $\beta = \sqrt{k^2 - k_y^2}$ as given by (2.17b). The wave admittance can be deduced from (A.2) or (A.4) as

$$Y_{TE} = \frac{H_y}{E_x} = \frac{\beta}{\omega\mu} = Y_{TE}\, Y_0 \qquad (A.9)$$

where

$$Y_{TE} = N\sqrt{1 - \frac{k_y^2}{k^2}} \qquad (A.10)$$

is the normalised TE wave admittance.

(c) TM wave

The tangential field components are H_x and E_y instead, but has similar value of β as TE wave. The wave admittance can be obtained from (A.1) or (A.5) as

$$Y_{TE} = -\frac{H_x}{E_y} = \frac{\omega\varepsilon}{\beta} = Y_{TM}\, Y_0 \qquad (A.11)$$

where

$$Y_{TM} = \frac{N}{\sqrt{1 - \frac{k_y^2}{k^2}}} \qquad (A.12)$$

is the normalised TM wave admittance.

A.2 Longitudinal Section Electric (LSE) Waves

The 2-D spatial Fourier transform discussed in section 5.2 shows that the Hermite - Gaussian modes can actually be decomposed into an infinite sum of LSE waves. The transverse field variations of these LSE waves vary as $\cos(k_x x)\cos(k_y y)$, $\cos(k_x x)\sin(k_y y)$, $\sin(k_x x)\cos(k_y y)$ and $\sin(k_x x)\sin(k_y y)$ for the TEM_{00}, TEM_{01}, TEM_{10} and TEM_{11} modes respectively. For linearly polarised TEM_{mp} modes propagating in the z-direction, these LSE waves are thus polarised in either x or y directions depending on the original polarisation of the TEM_{mp} mode assumed and the longitudinal propagation constant β is given by

$$\beta = \sqrt{k^2 - k_x^2 - k_y^2} \qquad (A.13)$$

as deduced from (2.15) (Note: $k = \omega\sqrt{\varepsilon\mu}$). It is found that the wave admittance of the LSE waves for all the TEM_{mp} modes polarised in same direction are ***identical.*** Thus, the following workings only show the derivations of the LSE wave admittance for the fundamental TEM_{00} mode. The reference for the co-ordinate system used in the derivations below are similar to that depicted in Fig. 4.1.

A.2.1 x-polarised LSE waves

For the fundamental TEM_{00} mode *polarised in the x-direction* and propagating in the longitudinal z-direction, the transverse electric fields components of the LSE waves are

$$E_x = \cos(k_x x)\cos(k_y y)\exp(-j\beta z) \qquad (A.14)$$

and $E_y = 0$. Substituting (A.14) into (A.3), H_z is thus given by

$$H_z = \frac{jk_y}{\omega\mu}\cos(k_x x)\sin(k_y y)\exp(-j\beta z) \qquad (A.15)$$

Then substituting (A.14) and (A.15) into (A.4), H_y can be deduced as

$$H_y = \left(\frac{\omega^2\varepsilon\mu - k_y^2}{\beta\omega\mu}\right) E_x \qquad (A.16)$$

From (A.16), the +z longitudinal wave admittance for the LSE wave polarised in the x-direction is thus expressed by

$$Y_{LSE,x} = \frac{H_y}{E_x} = \frac{k^2 - k_y^2}{\beta\omega\mu} = Y_0 \frac{\left(k^2 - k_y^2\right)}{\beta k_0} \tag{A.17}$$

where $(k/\omega\mu) = NY_0$. The normalised LSE wave admittance is thus given by

$$Y_{LSE,x} = \frac{N}{\beta k}\left(k^2 - k_y^2\right) \tag{A.18}$$

Subsequently, using(A.5) and (A.1) the other two field components H_x and E_z can be obtained by

$$H_x = \frac{k_x k_y}{\beta\omega\mu}\sin(k_x x)\sin(k_y y)\exp(-j\beta z) \tag{A.19}$$

$$E_z = \frac{j\,k_x}{\beta}\sin(k_x x)\cos(k_y y)\exp(-j\beta z) \tag{A.20}$$

A.2.2 y-polarised LSE waves

For the fundamental TEM_{00} mode *polarised in the y-direction* and propagating in the longitudinal z-direction, the transverse electric fields components of the LSE waves are

$$E_y = \cos(k_x x)\cos(k_y y)\exp(-j\beta z) \tag{A.21}$$

and $E_x = 0$. Substituting (A.22) into (A.3), H_z is thus given by

$$H_z = \frac{-jk_x}{\omega\mu}\sin(k_x x)\cos(k_y y)\exp(-j\beta z) \tag{A.22}$$

Then substituting (A.22) and (A.23) into (A.5), H_x can be deduced as

$$H_x = \left(\frac{k_x^2 - \omega^2\varepsilon\mu}{\beta\omega\mu}\right) E_y \tag{A.23}$$

From (A.24), the +z longitudinal wave admittance for the LSE wave polarised in the y-direction is thus expressed by

$$Y_{LSE,y} = -\frac{H_x}{E_y} = \frac{k^2 - k_x^2}{\beta\omega\mu} = Y_0 \frac{\left(k^2 - k_x^2\right)}{\beta k_0} \tag{A.24}$$

where the normalised LSE wave admittance is given by

$$Y_{LSE,y} = \frac{N}{\beta k}\left(k^2 - k_x^2\right) \tag{A.25}$$

Subsequently, using(A.5) and (A.1) the other two field components H_y and E_z can be obtained by

$$H_y = \frac{-k_x k_y}{\beta\omega\mu}\sin(k_x x)\sin(k_y y)\exp(-j\beta z) \qquad (A.26)$$

$$E_z = \frac{j k_y}{\beta}\cos(k_x x)\sin(k_y y)\exp(-j\beta z) \qquad (A.27)$$

Finally, note that although the LSE wave admittance are similar for all the TEM_{mp} modes polarised in the same directions, the expressions for the individual field components differ for each case.

Appendix B : High Index Contrast DBRs

Unlike other dielectric reflector stacks such as ZnSe/MgF or TiO_2/SiO_2 which have to be grown by plasma deposition, high index contrast ratio $Al_xGa_{1-x}As$ oxide/$Al_xGa_{1-x}As$ DBRs can be formed easily through a selective wet oxidation process. These types of oxide mirrors are especially valuable for VCSELs operating in the visible 650nm wavelength region and the telecommunication wavelength of 1550nm where the lattice-matched semiconductor DBR materials available provide little index contrast ratio. Using such oxide DBRs, only 4 or 5 mirror periods are needed to achieve reflectance in excess of 99%.

850nm Design

$Al_{0.2}Ga_{0.8}As$	613 Å
AlAs	1510 Å
$Al_{0.2}Ga_{0.8}As$	613 Å
Substrate	

X 5

650nm Design

$Al_{0.5}Ga_{0.5}As$	465 Å
AlAs	1191 Å
$Al_{0.5}Ga_{0.5}As$	3255 Å
AlAs	525 Å
Substrate	

X 5

Figure B.1 : Designs of AlAs oxide DBRs for operation at wavelengths of 850nm and 650nm

Figure B.1 shows the DBR designs used to demonstrate the feasibility of making high contrast Al_xO_y mirrors at wavelengths of 850nm and 650nm. It is assumed that the thickness of the oxidised AlAs layer shrinks by 12% after the oxidation process and the refractive index of Al_xO_y is 1.55. In the 650nm case, the existence of the first mirror pair AlAs/$Al_{0.5}Ga_{0.5}As$ closest to substrate is not related to the feasibility study discussed here. Fig B.2 and B.3 compare the experimental reflectivity spectra of these mirrors before and after oxidation with those predicted by theoretical simulations. Note that the curves for after oxidation have been offset from those before oxidation for the sake of clarity. Clearly, these mirrors look promising as the "after oxidation" experimental curves closely match the theoretical predictions from the viewpoint of stop-band bandwidth. The relative reflectance measured (not

explicitly shown in the figures due to offset) are also above 99% at the designed mirror central wavelength.

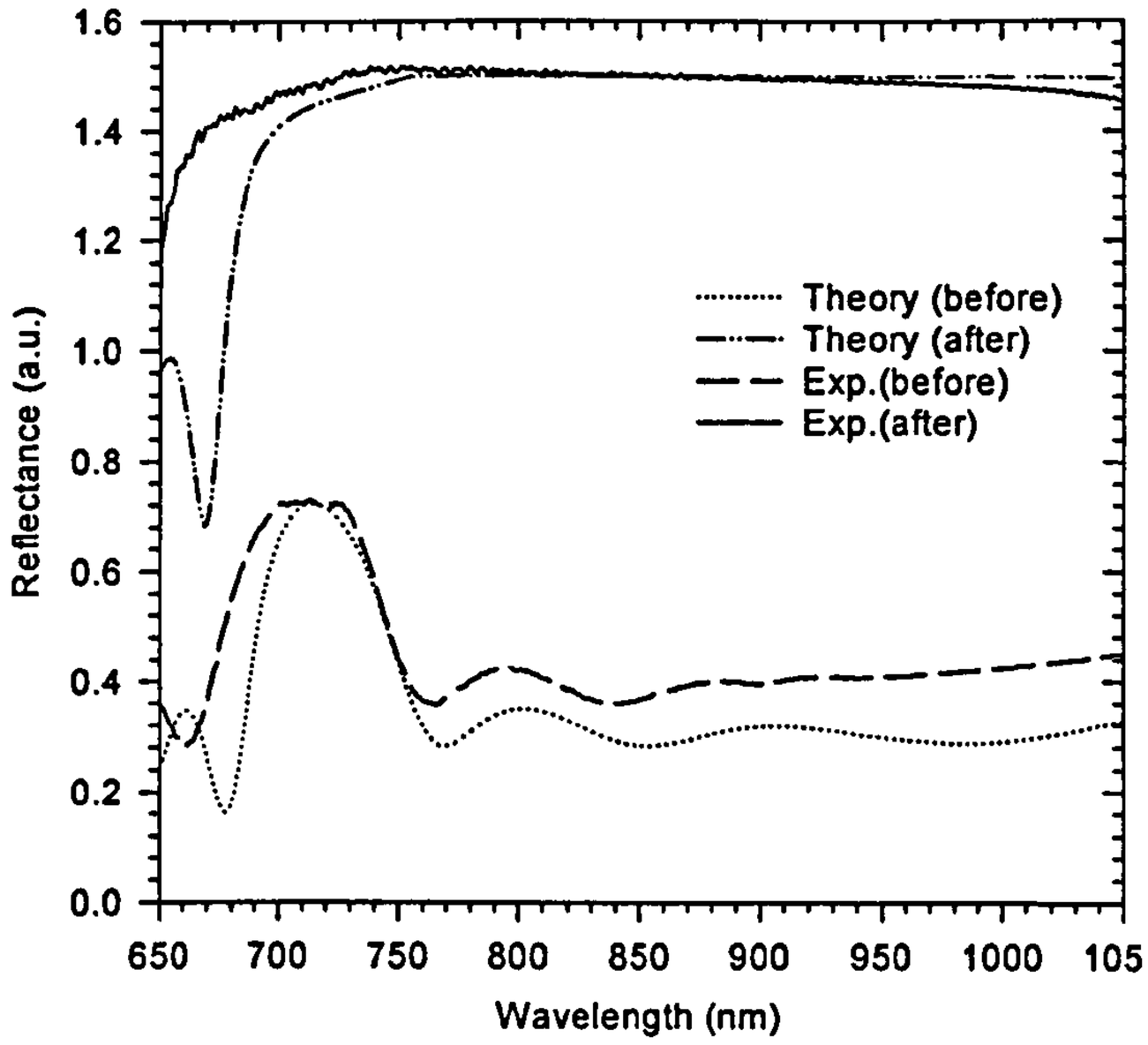

Figure B.2 : Reflectivity spectra of the 850nm oxide DBR before and after oxidation. The curves for "after oxidation" have been offset from those "before oxidation" for the sake of clarity

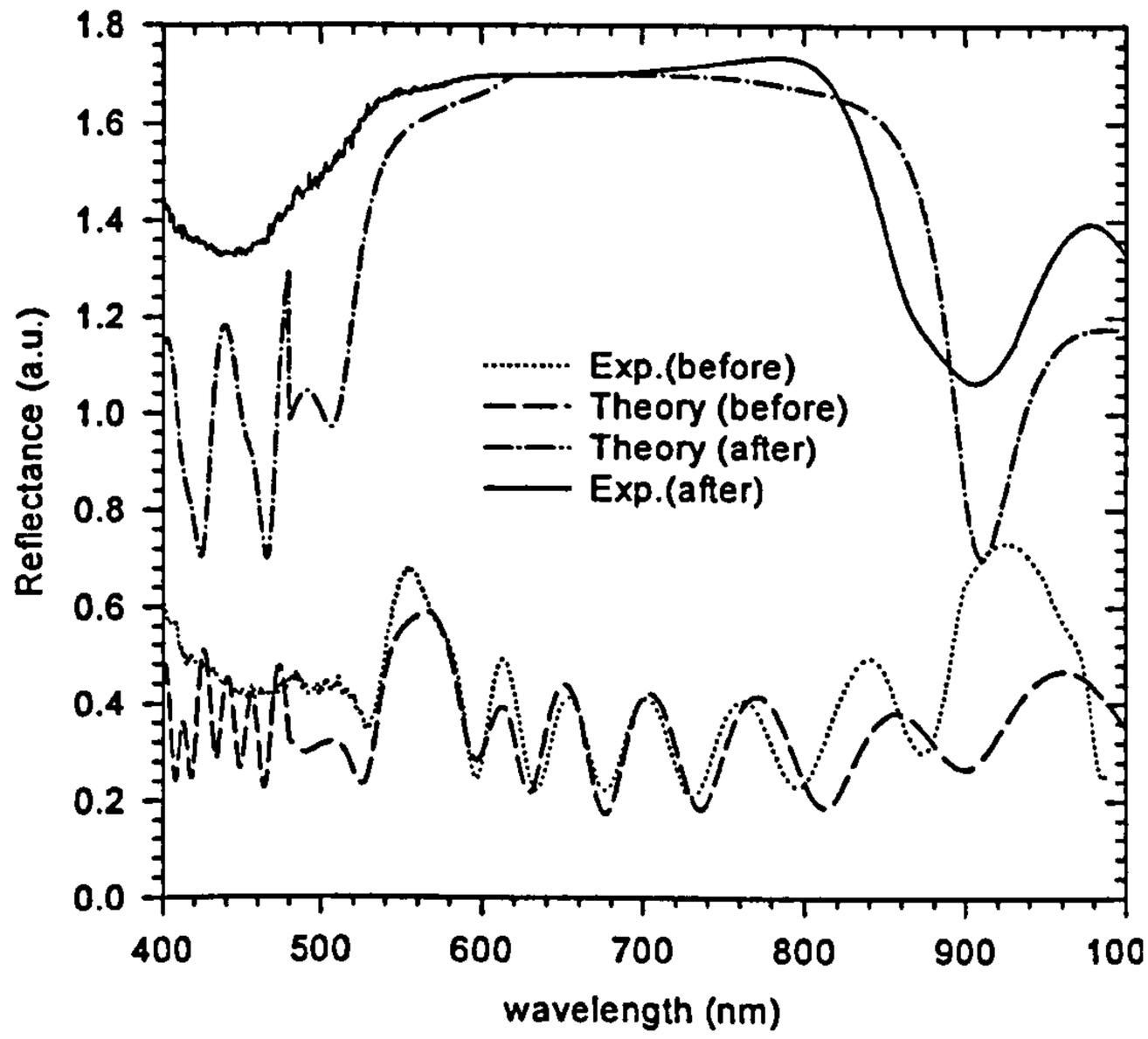

Figure B.3 : Reflectivity spectra of the 650nm oxide DBR before and after oxidation. The curves "for after oxidation" have been offset from those "before oxidation" for the sake of clarity

Appendix C : Stationary Property of Scalar Variational Formulae

In chapter 4, the scalar variational integral formulae for a resonator is derived as

$$\frac{\omega^2}{c^2} = \frac{\iiint_V \left[\left(\frac{\partial E}{\partial x}\right)^2 + \left(\frac{\partial E}{\partial y}\right)^2 + \left(\frac{\partial E}{\partial z}\right)^2\right] dxdydz}{\iiint n^2 E^2 \, dxdydz} \qquad (C.1)$$

Suppose now E is incremented by a small arbitrary function Δ, and consequently the resonant frequency term changes to $(\omega^2 + \delta)$. Rearranging, eqn. (C.1) thus becomes

$$\frac{(\omega^2 + \delta)}{c^2} \iiint_V n^2 (E + \Delta)^2 dV$$

$$= \iiint_V \left[\left(\frac{\partial (E+\Delta)}{\partial x}\right)^2 + \left(\frac{\partial (E+\Delta)}{\partial y}\right)^2 + \left(\frac{\partial (E+\Delta)}{\partial z}\right)^2\right] dxdydz \qquad (C.2)$$

Assuming that Δ and δ are sufficiently small that only the first order terms need to be considered, eqn. (C.2) can then be rewritten as

$$\frac{(\omega^2 + \delta)}{c^2} \iiint_V n^2 (E + 2E\Delta) \, dV$$

$$= \iiint_V \left[\left(\frac{\partial E}{\partial x}\right)^2 + \left(\frac{\partial E}{\partial y}\right)^2 + \left(\frac{\partial E}{\partial x}\right)^2 + 2\frac{\partial \Delta}{\partial x}\frac{\partial E}{\partial x} + 2\frac{\partial \Delta}{\partial y}\frac{\partial E}{\partial y} + 2\frac{\partial \Delta}{\partial z}\frac{\partial E}{\partial z}\right] dxdydz \qquad (C.3)$$

Expanding and rearranging, (C.3) becomes

$$\left\{\frac{\omega^2}{c^2} \iiint_V n^2 E \, dV - \iiint_V \left(\frac{\partial E}{\partial x}\right)^2 + \left(\frac{\partial E}{\partial y}\right)^2 + \left(\frac{\partial E}{\partial x}\right)^2 dV\right\} + \frac{\delta}{c^2} \iiint_V n^2 E \, dV$$

$$+ \frac{\omega^2}{c^2} \iiint_V 2n^2 E\Delta \, dV = \iiint_V 2\left[\frac{\partial \Delta}{\partial x}\frac{\partial E}{\partial x} + \frac{\partial \Delta}{\partial y}\frac{\partial E}{\partial y} + \frac{\partial \Delta}{\partial z}\frac{\partial E}{\partial z}\right] dxdydz \qquad (C.4)$$

where it is easy to recognise that the sum of the terms inside the curly bracket is equal to zero as can be deduced from (C.1). Hence, (C.4) can be reduced to

$$\frac{\delta}{2c^2}\iiint_V n^2 E\,dV + \frac{\omega^2}{c^2}\iiint_V n^2 E\Delta\,dV = \iiint_V \left[\frac{\partial\Delta}{\partial x}\frac{\partial E}{\partial x}+\frac{\partial\Delta}{\partial y}\frac{\partial E}{\partial y}+\frac{\partial\Delta}{\partial z}\frac{\partial E}{\partial z}\right]dxdydz \tag{C.5}$$

To proceed further, an extra term $\iiint_V (\nabla^2 E)\Delta\ dV$ is added to both sides of (C.5). This results in

$$\frac{\delta}{2c^2}\iiint_V n^2 E\,dV + \iiint_V \left\{\nabla^2 E + \frac{\omega^2 n^2}{c^2}E\right\}\Delta\ dV$$

$$= \iiint_V (\nabla^2 E)\Delta\,dV + \iiint_V \left[\frac{\partial\Delta}{\partial x}\frac{\partial E}{\partial x}+\frac{\partial\Delta}{\partial y}\frac{\partial E}{\partial y}+\frac{\partial\Delta}{\partial z}\frac{\partial E}{\partial z}\right]dxdydz \tag{C.6}$$

Again, it can be instantly recognised that the terms inside the curly bracket of (C.6) is the wave equation and thus equal to zero. Grouping the differential terms in respective axis together, eqn.(C.6) can then be simplified to

$$\frac{\delta}{2c^2}\iiint_V n^2 E\,dV = \iiint_V \left[\frac{\partial}{\partial x}\left(\Delta\frac{\partial E}{\partial x}\right)+\frac{\partial}{\partial y}\left(\Delta\frac{\partial E}{\partial y}\right)+\frac{\partial}{\partial z}\left(\Delta\frac{\partial E}{\partial z}\right)\right]dxdydz$$

$$= \iint_S \left[\left|\Delta\frac{\partial E}{\partial x}\right|_{\infty} - \left|\Delta\frac{\partial E}{\partial x}\right|_{-\infty}\right]dydz + \iint_S \left[\left|\Delta\frac{\partial E}{\partial y}\right|_{\infty} - \left|\Delta\frac{\partial E}{\partial y}\right|_{-\infty}\right]dxdz$$

$$+ \iint_S \left[\left|\Delta\frac{\partial E}{\partial z}\right|_{\infty} - \left|\Delta\frac{\partial E}{\partial z}\right|_{-\infty}\right]dxdy \tag{C.7}$$

Now, if Δ is zero on the boundary (i.e. the small perturbation in E-field also satisfies the boundary conditions, all the integral terms on the right hand side of (C.7) become zero. This means that δ is zero as well. In conclusion, there is no first order change in ω^2 for a small error Δ in the trial field.

Appendix D : Useful Integral Solutions for Gaussian Functions

Besides being sufficiently realistic in describing the field variation of the transverse modes supported by the VCSELs, the main advantage for using trial fields with Hermite-Gausian transverse functions in the variational integral formulae discussed in Chapter 4 is that the resulting integrals are always in handy, tractable forms. The list below gives the solutions and expressions that are necessary for the derivation of variational formulae discussed in section 4.2. Equations (D.1) to (D.6) give the solutions for the infinite integration of these functions, while equations (D.7) to (D.12) offer the expression for integrals involving variables. Based on the solution for the lower order functions, the expressions for higher order functions listed below were obtained through integration by parts.

I. Solutions for Infinite Integration

$$\int_0^\infty \exp\left(\frac{-2r^2}{r_0^2}\right) dr = \frac{1}{2}\sqrt{\frac{\pi}{2}}\, r_0 \tag{D.1}$$

$$\int_0^\infty r \exp\left(\frac{-2r^2}{r_0^2}\right) dr = \frac{r_0^2}{4} \tag{D.2}$$

$$\int_0^\infty r^2 \exp\left(\frac{-2r^2}{r_0^2}\right) dr = \frac{1}{8}\sqrt{\frac{\pi}{2}}\, r_0^3 \tag{D.3}$$

$$\int_0^\infty r^3 \exp\left(\frac{-2r^2}{r_0^2}\right) dr = \frac{r_0^4}{8} \tag{D.4}$$

$$\int_0^\infty r^4 \exp\left(\frac{-2r^2}{r_0^2}\right) dr = \frac{3}{32}\sqrt{\frac{\pi}{2}}\, r_0^5 \tag{D.5}$$

$$\int_0^\infty r^5 \exp\left(\frac{-2r^2}{r_0^2}\right) dr = \frac{r_0^6}{8} \tag{D.6}$$

$$\int_0^\infty r^7 \exp\left(\frac{-2r^2}{r_0^2}\right) dr = \frac{3r_0^8}{16} \tag{D.7}$$

II. Expressions for Integration involving Variable

$$\int_0^a \exp\left(\frac{-2r^2}{r_0^2}\right) dr = \frac{\sqrt{\pi}\, r_0}{2\sqrt{2}} \operatorname{erf}\left(\frac{\sqrt{2}\, a}{r_0}\right) \tag{D.8}$$

$$\int_a^\infty r \exp\left(\frac{-2r^2}{r_0^2}\right) dr = \frac{r_0^2}{4} \exp\left(\frac{-2a^2}{r_0^2}\right) \tag{D.9}$$

$$\int_0^a r^2 \exp\left(\frac{-2r^2}{r_0^2}\right) dr = \frac{\sqrt{\pi}\, r_0^3}{8\sqrt{2}} \left[\operatorname{erf}\left(\frac{\sqrt{2}\, a}{r_0}\right) - \frac{2\sqrt{2}\, a}{\sqrt{\pi}\, r_0} \exp\left(\frac{-2a^2}{r_0^2}\right)\right] \tag{D.10}$$

$$\int_a^\infty r^3 \exp\left(\frac{-2r^2}{r_0^2}\right) dr = \frac{r_0^4}{8}\left(1+\frac{2a^2}{r_0^2}\right) \exp\left(\frac{-2a^2}{r_0^2}\right) \tag{D.11}$$

$$\int_a^\infty r^5 \exp\left(\frac{-2r^2}{r_0^2}\right) dr = \frac{r_0^6}{8}\left(1+\frac{2a^2}{r_0^2}+\frac{2a^4}{r_0^4}\right) \exp\left(\frac{-2a^2}{r_0^2}\right) \tag{D.12}$$

Finally, note that the "seed" solution for all the integral solutions listed above is

$$\int_{-\infty}^{\infty} \exp(-t^2)\, dt = \sqrt{\pi} \tag{D.13}$$

(Reference : e.g. "Mathematical Methods in the Physical Science, by M.L.Boas, [John Wiley & Sons, 1993])

Appendix E : Spatial Fourier Transform Pairs of Hermite-Gaussian Functions

The general expressions for the one-dimensional Fourier transform pair in space are given by

$$F(k_x) = \int_{-\infty}^{\infty} f(x) \exp(-jk_x x)\, dx \qquad (E.1)$$

$$f(x) = \frac{1}{2\pi} \int_{-\infty}^{\infty} F(k_x) \exp(jk_x x)\, dk_x \qquad (E.2)$$

where x is the spatial distance and k_x is corresponding phase constant.

E.1 Spatial Fourier Transform of 1-D Hermite-Gaussian Functions

The spatial function of the fundamental order Gaussian function is expressed by

$$f_0(x) = \exp\left(\frac{-x^2}{r_0^2}\right) \qquad (E.3)$$

Its Fourier transform can then be obtained by substituting (E.3) into (E.1), which leads to

$$F_0(k_x) = \exp\left(-\frac{k_x^2 r_0^2}{4}\right) \int_{-\infty}^{\infty} \exp\left[-\frac{\left(x + jk_x r_0^2/2\right)^2}{r_0^2}\right] dx \qquad (E.4)$$

Now, if $\sqrt{2}\, s = x + jk_x r_0^2 / 2$ and thus $dx = \sqrt{2}\, ds$, eqn. (E.4) becomes

$$\begin{aligned} F_0(k_x) &= \sqrt{2} \exp\left(-\frac{k_x^2 r_0^2}{4}\right) \int_{-\infty}^{\infty} \exp\left(\frac{-2s^2}{r_0^2}\right) ds \\ &= \sqrt{\pi}\, r_0 \exp\left(-\frac{k_x^2 r_0^2}{4}\right) \end{aligned} \qquad (E.5)$$

where the integral solutions (D.1) has been exploited.

Next, the first order 1-D Hermite-Gaussian spatial function is given by

$$f_1(x) = x \exp\left(\frac{-x^2}{r_0^2}\right) = -\frac{r_0^2}{2}\frac{d f_0(x)}{dx} \tag{E.6}$$

Then, by making use of the fact that

$$F\left(\frac{df_0(x)}{dx}\right) = jk_x F_0(k_x) \tag{E.7}$$

, its spatial Fourier transform $F_1(k_x)$ can thus be deduced as

$$F_1(k_x) = \frac{-jk_x r_0^3\sqrt{\pi}}{2} \exp\left(-\frac{k_x^2 r_0^2}{4}\right) \tag{E.8}$$

E.2 Spatial "Inverse" Fourier Transform of 1-D Hermite-Gaussian Functions

Having obtained the spatial Fourier transforms in the spatial frequency domain (i.e. k-space), eqn.(E.2) can then be used to obtain the spatial "inverse" Fourier transform of the corresponding functions in the Fourier integral forms and written in terms of both distance and spatial frequency.

Beginning with the fundamental Gaussian function, the spatial Fourier integral functions f_0 is obtained by substituting (E.5) into (E.2),

$$\begin{aligned} f_0(x) &= \frac{\sqrt{\pi} r_0}{2\pi} \int_{-\infty}^{\infty} \exp\left(\frac{-k_x^2 r_0^2}{4}\right) \exp(jk_x x)\, dk_x \\ &= \frac{r_0}{\sqrt{\pi}} \int_0^{\infty} \exp\left(\frac{-k_x^2 r_0^2}{4}\right) \cos(k_x x)\, dk_x \end{aligned} \tag{E.9}$$

As for the first order Hermite-Gaussian function, the inverse Fourier transform of (E.8) leads to

$$\begin{aligned} f_1(x) &= \frac{-jr_0^3\sqrt{\pi}}{4\pi} \int_{-\infty}^{\infty} k_x \exp\left(\frac{-k_x^2 r_0^2}{4}\right) \exp(jk_x x)\ dk_x \\ &= \frac{r_0^3}{2\sqrt{\pi}} \int_0^{\infty} k_x \exp\left(\frac{-k_x^2 r_0^2}{4}\right) \sin(k_x x)\ dk_x \end{aligned} \tag{E.10}$$

Appendix F : Device Fabrication

Prior to the device fabrication process, the 2-inch MOCVD as-grown VCSEL wafer is usually first mapped to obtain the variation of the (plane) resonant wavelength using a standard photo-reflectance (PR) set-up. Room temperature and low temperature 10K photo-luminescene (PL) measurements are also carried out on a small piece of material to determine the PL peak wavelength and linewidth. The room temperature PL peak wavelengths of the three VCSEL layers used in this work are around 855nm, with a possible variation of ±6nm across the wafer [1]. The 10K PL linewidths are about 6 to 7 meV indicating reasonably good QW quality, as these values are comparable to previous successfully working VCSEL wafers [1]. After that, samples with typical sizes of about (9x9)mm are cleaved from the wafer region having a resonant wavelength close to the room temperature PL peak, and ready for device fabrication.

The fabrication process begins with deposition of the p-type Au/Zn/Au (top) and n-type InGe/Au (bottom) ohmic-contacts through thermal evaporation of metals and standard lift-off process. After the alloying process, etched mesas of different sizes and shapes that are aligned properly with respect to the metal contacts, are obtained through reactive ion etching (RIE) or wet etching using photo-resist as the etch masks. The etching process is controlled carefully (using an in-situ optical monitoring system in the case of RIE, and proper etch rate calibration in the case of wet-etching) so that the etched depth is sufficient to expose the AlAs layer to be oxidised, but does not penetrate too deeply into the bottom DBR to avoid increasing the device series resistance unnecessarily. The emulsion masks used in this work were designed and made in-house. The patterns on the masks are transferred from those defined on rubylith through an optical step and repeat process. The sizes/diameters of the square/circular mesas are increased from 48μm to 60μm in 1μm steps. Rectangular and elliptical mesas with 1μm to 3μm differences between the longer and shorter sides are also available within the same cell. After the etching process that exposes the AlAs layer, care is taken not to the subject the sample to excess heating during the subsequent sample cleaning procedure (such as removing the resist mask and wax at the back of substrate, etc.), prior to the selective wet oxidation process

itself. This is to avoid unintentional thermal oxidation in the uncontrolled environment, which has been found to give rise to oxide apertures with irregular edges after the subsequent wet oxidation process.

Compared to the other methods for providing current constriction in lasers e.g. proton implantation, selective wet oxidation is a relative simple and cheap procedure pioneered by N.Holonyak and J.M.Dallesasse from University of Illinois in 1990 [2]. They discovered that by simply exposing a high Al-content semiconductor such as $Al_xGa_{1-x}As$ to water vapor transported in an inert gas within an elevated temperature (350°C - 500°C) environment, a mechanically stable oxide with lower refractive index was formed [3]. While more sophisticated oxidation systems exist [4,5], Figure F.1 show the schematics of the comparatively simple oxidation apparatus used in this work.

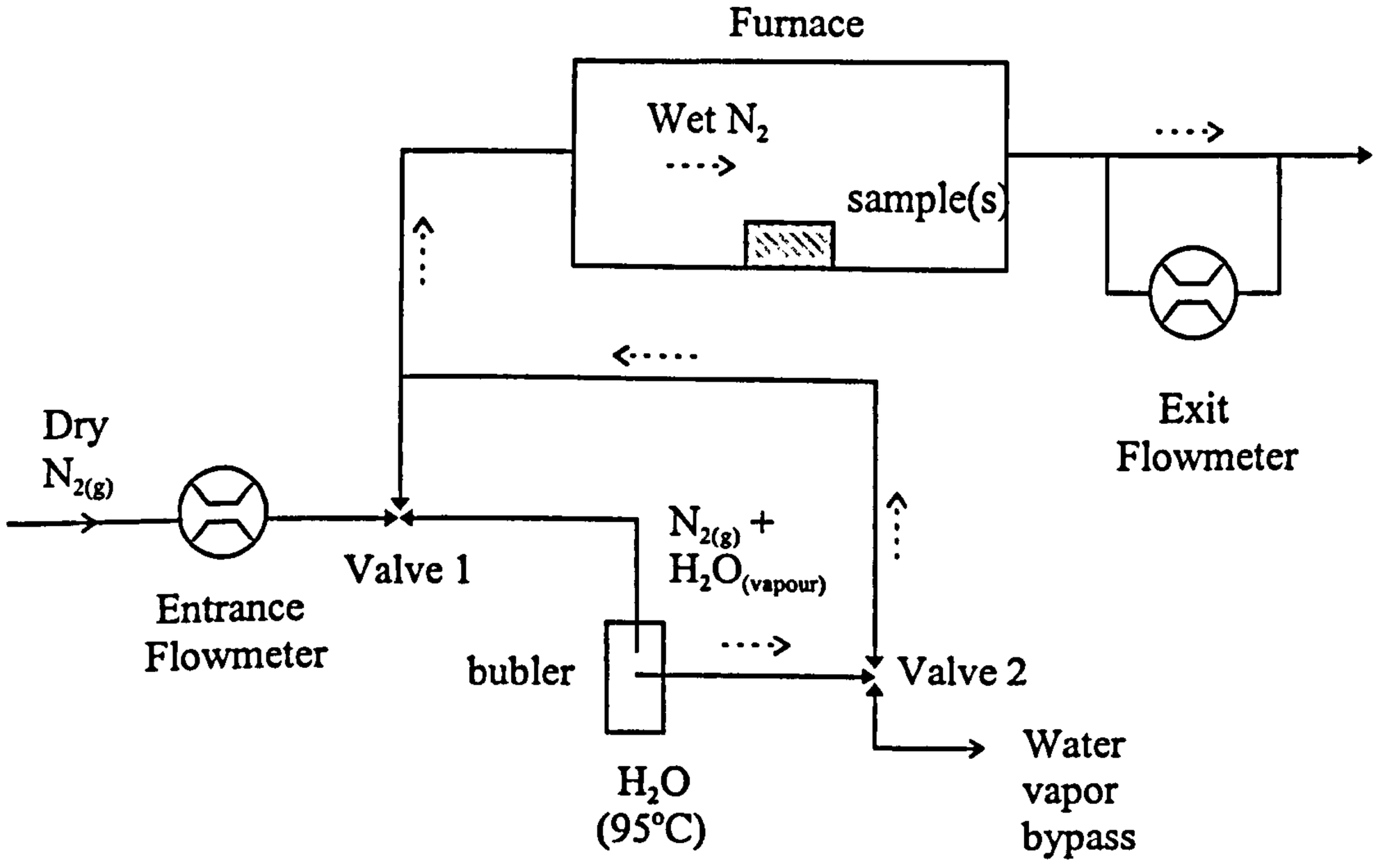

Figure F.1 : Schematics of oxidation setup used in this work. The hatched arrows show the flow of wet N_2 during oxidation

The oxidation is carried out in a 2-in. diameter quartz tube with a single heat zone furnace maintained at a temperature ranging from 380°C to 420°C, in wet nitrogen ambient. The furnace is preheated for about an hour until it stabilises and reaches the desired pre-set temperature. During this period, the quartz tube is flushed with pre-filtered dry nitrogen gas (99% purity) regulated by flow meters at the

entrance and the exit to ensure no leakage of gases from the tube. The temperature inside the tube is monitored by a thermocouple directly attached to beneath the center of a 0.25 inch thick- (3x3)cm quartz sample holder with a quartz push rod. To begin the wet oxidation process, the dry N_2 gas is diverted and bubbled through a 0.5-litre flask containing de-ionized water heated to 95±1°C by a heating mantle; thus acting as the carrier gas for the water vapor. The typical flow rate of the wet N_2 gas (i.e. N_2 + H_2O) used in this work is about 0.3 litre/min, although flow rate of as high as 0.70 liter/min can be used. The stainless steel tube leading to the furnace quartz tube from the bubbler and the front part of the quartz tube are heated by heating tapes to more than 100 °C to prevent condensation from affecting the stability of the water vapour supply. The end of the tube is capped except for an exhaust line, and the unheated exit flow meter is by passed once oxidation begins.

At the beginning of each oxidation run, the samples are left in the cool region of the tube (<100°C) while the tube is purged with the dry N_2 for about 15 minutes to get rid of any oxygen gas that might be present due to the sample loading process. Loaded with the samples to be oxidized, the quartz holder is then pushed into the vicinity of the furnace hot zone where the temperature is about 120°C (to avoid condensation on the sample) before the wet N_2 is allowed to start flowing. The oxidation furnace is then allowed to equilibrate with the wet N_2 gas for about 5 minutes during which time the temperature of the holder rose by about 45 degrees before stabilizing (This indicates that the wet N_2 is hotter than 120°C). Then the sample holder is pushed to the center (hottest part) of the hot zone and left to oxidize for the target period of time at the final temperature. At the end of the process, the sample holder is pulled out away from the hot zone immediately and the wet nitrogen supply is switched off. Dry nitrogen is then supplied at a maximum flow rate (0.70 liter/min) to flush out any residual water vapor left in the tube while the sample is cooling down. The samples were then removed from the tube when the temperature of the holder drops below 100°C. Figure 4.2 shows the typical temperature characteristic of the sample holder detected by the thermocouple during the heating up and cooling down transition period for target oxidation temperature of 400°C and 380°C. It is assumed that the temperature characteristic of the samples residing directly above the thermocouple are well represented by that of Fig. 4.2. The count time for these oxidation processes were clocked at 380°C or 360°C (95% of the final temperature)

respectively at which the rising temperature gradient of the sample holder has flattened considerably.

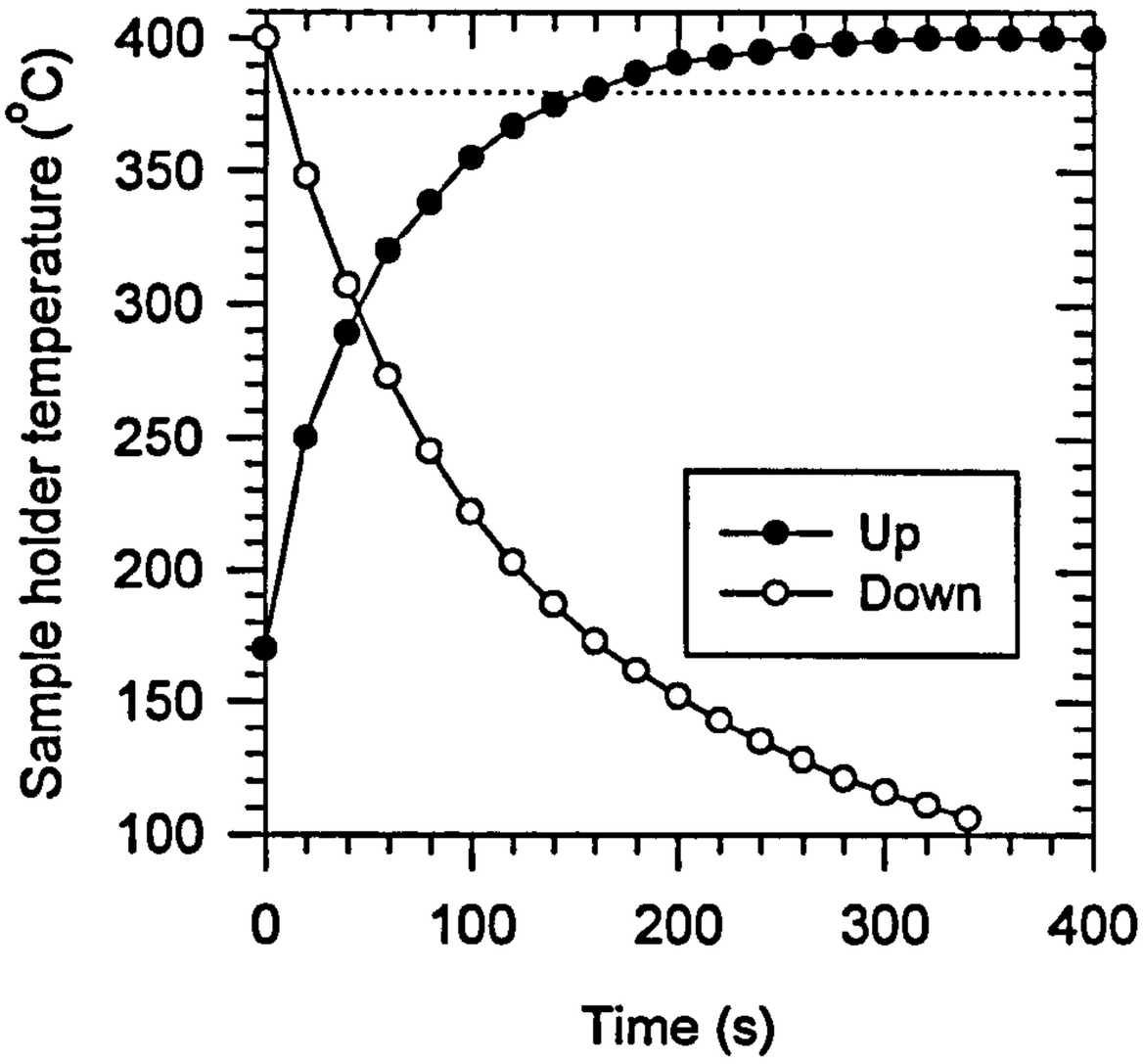

Figure F.2 : Typical temperature characteristics of the sample holder during the heating up and cooling down transition period for target oxidation of 400 °C.

It is well known that the selective wet lateral oxidation rate is affected by temperature, thickness and Al fraction in the oxidised $Al_xGa_{1-x}As$ layer [4-7], composition of embedding barrier layers [8], and to a certain extent doping type and concentration as well [9]. In this work, a simple test structure that is basically a single-pair DBR containing 600Å AlAs is used for calibration purposes. The order of the structure is as follows : 100Å GaAs/ 424Å $Al_{0.2}Ga_{0.8}As$ /200Å $Al_{0.5}Ga_{0.5}As$ / 600Å AlAs / 200Å $Al_{0.5}Ga_{0.5}As$ / 1000Å GaAs / substrate. After the oxidation, the visible contrast between the oxidized and unoxidised region can be observed clearly for this particular structure that has a relatively thin absorbing GaAs cap and $Al_{0.2}Ga_{0.8}As$ layer. This allows measurement of the lateral oxidation distance from the mesa edge as well as the aperture size directly using an optical microscope equipped with a calibrated eyepiece and a 100x microscope objective (numerical aperture, N.A. = 0.95). However, for the full VCSEL structure which has thick top DBR that is highly absorbing in the visible wavelength, an optical high-pass (wavelength) filter of 715nm is needed to observe the aperture. It is used to block off the visible light from the broad-band light source so that the contrast in the infra-red wavelengths can be picked

up by a sensitive black and white CCD camera connected to a monitor screen. The lateral oxidation distance or oxide aperture size is then deduced with reference to calibrated distance found on commercial calibrated gratings. The measured dimensions were obtained from the image on the monitor screen or printed image (on video printer paper).

After measuring the mesas of various sizes and shapes using both RIE and wet etching, the samples made from the test structure are loaded into the system for oxidation at temperature of 400°C. It is found that the oxide apertures resulting from square and circular mesas are always rectangular and elliptical in shapes respectively, with the longer side of the aperture parallel to the <110> crystal axis. For the square mesas that were oxidised for 15min, Figures F.3 illustrate the typical variations of the oxidation distance in the two orthogonal directions, measured from the mesa edges. Clearly, the asymmetry in the aperture shapes are less serious for the mesas with larger aperture size. This kind of crystallographic dependence of oxidation rate has also been observed by other researchers [3], and is believed to be due to the difference in surface reactivity presented by the crystallographic planes. By using lower Al content $Al_xGa_{1-x}As$ ($x < 0.94$) which was not available for this work as the oxide aperture, it is also claimed that this asymmetry in the aperture shape can be reduced [3]. Fortunately, it is found that by orientating the rectangular mesas along the direction with faster oxidation rate, the asymmetry in the aperture shape can also be reduced such that the ratio of the longer side to shorter side are improved to 1.07 or better. (Note that it was less successful to produce circular device by orientating the elliptical mesas along the direction with faster oxidation rate.) As discussed in chapter 4 and chapter 6, these nearly square devices are used for comparing the resonant frequencies, threshold and single mode performance of the strong, medium and weak guiding devices. The results in Fig. F.3 also imply that the lateral oxidation rate is dependent on the starting mesa size. Because of this, the successive final apertures sizes obtained are not in 1μm size steps, even in the case of devices with near-square apertures.

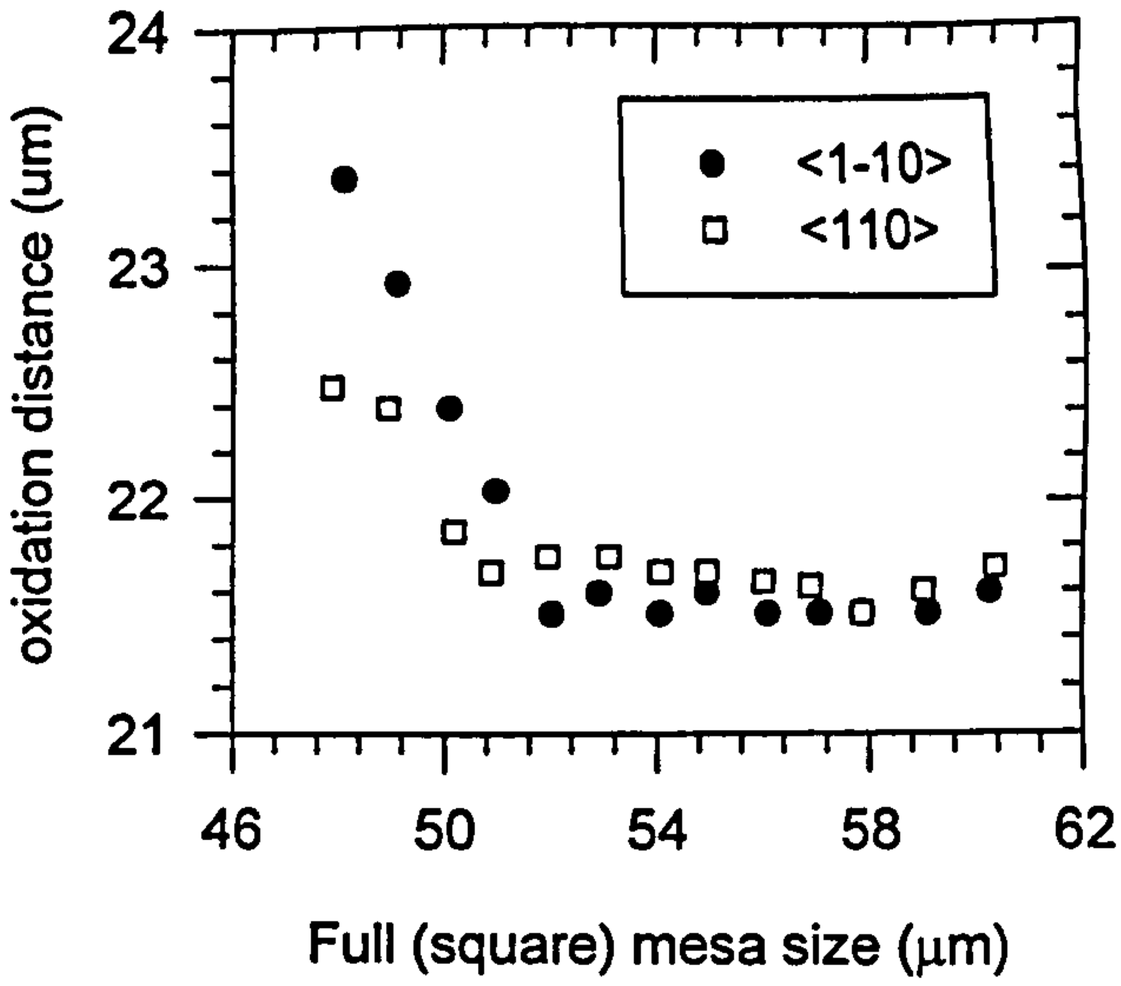

Figure F.3 : Typical variation of oxidation distances in the orthogonal $\langle 110 \rangle$ and $\langle 1\bar{1}0 \rangle$ directions as a function of the square mesa sizes, measured from a test structure sample.

Figure F.4 shows the variation of the oxidation distance along the $\langle 1\bar{1}0 \rangle$ direction obtained from test structure sample, as a function of oxidation period for mesa size of 50μm and 60μm. Note that the data points shown are the average of values taken over 3 or 4 runs. There is a run to run fluctuation of about ±1.5μm in the oxidation distance, leaving an uncertainty of ±3μm in the final aperture size. The most likely and apparent cause is the fluctuation in the temperature of the oxidising sample, reflected in the fluctuation in the sample holder temperature (±2°C) that are sometimes observed during the course of oxidation. This fluctuation might in turn be due to the changes in the ambient temperature, flow rate of wet N_2 or temperature of the heat zone itself. Obviously, if this selective oxidation process were to become commercially viable, the reproducibility of producing low threshold and single mode oxidised VCSELs with aperture size less than 4μm, has to be improved from what can be achieved by conventional systems like the one described above. By imposing more stringent temperature and gas flow control, it is claimed that the variation of the oxidation rate can be improved to just ±2% across a 3-inch wafer [4]. To define small features reliably, a novel low pressure steam furnace system with in-situ optical monitor system has also been demonstrated recently [5].

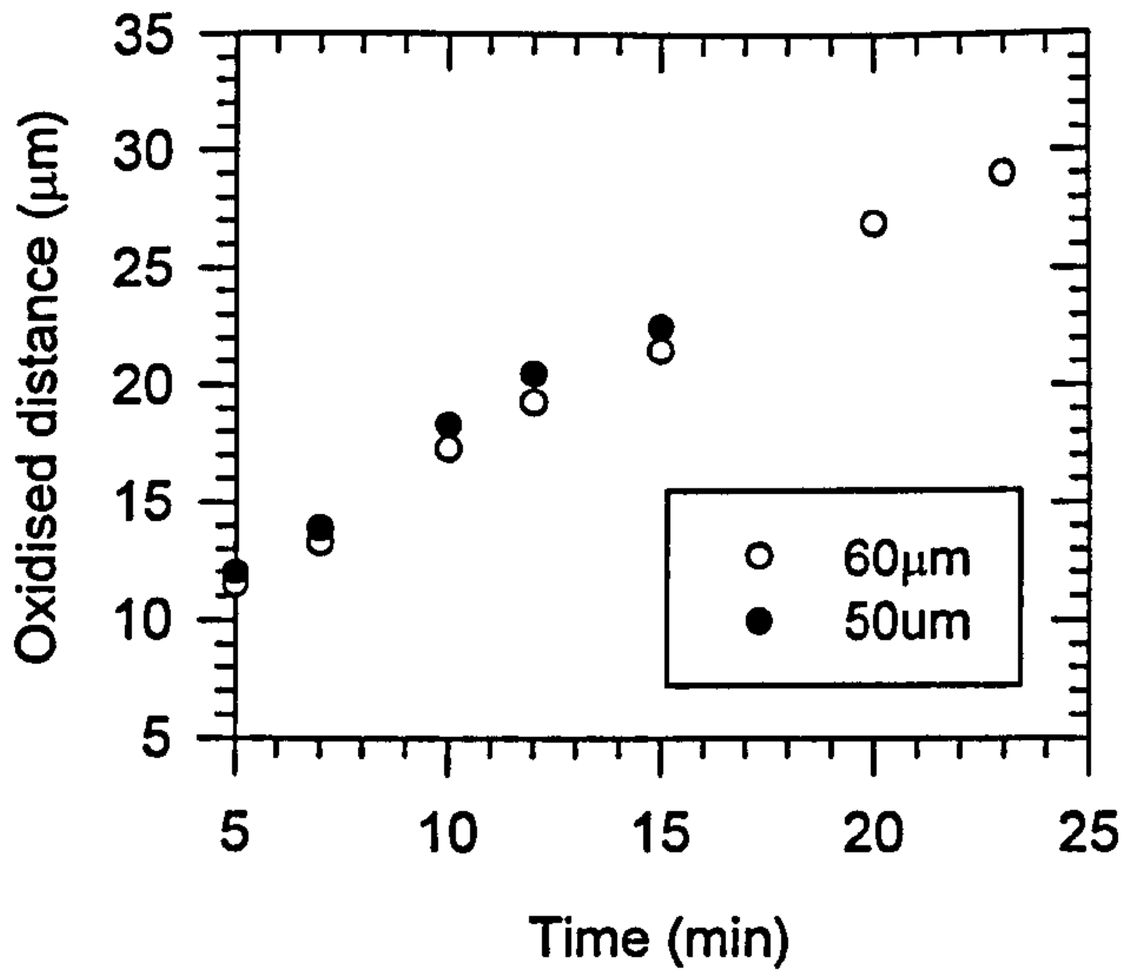

Figure F.4 : Lateral oxidation distance (along the $\langle 1\bar{1}0 \rangle$ direction) of the test structure samples (600Å AlAs), measured from 50μm and 60μm mesas as a function of time at the oxidation temperature of 400°C.

It is also found that the lateral oxidation rate obtained from the working VCSEL structures are different from that of the test structure to varying extents. For instance, for an oxidation period of 15min, the average oxidation rate (deduced from the longer oxidised distance) of a 60μm square mesa of the strong guiding VCSELs (600Å AlAs as well) is only slightly lower at about 1.35μm/min as compared to that of the test structure at 1.45μm/min. As for those VCSEL layers with 350Å (medium guiding) and 200Å (weak guiding) AlAs layers, however, the oxidation rates are more significantly lower at about 1.20 μm/min and 0.9 μm/min respectively. These results thus indicate that lateral oxidised distance for a given oxidation period is also dependent on the thickness of the AlAs. Similar observations have also been made by other researchers [6].

References for Appendix F

[1] T.E.Sale, "*Vertical Cavity Surface Emitting Lasers*", (Research Studies Press Ltd., 1995)

[2] J.M.Dallesasse, N.Holonyak, Jr, A.R.Sugg, T.A.Richard, and N.El-Zein, "Hydrolyzation oxidation of $Al_xGa_{1-x}A$-AlAs-GaAs quantum well heterostructures and superlattices", Appl. Phys. Lett., vol.57, pp. 2844-2846, Dec. 1990.

[3] N.Holonyak, Jr, and J.M.Dallesasse, U.S. Patent 5262360, 1993.

[4] K.D.Choquette, K.M.Geib, C.I.H.Ashby, "Advances in selective wet oxidation of AlGaAs alloys", IEEE Journal of Selected Topics in Quantum Electronics, vol.3, pp.916-926, June 1997.

[5] S.A.Feld, J.P.Loehr, R.E.Sherriff, J.Wiemeri, and R.Kaspi, "In situ optical monitoring of AlAs wet oxidation using a novel low temperature low pressure steam furnace design", IEEE Photon. Tech. Lett., vol.10, pp. 197-199, Feb 1998.

[6] J.H.Kim, D.H.Lim, K.S.Kim, G.M.Yang, K.Y.Lim and H.J.Lee, "Lateral wet oxidation of $Al_xGa_{1-x}As$/GaAs depending on its structures ", Appl. Phys. Lett., vol. 69, pp.3357-3359, Nov 1996.

[7] R.S.Burton and T.E.Schlesinger, "Wet thermal oxidation of $Al_xGa_{1-x}As$ compounds", J.Appl.Phys, vol.76, pp. 5503-5507, Nov 1994.

[8] O.Blum, C.I.H.Ashby and H.Q.Hou, "Barrier layer control of selective wet oxidation of AlGaAs for embeded optical elements", Appl. Phys. Lett., vol. 70, pp. 2870,-2872, May 1997.

[9] F.A.Kish, S.A.Maranowski, J.M.Dallesasse and K.C.Hsieh, "Dependence on doping type (p/n) of the water vapor oxidation of high gap $Al_xGa_{1-x}As$", Appl. Phys. Lett., vol.60, pp.3165-3167, June 1992.